Research on Engineering Structures Materials

Volume
9

Issue
2

June
2023

MM
Research Group

The International Journal of **Research on Engineering Structures and Materials (RESM**) is a peer-reviewed open access journal (p-ISSN: 2148-9807; o-ISSN: 2149-4088) published by MIM Research Group. It is published in February, June, September, and December.

The main objective of RESM is to provide an International academic platform for researchers to share scientific results related to all aspects of mechanical, civil, and material engineering areas.

RESM aims the publication of original research articles, reviews, short communications technical reports, and letters to the editor on the latest developments in the related fields.

All expenditures for the publication of the manuscripts are most kindly reimbursed by *MIM Research Group*. Thus, authors do not need to pay for publishing their studies in the journal.

The scope of the journal covers (but not limited to) behavior of structures, machines and mechanical systems, vibration, impact loadings and structural dynamics, mechanics of materials (elasticity, plasticity, fracture mechanics), material science (structure and properties of concrete, metals, ceramics, composites, plastics, wood, etc.,), nano-materials performances of new and existing buildings and other structural systems, design of buildings and other structural systems, seismic behavior of buildings and other structural systems, repair and strengthening of structural systems, case studies and failure of structural systems, safety and reliability in structural and material engineering, use of new and innovative materials and techniques in energy systems and mechanical aspects of biological systems (biomechanics and biomimetics).

The topics covered in RESM include:

- Structural Engineering
- Mechanical Engineering
- Material Engineering
- Earthquake Engineering
- Nano-technology
- Energy Systems (Focus on Renewable)
- Biomechanics and Biomimetics
- Environment (Material and Engineering System Related Issues)
- Computer Engineering and Data Science (Material and Engineering System Related Issues)

Abstracting and Indexing
Please visit http://www.jresm.org for more information.

Graphics and Design

Yunus Demirtaş   ydemirtas@jresm.net

RESEARCH on
ENGINEERING STRUCTURES &
MATERIALS

Research Group

RESEARCH on ENGINEERING STRUCTURES & MATERIALS

Editorial Board

Advisory Board Members

Jumrik Taipodia	NIT Arunachal Pradesh	India
Anna Chiaradonna	University of L'Aquila	Italy
Arindam Dey	Indian Institute of Technology Guwahati	India
Abbasali Sadeghi	Islamic Azad University	Iran
Peyman Beiranvand	Razi University	India
Aykut Tamer	Imperial College London	England
Denis Anders	Cologne University of Applied Sciences (TH Köln)	Germany
Cemal Kochan	Dokuz Eylul University	Turkey
Mohd Syahrul Hisyam Mohd Sani	Universiti Teknologi MARA	Malaysia
Suruchi Mishra	University of Maryland University College	Italy
Md. Zia Ul Haq	Panjab University	India
Natt Makul	Phranakhon Rajabhat University	Thailand
Dr Delsye Ching Lee Teo	Melbourne Polytechnic	Australia
Mehmet Ada	Usak University	Turkey
Yunika Kirana Abdul Khalik	University of Malaysia Sarawak	Malaysia
Khairul Anwar Mohamad Said	University of Malaysia Sarawak	Malaysia
H. Alperen Bulut	Erzincan University	Turkey
Azida Rashidi	University of Malaysia Sarawak	Malaysia
Tadesse Gemeda Wakjira	University of British Columbia	Canada
Lomesh Mahajan	Dr. Babasaheb Ambedkar Technological University	India
Divya Sharma	NITTTR Chandigarh	India
Ahmed Abdullahi	Higher Colleges of Technology	Dubai
Rini Mulyani	University Bung Hatta	Indonesia
	Advisory Board Members	
Dr Tahara Ramadzan Md Kassim	International Islamic University	Malaysia

Gökhan Gece	Bursa Technical University	Turkey
Harris Priya	-	-
Samuel Awe	Automotive Components Floby AB	Sweden
Saifulnizan Jamian	Universiti Tun Hussein Onn Malaysia	Malaysia
Mohsin Talib Mohammed	Kufa University	Iran
Ali Ercetin	Bandırma Onyedi Eylül University	Turkey
Siva Avudaiappan	University of Santiago	Chile
I Wiryadi	Mahasaraswati Denpasar University	Indonesia
Gustavo Bosel Wally	Federal University of Rio Grande do Sul	Brazil
Rajkumar Srinivasan	SRM TRP Engineering College Irungalur	India
Fatheali Shilar	-	-
Sharanabasava V. Ganachari	KLE Technological University	India
Qing Hong	Midwestern University	Glendale
Madeva Nagaral	Aircraft Research and Design Centre	India
E. Arunraj	Karunya Institute of Technology and Sciences	India
Yasmin Murad	University of Jordan Amman	Jordan
Uma Mageshwari	-	-
Hamide Tekeli	Süleyman Demirel University	Turkey
M.Helen Santhi	Vellore Institute of Technology	Chennai
Marwan Effendy	Universitas Muhammadiyah Surakarta	Indonesia
Mehmet Zerrakki Işık	Mechanical Eng. Department	Batman University
Mahmoud Mokhtar	Housing & Building National Research Center	Egypt
Mohammad Heydari Vini	Islamic azad university	Iran
Fadzli Mohamed Nazri	Universiti Sains Malaysia	Malaysia
Kavendra Pulkit	-	-
Thaer Alrudaini	University of Basrah	Iraq
Xinrong Chengil	-	-

In This Issue

ABSTRACTING / INDEXING

The international journal of Research on Engineering Structures and Materials (RESM) is currently Abstracted/Indexed by Asos Indeks, CiteFactor, Cosmos, CrossRef, Directory of Research Journal Indexing, Engineering Journals (ProQuest), EZB Electronic Journal Library, Global Impact Factor, Google Scholar, International Institute of Organized Research (I2OR), International Scientific Indexing (ISI), Materials Science & Engineering Database (ProQuest), Open Academic Journals Index, Publication Forum, Research BibleScientific Indexing Service, Root Indexing, Scopus, Ulakbim TR Index (Tubitak), Universal Impact Factor and under evaluation by many other respected indexes.

Check web site for current indexing info, www.jresm.org

Numerical study to evaluate the structural response of the basilica of St. Sotiri

Hüseyin Bilgin [*1,a], Zelina Fule[2,b], Hayri B. Özmen [3,c]

[1] Department of Civil Engineering, Faculty of Architecture and Engineering, EPOKA University, Tirana, Albania
[2] Consulting Engineer, Pristina City Center sh.a. St. Robert Doll No. 5, Pristina, Kosovo
[3] Civil Engineering Department, Engineering Faculty, Uşak University, Uşak 64300, Türkiye

Article Info	Abstract
	Basilicas constructed in the post-Byzantine time in Balkans cover a period of 400 years, from the 16th century to the 19th century. These masonry religious objects are of particular interest due to their different building typologies and historical value, so it is important that they be saved for future generations. This paper analyses the static and dynamic response of the Basilica of St. Sotiri near Gjirokastër (Albania). The static response and dynamic properties of the church have been assessed using FEM technique and the performance of the structure is investigated. As a result, important information is obtained to identify the critical regions of the structure and its seismic safety. The aim of this study is to point out that clear insight and information on interpreting the actual response of historical buildings can be obtained by numerical analysis methods. Authors believe that the approach and findings of this case study are useful to understand the load response of a wide range of monumental churches.

1. Introduction

The number of historical monumental structures in Europe and worldwide is huge. They are encountered in many seismic regions of the world in different states of integrity, ranging from undamaged to near -almost ruined. Nowadays, in Albania there are encountered many historical monuments which show masonry construction techniques that varies from century to century [1]. Starting from ancient structures such as Apollo Temple constructed during 5th century B.C in Apollonia, a large number of castles such as Gjirokastra's Castle, Rozafa Castle in Shkodra, Berat's Castle dating between 14th -16th century A.C, and a large number of churches, basilicas, monasteries and mosques are found throughout Albania [2]. During the past century, due to historical and political events that happened in the country, these buildings were almost forgotten, and no maintenance was done in order to preserve these cultural heritage buildings and rescue them from deterioration and amortization [3]. Some of them were able to continue to exist till today and the others were lost in the course of time partly by man-made actions and previous natural catastrophes [2].

Churches, mosques, city walls, castles, and clock towers built in various parts of the world are the key shapes of monumental ancient buildings [4-6]. They characterize a significant part of the Balkan cultural heritage, mainly vulnerable and prone to partial or complete failure under seismic loads as noted in some of the recent earthquakes in the region (Bosnia and Herzegovina-1969; Italy-1976; Montenegro-1979; Albania-2019) [7, 8]. These monuments are one of the most important key elements of our cultural diversity and preservation and restoration of them are essential engineering concern and duty to

guarantee the sustainable advancement and safety of our cultural funds to pass them onto upcoming generations [9-11].

An important portion of the Albanian cultural heritage is derived from the church masonry structures. The majority are in their original locations; most of them are still not in use [3]. However, natural or man-made hazards pose a severe threat to their survival [12]. Limitations in the ability to inspect the building or difficulties in extracting samples from buildings of historical value often caused restricted knowledge of the internal structure system or the properties of available materials. In addition, deterioration of material resistance and avoidance of deterioration are often witnessed throughout the life of ancient structures [13].

These historical buildings carry significant info to historical incidents, characters, history development, etc. [14-16]. They play a vital role in defining periods of engineering and architecture throughout history, including the advancement of construction techniques, ornamental patterns, building materials, and many other related topics [13].

Many of these structures deserve a specific structural analysis to evaluate their safety level under both static and dynamic loads. Also, the information obtained by the analyses of the individual structures may be used to determine more general interpretations about similar historical structures. In this regard, the aim of this paper is to bring into focus a historical basilica church from Gjirokastra which is a historical city remarkable for its great beauty, as well as its harmonious intercultural mix of Albanian, Byzantine and Ottoman heritage. The Church of the St. Sotiri's Basilica is selected to investigate its structural performance (Photo 1).
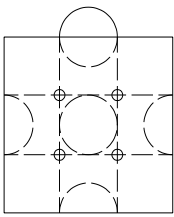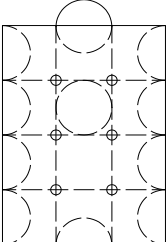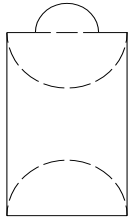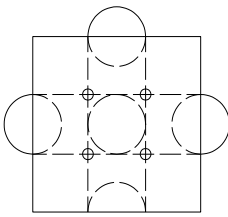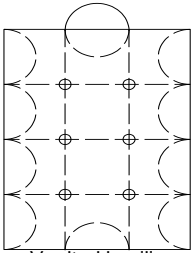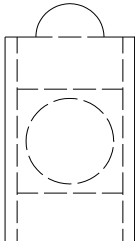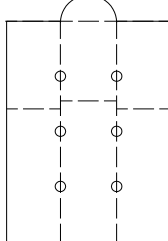
Photo 1. Church of the St. Sotiri's Basilica

It is one of the most remarkable religious monuments in the Gjirokastra district and is a type of three aisled barrel-vaulted basilica composed of the nave, the altar and the sanctuary which are composed in the same space dating back to the 17th-18th century. Firstly, current conditions of the structure are examined by in-situ inspection. Secondly, a global analysis of the structure has been prepared by utilizing the finite element (FE) modelling method. Then, the obtained results were compared with the visual inspection observations made on the load-bearing components of the church. It is believed that the findings could provide a case study that expands the understanding of the structural behavior of this structure typology. Considering its historical value, building developments, public and religious status make this study an important and interesting issue.

2. Church Types in Post-Byzantine Period

There are possible ways of classification based on different features of historical masonry structures. Material type, strength and stiffness of sections and the construction techniques are major properties of structural form. Typological classification contributes to the development of post-Byzantine architecture in time and space, the features that characterize this architecture in different periods and regions, the preference of certain types and forms in these periods, and the relationship between them. In classification, the criteria used in the study of Byzantine architecture and mainly based on plan and spatial composition are followed. (Table 1), [17].

Table 1. Classification of the churches in post-Byzantine period

Type \ Version	Single-Naved (T1)	Cross-in Squared (T2)	Basilicas (T3)
Version-1	Single nave	Cross-in-square single-apse	Domed basilica
Version-2	Single nave barrel vaulted	Cross-in-square tri-conch	Vaulted basilica
Version-3	Domed single-nave		Flat interior ceiling basilica
Type \ Version	Single-Naved (T1)	Cross-in Squared (T2)	Basilicas (T3)

Version-4

Cruciform roof
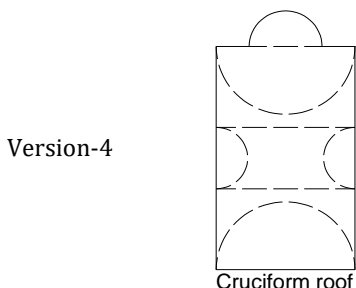
First, the type is defined according to the plan composition; Single Nave, Domed Square Cross churches and basilicas. The spatial composition of the interior, which is a very important component of the psychological and aesthetic understanding of religious buildings, helps to define different categories within each type. Thus, the first category of the first type includes churches without interior ceilings; the second category is churches with barrel vaulted interiors; the third category includes churches with or without vertically varying interiors with a central dome on a pulley; The fourth category includes churches whose interior lining system looks like a cross from the outside. The second type of the domed square-cross church is a very unified type when it comes to interior spatial composition. In this type, there are two categories in which plan differences affect the interior composition: churches with one apse and churches with three apses. Basilicas can be classified into three categories. The first category consists of domed basilicas (domes on a high drum). The second category includes basilicas whose interiors are covered with a system of vaults or curved structures. The third category is basilicas with flat ceilings [17].

2.1. Description of the St. Soitiri's Basilica

The St. Soitiri's Basilica is situated in the Old Bazaar beneath the great Castle of Gjirokastra, a city with a population of around 43000, notable for its great natural magnificence, as well as its harmonious inter-cultural mix of Albanian, Byzantine and Ottoman culture (Figure 1a-b). It was built in 1784 which used to be the seat of the local Orthodox bishop.
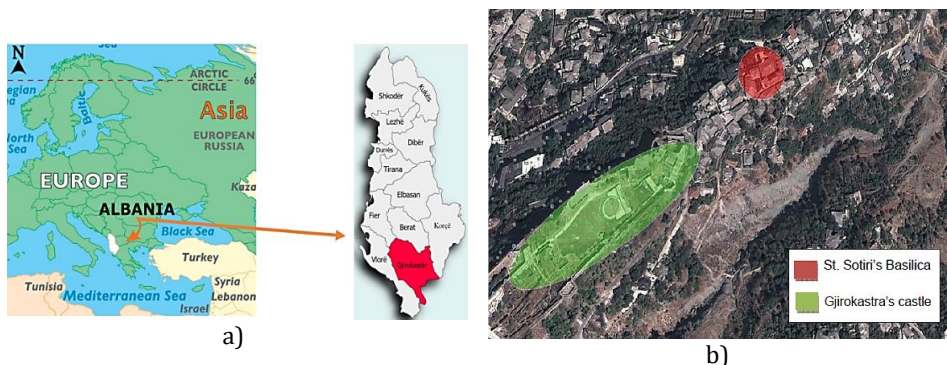
Figure 1. a) Location of the studied territory in Albanian map; b) Arial view of the castle and basilica

This study aims to assess the structural response of the church of the St. Sotiri's Basilica (Figure 2). Current situations of the church were studied by in-situ survey. The church is a three aisled barrel-vaulted basilica, with inner dimensions of 15.75 x 12.10 m and it is

composed of the nave, the altar and the sanctuary which are composed in the same space. St. Sotiri basilica falls in the type T3V2 of basilica's classification (Table 1).

a)   b)

Figure 2. a) East view of the Basilica; b) Iconostasis

Columns are connected to each other with two main arches that separate the central aisle from the side aisles. In the nave the aisles are covered with cylindrical vaults all along the length. The central space is composed of big vaults and side space of vaults. The altar is composed of three chambers. The narthex is divided into two levels, located at the west side of the basilica and it is separated from the nave by a series of arches. The eastern couple of columns and western couple of columns are thick square based columns and they are connected with transversal arches by creating the altar in the east and the narthex on the west.

The structural inspection of the church includes measurements of length and thickness of structural elements. The thickness of the load bearing walls is 1.0 meter. Sizes of the columns are 500 mm x 500 mm for the rectangular ones and 500 mm diameter for circular base columns. The thickness of vaults and arches are 300 mm. The height of the load bearing walls is 8.0 m. The heights of the columns are 4.6 m., and the maximum height of the basilica is 9.50 m, whereas the outer dimension of the structure is 17.60 m x 14.80 m. Plan view of the case study structure is given in Figure 3.
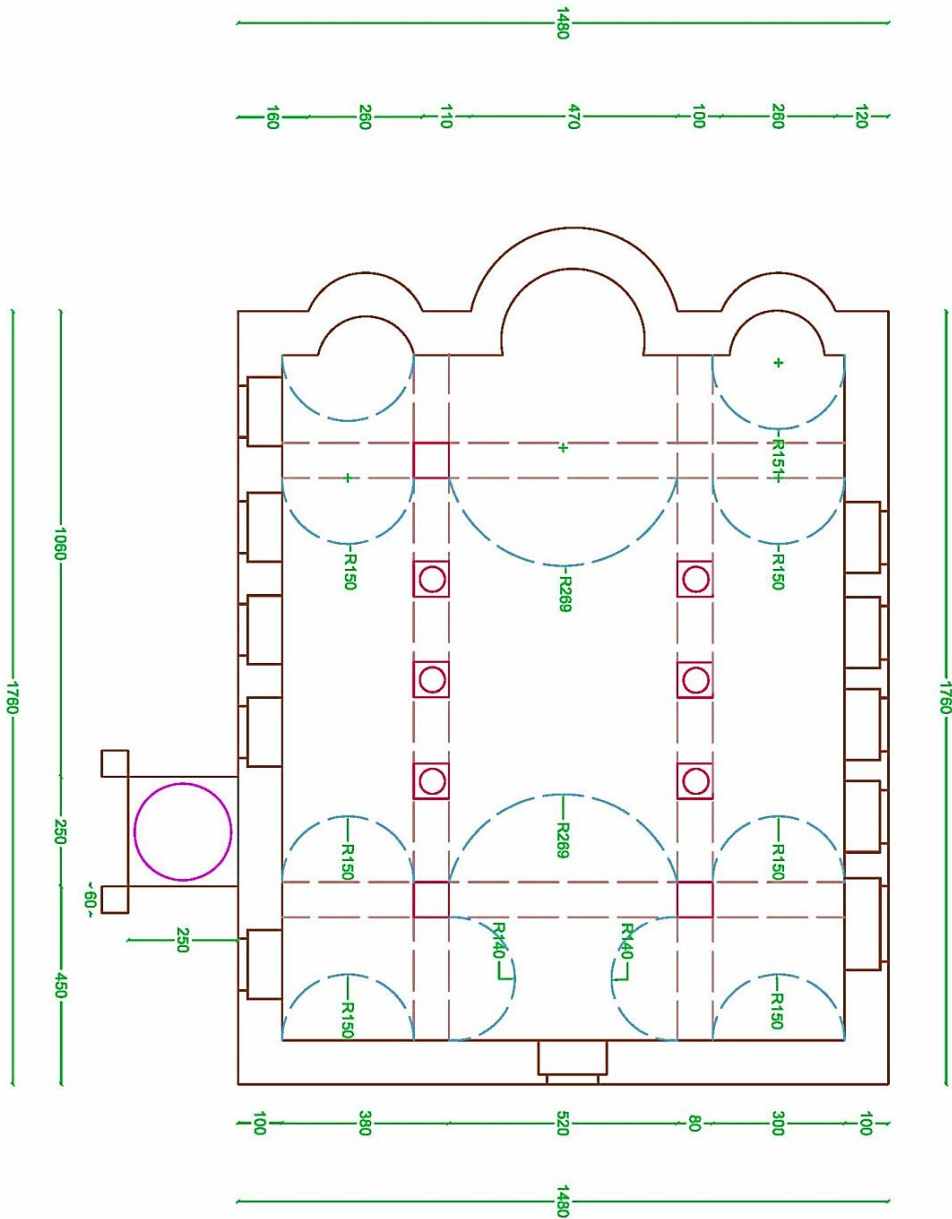
Figure 3. Plan view of the St. Sotiri's Basilica (Units in cm)

The narthex is divided into two levels. The eastern and western couple of columns are thick square (500 x 500 mm) based columns and they are connected with transversal arches by creating the altar in the east and the narthex on the west. In the basilica, there are three main parallel barrel type vaults which are placed in east-west direction, whereas two smaller vaults are constructed to the main ones in the north-east direction.

3. Damage Survey

On-site examination plays a crucial role in the structural evaluation of historical monumental structures, which aims to define the building's condition and describe a typical structural model [13].

In 1999 after an earthquake a slight misalignment and damage to the load-bearing walls occurred. The epicenter of the earthquake was 3.5 km from Gjirokastra, with a magnitude of 4.6 Richter scale and it is recorded by church authorities in basilica's archives. After repairing some parts of the load bearing walls of the basilica, it was added also the tower bell (Photo 2).

Photo 2. Church of the St. Sotiri's Basilica

The walls are reinforced with steel anchors passing from North to South direction. There are 8 steel anchors placed in two rows, four by four, and passing through the piers (they work as tensile members). Inherent material characteristics of the steel tie rods are reflected in the analytical model as given in Table 2.

Table 2. Material properties of steel tie rods

Characteristics	Steel tie rod
Modulus of Elasticity, E (GPa)	181.7
Poisson's Ratio	0.3
Tensile Strength (MPa)	542.3
Yield Strength (MPa)	363.2

As the geometrical characteristics of the basilica are determined, the structure is investigated on-site, and cracks and other irregularities are detected. Due to the architectural renovations, structural deficiencies cannot be identified easily. However, through the site checks, some of the cracks could be visualized.

In St. Sotiri Basilica, lime mortar is used in masonry walls. Lime mortar is composed of lime and sand, mixed with water and it has very large durability which is best shown in still-

standing ancient masonry structures. There is no uniformity in the distribution of mortar (Figure 4). In some places it is totally missing, and it is noticed that these places are rebuilt lately (Figure 5).

Figure 4. Western wall of the Basilica (left); Different colored stones, Eastern wall of the Basilica (right)

Figure 5. Northern wall

The middle three couples of columns have circular section while the outer columns have rectangular section.

There are three main parallel barrel type vaults which are placed in East – West direction. Then there are two other barrel type vaults with smaller dimensions, constructed perpendicular to the main ones, placed in North - South direction. From the inspection it resulted that the moisture is a significant problem especially during the rainy season (Figure 6).

Figure 6. Barrel vault over the South aisle, moisture concentration

The narthex is composed of two floors inside the basilica, located at the west side (Figure 7). In St. Sotiris Basilica the narthex is composed of two floors constructed with timber beams in the west side of the basilica and it is separated from the nave by a series of arches.

Figure 7. Narthex, Western side of the basilica

The nave and the side aisles are separated by a series of arches. The nave is covered with a barrel vault. The aisles are located on the sides of the Basilica. It can be found also in the west part of basilica in the role of narthex but in St. Sotiri Basilica they are found on the North and South sides. They are separated by the nave by a series of columns and arches above them.

4. Mathematical Modeling

4.1 Finite Element Modeling

As briefly mentioned formerly, determining the earthquake behavior of historic masonry structures is a challenging job for reasonable effects such as inadequate characterization of the inherent mechanical characteristics of the material, problems in mathematical modeling, and intricate architectural plans [18]. In technical literature, some physical models have been suggested to accurately predict the behavior of masonry material adopting numerous approaches [19].

Mathematical modeling is an important step in the analysis of monumental structures. The 3-D FE (finite element) model created by SAP2000 [20] is deployed using a set of finite elements. Considering the availability of resources, a modeling method should be chosen to define the state of safety of the building to be restored. Figure 8 illustrates three modeling approaches for modeling masonry structures.
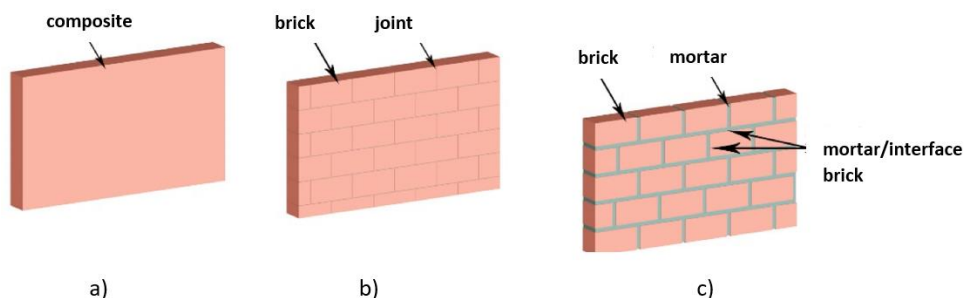
Figure 8. Modelling techniques of masonry: a) Macro modelling; b) simplified micro modelling; and c) micro modelling [19].

In this study, a simplified geometry of the church was adopted by following the macro-modeling technique since it is mostly used for analyzing large-scale structures and the effect of global factors. Such an approach was followed by several researchers [15]. The description of the geometry was accomplished through architectural plans and site measurements. The numerical model consists of main load-bearing volume as shown in Figure 9.
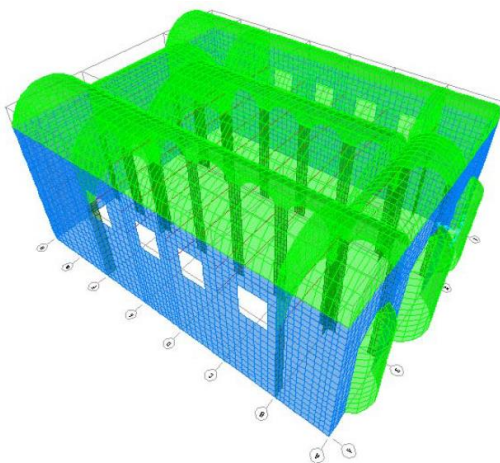
Figure 9. Three-dimensional finite element model of the Basilica St. Sotiri

5. Structural Assessment

Several methods and computational tools are available for the assessment of the mechanical response and current condition of the masonry structures. These methods use different theories or approaches, resulting in different levels of complexity, different costs, and different requirements [21]. The results of the different approaches may also be somewhat different. However, a complex analysis will not necessarily provide us always with better results than applying simplified approaches [18]. The method must be selected based on the chosen numerical model for the structure. A correct structural assessment should be based on a deep data of the following [21]:

- Building history and evolution,
- Geometry,
- Structural details,
- Material properties and construction techniques,
- Crack pattern and material decay map,
- Structural stability,

which can be accomplished through on-site measurements and investigation structural analysis with appropriate models and final diagnosis.

The research work for the material properties of the historical buildings in Albania was not satisfactory. There is a lack of information and laboratory tests, and there are limited possibilities to conduct experimental tests in order to determine the material properties and mechanical behavior of the masonry units. It is not easy to take specimens directly from the historical buildings for testing due to practical safety and official reasons to prevent further damage. In this case, research was made to find the appropriate data to be used in the FE model. Since the Basilica is constructed with tuff masonry, the research is focused on the mechanical properties of this material. Different experimental data are processed to calculate mean values of mechanical parameters of tuff masonry (Table 3).

Table 3. Material properties from previous studies

Properties	Betti et al., [22]	Lourenço et al., [19]	Portioli et al., [23]	Guler et al., [24]
Unit Weight, γ (kg/m³)	21	17	19	17
Modulus of Elasticity, E (MPa)	1740	1100	900	1000
Tensile Strength (MPa)	0.165	-	0.21	-
Compressive Strength (MPa)	1.7	-	2.1	-

Table 4. Selected material properties

Characteristics	Tuff masonry
Unit Weight, γ (kN/m3)	19.0
Modulus of Elasticity, E (MPa)	1100
Poisson's Ratio	0.071
Allowable Compressive Strength (MPa)	1.700
Allowable Tensile Strength (MPa)	0.165
Allowable Shear Strength (MPa)	0.530

The identification of the typology and characteristics of the material is used to associate it with the mechanical characteristics outlined in an assumed table, which is compiled based on the experimental data in the relevant literature (Table 4).

The other features in this research are the allowable compressive, tensile strength, and shear strength. Based on those physical characteristics, the Basilica structure is analyzed and checked for drawing final conclusions (Table 5).

Table 5. Selected allowable stresses

Allowable compressive stress (N/mm²)	Allowable tensile stress (N/mm²)	Allowable shear stress (N/mm²)
1.700	0.165	0.530

The dynamic analysis of the Basilica involves the response spectrum which is selected based on EC-8 with 0.25g acceleration, as presented in Figure 10.
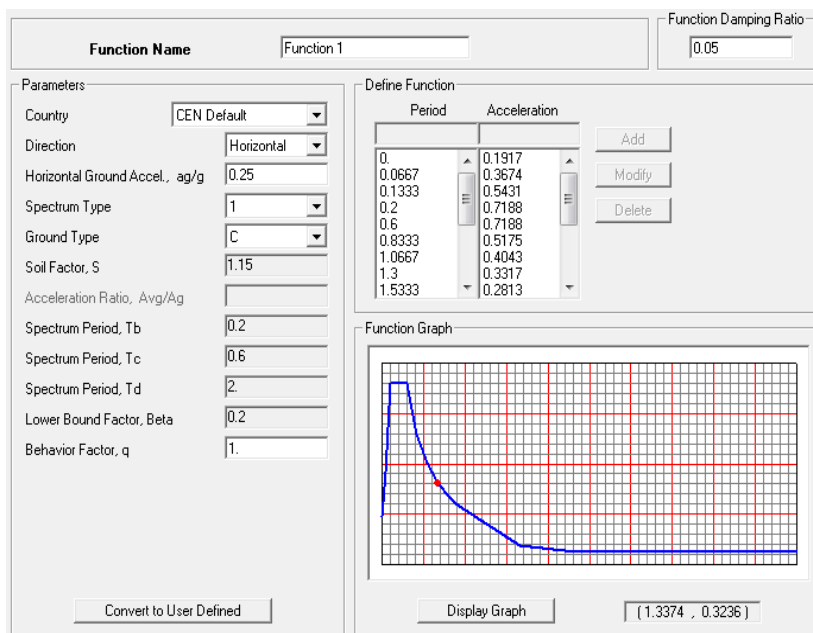
Figure 10. Response spectrum function

6. Results and Discussion

This part includes the analysis of stresses under static and dynamic loads. Linear analysis was used in this study. Static loads are characterized by the dead load of the building or its own weight, while dynamic loads are simulated by seismic loads represented by response spectrum function. All results are highly dependent on the macro modeling stage of the basilica.

For the Basilica St. Sotiri's analysis, two different loading conditions were considered, namely gravity load in x- and y- directions, and $G+EQ_x$ and $G+EQ_y$ for earthquake load, respectively. These loading conditions comprise of the dead load (self-weight) of the

structure and the seismic load defined by the response spectrum function for both orthogonal directions.

Firstly, the model has been subjected to vertical loads coming from masonry own weight. To check the deformation of the structure and the concentration of stresses, it is performed a linear static analysis with only dead load or in other terms, self-weight of the structure.

S_{MAX}	S_{MIN}
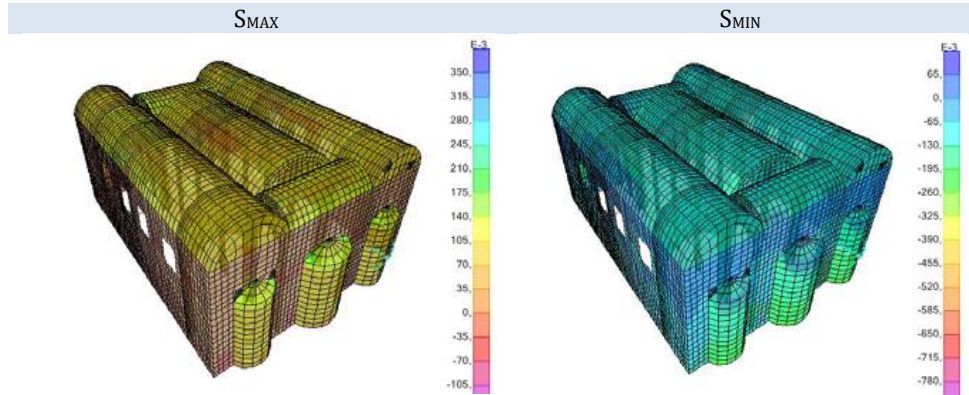
Figure 11. S_{MAX} and S_{MIN} Stresses diagram, (MPa)

The maximum values of S_{MAX} and S_{MIN} are seen at the top of the vaults and Northern and Eastern load bearing walls. The values of S_{MAX} and S_{MIN} are 0.349 MPa and 0.126 MPa for compressive stresses (Figure 11).

The basilica exhibits the maximum displacement at the top of the middle vault:

– -3 mm in X direction

– 2.9 mm in Y direction

– 2.5 mm in –Z direction.

Stresses under the dead load are below the allowable capacity which means they do not exceed the allowable limits. In the main vault over the nave, the stresses S_{MAX} and S_{MIN} are spread on the top of the vault.

S_{11}	S_{22}
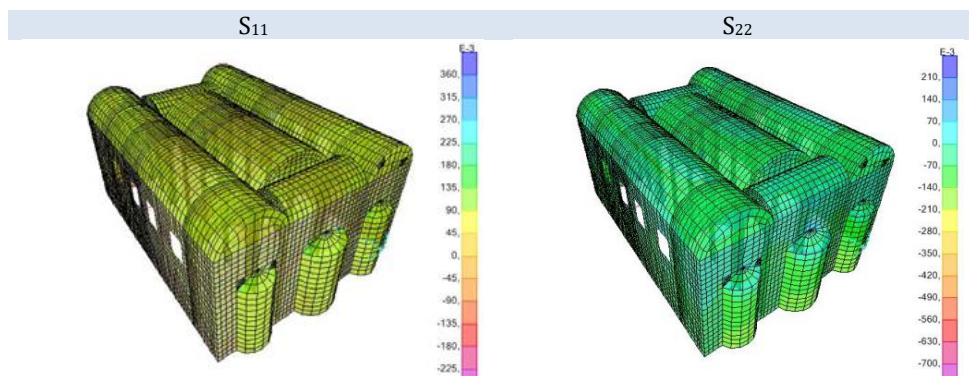
Figure 12. S_{11} and S_{22} stress diagrams under dead load, (MPa)

In the load bearing walls the S_{11} stresses vary from -0,227 MPa to 0,254 MPa. S_{22} stresses vary from -0.753 to 0.233 MPa (Figure 12). The most critical locations are the Northern and Southern load bearing walls which exhibit maximum concentration of stress.

The most potential danger on this structure comes from the S_{MAX} which may cause the structure to develop structural cracks and damages due to increasing tensile stresses. The locations of these concentrations of stresses are in the connection of vaults and load bearing walls, top of the main vault over the nave and in Eastern and Northern load bearing walls.

6.1 Modal Eigenvector Analysis Results

Eigenvector analysis determines the undamped free-vibration mode shapes and frequencies of the system. It is used FEM to perform this analysis because the basilica has a complicated geometry. These natural modes provide a good insight into the behavior of the structure.

Table 6. Modal characteristics

Mode Number	Period	U_X	U_Y	U_Z
1	0.242	8.981E-07	0.70494	5.913E-07
2	0.180	0.650	4.744E-07	0.00025
3	0.170	4.194E-08	0.0279	1.595E-07
4	0.169	0.000004	0.00102	3.909E-08
5	0.166	5.207E-08	0.00068	9.5E-10
6	0.165	0.000044	1.495E-07	0.000035
7	0.163	0.000071	3.792E-09	3.398E-08
8	0.162	3.484E-08	1.352E-08	2.218E-08
9	0.122	0.00039	0.000001	0.00925
10	0.122	0.000002	0.00163	0.000022
11	0.113	3.866E-08	0.00641	9.634E-07
12	0.111	1.95E-07	0.0049	8.327E-09

Table 6 summarizes the first twelve modal shapes obtained from modal eigenvector analysis. The 1st mode shape of the basilica involves the translation along the weakest transversal direction, with significant out-of-plane deformation of the orthogonal components. Figure 13 shows the first five modal shapes derived from modal eigenvector analysis.

1st mode   2nd mode   3rd mode   4th mode   5th mode
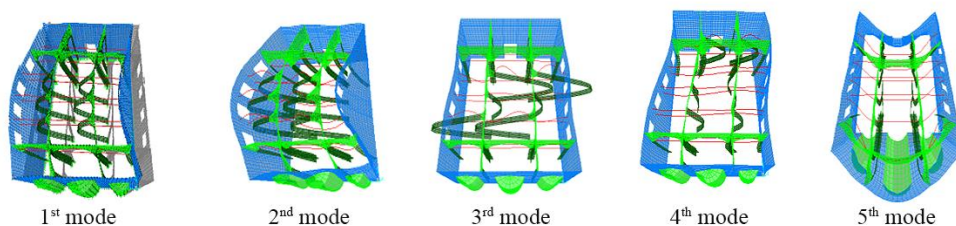
Figure 13. Modal shapes of the structure

6.2 Response Spectrum Analysis Results

Then, for more detailed results Basilica St. For Sotiri's analysis, two different loading conditions were considered, namely gravity load in x- and y- directions, and G + EQ$_x$ and

G+EQ$_y$ for earthquake load, respectively. These loading conditions comprise of the dead load (self-weight) of the structure and the seismic load defined by the response spectrum function for both orthogonal directions.

The considered element stresses are identified as S$_{11}$, S$_{22}$, S$_{12}$, S$_{13}$, and S$_{23}$. Shell internal stresses are reported for both the top and the bottom of the shell element. The top and bottom of the element are defined relative to the local 3-axis of the element. The positive 3-axis side of the element is considered to be the top of the element. The internal stresses and axes used in the definition of the shell element can be seen below Figure 14.
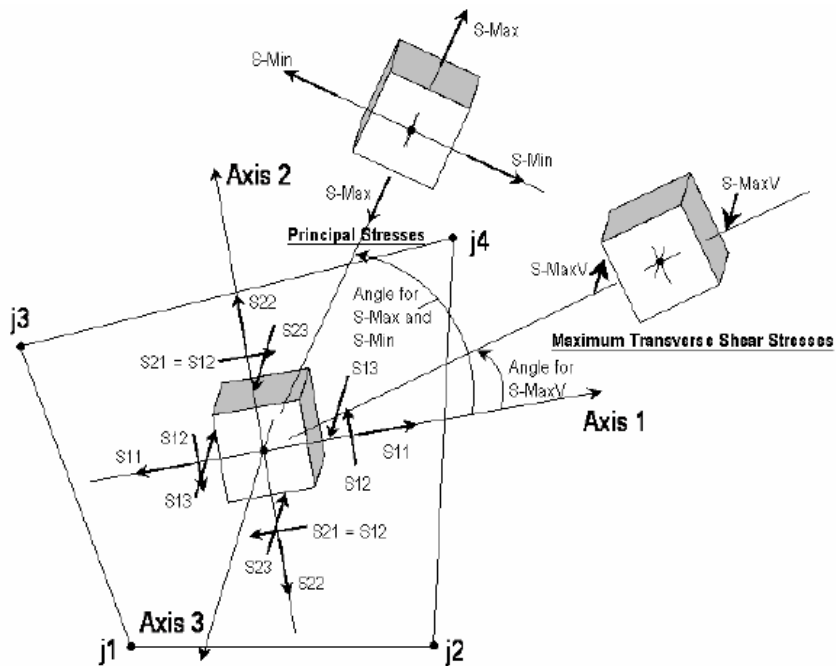
Figure 14. Internal stresses in shell element [20]

- S$_{11}$, stress acting on the positive and negative 1 face in the 1-axis direction - Hoop stress.

- S$_{22}$, stress acting on the positive and negative 2 faces in the 2-axis direction - Radial stress.

- S$_{12}$, shearing stress acting on the positive and negative 1 face in the 2-axis direction and acting on the positive and negative 2 faces in the 1-axis direction.

- S$_{MAX}$, maximum principal stress.

- S$_{MIN}$, minimum principal stress. By definition, principal stresses (S$_{MAX}$ and S$_{MIN}$) are oriented such that the associated shearing stress is zero.

- S$_{13}$, Out-of-plane shearing stress acting on the positive and negative 1 face in the 3-axis direction.

- S$_{23}$; Out-of-plane shearing stress acting on the positive and negative 2 faces in the 3-axis direction.
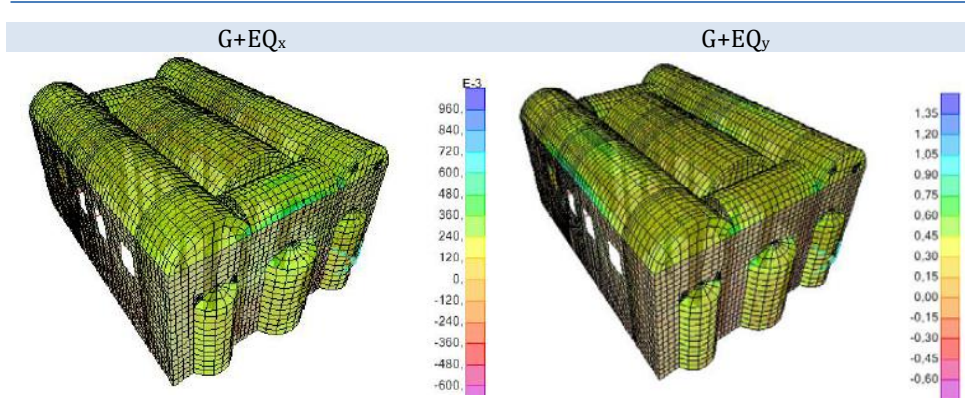
Figure 15. S_{22} tensile stresses distribution, (MPa)
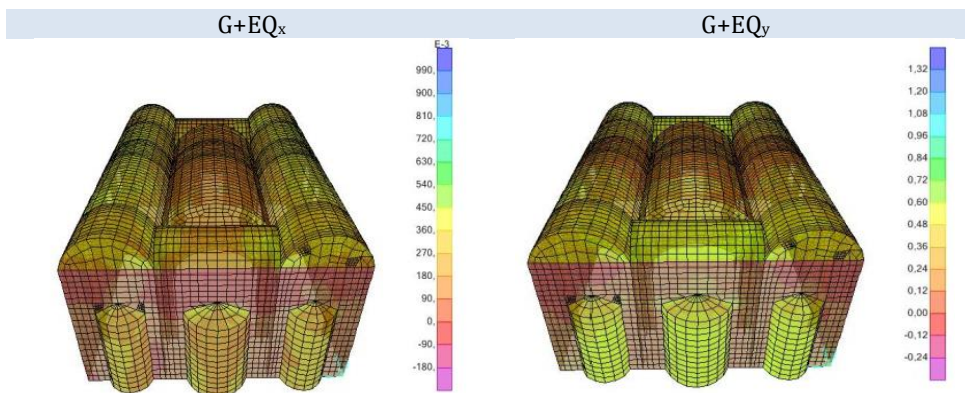
Figure 16. S_{12} tensile stresses distribution, (MPa)

S_{12} and S_{22} stresses for G+EQ$_x$ and G+EQ$_y$ loading cases acquired (Figure 15-17) at structural elements of the St. Sotiri's basilica are shown in Table 7-8.

Table 7. S_{12} and S_{22} stresses for the structural elements

			S_{12}		S_{22}	
Structural Elements			G+Eq$_x$ (MPa)	G+Eq$_y$ (MPa)	G+Eq$_x$ (MPa)	G+Eq$_y$ (MPa)
Vaults	Nave	Top surface				
		Tension	0.910	0.025	0.366	0.204
		Compression	0.259	0.027	0.306	0.388
		Bottom surface				
		Tension	0.416	0.015	0.303	0.426
		Compression	0.460	0.030	0.319	0.337
	Aisles	Top surface				
		Tension	0.268	0.019	0.088	0.221
		Compression	0.215	0.020	0.074	0.193
		Bottom surface				
		Tension	0.204	0.019	0.047	0.133
		Compression	0.219	0.028	0.015	0.151
	Narthex	Top surface				
		Tension	0.422	0.095	0.125	0.435
		Compression	0.402	0.047	0.098	0.356

	Bottom surface	Tension	0.356	0.193	0.046	0.269
		Compression	0.369	0.187	0.035	0.259
Sanctuary	Top surface	Tension	0.460	0.221	0.047	0.303
		Compression	0.204	0.219	0.019	0.088
	Bottom surface	Tension	0.305	0.388	0.015	0.221
		Compression	0.225	0.303	0.011	0.234
N-S Walls	Top surface	Tension	0.356	0.015	0.027	0.059
		Compression	0.303	0.193	0.460	0.047
	Bottom surface	Tension	0.435	0.088	0.015	0.019
		Compression	0.409	0.047	0.193	0.088
E-W Walls	Top surface	Tension	0.027	0.025	0.388	0.027
		Compression	0.021	0.221	0.303	0.204
	Bottom surface	Tension	0.035	0.460	0.256	0.185
		Compression	0.029	0.431	0.204	0.221
Columns	Top surface	Tension	0.303	0.219	0.439	0.015
		Compression	0.299	0.221	0.428	0.388
	Bottom surface	Tension	0.435	0.204	0.460	0.303
		Compression	0.420	0.027	0.419	0.299

(Left spanning labels: "Load bearing walls" spans N-S Walls and E-W Walls rows; "Columns" spans Columns rows.)

Table 8. Maximum and minimum stresses due to $G+EQ_x$ and $G+EQ_y$

	$G+Eq_x$ (MPa)		$G+Eq_y$ (MPa)	
	Max	Min	Max	Min
S_{11}	1.248	-0.205	2.194	-0.143
S_{22}	1.015	-0.610	1.413	-0.726
S_{12}	0.959	-0.259	1.388	-0.286
S_{13}	0.131	-0.017	0.124	-0.015
S_{23}	0.196	-0.033	0.139	-0.026

S_{12} (EQ$_y$) S_{22} (EQ$_y$)
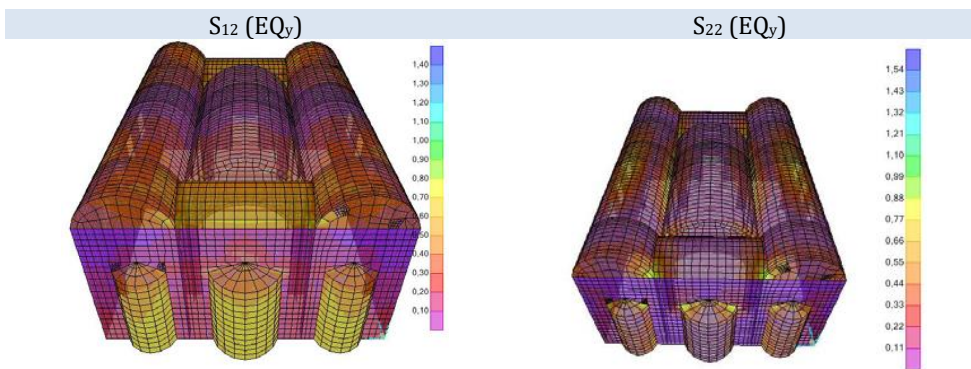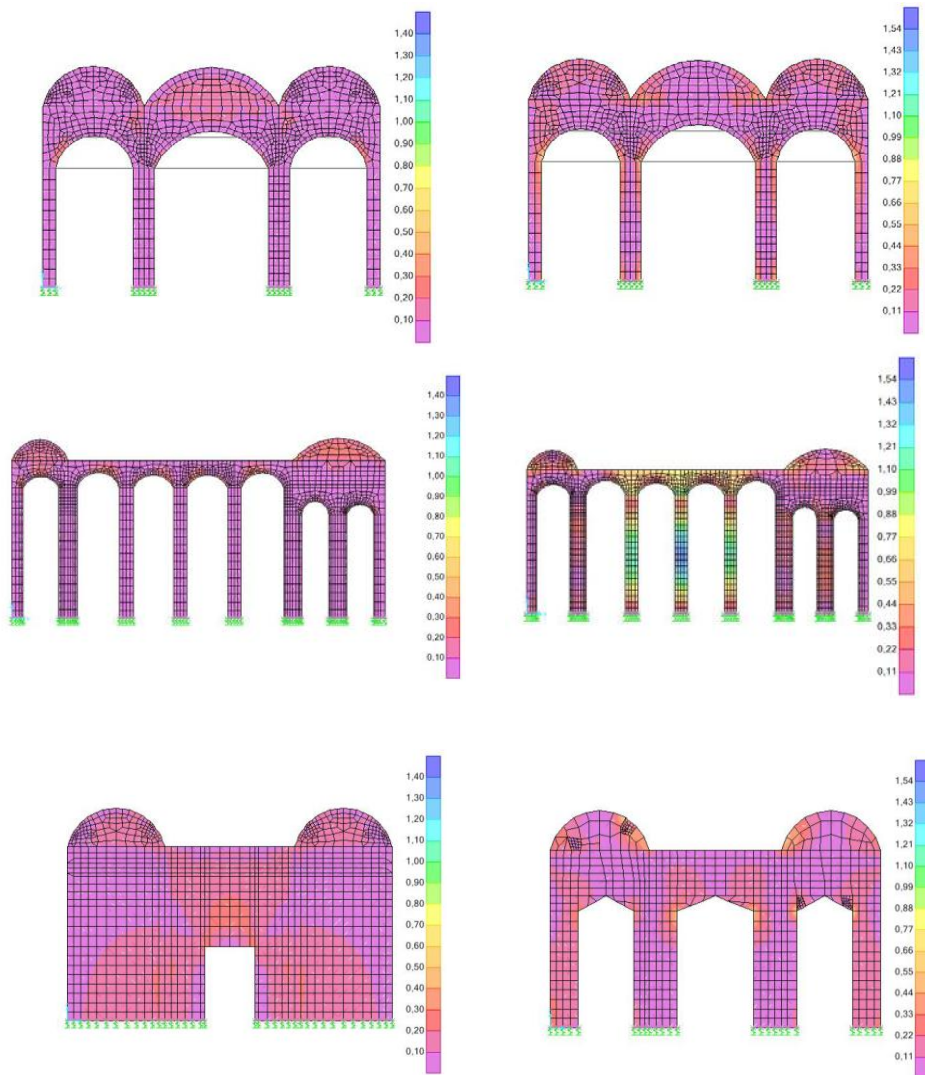
Figure 17. S_{12} and S_{22} for EQ_y loading case, (MPa)

The maximum displacement occurs at x- direction 7.5 mm when applying $G+EQ_x$ load case and at y- direction 11.8 mm when applying $G+EQ_y$ Load case (Table 9).

Table 9. Maximum and minimum stresses due to $G+EQ_x$ and $G+EQ_y$

EQ Load	Displacement (X-direction)	Displacement (Y-direction)
$G+EQ_x$	7.5 mm	6.5 mm
$G+EQ_y$	9.5 mm	11.8 mm

This value of displacement that occurs when applying the response spectrum analysis shows that the basilica is more prone to be damaged if the earthquake direction is along

the y- axis. Also, this result matches the real situation of the basilica. The most damages, cracks, misalignment of load bearing walls which are observed, are along the y- axis (N-S direction).

7. Conclusions

In this study, the structural response evaluation of the St. Sotiri Basilica is discussed. The methodology used in evaluation of the structure is visual inspection and simple measurement techniques of the entire structure and determination of the damaged structural members.

From the condition assessment of the St. Sotiri Basilica, it has been observed several damages to the load bearing walls, structural and non-structural cracks, humidity, misalignment, deterioration of surface plaster in vaults, deterioration of steel mechanical anchors etc. The most problematic part of the church is its roof which causes a leakage of water to the vaults and the walls beneath it. It is suggested to repair the damaged elements of the roof and the stone tiles urgently.

To have a better identification of stress distribution, FEM is prepared. Modeling is based on geometric data stored by the Historic Monuments Preservation Institute. Some of the missing data were substituted and assumed from other studies with similar geometrical properties. For analytical modeling, the macro-modeling approach is used. In other words, the results depend on the modeling of the structure.

The FEM prepared by SAP2000 involved assumed material properties due to inability to conduct tests. The maximum displacement obtained from the analysis shows a value of 7.5 mm for $G+EQ_x$ and 11.8 mm for $G+EQ_y$.

The results of the stresses in the basilica system exceed the allowable limits in various levels defined in the study. The findings provided by finite element analysis results support the observations regarding the damage conditions through visual inspections. The analysis of the structure using SAP 2000 has shown that the structure is safe under gravity loads, but it is not safe under seismic loading. The response spectrum analysis has shown that the assumed allowable strength of the materials is exceeded in vaults, Northern and Southern load bearing walls because of high concentration of stresses.

Since this study was based on the material properties and construction period obtained from different research and studies similar to this structure, St. The analysis of Sotiri Basilica can be done using real data that can be found through different laboratory tests and experiments. In addition, nonlinear analyzes can be performed for similar structural monuments after all data and tests, including foundation and soil properties, have been collected. Furthermore, this study proposes that various approaches for the analysis of historical monumental buildings should be compared to cover the inevitable unknowns that may affect the response of materials and mechanics.

Funding Declaration

Conflict of Interest

The authors have no affiliation with any organization with a direct or indirect financial interest in the subject matter discussed in the manuscript.

Acknowledgement

References

[1] Bidaj A, Bilgin H, Hysenlliu M, Premti I, Ormeni R. Performance of URM structures under earthquake shakings: Validation using a template building structure by the 2019 Albanian earthquakes. Res. Eng. Struct. Mater., 2022; 8(4): 811-834. http://dx.doi.org/10.17515/resm2022.440ea0531 .

[2] Z. Fule. A case study on structural assessment of St. Savior Basilica in Southern Albania. MSc Thesis, 83 pages, Epoka University, Tirana, Albania, 2013.

[3] Demaj A. Structural analysis of Post-Byzantine churches: A case study for southern Albania. MSc Thesis, 50 pages, Epoka University, Tirana, Albania. 2011.

[4] Betti M, Galano L, Vignoli A. Finite element modelling for seismic assessment of historic masonry buildings. In Earthquakes and Their Impact on Society; Springer International Publishing: Cham, Switzerland, 2015; 377–415.

[5] Usta P. (2021). Assessment of seismic behavior of historic masonry minarets in Antalya, Turkey. Case Studies in Construction Materials. 2021; e00665. https://doi.org/10.1016/j.cscm.2021.e00665

[6] Işık E, Harirchian E, Arkan E, Avcil F, Günay M. Structural Analysis of Five Historical Minarets in Bitlis (Turkey). Buildings. 2022; 12(2):159. https://doi.org/10.3390/buildings12020159 .

[7] Hrasnica M, Causevic A, Rustempašić N. Structural vulnerability and assessment of masonry building from Ottoman period in Bosnia and Herzegovina. 2019; 1142-1173. https://doi.org/10.4018/978-1-5225-7314-2.ch043

[8] Bilgin H, Shkodrani N, Hysenlliu M, Ozmen H.B, Işık E and Harirchain E. Damage and performance evaluation of masonry buildings constructed in 1970s during the 2019 Albania earthquakes. Engineering Failure Analysis, Volume 131, January 2022. https://doi.org/10.1016/j.engfailanal.2021.105824 .

[9] Bahreini V, Pouraminian M, Tabaroei A. Seismic sensitivity analysis of Musa Palas historic masonry arch bridge by Tornado diagram. J Build Rehabil. 2022; 7, 71. https://doi.org/10.1007/s41024-022-00215-9 .

[10] Betti M, Borghini A, Boschi S, Ciavattone A and Vignoli A. (2018) Comparative Seismic Risk Assessment of Basilica-type Churches, Journal of Earthquake Engineering, 22:sup1, 62-95, https://doi.org/10.1080/13632469.2017.1309602 .

[11] Formisano A, Di Lorenzo G, Krstevska L and Landolfo R. (2021) Fem Model Calibration of Experimental Environmental Vibration Tests on Two Churches Hit by L'Aquila Earthquake, International Journal of Architectural Heritage, 15:1, 113-131, https://doi.org/10.1080/15583058.2020.1719233 .

[12] Shkodrani N, Bilgin H, Hysenlliu M. Influence of interventions on the seismic performance of URM buildings designed according to pre-modern codes. Res. Eng. Struct. Mater., 2021; 7(2): 315-330. http://dx.doi.org/10.17515/resm2020.197ea0331 .

[13] Bilgin H, and Ramadani F. "Numerical Study to Assess the Structural Behavior of the Bajrakli Mosque (Western Kosovo)", Advances in Civil Engineering, vol. 2021, Article ID 4620916, 17 pages, 2021.

[14] Bilgin H, 'Structural Analysis of Domed Roof Systems in Architect Sinan's Works', Journal of Engineering Science and Technology. Selcuk University, p. 119-128 (2006).

[15] Valente M, Milani G. Seismic Response Evaluation and Strengthening Intervention of Two Historical Masonry Churches. In: Milani G, Taliercio A, Garrity S (eds) 10th International Masonry Conference. Milan. 2018

[16] Saloustros S, Pelà L and Roca P. (2020). Nonlinear Numerical Modeling of Complex Masonry Heritage Structures Considering History-Related Phenomena in Staged Construction Analysis and Material Uncertainty in Seismic Assessment. Journal of Performance of Constructed Facilities. 34. 10.1061/(ASCE)CF.1943-5509.0001494.

[17] Thomo, Pirro. Kishat Pasbizantine në Shqipërinë e Jugut. Tiranë : s.n., 1998.

[18] Kumar N, Barbato M, Rengifo-López EL, Matta F. Capabilities and limitations of existing finite element simplified micro-modeling techniques for unreinforced masonry. Res. Eng. Struct. Mater., 2022; 8(3): 463-490.
http://dx.doi.org/10.17515/resm2022.408st0226 .

[19] Lourenço P.B., P. Roca, C. Modena, S. Agrawal, Structural Analysis of Historical Constructions, New Delhi, 2006.

[20] CSI, 'SAP2000 Linear and Nonlinear Static and Dynamic Analysis and Design of Three-Dimensional Structures', Computers and Structures, (2012).

[21] J. DeJong M., Seismic Assessment Strategies for Masonry Structures, MIT, June 2009

[22] Betti M., Facchini L., Biagini P., Seismic Analysis of Masonry Structures, Meccanica dei Materiali e delle Strutture, Vol. 3 (2012), no.3, pp. 9-20, ISSN: 2035-679X

[23] F. Portioli, R. Landolfo, O. Mammana, F.M. Mazzolani; Finite Element Analysis on the Large Scale Model of Mustafa Pasha Mosque in Skopje Strengthened with FRP, Asia-Pacific Conference on FRP in Structures (APFIS 2007): 12-14 December 2007, Hong Kong, China.

[24] Guler K., Saglamer A., Celep Z., Pakdamar F., Structural earthquake response analysis of the little Hagia Sophia Mosque, 13th World Conference on Earthquake Engineering, 2004.

Research Article

Identification of distributed impact force using the finite element model based on regularization method

Abdelali El-Bakari[*1,2,3,a], Abdellatif Khamlichi [1,b], Eric Jacquelin[4,5,c]

[1]Department STIC, National School of Applied Sciences, Abdelmalek Essaadi University, Tetouan, Morocco
[2]Communication Systems and Detections Laboratory, FS, Abdelmalek Essaadi University, Tetouan, Morocco
[3]MASGC, National School of Applied Sciences, Abdelmalek Essaadi University, Tetouan, Morocco
[4]Université Claude Bernard Lyon, Villeurbanne, France
[5]IFSTTAR, UMR_T9406, LMBC Laboratoire de Biomécanique et Mécanique des chocs, Bron, France

Article Info	Abstract
	The aim of this paper is to invent a technique based on the finite element method which makes it possible to identify the impact load occurring on the elastic bodies. Identifying the periodical signal like a distributed pressure caused by an impact that occurs on the elastic plate can contribute to structural health monitoring. The inverse formulation of the objective function based on the finite element method has been established. The first part of this work will be devoted to modal analysis, the objective of which is to formulate the transfer function between the impact zone and the sensors implemented at known positions in the frequency domain. To switch from the frequency domain to the time domain, the inverse fast Fourier Transformation is used. Here, the identification of the impact force acting on linear elastic structures such as plates was considered. In the first place, it is convenient to look for the parameters that define the impact area using a minimization technique based on the Maxwell-Betti theorem. Once, the localization is determined, the reconstruction of the impact force-signal characteristics is done by the regularization methods. The regularization based on the truncation of the generalized singular values decomposition (TGSVD) has been adapted in this work. The TGSVD shows a relative error equal to 2.10%. This value is lower than that of literature value where Tikhonov regularization with the L-curve criterion was used & results in a relative error of about 40%". Further, the current work for a more complicated case that generates a non-punctual impact for the same type of force shows the efficiency of the TGSVD method to reconstruct the impact signal. The influence of sensor locations, modal truncation, noise level, and discrete transfer functions on the reconstructed impact characteristics are discussed.

1. Introduction

The direct measurement of the force developed during an impact is not possible, especially because the projectile is any kind and the impact zone is not known a priori. We can also note that the measure may be intrusive and difficult to perform in the case of a distributed force. On the other hand, the measurement of a vibration response at a point in the structure such as acceleration, displacement, or deformation can easily be performed. This is why indirect methods based on inverse problem-solving are the only viable methods for identifying the characteristics of an impact. The reconstruction of the characteristics of dynamic impact forces calls into question the ill-posed problem. The problem is generally solved by the regularization method [1]. Over the past decade years, we have seen the extensive application of the regularization-based inverse problem to identify the impact signal applied to engineering structures in order to monitor structural health [2-4].

*Corresponding author: aelbakari@uae.ac.ma
[a] orcid.org/0000-0002-4196-6640; [b] orcid.org/0000-0001-6954-774X; [c] orcid.org/0000-0001-8415-6712

Assessing random impact forces is very important because it helps to prevent system failures. In many practical situations, such as a high-speed impact of an object onto a structure, which can be assimilated to a non-punctual impact: a bird impacting the airplane fuselage, direct measurement of impact signal is complicated, prohibitive, and cumbersome, especially for large structures. While the main arguments concern the difficulty of installing the sensors and the changes in dynamic properties, the prior identification of impact zone characteristics can make investigations more efficient. The identification of the characteristics of the force generated by the impact can be used to better evaluate the monitoring of the structure, thus minimizing the experimental effort required [5- 7].

The identification of the impact force includes two relevant aspects, namely the reconstruction of the impact signal and the estimation of the impact force position. For the reconstruction of impact forces, the technique most used by many researchers in the elastic field is deconvolution based on the hypothesis that the response of a body subjected to impact force depends linearly on an impact force. This technique can be used both in the time domain and in the frequency domain. Based on the deconvolution problem Jacquelin et al. [8] used generalized singular value decomposition (GSVD) to reconstruct the impact force acting on a rectangular plate. Rezayat et al. [9] proposed an approach based on sparse regularization to identify dynamic forces in the frequency domain by grouping fast iterative shrinkage-thresholding algorithms. Qiao et al. [10] proposed a sparse regularization method to solve an arbitrary identification force by developing a dictionary composed of a set of basic functions such as sine, cosine, spline functions, and wavelets.

For its time domain applications, the dynamic responses provided by a remote sensor have been considered in He et al. [11]. They proposed a method based on empirical decomposition with intermittent criteria and finite element modeling for reconstruction impact force characteristics. For a linear elastic structure, the impact identification problem is usually solved in the time domain by using the deconvolution procedure method from the deformation response [12-13]. Doyle [14] proposed a wavelet deconvolution method for impact force identification, which produced a significantly more accurate solution than frequency-domain methods. However, the resolution of the above problems by the direct method for example the elimination of gauss gives unstable results; on the other hand, the method of least squares is widely used to improve the precision of the solutions [15-16]. In some cases, it is preferable to use a residual error minimization technique between the measured and numerically calculated responses in the time domain, instead of obtaining the history of the impact forces by the process of direct deconvolution of a convolution integral [17]. The finite element method was used in the approach proposed by Liu et al. [18] to characterize the impact force based on stress wave, they highlighted four sensors symmetrically implemented to measure responses in terms of time-varying strain. Employing fast Fourier transformation (FFT), we can associate a form of integral deconvolution problem in the frequency domain to predict the impact force on beams from the measured strain data [19-20]. He et al. [21] employed the regularization based on the TSVD method to identify the impact force in the frequency domain and remarked that the position of the respondent sensors strongly influenced the condition number of the FRF matrix. Liu et al. [22] proposed a nonconvex overlapping group sparsity to solve the impact force identification problem, and also compared the nonconvex regularization method and the standard L1-norm method.

Furthermore, for the location of the impact zone, several efficient methods have been proposed by many researchers based on the beam theory. In the case of a punctual impact, the location of the impact area can be easily achieved by minimizing the error between the measured and calculated responses. Inoue et al. [20] proposed a technique that uses the arrival time of each frequency component of a pulse detected through wavelet

transformation to determine the location of the force on the beam. Liu [23] proposed an algorithm for solving a force identification problem based on TSVD and the Tikhonov filter-LS schemes. Yen and Wu [24] used Green's functions to identify the characteristics of the impact area with a significant number of sensors implemented on the isotropic plate to measure deformation responses.

In most practical cases, the impact is distributed on a structural patch, the problem is more complex because it is to identify pressure distribution and not just a single force. Assuming uniform pressure, a new parameter appears in the problem representing the extent of the affected area. El-Bakari et al. [25] proposed an improvement approach based on heuristic optimization like a particle swarm optimization algorithm to minimize the fitness function that doesn't involve pressure. The technique is based on weighting coefficients to stabilize the objective function, four cases were proposed in their work. Liu et al. [26] employed the modified second-order Tikhonov regularization method (TRM) and the non-negativity of the identified loads, the non-negative least squares (NNLS) to identify the distributed loads acting on irregular structures.

In this work, we propose an efficient method in order to identify the history and location of impact forces occurring on a linear elastic plate. Localization has been resolved as a minimization problem. Modal analysis based on the finite element method has made it possible to derive FRF (frequency response functions) between the excitation points and the measured response by implementing sensors. Using the inverse fast Fourier transform (IFFT), the associated temporal response functions were computed. Then a Toeplitz matrix was created. It gives the displacement associated with the applied pressure acting on a rectangular patch of the plate. The robustness of this method will be discussed as a function of the noise level.

2. Theoretical Problem Formulation

We consider a homogeneous and isotropic elastic rectangular plate of dimensions $a \times b \times h$, with a = 0.6 m, b = 0.4 m, and $h = 5 \times 10^{-3}$m as shown in Fig. 1. The force modeling impact is selected to result from periodic dynamic load identification assuming a uniform pressure, $p(t)$ where t is time. it is applied to a rectangular patch in the middle of the plate which is centered on a point S_0 having a coordinate (a/2, b/2) and having length δa and width δb.
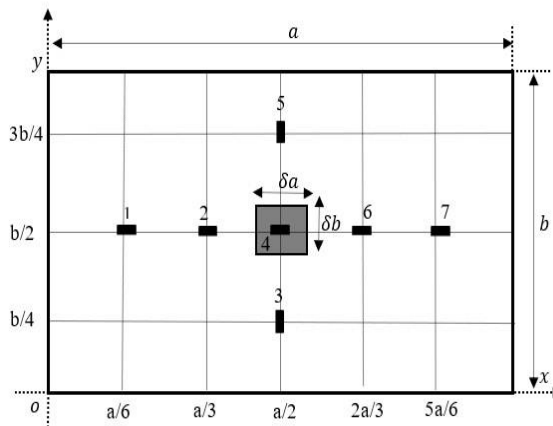
Fig. 1 Dimension of rectangular plate and sensors position

A finite element model of a rectangular plate is formulated in this part. As a result of the applied pressure, the displacement y is measured at certain points belonging to all points marked with symbol ■ which are shown in Fig. 1. The coordinates and node values of the sensors implemented on the structure are given in Table 1.

Table 1. Positions of sensors implemented on a rectangular plate

Sensors	#1	#2	#3	#4	#5	#6	#7
Coordinates	(a/6, b/2)	(a/3, b/2)	(a/2, b/4)	(a/2, b/2)	(a/2, 3b/4)	(2a/3, b/2)	(5a/6, b/2)
Nodes	121	231	368	363	358	473	583

Taking into account a sampled time interval of duration T_c and of length N the solution of the dynamical system is obtained by a linear convolution having the following form

$$y(k) = \sum_{i}^{k} h(j)p(k-j) \qquad k = 1,2, \dots, N \qquad (1)$$

where $y(k)$ is the discrete dynamic response as observed by the implemented sensor and $p(k)$ the discrete input pressure, h is a discrete system's impulse response function of the linear elastic system. The sampling rate is thus given by $\Delta t = T_c/(N-1)$.

In the frequency domain, there is also only a relationship with input/output defined by the assembling of the Eq. (1) for $k = 1,2, \dots, N$,

$$Y = HP \qquad (2)$$

where H is the Toeplitz-like transfer matrix, P is the pressure signal vector, and Y is the measured signal vector.

The H-matrix is obtained by employing a FEM of the plate. Designating the index i and j respectively the measurement DOF displacement, and any displacement DOF that is normal to the zone of applied impact, the FRF is collected from the calculated modes by FEM as

$$F_{ip}(\omega) = \sum_{j=1}^{N_{impact}} F_{ij}(\omega) \qquad (3)$$

with

$$F_{ij}(\omega) = \sum_{k=1}^{N_{modes}} \frac{\Phi_{ik}\Phi_{jk}}{\omega^2 - \omega_k^2 + 2i\beta_k\omega_k\omega} \qquad (4)$$

where N_{impact} is the number of total degrees of freedom of the normal displacements with respect to the affected area, N_{modes} the number total of modes that are selected in modal expansion, Φ_{ik} is the ith component of the kth mode normalized concerning mass, ω_k the kth mode angular frequency, β_k the damping coefficient for the kth mode, and the ω angular frequency.

Using the IFFT of the FRF given by Eq. (3)., the impulse function response h in the time domain can be obtained.

Generally, the matrix H can be written in the following form

$$H = \begin{bmatrix} h(1) & \cdots & h(N) \\ \vdots & \ddots & \vdots \\ h(N) & \dots & h(1) \end{bmatrix} \qquad (5)$$

In this study, the $N = 1024$ is selected in order to calculate easily the IFFT.

3. Regularization of The Inverse Problem

The direct inversion of the problem defined by Eq. (2) gives an unstable solution because the matrix is ill-conditioned. This means that its direct inversion of an ill-conditioned matrix can significantly amplify the error in the dynamic response. And as a result, lead to an unstable numerical solution that doesn't make physical sense. For the above reason, the deconvolution problem given in Eqs (2) and (5) needs to be regularized. The most popular ones are Tikhonov regularization [27] and Singular Value Decomposition (SVD) based methods [28], including truncated SVD (TSVD). In this work, the regularization technique based on the truncated generalized singular value decomposition (TGSVD) is considered. It should be mentioned that the simplest SVD method has not managed to regulate the identification problem considered in this work. The TGSVD-regularized solution of the problem given in Eqs (2) and (5) can be written like this

$$P = X\Phi\Delta^{-1}U^t W = H^* W \tag{6}$$

where X, Δ, U are the singular factors of H, Φ is the filter factor and $H^* = X\Phi\Delta^{-1}U^t$ is the regularized pseudo-inverse of H.

The presence of generalized singular values in the matrix H requires the introduction of the filter factors' goal in order to minimize the influence of the low amplitude of the latter. The Φ filter specified by the truncation method states:

$$\Phi_{ij} = f_i\delta_{ij} \quad i,j = 1, \dots, n \tag{7}$$

where $f_i = 0$ if $i \leq k$ and $f_i = 1$ otherwise.

To build the filter Φ within the framework of the truncation method, the rank k should be determined. Various criteria can be used for that. Here, when working with sinusoidal pressure signals, numerical experimentation has shown that $k \in [N - 10, N]$ with $N = 1024$.

4. Case Study

4.1. Description Problem

The rectangular plate shown in Fig. 1 is selected to have the following dimensions: length $a = 0.6$ m, width $b = 0.4$ m, and height $h = 5 \times 10^{-3}$m. It is supposedly embedded on these four edges. The material Young modulus is $E = 210$ GPa and the Poisson coefficient is $\mu = 0.3$. The density is $\rho = 7800$ kg. m^{-3}. The flexural rigidity modulus of the plate is given by $D = Eh^3/(12(1 - \mu^2))$.

A FEM simulation was carried out using the Abaqus software package. Since the type and size of mesh elements do not affect the displacement results, the simulation is performed using Abaqus eight-node linear brick, reduced integration with hourglass control (C3D8R). The C3D8R elements have only one point of integration which can pose a problem of convergence in terms of displacement. This is why in first-order, reduced-integration elements in Abaqus include hourglass control. The C3D8R elements and intermediate-size mesh for a linear 3D model of the rectangular plate do not affect the convergence in terms of the displacement node element. The mesh intermediate is described by the following properties:

- number of elements: 651;
- number of nodes: 1408;
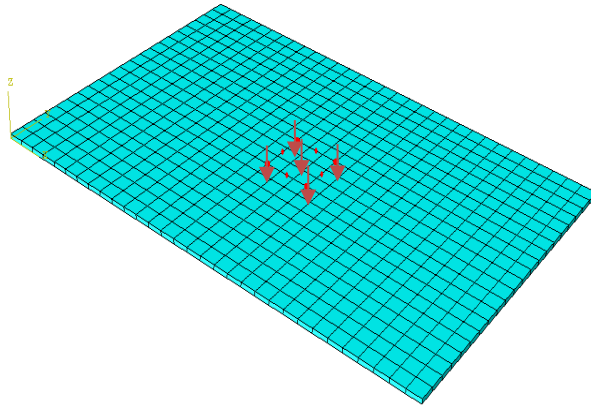
Fig. 2 Rectangular plate meshed; the impact zone (red color) subjected to the uniform pressure $p(t)$

Fig. 2 shows the intermediate mesh using the Abaqus-FEM model where the impact area is represented in red color. The latter extends over a surface (patch) in the middle of the plate simply supported. S_0, the coordinate of the impact center is given $S_0 = (0.3\text{m}, 0.2\text{ m})$, and the extents of the patch are defined by $\delta a = \delta b = 0.06$ m. The displacement measured by the sensors located on the x-axis and y-axis symmetry of the upper face of the plate having a normal parallel to the z-axis. Only the z-displacement is assumed to be measured.

The characteristics of a periodical-like sinus profile which represents the impact pressure are given in figure 3. The maximal peak value of the pressure is 3×10^4Pa, and the pulse width of each peak is $T = 0.02$s. The total duration of the signal considered in this study is $T_c = 6T$.

Fig. 4 shows the displacements in the z-direction measured by sensors implemented at different locations on the top face of the plate using the Abaqus implicit dynamic procedure: the nodes considered are located on the plane of symmetry of the top face, as indicated in Table 1.
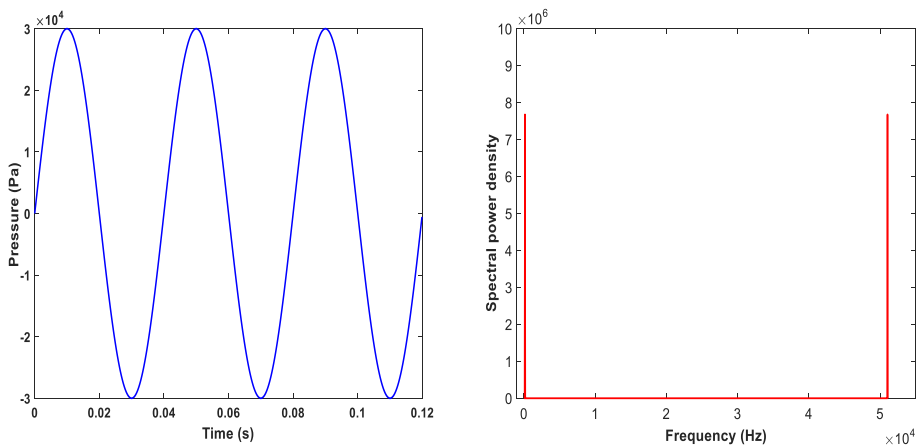
Fig. 3 Impact pressure signal characteristics; Pressure transient and Spectral content
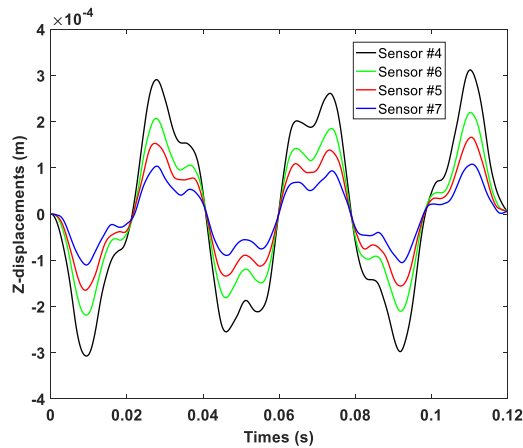
Fig. 4 Z-displacement as computed by using Abaqus dynamic implicit procedure

According to the study of convergence as a function of the size of the elements, an intermediate mesh was obtained without weighing down the machine by a refined mesh. Since the structure has no geometric defect at the time of the discretization the results remain unchanged vis-à-vis relation to the size of the element. The choice of the position of the sensors is not arbitrary it is an objective to show that the symmetry presents similar results. For this, it is enough to take the displacements given by sensors #3, #4, #6 et #7.

4.2. Modal Analysis

It is necessary to understand the vibration characteristics of a structure before proceeding with the identifying problem. This section focuses on the study of natural frequencies and structural modes shapes using the finite element method. This will allow us to determine the modes that have significant participation, as well as the corresponding frequencies, including the interest to develop the transfer function. The first 20 frequencies of the rectangular plate are given in Fig. 5. Fig. 6 illustrates some representative modes in the z-direction. The purpose of this modal study is to determine the maximum number of modes that contribute to the transfer function in order to complete the inverse formulation used to identify the impact force that occurs on the plate.
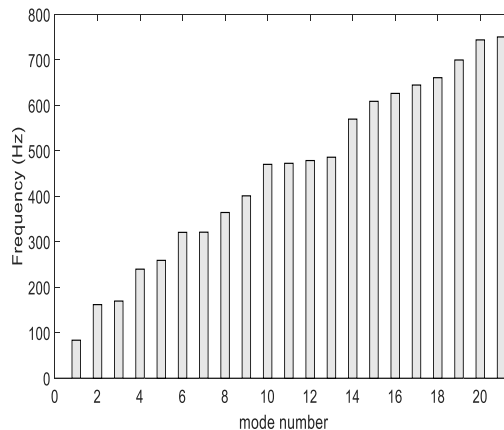
Fig. 5 Frequencies of the first 20 modes of the rectangular plate
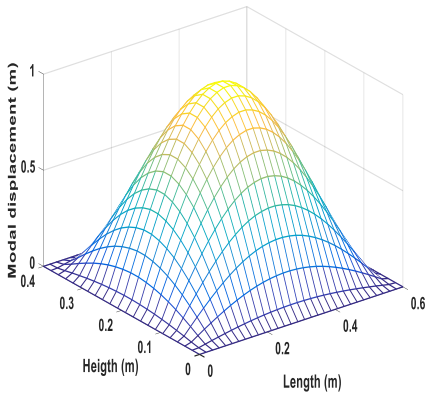
Mode 1
$f_1 = 83.592$ Hz
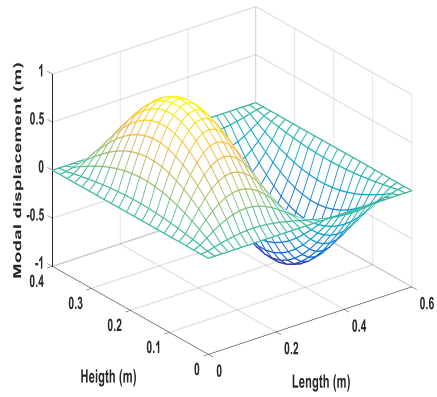
Mode 2
$f_2 = 161.84$ Hz
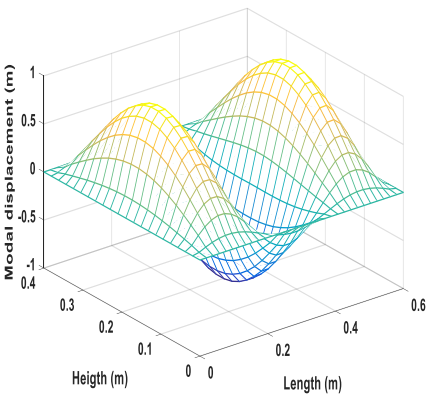
Mode 4
$f_4 = 239.84$ Hz
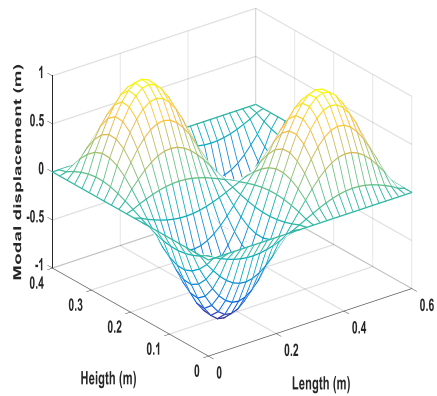
Mode 7
$f_7 = 321.15$Hz
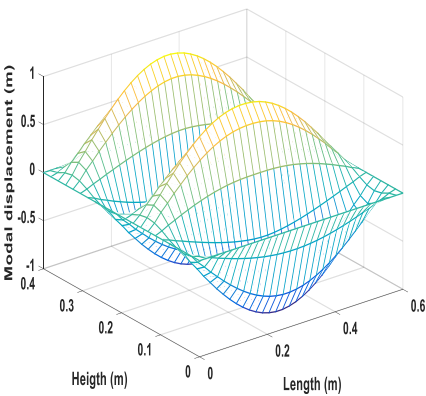
Mode 8
$f_8 = 364.44$ Hz
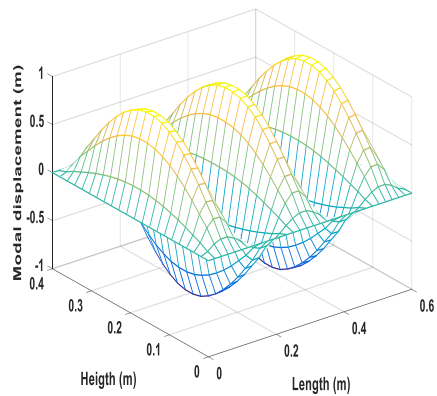
Mode 9
$f_9 = 401.07$ Hz

Fig. 6 Modes shapes of the plate, the z-displacement degrees of freedom are depicted
(a/h=120)

The frequency response function is calculated between the measurement sensor position and the excitation points using Eqs. (3)-(4). The $\beta_k = 5 \times 10^{-4}$ damping coefficient was used to avoid the singularities that may be present in the transfer matrix. Figure 7 gives the FRF for nodes 363 and 583 (according to the finite element mesh labeling).

Modal truncation convergence is reached here by considering only the first plate mode, but for the solution of the localization problem, it is necessary to keep three modes. The two signals compare well but a phase distortion can be noticed while computing the response using the discrete response function. The IFFT was calculated here by using N= 1024 points. The time domain used was [0,0.12s]. $\Delta f = 8,33$ Hz and $\Delta t = 1.1718 \times 10^{-4}$ s. With sufficient accuracy, one can assume now that the direct problem is well described by Eqs. (2)-(5) resulting from modal and fast Fourier analyses.

Node 363 is located at coordinate (a/2, b/2)	Node 583 is located at coordinate (5a/6, b/2)
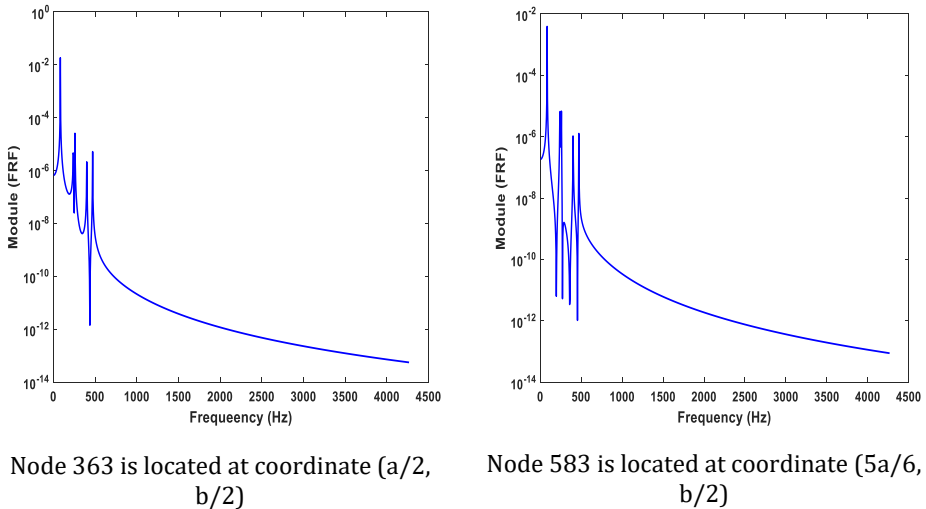
Fig. 7 FRF between sensor locations nodes and the impacted zone

4.3. Identification Problem

In this section, the formulation of inverse problem analysis was considered in two steps; the first one consists in finding the impact zone characteristics from measured displacement responses by the sensors placed on the top face of the rectangular plate. And in the second step, the reconstruction of the time history of the signal will be discussed through the regularization method. As regards the location, this means locating the impact zone and reconstructing the pressure signal. In the first step, searching the impact center position of the impacted zone, denoted here S_0, then as a second step the impact zone extensions δa and δb are determined.

To carry out this identification work, a flow chart summarizing the identification procedure is proposed in Fig.8.
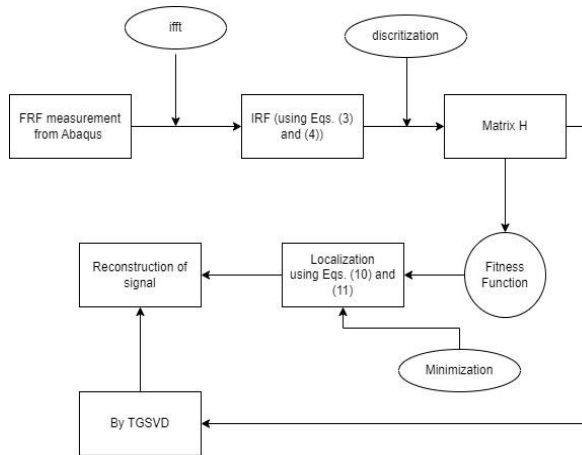
Fig. 8 Flow chart of the proposed identification method

4.3.1 Localization of impact force

Based on parametric modeling of dynamic responses associated, we consider a pair of points located on the plane of symmetry of the top face of the plate and having respectively a coordinate (x_i, y_i) and (x_j, y_j). The responses write

$$Y_i = H_i(S_0, \delta a, \delta b) \, Q$$
$$Y_j = H_j(S_0, \delta a, \delta b) \, Q \tag{8}$$

where Q is the resultant pressure force located at the unknown point (x, y), H_i and H_j are the Toeplitz matrices connecting this unknown point with the known senor locations i and j. Using commutative propriety $H_i(S_0, \delta a, \delta b)H_j(S_0, \delta a, \delta b) = H_j(S_0, \delta a, \delta b)H_i(S_0, \delta a, \delta b)$, one can prove the following Maxwell-Betti equation [18].

$$H_i(S_0, \delta a, \delta b)Y_j = H_j(S_0, \delta a, \delta b)Y_i \tag{9}$$

Parameter S_0 should then minimize the objective function

$$S_0 = \underset{x,y}{\mathrm{argmin}}\{\frac{\|H_i(S_0,\delta a,\delta b)Y_j - H_j(S_0,\delta a,\delta b)Y_i\|}{\|H_i(S_0,\delta a,\delta b)\| + \|H_j(S_0,\delta a,\delta b)\|}\} \tag{10}$$

where (x, y) are not located on the fixed boundary of the plate and $\| \ \ \|$ is the matrix norm 1. Having had determined S_0 a second minimization is performed in order to determine the limits of the impact interval in the x-axis (u_{10}, u_{20}) with parameter $\delta a = |u_{20} - u_{10}|$ and in the y-axis (v_{10}, v_{20}) with parameter $\delta b = |v_{20} - v_{10}|$ by solution of

$$(\delta a, \delta b) = \underset{x,y}{\mathrm{argmin}}\{\frac{\|H_i(u_1,u_2,v_1,v_2)Y_j - H_j(u_1,u_2,v_1,v_2)Y_i\|}{\|H_i(u_1,u_2,v_1,v_2)\| + \|H_j(u_1,u_2,v_1,v_2)\|}\} \tag{11}$$

It should be noted that, in order to avoid trivial solutions corresponding to the fixed boundaries and to points that are closer to them (because the modal displacements are small), the objective function is divided by the sum of norms of the Toeplitz matrices. One should also consider more than one mode in evaluating the FTF, otherwise, the numerator of the loss function is constant and minimization has a trivial multi-solution.

Isovalues of the objective function defined by Eq. (11) as a function of the nodes limiting the impact interval	Variation of the objective function defined by Eq. (10) as a function of the axial node number, the star shows the obtained minimum
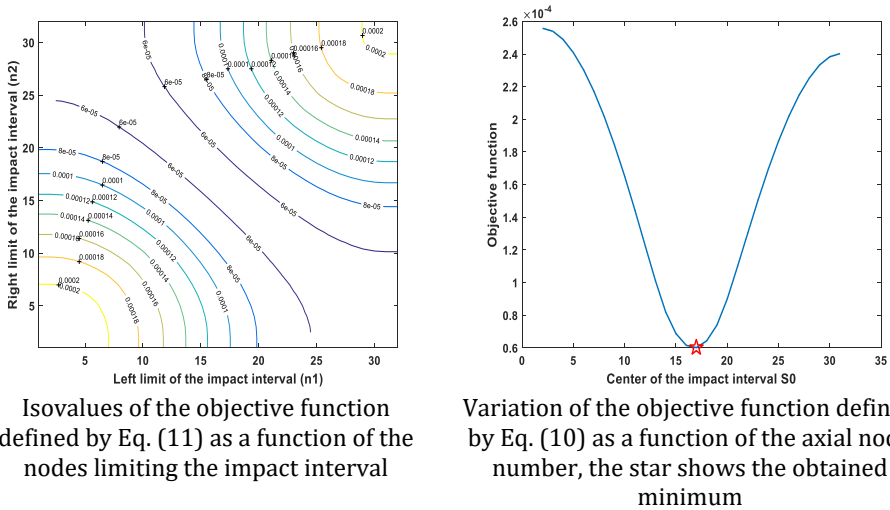
Fig. 9 Solutions of the minimization problems defined by Eqs (10) and (11)

Fig. 9 illustrates the objective function defined in Eq. (10) as a function of the local axial node number of the plate. This function is shown to have a minimum which is the point located at the coordinate distance $S_0(0.3m, 0.2m)$ corresponding to the center of the plate. The minimization of the fitness function gives the minimum at abscissa n=17 (the value of the objective function is $S_0 = 6.05 * 10^{-5}$) which corresponds to node 363 in the finite element mesh and has an index equal to 364.

Scanning all nodes (coordinate patch), we find the minimum of Eq. (10) obtained at n=17, this means that the minimum is obtained for all rectangular patch nodes. This technique makes it possible to find all areas of impact;

Minimization of the objective function defined by Eq. (11) yields the interval in:

- the x-axis $[0.2614285 \text{ m}, 0.3385715 \text{ m}]$ $(\delta a = 0.077143 \text{ m})$ which is not far from the exact solution $[0.27 \text{ m}, 0.33 \text{ m}]$
- y-axis $[0.161425 \text{ m}, 0.238575 \text{m}](\delta b = 0.07715 \text{ m})$ which is not far from the exact solution $[0.17 \text{ m}, 0.23 \text{ m}]$.
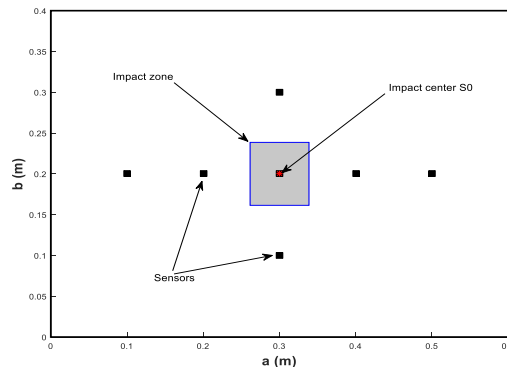
Fig. 10 Localization of impact force

Fig. 10 summarizes the problem of localization which has been challenged by Eqs. (9) and (10). It is clear that localization has been perfectly ensured by minimizing the objective functions defined by the Eqs. (9) and (10).

Now that S_0, δa and δb are calculated, the Toeplitz matrix $H_i(S_0, \delta a, \delta b)$ is completely known. The following section will be devoted to solving the inverse problem using the coupling FEM-TGSVD to reconstruct the impact signal.

4.3.2 Reconstruction of Signal Force

This part of the work analyzes the possibility of reconstruction force by using only the finite element method without the regularization technique. In the first order, the mains SPC is used to compare the different signals reconstructed. Figure 11 shows the SPC comparison with three positions of sensors implemented at points (j_1, j_2, and j_3) to measure the displacement response of the respective nodes (583, 358, 473), for each position we can only reconstruct the impact force. In Figures 11a, b, and c the first sensor is placed at i_1 corresponding to node 363 to give the excitation signal, and sensors measuring the displacement response are placed at j_1, j_2 and j_3 successively.
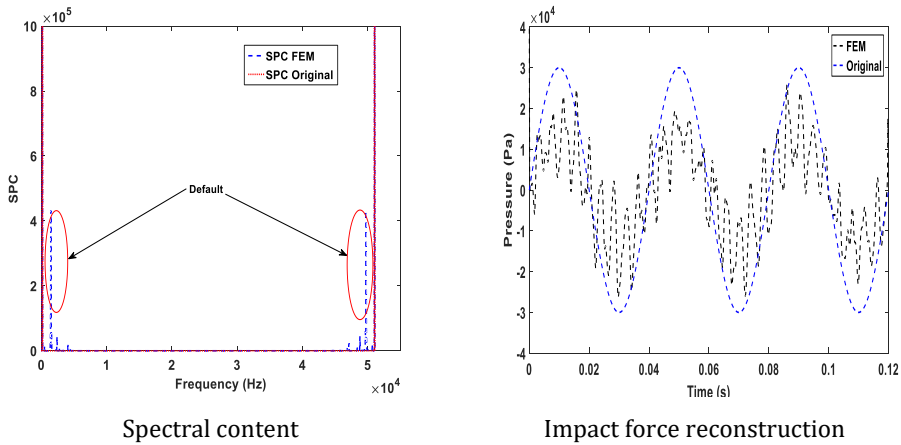
Spectral content · Impact force reconstruction

(a) Reconstruction of Impact pressure signal characteristics: Configuration 1 (#4, #7)

Spectral content · Impact force reconstruction

(b) Reconstruction of Impact pressure signal characteristics: Configuration 2 (#4, #5)
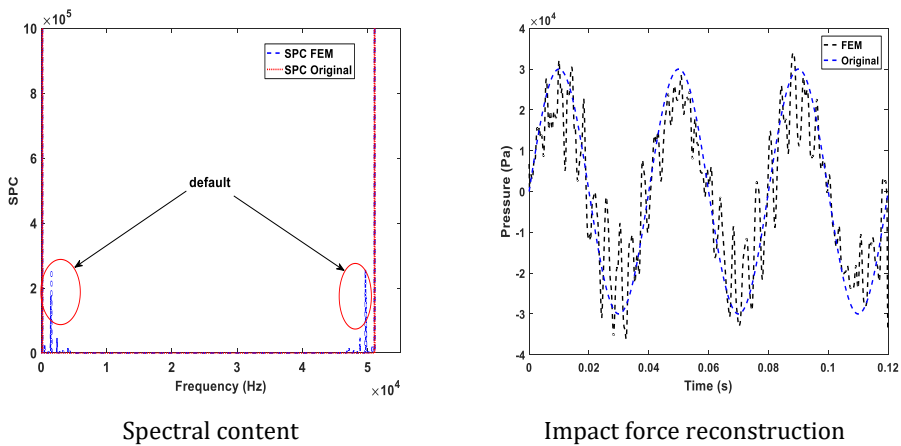
Spectral content   Impact force reconstruction
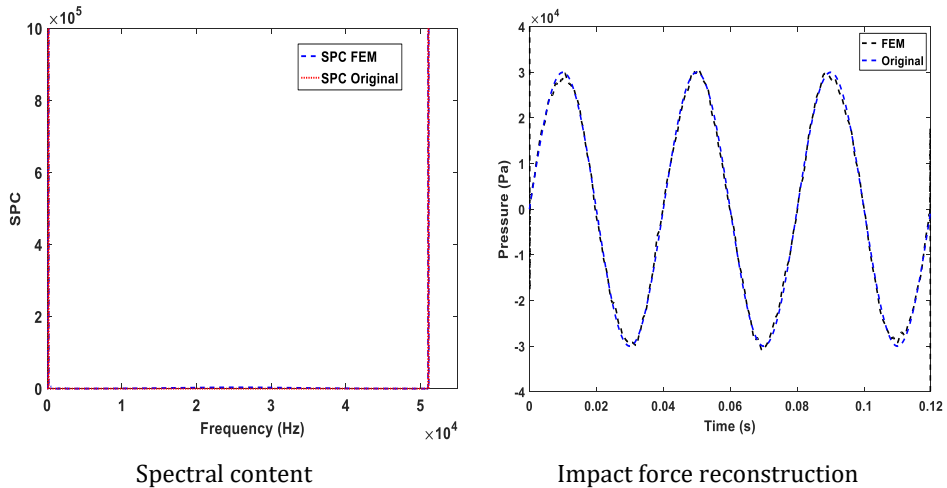
(c) Reconstruction of Impact pressure signal characteristics: Configuration 3 (#4, #6)
Fig. 11 Identification of impact force and a spectral of power by using three
configurations of position sensors

Fig. 11 shows the impact force identification by using only the finite element method as
stated by Eq. (8). The first point to make from Fig. 10 is that from the power spectrum, you
can predict the quality of the reconstructed signal. The reconstruction is poor in Figs. 10a
and 11b correspond to the first configuration when using the sensor excitation #4 (node
corresponding 363) and the sensor response #7 (node corresponding 358) and for the
second configuration (#4, #5). Configuration three (#4, #6) corresponding to the nodes
(363, 374) gives a very good reconstruction, which Can be explained by the following:

- The position of the measured response sensor is crucial.
- Do not be near or far from the impact area.
- The best result is for the displacement Y_{j1} measured by sensor #6 which is in node 474.
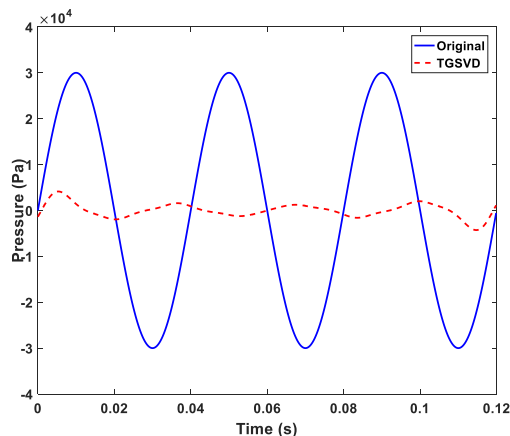
Fig. 12 Reconstruction of impact force when using 3 modes and filter truncation order
k=10
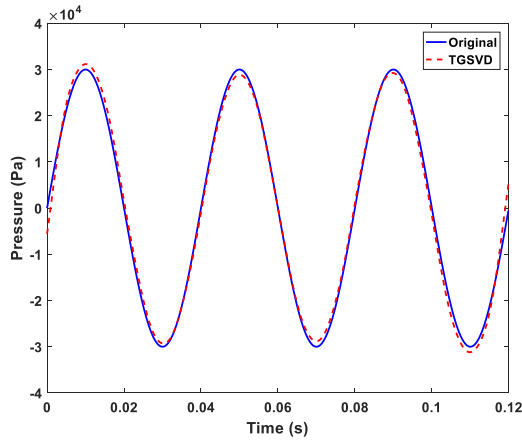
Fig. 13 Reconstruction of impact force when using 3 modes and filter truncation order k=20
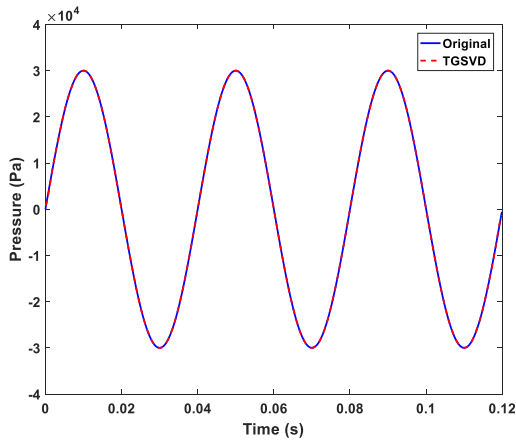
Fig. 14 Reconstruction of impact force when using 3 modes and filter truncation order k=80,

This method requires a laborious calculation and several tests in order to find the best place to implement the measurement sensor. This part was the object of a scanning calculation on the whole plate which is not easy in the case of any plate or structure that has rather large dimensions. To make the reconstruction method more reliable, we use the technique of generalized regularization in order of truncation.

Figs. 12, 13, and 14 illustrate the various results found by using the finite element method and TGSVD regularization method; it is important to remember that the position of the sensors in this method does not influence enough the good reconstruction of the impact signal. The only parameter that influenced the quality of the reconstructed signal is the truncation mode.

From figs. 12, 13, and 14 we can observe the effect of regularization in establishing the transfer function conducted to the reconstruction impact force. One can see that the reconstruction is bad without or with a wrong truncation filtering order. Those figures give a comparison with the signal reconstructed by using the TGSVD technique regularization and real impact force. For the filter, the truncation order equals 10 the reconstruction is

bad (Fig.12). For a truncation number equal to 20, the reconstructed signal takes a form that is very close to the real signal (Fig.13).

The signal profile obtained by the solution of the inverse problem coincides perfectly with the actual input force (Fig. 14). It is shown in this work that the mode number does not have much influence on the quality of the reconstructed signal, for this reason, the number of modes has been reduced to three. It is convenient to report that the best results obtained for the truncation filter order were equal to 80.

Compared to the work of Qiao et al. [10] who discussed the determination of a harmonic impact force for three types of sinusoidal forces at certain frequencies 60Hz, 80 Hz, and 150 Hz. In this identification procedure, they used SpaRSA identification and Tikhonov regularization with the L-curve criterion. they showed a clear advantage of SpaRSA over the Tikhonov method. This work for a more complicated case that generates a non-punctual impact for the same type of force shows the efficiency of the TGSVD method to reconstruct the impact signal. Moreover, the calculation of the relative error between the exact and identified forces is envisaged in order to test the performance of the TGSVD-based identification method and compare it with the work of Qiao et al. [10]. It is defined as

$$Relative\ error = \frac{\|F_{exact} - F_{identified}\|_2}{\|F_{exact}\|_2} \times 100\% \tag{12}$$

All calculations are completed and show a clear advantage of the TGSVD which shows a relative error equal to 2.10%. This value is lower than the one displayed in the work of Qiao et al. In addition to this, the Tikhonov method can generate a relative error of about 40% [10].

4.3.3 Effect of Noise Measurement

To test the robustness of the TGSVD regularization method, we consider four levels of measurement noise that affect the amplitude of the responses recorded by the sensors implement on the structure. The noise level considered is given by the following formula: $r = \alpha(-1 + ran\,d(\mu))$, with α representing the noise level considered in this study and μ varies randomly between [0,1].

Figs. 15, 16, and 17 show the noise effect on the quality of the reconstructed signal, in fact, to achieve a good quality impact signal reconstruction, the noise level must not exceed 1%.
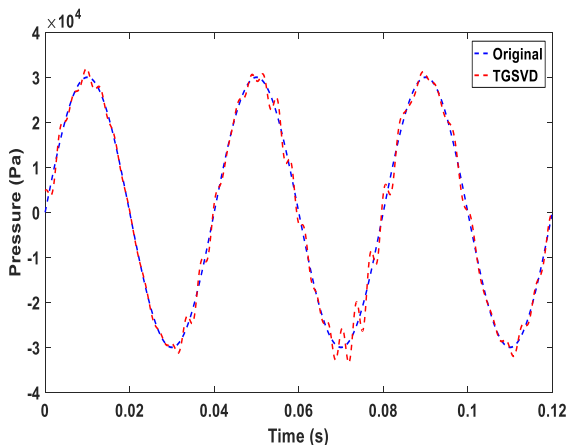
Fig. 15 Reconstruction of impact force when using 0.5% of measured noise (k=80),
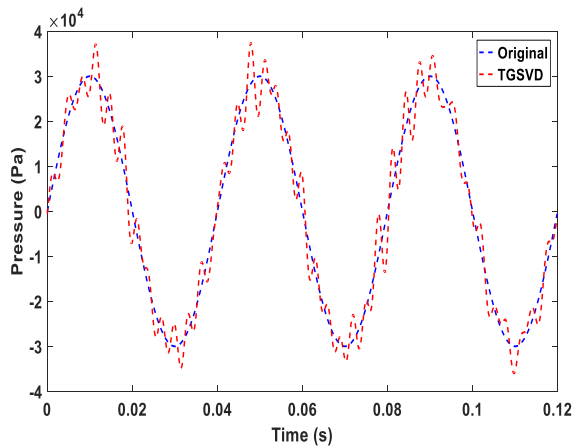
Fig. 16 Reconstruction of impact force when using 1% of measured noise (k=80),
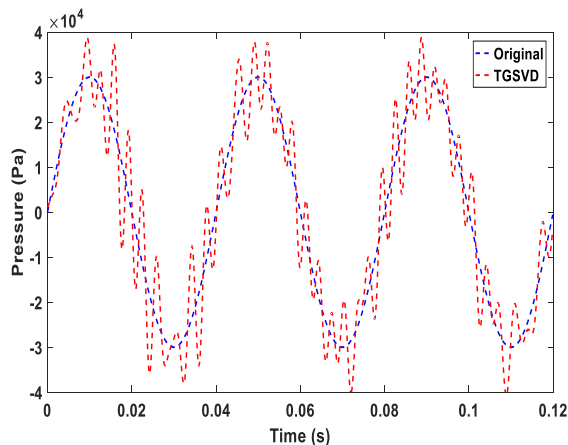
Fig. 17 Reconstruction of impact force when using 2% of measured noise (k=80),

It is clear from this part of the study which dealt with the influence of the noise level on the reconstructed signal quality, that a poor-quality sensor generates a significant noise that impacts the quality of the results and will not provide enough information about the impact signal. It should be noted that other case studies have been carried out in this work for a higher noise level and also for reconstruction based on the finite element method and the transient dynamic response. The latter gives a bad reconstruction from the first noise level. This makes the use of the TGSVD method essential in the reconstruction of the impact signal.

5. Conclusions

In this current study, the identification of a distributed impact acting on a patch of an elastic rectangular plate was performed. The identification procedure followed in this work is to decouple the reconstruction of impact force history from localization. The first step is to do optimization work ensured by a program under Matlab that allows localizing the impact area. whereas in the second step, the reconstruction of impact force history was performed using the finite element method (FEM) and then the truncated generalized singular value decomposition (TGSVD).

The proposed approach was applied to a homogeneous isotropic linear structure. The finite element method makes it possible to construct a modal or dynamic transient model. The generalized Toeplitz matrix was obtained by the IFFT of the FRF. After the reconstruction of the matrix elements, the minimization technique of the objective function was used in order de define the impact characteristics that define the impact zone. Localization has been solved for a linear structure. Once the impact zone is determined, the history of impact load is identified using the truncated generalized singular value decomposition (TGSVD) and finite element method. The impact force reconstruction is performed by two separate methods, trying to identify the history of the impact load by using just the finite element method without any means of regularization. It turned out that the reconstruction is possible for some sensors. This reconstruction is not resistant to the effects of low noise, it simply comes down to the sensitivity of the transfer matrix inversion. This makes the use of the regularization method mandatory for these kinds of identification problems.

The TGSVD shows a relative error equal to 2.10%. This value is lower than that of literature value where Tikhonov regularization with the L-curve criterion was used & results in a relative error of about 40%". Further, the current work for a more complicated case that generates a non-punctual impact for the same type of force shows the efficiency of the TGSVD method to reconstruct the impact signal.

The TGSVD was used to regularize the reconstruction problem. The efficiency of the approach used in this work was discussed in terms of the sensor's position when using only dynamical transitive responses without and with the TGSVD regularization technique, the modal truncation order and sensitivity of the measurement noise affected the responses. The modal convergence was achieved using only three modes. One should recall that the studied case is a symmetric problem and the impact frequency content is low. The proposed method can however be generalized to a more complicated situation without major problems.

Nomenclature

FEM- Finite Element Method

FRF- Frequency Response Function

TGSVD- Truncated Generalized Singular Value Decomposition

IFFT- Inverse Fast Fourier Transformation

P- the pressure signal vector

Y - the displacement vector

H - the Toeplitz matrix

j_i - positions sensors

T_c - the total duration of the signal

S_0 - impact center

$\delta a, \delta b$ - length and width of impact zone characteristics

E - elastic modulus

D - the flexural rigidity modulus of the plate

μ - Poisson ration

h -thickness of the plate

Φ_{ik}- the ith component of the kth mode normalized concerning mass

ω – angular frequency

β - damping coefficient

Competing Interests

The authors declare no competing financial interests.

References

[1] Calvetti D, Morigi S, Reichel L, et al. Tikhonov regularization and the L-curve for large discrete ill-posed problems. Journal of Computational and Applied Mathematics, 2000; 123(1-2): 423-446. https://doi.org/10.1016/S0377-0427(00)00414-3

[2] Nordström LJ. A dynamic programming algorithm for input estimation on linear time-variant systems. Computer Methods in Applied Mechanics and Engineering, 2006; 195: 6407-6427. https://doi.org/10.1016/j.cma.2006.01.002

[3] Qiao B, Liu J, Liu J, et al. An enhanced sparse regularization method for impact force identification. Mechanical Systems and Signal Processing, 2019; 126: 341-367. https://doi.org/10.1016/j.ymssp.2019.02.039

[4] Jia Y, Yang Z, Song Q. Experimental study of random dynamic loads identification based on weighted regularization method. Journal of Sound and Vibration, 2015; 342 :113-123. https://doi.org/10.1016/j.jsv.2014.12.010

[5] Chen Z, Chan THT, Yu L. Comparison of regularization methods for moving force identification with ill-posed problems. Journal of Sound and Vibration, 2020; 478:115349. https://doi.org/10.1016/j.jsv.2020.115349

[6] Hu N, Fukunaga H, Matsumoto S, at al. An efficient approach for identifying impact force using embedded piezoelectric sensors. International Journal of Impact Engineering, 2007; 34:1258-1271. https://doi.org/10.1016/j.ijimpeng.2006.05.004

[7] Wang L, Liu Y, Liu D, et al. A novel dynamic reliability-based topology optimization (DRBTO) framework for continuum structures via interval-process collocation and the first-passage theories. Computer Methods in Applied Mechanics and Engineering, 2021; 386: 114107. https://doi.org/10.1016/j.cma.2021.114107

[8] Jacquelin E, Bennani A, Hamelin P. Force reconstruction: analysis and regularization of a deconvolution problem. Journal of Sound and Vibration, 2003; 265 (1): 81-107. https://doi.org/10.1016/S0022-460X(02)01441-4

[9] Rezayat A, Nassiri V, Pauw BD, Ertveldt J, Vanlanduit S, Guillaume P. Identification of dynamic forces using group-sparsity in frequency domain. Mechanical Systems and Signal Processing, 2016; 70: 756-768. https://doi.org/10.1016/j.ymssp.2015.09.015

[10] Qiao B, Zhang X, Wang C, Zhang H, Chen X. Sparse regularization for force identification using dictionaries, Journal of Sound and Vibration, 2016; 368: 71-86. https://doi.org/10.1016/j.jsv.2016.01.030

[11] He J, Guan X, Liu Y. Structural response reconstruction based on empirical mode decomposition in time domain. Mechanical Systems and Signal Processing, 2012; 28:348-366. https://doi.org/10.1016/j.ymssp.2011.12.010

[12] W Feng, Q Li, Q Lu. Force localization and reconstruction based on a novel sparse Kalman filter. Mechanical Systems and Signal Processing, 2020, 144: 106890. https://doi.org/10.1016/j.ymssp.2020.106890

[13] Qiao B, Mao Z, Liu J, et al. Group sparse regularization for impact force identification in time domain. Journal of Sound of Vibration, 2019; 445: 44-63. https://doi.org/10.1016/j.jsv.2019.01.004

[14] Doyle JF. A wavelet deconvolution method for impact force identification. Experimental Mechanics, 1997; 37 (4): 403-408. https://doi.org/10.1007/BF02317305

[15] Chang C, Sun CT. Determining transverse impact force on a composite laminate by signal deconvolution. Experimental Mechanics, 1989; 29:414-419. https://doi.org/10.1007/BF02323860

[16] Xu B, He J, Rovekamp R, et al. Structural parameters and dynamic loading identification from incomplete measurements: approach and validation. Mechanical Systems and Signal Processing, 2012; 28: 244-257. https://doi.org/10.1016/j.ymssp.2011.07.008

[17] Yu Z, Mahdavi SH, Xu C. Time-domain spectral element method for impact identification of frame structures using enhanced GAs. KSCE Journal of Civil Engineering, 2019; 23: 678-690. https://doi.org/10.1007/s12205-018-0478-8

[18] Liu J, Hei C, Luo M, Yang D, Sun C, Feng A. A study on impact force detection method based on piezoelectric sensing. Sensors, 2022; 22: 5167. https://doi.org/10.3390/s22145167

[19] Doyle JF. An experimental method for determining the dynamic contact law. Experimental Mechanics ,1984; 24:10-16. https://doi.org/10.1007/BF02323199

[20] Inoue H, Harrigan J, Reid S. Review of inverse analysis for indirect measurement of impact force. Applied Mechanics Reviews, 2001; 54 (6): 503-524. https://doi.org/10.1115/1.1420194

[21] He Z, Lin X, Li E. A novel method for load bounds identification for uncertain structures in frequency domain. International Journal for Computational Methods, 2018; 15:1850051 ü. https://doi.org/10.1142/S0219876218500512

[22] Liu J, Qiao B, Chen Y, et al. Impact force reconstruction and localization using nonconvex overlapping group sparsity. Mechanical Systems and Signal Processing, 2022; 162: 107983. https://doi.org/10.1016/j.ymssp.2021.107983

[23] Liu Y, Shepard WS Jr. Dynamic force identification based on enhanced least squares and total least-squares schemes in the frequency domain. Journal of Sound of Vibration, 2005, 282: 37-60. https://doi.org/10.1016/j.jsv.2004.02.041

[24] Yen CS, Wu E. On the inverse problem of rectangular plates subjected to elastic impact, Part 1: method development and numerical verification. Journal of Applied Mechanics, 1995; 62: 692-698. https://doi.org/10.1115/1.2896002

[25] El-Bakari A, Khamlichi A, Dkiouak R, et al. Assessing impact force localization by using a particle swarm algorithm. Journal of sound of vibration. 2014; 333(6): 1554-1561. https://doi.org/10.1016/j.jsv.2013.11.032

[26] Liu H, Liu Q, Liu B, et al. An efficient and robust method for structural distributed load identification based on mesh superposition approach. Mechanical Systems and Signal Processing, 2021;151:107383. https://doi.org/10.1016/j.ymssp.2020.107383

[27] Tikhonov AN, Arsenin VY. Solutions of ill-posed problems. Wiley, New York, USA,1977.

[28] Hansen PC. Rank-deficient and Discrete Ill-Posed Problems: Numerical Aspects of Linear Inversion, vol. 4, Siam, USA, 2005.

Review of BS 8110, EC2, and the Improved EC2 shear resistance models for stirrup in reinforced concrete beams

Aderinwale Ayodeji[*1,a], Arum Chinwuba[1,b]

Department of Civil Engineering, Federal University of Technology, Akure, Nigeria

Article Info	Abstract
	The majority of beams used in construction have shear reinforcement provision. However, there exists a disparity in the results of the shear capacity guaranteed by the available shear design provisions. This is so because of the complex nature of the reinforced concrete shear mechanism. This study compares the BS 8110, EC2, and the Improved EC2 shear resistance models to ascertain the differences in their predictive ability when compared to experimental results. The EC2 is the most conservative at low level of shear reinforcement, i.e., shear reinforcement $\rho_w f_{ywm} \leq 1.3 \, MPa$, and at $\rho_w f_{ywm} \leq 2 \, MPa$ for mean value and design value predictions respectively. From the parametric trendline chart, the Improved EC2 predicts a higher shear capacity for lightly reinforced concrete beams than the EC2 shear model. A demerit point of 76 and 187 obtained respectively for the mean and design shear capacities of the BS 8110 shows that it is the most reliable of the three models in predicting the shear strength of stirrup-reinforced concrete beams.

1. Introduction

Shear failure is an undesirable mode of failure in reinforced concrete and usually occurs with a devastating consequence [1-2]. It is therefore a structural requirement that whenever the value of design shear stress exceeds the permissible shear stress of concrete, shear reinforcement must be provided [3-4]. Owing to the complexities involved in shear transfer mechanisms and their contributing variableness, a general shear theory is evasive [5-9]. The available analytical models regarding shear strength provide results that are often different from experimental results [10-12]. Shear reinforcements, also called stirrups, are employed to modify the shear resistance of reinforced concrete beams, thus transiting from brittle to a more ductile mode of failure [13-15].

Shear reinforcement comes into play after the formation of cracks [4, 16] and has been identified to perform three primary functions, which are, to restrict the growth of diagonal cracks, improve shear resistance through aggregate interlock, and also to increase the dowel capacity of longitudinal reinforcement [17]. While accurate assessment of the shear capacity of reinforced concrete is critically important for public safety, the traditional techniques available for this task are open to dispute [18]. None of the rational models proposed to date completely satisfies the three fundamental requirements of force equilibrium, strain compatibility, and material laws simultaneously [19].

This paper compares the predictive capabilities of the Improved EC2, BS 8110-1, and the EC2 shear method at their respective mean and design values, and with the experimental observations through the use of trendlines, total demerit points, statistical and parametric analysis. Experimental observations are from a database of 160 test results compiled by [20] on slender beams with stirrup failure. The database consists of simply supported

rectangular and flanged beams subjected to point loads that failed by diagonal tension and shear compression, and with a shear span to depth ratio (a/d) greater than 2.4. Details of the range of parameters captured in the experimental observations are summarized in Table 1.

Table 1. Range of parameters from 160 experimental observations presented by Olalusi [20]

Parameters	Minimum Value	Maximum Value
b_w (mm)	75	457
d (mm)	161	1369
f_{cm} (MPa)	13.40	125.30
ρ_l $(\%)$	0.14	5.20
$\rho_w\,f_{ywm}$ (MPa)	0.28	9.80
a/d	2.40	7.10
V_{exp} (KN)	81	1330

2. Shear Capacity for Reinforced Concrete Beams

There are different design procedures for calculating the shear capacity of reinforced concrete beams with stirrups [21-22]. Some prescribed shear capacity as the sum of both concrete and stirrup contributions, while others are based solely on stirrup contributions. Several models have been developed for shear in RC members as a result of its intricate nature [7, 23]. Pertinent models upon which current design standards are based are the 45-degree Truss Model [24], the Variable Angle Truss Model (VSIM) [25], and the Modified Compression Field Theory (MCFT) [26, 27]. Although BS 8110-1 has been retracted in the UK and replaced by EC2, it is still used in Nigeria as a guide for the design of reinforced concrete [28].

The EC2, which is based on the variable strut inclination method, has been identified to suffer drawbacks when predicting the shear capacity of lightly reinforced concrete beams due to neglect of the concrete contribution which otherwise is considered significant at low a level of shear reinforcement [29-33]. This has prompted Domenico and Ricciardi [34] to develop a shear strength model considered as an upgrade to the EC2 truss model with two inclinations of the compression strut, i.e., the lower inclination θ_1 and upper inclination θ_2 to ameliorate the limitations identified in the EC2 model.

2. 1. BS 8110 Shear Design Provision

The BS 8110 adopts an empirical model for its concrete contribution while the steel contribution is based on the 45° truss model. The concrete contribution v_c and that of the stirrups v_s adds up as being the nominal shear stress v_n [MPa] of the reinforced concrete beam as obtainable from Eqs. (1)-(2):

$$v_n = v_c + v_s \, [\text{MPa}] \tag{1}$$

$$v_n = \frac{0.75}{\gamma_c}\left(\frac{f_{cu}}{25}\right)^{1/3}\left(\frac{100A_s}{b_w d}\right)^{1/3}\left(\frac{400}{d}\right)^{1/4} b_w d + \frac{A_{sw} f_{yk} d}{\gamma_{ms} s} \quad [\text{MPa}] \tag{2}$$

where γ_c is the partial material safety factor for concrete ($\gamma_c = 1.25$); γ_s is the partial material safety factor for steel (γ_s=1.05); $100A_s/b_w d$ is the reinforcement ratio; f_{yk} is the yield strength of shear reinforcement; A_{sw} is the area of shear reinforcement; stirrup spacing $s \le 0.75$; f_{cu} is the characteristic concrete cube strength expressed as $f_{cu} = 0.8 f_c$, where f_c is the cylindrical concrete strength.

2.2 EN 1992 Eurocode 2: 2004 Shear Design Provision

Unlike the BS 8110, the EC2 computes its shear capacity by adopting variable strut inclination θ while neglecting the concrete contribution. The Variable Strut Inclination Method (VSIM) upon which the EC2 is based allows the concrete compressive angle θ to be varied between 21.8 and 45 degrees in a truss model according to derivations from plasticity theory [35 -37] The ultimate shear capacity of the shear reinforcement $V_{Rd,s}$, the web-crushing shear capacity $V_{Rd,max}$, and the strut angle θ can be determined by Eqs. (3)-(5):

$$V_{Rd,s} = \frac{A_{sw}}{s} z \frac{f_{ywk}}{\gamma_s 1.15} \cot\theta \qquad [KN] \qquad (3)$$

$$V_{Rd,\max} = \frac{\left(\frac{f_{ck}}{\gamma_c}\right) b_w z v_1 \alpha_{cw}}{(\cot\theta + \tan\theta)} \qquad [KN] \qquad (4)$$

$$\theta = \sin^{-1}\sqrt{\frac{A_{sw}\left(\frac{f_{ywk}}{\gamma_s}\right)}{\alpha_{cw} b_w s v_1 \left(\frac{f_{ck}}{\gamma_c}\right)}} \qquad [degrees\ ^0] \qquad (5)$$

where, A_{sw} is the cross-sectional area of the shear reinforcement, s is the stirrup spacing; f_{ck} and f_{ywk} are the characteristic values of the concrete compressive stenght respectively; internal lever arm is taken as $z = 0.9d$; v_1 may be taken to be $0.6\left(1 - \frac{f_{ck}}{250}\right)$; γ_c and γ_s are the partial material safety factor for concrete and steel; EC2 recommends the value of $\gamma_c = 1.5$ and $\gamma_s = 1.15$. The minimum shear reinforcement is as given in Eq. (6):

$$\rho_{w,\min} = 0.08 \frac{\sqrt{f_{ck}}}{f_{ywk}} \qquad [MPa] \qquad (6)$$

2.3 Improved Eurocode 2 Truss Model with Variable Inclination Struts

Domenico and Ricciardi [34] present a shear strength model which can be considered as an upgrade to the EC2 shear stress model. Though the underlying theoretical framework for the two models is similar, the Improved EC2 adopts two (rather than one) representative strut inclinations called θ_1 (lower inclination) and θ_2 (upper inclination), to capture the differences in the shear state along the web height of the beam as show in Fig. 1.
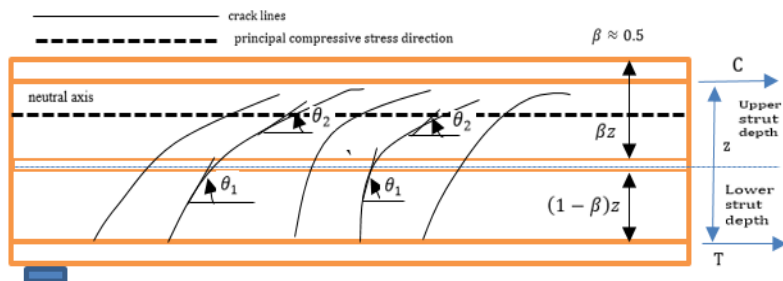
Fig 1. A rectangular beam showing the inclination angles Ө1 and Ө2 and transition depth z

By adopting a transition depth, $\beta = 1/2$, the closed-form expressions presented in Table 2 are easily adaptable for shear strength calculations for practical design and verification purposes and with less computational effort. For the Improved EC2 analysis, the efficiency factor $v_1 = 0.6(1 - f_{cm}/250)$, the mechanical ratio of the transverse reinforcement $w_w = \rho_w(f_{ywd}/f_{ywd})$, and the normalization parameters, $r = b_w z v_1 f_{cd}$ [in (N) units] are first computed. The calculated value of w_w is then checked against the limitations specified in Table 2. v_{Rd} is thus calculated based on the design region identified with the value of w_w. The shear strength of the beam, V_{Rd} [in (KN) units], is therefore obtained by multiplying the dimensionless strength of v_{Rd} computed with the normalization parameter r, $V_{Rd} = v_{Rd}r$

Table 2. Improved EC2 design regions and compression struts inclination by Domenico and Ricciardi [34]

Design region	ω_ω limitations	$cot\theta_1$	$cot\theta_2$	v_{Rd}
1	$0 \le \omega_\omega \le \omega_{\omega 1}$	$(cot\theta_1)_{max} = 2.5$	$(cot\theta_2)_{max} = 5$	$3.75\omega_\omega$
2	$\omega_{\omega 1} \le \omega_\omega \le \omega_{\omega 2}$	$\dfrac{5 + \sqrt{25 + 104\omega_\omega - 270}}{52\omega_\omega}$	$(cot\theta_2)_{max} = 5$	$\dfrac{5 + 260\omega_\omega + \sqrt{25 + 104\omega_\omega - 270\omega_\omega{}^2}}{104}$
3	$\omega_{\omega 2} \le \omega_\omega \le \omega_{\omega 3}$	$cot\theta_1{}^{opt} = \dfrac{\eta(\omega_\omega)}{2\sqrt{2\omega_\omega}}$	$cot\theta_2{}^{opt} = \dfrac{4\omega_\omega\sqrt{1+8\omega_\omega} + \sqrt{2\eta(\omega_\omega)}}{2\sqrt{2\omega_\omega}}$	$v_{Rd}{}^{opt} = \dfrac{\sqrt{2\eta(\omega_\omega)(1+8\omega_\omega - k(\omega_\omega) + 16\omega_\omega{}^2\sqrt{1+8\omega}}}{8(1 + 4\omega_\omega - k(\omega_\omega))}$
4	$\omega_{\omega 3} \le \omega_\omega \le \omega_{\omega,max}$	$cot\tilde{\theta}^{EC2} = \sqrt{\dfrac{1 - \omega_\omega}{\omega_\omega}}$	$cot\tilde{\theta}^{EC2} = \sqrt{\dfrac{1 - \omega_\omega}{\omega_\omega}}$	$v_{Rd}{}^{EC2} = \sqrt{\omega_\omega(1 - \omega_\omega)}$
5	$\omega_{\omega,max} \le \omega_\omega$	$cot\tilde{\theta}^{EC2} = 1$	$cot\tilde{\theta}^{EC2} = 1$	$v_{Rd}{}^{EC2}$

$where: \omega_{\omega 1} = 0.0716; \omega_{\omega 2} = 0.1136; \omega_{\omega 3} = 0.25; \omega_{\omega,max} = 0.5;$

$k(\omega_\omega) = \sqrt{1 + 8\omega_\omega - 16\omega_\omega{}^2 - 128\omega_\omega{}^3}; \eta(\omega_\omega) = \sqrt{1 + 4\omega_\omega - 8\omega_\omega{}^2 - k(\omega_\omega)}$

2.3 Design and Mean Shear Capacity

Design values are obtained by incorporating the characteristics material strength (f_{ck} and f_{ywk}) and the partial safety factor of concrete (γ_c) and steel (γ_s) into the expressions of the shear resistance model equations thus introducing a conservative bias into the design model [30]. The best estimate model/mean value predictions are obtained by neglecting all safety bias when calculating the shear resistance. For the mean value prediction, the characteristics material strengths f_{ck} and f_{ywk} are expressed at their mean values f_{cm} and f_{ywm} and partial safety factors γ_c and γ_s are equated to unity. The mean concrete strength as recommended by EN 1992-1-1 and the steel yield strength as recommended by Holicky [38] are given by Eqs. (7)-(8):

$$f_{cm} = f_{ck} + 8 \quad \text{[MPa]} \tag{7}$$

$$f_{ywm} = f_{ywk} + 2\sigma_{fyw} \quad \text{[MPa]} \tag{8}$$

where, $\sigma_{fyw} = 0.1f_{fywm}$ and $2\sigma_{fyw}$ is the standard deviation of steel yield strength stipulated by practice standard in Europe.

3. Results and Discussions

3.1 Comparison of the Trendline of Normalized Experimental Observations to Design Value Predictions of the Improved EC2 Model and the Codified EC2 and BS 8110 Standards

The trend line of the normalized experimental shear stress observations was compared to that of the EC2, BS 8110, and the Improved EC2 design shear stress capacity predictions (V/bd) as shown in Figure 2 at varied amount of shear reinforcement $(\rho_w f_{ywm})$. Judging from the plot, the BS 8110 trendline depicts a consistent relative increase of shear stress over the parametric range of shear reinforcement $(\rho_w f_{ywm})$ under consideration; while the trend line pattern of both the Improved EC2 and EC2 does not depict similar consistent level of appreciable increase over the entire parametric range of $(\rho_w f_{ywm})$ increases. At a range of $\rho_w f_{ywm} \leq 2$, EC2 has the most conservative trendline of all the models considered. At $\rho_w f_{ywm} > 0.3$, the Improved EC2 has the least conservative trendline which shows an approximate closeness to the experimental observations. Based on the premise that the Improved EC2 is based on the same theoretical principles as EC2 capacity predictions, the trendlines for these models possess similar curvilinear pattern.
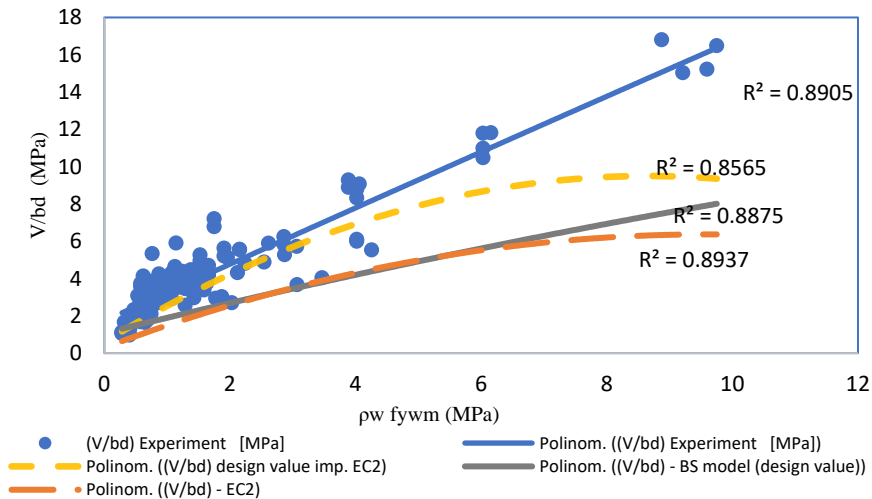
Fig. 2 Experimental and Predicted Design Value Shear Strength by Improved EC2, EC2 and BS 8110

3.2 Comparison of the trendline of normalized experimental observations to the mean value predictions of the Improved EC2 model and the codified EC2 and BS 8110 standards

The trend line of the normalized experimental shear stress observations was compared to that of the EC2, BS 8110 and the Improved EC2 mean value prediction (V/bd) as shown in Figure 3. The mean shear capacity predictions of EC2 below shear reinforcement range of 1.2 Mpa i.e $\rho_w f_{ywm} \leq 1.2\ Mpa$, is the most conservative. Above this, its trendline maintains a curvilinear pattern which though conservative, approximates the trendline of the experimental observations at $\rho_w f_{ywm} \leq 6\ Mpa$. The trendline of the improved EC2 mean predictions becomes unconservative at a parametric range of $1.1 \geq \rho_w f_{ywm} \leq 5.5\ Mpa$. The Improved EC2 thus over-predicts the shear capacity at the stated parametric range. The BS 8110 code mean predictions maintain a conservative trendline over the entire range of $\rho_w f_{ywm}$ observed.
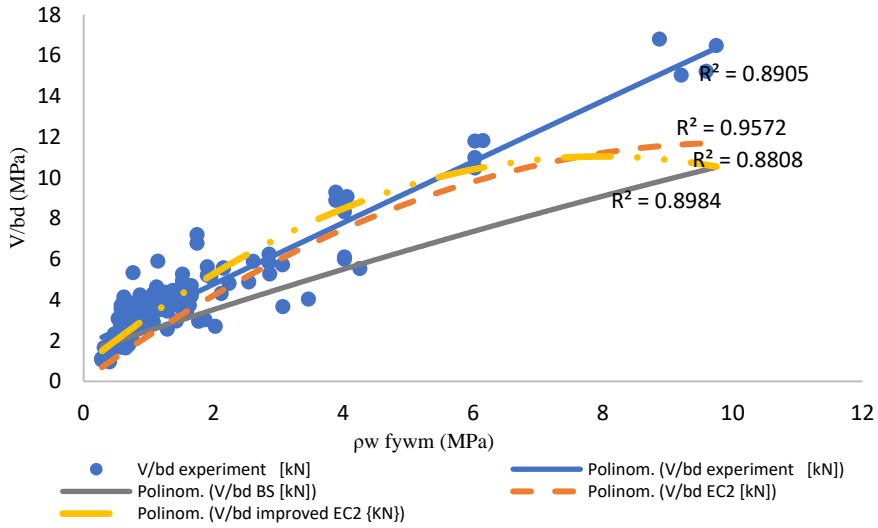
Fig. 3 Experimental and Predicted Design Value Shear Strength by Improved EC2, EC2 and BS 8110

3.3 Comparison of the Design value shear strength predictions and the mean value shear strength predictions

The design value shear strength predictions as captured in Figure 2 depicts a general conservative trendlines with the Improved EC2 as its least conservative model prediction at a range of $\rho_w f_{ywm} \geq 0.3\ Mpa$. The mean value predictions in Figure 3 depict a less conservative trendline for all the models considered with the Improved EC2 being unconservative at a parametric range of $1.1 \geq \rho_w f_{ywm} \leq 5.5 MPa$ when compared to the experimental trendline.

3.4 Total Demerit Point Analysis

Demerit point analysis introduced by Collins [39] for the performance assessment of shear strength methods assigns demerit points, within a specified range, to the ratio of experimental observations and predicted shear strength method under consideration $V_{\exp}/V_{pred}$ as given in Table 3.

Table 3. Demerit Points Classification [39]

S/N	Classification	$\left(\dfrac{v_{exp}}{v_{pred}}\right)$ Range	DP
1	Extremely dangerous	<0.5	10
2	Dangerous	0.50-0.65	5
3	Low safety	0.65-0.85	2
4	Appropriate safety	0.85-1.30	0
5	Conservative	1.3-2.00	1
6	Extremely conservative	>2.0	2

The corresponding values are then summed as the Total Demerit Point (TDP). The TDP shows the overall performance of each shear strength method as shown in Fig 4. A smaller value of the TDP indicates the shear strength evaluation method to be more reliable in

predicting the shear strength of reinforced concrete beams under this condition. More so, Improved EC2 maintains a low variability between its design and mean shear strength. From Table 4, it can be observed that EC2 largely underpredicts shear capacity with the highest distribution of experimental to estimated shear capacity ($V_{\exp}/V_{pred}$) in the extremely conservative class both for its mean and design value predictions which is due to the conservation provided by the strut angle(θ).

Table 4. Demerit Points Classification [39]

Range	Classification	DP	BS 8110 Mean Value Points	Design Value Points	EC2 Mean Value Points	Design Value Points	Improved EC2 Mean Value Points	Design Value Points
<0.5	Extremely dangerous	10	0	0	0	0	10	0
0.5-0.65	Dangerous	5	0	0	5	0	35	5
0.65-0.85	low safety	2	4	0	10	0	52	20
0.85-1.30	Appropriate safety	0	0	0	0	0	0	0
1.30-2.00	Conservative	1	66	99	78	40	35	76
>2.0	Extremely conservative	2	6	88	64	228	2	24
Total Demerit Points (TDP)			76	187	157	268	134	125
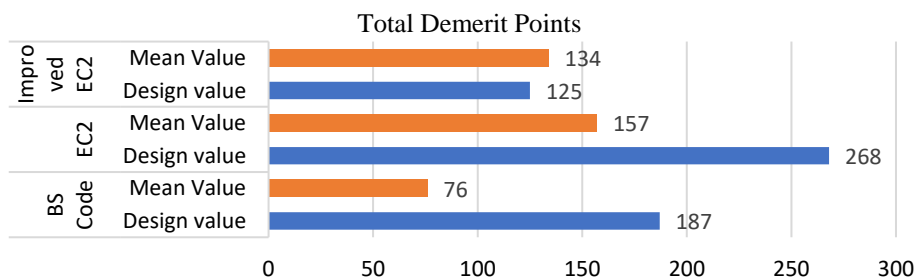
Fig. 4 Demerit point analysis

3.5 Statistical Properties

From Table 5, the sample mean of the improved EC2 has the lowest value at 1.10 and 1.30 respectively for both mean and design value predictions, followed be the BS 8110 at 1.34 and 1.77, then the EC2 at 1.58 and 2.34. The Improved EC2 thus performs best as the least conservative design method and with the lowest variability at 0.30 and 0.37 standard deviation for its best estimate and design value predictions respectively.

Table 5. Statistical Properties of BS 8110, EC2 and Imp. EC2

		Mean (μ)	Standard Deviation (σ)
BS 8110	Mean Value	1.3	0.32
	Design Value	1.77	0.43
EC2	Mean Value	1.5	0.47
	Design Value	2.34	0.65
Imp. EC2	Mean Value	1.10	0.30
	Design Value	1.36	0.37

3.5 Parametric Variation

In a bid to further examine the influence of shear reinforcement, beam size and concrete strength as its concerns the models under consideration, parametric analysis was

conducted across practical ranges of the aforementioned parameters. A lot of the mean, and the design shear value of a given test section will be varied across the percentage shear reinforcement $\rho_w f_{ywm}$ as depicted in Figs. (5) to (8).
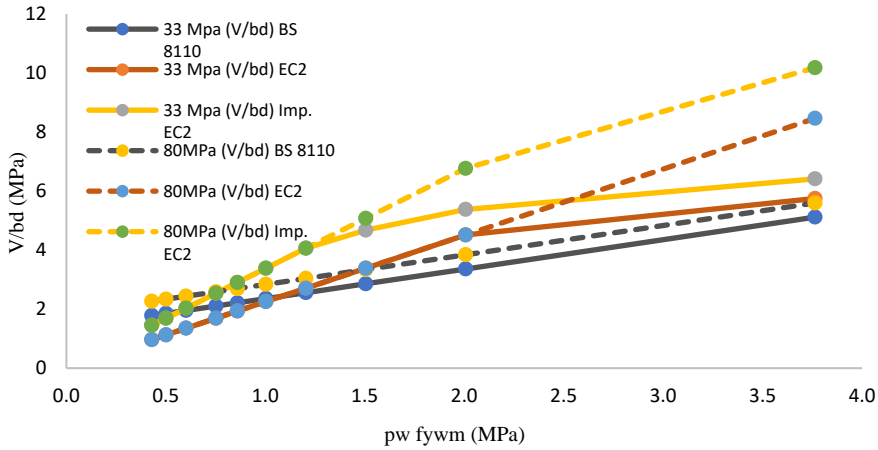
Fig. 5 Mean value parametric variation:300x450mm at $fcm = 33 \ and \ 80MPa$
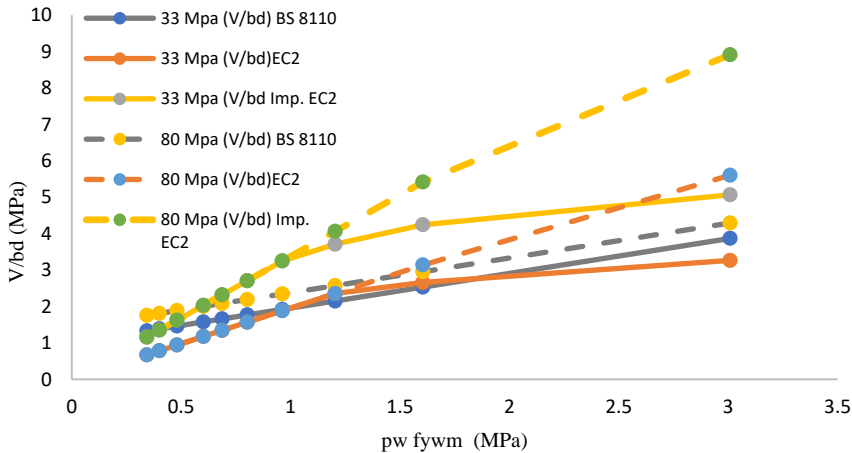
Fig. 6 Design value parametric variation:300x450mm at $fcm = 33 \ and \ 80MPa$

The test beam for the parametric analysis in Figure 4 and 5 had the following section properties: $b_w = 300mm, \ d = 450mm, \ f_{ywm} = 460MPa, \ a/d = 2.5, \ \rho_l = 3.5\%, \ f_{cm} = 33 \ and \ 80MPa$ respectively. The test beam for Figure 6 and 7 had the following properties: $b_w = 600mm, d = 900mm, f_{ywm} = 460MPa, a/d = 2.5, \rho_l = 3.5\%, f_{cm} = 33 \ and \ 80MPa$ respectively. Observations from the mean value plot in Figure 4 shows that the trendlines of the EC2 and the Improved EC2 model were not affected by the concrete strength (33 and 80MPa) at $\rho_w f_{ywm} \leq 2MPa$ and $\rho_w f_{ywm} \leq 1.2MPa$ respectively above which noticeable variation is observed as the amount of shear reinforcement increases. For the design plot in Figure 5, the EC2 and the Improved EC2 remained unaffected by the varied concrete

strength at a low shear reinforcement $\rho_w f_{ywm} \leq 1.2 MPa$ and $\rho_w f_{ywm} \leq 0.9 MPa$ respectively. The BS 8110 maintains an appreciable increase over the entire range of shear reinforcement both for the mean and design value plots at f_{cm} of 33 and 80 MPa without sudden slope change.
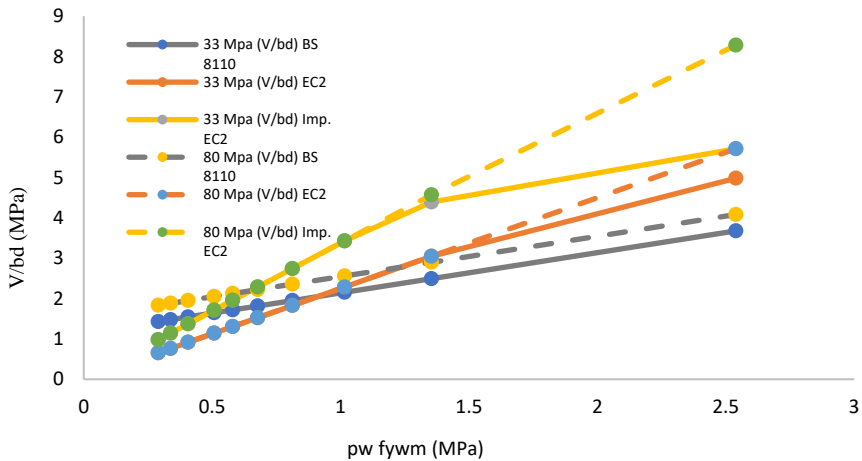
Fig. 7 Mean value parametric variation: 600x900mm at $fcm = 33\ and\ 80 MPa$
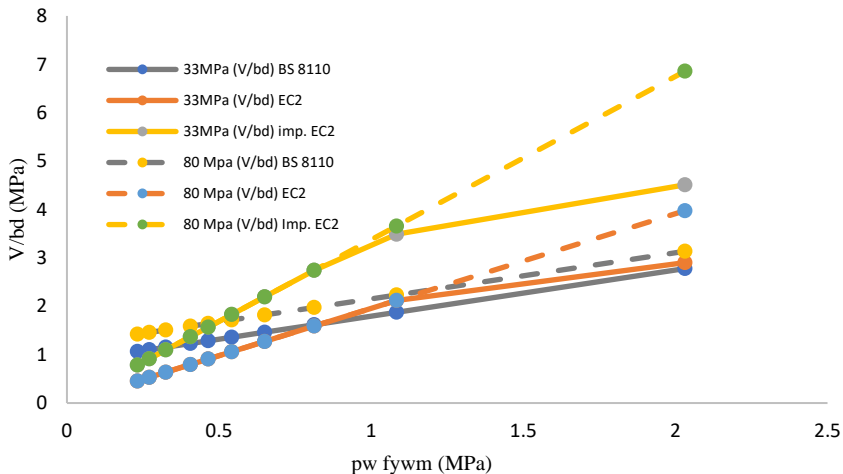
Fig. 8 Design value parametric variation: 600x900mm at fcm=33 and 80MPa

Observations from the mean value plot in Figure 6 shows that at $\rho_w f_{ywm} \leq 0.3 MPa$ and $\rho_w f_{ywm} \leq 1 MPa$ the trendlines is unaffected by the variations in concrete strength at 33 and 80 MPa respectively. For the design plot in Figure 7, the trendlines for the EC2 at $\rho_w f_{ywm} \leq 1.1 MPa$ and the Improved EC2 at $\rho_w f_{ywm} \leq 0.8 MPa$ remained unaffected by the changes in the concrete shear strength (33 and 80 MPa), and above these shear reinforcement values, concrete strength had a tolerable influence on their respective trendlines as the amount of shear reinforcement increases.

5. Conclusions

This study compares the Improved Eurocode 2 truss model having two variable inclination compression struts with Eurocode 2 and BS 8110 shear capacity prediction methods for reinforced concrete beams with stirrups. From the trendline analysis conducted in this study, the design value trendline for Improved EC2 is the least conservative which best approximates the experimental observation. The mean value prediction for the Improved EC2 between the ranges of $1.1 \geq \rho_w f_{ywm} \leq 5.5\ MPa$ is largely unconservative with shear capacity predictions exceeding experimental observations.

From the Total demerit point analysis, the Improved EC2 has the least variability between its mean and design value at 134 and 125 respectively. Though the BS 8110 gave the least mean value demerit point of 76, its design value demerit point of 187 is higher than that obtained for the Improved EC2 at 125. From the statistical analysis, the Improved EC2 had the lowest sample mean both for its design and mean value predictions when compared to the EC2 and BS 8110 shear strength methods. Also, it has the least variability of 0.30 and 0.37 standard deviation for its mean and design value predictions respectively.

From the parametric analysis, the trendlines of BS 8110 maintain an appreciable increase over the entire range of shear reinforcement both for the mean and design value plots of the two test beams under consideration without a sudden slope change. The trendline of the EC2 and the Improved EC2 follow almost the same pattern. This further confirms the underlying assumption that the two models were based on the same theoretical framework. The Improved EC2 predicts higher shear stresses than the EC2 model over the parametric range of the shear reinforcement considered on the plots. The Improved EC2 might lead to considerable savings in the amount of shear reinforcement consumed in construction works, especially for lightly reinforced concrete where the EC2 shows weakness.

References

[1] Arabzadeh A, Hizaji RA. Simple approach to predict the shear capacity ad failure mode of fixed-end RC deep beams based on experimental study. International Journal of Engineering (IJE), IJE Transactions A: Basics, 2019; 32(4): 474-483 https://doi.org/10.5829/ije.2019.32.04a.03
[2] Zhang M, Deng M, Yang J, Zhang Y. Experimental study on the shear behaviour of reinforced highly ductile fiber-reinforced concrete beams with stirrups. Buildings, 2022; 12(8): 1264. https://doi.org/10.3390/buildings12081264
[3] Zamri NF, Mohammed RN, Khalid N, Chiat KY. The Effects of Inclined Shear Reinforcement in Reinforced Concrete Beam. Malaysian Journal of Civil Engineering, 2018; 30(1): 85-96. https://doi.org/10.11113/mjce.v30.169
[4] Rahal KN, Al-Shaleh K. Minimum transverse reinforcement in 65 MPa concrete beams. ACI Structural Journal, 2004; 101(6): 872-878. https://doi.org/10.14359/13463
[5] Talib HY, and Al-Salim NH. Improving punching shear in flat slab by replacing punching shear reinforcement by ultrahigh performance concrete. International Journal of Engineering, Transaction B: Applications, 2022; 35(8): 1619-1628, https://doi.org/10.5829/IJE.2022.35.08B.18
[6] Victor S, Bentz E, Ruiz M, Foster S, Muttoni A. Background to the fib Model Code 2010 shear provisions-part 1; beams and slabs. Journal of Structural concrete, 2013; 14(3): 195-203. https://doi.org/10.1002/suco.201200066
[7] Hawkins N, Kuchma D, Mast F, Marsh L. and Reineck, K. H. Simplified Shear Design of Structural Concrete Members: Appendixes. Transportation Research Board of the National Academies, University of Illinois, Urbana, Illinois, 2004.

[8] Słowik M. Shear Failure Mechanism in Concrete Beams. Procedia Materials Science, 2014; (3): 1977-1982. https://doi.org/10.1016/j.mspro.2014.06.318

[9] Zhang T, Visintin P, Oehlers DJ. Shear strength of RC beams with steel stirrups. Journal of Structural Engineering, 2015; 14(2): 04015135. https://doi.org/10.1061/(ASCE)ST.1943-541X.0001404

[10] Ghafar A, Javed A, Rehman H, Ahmed K. Ilyas M. Development of shear capacity equations for rectangular reinforced concrete beams. Pakistan Journal of Engineering and Applied Sciences. 2010; 6: 1-8.

[11] Wei W, Che Y, Gong J. Shear strength model for reinforced concrete beams web reinforcement. Magazine of Concrete Research, 2011; 63(6): 423-431. https://doi.org/10.1680/macr.10.00020

[12] EI-Chabib, H, Nehdi, M, Saïd A. Predicting the effect of stirrups on shear strength of reinforced normal-strength concrete (NSC) and high-strength concrete (HSC) slender beams using artificial intelligence. Canadian. Journal of Civil Engineering. 2006; 33: 933-944. https://doi.org/10.1139/l06-033

[13] Collins M, Bentz E, Sherwood E. Where is shear reinforcement required? Review of research results and design procedures. ACI Structural Journal. 2008; 10(5): 590-600.

[14] Park MK, Lee DH, Ju, H, Hwang JH, Choi SH, Kim KS. Minimum shear reinforcement ratio of prestressed concrete members for safe design. Journal of Structural Engineering and Mechanics, 2015; 56(2): 317-340 https://doi.org/10.12989/sem.2015.56.2.317

[15] De Domenico D, Ricciardi G. A stress field approach for the shear capacity of RC beams with stirrups. Journal of Structural Engineering and Mechanics, 2020; 73(5): 515-527

[16] Yoon Y, Cook W, Mitchell D. Minimum Shear Reinforcement in Normal, Medium, and High-Strength Beams. ACI Structural Journal. 1996; 93(5): 576-584. https://doi.org/10.14359/9716

[17] Wang H. Reinforced concrete beam design for shear. University of Calgary, Alberta, Canada, 2002.

[18] Collins MP, Mitchell D. Shear design and evaluation of concrete structures. Concrete in Australia, 2014; 40(1): 28-38.

[19] Yang, KH, Ashour AF. Load capacity of reinforced concrete continuous deep beams. Journal of Structural Engineering, 2008; 134(6): 919-929. https://doi.org/10.1061/(ASCE)0733-9445(2008)134:6(919)

[20] Olalusi OB. Reliability Assessment of shear design provisions for reinforced concrete beams with stirrups, PhD Thesis, Dept. of Civil Engineering University of Stellenbosch, South Africa, 2018.

[21] Sagaseta J, Vollum R. Influence of beam cross-section, loading arrangement and aggregate type on shear strength. Magazine of Concrete Research, 2011; 63(2): 139-155. https://doi.org/10.1680/macr.9.00192

[22] Collins M, Bentz E, Sherwood E, Xie L. An Adequate theory for the shear strength of reinforced concrete structures. Magazine of Concrete Research, 2008; 60: 635-650, https://doi.org/10.1680/macr.2008.60.9.635

[23] American Concrete Institute - American Society of Civil Engineers (ACI ASCE) Committee 445. Report on Shear and Torsion. Recent Approaches to Shear Design of Structural Concrete. ACI Structural Journal, 1998; 124: 1375-1416. https://doi.org/10.1061/(ASCE)0733-9445(1998)124:12(1375)

[24] BS 8110-1, Structural use of Concrete-Part 1: code of practice for design and construction. British Standards Institution, UK, 1997.

[25] EN-1992-1-1: Eurocode 2 - Design of concrete structures - Part-1-1: General rules and rules for buildings. European committee for standardization, Brussels, 1991.

[26] ACI for structural Design ACI Committee 318. Building code requirements for structural concrete (ACI 318-11M) and Commentary. American Concrete Institute, 2011.

[27] CSA Standard A23.3-04. Design of concrete structures for buildings, Canadian Standards Association, Ontario, Canada, 2004.

[28] Mensah K. Reliability Assessment of structural concrete with special reference to stirrup design", PhD Thesis, University of Stellenbosch, South Africa, 2015.

[30] Viljoen C, Retief JV, Sykora M. Assessment of alternative shear resistance models for reinforced concrete sections. Conference: fib Symposium, Cape Town, 2016.

[31] Cladera A, Marí A. Shear strength in the new Eurocode 2. A step forward. Journal of Structural Concrete, 2007; 8(2): 57-66. https://doi.org/10.1680/stco.2007.8.2.57

[32] Todisco L, Reineck KH, Bayrak O. European design rules for point loads near supports evaluated with data from shear tests on non-slender beams with vertical stirrups", Journal of Structural Concrete, 2016; 17(2): 135-144. https://doi.org/10.1002/suco.201500089

[33] Marí A, Bairán J, Cladera A, Oller E, Ribas C. Shear-flexural strength mechanical model for the design and assessment of reinforced concrete beams. Journal of Structure and Infrastructure Engineering, 2015; 11(11): 1399-1419. https://doi.org/10.1080/15732479.2014.964735

[34] De-Domenico D, Ricciardi G. Shear Strength of RC beams with Stirrups using an Improved Eurocode 2 Truss Model with Two Variable-Inclination Compression Struts. Journal of Engineering Structures, 2019; 198: 109359.

[35] Reineck KH, Bentz E, Fitik B, Kuchma DA, Bayrak O. ACI-DAFstb databases for shear tests on slender reinforced concrete beams with stirrups. ACI Structural Journal, 2014; 111(5): 1147. https://doi.org/10.14359/51686819

[36] Jensen B, Lapko A. On shear reinforcement design and structural concrete beams on the basis of the theory of plasticity. Journal of Civil Engineering and Management, 2009; 15(4): 395-403. https://doi.org/10.3846/1392-3730.2009.15.395-403

[37] Mosley B, Bungey J, Hulse R. Reinforced Concrete Design to Eurocode 2. 6th Ed. Palgrave Macmillan, New York, USA, 2007.

[38] Holicky M. Reliability analysis for structural design. SUN MeDIA, South Africa, 2009.

[39] Collins MP. Evaluation of shear design procedures for concrete structures. A report prepared for CSA technical committee on reinforced concrete design, Canada, 2001.

Research Article

Seismic performance of masonry buildings in Iraq

Frak S. Alkenanee [1,a], Thaer M. S. Alrudaini[*2,b]

[1]Department of School Buildings. Directorate General for Education of Dhi Qar, Dhi Qar, Iraq.
[2]Department of Civil Engineering, College of Engineering, University of Basrah, Basrah, Iraq.

Article Info	Abstract
	Masonry buildings in seismic active regions experienced severe damages and collapses during earthquakes. Many researches were published concerning the seismic assessment of masonry buildings. Almost, all previous studies focused on historical buildings located in different regions in the world. This paper evaluates the seismic performance of ordinary residential masonry buildings located in three different regions in Iraq with various seismic intensities. Masonry buildings included houses, public and commercial buildings are common construction practice in Iraq. A three dimensional finite element modeling was adopted for the investigations in which nonlinear static pushover analyses were conducted to derive capacity curves of the building models. The finite element model was verified against experimental results presented in the literature. Capacity curves were compared with seismic capacity demands derived for each building model in both perpendicular principle axes. Two house building models with semi-regular and irregular plan layouts were considered in the investigations. The influence of the strength of the local clay bricks and the quality of the mortar on the seismic performance of the buildings was considered. Investigations have demonstrated that the plan layout and the strength of bricks and mortar are significantly influencing the seismic performance of the considered masonry buildings. For the considered models, the base shear capacity of the semi-regular house and that for the irregular house model have increased up to 233 % and 100 %, respectively by increasing strength of clay bricks from 9 MPa to 18 MPa. Using cement sand mortar with a compressive strength of 15.2 MPa rather than lime mortar that have compressive strength equal to 3.1 MPa contributes in increasing building shear capacity up to 20 %. Seismic vulnerability of masonry buildings in the considered cities with low to medium seismic intensities could be averted by using relatively high strength mortar and brick as well as adopting regular plans.

1. Introduction

Past earthquakes that occurred in many parts in the world cause severe damages and collapses to masonry buildings. In the last few decades, many researches have been conducted to investigate the efficient measures to mitigate the risk of earthquakes on buildings. Regarding to masonry buildings, the attention was relatively low with prime focus on historical buildings [1–8]. Investigations showed that the building is susceptible to heavy damages and collapse when subjected to the specified moderate to high seismic intensities. The past investigations have revealed the noncompliance of the built masonry buildings with requirements of design codes and standards especially for the moderate to strong earthquakes. Most of the previous studies were focused on old and heritage buildings with thick walls and four to five floors and located in moderate to high intensity earthquake regions. A great attention on seismic behavior of heritage and historical is

clear in recent studies. Among of these resent studies; Michele Betti et al. [9] used nonlinear static pushover analysis for the seismic assessment of basilica-type masonry church considering the Italian seismic guidelines. Also, Gianni Bartoli et al. [10] studied the seismic performance of historic masonry towers considering the Italian seismic guidelines. The Italian seismic guidelines specified three levels for seismic assessments. Gianni Bartoli et al. [10] reported and compared results of first and third specified levels of assessments and draw the conclusions based on the third level that involves nonlinear static pushover analysis. Francisco Brandão et al. [11] investigated the seismic resistance of the historical Nossa Senhora das Dores Church in Brazil using three dimensional finite element modeling. Linear time-history analyses were conducted considering two actual earthquake records. The results showed large displacements and high stresses in many parts of the church in which the potential damages were identified. These investigations provide the indications for the demanded retrofitting measures. Giulio Castori et al. [12] investigated the seismic vulnerabilities and defects of a multistory medieval building, located in Perugia, Italy. The investigations included simulating the building using three dimensional finite elements and the analysis were conducted by adopting nonlinear static pushover analysis. The analysis results showed poor seismic resistance compared to the demanded resistance. Motsa et al. [13] proposed a numerical investigation procedure for the seismic assessment of ancient monuments made of megalithic stones considering middle temple of the Mnajdra Megalithic structure. Demirlioglu et al. [14] studied the seismic behaviour of a historic brick masonry building using both linear and nonlinear pushover analyses considering equivalent frame method and finite element modeling. Bilgin and Ramadani [15] evaluated the structural behavior of historical Bajrakli Mosque located in western of Kosovo using static and dynamic analyses and considering both gravity and lateral seismic loads. Tomic´ et al. [16] suggested parametric investigations to assess the seismic behavior of historical masonry buildings that mainly affected by the uncertainty in material properties, construction details and modeling parameters. Usta [17] used three dimensional finite element modeling and fragility analysis to study the seismic performance of historical minarets in Antalya, Turkey. Hökelekli [18] conducted linear and nonlinear time history dynamic analysis considering actual earthquake records in Turkey to investigate the seismic performance of historical minaret in Turkey. Maras et al. [19] assessed the performance of historical Sütlü minaret mosque in Turkey using three dimensional finite element modeling and dynamic analysis. Six earthquake excitation records were applied to the model in which the performance was investigated. Further studies focused on public masonry buildings. among these studies; Estêvão and Tomás [20] studied the seismic performance of masonry school buildings in the region of Algarve (Portugal) according to provisions of Eurocode 8 (EC8) and based on nonlinear pushover analysis.

It is obvious that almost all the previous studies deal with seismic assessment of historical and heritage buildings in different regions in the world. In contrast; very little attention on investigating ordinary commercial or residential masonry buildings. In this paper, a focus is made on the seismic performance of ordinary masonry residential buildings in three different regions in Iraq. In Iraq, houses and some public and commercial buildings are limited to two stories and constructed using structural bearing wall systems. Bearing walls used for buildings in Iraq usually constructed using different types of clay brick units and concrete block units. Usually, the brick wall buildings in Iraq are constructed with slender walls of thickness equal to 0.25 m, height equal to 3 m and length up to 8 m and constructed without any consideration to the lateral loads. Iraq is located within a region of low to moderate seismic action [21]. During the last two decades, several low intensity earthquakes occurred in Iraq. Fortunately, the recorded intensity of the earthquakes was low and resulted in minor damages to some buildings [22]. Resent seismic events as well

as the new design requirements for buildings in Iraq demands the seismic evaluation of masonry buildings in Iraq. This paper presents a study on the seismic performance of ordinary masonry residential buildings (brick bearing wall type) considering the specified intensities of earthquakes in three different regions in Iraq. The investigations are focused on two storey residential houses constructed using clay brick units that represent the majority of masonry buildings in Iraq. The influence of different types of local clay bricks (Type A, Type B and Type C) and mortar strength on the seismic performance of the building models are also considered in this study. Nonlinear static pushover analysis method recommended by FEMA 356 [23] guidelines is adopted for the investigations. Macro model of the masonry walls is developed and adopted in this study by utilizing multi-purpose commercial finite element software ANSYS 11.0 [24]. Initially, the developed finite element model has been verified against experimental and numerical results published in the literature. Capacity curves that represent the varying drift at the top of the building with base shear are derived by conducting pushover analyses considering two principal directions. The pushover analysis approach was widely adopted in the previous studies [8,12,25–27]. Also, Capacity demands of the building model in different regions in Iraq are derived based on seismic intensity of each region, soil properties and the building model characteristics. Then the building models are assessed by comparing results of the capacity curves with the capacity demand of those considered building models. In the following sections, a model for masonry representation and verification of the developed model are presented. Also, analysis procedure, details of the considered models as well as the investigation results are presented and discussed. Finally, study considerations are highlighted and main conclusions points are drawn.

2. Masonry Representation

Masonry walls are modeled using equivalent homogeneous isotropic macro model that has properties accounting for the interaction effect of both bricks and mortar. The modeling is conducted by using the multi-purpose finite element software ANSYS 11.0 [24] in which the masonry walls are modeled using three dimensional solid elements (SOILD 65). The three dimensional brick (SOLID 65) elements with rectangular parallelepiped or cube shapes that have eight nodes at the corners is considered in this study. Each node has three translational degrees of freedom with capability of accounting cracking in tension and crushing in compression. In this study, the walls are discretized using the solid elements (SOLID 65) in which both linear elastic and nonlinear properties as well as failure criteria are defined for the elements. Elastic properties and nonlinear parameters for the solid elements represent the properties of masonry prism that accounting for the combined effect of brick units and mortar. Also, nonlinear stress strain curve is defined to model the nonlinear response of masonry walls that simulates the combined effect of bricks and mortar. This model was previously presented by Betti and Vignoli [2] and Betti and Galano [3] and Avossa and Malangone [28] to simulate masonry walls in which equivalent Drucker-Prager elastic perfectly plastic model along with William and Warnke [29] failure criteria were considered. In this study, macro model of masonry walls is developed considering stress-strain relation along with William and Warnke [29] failure criteria. The masonry walls are defined by the average stress strain relations of the constitutive materials involving bricks and mortar. The elastic modulus of masonry prism (E_m) and the compressive strength of a masonry prism (f'_m) in MPa are defined by the following relations [30]:

$$E_m = 550\, f'_m \qquad\qquad\qquad\qquad (1)$$

$$f'_m = 0.63.\, f_b^{\,0.49}.\, f_j^{\,0.32} \qquad\qquad\qquad (2)$$

where f_b = compressive strength of bricks in (MPa) and f_j = compressive strength of mortar in (Mpa).

A stress-strain curve of masonry prism is modeled using multi-linear relation for compression as depicted in Figure 1. The ascending part (first part) of the curve is defined by [30]:

$$f_m = f''_m \left(2\left(\frac{\varepsilon_m}{\varepsilon'_m}\right) - \left(\frac{\varepsilon_m}{\varepsilon'_m}\right)^2\right) \qquad \text{for} \qquad \varepsilon_m \le \varepsilon'_m \qquad (3)$$

where: $f''_m = 0.75\, f'_m$, ε'_m = strain at the ultimate stress f''_m, ε_m = strain corresponding to stresses f_m below ultimate value.

In this study, a constant strength of masonry prism equal to f''_m is assumed after the ultimate strength (f''_m) for the second part of the stress-strain curve in which (see Figure 1):

$$f_m = f''_m \qquad\qquad \varepsilon'_m < \varepsilon_m \le \varepsilon_{mu} \qquad\qquad (4)$$

The tension part is modeled using linear brittle stress strain relation up to ultimate tension strength that equal to $0.1\, f''_m$. The Poisson's ratio for masonry is set equal to (0.18) [28].
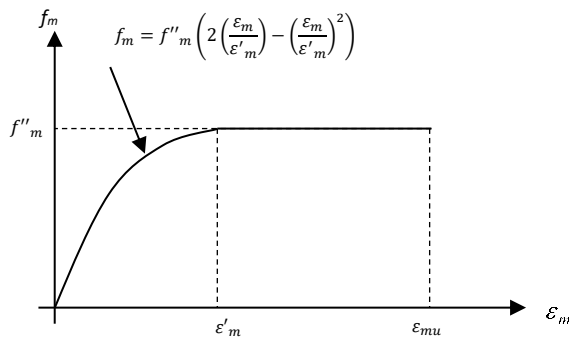
Fig. 1 Idealized stress-strain relationship of masonry prism

3. Verification of The Developed FEM Model of Wall Panels

The developed model is verified via experimental results of masonry wall specimen presented in Avossa and Malangone [28]. The studied model consisted of plane wall with two vertical flanges at the two ends of the wall. The dimensions of the wall model were 3.6 m length, 2.0 m height and 0.15 m thickness. The dimensions of the two flanges were 0.6 m width and 0.15 m thickness. In addition; two concrete slabs were placed at the top and beneath the wall specimen. The dimensions of the top slab were 0.16 m x 1.4 m x 4.0 m;

while that of the bottom slab were 0.18 m x 0.9 m x 4.0 m. Material properties include modulus of elasticity of the masonry wall E_m= 2460 MPa, compressive strength f'_m = 5.576 MPa, Poisson's ratio $v = 0.18$, density of the masonry wall $= 1.8 \times 10^{-5}\ N/mm^3$ and tensile strength of the masonry wall (f_t) =0.194 MPa. The finite element of the considered masonry wall is shown in Figure 2. In this study a cube brick element is adopted with dimensions equal to 150 x 150 x 150 mm³. This model has been verified against experimental and numerical analysis and provide very good agreement. Several preliminary trials with other models were considered with different smaller size elements equal to 50 x 50 x 50 mm³ and 75 x 75 x 75 mm³ in which took much longer time with slightly different results that make the analysis very tedious. The lateral load was applied at the top slab in the direction parallel to the plane of the wall. The experimental and numerical results of the lateral load versus lateral displacement that presented by Avossa and Malangone [28] are illustrated in Figure 3. Also, the numerical results obtained by using the developed FEM model in this study are illustrated in Figure 3. It is obvious from Figure 3, that the predicted results of the load displacement curve have a good agreement with the previous experimental and numerical results.
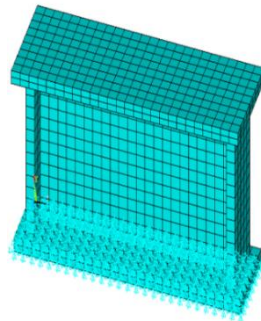
Fig. 2 Finite element modeling model of in-plane loaded masonry wall with end flanges
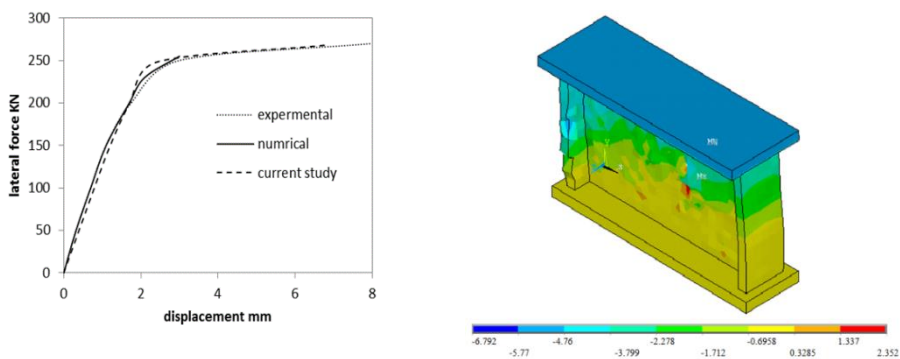
Fig. 3: a) Load- displacement curve; b) deformation shape of the wall model

In addition, experimental test of a simple model of in- plane loaded masonry wall panel with central opening that presented by Akhaveissy [31] is considered for the verification of the developed model. The wall was made from clay brick units had dimensions equal to

210 mm x 52 mm x 100 mm. The mortar thickness was 10 mm. The height/width ratio of wall was equal to about one in which the height and the width of the wall were equal to 1000 mm and 990 mm, respectively. Two relatively stiff steel beam sections were installed for clamping the top and bottom boundaries of the wall for the laboratory test. The masonry have modulus of elasticity E_m= 7635 MPa, compressive strength of masonry prism f'_m=10.5 MPa, Poisson's ratio $v = 0.15$ and tensile strength f_t=1.05 MPa. The finite element idealization and boundary conditions are shown in Figure 4. A vertical pressure of 0.3 MPa was applied at the top of the wall before applying the horizontal load. Pushover horizontal load was applied gradually (considering 10 kN each load step) at the top steel beam section in which the drift was recorded versus the load. Analysis results including deformed shape as well as the load – displacement curve are presented in Figure 5. Also, comparison with previous experimental and numerical results are given in Figure 5. An excellent agreement between the results obtained from the developed model with previous experimental and numerical model has demonstrated as shown in Figure 5.

(a)   (b)
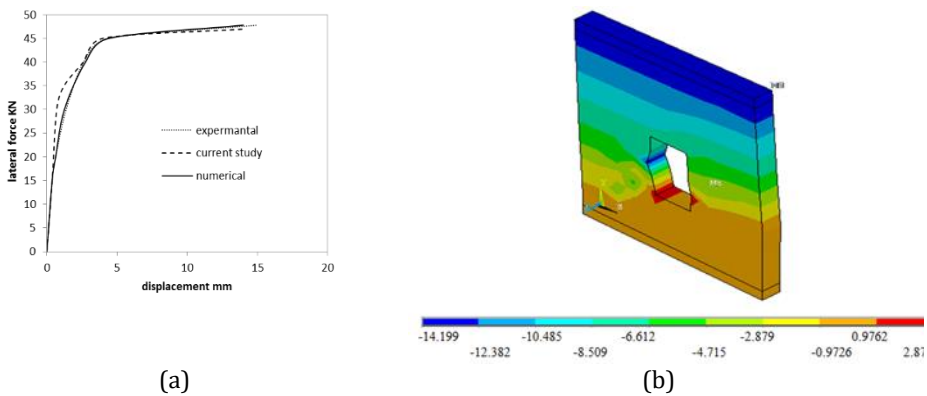
Fig. 4 Finite element modeling of in-plane loaded masonry wall with central opening
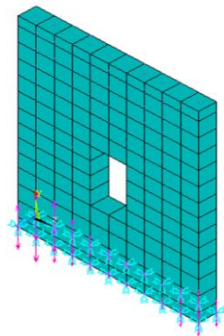
Fig. 5   a) Load- displacement curve; b) deformation shape of the wall model

4. Non-Linear Pushover Analysis

This study is limited to nonlinear static push over approach for evaluating seismic performance of masonry buildings. The nonlinear static pushover approach was used to investigate the ultimate base shear. Then determined base shear was compared with demanded base shear to evaluate the seismic performance of the considered model. A non-linear static pushover analysis is conducted to derive lateral load displacement capacity

curves of building models. The pushover capacity curves refer to the relation between base shear and horizontal displacement at the top of the building (the control point at the roof). The seismic performance of the building is evaluated by comparing the base shear capacity with the seismic base shear demand corresponding to the brittle behavior. However, the ultimate displacement is compared with displacement demand for the ductile behavior. The safe performance of the building is achieved by satisfying either the base shear demand for brittle response or the displacement demand for ductile response [32]. The seismic base shear demand is determined using the procedure specified in FEMA 356 [23]. This study focuses only on base shear demands in which masonry buildings exhibit brittle behavior that demonstrated by very small ultimate lateral displacements. In the non-linear static analysis, initially the gravity loads are placed and kept constant for a specific period of time, subsequently the lateral forces that represent seismic action are applied gradually considering load time steps. In this study, each load step equal to 0.1 of demanded base shear is considered in this study. The analysis is conducted by applying the lateral forces in two perpendicular directions, not acting simultaneously. Pushover analysis is conducted twice on each house buildings along two orthogonal directions. At the beginning, the pushover analysis is performed by applying lateral loads along transverse direction. Then the pushover analysis is performed by applying lateral loads along longitudinal direction. The lateral loads are distributed along the building height and applied at the floors level by adopting the lateral load distribution formula specified by FEMA 356 [23]. The seismic base shear demand is obtained using the following equation [33]:

$$V = C_s \ W \tag{8}$$

where; C_s = seismic response coefficient and W = effective seismic weight. Both seismic response coefficient and the effective seismic weight are computed using the procedure specified in ASCE 7-17 [33] based on the soil properties of the region and the earthquake spectral acceleration at the considered region.

5. Building Models

In this study, two house models each with two storeys are considered. Figure 6 illustrates two typical plans of considered house models including dimensions, locations of doors and windows. The first house represents simple typical semi regular house model, while the second house represents typical irregular house.

The height of storey is 3 m, the dimensions of all the doors are 1 m width and 2.1 m height and the dimensions of the windows are 2 m width and 1.5 m height. In Iraq, it is common of practice casting continuous reinforced concrete lintel beam along the walls at the level above the openings (doors and windows). The lintel dimensions are 0.24 m width and 0.3 m depth. The walls are constructed using clay brick units in either lime mortar or cement sand mortar. In this study, the influence of the strength of brick units and mortar on the seismic performance of masonry buildings in Iraq is considered. In Iraq, clay bricks are classified into three types according to the strength that include type A, type B and type C that have compressive strength of 18 MPa, 13 MPa and 9 MPa, respectively. Two types of mortars are considered including lime mortar has strength equal to 3.1 MPa denoted by mortar 1 and cement sand mortar with a compressive strength equal to 15.2 MPa and denoted by mortar 2.

Table 1 illustrates the properties of the materials corresponding to the considered models. The houses are subjected to both live loads (2 kN/m²) and dead loads (7.6 kN/m² and 4.8 kN/m² for roof and floor; respectively, including self-weight). The houses are studied for seismic demand of three regions including Baghdad city, Kirkuk city and north of Amara city. Spectral response acceleration at short period (Ss) are 0.3, 0.6 and 1.0 for Baghdad city, Kirkuk city and north of Amara city, respectively [34]. Site class D for soil properties is adopted in this study as recommended by ASCE 7-17 [33] when the details of soil properties are unknown. The finite element models of the considered houses are shown in Figure 7. Masonry walls are modeled using the developed model in previous section. Slabs and the continuous lintel are modeled using linear elastic material considering properties of concrete. house.
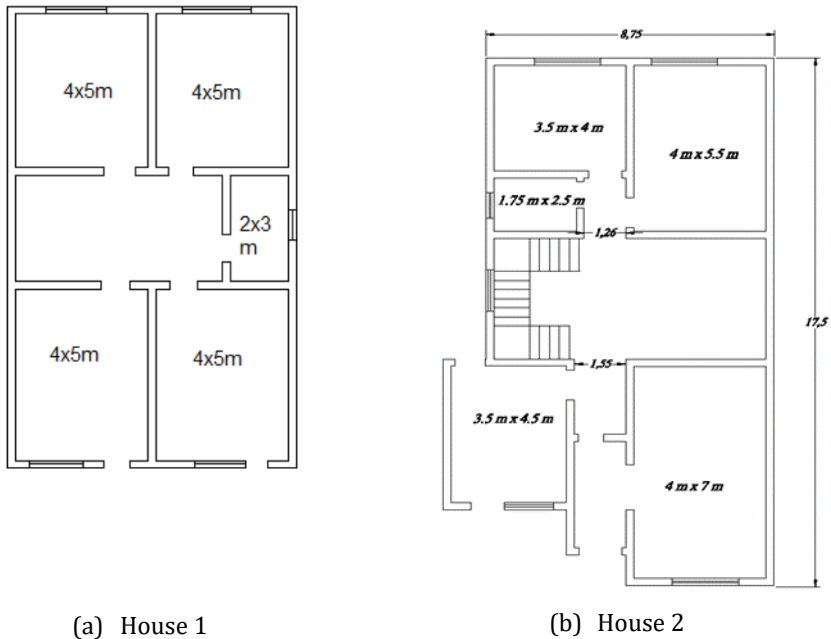
(a) House 1   (b) House 2

Fig. 6 The details and dimensions of the typical house models

Table 1. Strength of mortar, brick and masonry prism

Brick Type	Mortar	Compressive strength (MPa)		
		Mortar fj	brick fb	Wall f''_m
A	1	3.1	18	2.79
B	1	3.1	13	2.38
C	1	3.1	9	1.99
A	2	15.2	18	4.65
B	2	15.2	13	3.96
C	2	15.2	9	3.31

(a) House 1   (b) House 2
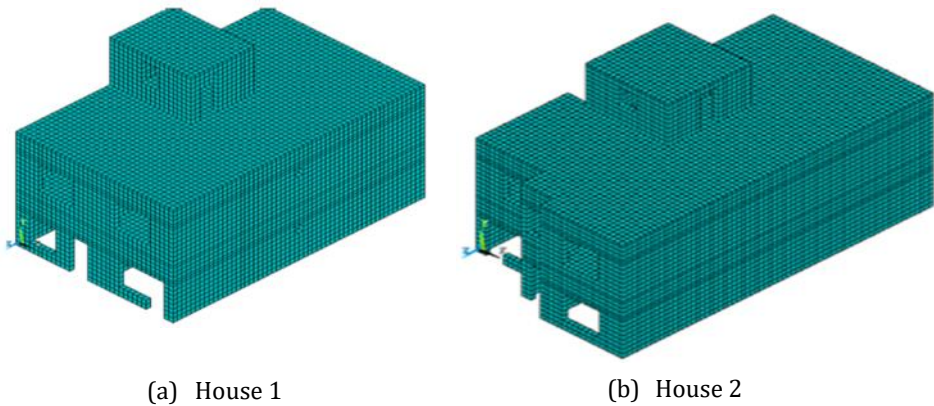
Fig. 7 Finite element modeling of the houses

6. Analysis Results

Pushover analysis is conducted twice on each house buildings along two orthogonal directions. At the beginning, lateral loads were applied along transverse direction in which the analysis was conducted and the results were predicted. Another analysis was conducted separately by applying the lateral loads along the longitudinal direction. The load is applied gradually considering load time steps. In this study, each load step equal to 0.1 of demanded base shear is considered in this study. Results of pushover analysis in terms of final deformations pattern are illustrated in Figures 8 and 9 for both house models. The capacity curves that represent base shear versus lateral displacement of the house models are illustrated in Figures 10 and 11. Tables 2 to 5 illustrate the comparison results of the ultimate base shear determined from pushover analysis with the seismic base shear demand. The seismic demand in Tables 2 to 5 are obtained based on the spectrum accelerations recommended by Iraqi seismic code. The capacity curves illustrated in Figures 10 and 11 show that both house models exhibit better seismic performance in longitudinal direction (z- direction) than in the transverse direction (x-direction). Also, it is obvious from Figures 10 and 11 and Tables 2-5 that the performance of the house models has significantly improved by using brick type A instead of using brick type B and brick type C due to the increase in compressive strength of the brick type A over those of brick types B and C. Also, Tables 2-5 show a significant increase in base shear capacity of the house models by using mortar 2 rather than mortar 1 due to increase in compressive strength. For instance, Table 2 shows that base shear capacity of the house 1 with mortar 1 have increased up to 233.3 % and 225 % in the longitudinal and transversal directions, respectively by using brick type A over that of using brick type C. On the other hand, Table 3 shows that base shear capacity of the house 1 with mortar 2 has increased up to 71.4 % and 50 % in the longitudinal and transversal directions, respectively by using brick type A over that of using brick type C. Also, Tables 2 and 3 show that using stronger cement sand mortar rather than the weak lime mortar results in increase in base shear capacity of the house 1 with brick type A by about 20 % and 15.4 % in the longitudinal and transversal directions, respectively. Furthermore, Tables 2-5 illustrate the seismic performance of the adopted house models in terms of potential collapse.
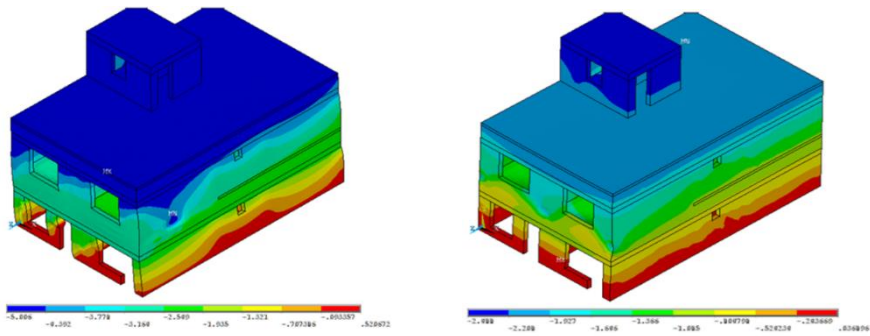
(a) Transverse action, brick Type C (b)Longitudinal action, brick Type C

Fig. 8 Deformation shapes of the house 1
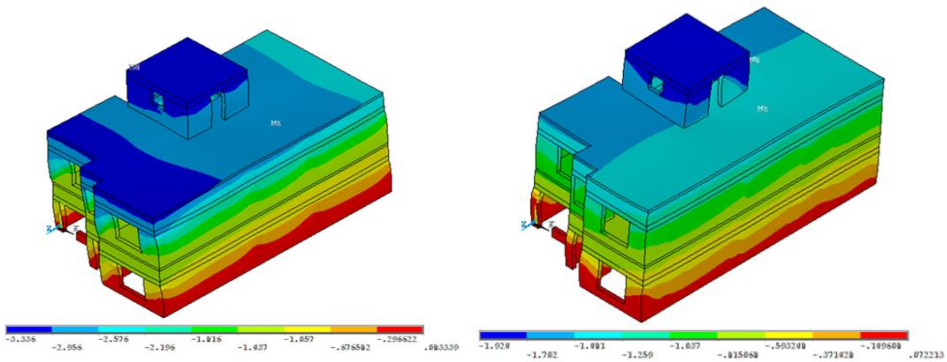
(a) Transverse action, brick Type C (b)Longitudinal action, brick Type C

Fig. 9 Deformation shapes of the house 2
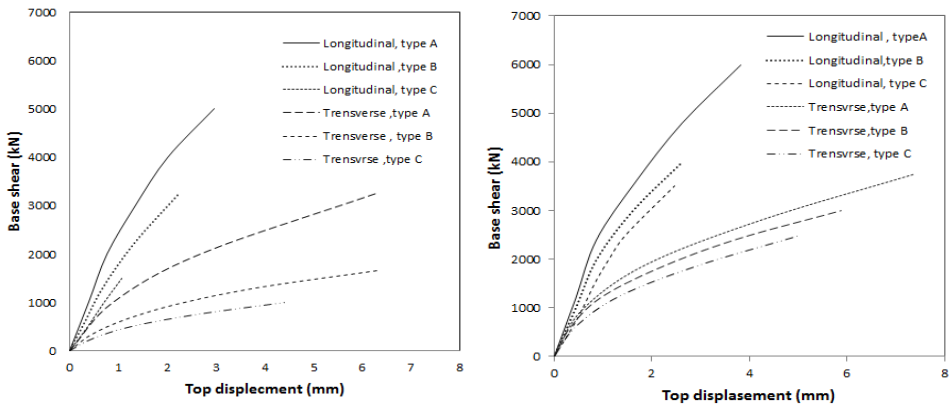
(b) Transverse action, brick Type C (b)Longitudinal action, brick Type C

Fig. 10 Capacity curves corresponding to house 1

Regarding the seismic performance of the house 1, Table 2 shows that the house 1 with brick type A has survived the collapse in which the base shear capacity is larger than the demanded base shear. However, the collapse of the house 1 with brick type C and lime mortar 1 in north of Amara city has demonstrated due to the higher demand base shear compared with the house base shear capacity. In contrast, Tables 4 and 5 show that the house 2 performs well along the longitudinal direction while the collapse has demonstrated in the perpendicular direction except for case with brick type A and cement sand mortar in Baghdad city in which has the lowest shear demand. The poor performance along the transversal direction compared to the longitudinal direction of the house 2 stems from its irregular plan that causing additional torsional stresses.

(a)Transverse action, brick Type C   (b)Longitudinal action, brick Type C
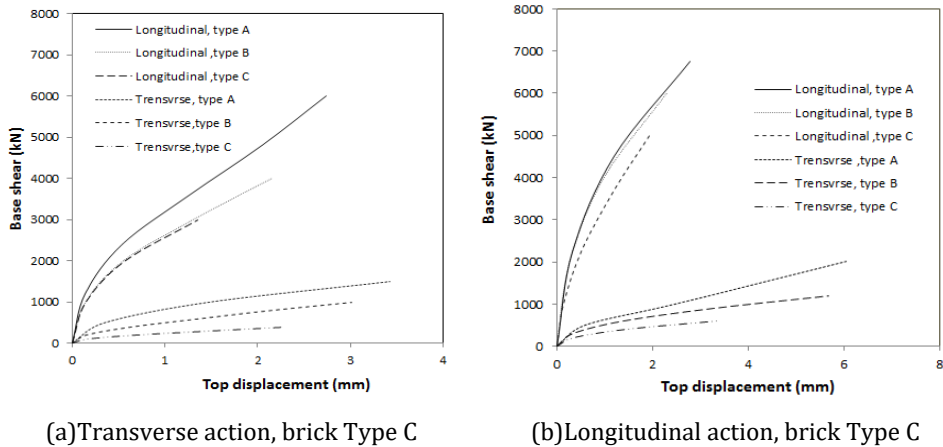
Fig. 11 Capacity curves corresponding to house 2

Table 2. Ultimate capacity of the house1versus seismic demands considering mortar 1

Brick Type	City	Demand Base shear (kN)	Base shear capacity (kN)		Result
			Short direction	Long direction	
A	Baghdad	732	3250	5000	Survived from collapse
	Kirkuk	1267	3250	5000	Survived from collapse
	North of Amara	1785	3250	5000	Survived from collapse
B	Baghdad	732	1667	3250	Survived from collapse
	Kirkuk	1267	1667	3250	Survived from collapse
	North of Amara	1785	1667	3250	Collapse along short
C	Baghdad	732	1000	1500	Survived from collapse
	Kirkuk	1267	1000	1500	Collapse along short
	North of Amara	1785	1000	1500	collapse

Table 3. Ultimate capacity of the house1versus seismic demands considering mortar 2

Brick Type	City	Demand Base shear (kN)	Base shear capacity (kN)		Result
			Short direction	Long direction	
A	Baghdad	732	3750	6000	Survived from collapse
	Kirkuk	1267	3750	6000	Survived from collapse
	North of Amara	1785	3750	6000	Survived from collapse
B	Baghdad	732	3000	4000	Survived from collapse
	Kirkuk	1267	3000	4000	Survived from collapse
	North of Amara	1785	3000	4000	Survived from collapse
C	Baghdad	732	2500	3500	Survived from collapse
	Kirkuk	1267	2500	3500	Survived from collapse
	North of Amara	1785	2500	3500	Survived from collapse

Table 4. Ultimate capacity of the house 2 versus seismic demands considering mortar 1

Brick Type	City	Demand Base shear (kN)	Base shear capacity (kN)		Result
			Short direction	Long direction	
A	Baghdad	1021	1500	6000	Survived from collapse
	Kirkuk	1768	1500	6000	Collapse along short direction
	North of Amara	2490	1500	6000	Collapse along short direction
B	Baghdad	1021	1000	4000	Collapse along short direction
	Kirkuk	1768	1000	4000	Collapse along short direction
	North of Amara	2490	1000	4000	Collapse along short direction
C	Baghdad	1021	460	3000	Collapse along short direction
	Kirkuk	1768	460	3000	Collapse along short direction
	North of Amara	2490	460	3000	Collapse along short direction

The presented investigation results in Tables 2-5 represent the global performance of masonry buildings considering nonlinear static analysis. Considering the global seismic performance of the buildings in this study is in line with several previous published studies [10,16,20]. In contrast, investigations presented in Francisco Brandão et al. [11], Hökelekli [18] and Maras et al. [19] considered local damages in buildings using stress analysis by adopting linear or/and nonlinear time history analyses. On the other hand, several previous investigations considered both local and global performance of buildings [9,17]. Investigation results have demonstrated various performance of masonry buildings due to various earthquake intensities as well as various building plans and structural characteristics of the buildings that stem from using various construction methods and materials. This study focused on modern ordinary masonry buildings located in three cities

in Iraq while almost all previous studies had focused on old and historical masonry buildings [9-20] located in different regions in the world.

Table 5. Ultimate capacity of the house 2 versus seismic demands considering mortar 2

Brick Type	City	Demand Base shear (kN)	Base shear capacity (kN)		Result
			Short direction	Long direction	
A	Baghdad	1021	2003	6750	Survived from collapse
	Kirkuk	1768	2003	6750	Survived from collapse
	North of Amara	2490	2003	6750	Collapse along short direction
B	Baghdad	1021	1200	6000	Survived from collapse
	Kirkuk	1768	1200	6000	Collapse along short direction
	North of Amara	2490	1200	6000	Collapse along short direction
C	Baghdad	1021	600	5000	Collapse along short direction
	Kirkuk	1768	600	5000	Collapse along short direction
	North of Amara	2490	600	5000	Collapse along short direction

7. Conclusions

Almost, the majority of building construction in Iraq were designed and constructed without adopting any seismic provisions especially residential masonry buildings. During the last two decades, several earthquakes occurred in Iraq. Fortunately, the recorded intensity of the earthquakes was low and resulted in minor damages to some buildings. However, Iraq is located within low to moderate seismic action region. Therefore, the seismic design and assessment of buildings is demanded according to the new design requirements for buildings in Iraq. In this study, the seismic performance of unreinforced masonry building models in Iraq is investigated considering three regions with different seismic levels. In Iraq, houses and some public and commercial buildings are limited to two stories and constructed using structural bearing wall systems. Bearing walls used for buildings in Iraq usually constructed using different types of clay brick units and concrete block units. A three dimensional finite element simulation is adopted for the investigations using multi-purpose finite element software ANSYS. The finite element model is verified against experimental results of masonry wall models available in the literature. Two typical house models constructed using local clay brick unites represent an important percentage of masonry building stock in Iraq are considered in this study. Three types of local clay brick units including type A, type B and type C that classified in Iraqi Standards according to their strength are considered in the parametric investigations. Also, two typical mortar types including lime mortar and cement sand mortar with different compressive strengths are considered in the parametric investigations. The two house models involve two storey houses, one with semi regular plan and the other with irregular plan. Capacity curves representing base shear versus lateral displacement at the top of the building models are derived using pushover analysis conducted in two principal directions and compared with the seismic demands in different regions in Iraq.

Based on the numerical analysis results, the following conclusions can be drawn:

1. The verification analysis results show that homogenized three-dimensional model that developed in this study have been successfully predict the nonlinear behavior of the masonry walls under lateral loads.

2. The base shear capacity of the brick wall buildings is very sensitive to the building layout as well as material properties and site location.

3. For the considered models, the base shear capacity along the longitudinal direction of the semi-regular house 1 model have been increased up to 233 % by increasing strength of clay bricks from 9 MPa to 18 MPa that representing strength of clay brick types C and A, respectively. In contrast, the base shear capacity of the irregular house 2 model has shown an increase of up to 100 % by increasing strength of clay bricks from 9 MPa to 18 MPa that representing strength of clay brick types C and A, respectively.

4. Using cement sand mortar with a compressive strength of 15.2 MPa rather than lime mortar that have compressive strength equal to 3.1 MPa contributes in increasing building shear capacity up to 20 %.

5. The seismic vulnerability has demonstrated along the short length of the building more than along the long direction regardless the total length of the walls along any direction.

6. House model with semi regular plan perform better than that with irregular plan due to producing torsional response that increases the stresses especially along the short direction.

7. Seismic vulnerability of masonry buildings in the considered cities with low to medium seismic intensities could be averted by using relatively high strength mortar and Type A brick as well as adopting regular plans.

The above conclusions were drawn based on nonlinear static pushover analysis and limited to only two storey houses with typical plans. Further investigations are recommended for future study considering public buildings such as one and two storey masonry schools, health centers and two storey office buildings that are common practice masonry buildings in Iraq. Also, further investigations are required by adopting nonlinear time history analyses considering actual recorded earthquake excitations.

Acknowledgement

References

[1] Lopes M. Evaluation of the seismic performance of an old masonry building. 11th World Conf. Earthq. Eng., 1996, p. 1484.

[2] Betti M, Vignoli A. Numerical assessment of the static and seismic behaviour of the basilica of Santa Maria all'Impruneta (Italy). Constr Build Mater 2011;25:4308-24. https://doi.org/10.1016/j.conbuildmat.2010.12.028

[3] Betti M, Galano L. Seismic analysis of historic masonry buildings: The Vicarious Palace in Pescia (Italy). Buildings 2012;2:63-82.

https://doi.org/10.3390/buildings2020063

[4] Khadka SS. Seismic Performance of Tradational Unreinforced Masonry Building in Nepal. Kathmandu Univ J Sci Eng Technol 2013;9:15-28.

[5] Clementi F, Gazzani V, Poiani M, Lenci S. Assessment of seismic behaviour of heritage masonry buildings using numerical modelling. J Build Eng 2016;8:29-47. https://doi.org/10.1016/j.jobe.2016.09.005

[6] Kocaman I, Kazaz I, Kazaz E. Seismic load capacity of historical masonry mosques by rigid body kinetics. Int J Archit Herit 2019. https://doi.org/10.1080/15583058.2019.1570389

[7] Bilgin H, Korini O. Seismic capacity evaluation of unreinforced masonry residential buildings in Albania. Nat Hazards Earth Syst Sci 2012;12:3753-64. https://doi.org/10.5194/nhess-12-3753-2012

[8] Bartoli G, Betti M, Monchetti S. Comparative seismic assessment of masonry towers through nonlinear analysis: The RiSEM experience. Brick Block Mason. Proc. 16th Int. Brick Block Mason. Conf. Padova, Italy, 26-30 June 2016, CRC Press; 2016, p. 87-94. https://doi.org/10.1201/b21889-9

[9] Betti M, Borghini A, Boschi S, Ciavattone A, Vignoli A. Comparative seismic risk assessment of basilica-type churches. J Earthq Eng 2018;22:62-95. https://doi.org/10.1080/13632469.2017.1309602

[10] Bartoli G, Betti M, Monchetti S. Seismic Risk Assessment of Historic Masonry Towers: Comparison of Four Case Studies. J Perform Constr Facil 2017;31:4017039. https://doi.org/10.1061/(ASCE)CF.1943-5509.0001039

[11] Brandão F, Diógenes A, Fernandes J, Mesquita E, Betti M. Seismic behavior assessment of a brazilian heritage construction. Frat Ed Integrita Strutt 2018;12:14-32. https://doi.org/10.3221/IGF-ESIS.45.02

[12] Castori G, Corradi M, Borri A, Sisti R, De Maria A. Macro element and dynamic seismic analysis of the medieval government building of Perugia, Italy. Int J Mason Res Innov 2019;4:297-311. https://doi.org/10.1504/IJMRI.2019.102529

[13] Motsa SM, Drosopoulos GA, Stavroulaki ME, Maravelakis E, Borg RP, Galea P, et al. Structural investigation of Mnajdra megalithic monument in Malta. J Cult Herit 2020;41:96-105. https://doi.org/10.1016/j.culher.2019.07.004

[14] Demirlioglu K, Gonen S, Soyoz S, Limongelli MP. In-Plane Seismic Response Analyses of a Historical Brick Masonry Building Using Equivalent Frame and 3D FEM Modeling Approaches. Int J Archit Herit 2020;14:238-56. https://doi.org/10.1080/15583058.2018.1529208

[15] Bilgin H, Ramadani F. Numerical Study to Assess the Structural Behavior of the Bajrakli Mosque (Western Kosovo). Adv Civ Eng 2021;4620916. https://doi.org/10.1155/2021/4620916

[16] Tomić I, Vanin F, Beyer K. Uncertainties in the seismic assessment of historical masonry buildings. Appl Sci 2021;11:1-36. https://doi.org/10.3390/app11052280

[17] Usta P, Bozdağ Ö, Işil Çarhoğlu A. Appraisal of structural behavior of afyon sandıklı ulu mosque. El-Cezeri J Sci Eng 2020;7:871-81.

[18] Hökelekli E, Demir A, Ercan E, Nohutçu H, Karabulut A. Seismic assessment in a historical masonry minaret by linear and non-linear seismic analyses. Period Polytech Civ Eng 2020;64:438-48. https://doi.org/10.3311/PPci.15126

[19] Maras MM, Özmen A, Sayın E, Ayaz Y. Seismic Assessment of the Historical Sütlü Minaret Mosque. Period Polytech Civ Eng 2022;66:445-59.

https://doi.org/10.3311/PPci.19400
[20] Estêvão JMC, Tomás B. Ranking the Seismic Vulnerability of Masonry School Buildings according to the EC8-3 by Using Performance Curves. Int J Archit Herit 2021:1-16. https://doi.org/10.1080/15583058.2021.1904458
[21] Sissakian VK, Abdul Ahad AD, Hamid AT. Geological Hazards In Iraq. Classification And Geographical Distribution. 2011.
[22] Jasim NA. Seismicity Evaluation of Central and. Iraqi J Sci 2010;54:911-8.
[23] FEMA. Prestandard and Commentary for the Seismic Rehabilitation of Buildings. Rehabil Requir 2000:1-518.
[24] ANSYS 11.0 Inc., "ANSYS user's manual", Version 11.0, U.S.A.
[25] D'Ayala D. Assessing the seismic vulnerability of masonry buildings. Handb. Seism. risk Anal. Manag. Civ. Infrastruct. Syst., Elsevier; 2013; 334-65. https://doi.org/10.1533/9780857098986.3.334
[26] Castori G, Borri A, De Maria A, Corradi M, Sisti R. Seismic vulnerability assessment of a monumental masonry building. Eng Struct 2017;136:454-65. https://doi.org/10.1016/j.engstruct.2017.01.035
[27] Aşıkoğlu A, Vasconcelos G, Lourenço PB, Pantò B. Pushover analysis of unreinforced irregular masonry buildings: Lessons from different modeling approaches. Eng Struct 2020;218:110830. https://doi.org/10.1016/j.engstruct.2020.110830
[28] Avossa AM, Malangone P, Civile I, Ingegneria F, Università S, Ce A. a New Model for the Seismic Performance Assessment of Masonry Structures. IX Int Forum Le Vie Dei Merc SAVE Heriatage, Aversa, Capri 2002;1:1-10.
[29] Chen WF, Saleeb AF, Dvorak GJ. Constitutive Equations for Engineering Materials, Volume I: Elasticity and Modeling. J Appl Mech 1983;50:703-703. https://doi.org/10.1115/1.3167127
[30] Kaushik HB, Rai DC, Jain SK. Uniaxial compressive stress-strain model for clay brick masonry. Curr Sci 2007;92:497-501.
[31] H. Akhaveissy A. The DSC Model for the Nonlinear Analysis of In-plane Loaded Masonry Structures. Open Civ Eng J 2012;6:200-14. https://doi.org/10.2174/1874149501206010200
[32] Engineering AS of C. Seismic rehabilitation of existing buildings, American Society of civil engineers; 2007.
[33] Engineers AS of C. Minimum design loads and associated criteria for buildings and other structures. American Society of Civil Engineers; 2017.
[34] Jasim ML, Yassin LA, Resheq AS. Seismic Maps in the Iraqi Seismic Codes and their Impact on Buildings. Cent ASIAN J Theor Appl Sci 2022;3:137-46.

Research Article

Friction limit prediction of high-strength bolted connections using finite element method

Mojtaba Hosseini[a], Amir Mohammad Amiri[b], Peyman Beiranvand[c], Esfandiyar Abasi [d]

Department of Civil Engineering, Lorestan University, Khorramabad, Iran

Article Info	Abstract
	In this study, the aim is to deduce the static friction limit of contact interfaces in bolt friction joints by analyzing other bolt friction joints with the same contact surface but in a different shape. By using the Weibull mathematical distribution to deal with microelements on the contact surface, the friction limit of a certain type of bolt connection was statistically predicted from other types of bolt connections with the same contact surface. As a result, this research succeeded to predict the friction limit of bolt joints with different numbers of contact surfaces and with different numbers of bolt rows. Another result of this research both the stress ratio and the Weibull stress ratio showed a high prediction accuracy.

1. Introduction

High-strength bolted friction (HSF) joints are widely used as field joints for structural members of steel bridges. HSF joints have many advantages such as easy construction, good rigidity, and good fatigue resistance. HSF joints have become one of the main connection types in steel bridges. Although three different Chinese specifications [1–3] and other specifications in the world [4,5] have specified design concepts of HSF joints, there still exist many issues remaining to be solved: such as the detailed stress state of the connected plate, the load transfer factor of each bolt, and the friction stress distribution of the contact surfaces. The bolt friction joints are widely used in steel structures. The friction coefficient is often used to evaluate the loading capacity of bolt friction joints and it is only decided by the contact surface specification like 0.45 for an organized zinc-rich paint surface (IOZ) and 0.4 for the blasted surface in design. However, experimentally obtained friction coefficients μ have dispersion even if they have been made by the same contact surface specification. It could be considered that the micro surface condition is ununiformed for many reasons, for example, the spatial dispersion in one surface [6], the number of contact surfaces [7], bolt columns [8], and so on. Experimental results showed that the friction coefficient of a double-lap bolt joint is slightly higher than that of a single-lap bolt joint both in IOZ and blasted surface [7], and friction coefficients also varied when the number of bolt columns changed [8].

Based on these issues, not only the contact surface specification but also many other reasons should also be considered in a real situation so that we can get a rational friction limit considering relationships between local stress and dispersion of micro surface condition. To achieve that, the computational simulation could be considered because it

provides detailed local stresses in contact surfaces and may efficiently save experimental costs at the same time.

Recently, the finite element (FE) method was used to investigate the behavior of this type of connection. Citipitioglu et al. [9] studied the influence of bolt pretension and the effect of friction and friction between the connection components on the behavior of such connections by using the FE method. In their FE models, all connection components were modeled using brick elements, while the effect of adjacent surfaces was considered. A FE model with 3-Dsolid elements was established to investigate the bearing failure of cold-formed steel bolted connections under shear by Chung a dip [10]. Ju et al. [11] used the 3-D elastoplastic FE method to study the structural behavior of the butt-type steel bolted joint. The numerical results were compared with AISC specification data.

Soo et al. [12] used the ABAQUS program to establish FE models with 3-D solid elements. Non-linear material and non-geometric analyses were carried out to predict the load-displacement curves of bolted connections. Su et al. [13] developed an iterative procedure through a computer program to calculate the non-linear deformation of bolt groups under in-plane eccentric loads based on the assumptions of elastoplastic behavior of bolts and rigid body movement of the bolt group. Yu et al. [14] explored the use of an explicit dynamic solver to analyze bolted steel connections. By comparing the results with those from static analysis and tests, it was shown that the explicit dynamic solver, with proper control, gives satisfactory predictions of the responses of steel connections up to post-failure deformations. Bouchair et al. [15] studied the behavior of stainless steel bolted connections.

This research focuses on the friction coefficients of different kinds of bolted joints with the same contact surface specification. This research aims to find a local approach-based rational method to predict the friction limit of many types of different high-strength bolt joints from experimentally obtained friction coefficients of one type of joint with the same contact surface specification. This research firstly speculates the friction limit of single-lap bolt joints from double-lap bolt joints and secondly speculates the friction limit of multi-rows bolt joints from 2-rows bolt joints.

2. Method and Materials

2.1. Subject Description

Fig. 1 shows the geometry of experimental specimens, and Table 1 shows their specifications. P2-15 and B2-10 (PB) are 2face friction joints, the former with inorganic zinc and the latter with blasted specimens. P1-15 and B1-10 (PB) are 1-face friction joints, the former with inorganic zinc and the latter with blasted specimens [7]. A structural steel SM490Y was used for the base plate and a connecting plate of the specimens, and F10T high-strength bolts (nominal diameter M22, length beneath the head 90 mm) were used. For the sliding side, a higher bolt axial force was introduced so that the main friction would precede on the friction side where the bolt axial force was controlled.

Rows of friction joints with blasted contact surfaces. SS41 was used for the base plate and connecting plates of the specimens, and F10T high-strength bolts (nominal diameter M20, length beneath the head 85 mm) were used and tightened to standard bolt tension (nominal value 18.2 t) on the sliding side [8]. If the ratio of friction/yield strength is smaller than 1 means bolt joints will have friction before baseboard yield when designed.
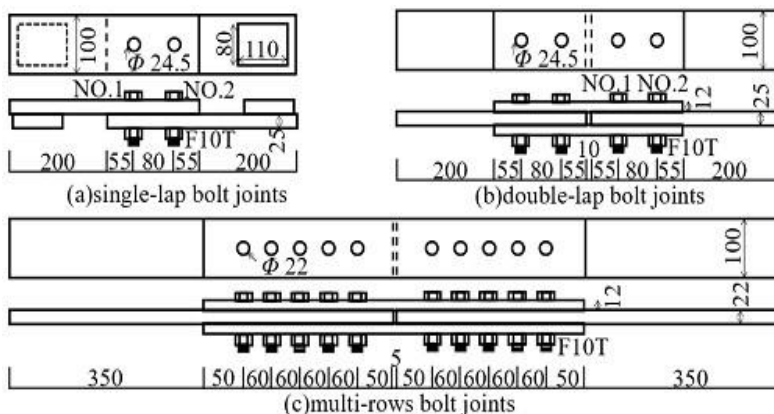
Fig. 1 Experimental specimens

Table 1. Specifications of experimental specimens

Specimens name	Contact surface	Number of contact surfaces	Rows of bolts	The ratio of friction/yield strength	Number of specimens
P1-15	IOZ	1	2	0.31	3
P2-15	IOZ	2	2	0.61	3
B1-10	Blast	1	2	0.24	3
B2-10	Blast	2	2	0.49	3
MB-20-2-12	Blast	2	2	0.8	2
MB-20-3-12	Blast	2	3	1.2	2
MB-20-4-12	Blast	2	4	1.6	2
MB-20-5-12	Blast	2	5	2.0	2

2.2. Experimental Methods and Results

In the friction capacity experiment of specimen PB, the bolt axial force was measured by strain gauges attached to the bolt shaft on the friction side immediately before loading, and the average strain on the front and back of the base plate was measured by strain gauges attached to the front and back of the base plate during the test, the amount of friction was measured by a clip gauge attached to the first bolt position on the friction side, and the load was measured by the load cell of the testing machine. A tensile load was applied at a loading rate of approximately 2kN/s until the main friction occurred.

In the friction capacity experiment of specimens MB, a 100-ton universal testing machine was used to apply a monotonic tensile force to the specimens. The average elongation of the joints of the specimens and the axial force of each bolt were measured with a strain gauge during the force application. Strain gauges were also attached to the shaft of the base plate, the base plate of the first bolt, and the connecting plate of the n-th bolt to measure the axial strain.

The results of the friction capacity test are shown in Table 2. In the PB experiment, his bolt axial force immediately before the test decreased significantly with time of more than one month after bolting. The coefficient of friction tended to be higher for the blasted specimens, and both the IOZ and blasted specimens showed a slightly higher coefficient of

friction for the specimens with single-lap bolt joints. The bending strain (the difference in strain between the front and back of the base plate divided by two) at the onset of main friction (when the friction capacity is reached) was about 1000µ for the specimens with single-lap bolt joints. In the MB experiment, the axial force variation during the experiment was measured with strain gauges at the bolt heads.

Table 2. The results of the friction capacity test

Specimens name		No.1 Bolt Load [kN]	No.2 Bolt Load [kN]	Average Bolt Load [kN]	Friction resistance [kN]	µ	Average µ
P1-15	-1	223	233	228.0	256	0.561	
	-2	230	215	222.5	236	0.530	0.543
	-3	217	231	224.0	241	0.538	
P2-15	-1	219	213	216.0	460	0.532	
	-2	212	208	210.0	430	0.512	0.516
	-3	221	226	223.5	450	0.503	
B1-10	-1	221	220	220.5	314	0.712	
	-2	230	223	226.5	271	0.598	0.658
	-3	229	225	227.0	302	0.665	
B2-10	-1	229	220	224.5	574	0.639	
	-2	226	220	223.0	521	0.584	0.602
	-3	227	215	221.0	516	0.584	
MB-20- 2-12	-1			181.6	521	0.718	0.670
	-2			181.2	451	0.622	
MB-20- 3-12	-1			184.1	570	0.516	0.518
	-2			185.0	576	0.519	
MB-20- 4-12	-1			183.8	635	0.432	0.431
	-2			179.8	620	0.431	
MB-20- 5-12	-1			181.3	658	0.366	0.368
	-2			182.2	674	0.370	

2.3. Analysis Conditions

The model that reproduces the behavior of each test piece up to the occurrence of main friction was created and used a high Static friction coefficient to fix friction displacement of the joint contact surface (using commercial software ABAQUS 2020).

Fig.2 shows an analytical model that reproduces the 1/2 region of the PB specimen and the 1/8 region of the MB specimen, in consideration of symmetry. Reduced integral first-order solid elements were used throughout. The contact surfaces were reproduced as flat surfaces with no surface roughness or coating. For the PB specimen model, the elements were divided to the thickness of 5mm for the base and connecting plate, and the circumference of the bolt holes was divided into small sections with a length of 3.5 mm. For the MB specimen, it was 4mm for thickness and 2.5mm for the area near bolt holes. Fig.3 shows the element partitioning around the bolt holes in multi rows bolt joints as an example test model. In the contact analysis, the base plate, connecting plate, and fasteners

(bolts, nuts, and washers integrated) were mobilized as independent elastic bodies with uniform material properties (Young's modulus 200GPa, Poisson's ratio 0.3), and contact conditions were applied to the interface between the base plate and connecting plate (contact surface of the joint) and between the connecting plate and the washer portion.

The static friction coefficients for the PB and MB joints surfaces were set to 20 and 30 percent respectively. This is determined by the specific situation of each specimen, to make the coefficient of friction of each element less than the set value at the moment of sliding, which means no relative sliding will occur. Using a higher coefficient of static friction, a similar solution will be obtained, but it will be more difficult to obtain the convergence solution.
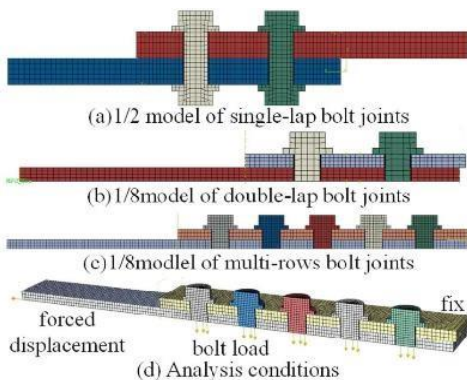
Fig. 2 Analysis models
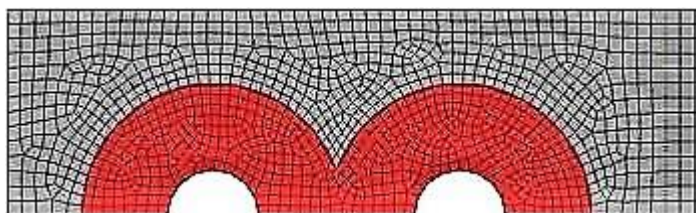
Fig. 3 Mesh near the bolt holes

The contact determination is based on the penalty and extended Lagrange methods. Local friction is determined by the maximum frictional shear stress, which is determined by the contact pressure and the static friction coefficient.

The displacement was fixed at the end of the fixed base plate and the initial axial force during the test based on Table 2 was imposed at the bolt axial part by ABAQUS bolt load. The loading was then reproduced by applying a joint axial tension-forcing displacement to the end of the base plate on the friction side. Since this is a boundary nonlinear problem with contact conditions, it was solved statically as a sequential analysis with the maximum forced displacement increment set to 1/100 of the maximum forced displacement.

2.4. Method

2.4.1 Hypothesize

The main friction in high-strength bolt joints is friction that propagates instantaneously across single or multiple contact surfaces and generates large relative displacements between steel plates, often resulting in a sudden decrease in the axial stiffness of the joint.

In joints that exhibit a well-defined friction resistance point, the initiation of principal friction causes the axial stiffness of the joint to instantaneously turn negative and the relative displacement between the steel plates to increase rapidly.

Although the mechanism of occurrence of such principal friction is not always clear, this study assumes that it is an unstable phenomenon in which loss of shear stiffness and localized friction occur in a chain model starting from a microscopic region where a certain limit state is first reached on the joint surface (starting point) and propagate to the surrounding area. The main friction is assumed to originate from the region of high frictional shear stress.

This study focuses on whether a limit state for local friction is established at the assumed onset point. Coulomb's law is assumed as the local limit state. Coulomb's law states that the following equation holds for the maximum value of frictional shear stress τ transmitted by a small surface area.

$$Max \ (\tau interface) = \mu pinterface \tag{1}$$

Where μ and *pinterface* are respectively the static friction coefficient and the contact pressure of the small surface area.

From (1), we can assume $\tau interface \ / \ pinterface$ as the driving parameter for the generation of localized friction. The present study applies a local approach to consider this local trigger introducing two parameters, stress ratio, and Weibull stress ratio, as described later.

2.4.2 Stress Ratio

This study investigates the possibility of estimating the occurrence of local friction based on the stress values evaluated at the integration points of finite elements to investigate a method to evaluate the limit of principal friction occurrence from a simple finite element analysis. The $\tau interface \ / \ pinterface$ (the stress ratio) is defined for a small surface area, which is the ratio of the shear stress τIP to the direct stress σIP evaluated at the integration point of the finite element forming the surface layer.

$$\rho = \tau IP / \sigma IP \tag{2}$$

Eq. (2) focuses on the maximum stress ratio at the onset of friction resistance around the bolt holes of the contact surface and examines whether the maximum stress ratio can be used to evaluate the main friction onset limit state. If the contact surfaces are finished similarly, the friction limit's stress ratios should match. In other words, in the case of the PB specimen, the stress ratio of the friction limit of the single-lap bolt joints should match the stress ratio of the friction limit of the double-lap bolt joints. In the MB specimen, the stress ratio of the friction limit of the 345-rows joints should match the stress ratio of the friction limit of the 2-row joints.

2.4.3 Weibull Stress Ratio

The prediction accuracy of the limit of occurrence of principal friction may be improved by considering local variations in surface properties at the joint surface of a high-strength bolt joint. In this study, the Weibull stress concept, which has been used to evaluate the failure limit of brittle materials [16], is applied to the evaluation of the occurrence limit of principal friction at the joint surface. Weibull stress is formulated based on the weakest link hypothesis, which states that brittle fracture of a material is induced when the basic volume containing defects fails due to equivalent stress in a material-specific probability distribution and that the relationship between generated stress and material failure probability follows a Weibull distribution [17]. In this study, the Weibull stress ratio is

defined as the equivalent stress to the stress ratio for the element in the surface layer as shown in the following equation to apply to the principal friction.

$$\sigma_w = \left(\sum_{i=1}^{n} \rho_i^m S_i\right)^{\frac{1}{m}} \tag{3}$$

Here, n is the number of surface finite elements in the region Ω where high shear stress is generated. The threshold Ω of shear stress is discussed in the next section. ρ And S is the stress ratio of finite elements in the area of the surface. Weibull parameter m gets bigger when the dispersion in each specimen gets smaller. The Weibull stress ratio is higher when the maximum value of the stress ratio is higher and when Ω is wider. Fig. 4 illustrates the Weibull stress ratio concept. The Weibull stress ratio concept models the contact surface as a series of basic surface areas, including defects, and considers that an increase in the stress ratio induces the main friction across the entire contact surface by causing one of the basic surface areas to friction.
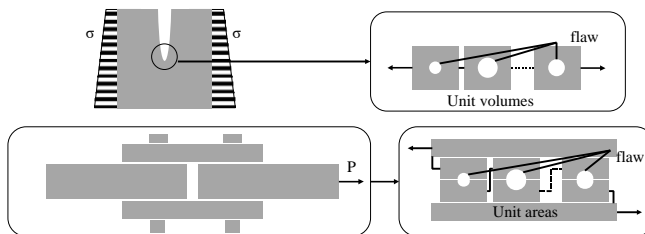
Fig. 4 Concept of Weibull stress ratio

Based on (3), if the contact surfaces are finished in the same way, the Weibull stress ratios at the friction limit should match. In other words, in the case of the PB specimen, the Weibull stress ratio of the friction limit of the single-lap bolt joints should match the Weibull stress ratio of the friction limit of the double-lap bolt joints. In the MB specimen, the Weibull stress ratio of the friction limit of the 345-row joints should match the Weibull stress ratio of the friction limit of the 2-row joints.

3. Results and Discussion

3.1. Calculation Region

The region Ω is mainly determined by the portion of the contact surface in the resolution that is actually in contact. Some of the unstable outermost elements are removed according to the actual situation. The region Ω was calculated for multiple loads and was selected to satisfy the above conditions at any load level, although it was calculated densely around loads equivalent to the friction capacity.

Fig. 5 shows the threshold values for the direct stress σ and the distribution of direct stresses on the joint surface at the friction force. As an example of the blasted specimen, the area Ω determined by the threshold values in the figure generally corresponds to the area of damage on the contact surface after the test, which means the Copen of the element is smaller than 0.

3.2. Varying Numbers of Contracting Surface Prediction by Stress Ration

Fig. 6 shows the relationship between the maximum value of stress ratio ρ and load in the region Ω obtained from the analysis results. Single/double-lap bolt joint specimens are shown separately for each contact surface specification. The maximum stress ratio increases monotonically with load in all specimens, and the location of the point of

maximum stress ratio at the load value equivalent to friction capacity is close to each other among the three specimens of the same type, indicating that the friction capacity and the friction coefficient of the specimens can be estimated from the maximum stress ratio. For the specimens with double-lap bolt joints, it is shown that the prediction of the main friction limit can be obtained.

(a)Copen at slip time increment

(b)Base plate after slip experiment

Fig. 5 Result for B2-10-1

(a) IOZ double-lap bolt joints

(b) IOZ single-lap bolt joints

(c) Rust double-lap bolt joints

(d) Rust single-lap bolt joints

Fig. 6 Stress ratio results for different numbers of surfaces

Based on the average of the maximum stress ratios at the friction capacity points for the specimens with double-lap bolt joints, the critical maximum stress ratios for principal friction for the IOZ and blasted specimens were respectively 1.468 and 1.829 for the analysis. According to section 4.2, the friction capacity and coefficient of friction estimated from the maximum stress ratios at the friction capacity points of the double-lap bolt joints

and the identified critical maximum stress ratio of the single-lap bolt joints are shown in Table 3.

Table 3. The prediction result in different numbers of contact surface by using stress rations

Specimens name	The limit value of the stress ratio	Estimated friction Reaction force [kN]	Estimated friction coefficient	Estimation error	Average error
P1-15-1	1.468	124	0.454	-2.87%	6.28%
P1-15-2		132	0.595	12.17%	
P1-15-3		132	0.591	9.84%	
B1-10-1	1.829	133	0.606	-14.90%	-4.82%
B1-10-2		142	0.628	5.00%	
B1-10-3		144	0.635	-4.56%	

Fig. 7 shows the relationship between the Weibull stress ratio ρ and load in the region obtained from the analysis results. Same with the maximum stress ratio, the Weibull stress ratio ρ at a load value equivalent to the friction capacity and the monotonic increase in the Weibull stress ratio ρ with increasing load indicates that the Weibull stress ratio ρ can estimate the friction capacity as well as the friction coefficient. For the specimens with double-lap bolt joints, it is shown that the prediction of the main friction limit can be obtained.

(a) IOZ double-lap bolt joints   (b) IOZ single-lap bolt joints

(c) Rust double-lap bolt joints   (d) Rust single-lap bolt joints
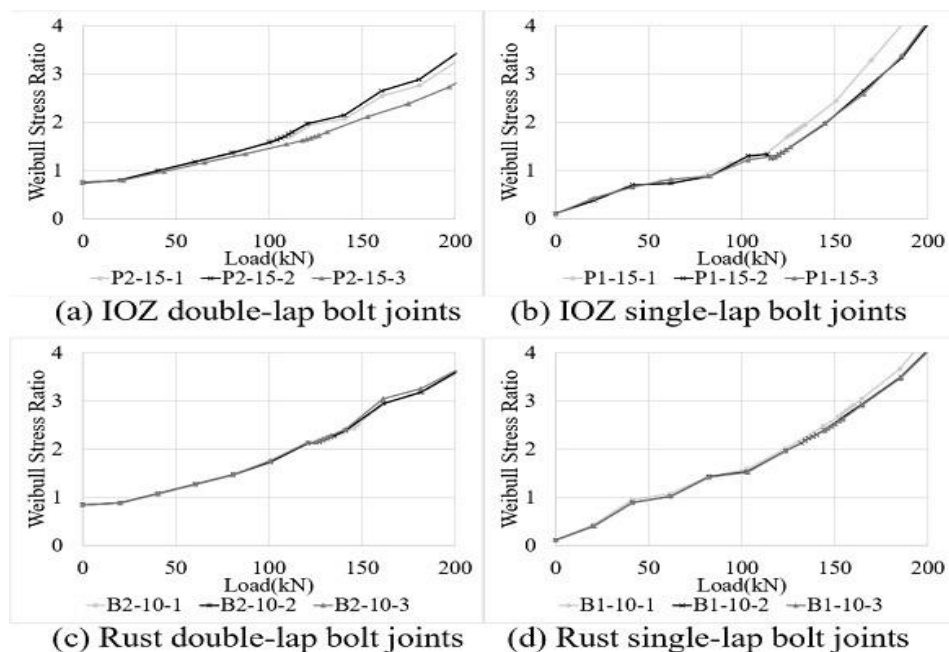
Fig. 7 Weibull stress ratio results for different numbers of surfaces

Based on the average of the Weibull stress ratios at the friction capacity points for the specimens with double-lap bolt joints, the critical maximum stress ratios for principal friction for the IOZ and blasted specimens were respectively 1.721 and 2.285 for the analysis. According to section 4.2, the friction capacity and coefficient of friction estimated

from the Weibull stress ratios at the friction capacity points of the double-lap bolt joints and the identified critical maximum stress ratio of the single-lap bolt joints are shown in Table 4.

Table 4. The prediction result in different numbers of contact surface by using Weibull mathematical stress rations

Specimens name	Limit value of Weibull stress ratio	Estimated friction Reaction force [kN]	Estimated friction Coefficient	Estimation error	Average error
P1-15-1		125	0.549	-2.14%	
P1-15-2	1.721	133	0.600	13.05%	6.92%
P1-15-3		132	0.591	9.84%	
B1-10-1		133	0.606	-14.90%	
B1-10-2	2.285	140	0.619	3.48%	-6.24%
B1-10-3		140	0.617	-7.29%	

(a) 2 rows bolt joints

(b) 3 rows bolt joints

(c) 4 rows bolt joints

(d) 5 rows bolt joints

Fig. 8 Stress ratio results for different numbers of bolts

Fig. 8 shows the relationship between the maximum value of stress ratio ρ and load in the region Ω obtained from the analysis results. Single/double-lap bolt joint specimens are shown separately for each contact surface specification. The maximum stress ratio increases monotonically with load in all specimens, and the location of the point of maximum stress ratio at the load value equivalent to friction capacity is close to each other among the three specimens of the same type, indicating that the friction capacity and the friction coefficient of the specimens can be estimated from the maximum stress ratio. For

the specimens with double-lap bolt joints, it is shown that the prediction of the main friction limit can be obtained.

Based on the average of the maximum stress ratios at the friction capacity points for the specimens with double-lap bolt joints, the critical maximum stress ratios for principal friction for 2 rows of bolt joints specimens is 8.505 for the analysis. According to section 4.2, the friction capacity and coefficient of friction estimated from the maximum stress ratios at the friction capacity points of the 2-rows bolt joints and the identified critical maximum stress ratio of the 3,4,5 rows bolt joints are shown in Table 5.

Table 5. The prediction result in different numbers of bolt rows by using stress rations

The limit	The limit value of the stress ratio	Estimated friction Reaction force [kN]	Estimated friction coefficient	Estimation error	Average error
MB-20-3-12-1	8.340	576	0.521	0.99%	0.47%
MB-20-3-12-2		576	0.519	-0.04%	
MB-20-4-12-1	9.941	564	0.384	-11.12%	-10.10%
MB-20-4-12-2		564	0.392	-9.08%	
MB-20-5-12-1	10.477	468	0.258	-28.83%	-29.68%
MB-20-5-12-2		468	0.257	-30.54%	

Fig. 9 Weibull stress ratio results for different numbers of bolts

Fig. 9 shows the relationship between the Weibull stress ratio ρ and load in the region obtained from the analysis results. Same with the maximum stress ratio, the Weibull

stress ratio ρ at a load value equivalent to the friction capacity and the monotonic increase in the Weibull stress ratio ρ with increasing load indicates that the Weibull stress ratio ρ can estimate the friction capacity as well as the friction coefficient. For the specimens with double-lap bolt joints, it is shown that the prediction of the main friction limit can be obtained.

Table 6. The prediction results in different numbers of bolt rows by using Weibull mathematical stress rations

Specimens name	Limit value of Weibull stress ratio	Estimated friction Reaction force [kN]	Estimated friction coefficient	Estimation error	Average error
MB-20-3-12-1	9.941	584	0.529	2.39%	2.18%
MB-20-3-12-2		587.6	0.529	1.97%	
MB-20-4-12-1	11.844	573.2	0.390	-9.67%	-9.38%
MB-20-4-12-2		564	0.392	-9.08%	
MB-20-5-12-1	12.351	478	0.264	-27.31%	-28.18%
MB-20-5-12-2		478	0.262	-29.05%	

Based on the average of the Weibull stress ratios at the friction capacity points for the specimens with two-row bolt joints, the critical maximum stress ratio for principal friction is 10.315 for the analysis. According to section 4.2, the friction capacity and coefficient of friction estimated from the Weibull stress ratios at the friction capacity points of the 2 rows of bolt joints and the identified critical maximum stress ratio of the 3, 4, and 5 bolt joints are shown in Table 6.

4. Conclusions

In this research, replacing the friction coefficient, two new parameters, the stress ratio, and the Weibull stress ratio, are introduced to infer the friction limit of bolt joints. For each method, two prediction scenarios were considered: different numbers of contact surfaces and different numbers of bolt columns. Positive results for prediction accuracy were observed. The findings could be summarized as follows.

- For varying numbers of contact surfaces prediction, the slip limit of single-lap bolt joints with IOZ and blasted surface were inferred from those of double-lap bolt joints. The stress and Weibull stress ratios showed a high prediction accuracy.
- For varying numbers of joint rows prediction, the friction limit of 3, 4, and 5 rows of bolt joints with blasted material were inferred from those of 2 rows of bolt joints. Both the stress ratio and the Weibull stress ratio showed higher prediction accuracy than friction coefficients in the prediction of 3-column joints. On the other hand, the accuracy of both the stress ratio and the Weibull stress ratio was low in the 4 and 5 columns joints prediction. It could be considered that the friction/yield ratio is much larger than 1 which means yield happens. Future research is needed to find out explanations for the different results and raise the accuracy by using plastic materials in simulation.

The feasibility of the two new methods was confirmed. They could currently be applied to predict friction limits of bolt joints in different numbers of contact surfaces and joint rows. Their feasibility for other situations will be researched in the future, such as bolt joints with large eccentric or over double-laps.

References

[1] Ministry of Construction of the People's Republic of China. Code for design of steel structures (GB 50017-2003). Beijing. 2003 [in Chinese].

[2] Ministry of Construction of the People's Republic of China. Specification for design, construction, and acceptance of high-strength bolt connections in steel structures (JGJ 82-91). Beijing. 1992 [in Chinese].

[3] Ministry of Railways of the People's Republic of China. Code for design on the steel structure of Railway Bridge (TB10002.2-2005). Beijing. 2005 [in Chinese].

[4] American Institute of Steel Construction. Specification for Structural Steel Buildings. Chicago (IL). 2005.

[5] Kitada T, Yamaguchi T, Matsumura M, et al. New technologies of steel bridges in Japan. Journal of Constructional Steel Research 2002; 58(1):21-7 https://doi.org/10.1016/S0143-974X(01)00029-3

[6] Y. Tamba, S. Yukito, S. Kimura, T. Yamaguchi, K. Sugiura, "Slip coefficient for high strength bolted frictional joints with the roughened steel surface and inorganic Zinc-rich painted surface, Journal of JSCE, A1, Vol. 3, 2015, pp. 19-32. https://doi.org/10.2208/journalofjsce.3.1_19

[7] K. Minami, H. Tamura, N. Yoshioka, D. Uchida, M. Moro, K. Ando, A study on initial bolt pretensions of high strength bolted joints considering a number of contact surfaces. Journal of JSCE, A1, Vol. 75, No.1, 2019, pp. 46-57. https://doi.org/10.2208/jscejseee.75.46

[8] S. Tsujioka, W. Kozo, Strength of M20, and F10T High-Strength Multi bolted slip-Type Joints, Journal of Structural Engineering. B, Vol.40, 1994, pp. 495-500.

[9] Citipitioglu Am H.R.W.D. Refined 3D finite element modeling of partially restrained connections including friction. Journal of Constructional Steel Research2002; 58(8):995-1013. https://doi.org/10.1016/S0143-974X(01)00087-6

[10] Chung KF, Ip KH. Finite element investigation on the structural behavior of cold-formed steel bolted connections. Engineering Structures 2001; 23:1115-25. https://doi.org/10.1016/S0141-0296(01)00006-2

[11] Ju SH, Fan CY, Wu GH. Three-dimensional finite elements of steel bolted connections. Engineering Structures 2004; 26(3):403-13. https://doi.org/10.1016/j.engstruct.2003.11.001

[12] Soo Kim T, Kuwamura H. Finite element modeling of bolted connections in thin-walled stainless steel plates under static shear. Thin-Walled Structures2007; 45(4):407-21. https://doi.org/10.1016/j.tws.2007.03.006

[13] Su RKL, Siu WH. Nonlinear response of bolt groups under in-plane loading. Engineering Structures 2007; 29(4):626-34. https://doi.org/10.1016/j.engstruct.2006.06.003

[14] Yu H, Burgess IW, Davison JB, et al. Numerical simulation of bolted steel connections in fire using explicit dynamic analysis. Journal of Constructional Steel Research 2008; 64(5):515-25. https://doi.org/10.1016/j.jcsr.2007.10.009

[15] Bouchair A, Averseng J, Abidelah A. Analysis of the behavior of stainless steel bolted connections. Journal of Constructional Steel Research 2008; 64(11):1264-74. https://doi.org/10.1016/j.jcsr.2008.07.009

[16] F. Minami, Fracture assessment method using the Weibull stress- Part I, Journal of the Japan Welding Society, Vol.75, No.5, 2005, pp. 416-446. https://doi.org/10.2207/jjws.75.416

[17] C.He, H. Tamura, H. Yamada, H. Katsuchi, Analytical simple estimation of slip coefficient of high strength bolt joints, Journal of Construction Steel, Vol 28, 2020.11, pp. 146-157.

Technical Note

Development of high-performance self curing concrete using super absorbent polymer and silica fume additives

Anju Mary Ealias[1,a], Emlin V[2,b]

[1]Department of Civil Engineering, SCMS School of Engineering and Technology, Kerala, India
[2]Department of Mechanical Engineering, School of Engineering, CUSAT, Kerala, India

Article Info	Abstract
	Curing plays a vital role in determining the mechanical properties of hardened concrete. The use of Super Absorbent polymer (SAP) has been found to be highly effective in reducing the water requirement for curing. Silica Fume (SF) is commonly used as a mineral admixture in High Performance Concrete (HPC) to improve mechanical and durability properties. But when silica fume was incorporated in SAPs, contradictory results with respect to strength after curing has been reported and this study aims to evaluate the effect of altering dosage of SAP and SF to maximize the strength and to reduce the water requirements in HPC. Concrete tested include traditional HPC and specimens of HPC with SAP, HPC with SF and HPC with combined dosage of SAP and SF. Compressive strength test, Split Tensile test and Sulphate attack test were conducted as per relevant Indian Standards. The dosage of SAP and SF were individually varied in the initial stage and from the experimental results, optimal dosage of SAP and SF was determined. The combined specimen with the optimal dosage of SAP and SF was tested in the final stage. The results showed that self-curing effect of SAP and the filler effect of SF maximize the compressive and tensile strength of hardened concrete. The optimal dosage was derived as 0.35% (by weight of cement) for SAP and 10% (by weight of cement) for SF and higher SAP or SF content in HPC was found to be detrimental with respect to strength.

1. Introduction

As concrete is one of the most widely used construction materials, ensuring its' optimum performance is of prime importance. Curing of concrete play a major role in determining the final microstructure of concrete and proper curing ensures its durability and performance. However, in practice good curing is not easy to achieve all the time owing to water shortage. In such a scenario, self-curing or internal-curing is desirable, where some curing agents are introduced in order to reduce the evaporation of water from concrete, thereby increasing the water retention capacity of the concrete.

The control of properties of cement-based materials in different stages of hardening can be achieved using chemical admixtures. Among the various chemical admixtures available, Super Absorbent Polymer (SAP) possess several desirable properties and the use of water-soluble polymers as self-curing agents in concrete has found several applications recently [1]. SAP is a polymer-based material that can absorb a considerable quantity of water from the surroundings, resulting in the swelling of the polymer matrix

and thus retain water without dissolving. It can take up water during the mixing process, enabling it to be used as a dry concrete admixture.

The pioneering studies with respect to the application of SAP in self-curing were done by Tsuji et al. [2] and Jensen et al. [3]. The water uptake capacity of SAP was reported to be more than 100 times its weight [3] and hence, sometimes, it is referred to as hydrogels. SAP can be used as an alternative to low density aggregate for self-curing. In addition to self-curing, studies have shown that SAPs can influence the properties of fresh and hardened concrete [3]. The process of bulk polymerization is employed for the preparation of majority of SAPs and the resultant product consists of crosslinked bulk of randomly composed copolymers with irregular shape [4]. Inverse suspension polymerization involving dispersion of reaction mixture with water droplets in oil phase can be used to produce SAPs of regular shapes, like spherical ones. However, this process is more complicated and use of a surfactant is necessary to stabilize water droplets. Such additions can badly affect the cement chemistry as reported by Laustan et al. [5].

The physico-chemical mechanism of sorption in SAPs was investigated by Toyoicki Tanaka [6] and he concluded that the favorable interactions between water and the polymer network depends on electronegativity of atoms in the network. The positively charged atoms like Na^+, K^+ were found to be having higher affinity towards water. The driving force of sorption can be described based on net osmotic pressure across the semipermeable polymer network. Most of SAPs are prepared from natural or synthetic monomers and commercially available SAPs are mostly acrylate-based. The mechanism of sorption in acrylic acid-based SAPs was studied by Zhu et al. [7]. They reported that SAP compositions that contained higher concentrations of acrylic acid had large swelling capacities. They also found that such SAPs were very sensitive to the presence of cations in the salt solution, especially, Ca^{2+}, Al^{3+}, etc. which can reduce sorption due to ion exchange. Lee et al. [8] reported that higher alkalinity inhibits ion exchange and hence by increasing the concentrations of Na^+ and K^+, resultant SAPs can retain more water for a longer period.

Several researchers have incorporated mineral and chemical admixtures to modify the SAP sorption properties. Silica Fume (SF) admixture is commonly used in HPC as it has an amorphous state and it has extreme fineness as compared to other mineral admixtures which improves mechanical and durability properties of HPC. A study conducted by Smarzewski et al. [9] concluded that SF can be used as an effective replacement of cement and significant improvement in strength was reported by adding up to 10% (by weight of cement) SF in HPC. However, when silica fume was incorporated with SAPs, contradictory results with respect to strength after curing was reported. The study by Bose et al. [10] reported an increase in mechanical properties while another study reported a decrease of the same [11]. The control of dosage of silica fume plays a dominant role in the development of superior mechanical properties in HPC.

The possibility of developing a HPC mix with combined addition of SAP and SF, to achieve the twin objectives of improving mechanical properties and simultaneously minimizing the water requirement for curing is yet to be explored in detail. The purpose of this study is to experimentally determine the effects of different proportions of SF, SAP and their combined form (SF+SAP) as a partial replacement of cement on the various properties of fresh and hardened concrete. In the present study, the mechanical properties of HPC were investigated with the addition of SAP and silica fume in two stages. In the initial stage, the SAP and SF dosage in HPC were individually varied to derive an optimal dosage of both and a specimen with both SAP and SF in their respective optimal dosage was prepared for the final stage of testing. To this end, a systematic experimental plan was formulated; starting with material characteristic test followed by mix design for HPC.

Mechanical properties tests including compressive strength, tensile strength tests were carried out and to assess the durability, Sulphate attack test was also carried out for various concentrations of SAP and SF mineral admixture.

2. Materials

This section deals with the materials used and properties of the material tested. The study involves the use of OPC cement, coarse and fine aggregates, SF and SAP for making concrete mixes.

2.1 Ordinary Portland Cement

Ordinary Portland Cement of OPC 53 grade as per IS 269-2015 [12] was used along with SAP and silica fume. The laboratory tests conducted on OPC were Specific gravity test, Initial and Final setting time test and Standard consistency test. The physical properties of cement determined in this study are given in Table 1.

Table 1. Properties of cement

Test	Result	Permissible limit as per IS 269-2015
Standard consistency	32%	22-33 %
Specific gravity	3.19	3.13-3.19
Initial setting time	26 min	Should not be greater than 30 minutes
Final setting time	590 min	Should not be greater than 600 minutes

2.2 Coarse and Fine Aggregates

Coarse aggregate used in the present work was crushed aggregate with a maximum nominal size of 20 mm. Material properties of coarse aggerate was determined using specific gravity, sieve analysis and water absorption tests. M-sand was used as fine aggregate with aggregate size less than 4.75 mm. Sieve Analysis of Fine aggregate is presented in Table 2 and from the percentage weight retention, Fineness Modulus was calculated. The consolidated properties of aggregates are shown in Table 3.

Table 2. Sieve analysis of fine aggregate

Sieve size(mm)	Weight retained(g)	Percentage weight retained	Percentage Cumulative weight
4.75	11.2	1.1	1.1
2.36	25.5	2.507	3.607
1.18	18.5	1.819	5.426
600	53.9	5.3	10.726
300	248.4	24.42	35.146
150	266.9	26.24	61.386
75	339.4	33.37	94.756
Pan	53.2	5.231	100

Table 3. Properties of coarse and fine aggregate

Test	Result	
	Coarse Aggregate	Fine Aggregate
Specific gravity	2.74	2.67
Fineness modulus	6.15	3.17
Water Absorption	0.49%	0.61%

2.3 Silica Fume Admixture and SAP

Silica Fume (SF) was added in the present study as mineral admixture and SAP was used for internal curing. The specific density of silica fume was estimated as 1.91 g/cm³. SAP used is Acryl amide/acrylic acid-based copolymer and the average size of SAP particles used was approximately 1 mm.

3. Mix Design and Specimen Details

A total of 8 combinations were considered for the study using HPC grade including the control specimen of traditional HPC. SF content used were 0%, 5%, 10%, 15% (by weight of cement) and SAP content used in the present study were 0.3%, 0.35% and 0.4% (by weight of cement). HPC grade was prepared by setting the Water to Cement ratio as 0.35. The total cementitious material used was 448 kg/m³ and amount of Fine Aggregate as percentage of total Aggregate was selected as 33% (by weight of cement).

The required quantity of cement, SAP, m-sand, coarse aggregate and water were measured and kept aside prior to the mixing for each mix proportion. The raw materials were weighed after oven drying to eliminate the error introduced by moisture content. Mixing of all materials was done manually. Care was taken to ensure uniform mixing and to prevent the formation of lumps and dehydration of the mix. The concrete mix was transferred to prefabricated moulds of size 15x15x15 cm for cubes and 15 cm diameter and 30 cm height for cylinder for testing as per Indian Standard code IS 516:2000 [13]. The moulds were oiled prior to transferring of the mix. The transferred mix was compacted manually using the trowel and kept aside for a day. The specimen was removed from the mould after 24 hours and was transferred to a water basin for the curing. The water used for curing conforms to standard IS 156:2000. The HPC with SAP content was cured in air itself i.e self-curing was allowed. After the curing period the specimens were taken out from the water basin and were tested. Three specimens of each mix were made and tested for repeatability. Specimens with optimal SAP and SF content were selected for self-curing study. A total of 96 cubes and 48-cylinder specimens were casted for this work.

4. Experimental Procedure

The procedures for conducting the experiments are detailed in this section. In the study, compressive strength test, split tensile strength test, sulphate attack test were conducted to ascertain the mechanical and durability properties of concrete.

4.1 Compressive Strength and Split tensile Strength

Cube specimens with side of 150 mm were produced and stored immediately after mixing in a climate room. The compressive strength of the specimen was evaluated at 7, 14 and 28-days as per IS 516:2000. The test setup used is shown in Figure 1. For split tensile strength, cylindrical concrete specimens were used and the testing procedure was in accordance with IS 5816:1999 [14]. The split tensile strength was tested after 7 days and 28 days using the test setup shown in Figure 2.

4.2 Sulphate Attack Test

Magnesium sulphates and sodium sulphate solutions were used in Sulphate attack test. The cubical specimens after proper curing of 28 days were immersed in water containing 5% sodium sulphate and magnesium sulphate separately for 14 days. The degree of sulphate attack was then evaluated by testing the compressive strength of specimen using compression testing machine.

Fig. 1 Test setup for compressive strength

Fig. 2 Test setup for split tensile strength

5. Results and Discussion

5.1 Compressive Strength

The results of compressive strength test are detailed in Table 4. Specimen IDs from 1 to 8 were given for identifying different mixes of concrete used. The curing medium used and

compressive strength of concrete obtained after 7,14 and 28 days are detailed in Table 4. The average strength of three specimens in each mix is reported in Table 4.

5.2 Split Tensile Strength

The results of split tensile strength test are detailed in Table 5. The curing medium used and average compressive strength of three specimens of concrete obtained after 7 and 28 days are shown in Table 5.

Table 4. Compressive strength results

Specimen Id	Mix	Curing Medium	7th day Strength N/mm²	14th day Strength N/mm²	28th day Strength N/mm²
1	HPC	Water	45.11	47.33	55.33
2	SAP (0.3%)	Air	37.50	45.11	54.44
3	SAP (0.35%)	Air	43.77	50.02	58.22
4	SAP (0.4%)	Air	37.11	44.66	55.22
5	SF (5%)	Water	45.54	48.54	56.45
6	SF (10%)	Water	46.11	49.51	57.14
7	SF (15%)	Water	45.73	48.78	56.82
8	SAP (0.35%) + SF (10%)	Air	44.98	49.82	59.13

Table 5. Split Tensile strength results

Specimen Id	Mix	Curing Medium	7th day Strength N/mm²	28th day Strength N/mm²
1	HPC	Water	2.55	3.22
2	SAP (0.3%)	Air	2.19	2.97
3	SAP (0.35%)	Air	2.66	3.34
4	SAP (0.4%)	Air	2.21	3.11
5	SF (5%)	Water	2.59	3.26
6	SF (10%)	Water	2.62	3.30
7	SF (15%)	Water	2.48	2.98
8	SAP (0.35%) + SF (10%)	Air	2.59	3.33

5.3 Sulphate attack Test

The results of sulphate attack test are detailed in Table 6. The specimen 28-day compressive strength after the sulphate attack is presented. The average percentage loss in compressive strength of the three specimens used in the study is calculated by using the test results of sulphate treated and untreated specimens and the results are shown in Table 6.

5.4 Comparison of results

The results in Figure 3 shows the comparison of properties between specimens used in the experimental study. It can be found that addition of SAP led to increase in compressive strength when compared to control specimen of HPC (Specimen 1). However, the increase was noted till 0.35% SAP addition (Specimen 2, 3) and further increase in SAP content (Specimen 4) did not improve the compressive strength. It can be postulated that at 0.3% SAP content, there was insufficient water release for self-curing. However, at 0.4% SAP content, there was reduction in compressive strength due to large voids in concrete due to excess release of water. It was confirmed by measuring the density of the specimens 1, 2, 3, 4. Specimen 4 (0.4% SAP) reported nearly 7 % reduction in density over the specimen 3 (0.35% SAP). The maximum improvement in compressive strength over control specimen that was obtained with SAP addition was 5.22%. Similar trend in compressive strength of HPC with SAP addition was reported by other researchers [15,16].

Table 6. Compressive strength of cubes after sulphate attack

Specimen Id	Mix	28th Day Strength N/mm²	Loss In Compressive Strength (%)
1	HPC	43.87	20.7
2	SAP (0.3%)	46.00	15.5
3	SAP (0.35%)	50.51	12.9
4	SAP (0.4%)	47.21	14.5
5	SF (5%)	45.83	18.8
6	SF (10%)	47.37	17.1
7	SF (15%)	47.79	15.9
8	SAP (0.35%) + SF (10%)	50.26	15.1
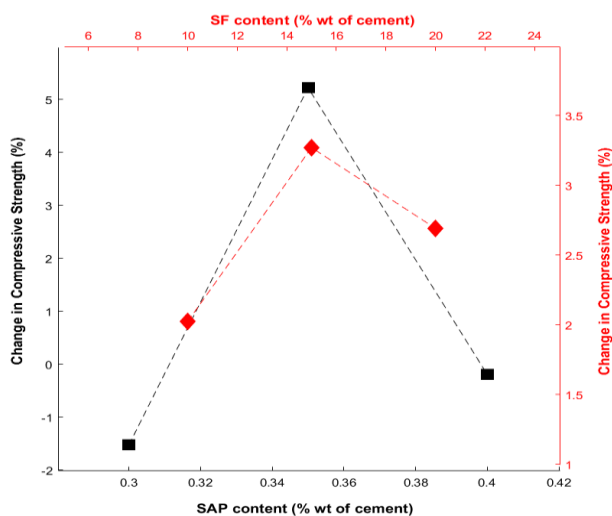
Fig. 3 Comparison of compressive strength

From Figure 3, it is also clear that the specimens 5,6,7 with SF content show higher compressive strength compared to control specimen no. 1. It can be attributed to the pozzolanic effect and filler effect provided by SF. Similar results were reported by Mazloom et al. [17] and Onuaguluchi and Panesar [18]. However, it can be found that with SF content above 10% does not improve compressive strength. This can be attributed to the reduction in C_3S and C_2S amount in the cementitious material, which lowers the concrete strength. Similar trends were reported in [19]. A specimen with 0.35% SAP and 10% SF gives the best compressive strength (6.87% increase over HPC) without water curing owing to advantageous properties of SAP and SF. The filler effect and proper amount of water released ensured proper curing and development of 28-day compressive strength.
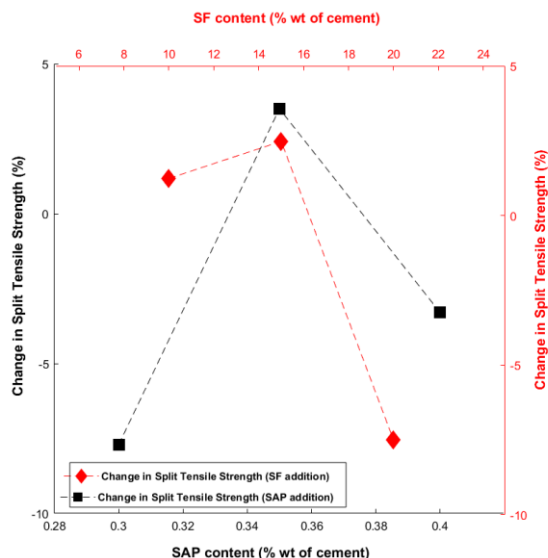
Fig. 4 Comparison of split tensile strength

From Figure 4, it can be found that addition of SAP leads to increase in split tensile strength. It can be noted that the improvement over control specimen is highest with 0.35 % SAP composition (specimen 3) and the maximum increase was 3.73%. The effect of SAP and SF addition on split tensile strength was found to show similar trend as the compressive strength, strength increased with addition till an optimal value and then starting to reduce. In this study, the replacement of the cement with SF significantly increased the splitting-tensile strength till 10% of SF (specimens 5,6). However, beyond 10% SF, it can be postulated that cement paste was not getting hardened due to loss of cementitious materials with increase in silica fume content, making it weaker in tension [20]. The combined specimen with 10% SF and 0.35% SAP gave almost same split tensile strength as specimen with 0.35% SAP which highlighted the minor influence of SF on split tensile strength.

The comparison of various specimen with respect to loss of compressive strength on sulphate attack test, is shown in Figure 5. It is clearly visible that self-curing concrete with SAP and SF can retain compressive strength in adverse conditions compared to HPC. The loss of compressive strength is only 12.9% with SAP content of 0.4% compared to 20.7% in HPC. The self-healing effect provided by SAP in specimens 2,3,4 may be the reason for reduction in loss of compressive strength in harsh environment. This effect was analyzed in [21] and various aspects of water transfer between SAP macro voids

resulting in healing of cracks was explained. Similar trend was observed with SF addition even though the strength was lower than that of self-cured specimens. It is postulated that the pozzolanic reaction of SF prevents the diffusion of sulfate ions in the cement matrix, which can reduce the decalcification of hydration products thereby reducing the damage to concrete [22]. A reasonably good results of specimen 8 with respect to sulphate attack showed the importance of optimizing the SAP and SF content to maximize the performance of HPC and minimize the use of water simultaneously.
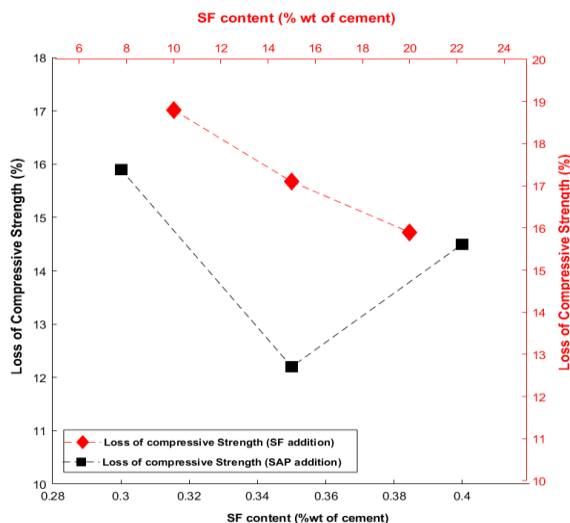
Fig. 5 Loss in compressive strength

6. Conclusions

Self-curing of concrete and its effect on mechanical properties has been a subject of research for a long period with the aim of reducing water requirements for construction. SAP offered significant potential in this area and the study highlighted the importance of the same through meticulously designed experiments. The addition of SF as filler material offered improvement in HPC compressive strength and allowed the reduction of expensive cementitious content. The combined effect of SAP and SF was also investigated in this study.

The compressive strength after 28 days with water curing on a control specimen of HPC was compared with specimens containing only SAP, only SF and a combination of SF and SAP. The optimal content of SAP for best compressive strength was found to be 0.35% with improvement of above 5% in strength over control specimen. Improvement was maximized with SF content of 10% and further addition of SF lowered the strength. Almost similar results were obtained in split tensile strength study of the specimens. A specimen with 0.35% SAP and 10% SF was selected as representative case to study combined effect of additives considering the results of individual groups. An increase in compressive strength of 6.87% over control specimen was obtained with the specimen. The sulphate attack test results also highlighted the importance of selecting the optimal concentration of SAP and SF. SAP content above 0.35% and SF content above 10% is not recommended based on the experimental results.

Even though many researchers reported beneficial results, the application of SAP and SF in the field is limited at present, primarily on account of lack of formal standards and

regulations. Additional studies can be carried out in this area by replacing SAP with other self-curing agents like calcium lignosulfonates. The study of microstructure of the concrete with SAP and SF, especially after sulphate attack test, can also be taken up to gain valuable insights on the various mechanisms to better explain the results of the experimental work.

References

[1] Schröfl C, Erk KA, Siriwatwechakul W, Wyrzykowski M, Snoeck D. Recent progress in superabsorbent polymers for concrete, Cement and Concrete Research, 151, 2022, 106648. https://doi.org/10.1016/j.cemconres.2021.106648

[2] Tsuji M, Shitama K, Isobe D. Basic studies on simplified curing technique, and prevention of initial cracking and leakage of water through cracks of concrete by applying superabsorbent polymers as new concrete admixture, Zairyo 48 (11), 1999 1308-1315. https://doi.org/10.2472/jsms.48.1308

[3] Jensen OM, Hansen PF. Water-entrained cement-based materials I. Principles and theoretical background, Cement and Concrete Research, 31 (4), 2001,647-654 .https://doi.org/10.1016/S0008-8846(01)00463-X

[4] Justs J, Wyrzykowski M, Winnefeld F, Bajare D, Lura P. Influence of superabsorbent polymers on hydration of cement pastes with low water-to-binder ratio, J. Therm. Anal. Calorim. 115 (1), 2014, 425-432. https://doi.org/10.1007/s10973-013-3359-x

[5] SLaustsen S, Hasholt MT, Jensen OM. Void structure of concrete with superabsorbent polymers and its relation to frost resistance of concrete, Mater. Struct. 48 (1-2), 2015, 357-368. https://doi.org/10.1617/s11527-013-0188-0

[6] Tanaka T. Collapse of gels and the critical endpoint, Phys. Rev. Lett. 40 (12), 1978, 820-823. https://doi.org/10.1103/PhysRevLett.40.820

[7] Zhu Q, Barney CW, Erk KA. Effect of ionic crosslinking on the swelling and mechanical response of model superabsorbent polymer hydrogels for internally cured concrete, Mater. Struct. 48 (7), 2015, 2261-2276. https://doi.org/10.1617/s11527-014-0308-5

[8] Lee HXD, Wong HS, Buenfeld NR., Effect of alkalinity and calcium concentration of pore solution on the swelling and ionic exchange of superabsorbent polymers in cement paste, Cem. Concr. Compos. 88, 2018, 150-164. https://doi.org/10.1016/j.cemconcomp.2018.02.005

[9] Smarzewsk P. ICSI 2019 The 3rd International Conference on Structural Integrity, Influence of silica fume on mechanical and fracture properties of high performance concrete. https://doi.org/10.1016/j.prostr.2019.08.002

[10] Bose B, Davis CR, Erk KA. Microstructural refinement of cement paste internally cured by polyacrylamide composite hydrogel particles containing silica fume and nanosilica, Cem. Concr. Res., 143, 2021, 106400. https://doi.org/10.1016/j.cemconres.2021.106400

[11] Vafaei B, Farzanian K, Ghahremaninezhad A. Effect of hydrogels containing nanosilica on the properties of cement pastes, J Compos Sci 5 (4), 2021, 105-115 https://doi.org/10.3390/jcs5040105

[12] Bureau of Indian Standards. Ordinary Portland Cement - Specification (Sixth Revision), 2015.

[13] Bureau of Indian Standards IS 516:2014. Method of Tests for Strength of Concrete, 2014.

[14] Bureau of Indian Standards. Method of Test Splitting Tensile Strength of Concrete. IS 5816: 1999, 2018 .

[15] Dudziak, L, Mechtcherine, V. Reducing the cracking potential of ultra-high performance concrete by using super absorbent polymers (SAP). Proceedings of the

International Conference on Advanced Concrete Materials, 2009, 17-19. https://doi.org/10.1201/b10162-4

[16] Mousa MI, Mahdy MG, Abdel-Reheem AH, Yehia AZ. Self-curing concrete types; water retention and durability. Alexandria Eng. J., 54 (3), 2015, 565-575 https://doi.org/10.1016/j.aej.2015.03.027

[17] Mazloom M, Ramezanianpour AA, Brooks JJ. Effect of silica fume on mechanical properties of high-strength concrete, Cem. Concr. Compos. , 26 (4), 2004, 347-357 https://doi.org/10.1016/S0958-9465(03)00017-9

[18] Onuaguluchi O, Panesar DK. Hardened properties of concrete mixtures containing pre-coated crumb rubber and silica fume, J. Cleaner Prod. 82 (22), 2014, 125-131 https://doi.org/10.1016/j.jclepro.2014.06.068

[19] Khodabakhshian A, Ghalehnovi M, Brito JD, Shamsabadi EA. Durability performance of structural concrete containing silica fume and marble industry waste powder, J. Cleaner Prod., 170, 2018 https://doi.org/10.1016/j.jclepro.2017.09.116

[20] Luo T, Hua C, Liu F, Sun Q, Yi Y, Pan X. Effect of adding solid waste silica fume as a cement paste replacement on the properties of fresh and hardened concrete, Case Studies in Construction Materials, 16, 2022, e01048 https://doi.org/10.1016/j.cscm.2022.e01048

[21] Mousavi SS, Guizani L, Bhojaraju C, Ouellet-Plamondon C. The effect of air-entraining admixture and superabsorbent polymer on bond behaviour of steel rebar in pre-cracked and self-healed concrete, Construction and Building Materials, 281, 2021, 122568 https://doi.org/10.1016/j.conbuildmat.2021.122568

[22] Zhang S, Cao K, Wang C, Wang X, Wang J, Sun B. Effect of silica fume and waste marble powder on the mechanical and durability properties of cellular concrete, Construction and Building Materials, 241, 2020, 117980 https://doi.org/10.1016/j.conbuildmat.2019.117980

Research Article

Effect of SCBA and GGBFS on the performance of binary and ternary blended concrete

Satish M. Palaskar*[a], Dr. Gaurang R. Vesmawala[b]

Department of Civil Engineering, Sardar Vallabhbhai National Institute of Technology, Surat, India

Article Info	Abstract
Article history: Received 29 Dec 2022 Revised 17 Jan 2023 Accepted 17 Jan 2023 *Keywords:* *Binary and ternary blended concrete;* *SCBA;* *GGBFS;* *Fresh properties;* *Mechanical properties;* *Microstructural properties*	The present studies focus on the characteristics of binary and ternary concrete in plastic and hardened stage for a mix of grade M25. Two mineral admixtures were used, sugarcane bagasse ash (SCBA) and ground granulated blast furnace slag (GGBFS). In preparing binary and ternary blended concrete, these admixtures partially substituted cement. Cement was replaced with SCBA and GGBFS, with the substitution percentage being 15%, 20%, 25%, and 30% by mass. Fresh properties were evaluated in terms of slump cone and setting time. Moreover, the mechanical characteristics were assessed concerning the strength of concrete in compression, split, and flexure. The microstructural properties were investigated in terms of scanning electron microscope (SEM) images. The experimental result indicated that the inclusion of SCBA and GGBFS improves workability and strength in compression while strength in the split and flexural hampered in binary as well as ternary concrete.

1. Introduction

Ordinary Portland cement (OPC) is the world's leading cement. According to statistics from the U.S. government, approximately 4.1 billion tonnes of OPC were generated globally in 2015 alone. Since the creation of concrete, OPC has been integrated as the primary binder material [1]. OPC's financial and environmental issues have motivated scientists to find other product to replace OPC. Supplementary cement products are helpful for concrete properties and play a role in some extra production of calcium silicate hydrate (C-S-H) gel. The concept of partly substituting OPC with supplementary products may be backed by the reality that's there a considerable quantity of unwanted material generated by different sectors with appropriate characteristics for use in concrete. These waste materials generally require a lot of effort and energy for disposal. Among the most widely used industrial waste in concrete are fly ash and GGBFS. Along with industrial waste, certain farming waste has revealed excellent performance when utilized in concrete, such as rice husk ash (farming waste of the rice milling sector) [2].

Sugarcane crops are cultivated all over the world to produce sugar, ethanol, and much more. The bagasse, waste material after drying in the sugar sector, is generally used as fuel for boilers. Sugarcane bagasse ash is commonly found in boilers under non-controlled burning situations. When the bagasse is heated under controlled circumstances, it can generate ash with more excellent amorphous silica[3]. GGBFS is a waste generated in iron-making blast furnaces. Iron-ore, coke, and limestone melt in blast

furnaces, producing molten iron and slag. Mostly silicates and alumina are included in the molten slag. The slag granulation method includes refrigerating molten slag with water jets with high pressure. This quickly quenches the formation of slag as well as granular particles. The granulated slag is further dried and ground to an extremely fine particle in a revolving ball mill called "GGBFS." The variables determining a slag's cementitious characteristics are the slag's chemical composition and the fineness of the slag[4].

The employment of supplementary cementitious material considerably improves the concrete microstructure. Reactive silica in these materials reacts with calcium hydroxide when using pozzolanic materials and produces extra C-S-H gel. Due to pore enhancement and extra C-S-H formation, concrete permeability is significantly reduced. Grinding of the burnt sample of SCBA at 700°C presented maximum pozzolanic activity. SCBA in concrete significantly enhance durability [5]. It has been shown to have greater strength in compression at 20% substitution of cement with SCBA[6]. Besides the increase in strength, there are cost savings of 35.62%, as noted by Tayyab Akram et al. [7]. Workability is seen to be increased up to 25% cement replacement, as noted by R. Srinivasan et al. also, strength in compression, split and flexural increases up to 10% replacement [8]. There will significantly enhance workability, compressive strength, and tensile strength by using GGBFS and rice husk ash [9]. Moulshree Dubey et al. found the addition of GGBFS and metakaolin in binary concrete enhances the concrete performance [10]. G. C. Cordeiro et al. found significant pozzolanic activity corresponding to be mechanical as well as a chemical method of evolution [11]. Noorul Amin et al. showed activation of bagasse ash in which mechanical activation was done using grinding and chemical by different alkalis. Strength increases with fineness and decreases by chemical activation [12]. Chemical test outcomes indicate SCBA has pozzolanic characteristics when burned at 700°C and sieved through a 45-micron sieve [13]. Setting time is slightly affected by use of SCBA at 50% and strength in compression is up to 90% of reference concrete for 50% replacement. There is an increase in durability properties especially chloride ion penetration [14]. Strength in compression is higher for 10% substitution of cement by SCBA while flexural strength is lower when revealed to temperature from 300°C to 500°C for two hours [15]. The influence of residual rice husk ash and SCBA in binary and ternary blended concrete permitted attainment of high intensity of cement substitution and retained steady or improved strength in compression [16]. Ashhad Imam et al. developed several synergic equations using micro silica, marble dust, and rice husk ash. These equations could explain the early and long-term strength [17]. Mateusz Radlinski and Jan Olek used fly ash and silica fume in ternary concrete. They found improved compressive strength and resistance to chloride ion penetration with a reduced water adsorption rate [18]. G.C. Isaia et al. found increased pozzolanic and physical effects when fly ash, rice husk ash, and limestone filler are increased in concrete. These effects are higher at 91 days compared to 28 days [19]. Shweta Goyal et al. used silica fume and fly ash with different water-cement ratios, along with water cured to continuously air-cooled regime, and found the economic combination of silica fume and fly ash [20]. There will be an increase in compressive and flexure strength when silica fume and fly ash are used in concrete at a different water-cement ratio, as noted by Muhannad Ismeik. At a later age, fly ash incorporation showed better results [21]. OPC was substituted by ground fly ash and ground bagasse ash. Compressive strength at 20% replacement by both ashes is similar to reference concrete; water permeability is reduced, and resistance to chloride penetration is improved [22]. Microstructural studies revealed that fly ash and bagasse ash fiber equally dispersed throughout the matrix. Both strengths in compression and flexure decrease. Bagasse fiber exhibits better tensile strength and decreased density [23]. Calcium carbide residue and bagasse ash mixture in concrete reduce cement consumption up to 70% with similar mechanical properties [24]. SCBA produces more viscous and plastic binary paste when used in the binary and

ternary systems, along with cement and fly ash [25]. There is a decrease in strength for compression, flexure, and split at three days of curing but at 7, 28, and 90 days it increases when GGBFS partially replaces cement. Abrasion resistance also increases with curing age [26]. The flowability of ultra-high-performance concrete increases steadily with GGBFS and fly ash content. Under standard curing, there is limited influence on compressive strength by incorporating fly ash [27]. Workability decreases for 10% micro silica and 30% GGBFS, while compressive strength is maximum for 5% microsilica and 30% GGBFS when used as a cementitious material in concrete [28]. The incorporation of fly ash and GGBFS decrease permeability and improve sulfate attack resistance under any curing condition [29]. It was found that compressive strength is maximum when manufactured sand is used in concrete containing GGBFS. Abrasion resistance was influenced by strength irrespective of GGBFS and manufactured sand content [30]. The consistency of cement decreases with increases in GGBFS amount while workability and setting time increases. GGBFS speeds up the hydration of OPC at the initial time of hydration. Sulfate resistance is superior as compared with normal concrete [4]. Compressive strength is seen to be maximum for 90 days of curing for cement replacement by slag [31]. Zheng et al. used a fly ash and silica fume combination and found a significantly higher strength retention ratio [32]. The mixture of calcium carbide residue and fly ash was used by Kittiphong Amnadnua et al., who found improved compressive strength with lower water permeability [33]. Liwa Mo et al. used ground granulated blast furnace slag, fly ash, and magnesia and found the same or higher mechanical strength at 28 days and 90 days [34]. The chloride permeability was low to moderate when quarry dust powder, silica fume, and fly ash were used in concrete by H.A.F Dehwah et al. [35].

2. Research Significance

The construction industry is currently concentrating on replacing cement with locally available environmental friendly products. The main emphasis is on reducing the quantity of consumption of cement content in the production of concrete, which in turn decreases the release of greenhouse gases into the atmosphere. The utilization of these products also assists in preventing the difficulties of disposal and landfill that cause significant environmental problems. The use of these products in a lucrative manner as an alternative to cement is essential for preserving sustainability. Many investigators concentrated on alternative cemented materials and concluded that the usage of these materials revealed improved strength along with durability properties. A comprehensive analysis of the literature suggested that fly ash is a significant material used to replace cement in mixed concrete partially. Only a few emphasized using SCBA as one of the complementary cement components in producing cement concrete mixture together with GGBFS. The application of these products is a significant benefit in environmental and economic terms. It also answers the problems of landfill and global warming and their applicability in the construction sector. It is planned to consider the above aspects to address the following issues. Whether the use of SCBA, a sugar industry by-product, along with GGBFS, may or may not be used in the preparation of blended concrete mix? How does this substitute affect the strength and microstructural properties?

3. Objectives and Methodology

The goal of the current research is to find out blended cementitious concrete via two materials. The materials are SCBA and GGBFS. The mechanical and microstructural characteristics are evaluated concerning the reference mix. To accomplish the research goals, a comprehensive experimental program was scheduled. The research aims to identify the optimal amounts of SCBA and GGBGS that can be substituted in cement. The

concrete blend of target strength in compression of 25MPa was designed with no mineral admixtures. Initially, sugarcane bagasse ash was optimized from 0 to 30% cement. Ternary blended cement concrete mix proportion was established utilizing SCBA and GGBFS as partial substitution of cement from 0 and 30%. This optimization method substantially improves the volume of cement use and can decrease at least some quantity of carbon dioxide released due to cement production. The mechanical and microstructural properties were assessed and correlated with the reference mix. An assessment of binary and ternary blended composite with reference mix was conducted by evaluating mechanical performance by preparing cubes, cylinders, and standard-size beams.

4. Materials and Mix Proportion

The materials utilized in this investigation are cement, aggregate, SCBA, GGBFS, and water. OPC affirming IS12269-1987 [36] was used in the investigation. The grade was 55, and specific gravity was 3.15 having a setting time of 200 min as initial and 312 min as final. The fine aggregate affirming Zone-II of IS: 383-1970 [37] was utilized. The fine aggregate so employed was obtained from the local river source. Well-graded crushed granite having size confirming to IS: 383-1970 [37] was used, which was obtained from the local crushing unit. The physical properties of fine and coarse aggregate are shown in Table. 1. For this investigation, SCBA was collected from Prasad Sugar and allied Agro-Products limited, Maharashtra (India). SCBA is burnt at 700°C for two hours in a muffle furnace, and then ground to make it fine. The chemical properties of SCBA are presented in Table 2.

Table 1. Physical properties of aggregate

Property	Fine Aggregate	Coarse Aggregate	Coarse Aggregate
Particle Shape, Size	Round,< 4.75 mm	Crushed angular, 20 mm	Crushed angular, 10 mm
Fineness modulus	6.63	6.79	6.57
Silt content (%)	1.0	Nil	Nil
Specific Gravity	2.81	2.82	2.79
Surface moisture	Nil	Nil	Nil
Water absorption (%)	1	1.33	1.45

GGBFS was collected from Guru Corporation Ahmedabad, Gujarat (India). The chemical properties of GGBFS are presented in Table 2. Portable water affirming to IS 456-2000 [38], was utilized for mixing and curing. Concrete mix design is done concerning the Indian standard code [39] for M25 grade. A water-cement ratio of 0.5 was used. Mix proportions for binary and ternary blended concrete are presented in Table 3.

Table 2. Chemical properties of SCBA and GGBFS

Content	SiO_2	Al_2O_3	Fe_2O_3	CaO	MgO	SO_3
SCBA	85.23	12.62	0.60	2.34	1.04	0.001
GGBFS	34.12	18.95	0.23	35.46	8.2	0.45

Table 3. Concrete mix proportion for binary and ternary blended concrete

Mix Designation	Cement (kg/m³)	SCBA %	GGBFS %	SCBA (kg/m³)	GGBFS (kg/m³)
P	394.32	0	0	0	0
B15	368.69	15	0	65.06	0
B20	347.00	20	0	86.75	0
B25	325.31	25	0	108.44	0
B30	303.62	30	0	130.13	0
G15	368.69	0	15	0	65.06
G20	347.00	0	20	0	86.75
G25	325.31	0	25	0	108.44
G30	303.62	0	30	0	130.13
B10G05	368.69	10	05	43.38	21.69
B10G10	347.00	10	10	43.38	43.37
B10G15	325.31	10	15	43.38	65.06
B10G20	303.62	10	20	43.38	86.75
B15G05	347.00	15	05	65.06	21.69
B15G10	325.31	15	10	65.06	43.38
B15G15	303.62	15	15	65.06	65.06
B20G05	325.31	20	05	86.75	21.69
B20G10	303.62	20	10	86.75	43.38
B25G05	303.62	25	05	108.45	21.69

5. Result and Discussion

5.1. Workability and Setting Time

The workability of concrete was obtained concerning IS 1199-1959 [40]. As shown in Fig. 1, the test result noticed that concrete without SCBA and GGBFS i.e. [P], had the lowest slump of 140 mm compared with binary concrete. At the same time, a lower slump of 145 mm and 140 mm was noticed in binary composite with substitution of cement at 15% and 30% by SCBA & GGBFS, respectively. In ternary composite, the lowest and highest slump value was noticed at B10G20 (cement replaced by 10% SCBA and 20% GGBFS) and B15G10 (cement replaced by 15% SCBA and 10% GGBFS), which are 100 mm and 160 mm, respectively. It was also noticed that the slump increases as SCBA content increases and decreases as GGBFS content increases. The initial and final setting times are found concerning IS 4031-1988 [41]. As shown in Fig. 2 Initial setting time (191 min) was noticed to be less against the 15% substitution of cement with SCBA, but the final setting time (380 min) will be more for concrete without any replacement. However, incorporating GGBFS resulted in a lower setting time at 30% and a higher one at 15%. Ternary blended concrete exhibited lower initial setting times at B15G10 and B25G05 while final setting times were higher at all replacement levels. The increase in setting

time may be due to carbon content and crystalline particles. As SCBA was a burnt material, the carbon content was found to be reduced, producing amorphous silica content that may be active. This can be attributed to the slowing down of the initial hydration process due to excess water. Genesan et al. 2007 reported a rise in setting time with an increase in bagasse ash because of the dilution effect [42]. The water requirement of the SCBA blended mix was more than the control mix due to the presence of large fibrous particles [5].
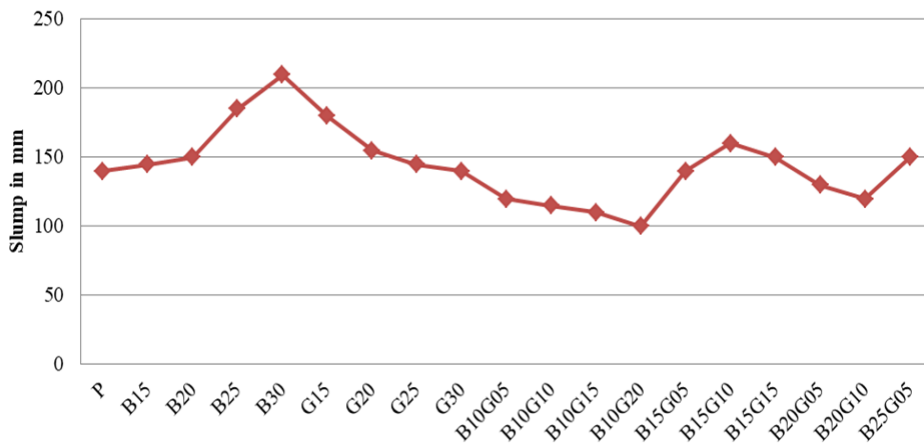
Fig. 1 Slump for various binary and ternary mixes of SCBA & GGBFS
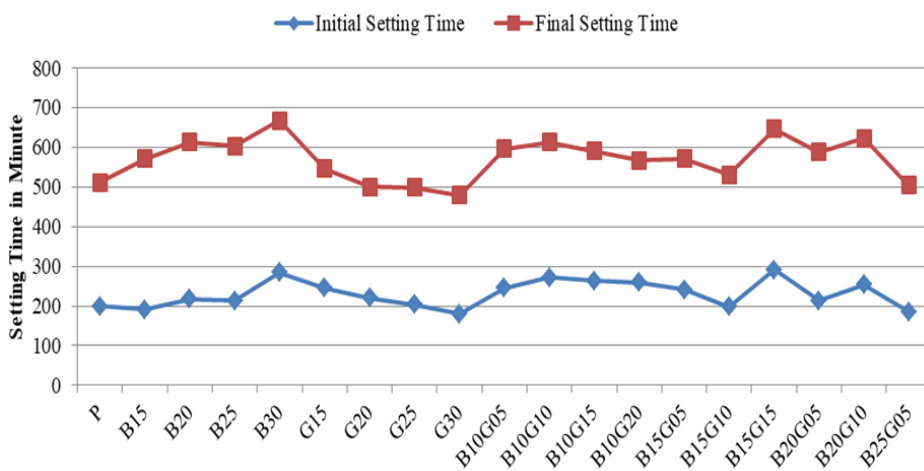
Fig. 2 Setting time for various binary and ternary mixes of SCBA & GGBFS

5.2. Compressive Strength

Concrete is well known for its strength in compression, as, in most places, it is used due to this property only. Concrete properties influence the structures' service life in harden stage. The strength of concrete in compression was measured at 7 and 28 days as per the procedure of IS 516-1959 [43]. The addition of SCBA increases the strength in compression at 15% substitution whereas addition of GGBFS increases the strength in compression at 15% and 20%. For all other substitutions, there is a reduction in strength in compression. Ternary blended concrete exhibit higher strength in compression at 20%

(B15G05) substitution. These results showed a substantial effect of SCBA and GGBFS on seven days of compressive strength which is lower for all replacement levels. Improvement in strength results with SCBA and GGBFS may have been caused by the filler effect and the pozzolanic reaction between $Ca(OH)_2$ from cement hydration and reactive SiO_2 from SCBA. The dilution effect may cause a decrease in strength in compression. Govindarajan and Jayalakshmi 2011 also observed an increase in strength at 5, 10, and 15% replacement.
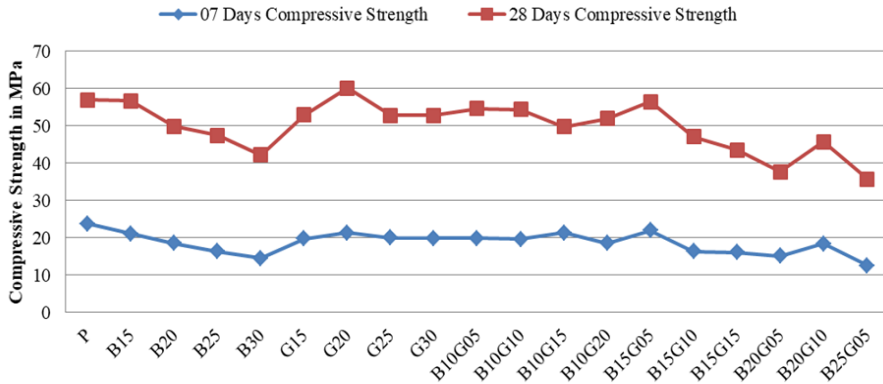
Fig. 3 Strength in compression of concrete for various binary and ternary mixes of SCBA & GGBFS
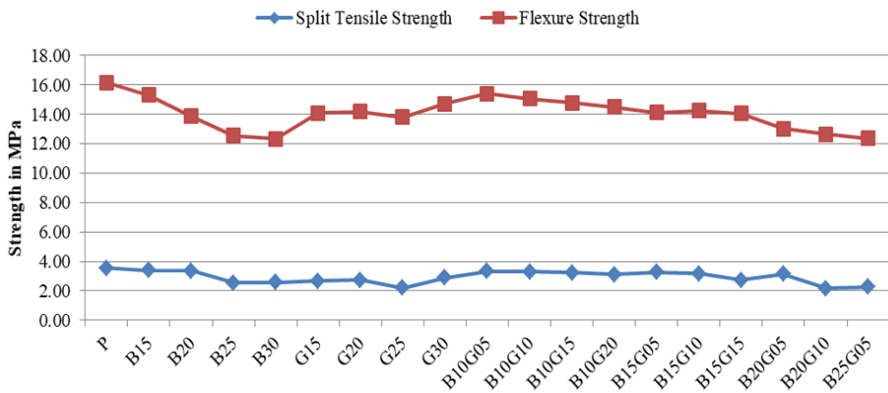
Fig. 4 Strength in flexural and split tensile of concrete for various binary and ternary mixes of SCBA & GGBFS

A sample of SCBA showed that when C-S-H increased (strength improved), peaks of $Ca(OH)_2$ diminished, indicating that a pozzolanic reaction occurred between $Ca(OH)_2$ & amorphous silica present in SCBA [44]. The reason for the improvement in the strength of SCBA may be attributed to silica content, fineness, and pozzolanic reaction between calcium hydroxide and reactive silica in SCBA. Similar behaviour was reported in previous work [45-46].

Flexural strength is measured following IS 516-1959 [43] on a 100 X 100 X 500 mm beam, and split tensile strength is carried out as per IS 5816-1999 [47] on 150 mm dia. X 300 mm height Cylinders. The result illustrated in Fig. 4 shows that adding SCBA and GGBFS causes a decrease in the average value of flexure and split tensile strength.

5.3. Microstructural Properties

To observe the microstructure of binary and ternary blended concrete specimens with SCBA and GGBFS, SEM and Energy Dispersive Spectroscopy (EDS) analysis were performed in the field emission scanning electron microscope laboratory of the College of Engineering Pune. Fig.5-13 shows the SEM/EDS micrographs. For the specimen with 20% and 30% of SCBA, unreacted bagasse ash particle was observed, leading to lesser compressive strength. Moreover, voids were also detected, representing permeable concrete. With the rise in the replacement amount, the unreacted particle of SCBA will rise and decrease the compressive strength. Binary concrete containing GGBFS have less voids than binary concrete containing SCBA, indicating a compacted and dense matrix. Crystalline particles were observed at high magnification as coated by a rough layer pertaining to the additional C-S-H product. The internal structure of reference concrete and concrete containing SCBA and GGBFS is dense at B20, G20, and B10G20 mixes, and C-S-H gel exists in the form of continuous block [48]; this results in higher compressive strength. Chemical compound analysis by EDS was investigated and shown in Fig. 5-13. The ratio of Si/Al was calculated from the EDS analysis. The ratio of Si/Al for ternary concrete with 10% SCBA and 10% GGBFS was observed to be higher, making it more rigid in terms of its microstructure. Similar behaviour in the cementitious medium is clearly defined by P. C. Hewlett (2004) [49]. The Ca/Si ratio represents the overall cementitious medium properties. Ca/Si ratio was found to be decreasing with an increase in replacement level for both binary and ternary blended concrete. Ca content decreased with an increase in SCBA and GGBFS in binary and ternary concrete. Fe content was found to be increased up to 20% SCBA replacement, and then it started decreasing. The pozzolanic nature of SCBA with C-H can be confirmed with an increase in the concentration of ferrous content with the inclusion of SCBA and GGBFS content [50].
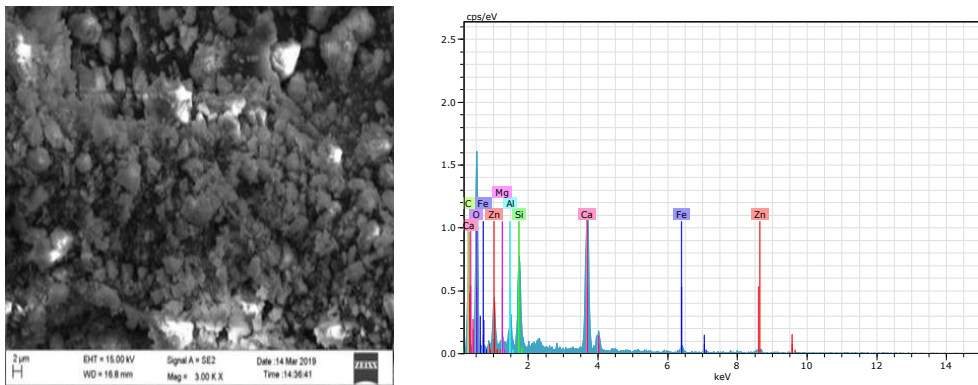
Fig. 5 SEM evaluation of concrete specimen using OPC
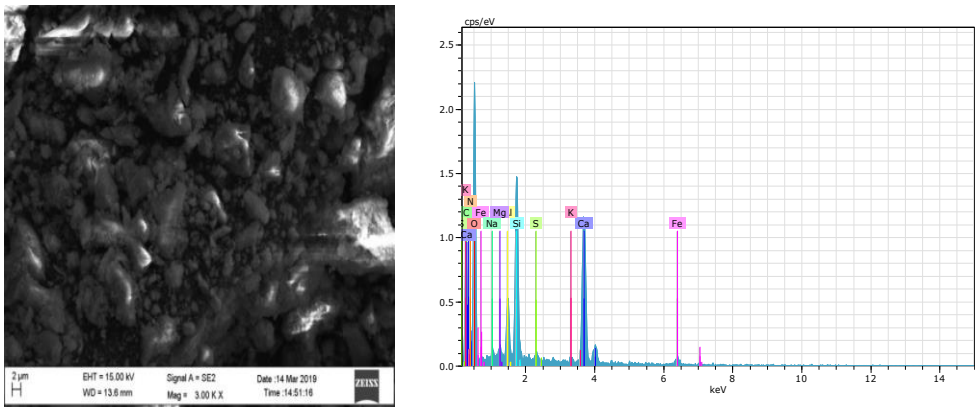
Fig. 6 SEM evaluation of concrete specimen using OPC by 20% SCBA
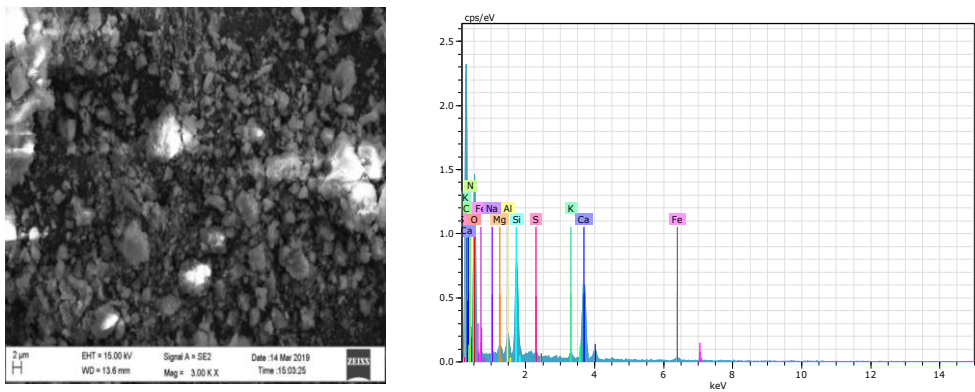
Fig. 7 SEM evaluation of concrete specimen using OPC by 30% SCBA
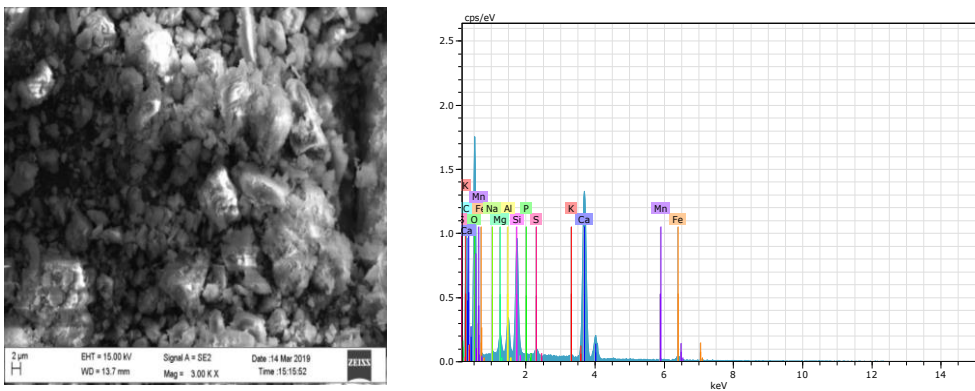
Fig. 8 SEM evaluation of concrete specimen using OPC by 20% GGBFS

413
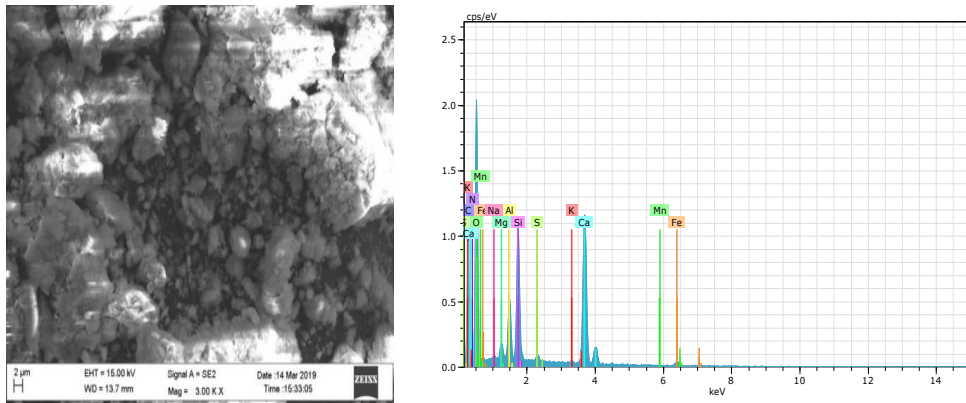
Fig. 9 SEM evaluation of concrete specimen using OPC by 30% GGBFS
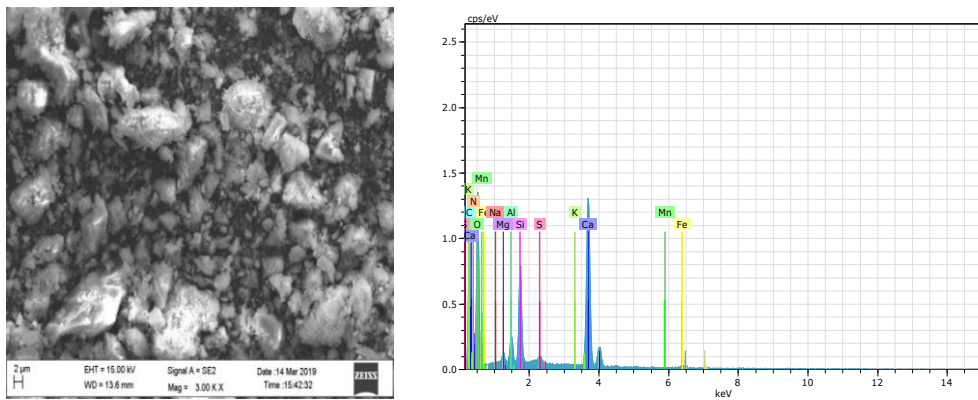
Fig. 10 SEM evaluation of concrete specimen using OPC by 10% SCBA & 10%GGBFS
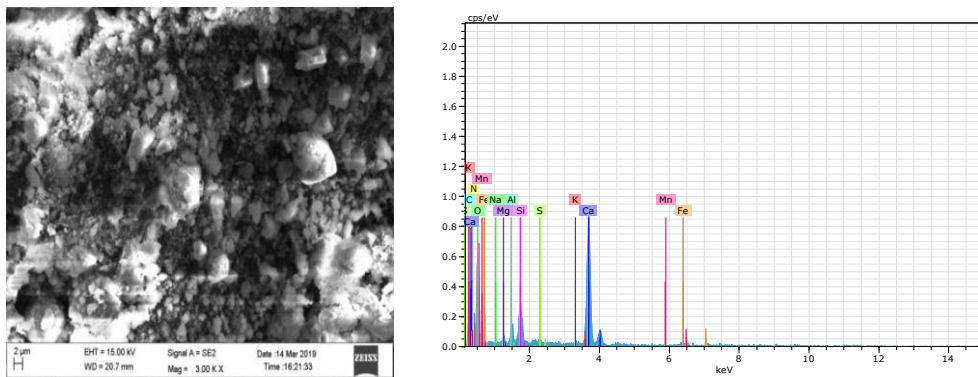
Fig. 11 SEM evaluation of concrete specimen using OPC by 10% SCBA & 20% GGBFS
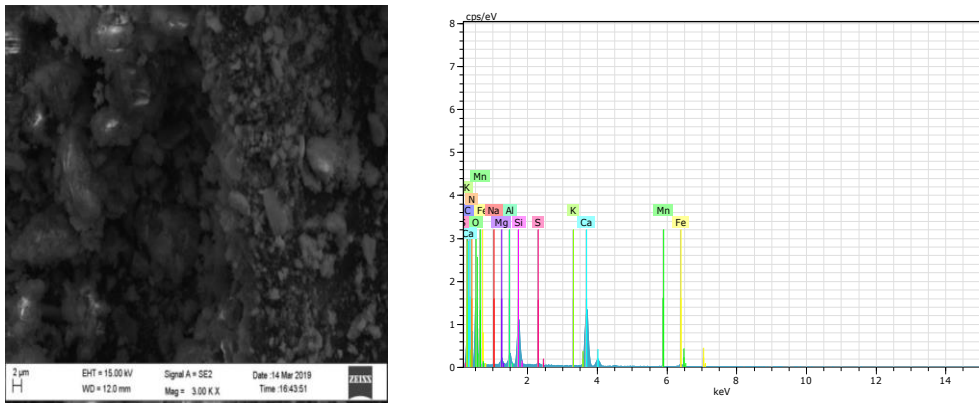
Fig. 12 SEM evaluation of concrete specimen using OPC by 15% SCBA & 15% GGBFS
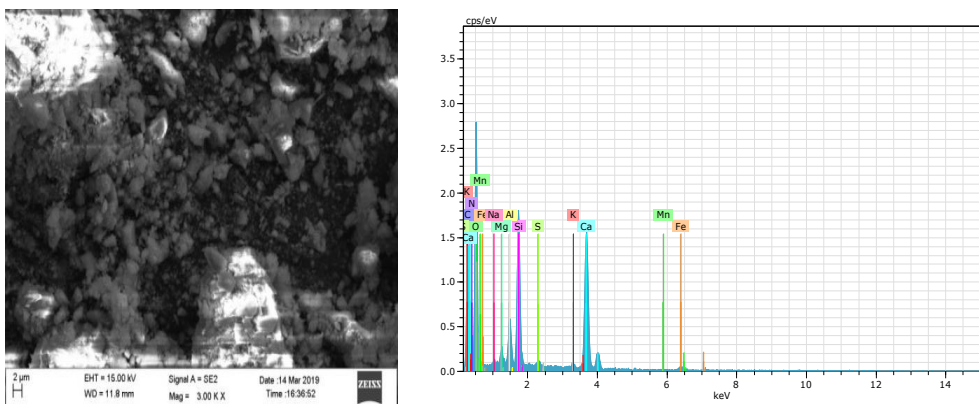
Fig. 13 SEM evaluation of concrete specimen using OPC by 20% SCBA & 10% GGBFS

Fe content in the present study was found more for the B20 mix than the B30 blend; also, for ternary concrete, it was found more for the B10G20 combination. This investigation supports explaining and relating the strength enhancement due to SCBA and GGBFS inclusion.

6. Conclusions

This research focussed on the effect of different pozzolanic materials on the properties of binary and ternary blended concrete in fresh and hardened stages. Pozzolanic materials are agriculture and industrial waste. Sugarcane bagasse ash was heated and ground before using it. The chemical properties of SCBA were determined, and for GGBFS, they were obtained from the supplier. Concrete mixes were cast using % variation up to 30% replacement in binary and ternary concrete. Experimental data were also analysed by using microstructural studies.

- The workability of binary concrete mixes follows an increasing trend with a rising percentage of SCBA and a decreasing trend with a rising percentage of GGBFS. A maximum slump was obtained for 30% replacement of cement. However, for the optimum replacement percentage, the slump obtained was 145 mm and 155 mm in binary concrete, whereas 140 mm in ternary concrete.

- The setting time of binary concrete mixes follows an increasing trend with a rising percentage of SCBA and a decreasing trend with a rising percentage of GGBFS. The value of both setting times is more for all binary and ternary mixes than concrete without any cement replacement.
- The optimum value for compressive strength was obtained at 15% SCBA and 20% GGBFS in binary concrete and 15%SCBA + 5%GGBFS in ternary concrete. At this replacement, the compressive strength value at 28 days was observed as 35.6MPa, 38.7MPa, and 34.5MPa. Similarly, for flexure and split tensile strength, the value obtained are 11.93MPa, 11.45MPa, 10.85MPa, 3.38MPa, 2.72MPa, and 3.26MPa, respectively.
- Microstructural studies indicate that extra calcium-silicate-hydrate gel, which is responsible for compressive strength development, was found in concrete containing SCBA and GGBFS, due to which compressive strength increases for 15% SCBA and 20%GGBFS use in concrete.

Considering the excess amount of sugarcane bagasse ash and ground granulated blast furnace slag, the amount of cement in concrete can be lowered. The partial substitution of cement by SCBA and GGBFS has an economic and environmental benefits. Concrete properties are improved using these materials; therefore, both are better in binary and ternary concrete. Studies on using these agricultural and industrial wastes open the path for creating sustainable construction materials. This research work can be extended using sodium hydroxide and sodium silicate solution while manufacturing concrete.

References

[1] Part WK, Ramli M, Cheah CB. An Overview on the Influence of Various Factors on the Properties of Geopolymer Concrete Derived From Industrial Byproducts. Handb Low Carbon Concr 2016;77:263–334.
https://doi.org/10.1016/B978-0-12-804524-4.00011-7

[2] Joseph B, Mathew G. Influence of aggregate content on the behavior of fly ash based geopolymer concrete. Sci Iran 2012;19:1188–1194.
https://doi.org/10.1016/j.scient.2012.07.006

[3] Frías M, Villar E, Savastano H. Cement & Concrete Composites Brazilian sugar cane bagasse ashes from the cogeneration industry as active pozzolans for cement manufacture 2011;33:490–496. https://doi.org/10.1016/j.cemconcomp.2011.02.003

[4] Siddique R, Bennacer R. Use of iron and steel industry by-product (GGBS) in cement paste and mortar. Resour Conserv Recycl 2012;69:29–34.
https://doi.org/10.1016/j.resconrec.2012.09.002

[5] Bahurudeen A, Santhanam M. Performance Evaluation of Sugarcane Bagasse Ash-Based Cement for Durable Concrete 2014 https://doi.org/10.5703/1288284315412

[6] Chusilp N, Jaturapitakkul C, Kiattikomol K. Utilization of bagasse ash as a pozzolanic material in concrete. Constr Build Mater 2009;23:3352–3358.
https://doi.org/10.1016/j.conbuildmat.2009.06.030

[7] Akram T, Memon SA, Obaid H. Production of low cost self compacting concrete using bagasse ash. Constr Build Mater 2009;23:703–712.
https://doi.org/10.1016/j.conbuildmat.2008.02.012

[8] Srinivasan R, Sathiya K. Experimental Study on Bagasse Ash in Concrete. Int J Serv Learn Eng 2010;5:60–6. https://doi.org/10.24908/ijsle.v5i2.2992

[9] Ganesh AC, Kumar MV, Mukilan K, Kumar AS, Kumar KA. Investigation on the effect of ultra fine rice husk ash over slag based geopolymer concrete. Res Eng Struct Mater 2022;x:1–15. https://doi.org/10.17515/resm2022.501ma0814

[10] Dubey M, Deo S V., Ramtekkar G. Effect of metakaolin and steel slag on performance of binary blended concrete. Res Eng Struct Mater 2022;8:603–614. https://doi.org/10.17515/resm2022.389ma0120

[11] Cordeiro GC, Filho RDT, Fairbairn EMR. Effect of calcination temperature on the pozzolanic activity of sugar cane bagasse ash. Constr Build Mater 2009;23:3301–3303. https://doi.org/10.1016/j.conbuildmat.2009.02.013

[12] Amin N, Khan AW, Alam S. Activation of bagasse ash in cement using different techniques 2011;164:199–204. https://doi.org/10.1680/coma.900035

[13] Abdulkadir TS et al. evaluation of sugarcane bagasse ash as a replacement for cement in concrete works. Acta Teh Corviniensis – Bull Eng 2014;7:1–21

[14] Rerkpiboon A, Tangchirapat W, Jaturapitakkul C. Strength, chloride resistance, and expansion of concretes containing ground bagasse ash. Constr Build Mater 2015;101:983–989. https://doi.org/10.1016/j.conbuildmat.2015.10.140

[15] Soares MMNS De, Garcia DCS, Figueiredo RB, Teresa M, Aguilar P, Cetlin PR. Comparing the pozzolanic behavior of sugar cane bagasse ash to amorphous and crystalline SiO 2. Cem Concr Compos 2016;71:20–25. https://doi.org/10.1016/j.cemconcomp.2016.04.005

[16] Cordeiro GC, Filho RDT, Tavares LM, Fairbairn EMR. Experimental characterization of binary and ternary blended-cement concretes containing ultrafine residual rice husk and sugar cane bagasse ashes. Constr Build Mater 2012;29:641–646. https://doi.org/10.1016/j.conbuildmat.2011.08.095

[17] Imam A, Kumar V, Srivastava V. Empirical predictions for the mechanical properties of Quaternary Cement Concrete. J Struct Integr Maint 2018;3:183–196. https://doi.org/10.1080/24705314.2018.1492668

[18] Radlinski M, Olek J. Investigation into the synergistic effects in ternary cementitious systems containing portland cement, fly ash and silica fume. Cem Concr Compos 2012;34:451–459. https://doi.org/10.1016/j.cemconcomp.2011.11.014

[19] Isaia GC, Gastaldini ALG, Moraes R. Physical and pozzolanic action of mineral additions on the mechanical strength of high-performance concrete. Cem Concr Compos 2003;25:69–76. https://doi.org/10.1016/S0958-9465(01)00057-9

[20] Goyal S, Kumar M. Effect of relative proportion of pozzolana on compressive strength of concrete under different curing conditions. Bhattacharjee Int J Eng 2008:20

[21] Ismeik M. Effect of mineral admixtures on mechanical properties of high strength concrete made with locally available materials. Jordan J Civ Eng 2009;3:78–90.

[22] Somna R, Jaturapitakkul C, Amde AM. Effect of ground fly ash and ground bagasse ash on the durability of recycled aggregate concrete. Cem Concr Compos 2012;34:848–854. https://doi.org/10.1016/j.cemconcomp.2012.03.003

[23] Verma D, Chandra P. Mechanical Properties and Morphological Study of Fly-Ash – Bagasse Composites 2013;93:65–71. https://doi.org/10.1007/s40033-012-0013-x

[24] Rattanashotinunt C, Thairit P, Tangchirapat W, Jaturapitakkul C. Use of calcium carbide residue and bagasse ash mixtures as a new cementitious material in concrete. J Mater 2013;46:106–111. https://doi.org/10.1016/j.matdes.2012.10.028

[25] Jiménez-Quero VG, León-Martínez FM, Montes-García P, Gaona-Tiburcio C, Chacón-Nava JG. Influence of sugar-cane bagasse ash and fly ash on the rheological behavior of cement pastes and mortars. Constr Build Mater 2013;40:691–701. https://doi.org/10.1016/j.conbuildmat.2012.11.023

[26] Rao SK, Sravana P, Rao TC. Abrasion resistance and mechanical properties of Roller Compacted Concrete with GGBS. Constr Build Mater 2016;114:925–933. https://doi.org/10.1016/j.conbuildmat.2016.04.004

[27] Wu Z, Shi C, He W. Comparative study on flexural properties of ultra-high performance concrete with supplementary cementitious materials under different

curing regimes. Constr Build Mater 2017;136:307–313. https://doi.org/10.1016/j.conbuildmat.2017.01.052

[28] Vijaya Bhaskar Reddy S, Srinivasa Rao DP. Experimental studies on compressive strength of ternary blended concretes at different levels of micro silica and ggbs. Mater Today Proc 2016;3:3752–3760. https://doi.org/10.1016/j.matpr.2016.11.024

[29] Zhang Z, Wang Q, Chen H, Zhou Y. Influence of the initial moist curing time on the sulfate attack resistance of concretes with different binders. Constr Build Mater 2017;144:541–551. https://doi.org/10.1016/j.conbuildmat.2017.03.235

[30] Rao SK, Sravana P, Rao TC. Investigating the effect of M-sand on abrasion resistance of Roller Compacted Concrete containing GGBS. Constr Build Mater 2016;122:191–201. https://doi.org/10.1016/j.conbuildmat.2016.06.054

[31] Dinakar P, Sethy KP, Sahoo UC. Design of self-compacting concrete with ground granulated blast furnace slag. Mater Des 2013;43:161–169. https://doi.org/10.1016/j.matdes.2012.06.049

[32] Zheng DD, Ji T, Wang CQ, Sun CJ, Lin XJ, Hossain KMA. Effect of the combination of fly ash and silica fume on water resistance of Magnesium-Potassium Phosphate Cement. Constr Build Mater 2016;106:415–421. https://doi.org/10.1016/j.conbuildmat.2015.12.085

[33] Amnadnua K, Tangchirapat W, Jaturapitakkul C. Strength, water permeability, and heat evolution of high strength concrete made from the mixture of calcium carbide residue and fly ash. Mater Des 2013;51:894–901. https://doi.org/10.1016/j.matdes.2013.04.099

[34] Mo L, Liu M, Al-Tabbaa A, Deng M, Lau WY. Deformation and mechanical properties of quaternary blended cements containing ground granulated blast furnace slag, fly ash and magnesia. Cem Concr Res 2015;71:7–13. https://doi.org/10.1016/j.cemconres.2015.01.018

[35] Dehwah HAF. Corrosion resistance of self-compacting concrete incorporating quarry dust powder, silica fume and fly ash. Constr Build Mater 2012;37:277–282. https://doi.org/10.1016/j.conbuildmat.2012.07.078

[36] IS 12269-1987: Specification for ordinary Portland cement. Bureau of Indian Standards, New Delhi, India.

[37] IS 383-1970: Specification for coarse and fine aggregates from natural sources for concrete. Bureau of Indian Standards, New Delhi, India.

[38] IS 456-2000: Code of practice for plain and reinforced concrete. Bureau of Indian Standards, New Delhi, India.

[39] IS 10262-2009: Recommended guidelines for concrete mix design. Bureau of Indian Standards, New Delhi, India.

[40] IS 1199-1959: Method of Sampling and Analysis of Concrete. Bureau of Indian Standards, New Delhi, India

[41] IS 4031(Part 5)-1988: Methods of physical tests for hydraulic cement: Determination of initial and final setting times. Bureau of Indian Standards, New Delhi, India.

[42] Ganesan K, Rajagopal K, Thangavel K. Evaluation of bagasse ash as supplementary cementitious material. Cem Concr Compos 2007;29:515–524. https://doi.org/10.1016/j.cemconcomp.2007.03.001

[43] IS 516-1959: Method of Tests for Strength of Concrete. Bureau of Indian Standards, New Delhi, India

[44] Govindarajan D, Jayalakshmi G. XRD, FTIR and Microstructure Studies of Calcined Sugarcane Bagasse Ash. Adv Appl Sci Res 2011;2:544–549

[45] Chu I, Kwon SH, Amin MN, Kim JK. Estimation of temperature effects on autogenous shrinkage of concrete by a new prediction model. Constr Build Mater 2012;35:171–182. https://doi.org/10.1016/j.conbuildmat.2012.03.005

[46] Cordeiro GC, Toledo Filho RD, Tavares LM, Fairbairn EMR. Pozzolanic activity and filler effect of sugar cane bagasse ash in Portland cement and lime mortars. Cem Concr Compos 2008;30:410–418. https://doi.org/10.1016/j.cemconcomp.2008.01.001

[47] IS 5816:-1999: Method of Tests for Splitting Tensile Strength of Concrete. Bureau of Indian Standards, New Delhi, India

[48] Zheng W, Li H, Wang Y. Compressive behaviour of hybrid fiber-reinforced reactive powder concrete after high temperature. Mater Des 2012;41:403–409. https://doi.org/10.1016/j.matdes.2012.05.026

[49] Hewlett, P. C. (2004). Lea's Chemistry of Cement and Concrete. Elsevier Butterworth Heinemann Publication, Oxford (UK).

[50] Najimi M, Sobhani J, Pourkhorshidi AR. Durability of copper slag contained concrete exposed to sulfate attack. Constr Build Mater 2011;25:1895–1905. https://doi.org/10.1016/j.conbuildmat.2010.11.067

Research Article

Morpho-structural and compressive mechanical properties of graphene oxide reinforced hydroxyapatite scaffolds for bone tissue applications

Ferzan Fidan[1,a], Naim Aslan[1,2,b*], Mümin Mehmet Koç[3,4,c]

[1]Department of Strategic Raw Materials and Advanced Technology Applications, Institute of Post Graduate Education, Munzur University, Tunceli, Turkey
[2]School of Tunceli, Department of Machinery and Metal Technologies, Munzur University, Tunceli, Turkey
[3]School of Medical Service, Department of Medical Service and Techniques Kirklareli University, Kırklareli, Turkey
[4]Department of Physics, Faculty of Arts and Sciences, Kırklareli University, Kırklareli, Turkey

Article Info	Abstract
	Hydroxyapatite (HA) is a unique material that has the potential to be used to replace bones and teeth in the field of orthopedics and dentistry since HA exhibits quite similar biological and chemical characteristics to human bone. Hydroxyapatite ceramics are bioactive materials used to repair damaged human tissue. The pores in the porous hydroxyapatite ceramics provide a mechanical interlock, enabling a solid bond and fixation between the implant and bone. In this study, 0.5wt%, 1wt%, and 1.5wt% graphene oxide (GO) reinforced porous HA structures were obtained using the space-holder method to increase the strength of hydroxyapatite with low mechanical strength. NaCl was used as a spacer, and PEG 400 as a binder. Scaffold structures with 40% porosity rates were sintered at 1000 ºC under vacuum. Finally, a compression test was applied to the samples which were previously analyzed by SEM, EDS and XRD. The compressive strengths of 0.5%, 1%, and 1.5% graphene oxide reinforced porous HA samples were determined between 8.04 and 31.14 MPa. The highest compressive strength was recorded as 31.14 MPa in the 1% GO added sample, and the lowest compressive strength was recorded as 8.04 MPa in the 1.5% GO added sample. In addition, it was understood that the mechanical properties did not increase regularly with the increase of graphene oxide reinforcing.

1. Introduction

Scaffold structures are porous structures which were extensively used in tissue engineering applications such as bone repair, cellular infiltration, angiogenesis, nutrient transfer, and disposal of metabolic waste [1]. When tissue is implanted in the body, scaffold structures provide a mechanically stable environment that promotes cell migration, adhesion, and growth because of their interconnected pores [2]. Hydroxyapatite (HA), which is widely used as a bio ceramic, is known as an essential bio ceramic material with chemical and crystallography similarities to the bone matrix [3]. This material is used as the major inorganic component for bones, teeth, and hard tissue restoration and as a bio ceramic implant in orthopedic and dental applications [4, 5]. However, their mechanical properties such as low fracture toughness and low compressive and tensile stress are known to be significant disadvantages [3]. To improve the low mechanical properties of hydroxyapatite, additives such as carbon nano-tube (6), Al_2O_3 [7], ZrO_2, etc. were used as reinforcing material [8]. Among those reinforcing materials, graphene (Gr) and graphene oxide (GO) have recently attracted the attention of researchers because of its unique

mechanical, thermal, and electrical properties. GO is an astonishing 2D material which shows astonishing mechanical resistance due to its sp^2 hybrid binding structure. GO is carbon based material; hence, it is non-toxic [9–11]. Gr and GO are also light, flexible, and biocompatible; therefore, it stands out as a promising material in the production of functional bioceramics used in biomedical applications [12]. Mechanical properties and biocompatibility characteristics of Gr and GO-HA composite structures have been reported by several researchers in the literature where different GO additive ratios were evaluated for different scenarios. It was observed that with 0.5wt%, 1wt%, and 1.5wt% GO reinforcing, the elastic modulus and the fracture toughness increased by 86% and 40% (compared to pure HA), respectively; GO addition had also an improving effect on biocompatibility [13, 14].

Powder metallurgy techniques are one of the most common techniques used in the production of porous or scaffold structures due to their low cost and flexibility in combining different components and compounds [15, 16]. Powder metallurgy techniques and space-holder methods are trending methods preferred by researchers for the production of scaffold structures, since such methods provide low processing cost, and high biological activity which enable producers to manufacture materials in desired pore size distribution with well controlled pore shape [16, 17]. NaCl is an affordable material with good biocompatibility and therefore, often preferred as a spacer to obtain scaffold structures. The NaCl keeps its shape under a high pressure, and it can be removed from the structure before sintering via hot water washing [18–20].

Graphene and graphene oxide-reinforced composite structures are a trending topic in the literature; however, investigation of the properties of the HA scaffold structures obtained by the space-holder method in the existence of graphene oxide (GO) has not been discussed. In this study, HA scaffold structures, 0.5wt%, 1wt%, and 1.5wt% GO reinforced HA scaffold structures with 40% porosity were produced by using powder metallurgy and the NaCl spacer hybrid method. The morphological, structural, and mechanical characterizations of the scaffold structures were investigated.

2. Experimental Details

2.1. Production of Scaffold Structures

In this study, hydroxyapatite (<30 μm, Sigma Aldrich) powders were used as a matrix material, and NaCl (100-150 μm, Supelco) particles by volume were used at a rate of 40%. GO, which is used as a reinforcement material, was obtained by the modified hammers method [21]. Graphene reinforcement ratios in GO/HA structures were determined as 0.5wt%, 1wt%, and 1.5wt% by weight.

Firstly, 0.5wt%, 1wt% and 1.5wt% GO powders were added to separate beakers containing 15 ml of distilled water and mixed ultrasonically for 60 minutes. Then, HA powders and GO additives were added to the beakers at determined rates. In order to adjust the pH of the mixture to 7.4, it was mixed with aqueous NaOH buffer solution using a magnetic stirrer for 60 minutes. Then, the mixture was subjected to the ultrasonic homogenizer for 10 minutes. 0.5wt%, 1wt%, and 1.5wt% GO-reinforced HA mixtures were left to dry in an oven at 70 ∘C for 24 h. NaCl space-holder particles were added to the dried GO-reinforced HA powders at a rate of 40% (v/v). In order to ensure the binding of the materials in the mixture, the polymer PEG400 (polyethylene glycol 400) binder was added to the mixture, and the mixture was stirred with a magnetic stirrer. Then, 450 MPa cold press was applied to the unreinforced HA (P40-HA), 0.5wt% (P40-HA/0.5GO), 1wt% (P40-HA/1GO) and 1.5wt% (P40-HA/1.5GO) GO reinforced HA composites, respectively. It should be noted that all samples have 40% porosity which was obtained with NaCl spacer. To dissolve the NaCl particles, which promotes spacing in the pressed HA-based samples,

composite samples were kept in distilled water for 60 minutes. Then, they were placed in an oven at 80 ∘C for 12 hours for the drying process. Finally, the samples were sintered at 1000 ∘C for 1 hour with the help of a vacuum tube furnace (MSE furnace, 1600 ∘ C). The resulting illustrations and producing schematic of the pure HA and HA/GO scaffolds are presented in Figures 1 and 2, respectively.
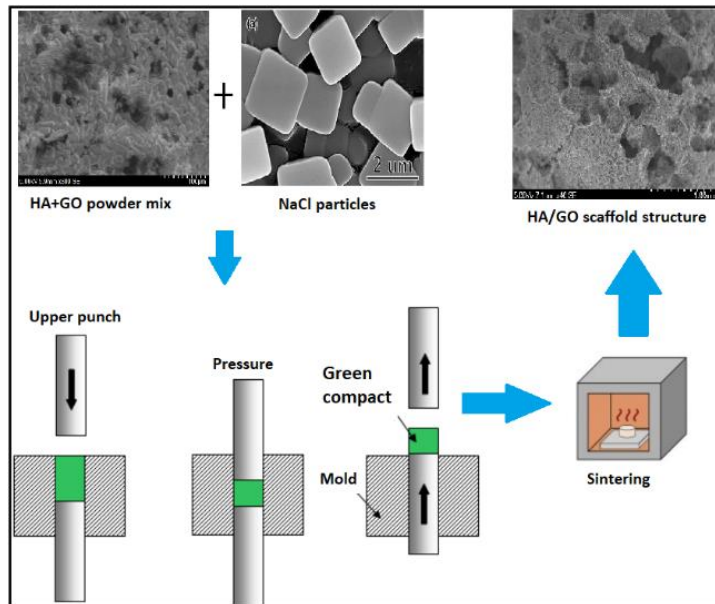
Fig. 1 Production scheme of scaffold structures
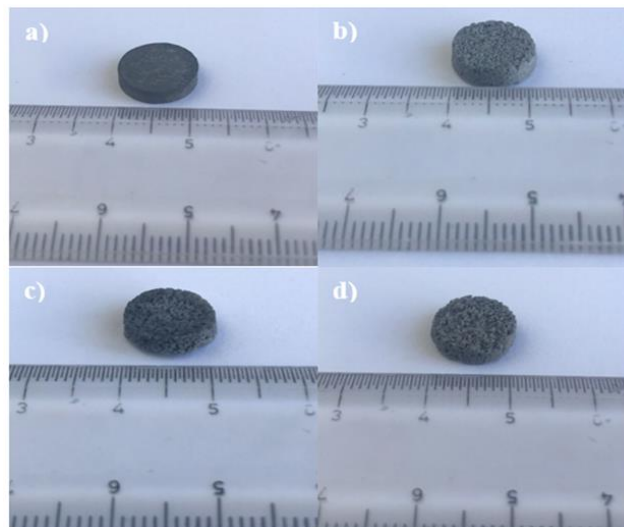
Fig. 2 Images of (a) P40-HA, (b) P40-HA/0.5GO, (c) P40-HA/1GO, (d) P40-HA/1.5GO samples

2.2. Characterization of HA/GO Scaffold Structures

For the structural characterization of the sintered samples, X-ray diffraction analysis (XRD, Rigaku miniflex600) patterns were taken at a scanning speed of 2 degrees/min and in the range of 10-80 degrees. For morphological and elemental analysis, scanning electron microscopy (SEM, Hitachi SU3500) and SEM-dependent energy dispersive X-ray spectroscopy (EDS, Oxford) were used. The tensile device (100 kN, Shimadzu) was used for compression strength. The compression tests were performed on dimensions 10 mm x 6 mm at a speed of 1 mm.min^{-1}.

3. Results and Discussion

3.1. Morphological and structural characterizations of scaffold structures

In this study, HA based, 0.5wt%, 1wt%, and 1.5wt% GO reinforced HA-based porous structures were obtained by using 40% NaCl spacers by volume. The SEM-EDS structural images obtained for the HA sample (P40-HA) and shown in Figure 3a. As illustrated in the figure, porous structures and microcracks were observed on the surfaces following the removal of the NaCl spacer. It is believed that microcrack formation is caused by phase separation by the high temperature heat treatment effect on HA. In fact, it is also known that cracks in HA can negatively affect mechanical strength [3]. In addition, the presence of Cl in the EDS spectrum means that NaCl could not entirely be separated from the structure. To prevent the residual NaCl related peak, the NaCl structure should be fully eliminated by keeping the samples in the water for a longer period of time before the sintering process. SEM-EDS analysis of the 0.5% by weight GO reinforced (P40-HA/0.5GO) scaffold sample is shown in Figure 3b. No cracks in the scaffold structures were seen in the SEM images. The pores in the scaffold structures were found to be relatively smaller. No volumetric shrinkage in samples was observed. As expected, no carbon peak was observed in the P40-HA sample without GO additive in the EDS spectrum, while a significant carbon peak was observed in the GO-reinforceed scaffold structures. Therefore, the presence of the carbon (C) peak in the EDS may be an indication of the GO additive. It is also seen that the peak C is 15% by weight. Such a strong C related peak may also be attributed to the PEG debris which may be stuck to the free GO radicals on the surface of scaffold structures. The SEM images and EDS spectrum of the 1 wt% reinforced GO (P40-HA/1GO) structures are shown in Figure 3c. The SEM image showed a morphological structure with random pores and no cracks. Furthermore, the presence of C in the EDS spectrum almost doubled in comparison to the P40-HA/0.5GO. The presence of Cl was also observed in the P40-HA/1GO scaffold structure.
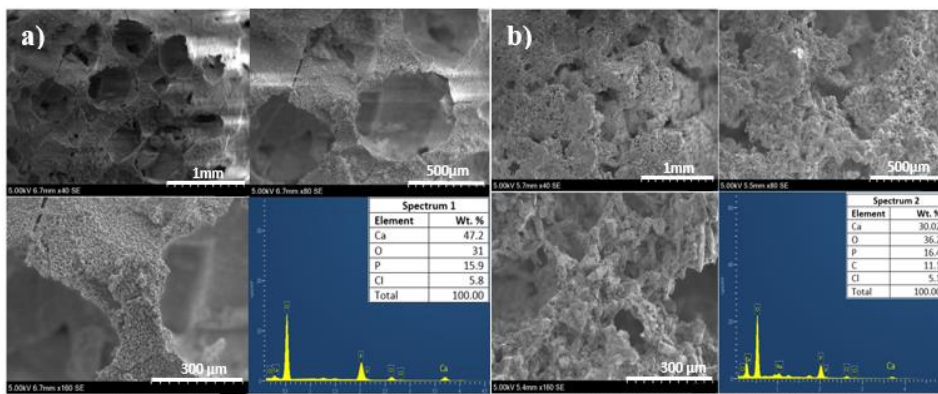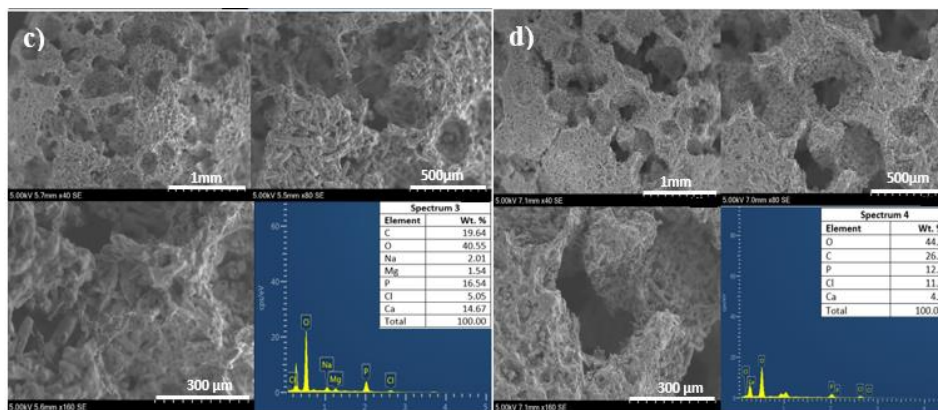
Fig. 3 SEM images and EDS spectra of (a) P40-HA, (b) P40-HA/0.5GO, (c) P40-HA/1GO, (d) P40-HA/1.5GO structures

The SEM images and EDS spectrum of the P40-HA/1.5GO sample reinforced with 1.5 wt% GO are presented in Figure 3d. P40-HA/1.5GO scaffold showed slightly different morphology than those of the P40-HA/0.5GO and P40-HA/1GO structures, as well as the presence of dimensional reduction and crack-forming pores. Overall surface and active sites seemed to be more homogeneous and uniform. It can be attributed to the fact that the GO additive can be formed after 1wt% with its high coefficient of expansion and strong binding of apatite forms to itself [12]. It is believed that the dosage of GO additive can be a limiting entity and can create a disadvantage when higher levels of additive are achieved.
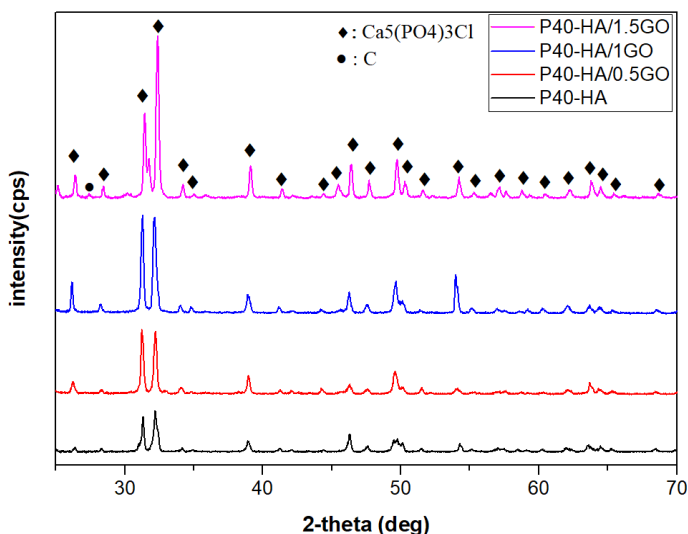
Fig. 4 XRD analysis results of P40-HA, P40-HA/0.5GO, P40-HA/1GO and P40-HA/1.5GO samples

X-ray diffraction patterns were used to determine the elemental analysis of the pore structures obtained. The XRD spectra of P40-HA, P40-HA/0.5GO, P40-HA/1GO, and P40-HA/1.5GO samples by weight are given in Figure 4. As shown in the figure, characteristic peaks of chlorapatite due to heat treatment were observed. In addition, it was observed that the C peak occurred as a result of GO reinforcement. The presence of carbon peak

became more apparent with the rise of GO reinforcement. Again, Tricalcium phosphate (TCP) and CaHPO$_4$ structures, which can be formed due to heat treatment [10,12], were not found in porous structures. The sharp peaks formed by both HA and GO reinforced HA porous structures can be explained by the presence of crystallinity of these structures. After sintering, the characteristic peaks became more pronounced with the removal of water and moisture from the structures.

3.2. Mechanical Measurements

The compression test was applied to the P40-HA, P40-HA/0.5GO, P40-HA/1GO, and P40-HA/1.5GO scaffold structures and the force-elongation values were obtained. The stress-strain curves and compressive strength graphs derived from these force-elongation values are given in Figure 5. The compressive strength of the P40-HA, P40-HA/0.5GO, P40-HA/1GO, and P40-HA/1.5GO scaffolds were measured as 24.6, 28.4, 31.14, and 8.04 MPa, respectively.
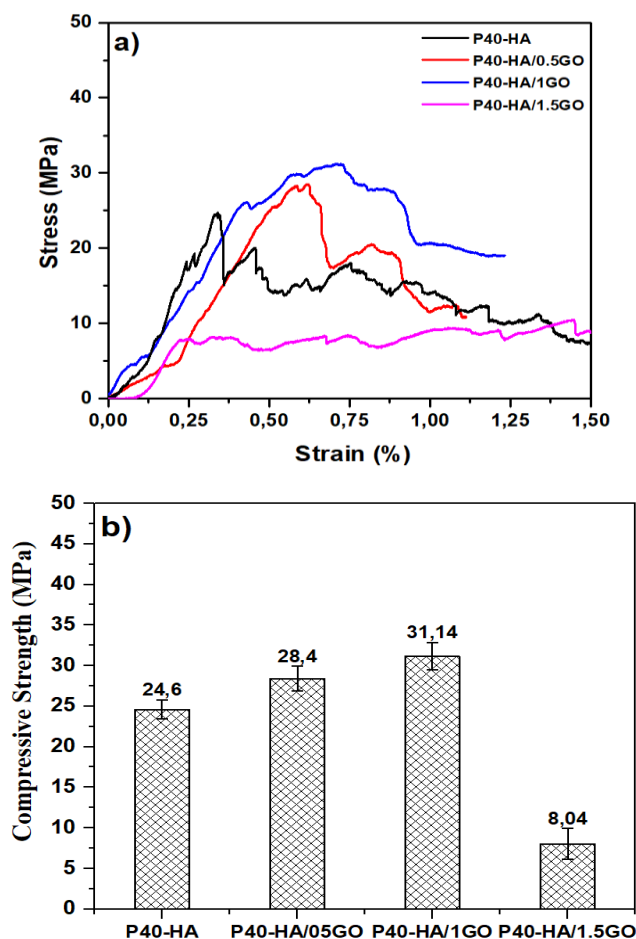
Fig. 5. (a) stress-strain curve and (b) compressive strength values of P40-HA, P40-HA/0.5GO, P40-HA/1GO and P40-HA/1.5GO samples

It is found that there is an increase in mechanical strength with 0.5wt% GO reinforcement and it achieves the highest level in 1wt% GO reinforcement. However, there was a significant reduction in the mechanical strength for 1.5wt% GO reinforcement. This can be

attributed to HA cracks in the scaffold structure and supports our claim that surface cracks increase with the GO reinforcement in Figure 3. Furthermore, it is considered that the addition of GO with sp^2 hybrid bond structure increases the coefficient of expansion, thus tending to bind more to HA and increase cracks [12]. As a matter of fact, the increase in the amount of GO in the matrix material HA (especially over 1wt%) makes it possible to create cracks and negatively affect the mechanical properties due to the fact that the very strong carbon bonds form a tighter bond with the HA forms together with the heat treatment [10, 21].There are various studies in the literature to improve the mechanical strength of HA composite structures. Gr nanoplatlet-nHA composites with various reinforcing ratios were produced by Kumar et al. While the resulting compression strength values were 87 MPa in the undoped HA structure, the highest compression strength value was measured as 96 MPa in the 0.5wt% Gr nanoplates reinforced HA composite structure [23]. In another study, as a result of the compressive strength test applied to PEEK/HA composite structures with different ratios of GO, the lowest value was measured as 45 MPa in the 0.25% GO reinforcing sample, while the highest value was measured as 65.41 MPa in the 1% GO composite structure [24]. Due to the high pores of the obtained scaffold structures, it is possible that the mechanical values of these scaffold structures are lower than Gr/GO-reinforced HA composites.

4. Conclusion

In our study, we used GO as a reinforcement material to enhance the mechanical properties of the HA scaffolds. Unreinforced HA scaffold, 0.5 wt%, 1wt%, and 1.5wt% GO reinforced HA scaffold structures were obtained by powder metallurgy and 40% (v/v) NaCl spacers. The morpho-structural and mechanical properties of the unreinforced HA scaffolds, 0.5wt%, 1wt%, and 1.5wt% GO reinforced HA scaffold structures were investigated. As a result of the morpho-structural characterizations, it was observed that the cracks on the surface increased with the increase of GO additive and the rate of cracks was slightly higher in the 1.5wt% GO added sample. It was observed that the carbon contents of the HA scaffold structures with 0.5%, 1% and 1.5% GO by weight were higher than the amount of additives in the EDS spectrum. This may be because some residues remain on the scaffold structures in the tube furnace when the polymer binder is removed by vacuum heat treatment. As a result of the XRD analysis, chlorapatite peaks were prominently formed in the structure due to the heat treatment and the C peak was observed due to the GO contribution. In both EDS and XRD analysis, in order to minimize the presence of Cl in apatite forms, the NaCl particles in HA can be dissolved in water before heat treatment and completely removed. Stress-strain curves of porous P40-HA structures with 0.5 wt%, 1 wt% and 1.5 wt% GO additives by weight were given and the compression strength values obtained from these curves were calculated. The compressive strengths of the 40% porous HA-GO composite structures were measured between 8.04 and 31.14 MPa. The highest compressive strength was obtained with 31.14 MPa in the 1wt% GO added sample, while the lowest value was measured as 8.04 MPa in the 1.5wt% GO added sample. Our results were compared with the previous results which was similar to our works. It was seen that our results were coherent with the previously published reports where GO was used as reinforcement material in HA scaffolds. Our results suggest that GO-HA scaffold structures can be a potential candidate for cancellous bone tissue implant applications.

References

[1] Feng C, Zhang K, He R, Ding G, Xia M, Jin X, et al. Additive manufacturing of hydroxyapatite bioceramic scaffolds: Dispersion, digital light processing, sintering, mechanical properties, and biocompatibility. J Adv Ceram 2020 93. 2020 Jun 5 [cited 2022 May 30];9(3):360-73. https://doi.org/10.1007/s40145-020-0375-8

[2] Baino F, Novajra G, Vitale-Brovarone C. Bioceramics and scaffolds: A winning combination for tissue engineering. Front Bioeng Biotechnol. 2015;3:202. https://doi.org/10.3389/fbioe.2015.00202

[3] Zhou H, Lee J. Nanoscale hydroxyapatite particles for bone tissue engineering. Acta Biomater. 2011 Jul 1;7(7):2769-81. https://doi.org/10.1016/j.actbio.2011.03.019

[4] Prakash C, Singh G, Singh S, Linda WL, Zheng HY, Ramakrishna S, et al. Mechanical Reliability and In Vitro Bioactivity of 3D-Printed Porous Polylactic Acid-Hydroxyapatite Scaffold. J Mater Eng Perform. 2021 Jul 1 [cited 2022 Apr 30];30(7):4946-56. https://doi.org/10.1007/s11665-021-05566-x

[5] Senthilkumaran CK, Sugapriya S. Hydroxyapatite Formation on the Antase Phasetitanium Dioxide Nanoparticles. Proceedings of the First International Conference on Combinatorial and Optimization, ICCAP 2021, https://doi.org/10.4108/eai.7-12-2021.2314715

[6] Balani K, Zhang T, Karakoti A, Li WZ, Seal S, Agarwal A. In situ carbon nanotube reinforcements in a plasma-sprayed aluminum oxide nanocomposite coating. Acta Mater. 2008 Feb 1;56(3):571-9. https://doi.org/10.1016/j.actamat.2007.10.038

[7] Tercero JE, Namin S, Lahiri D, Balani K, Tsoukias N, Agarwal A. Effect of carbon nanotube and aluminum oxide addition on plasma-sprayed hydroxyapatite coating's mechanical properties and biocompatibility. Mater Sci Eng C. 2009 Aug 31 [cited 2022 Jul 10];7(29):2195-202. https://doi.org/10.1016/j.msec.2009.05.001

[8] Lahiri D, Singh V, Keshri AK, Seal S, Agarwal A. Carbon nanotube toughened hydroxyapatite by spark plasma sintering: Microstructural evolution and multiscale tribological properties. Carbon N Y. 2010 Sep 1;48(11):3103-20. https://doi.org/10.1016/j.carbon.2010.04.047

[9] Silva M, Alves NM, Paiva MC. Graphene-polymer nanocomposites for biomedical applications. Polym Adv Technol. 2018 Feb 1 [cited 2022 Nov 25];29(2):687-700. https://doi.org/10.1002/pat.4164

[10] Aslan N, Aksakal B, Dikici B, Sinirlioglu ZA. Graphene reinforced hybrid-bioceramic coatings on porous-Ti6Al4V for biomedical applications: morphology, corrosion resistance, and cell viability. J Mater Sci. 2022 Sep 1 [cited 2022 Nov 25];57(35):16858-74. https://doi.org/10.1007/s10853-022-07695-7

[11] Eivazzadeh-Keihan R, Alimirzaloo F, Aghamirza Moghim Aliabadi H, Bahojb Noruzi E, Akbarzadeh AR, Maleki A, et al. Functionalized graphene oxide nanosheets with folic acid and silk fibroin as a novel nanobiocomposite for biomedical applications. Sci Rep. 2022 Dec 1 [cited 2022 Nov 25];12(1). https://doi.org/10.1038/s41598-022-10212-0

[12] Aslan N, Aksakal B. Effect of graphene reinforcement on hybrid bioceramic coating deposited on the produced porous Ti64 alloys. J Porous Mater. 2021 Aug 1 [cited 2022 Apr 30];28(4):1301-13. https://doi.org/10.1007/s10934-021-01081-5

[13] Zhang L, Liu W, Yue C, Zhang T, Li P, Xing Z, et al. A tough graphene nanosheet/hydroxyapatite composite with improved in vitro biocompatibility. Carbon N Y. 2013 Sep 1;61:105-15. https://doi.org/10.1016/j.carbon.2013.04.074

[14] Baradaran S, Moghaddam E, Basirun WJ, Mehrali M, Sookhakian M, Hamdi M, et al. Mechanical properties and biomedical applications of a nanotube hydroxyapatite-reduced graphene oxide composite. Carbon N Y. 2014 Apr;69:32-45. https://doi.org/10.1016/j.carbon.2013.11.054

[15] Choy MT, Tang CY, Chen L, Wong CT, Tsui CP. In vitro and in vivo performance of bioactive Ti6Al4V/TiC/HA implants fabricated by a rapid microwave sintering technique. Mater Sci Eng C. 2014 Sep 1;42:746-56. https://doi.org/10.1016/j.msec.2014.06.015

[16] Aslan N, Aksakal B, Findik F. Fabrication of porous-Ti6Al4V alloy by using hot pressing technique and Mg space holder for hard-tissue biomedical applications. J Mater Sci Mater Med. 2021 Jul 1 [cited 2022 Apr 30];32(7):1-11. https://doi.org/10.1007/s10856-021-06546-2

[17] Topuz M, Dikici B, Gavgali M. Titanium-based composite scaffolds reinforced with hydroxyapatite-zirconia: Production, mechanical and in-vitro characterization. J Mech Behav Biomed Mater. 2021 Jun 1;118:104480. https://doi.org/10.1016/j.jmbbm.2021.104480

[18] Ye B, Dunand DC. Titanium foams produced by solid-state replication of NaCl powders. Mater Sci Eng A. 2010 Dec 15;528(2):691-7. https://doi.org/10.1016/j.msea.2010.09.054

[19] Jha N, Mondal DP, Dutta Majumdar J, Badkul A, Jha AK, Khare AK. Highly porous open cell Ti-foam using NaCl as temporary space holder through powder metallurgy route. Mater Des. 2013 May 1;47:810-9. https://doi.org/10.1016/j.matdes.2013.01.005

[20] Topuz M, Dikici B, Gavgali M, Yilmazer Y. Effect of hydroxyapatite:zirconia volume fraction ratio on mechanical and corrosive properties of Ti-matrix composite scaffolds. Trans Nonferrous Met Soc China. 2022 Mar 1 [cited 2022 Apr 30];32(3):882-94. https://doi.org/10.1016/S1003-6326(22)65840-0

[21] Hummers WS, Offeman RE. Preparation of Graphitic Oxide. J Am Chem Soc. 1958 Mar 1;80(6):1339. https://doi.org/10.1021/ja01539a017

[22] Liu Y, Huang J, Li H. Synthesis of hydroxyapatite-reduced graphite oxide nanocomposites for biomedical applications: Oriented nucleation and epitaxial growth of hydroxyapatite. J Mater Chem B. 2013 Apr 7;1(13):1826-34. https://doi.org/10.1039/c3tb00531c

[23] Kumar S, Gautam C, Mishra VK, Chauhan BS, Srikrishna S, Yadav RS, et al. Fabrication of Graphene Nanoplatelet-Incorporated Porous Hydroxyapatite Composites: Improved Mechanical and in Vivo Imaging Performances for Emerging Biomedical Applications. ACS Omega. 2019 Apr 24;4(4):7448-58. https://doi.org/10.1021/acsomega.8b03473

[24] Peng S, Feng P, Wu P, Huang W, Yang Y, Guo W, et al. Graphene oxide as an interface phase between polyetheretherketone and hydroxyapatite for tissue engineering scaffolds. Sci Reports 2017 71. 2017 Apr 20 [cited 2022 Sep 1];7(1):1-14. https://doi.org/10.1038/srep46604

Research Article

Machine learning approaches for predicting compressive strength of concrete with fly ash admixture

Lomesh Mahajan*, Sariputt Bhagat

Department of Civil Engineering, Dr. Babasaheb Ambedkar Technological University, 402103, India

Article Info	Abstract
	As worldwide environments differ from place to place, the cementitious composites change their initial characteristics. That's why it's crucial to understand their mechanical qualities for protection. In the case of concrete, the Compressive strength (C.S) is among the most crucial properties. Nowadays Machine learning (M-L) methods have been significant tools to predicting the C.S of concrete rather than traditional methods. In this study, the experimental investigation is compiled and M-L approaches are used to predict the C.S of fly ash-containing concrete. All of the materials in this research were analyzed for their chemical and physical characteristics and supervised machine learning techniques are the focus for predicting concrete C.S. Outcome prediction techniques like Artificial neural networks (A N N), Gene expression programming (G E P), and Decision trees (D-T) were studied. To run the models with proper datasets, concrete samples (cylinders) with varying mix ratios were cast and evaluated at different ages. The 07 input elements (Cement, fly ash, superplasticizer, coarse aggregate, fine aggregate, water, and curing days) were used to forecast the output element C.S. A total of 100 data points were used to predict CS. Furthermore, the experimental evidence is validated by study of Root mean error (RME), Root mean square error (R M S E). and k-fold Cross validation (R^2), The statistical tests were included to see how well the adopted model was performed. The bagging algorithm method outperforms GEP, ANN, and DT in terms of prediction accuracy, as shown by an R^2 value of 0.97 vs 0.82, 0.81, and 0.78, respectively.

1. Introduction

Concrete is perhaps the tremendously used materials for constructing buildings of every kind, and it can be used in a myriad of different ways across the construction sector. The main components of regular concrete are cement, water, and various sizes of rocks and gravel [1-3]. Globally, cement manufacturing and usage in building projects are the leading causes of greenhouse gases (GHG) [4]. Cement industries are a major CO_2 emitter, Have a significant influence on the environment [5]. As four billion tons of cement production are generated per year, the equal amount of CO2 released in the surrounding region [6]. To limit this impact with using discarded or recycled material is recommended [7]. Not just reduce the need for concrete but its deterioration of the environment will stop [8]. Cement may be replaced by many industrial operational residues (e.g. G G B S, Granite Powder, Fly Ash (F-A) [9]. These additional raw resources will enhance the Hardened concrete and flawlessly reduce carbon footprint up to 80%.

When it comes to the design and research of concrete buildings, the concrete compressive strength (also known as C C S) is considered to be one of the most essential characteristics. The fundamental components of concrete may be enhanced by adding supplementary components like chemical or mineral admixtures, either before or after

the concrete has been set. Cementitious mixtures affect concrete quality [10]. Every project requires a lab strength study to determine concrete quality [11]. Predicting concrete strength is a major difficulty in concrete manufacturing units. For heterogeneous construction, the strength is an essential criterion since ancient time [12]. The mineral admixture added to concrete has a key role in the environment due to global requirements and sustainability [13]. Sustainable materials like fly ash are a reliable alternative for cement in retrofitting, repairs, and big construction. It improves concrete's mechanical and rheological qualities [14].

Because the compressive strength (C.S) of concrete requires a lot of time and effort, It's not easy to find a balance between cost and quality when deciding how much of each appropriate concrete material to use. To save time and money in the lab, scientists have invested more than one decade developing artificial methods for choosing the best strength prediction techniques [15]. It's hard to find or forecast concrete's C.S of complicated mix-ups. Concrete's C.S is evaluated in the lab by breaking the cylinders and standard-sized cubes for a certain amount of time after casting the specimens [16]. The use of this technique has been universally adopted. However, performing testing in a laboratory is likely to be time consuming and money consuming. The traditional accepted lab methods involve lots of time and money for machinery setup and actual specimen testing.

In recent years, aids of advance technologies like artificial intelligence (A-I) and Machine learning (M-L) have been focused into predictive scenario of several mechanical characteristics in concrete [15,17]. M-L approaches such as supervised learning (regression, classification), Unsupervised learning, clustering, and reinforcement learning can be useful to estimate the many other parameters with varying degrees of effectiveness, and they can also assist in predicting the C.S with exact accuracy [22].

2. Machine Learning Overview

The most advanced kind of A-I is machine learning, which has the highest creation of predictive algorithms should be the primary emphasis. This is as a result of the objective recognition of a variety of patterns present in massive datasets for a specific activity that must be completed. This man-made region is designated as Intelligence enables computers to carry out those difficult and complex tasks. Complicated jobs that required a fine level of precision from the robots. These algorithmic processes developed an algorithm that, rather than manually identifying patterns, could learn them from the data. These algorithms individually learned logics from available data, so it perform better than human program interference. These algorithms are built on computer training, which allows learning attributes to make the data point for interpret knowledge and easily create solutions of other accessible datasets. If an algorithm is taught to distinguish benign from malignant lesions on imaging, it may be used with additional image data to malignant based on learned criteria.

The A-I subfields are organized hierarchically as shown in Fig 1. The following is a list of general categories that may be applied to M-L models. Similarly, the M-L branches are categorized in various ways. It is mainly divided into three categories namely Supervised Learning, Unsupervised learning and reinforcement learning.

The model presentation in supervised learning-based tasks starts with the annotated data collection (also known as a feature vector) to imply that datasets include instances of observations and based on what they were anticipating. In order for these models to generate a result of inferring a function that translates feature vectors to label vectors. Standard and well-liked methods of supervised machine learning include the decision

tree, boosting, S V M, AdaBoost, bagging, artificial neural networks, and manipulation of gene expression.
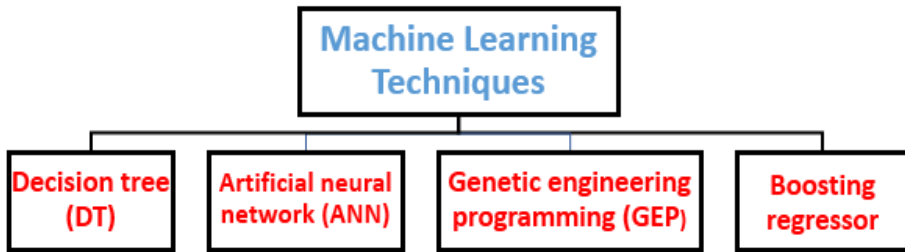
Fig. 1 Artificial intelligence's hierarchical structure and the several subfields

For unsupervised learning, the available datasets are often quite limited for the output labels are scant or nonexistent in several cases. The purpose of these models is rather to determine the interrelationship and/or expose the dormant parameters based on the findings.

3. Literature Review and Machine Learning Techniques

For forecasting of a variety of scientific issues, the hottest trends in machine learning technology commonly used are A N N, G E P and D-L (deep learning) [23-24]. S V M is built to handle nonlinear regression situations better, which helps it overcome the limitations of other methods [25]. It is capable of a superior global optimum solution and has excellent generalizability. In spite of the fact that the Decision tree (D-T) and Random Forest (R-F) is structured like a tree and employs nodes and roots to distribute data. the outcomes of the prediction [26]. DT makes use of an exhaustive database that contains the variable that is of interest to it, while the selection of unique particulars within the factors that create the trees used for prediction in R-F is based on randomization. After then, a correct forecast is shown by connecting the averaged prediction with as many voters as possible. One of the most recent machine learning (M-L) computer algorithms, GEP, was developed by imitating the Darwinian evolutionary process [27]. It does it by expressing the non-linear nature of the connection via an expression tree. Methods that are associated with machine learning (M-L) are often used in order to extract undiscovered trends, necessary data, and relationships from a huge database. Despite this, the procedure makes use of database systems, in addition to machine learning and statistical investigation. Both modeling and prediction may be accomplished via the use of two distinct methods. One among them is a conventional method that is based on a solitary model all on its own, while the other is a methodology that is recognized as the ensemble algorithm method [28]. Early literature on these algorithms suggests that ensemble strategies appear to be more precise when compared to the standard standalone ML models [29]. All weak learners in ensemble learning models are first trained with the use of training data, and then combined these weaker/Slow learners with other learners to form a perfect learner [30].

Though many years ago, numerous machine learning algorithms have been used for the purpose of predicting the performance of different factors. Despite this, there has been a discernible shift toward a greater use of them in the field of civil engineering over the time of the last several years. It is owing to the great level of precision that they possess in their forecasting of properties (mechanical). The working theory of M-L is quite similar to that of traditional algorithms; however, since nonlinear behaviour is more accurate than linear behaviour, the working principle of ML is exactly the same. Evaluation of

tangible mechanical properties frequently makes use of A N N, decision tree algorithm D-T, support vector machines S V M, R-F, G E P, and D-L [31]. Researcher [32] took 11 different algorithms in order to determine the shear strength in the steel fibres reinforced concrete beams. In order to make an accurate prediction of the mechanical characteristics of silica fume concrete, Researcher [33] employed ANN in conjunction with multi-objective grey wolves optimizer. Researcher [34] used D-T, A N N and S V M in order to estimate the C.S of concrete.

Researcher [35] evaluated the C.S and tensile strength of waste concrete using an ANN algorithm. The concrete C.S in marine environments was predicted [36] by using SVM, and the results were compared to those obtained by utilizing ANN and DT models. Using a variety of different machine learning algorithms, [37] were able to forecast the strength properties of lightweight foamed concrete. Researcher [38] made use of a machine learning approach for finding durability property in reinforced concrete. The use of machine learning helped Suguru. [39] to construct an automated detector of fractures in concrete structures. For the purpose of gathering research data, images of the concrete were employed, whereas the use of deep learning was used for the crack detection. Researcher [40] determine the degree of precision achieved by the machine learning models. To make their prediction of the interfacial bond, [41] employs M L R, S V M, and A N N. comparison between fiber-reinforced polymers (FRPs) and concrete in terms of strength.

An A N N, which are effective methods for addressing heterogeneity in the testing model [42]. Many scholars are in favor of the widespread use of A N N in C.S prediction. The input, hidden, and output layers are all components of the feed forward ANN class, which is often referred to as multilayer perception (M L P). These conventional kinds of neural nodes are simpler to work with in the power prediction model [43-44]. This study incorporates a number of categorical criteria for the purpose of predicting the C.S of fly ash concrete mixes. This is done in order to facilitate the development of a unified M-L model that can account for a wide variety of mixture features. In addition, rather than relying on the findings of previous research, the models will make use of a variety of Fly Ash concrete combinations. Since a cemented composite is intended to be used mainly for compression as a building material, the mechanical strength of the material is considered to be the most important feature it possesses. In the research that was done, typical compressive strengths were found to range from around 25 to 115 MPa [45-49].

4. Research Significance

The computational methods have been more productive in the recent decade and minimizes physical efforts due to their time saving techniques. This era of interdisciplinary domain use is emerging field having less validations available in the civil engineering hands. The minute research work available on the ANN tactics and its use in the field of C.S prediction. The Advanced M-L technics can effectively save laboratory handmade workouts and excessive material costing. Aspects of this study's is very significant and innovative due to following reasons (a) originality (b) relevance include its ASTM's experimental works for fly ash concrete (FAC) (c) developing a FAC model with the use of machine learning (M-L) algorithms.

This study focuses on strength predictions by using M-L (DT, ANN, boosting) approaches. Fly ash mixed concrete considered for whole experimental program. M-L was used to predict and compare actual results. Relevance of this quality of the results produced by different M-L algorithms. Another thing that this study does provides a method for contrasting individual and ensemble M-L methods and the outcomes of the experimentation. Each Statistical checks and K-fold performance model assessed for

cross-validation. The goal of this study is to investigate the relationship between the input parameters and the precision of the predicted output. Applications like this were used to make comparisons the accuracy with which various methods make predictions.

Table 1. Trends of adopting M-L techniques for the prediction of various mechanical properties

Sr No	Reference and Year	Algorithm and Method adopted by Researchers	Dataset Used	Output (Prediction Parameter)	alternative mineral admixture used)
1	Researcher [50]	Convolutional Neural Network Regression (CNN), Ensemble Regression models	345	Compressive Strength (C-S)	sludge-cement
2	Researcher [51]	A N N, G E P, and Gradient boosting tree (GBT) models	232	C-S	demolition waste
3	Researcher [52]	support vector regression (SVR), grid search (GS) optimization algorithm,	559	C-S	Not Used
4	Researcher [53]	ensemble deep neural network models	270	C-S	Fly ash
5	Researcher [54]	Back propagation neural network (BPNN), multivariate adaptive regression spline (MARS), Relevance vector machine (RVM)	629	C-S	Not Used
6	Researcher [55]	Individual and ensemble algorithm (GEP, DT and Bagging)	270	(C-S)	Fly ash
7	Researcher [21]	Individual and ensemble modelling (A N N, bagging and boosting)	1030	C-S	Fly ash
8	Researcher [18]	Individual algorithm (A N N, GEP, D-T)	642	Chloride Concentration	Fly ash
9	Researcher [56]	Data Envelopment (DEA)	114	C-S, Slump Value, L-box and V-funnel test	Fly ash
10	Researcher [57]	Multivariate (MV)	21	C-S	Crumb Rubber
11	Researcher [58]	Support vector machine (S V M)	25	C-S	Fly Ash
12	Researcher [59]	SVM	115	Slump Value, L-box and V-funnel test	Fly Ash
13	Researcher [60]	Adaptive neuro fuzzy inference system (ANFIS-ANN)	7	C-S	POFA
14	Researcher [20]	Gene expression programming (GEP)	277	Axial Capacity	Not Used

Table 1 (Cont.) Trends of adopting M-L techniques for the prediction of various mechanical properties

Sr No	Reference and Year	Algorithm and Method adopted by Researchers	Dataset Used	Output (Prediction Parameter)	alternative mineral admixture used)
15	Researcher [61]	G E P	357	C-S	Not Used
16	Researcher [62]	R-F and G E P	357	C-S	Not Used
17	Researcher [63]	A N N	205	C-S	Fly Ash, GGBFS, SF, RHA
18	Researcher [64]	Intelligent rule enhanced multiclass SVM and fuzzy rules (IREMSVM-FR)	114	C-S	Fly Ash
19	Researcher [65]	R-F	131	C-S	Fly ash, GGBFS
20	Researcher [66]	M A R S	114	C-S, Slump value, L-box test	Fly ash
21	Researcher [67]	Random Kitchen Sink Algorithm (RKSA)	40	C-S, Slump value, V-funnel and J-ring test	Fly Ash
22	Researcher [68]	Adaptive neuro fuzzy inference system (ANFIS)	55	C-S	Not Used
23	Researcher [69]	A N N	114	C-S	Fly Ash
24	Researcher [70]	A N N	69	C-S	Fly Ash
25	Researcher [71]	A N N	169	C-S	Fly Ash, GGBFS, RHA

5. Experimental Program

The basic concrete making elements such as water, cement, fly ash, sand, coarse aggregate priory examined with IS Code and ASTM standards. Type-1; 53Grade cement (Ordinary Portland) was used for experimental study. The standard specification stated as per ASTM C150 has been considered for cement used and research work. To avoid effect of surrounding moisture the cement bags were covered with air tight polythene sheets. The fly ash and cement physical-chemical properties are mention in the Table 2 and Table 3.

In order to establish the fine aggregate's qualities, testing was conducted in accordance with the ASTM standard. The concrete mix that was prepared in accordance with ASTM requirements included coarse aggregates that were readily accessible in the surrounding area and had a maximum nominal size of 20 mm. Table 4 includes the physical properties of Coarse Aggregate (CA) and Fine Aggregate (Fa).

The various mix proportions conducted for examination are tabulated in Table 5(a,b,c). The cylindrical Specimen size of 100mm dia and 200 mm height were casted for w/c ratio 0.4 to 0.6. The curing of specimens done at room temperature 27 degree Celsius for period of 3,7,14, 28, and 90days. After proper curing, the C.S carried out according to

ASTM C39. The hit and trial method considered with superplasticizer dose to fulfill desire workability property of mix. The glimpse of laboratory work shown in Fig. 2.

Fig. 2 shows a glimpse of experimental work that were subjected to compressive testing

Table 2. Physical properties of cement and fly ash used

Sr No	Material	Property	Measured Unit	Obtained Value
1	Cement	Specific surface area	Cm2/gm	8299
2	Cement	Specific Gravity	gm/cm2	3.1
3	Cement	Insoluble residue	Percent	0.5
4	Cement	Particle Size	μm	1.65
5	Cement	Loss of Ignition	Percent	2.29
6	Fly Ash	Retention on 45 micron Sieve	Percent	33
7	Fly Ash	Lime Reactivity	N/mm2	7
8	Fly Ash	Soundness test using Autoclave Expansion	Percent	0.06
9	Fly Ash	Drying Shrinkage	Percent	0.05
10	Fly Ash	C.S compare to cement mortar cube	Percent	81

Table 3. Chemical properties of fly ash and cement

Sr No	Chemical Compound	Cement	Fly ash
1	Calcium Oxide-(CaO)	65.82	2.35
2	Iron Oxide-(Fe2O3)	3.63	26.87
3	Silica-(SiO2)	18.99	50.9
4	Alumina-(Al2O3)	6.94	4.27
5	Magnesium Oxide -(MgO)	1.98	1.52
6	Sodium Oxide-(Na2O)	0.10	0.11
7	Potassium Oxide- (K2O)	0.45	1.47

Table 4. Physical properties of Coarse Aggregate (CA) and Fine Aggregate (Fa)

Sr No	Aggregate Type	Property	Measured Unit	Result	Standards Followed
1	CA	Bulk Specific Gravity	No Unit	2.75	ASTM C128, C127
2	Fa	Bulk Specific Gravity	No Unit	2.65	ASTM C128, C127
3	CA	Moisture Content	Percent	0.75	ASTM C566
4	Fa	Moisture Content	Percent	1.10	ASTM C566
5	CA	Moisture Absorption	Percent	1.40	ASTM C128/ C127
6	Fa	Moisture Absorption	Percent	1.10	ASTM C128/ C127
7	CA	Fineness Modulus	No Unit	-	ASTM C136
8	Fa	Fineness Modulus	No Unit	2.45	ASTM C136
9	CA	Nominal Maximum Size	mm	20	-
10	Fa	Nominal Maximum Size	mm	4.70	-
11	CA	Rodded Unit Weight	kg/m³	1580	ASTM C29
12	Fa	Rodded Unit Weight	kg/m³	-	-

The modeling work performed according to 07 input parameters and 01 output (i.e. C.S). This input dataset consists various variables, which mentioned in the Table 6. The details of frequency distribution also presented in the Table 6 and statistical distribution mentioned in Table 7. The concentration used for computing the C-S is graphically represented by using Histogram as shown in Fig. 4.

Table 5a. Mix proportions conducted of specimens (sr. no 1 to 33)

Sample no	Cement (kg/m³)	Flyash (kg /m³)	Water (kg/m³)	Superplast icizer (Kg/m³)	Coarse aggregate (kg/m³)	Fine aggregate (kg /m³)	Curing Period (days)	CS (N/mm²)
1	185.5	102	166.6	7.7	1009.5	908.5	90	39.4
2	170.5	127.9	161.5	8	1093.1	801.6	3	18.23
3	180.5	127.9	165.8	8	1093.1	801.7	14	24.46
4	160.5	127.9	161.8	8	1093.1	807.1	28	28.53
5	241.9	126.1	184	5.9	1060.7	782.4	14	23.03
6	211.9	126.1	183.9	5.9	1060.7	782.4	28	22.93

7	211.9	125.1	183.9	5.9	1060.7	782.4	56	34.33
8	239.8	118.8	191.6	4.8	1032.5	761.7	90	33.43
9	195.1	124.7	160.5	10.1	1091.2	805.7	3	10.61
10	190.5	124.7	161.6	10.1	1091.2	805.7	14	24.22
11	167.9	168.8	172.1	4.7	1061.7	783.2	3	12.9
12	135.9	163.8	176.2	4.7	1061.7	783.2	14	28.61
13	165	161.8	172.1	4.7	1061.7	783.2	28	26.32
14	230.4	118.7	194.9	6.3	1031.2	760.7	3	16.59
15	228.5	119.7	191	6.3	1031.2	760.7	14	22.43
16	229.5	118.7	194.9	6.3	1031.2	760.7	90	43.49
17	247.9	94.6	186.4	7.2	953	850.1	3	22.55
18	237.9	92.6	188.4	7.2	953	850.1	14	27.72
19	247.9	92.6	186.4	7.2	953	850.1	90	48.95
20	250.3	96.2	187.1	5.7	960	864.3	3	13.9
21	250.8	96.2	186.2	5.7	960	864.3	14	28.52
22	212.3	125.4	158.7	8	1088.5	802.6	3	19.54
23	212.4	125.2	181.6	6	1031.5	760.8	14	32.04
24	251.6	124.7	188.2	6.6	1031.5	813.8	56	36.02
25	251.7	123.3	181.3	6.6	1031.5	760.8	90	46.32
26	181.6	123.3	169.3	7.8	1058.7	813.8	3	15.73
27	181.6	123.3	170.3	7.8	1058.7	813.8	14	24.05
28	181.6	123.3	169.3	7.8	1058.7	780.9	28	29.91
29	182.3	124.9	170.3	7.8	1058.7	780.9	56	38.89
30	181.2	122.3	169.3	7.8	1058.7	780.9	90	47.89
31	249.9	125.3	168	9.6	964.3	868.1	90	47.11
32	229.9	125.3	160.3	12	977	878.7	3	23.23
33	220.6	125.3	145.8	12.6	1009.1	902.9	28	32.86
34	210.6	125.3	143	12.2	1089.9	804	56	63.67
35	220.6	125.2	140.8	12.2	1089.9	804	90	63.44
36	213.5	125.2	154.5	10.4	1056.6	779.5	28	44.27
37	213.5	125.3	154.7	10.4	1056.6	779.5	56	48.26
38	213.5	125.3	154.5	10.4	1056.6	779.5	90	55.21
39	213.3	125.3	155.3	11.9	1055.4	778.6	3	20.76
40	213.3	125.3	154.3	11.9	1055.4	803.1	14	38.1

Table 5b. Mix proportions conducted of specimens (sr. no 34 to 66)

Sample no	Cement (kg/m^3)	Flyash (kg /m^3)	Water (kg/m^3)	Superplasti cizer (Kg/m^3)	Coarse aggregate (kg/m^3)	Fine aggregate (kg /m^3)	Curing Period (days)	CS (N/mm^2)
41	213.3	125.3	155.4	11.9	1055.4	803.1	28	43.56
42	213.3	125.3	154.3	11.9	1055.4	803.6	56	50.55
43	213.3	125.3	155.2	11.9	1055.4	803.1	90	59.52
44	218.7	125.3	158.2	11.5	1081.8	798	56	41.33
45	218.7	125.3	159.8	11.5	1081.8	798	90	46.37

46	375.8	125.3	216.4	0	1006.6	765.5	3	20.1
47	190.1	125.3	165.3	10.1	1082.1	802	14	21.34
48	164.8	125.3	163.5	0	1008.7	904	28	27.23
49	190.1	125.3	165	10.1	1082.1	802	28	27.79
50	249.8	125.3	192.5	5.5	952	860.3	28	29.33
51	213.3	125.3	158.9	11.9	1046.7	775	28	45.73
52	194.5	125.3	171.2	7.7	1001.1	904.9	28	40.39
53	251.2	125.3	192.6	6	1046.7	757.4	28	38.11
54	309.8	125.3	189.6	0	939.3	715.3	28	42.06
55	279.8	125.3	189.6	0	939.3	703.1	7	37.69
56	290	125.3	183.3	0	1072.3	757.4	7	24.3
57	252.3	125.3	186.4	0	1114.7	787.4	7	14.23
58	338.8	125.3	196.7	0	971.1	803.1	3	19.36
59	256.8	125.3	192.5	0	971.1	859.6	90	28.66
60	253.8	125.3	192.4	0	971.1	802.8	90	29.78
61	306.8	125.3	193.2	0	971.1	802.6	28	30.45
62	306.8	125.3	190.9	0	971.1	802.6	90	37.04
63	289.8	125.3	191.9	0	939.1	758.1	28	47.41
64	296.8	125.3	191	0	939.1	758.1	90	52.3
65	298.8	125.3	187	0	969.1	766.1	3	18.23
66	287.8	125.3	188.3	0	969.1	761.1	7	22.33
67	288.8	125.3	188.3	0	969.1	762.1	14	30.34
68	291.8	125.3	187	0	969.1	766.1	28	34.67
69	330.8	125.3	191.9	0	981.1	804.1	90	41.22
70	348.8	125.3	191.9	0	1050.1	809.1	3	17.71
71	294.8	125.3	185	0	1072.1	772.5	28	28.31
72	237.8	125.3	184.9	0	1121.1	792.1	28	17.96
73	295.8	125.2	191	0	1088.1	768.6	7	17.95
74	322.3	125.3	203.1	0	977.1	843.1	14	25.23
75	321.8	124.9	201.2	0	977.1	803.3	28	27.27
76	321.8	125.2	202.4	0	977.1	823.1	90	31.69
77	301.8	125.3	202.4	0	977.1	820.1	28	27.23
78	312.3	125.1	182.1	0	1043.1	737.1	28	41.2
79	316.8	125.3	192.2	0	939.1	724.1	3	27.41
80	209.8	125.3	142.2	0	899.1	899.1	7	50.53

Table 5c. Mix proportions conducted of specimens (sr. no 34 to 66)

Sample no	Cement (kg/m³)	Flyash (kg /m³)	Water (kg/m³)	Superplasticizer (Kg/m³)	Coarse aggregate (kg/m³)	Fine aggregate (kg /m³)	Curing Period (days)	CS (N/mm²)
81	220.7	125.3	142.2	0	899.1	899.1	28	73.23
82	143.8	125.3	157.9	18.2	946.1	847.1	28	18.54
83	147.8	125.3	158.1	16.2	1005.1	833.1	28	21.07
84	325.8	125.1	198.8	11.2	804.1	795.1	28	40.9
85	289.8	125.3	220.2	11.2	901.1	716.1	28	10.71
86	299.6	125.3	211.2	10.1	881.3	730.7	28	26.93

87	147.9	125.1	158.9	16.3	1004.9	833.2	28	20.1
88	326.3	125.3	193	11	804.2	795.6	28	36.73
89	276.2	125.3	217.1	11.2	900.8	716	28	10.67
90	150.5	125.3	164.3	15.8	1077.6	690.1	28	16.56
91	190.6	125.3	184.8	11.3	982.6	814.1	28	16.33
92	190.7	125.3	167.9	11.8	994.3	787.1	28	19.78
93	188.5	125.3	182.1	11.9	1026.4	735.1	28	21.13
94	297.9	125.1	189.1	6.3	882.1	818.1	28	42.76
95	318.7	125.3	212.4	5.9	863.6	728.1	28	37.21
96	355.7	125	196	11.2	804.5	772.1	28	37.39
97	199.6	125.3	185.1	12.8	852.4	859.6	28	19.13
98	278.5	125.3	170	10.3	928.4	785.1	28	42.28
99	305.5	125	217	10.6	942.2	796.3	28	42.89
100	318.5	125.3	196	11.2	856.3	736.5	28	43.6

Table 6. Dataset properties for Input- output variables

Parameter	Min value	Max value
Cement (kg/m³)	135.9	375.8
Water content (kg/m³)	141.4	220.9
Fly ash (kg/m³)	92.6	168.8
Superplasticizer (% by mass)	0	18.2
Fine Aggregate (kg/m³)	690.1	908.5
w/c ratio	0.4	0.6
Curing period (days)	3	90
Course Aggregate (kg/m³)	804.1	1121.1
C.S (MPa)	10.6	73.23

The models were executed via the usage of the anaconda programme. The detail names of algorithms used to compute C.S are i) boosting algorithm, ii) Artificial neuron network (A N N), iii) Genetic engineering programming (G E P), and iv)Decision tree (D-T). The simple algorithm flowchart of D-T and A N N Technique in schematic form is mentioned in Fig.3

Table 7. Details of parameters study

Sr. No.	Parameters	Cement kg/m³	Fly Ash kg/m³	Water kg/m3	Super Plasticizer kg/m³
1	Mean or Avg	241.2	123.854	178.77	6.426
3	Median	230.35	124.8	184.2	7
2	Std. Deviation	55.62	10.13	18.01	4.94
2	Std. Error	5.62	1.02	1.82	0.50
4	Mode	213.5	124.8	191.3	0
6	Sample Variance	3093.85	102.65	324.33	24.44
7	Kurtosis	-0.8	9.8	-0.6	-1.1
8	Skewness	0.27	0.55	-0.08	-0.02
9	Maximum	376	168.3	220.5	18
10	Minimum	136.1	92.1	141.1	0
11	Range	239.9	76.2	79.4	18
12	Sum	24120	12385.4	17877.1	642.6
13	Count	100	100	100	100

Table 7(Con.). Details of parameters study

Sr. No.	Parameters	Coarse Aggregate kg/m³	Fine Aggregate kg/m³	Days	Comp. Strength MPa
1	Mean or Avg	1001.3	793.273	33.67	30.49
3	Median	1006.2	794.9	28	27.52
2	Std. Deviation	71.36	48.00	28.81	13.00
2	Std. Error	7.21	4.85	2.91	1.31
4	Mode	1055.6	800	28	17.11
6	Sample Variance	5092.88	2304.07	830.20	169.06
7	Kurtosis	0.3	0.7	-0.1	0.2
8	Skewness	-0.77	0.17	1.06	0.67
9	Maximum	1118	905.4	90	72.11
10	Minimum	801	650	3	9.49
11	Range	317	255.4	87	62.62
12	Sum	100130	79327.3	3367.0	3049.3
13	Count	100	100	100	100

The decision tree is widely recognized as both one of the most simple and effective classification methods. It is a model that resembles a tree that divides data points into a variety of classes based on whether or not the data points fulfil a set of predetermined criteria. D-T manages the categorization job based on criteria derived from the characteristics of the incoming data. The behaviour of the decision tree is designed for no similarities whatsoever in the classification and regression trees.

Artificial neural systems (A N N's), on the contrary hand, are capable of learning similar to the human brain. Artificial intelligence (A-I) relies on A N N as its backbone in order to effectively address difficult issues. ANN has the ability to improve its output via a learning process that it can carry out on its own. Back propagation is a standard set of training rules used by ANNs, just as humans need standard specifications or guidelines to arrive at the correct result or output. For this ANN analysis, hidden layer size taken as (20 nos , 20 nos). The activation function intentionally relu was used and solver kept Adam with alpha-value 0.0001.

The concept of genetic programming was firstly introduced by Ferreira [72]. In comparison to earlier generations of genetic algorithms, Gene expression programming (G E P) can quickly gather massively increased data. Since genetic operators are directly affecting the chromosome, the process is more open. It all starts off with the first population's chromosomes, which are created at random. After the chromosomes are uncovered, fitness cases are used to determine each person's starting point for strength. They are picked out based on how well they can be reproduced and altered. Synthesis of the genomes finally replication with alterations until appropriate results are obtained are all applied to the new chromosomes. The first chromosomes for the population are generated at random. Once a person's chromosomal makeup has been determined, a fitness case is utilized to provide a baseline for their physical ability. Selection criteria include ease of duplication and tampering potential. The new chromosomes go through synthesis, conflict with the selection environment, selection, and eventually replication with changes until the desired outcomes are achieved [72].
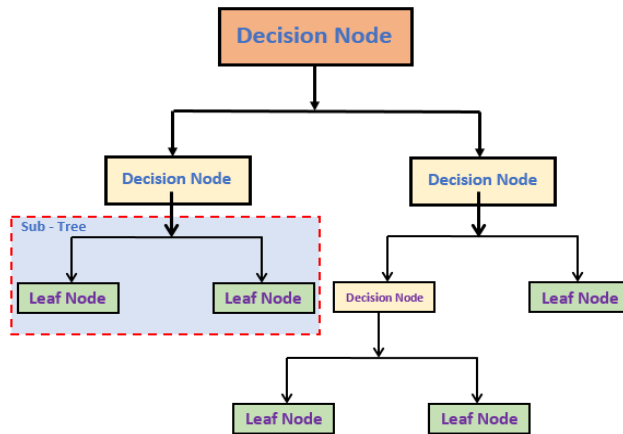
(a)
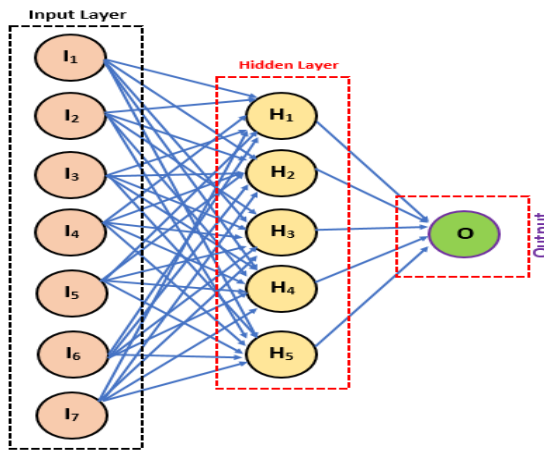
(b)

Fig. 3 Flow Chart of Decision Tree Technique (D-T) and Artificial Neural Network Technique (A N N)

6. Results and Discussion

Figure 5 depicts the findings of the predictive model of fly ash Binder concrete with the help of a decision tree. According to Fig. 5(a), the DT provides a more improved coefficient of correlation $R^2 = 0.76$ when predicting the concrete C-S. In addition, the modelled error distribution indicates value of the average error found 4.22 MPa, with the range 0.001 MPa to 21.40 MPa. In addition, the performance of the model can be evaluated based on its output results. It reveals that the majority of a data points are found within 7 MPa, with a precision of 2/3 results; 1/3 percent of the data is located within the range of 7MPa to 10 MPa; and one data point reveals that space exists more than 20Mpa.

As can be seen in Figure 5 (b), the ANN algorithm's prediction of the C.S produces a value that has a very strong association both with the experimental value and with the value

that was anticipated. The model found an R2 value equal to 0.88 and seen a low error. While the smallest and highest errors were found to be 0.0 MPa (Zero) and 21.4 MPa, respectively. Similarly, one value of distribution error values of model found above 20 MPa and remaining 95 percent as depicted less than 10MPa.

Figure 5 (c) is an illustration of the impact that the factors have on the linear regression model used. The GEP succeeded more correctly than the earlier algorithms by displaying a better value for the coefficient of determination with R square equal to 0.86. Otherwise stated, the GEP outperformed the earlier algorithms. The lowest value of errors is close to 0.77 MPa, average distribution value close to 3.353 MPa and the highest value of errors is equivalent to 5.99 MPa. In addition, the conclusion of the expected error reveals that one hundred percent of the datasets are below 5.99 MPa, demonstrates that the model is accurate.
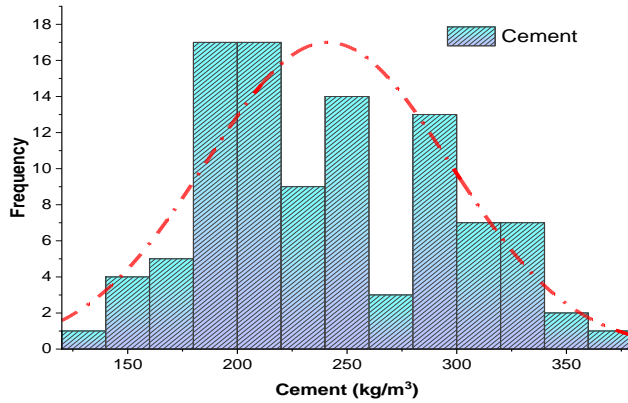
(a)
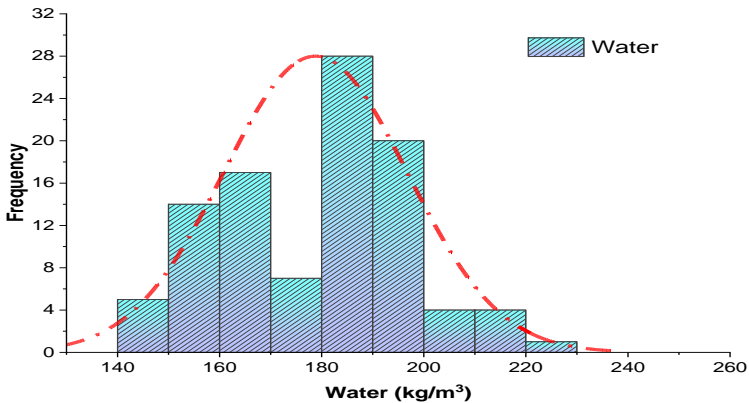
(b)
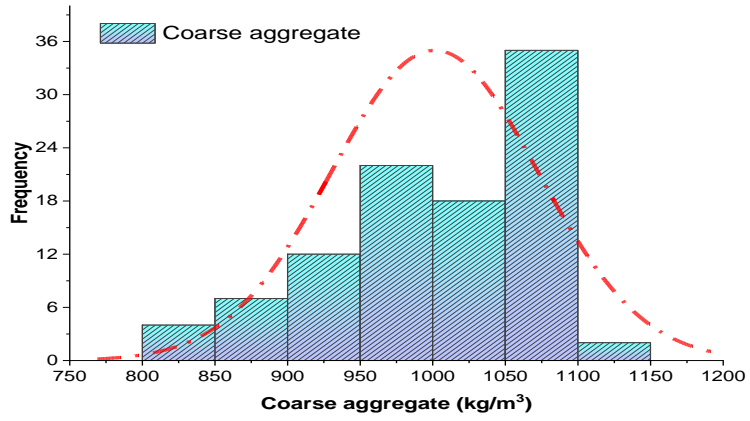
(c)
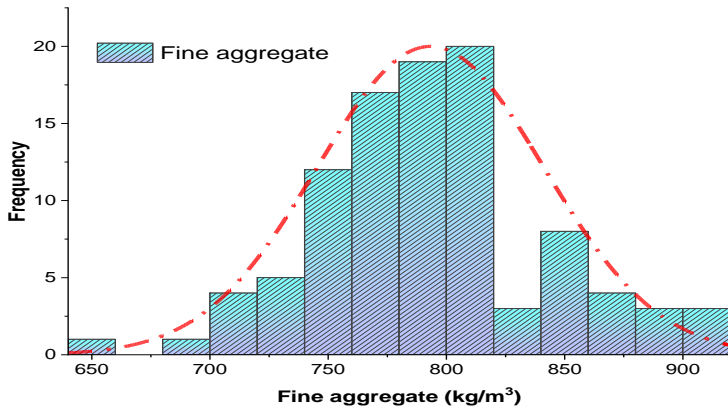
(d)
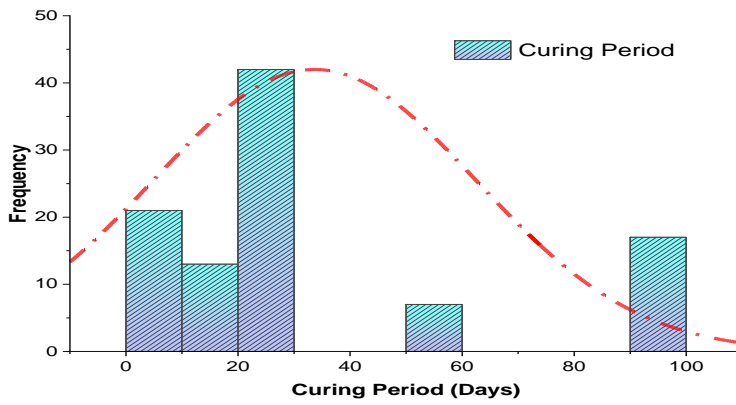
(e)
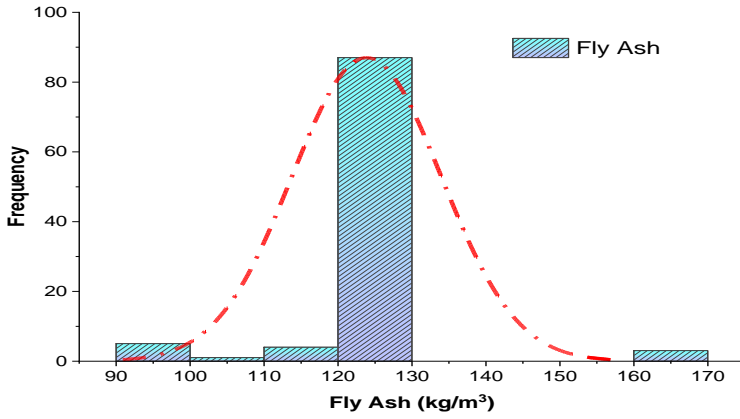
(f)
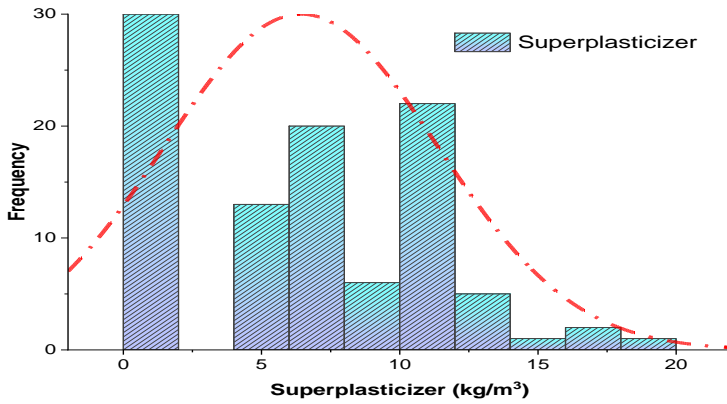
(g)
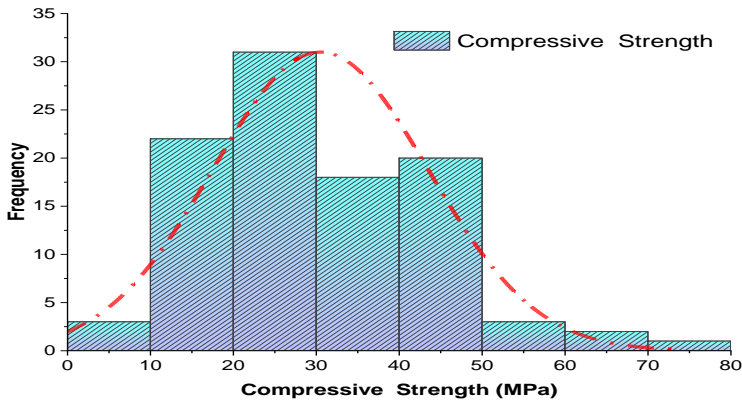
(h)

Fig. 4 Histogram of concentration used for computing the C-S

When compared to the individual machine learning strategies that were used for this research, the performance of the ensemble (boosting) machine learning algorithm that was used to predict the C.S of concrete was much superior. Figure 5(d), which depicts the correlation between the actual and desired output, provides a glimpse of its performance. While Fig. 5(d) provides details concerning the error distribution, which indicates that the highest and lowest values of the error are equal to 3.0 MPa and 0.57 MPa, respectively, including an average error of estimated 2.0 MPa. In addition, the fact that one hundred percent of the error data are below 4 MPa proves how accurate the model is.

6.1 K-fold Cross Validation

The J. knife test and K-fold cross validation algorithm test can be applied for a variety of purposes, such as the lesser of biases in a random training data selection, the attempting to hold out of the data set, and the minimization of the overfitting problems. The stratified 10-fold validation technique is recognized as accurate and is often used for the purpose of achieving the most efficient use of computer resources. The same ten-fold analysis is also used in this research, but it does so by dividing the data into k-groups. It then takes nine out of ten of those subgroups to analyses the data, thus the total number of subsets is ten. The model can only be validated using a single subset of data. This procedure must be carried out a total of 10 times before an average result can be determined. In addition to this, the results of the statistical checks were used to assess the response of the models that were implemented. The evidence on the model's performance was obtained by the use of the formulae, which were developed in line with the relevant research.

In order to investigate whether or not the bias as well as variance of the test set have decreased, the tried-and-true method of k-fold cross validation is being used. In contrast, the output of each of the machine learning algorithms demonstrates some level of variability. In contrast to the A N N and decision tree models, the G E P model has much less errors and a significantly higher R^2 value. Based on the range shown in Fig. 6 (a), the average R^2 value for G E P modelling is 0.82, with values ranging from 0.95 to 0.65. In contrast, the A N N model delivers an average R^2 value of 0.81 over 10 folds, with highest and lowest scores of 0.92 and 0.66. Moreover, as shown in Fig. 6(c), the average R2 value for the Decision tree (D-T) model is 0.78, whereas the highest and lowest values are 0.90 and 0.58, respectively. Reduced error rates in validation are a reflection of improved models. Results from the validation indicators show that the GEP has an average MAE, MSE, and RMSE of 7.89 MPa, 7.80 MPa, and 2.78 MPa, respectively (see Fig. 6 (a)).

The figures 6 (b) for ANN's mean absolute error, mean standard error, and root mean squared error averages are 8.24 MPa, 8.17 MPa, and 2.854MPa, respectively. Similarly, Figure 6 (c) shows the decision tree values of 8.08 MPa, 8.04 MPa, and 2.82 MPa, respectively. While Fig. 6(d) shows that the highest possible value of average R^2 for the boosting regressor is 0.82, the lowest possible value is 0.62, and the max value is 0.97. As can be seen in 11(d), the lowest average values for BR's MAE, MSE, and RMSE were consecutively 6.714 MPa, 6.8 MPa, and 2.59 MPa. The statistical indicator was performed for K-fold cross-validation may be seen shown in Figure 6 (a) to (d).
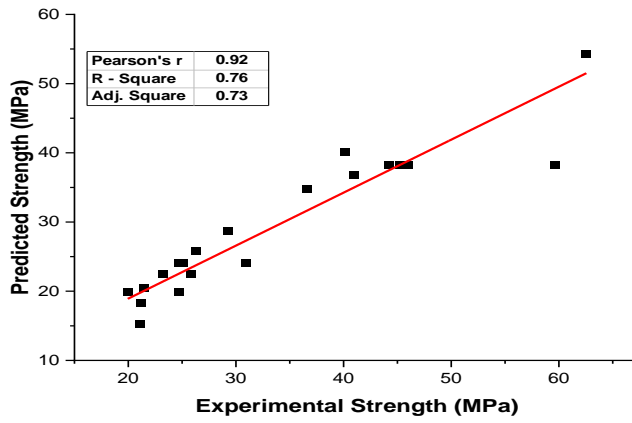
(a)
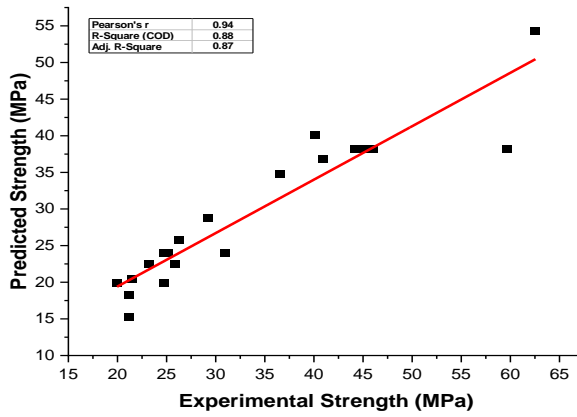
(b)
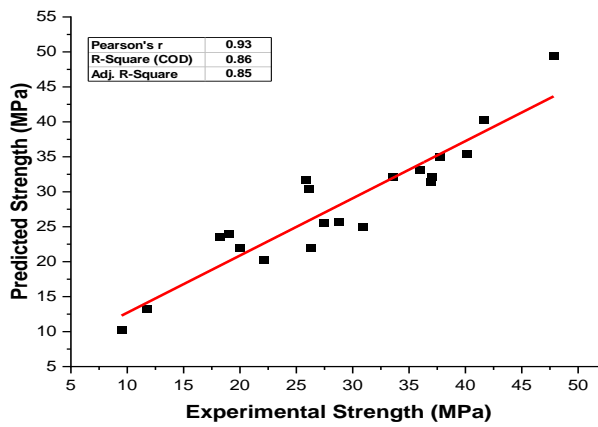
(c)
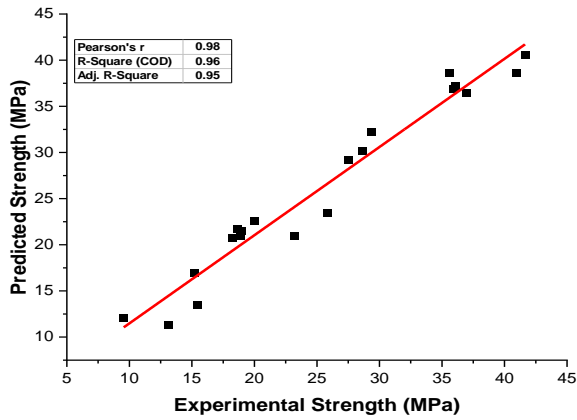
(d)

Fig. 5 (a) Performance of DT algorithm (b) ANN algorithm (c) GEP algorithm (d) Boosting Regressor algorithm , Relation between the predicted and experimental values of the compressive strength

In moreover, statistical tests that were performed on the dataset revealed that the ensemble ML method has lower error rates compared to the other three individual algorithms that were implemented (G E P, A N N, and D-T). The mean absolute error, the mean standard error, and the root mean squared error for the bagging regressor (B-R) come to 3.69 MPa, 24.76 MPa, and 4.79 MPa, respectively, when statistical tests are performed. In contrast to one another, the G E P, A N N, and D-T all display pattern vice with a lower degree of deviation among themselves. This check has a direct connection to the coefficient of correlation (R^2); a lower error value indicates a highest R^2 value again for model.
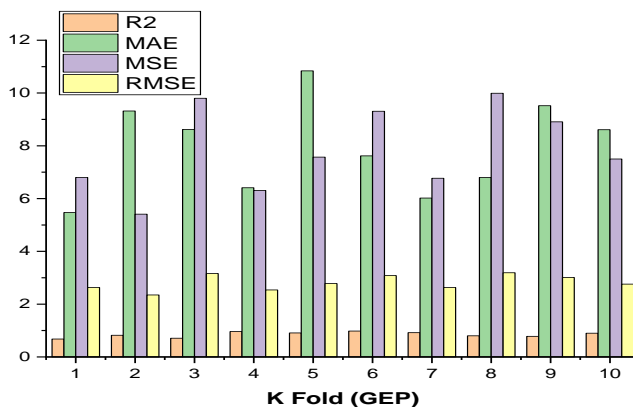
(a)
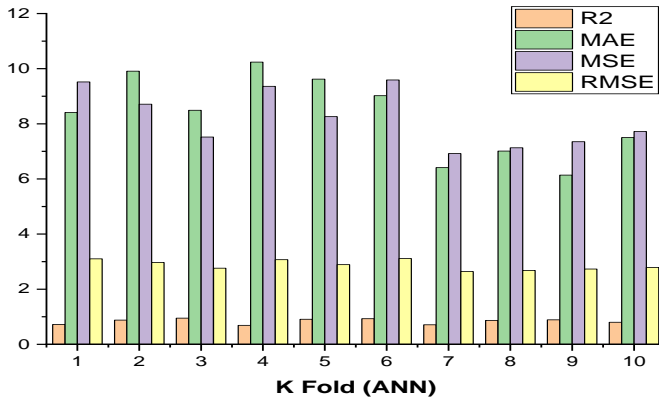
(b)
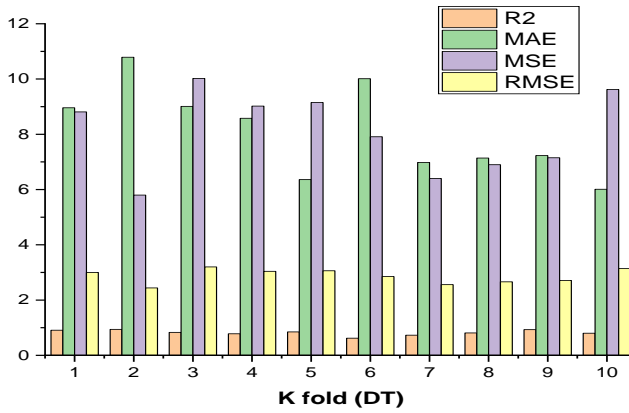
(c)
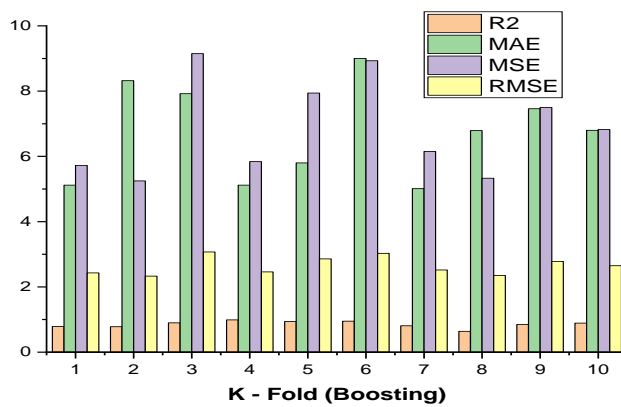
(d)

Fig.6 "K-fold" cross-validation; (a) ANN model and (b) GEP model cross-validation (c) DT model and (d) Boosting regressor

6. Conclusion

This study is predicated on a comparative evaluation of M-L algorithms applied to concrete made with fly ash as its primary component. For the purpose of predicting the C.S of fly ash-mixed concrete, supervised machine learning techniques such as decision tree (D-T), artificial neural network (A N N), genetic engineering programming (G E P), and bagging regressor (B-R) were examined. In addition, the individual machine learning algorithms were contrasted with the ensemble machine learning technique in order to get a deeper comprehension of their capabilities.

- The individual machine learning algorithms demonstrate improved performance, with a less amount of variation between the real and expected results. In comparison to regression, it has the ability to handle many outputs and responses, while regression models can only handle one response at a time. The purpose of this discipline is to study how to replicate and apply some of the cognitive functions of the machine learning tool, so that people may produce technological goods and establish applicable theories.
- However, when the overall accuracy of the independent ML techniques was compared with that of the algorithm employed by the ensemble (bagging regressor), the ensemble was found to be a relatively strong and much more accurate method, as indicated by the value of its coefficient correlation (R^2), and this was equal to 0.97. The G E P, A N N, and D-T each have average R^2 value of 0.82, 0.81, and 0.78, respectively.
- The lower values of the errors, including the mean absolute error (3.6 MPa), the mean squared error (24.6), and the root mean squared error (4.9), further support the excellent accuracy of the bagging regressor, while alternative techniques exhibit greater values for these misjudgments.
- The K-fold cross validation technique, which was used to verify the correctness of the model, also demonstrates that the bagging regressor was beneficial.
- Statistical tests that were performed on the dataset revealed that the ensemble ML method has lower error rates compared to the other three individual algorithms that were implemented (G E P, A N N, and D-T)
- The use of statistical checks additionally verifies that bagging regressor shows an improvement in model performance by reducing the amount of error that exists between the outcomes that were sought and those that were predicted.
- It has been shown that ML algorithms are an effective and practical tool for tackling many structural engineering issues and are predicted to continue to be used in the future.

References

[1] Possan, E, Thomaz WA, Aleandri GA, Felix EF, dos Santos AC. CO2 uptake potential due to concrete carbonation: A case study. Case Stud. Constr. Mater. 2017, 6, 147-161. https://doi.org/10.1016/j.cscm.2017.01.007
[2] Barkhordari, MS, Tehranizadeh M, Scott MH. Numerical modelling strategy for predicting the response of reinforced concrete walls using Timoshenko theory. Mag. Concr. Res. 2021, 73, 988-1010. https://doi.org/10.1680/jmacr.19.00542
[3] Venkateswarlu K, Deo S, Murmu M. Effect of Super absorbent polymer on workability, strength and durability of Self consolidating concrete. Int. J. Eng. 2021, 34, 1118-1123. https://doi.org/10.5829/ije.2021.34.05b.05
[4] Yan H, Shen Q, Fan LCH, Wang Y, Zhang L. Greenhouse gas emissions in building construction: a case study of one peking in Hong Kong, Build. Environ. 45, 2010, 949-955. https://doi.org/10.1016/j.buildenv.2009.09.014

[5] Xiao H, Duan Z, Zhou Y, Zhang N, Shan Y, Lin X, Liu G. CO2 emission patterns in shrinking and growing cities: a case study of Northeast China and the Yangtze River Delta, Appl. Energy. 251, 2019, 113384. https://doi.org/10.1016/j.apenergy.2019.113384

[6] Benhelal E, Zahedi G, Shamsaei E, Bahadori A. Global strategies and potentials to curb CO2 emissions in cement industry, J. Clean. Prod. 51 ,2013, 142-161. https://doi.org/10.1016/j.jclepro.2012.10.049

[7] Kajaste R, Hurme M. Cement industry greenhouse gas emissions - Management options and abatement cost, J. Clean. Prod. 112, 2016, 4041-4052. https://doi.org/10.1016/j.jclepro.2015.07.055

[8] Batayneh M, Marie I, Asi I. Use of selected waste materials in concrete mixes, Waste Manag. 27, 2007, 1870-1876. https://doi.org/10.1016/j.wasman.2006.07.026

[9] Shubbar AA, Jafer H, Dulaimi A, Hashim K, Atherton W, Sadique M. The development of a low carbon binder produced from the ternary blending of cement, ground granulated blast furnace slag and high calcium fly ash: an experimental and statistical approach, Constr. Build. Mater. 187, 2018, 1051-1060. https://doi.org/10.1016/j.conbuildmat.2018.08.021

[10] Gursel AP, Masanet E, Horvath A, Stadel A. Life-cycle inventory analysis of concrete production: a critical review. Cement and Concrete Composites,51, 2014, 38-48. https://doi.org/10.1016/j.cemconcomp.2014.03.005

[11] Mehta PK. Greening of the concrete industry for sustainable development. Concrete International, 24, 2002,7 23- 28.

[12] Mahajan LS, Bhagat SR. Strength Assessment of Concrete using Fly Ash and Metakaolin, In proceeding: International Conference on Advances in Concrete Technology materials and construction practices, Excel India Publishers, New Delhi, 2016, 113-114.

[13] Li VC, Wang S, Wu C. Tensile Strain-Hardening Behavior of Polyvinyl Alcohol Engineered Cementitious Composite (PVA-ECC). Materials Journal, 2001; 98: 483-492 https://doi.org/10.14359/10851

[14] Wang S, Li VC. Engineered Cementitious Composites with High-Volume Fly Ash., ACI Materials Journal,104, 2007, 233-241 https://doi.org/10.14359/18668

[15] Mahajan L, Bhagat S. An artificial neural network for the prediction of the strength of supplementary cementitious concrete. Res. Eng. Struct. Mater., 8(2), 2022, 421-430. https://doi.org/10.17515/resm2022.341st0918tn

[16] Li M, Hao H, Shi Y, Hao Y. Specimen shape and size effects on the concrete compressive strength under static and dynamic tests, Constr. Build. Mater. 161, 2018, 84-93. https://doi.org/10.1016/j.conbuildmat.2017.11.069

[17] Feng DC, Liu ZT, Wang XD, Chen Y, Chang JQ, Wei DF, Jiang ZM. Machine learning-based compressive strength prediction for concrete: an adaptive boosting approach, Constr. Build. Mater. 230, 2020, 117000. https://doi.org/10.1016/j.conbuildmat.2019.117000

[18] Ahmad A, F. Farooq, KA. Ostrowski, K. 'Sliwa-Wieczorek, S. Czarnecki, Application of novel machine learning techniques for predicting the surface chloride concentration in concrete containing waste material, Materials (Basel). 14, 2021, 2297. https://doi.org/10.3390/ma14092297

[19] Khan MA, Memon SA, Farooq F., Javed MF, Aslam F., R. Alyousef, Y. Sun, Compressive strength of fly-ash-based geopolymer concrete by gene expression programming and random forest, Adv. Civ. Eng. 2021, 1-17. https://doi.org/10.1155/2021/6618407

[20] Javed MF, Farooq F, Memon SA, Akbar A, Khan MA, F. Aslam, R. Alyousef, H. Alabduljabbar, S.K.U. Rehman, S.K. Ur Rehman, S. Kashif, U. Rehman, New prediction model for the ultimate axial capacity of concrete-filled steel tubes: anevolutionary approach, Crystals. 10, 2020, 1-33. https://doi.org/10.3390/cryst10090741

[21] Farooq F, Ahmed W, Akbar A, Aslam F, Alyousef R., Predictive modeling for sustainable high-performance concrete from industrial wastes: a comparison and optimization of models using ensemble learners, J. Clean. Prod. 292, 2021, 126032. https://doi.org/10.1016/j.jclepro.2021.126032

[22] Javed MF, Amin MN, Shah MI, Khan K, Iftikhar B, Farooq F, Aslam F, Alyousef R, Alabduljabbar H, Applications of gene expression programming and regression techniques for estimating compressive strength of bagasse ash based concrete, Crystals. 10, 2020, 1-17. https://doi.org/10.3390/cryst10090737

[23] Foucquier A, Robert S, Suard F, St'ephan L, Jay A, State of the art in building modelling and energy performances prediction: a review, Renew. Sustain. Energy Rev. 23, 2013, 272-288. https://doi.org/10.1016/j.rser.2013.03.004

[24] Bhagat SR, Suryawanshi GA, Monali Mahajan, Lomesh S. Mahajan, Artificial neural network techniques for evaluation of pollution, IOP Conf. Series: Earth and Environmental Science 796, 2021. https://doi.org/10.1088/1755-1315/796/1/012052

[25] Lv Y, Liu J, Yang T, Zeng D., A novel least squares support vector machine ensemble model for NOx emission prediction of a coal-fired boiler, Energy. 55, 2013, 319-329. https://doi.org/10.1016/j.energy.2013.02.062

[26] Dou J., Yunus AP, Tien Bui D, A. Merghadi, M. Sahana, Z. Zhu, C.W. Chen, K. Khosravi, Y. Yang, B.T. Pham, Assessment of advanced random forest and decision tree algorithms for modeling rainfall-induced landslide susceptibility in the Izu-Oshima Volcanic Island, Japan, Sci. Total Environ. 662, 2019, 332-346. https://doi.org/10.1016/j.scitotenv.2019.01.221

[27] Zhang D, Tsai JP, Machine learning and software engineering, Softw. Qual. J. 11 , 2003, 87-119. https://doi.org/10.1023/A:1023760326768

[28] J.S. Chou, A.D. Pham, Enhanced artificial intelligence for ensemble approach to predicting high performance concrete compressive strength, Constr. Build. Mater. 49 ,2013, 554-563. https://doi.org/10.1016/j.conbuildmat.2013.08.078

[29] Galar M, Fernandez A, Barrenechea E, Bustince H, Herrera F., A review on ensembles for the class imbalance problem: bagging-, boosting-, and hybrid-based approaches, IEEE Trans. Syst. Man Cybern. Part C Appl. Rev. 42, 2012, 463-484. https://doi.org/10.1109/TSMCC.2011.2161285

[30] Gomes HM, Barddal JP, Enembreck F, Bifet A., A survey on ensemble learning for data stream classification, ACM Comput. Surv. 50, 2017, 1-36. https://doi.org/10.1145/3054925

[31] Rahman J, Ahmed KS, Khan NI, Islam K, Mangalathu S., Data-driven shear strength prediction of steel fiber reinforced concrete beams using machine learning approach, Eng. Struct. 233,2021, 111743. https://doi.org/10.1016/j.engstruct.2020.111743

[32] Jesika Rahman, Khondaker Sakil Ahmed, Nafiz Imtiaz Khan, Kamrul Islam, Sujit Mangalathu, Data-driven shear strength prediction of steel fiber reinforced concrete beams using machine learning approach, Engineering Structures, Volume 233, 2021, 111743. https://doi.org/10.1016/j.engstruct.2020.111743

[33] Behnood A, Golafshani EM, Predicting the compressive strength of silica fume concrete using hybrid artificial neural network with multi-objective grey wolves, J. Clean. Prod. 202, 2018, 54-64. https://doi.org/10.1016/j.jclepro.2018.08.065

[34] Güçlüer K, ¨Ozbeyaz A, S. G¨oymen, O. Günaydın, A comparative investigation using machine learning methods for concrete compressive strength estimation, Mater. Today Commun. 27, 2021, 102278. https://doi.org/10.1016/j.mtcomm.2021.102278

[35] Getahun MA, Shitote SM, Abiero Gariy ZC, Artificial neural network based modelling approach for strength prediction of concrete incorporating agricultural and construction wastes, Constr. Build. Mater. 190, 2018, 517-525. https://doi.org/10.1016/j.conbuildmat.2018.09.097

[36] Ling H, Qian C, Kang W, Liang C, Chen H, Combination of support vector machine and K-Fold cross validation to predict compressive strength of concrete in marine environment, Constr. Build. Mater. 206 ,2019, 355-363. https://doi.org/10.1016/j.conbuildmat.2019.02.071

[37] Zaher M. Yaseen, RC. Deo, A. Hilal, AM. Abd, LC. Bueno, S. Salcedo-Sanz, ML. Nehdi, Predicting compressive strength of lightweight foamed concrete using extreme learning machine model, Adv. Eng. Softw. 115, 2018, 112-125. https://doi.org/10.1016/j.advengsoft.2017.09.004

[38] Taffese WZ, Sistonen E, Machine learning for durability and service-life assessment of reinforced concrete structures: recent advances and future directions, Autom. Constr. 77,2017, 1-14. https://doi.org/10.1016/j.autcon.2017.01.016

[39] Yokoyama S, Matsumoto T., Development of an automatic detector of cracks in concrete using machine learning, in, Procedia Eng., Elsevier Ltd, 2017, 1250-1255. https://doi.org/10.1016/j.proeng.2017.01.418

[40] Ben W, Chaabene, Flah M, Nehdi ML, Machine learning prediction of mechanical properties of concrete: critical review, Constr. Build. Mater. 260, 2020, 119889. https://doi.org/10.1016/j.conbuildmat.2020.119889

[41] Su M, Zhong Q, Peng H, Li S, Selected machine learning approaches for predicting the interfacial bond strength between FRPs and concrete, Constr. Build. Mater. 270, 2021, 121456. https://doi.org/10.1016/j.conbuildmat.2020.121456

[42] Gunasekara C, Setunge S, Law DW, Willis N, Burt T. Engineering Properties of Geopolymer Aggregate Concrete. Journal of Materials in Civil Engineering, 30, 2018, 11 04018299. https://doi.org/10.1061/(ASCE)MT.1943-5533.0002501

[43] Peng CH, Yeh IC, Lien LC. Building Strength Models for High-Performance Concrete at Different Ages using Genetic Operation Trees, Nonlinear Regression, and Neural Networks. Engineering Composites,26, 2010, 61-73. https://doi.org/10.1007/s00366-009-0142-5

[44] Shi L, Lin STK, Lu Y, Ye L, Zhang YX. Artificial Neural Network Based Mechanical and Electrical Property Prediction of Engineered Cementitious Composites. Construction and Building Materials, 174, 2018, 667-74. https://doi.org/10.1016/j.conbuildmat.2018.04.127

[45] Bilim C, Atis CD, Tanyildizi H, Karahan O. Predicting the Compressive Strength of Ground Granulated Blast Furnace Slag Concrete using Artificial Neural Network, Adv. Eng. Soft. 40 (5), 2009,334-340. https://doi.org/10.1016/j.advengsoft.2008.05.005

[46] Sahoo S, Das BB, Mustakim S. Acid, Alkali, and Chloride Resistance of Concrete Composed of Low-Carbonated Fly Ash. Journal of Materials in Civil Engineering, 29(3), 2016; 1-12, 04016242. https://doi.org/10.1061/(ASCE)MT.1943-5533.0001759

[47] Mahajan LS, Bhagat SR. Investigation of the Relationship between Splitting Tensile Strength and Compressive Strength for Prediction of Splitting Tensile Strength of Fy Ash Concrete, In: Proceedings, 3rd International Conference on Innovative Technologies for Clean and Sustainable Development at NITTTR, Chandigarh, India 2020.

[48] Ankur M, Rafat S, Pratap SB, Salima A, Grzegorz L, Danuta BH. Influence of Various Parameters on Strength and Absorption Properties of Fly Ash Based Geopolymer Concrete Designed by Taguchi Method, Construction and Building Materials,150, 2017, 817-824 https://doi.org/10.1016/j.conbuildmat.2017.06.066

[49] Hashmi AF, Shariq M, Baqi A. Haq Moinul, Optimization of Fy Ash Concrete Mix - a Solution for Sustainable Development, Materials Today: Proceedings, 26(2), 2020; 3250-3256. https://doi.org/10.1016/j.matpr.2020.02.908

[50] Jinrui Zhang, Wenjun Niu, Youzhi Yang, Dongshuai Hou, Biqin Dong, Machine learning prediction models for compressive strength of calcined sludge-cement

composites, Construction and Building Materials, Volume 346, 2022, 128442. https://doi.org/10.1016/j.conbuildmat.2022.128442

[51] Babatunde Abiodun Salami, Mudassir Iqbal, Abdulazeez Abdulraheem, Fazal E. Jalal, Wasiu Alimi, Arshad Jamal, T. Tafsirojjaman, Yue Liu, Abidhan Bardhan, Estimating compressive strength of lightweight foamed concrete using neural, genetic and ensemble machine learning approaches, Cement and Concrete Composites, Volume 133, 2022, 104721. https://doi.org/10.1016/j.cemconcomp.2022.104721

[52] Woubishet Zewdu Taffese, Leonardo Espinosa-Leal, Prediction of chloride resistance level of concrete using machine learning for durability and service life assessment of building structures, Journal of Building Engineering, Volume 60, 2022, 105146. https://doi.org/10.1016/j.jobe.2022.105146

[53] Mohammad Sadegh Barkhordari, Mohsen Tehranizadeh, Response estimation of reinforced concrete shear walls using artificial neural network and simulated annealin algorithm, Structures, Volume 34, 2021, 1155-1168. https://doi.org/10.1016/j.istruc.2021.08.053

[54] Panagiotis G. Asteris, Athanasia D. Skentou, Abidhan Bardhan, Pijush Samui, Paulo B. Lourenço, Soft computing techniques for the prediction of concrete compressive strength using Non-Destructive tests, Construction and Building Materials, Volume 303, 2021, 124450. https://doi.org/10.1016/j.conbuildmat.2021.124450

[55] Ahmad A, Farooq F, Niewiadomski P, Ostrowski K, Akbar A, Aslam F, Alyousef R., Prediction of compressive strength of fly ash based concrete using individual and ensemble algorithm, Materials (Basel). 14, 2021, 1-21. https://doi.org/10.3390/ma14040794

[56] Balf FR, Kordkheili HM, Kordkheili AM, A new method for predicting the ingredients of self-compacting concrete (SCC) including fly ash (FA) using data envelopment analysis (DEA), Arab. J. Sci. Eng. ,2020, 1-22. https://doi.org/10.1007/s13369-020-04927-3

[57] Buˇsi'c R, Benˇsi'c M, Miliˇcevi'c I, Strukar K, Prediction models for the mechanical properties of self-compacting concrete with recycled rubber and silica fume, Materials (Basel). 13, 2020, 1821. https://doi.org/10.3390/ma13081821

[58] Azimi-Pour M, Eskandari-Naddaf H, Pakzad A, Linear and non-linear SVM prediction for fresh properties and compressive strength of high volume fly ash self-compacting concrete, Constr. Build. Mater. 230, 2020, 117021. https://doi.org/10.1016/j.conbuildmat.2019.117021

[59] Saha P, Debnath P, Thomas P, Prediction of fresh and hardened properties of selfcompacting concrete using support vector regression approach, Neural Comput. Appl. 32, 2020, 7995-8010. https://doi.org/10.1007/s00521-019-04267-w

[60] Al-Mughanam T, Aldhyani THH, B. Alsubari, M. Al-Yaari, Modeling of compressive strength of sustainable self-compacting concrete incorporating treated palm oil fuel ash using artificial neural network, Sustain. 12, 2020, 1-13. https://doi.org/10.3390/su12229322

[61] Aslam F, Farooq F, Amin MN, Khan K, Waheed A, Akbar A, Javed MF, Alyousef R, Alabdulijabbar H., Applications of gene expression programming for estimating compressive strength of high-strength concrete, Adv. Civ. Eng. 2020, 1-23. https://doi.org/10.1155/2020/8850535

[62] Farooq F, Amin MN, Khan K, Sadiq MR, Javed MF, Aslam F, Alyousef R, A comparative study of random forest and genetic engineering programming for the prediction of compressive strength of high strength concrete (HSC), Appl. Sci. 10, 2020, 1-18, https://doi.org/10.3390/app10207330. https://doi.org/10.3390/app10207330

[63] Asteris PG, Kolovos KG, Self-compacting concrete strength prediction using surrogate models, Neural Comput. Appl. 31, 2019, 409-424. https://doi.org/10.1007/s00521-017-3007-7

[64] Selvaraj S, Sivaraman S., Prediction model for optimized self-compacting concrete with fly ash using response surface method based on fuzzy classification, Neural Comput. Appl. 31, 2019, 1365-1373. https://doi.org/10.1007/s00521-018-3575-1

[65] Zhang J, Ma G, Huang Y, Sun J., F. Aslani, B. Nener, Modelling uniaxial compressive strength of lightweight self-compacting concrete using random forest regression, Constr. Build. Mater. 210, 2019, 713-719. https://doi.org/10.1016/j.conbuildmat.2019.03.189

[66] Kaveh A, Bakhshpoori T., Hamze-Ziabari SM, M5' and mars based prediction models for properties of selfcompacting concrete containing fly ash, Period. Polytech Civ. Eng. 62, 2018, 281-294. https://doi.org/10.3311/PPci.10799

[67] Sathyan D, Anand KB, Prakash AJ, Premjith B, Modeling the fresh and hardened stage properties of self-compacting concrete using random kitchen sink algorithm, Int. J. Concr. Struct. Mater. 12, 2018, 1-10. https://doi.org/10.1186/s40069-018-0246-7

[68] Vakhshouri B, Nejadi S, Prediction of compressive strength of self-compacting concrete by ANFIS models, Neurocomputing. 280, 2018, 13-22. https://doi.org/10.1016/j.neucom.2017.09.099

[69] Belalia Douma O, Boukhatem B, Ghrici M, Tagnit-Hamou A, Prediction of properties of self-compacting concrete containing fly ash using artificial neural network, Neural Comput. Appl. 28, 2017, 707-718. https://doi.org/10.1007/s00521-016-2368-7

[70] Abu Yaman M, Abd Elaty M, Taman M, Predicting the ingredients of self compacting concrete using artificial neural network, Alexandria Eng. J. 56, 2017, 523-532. https://doi.org/10.1016/j.aej.2017.04.007

[71] Asteris PG, Kolovos KG, Douvika, MG, Roinos K, Prediction of self-compacting concrete strength using artificial neural networks, Eur. J. Environ. Civ. Eng. 20(2016) s102-s122. https://doi.org/10.1080/19648189.2016.1246693

[72] Ferreira, C. Gene Expression Programming in Problem Solving. In: Roy, R., Köppen, M., Ovaska, S., Furuhashi, T., Hoffmann, F. (eds) Soft Computing and Industry. Springer, London, 2002. https://doi.org/10.1007/978-1-4471-0123-9_54

Research Article

Influence of PVA and PP fibers addition on the durability and mechanical properties of engineered cementitious composites blended with silica fume and zeolite

H. Emamjomeh[a], K. Behfarnia[b], A. Raji[c], M. Almohammad-albakkar[*,d]

Department of Civil Engineering, Isfahan University of Technology, Isfahan 84156-83111, Iran

Article Info	Abstract
	Over the past two decades the effects of different admixtures have been investigated on mechanical properties and durability of engineered cementitious composites (ECC). Despite this, materials such as silica fume and zeolite have not been thoroughly investigated. The present study was designed and implemented to evaluate the effects of silica fume, zeolite, and blast furnace slag (BFS) on engineered cementitious composites and to compare the mechanical properties and durability of the polyvinyl alcohol-ECC (PVA-ECC) and polypropylene-ECC (PP-ECC) specimens. For this purpose, specimens were subjected to adverse conditions in a 5% magnesium sulfate solution and lab conditions as the reference treatment to measure the post-treatment variations in their compressive strength, flexural strength, and mid-span deflection (MSD). Results demonstrated that PP-ECC was not only easier to manufacture but outperformed PVA-ECC in some respects as well. It was also observed that MSD increased in the PVA-ECC specimens but declined in the PP-ECC ones under identical increments in their BFS contents. Finally, all the specimens maintained under the lab conditions displayed the best performance in terms of strength and durability when 3% silica fume was added to their mixtures while the same addition led to the worst performance in the sulfate medium.

1. Introduction

Although concrete has a history of more than a century in the construction industry, its durability has only recently been investigated. Degradation of concrete structures under such harmful conditions as sulfate, acidic, or chloride ion attacks, as typically occurs in coastal areas, has motivated a lot of research aimed at improving the durability of cement-based materials. Concrete deterioration in coastal areas often takes long years due to the low concentrations of aggressive ions in seawater. Most hydraulic structures are designed for a service life of 50 to 100 years depending on the intended use. Poor durability of cement-based materials, however, causes such structures to deteriorate long before their planned service life is reached [1]. This is especially true for structures in coastal areas or in aquatic environments where aggressive agents continually damaging structures are varied. The Gutianxi II Hydropower Station in China is a clear example of accelerated concrete deterioration only after 30 years of operation that incurred more than four million dollars of payouts on structural repairs [2].

One of the adverse environmental conditions most influencing the durability of concrete hydraulic structures is sulfate attack [3]. The chemical reactions between cement hydration products and sulfate ions produce expansive chemical compounds that cause

*Corresponding author: m.almohammadalbakkar@cv.iut.ac.ir
[a] orcid.org/0000-0003-3962-7559; [b] orcid.org/0000-0003-0881-9849; [c] orcid.org/0000-0002-3372-8239; [d] orcid.org/0000-0003-1684-3080

cracks in concrete that, in turn, allow sulfate ions or water to infiltrate into the inner parts of the structure, thereby accelerating the deterioration process [4] .

A wide variety of causes have been cited for concrete cracking under field conditions. These include mechanical loading, thermal shocks, shrinkage, unequal foundation settlement, and chemical attacks [5] , with sulfate attack being the most common cause of cracks developing within the cement-based materials that ultimately give rise to the poor durability of concrete in hydraulic structures [6, 7]. Even though cracks accelerate concrete deterioration by allowing easier penetration of aggressive ions [8-11], the impacts of cracks on the deterioration process may be trivial when they within a relatively small width range. When crack widths exceed 100 μm, however, corrosion rate grows to a large extent [12, 13]. Wang et al. reported that concrete permeability gradually increased from an uncracked state to that of crack widths 50 μm in size, beyond which a sharp increase was observed in permeability with rising crack widths from 50 to 200 μm [14]. Study has shown that, from the viewpoint of concrete durability, a crack width below 200 μm (and ideally, one below 50 μm) is desirable for hydraulic concrete structures because concrete permeability scales with the 3rd power of crack widths above 50 μm [8, 15-17]. Using electrochemical impedance spectroscopy as a non-destructive test, Zhu et al. [18] investigated the differences between engineered cementitious composites (ECC) and plain mortar in their cracking behavior. Given the fact that cracking in cement-based materials almost inevitably occurs under mechanical loading or adverse environmental conditions, it will be essential in such applications to use construction materials such as engineered cementitious composites (ECC) with potentially low crack widths. This is while ECCs offer the additional advantages of high toughness, spalling resistance, and low permeability [19-26]. Oil-coated polyvinyl alcohol (PVA) fibers have been most commonly used in the manufacture of ECC; however, recent studies show that highly ductile ECCs could also be developed using the non-oil-coated, low tensile strength PVA fiber by re-tailoring the matrix [27]. In a more recent study by Arulanandam et al. [28], an approach using a thorough analytical and finite element analysis (FE) has been used to study the performance of engineered cementitious composite (ECC) beams with and without transverse reinforcements. In a follow-up study by Maheswaran et al. [29], the shear behavior of engineered cementitious composite beams with a hybrid mix of polyvinyl alcohol (PVA) and polypropylene (PP) fibers was investigated experimentally and numerically. The primary objective of their study is to understand how ECC beams with mono and hybrid fiber combinations behave in shear under different shear scenarios. Based on the results, hybrid PVA-PP fibers were found to enhance the performance of ECC beams by improving their performance in terms of strength and ductility in comparison with steel and PP-fibers. moreover, a failure transition from brittle diagonal tension to ductile bending was observed when hybrid fibers were incorporated into ECC beams [29]. Additionally, ABAQUS software was utilized to conduct a detailed nonlinear finite element analysis [29].

Although the mechanical properties and durability of ECCs under different conditions have been investigated in recent years [30-33], only few studies, have been conducted to determine the effects of silica fume, zeolite, blast furnace slag (BFS), and different fiber types on the mechanical and durability properties of ECC. In order to fill this gap, this study examines the effects of silica fume and zeolite on ECCs in 5% magnesium sulfate solution, which is considered the most destructive environment for cement-based materials. In this context, zeolite and silica fume were selected and added to ECCs since they can improve the microstructure of the evaluated concrete; thereby enhancing its performance and permeability properties. In addition, to determine the difference between the performance of the (polyvinyl alcohol) PVA-ECC specimens subjected to the sulfate medium and lab conditions and those of the (polypropylene) PP-ECC specimens, compressive strength,

flexural strength, and midspan deflection were measured at four (28, 150, 180, and 210 days) concrete ages.

2. Experimental Program

2.1. Materials and Mix Designs

To make the ECC mixtures required in this study, type II Portland cement, silica fume, zeolite, blast furnace slag (BFS), and limestone powder (LSP) are used. In parallel, high-range water-reducing admixtures (HRWRA), polyvinyl alcohol (PVA) fibers, or polypropylene (PP) fibers were added. In addition to their great pozzolanic activity, the pozzolans used are cheap and abundant in Iran. The chemical compositions and physical properties of the powder materials are reported in Table 1 and Table 2, respectively.

Table 1. Chemical composition of the materials used (%)

Material	SiO_2	Al_2O_3	Fe_2O_3	CaO	MgO	SO_3	Na_2O	K_2O	$CaCO_3$
Cement	22.00	5.00	3.82	64.00	1.90	1.50	0.25	0.49	-
Zeolite	63.30	11.70	0.32	3.60	1.20	0.09	-	-	-
Silica fume	92.50	0.90	0.80	1.00	1.60	-	0.40	0.35	-
LSP	0.23	0.08	0.09	55.31	0.21	-	-	-	98.72
BFS	34.70	10.93	-	38.37	10.30	2.53	0.60	0.60	-

Table 2. Physical properties of the materials used

Material	Specific gravity (gr/cm³)	Av. size (μm)	Specific surface area (m^2/kg)	L.O. I[1]
Cement	3.15	16.20	300	1.00
Zeolite	2.20	16.84	320	8.49
Silica fume	2.00	0.23	22500	1.70
LSP	2.71	13.40	460	43.43
BFS	2.80	10.60	400	0.56

[1]Loss On Ignition

Clearly, no aggregate was used in the mixtures in order to reduce the fracture toughness of the matrix formed because the presence of aggregates would increase the tortuosity of the fracture path in the ECC.

While both the fibers used were 12 mm in length, the PVA fiber measured significantly higher values of tensile strength and elasticity modulus than did the PP one. The most important difference between the fibers with regards to the properties of the ECCs produced, however, is their surface properties that make them either hydrophobic or hydrophilic. To make the PVA fibers less hydrophilic, a solution containing anti-static materials was sprayed on the fibers. Table 3 reports the mechanical properties of the fibers used in this research. A total number of 280 cube specimens, 70 mm on each side, and 280 prism ones, 350 mm × 100 mm × 30 mm in size, were cast using eight different mix designs.

Table 3. Properties of the fibers used

Fiber	Modulus of elasticity (GPa)	Tensile strength (MPa)	Tensile strain (%)	Specific gravity (gr/cm³)	Length (mm)	Diameter (μm)
PVA	35	1588	6	1.3	12	15
PP	4.1	400	8-10	0.91	12	19

Table 4 reports the mix design proportions. The letters L, S, Z, and M in the designations used for the mix designs represent LSP, BFS, zeolite, and silica fume, respectively. The digits following each letter represent the percentage of the admixture represented relative to the whole cementitious materials used in the specimen; for example, the mixture L30 S40 M3-PVA contained 30% LSP, 40% BFS, and 3% silica fume with the remaining content being Type II Portland cement. Finally, PVA indicates that the specimen was reinforced with PVA fibers.

Table 4. ECC mix design proportions (kg/m³)

Mix ID	Cement	BFS	LSP	Zeolite	SF	Water	HRWRA	PVA	PP
L30 S43-PVA	400	637	445	0	0	474	8	25	0
L30 S47 Z3-PVA	294	691	441	44	0	470	11	25	0
L30 S40 Z3-PVA	399	590	443	44	0	472	11	25	0
L30 S40 M3-PVA	400	593	445	0	44	474	8	25	0
L30 S43-PP	400	637	445	0	0	474	7	0	17
L30 S47 Z3-PP	294	691	441	44	0	470	8	0	17
L30 S40 Z3-PP	399	590	443	44	0	472	8	0	17
L30 S40 M3-PP	400	593	445	0	44	474	5	0	17

The parameters studied included the strength, ductility, and durability of the specimens in a medium of 5% magnesium sulfate solution. Previous study had indicated that the 5% magnesium sulfate solution was more destructive to concrete than such other sulfate solutions as sodium sulfate, particularly with respect to their effects on reducing compressive strength [34-39] . The higher values of high-range water-reducing admixture (HRWRA) reported in Table 4 for the mixtures containing zeolite are due to the porous and platy microstructure of natural zeolite.

2.2. Mixing

The materials used, mixing ratios, mixing method, ECC casting method, and its curing method are the factors with strong effects on ECC performance, especially its ductility. It may, however, be confidently maintained that the mixing method employed is the one with the greatest effect on ECC ductility. For example, in the absence of a proper mixing method, fiber balling will occur in ECC specimens with no subsequent multiple cracking and strain hardening even if all the other factors, including the materials used and their mix proportions, are ideal. Improper mixing has, indeed, a greater negative effect on ECC ductility than it does on other mechanical properties such as compressive strength. Overall, preparing good ECC specimens strongly relies on such important factors as mixing sequence, duration of each mixing step, mixer speed, mortar viscosity during fiber addition, and the rate at which fibers are added into the mixture. In the present

experiment, the following sequence was adopted for mixing the ingredients of the ECC specimens:

- Initially, all the powder constituents including cement, slag, lime powder, and silica fume or zeolite were mixed for 1 minute at 70 rpm.
- Two-thirds to three-quarters (depending on the mix design) of the water and HRWRA were added to the cementitious materials and mixed initially at 140 rpm for 2 minutes followed by mixing at 300 rpm for 1 minute.
- All the fibers were gradually added into the mixture over a period of 10 minutes while being mixed at 140 rpm. At appropriate intervals, the remaining (one-third or one-quarter) water was added to the mixture in 3 to 5 steps (depending on the mix design) and the mixer speed at each step was raised to 300 rpm for 30 seconds.
- Finally, the mixture thus obtained was mixed at 300 rpm for 3 minutes.

2.3. Testing

The ECC specimens were removed out of their molds after 48 hours to be cured in water for 26 days. Five cubes and five prisms from each mix design were subsequently tested and their compression strength and toughness were measured while half of the remaining specimens were transferred into the 5% magnesium sulfate solution and the rest were stored under lab conditions (50±5 relative humidity, 23±2° C). To avoid changes in solution concentration through time due to sulfate precipitation, the sulfate solution was regularly mixed using a timer that would turn on the water pump for 20 min per hour. In addition, all the specimens in the solution were kept adequately spaced from each other using plastic shields.

In order to compare the durability performance of different ECC mixtures treated in the magnesium sulfate solution, the variation in compressive strength, flexural strength, and MSD (MSD corresponding to maximum flexural strength) were calculated at concrete ages of 150, 180, and 210 days. In this study, all the reported results of each parameter were the averages of five measurements and compared with the control mixtures, which were also made with the same constituents and treated under lab conditions.

3. Results and Discussion

3.1. Compressive Strength

Using 70-mm cubic specimens, the compressive strengths of each mix design were measured at the ages of 28, 150, 180, 210 days. Fig. 1and Fig. 2 depict the high ability of the ECC specimens to withstand compressive strains and their cracking patterns, respectively, after the compressive test. Fig. 3 shows the compressive strengths of ECC specimens of different ages treated under lab conditions while Fig.4 presents the reductions in the compressive strength of specimens cured in the sulfate medium. In Fig.4 similar mix designs (those containing the same cementitious constituent but reinforced with different fibers) are shown by similar patterns next to each other but differentiated by different colors (the lighter color represents PP-ECC).

Fig. 1 ECC high ability to withstand compression

Fig. 2 Cracking pattern in ECC specimens due to compressive test

According to Fig. 3, at all the concrete ages tested, the mixtures reinforced with PP fibers recorded higher compressive strengths than those measured in the corresponding ones but reinforced with PVA fibers. The differences could have been due to the presence of the anti-static solution on PVA fibers that formed small air bubbles when mixed with water.
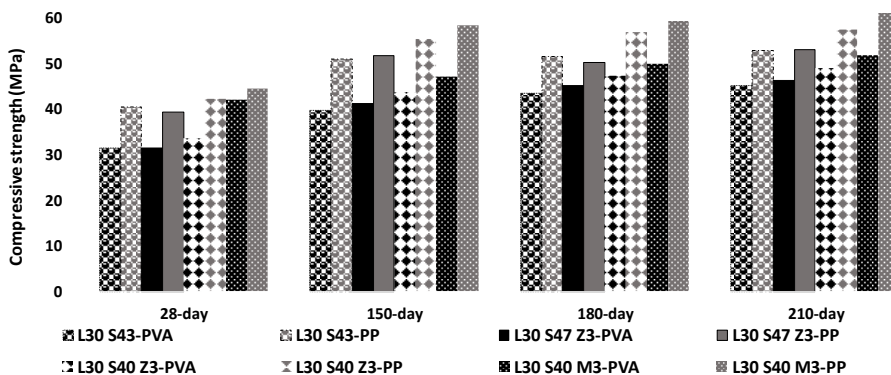
Fig. 3 Compressive strengths of the specimens of different ages treated under lab condition

This is while higher compressive strengths were recorded at all concrete ages and regardless of the fiber type used for the mixture containing silica fume (L30 S40 M3) than those recorded for the mixture containing the same amount of zeolite (L30 S40 Z3), probably due to the higher pozzolanic activity of silica fume than that of zeolite. It must be

noted that an increase of 18% in BFS used in L30 S47 Z3, compared with L30 S40 Z3, reduced its compressive strengths at all ages regardless of the fiber type used; again, this might have been due to the weaker pozzolanic activity of BFS compared to other mixture constituents.
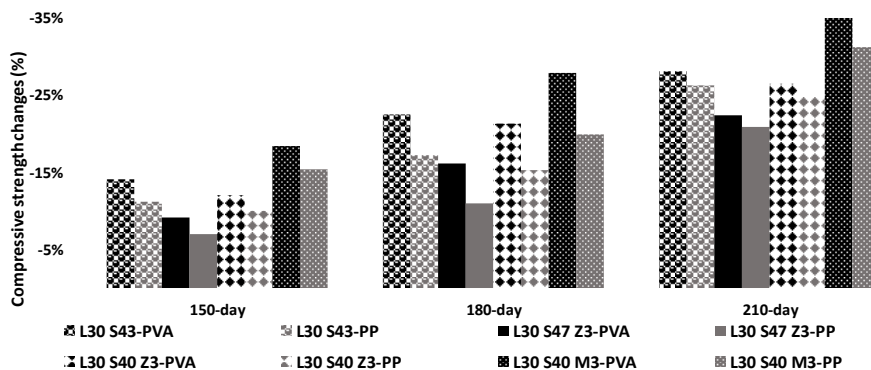
Fig. 4 Variations in the compressive strength of specimens cured in the 5% magnesium sulfate solution relative to the values measured for the control mixes

According to Fig.4, however, the increase in BFS in the specimens treated in the sulfate medium led to their better performance at all concrete ages, indicating the efficacy of BFS in maintaining ECC compressive strength when exposed to the 5% magnesium sulfate solution. This is principally attributed not only to the reduced calcium hydroxide present in the cement paste due to reaction with BFS but also to the pore structure and pore size distribution of the cement paste that were modified by BFS. Moreover, a reduction of 26.5% was observed in the compressive strength of the L30 S40 Z3-PVA specimens at the age of 210 days while the same parameter showed reductions of 24.9% in L30 S40 Z3-PP which indicate compressive strength values by 6% higher in the PP-ECC specimens subjected to a sulfate attack relative to those recorded for the PVA-ECC ones.

It may be figured out from Fig. 4 that the greatest reduction in compressive strength observed for all the three concrete ages due to treatment in the sulfate medium belonged to mixtures containing silica fume, indicating the outperformance of zeolite over silica fume in maintaining the durability of specimens treated in the magnesium sulfate solution. This is probably due to the deterioration of the cement paste as a result of C-S-H conversion into magnesium silicate hydrate (M-S-H) in mixtures containing silica fume. The better performance of the mixtures containing zeolite in sulphate medium undergoes its pozzolanic activity due to its high quantity of reactive SIO_2 and Al_2O_3, which combines with Ca $(OH)_2$ to form additional C-S-H gel. Comparison of L30 S43 and L30 S40 Z3 reveals that 3% zeolite used as a substitute for BFS led to a considerable improvement in the compressive strength of the specimens treated in the sulfate medium, mainly due to the limited formation of ettringite in the presence of zeolite.

A reduction of 22.4% in the compressive strength was recorded for the 210-day L30 S47 Z3-PVA specimen subjected to the sulfate attack while the same measurement for L30 S40 Z3-PVA showed 18.9% reduction. These values indicate that an 18% increment in BFS (L30 S47 Z3 vs L30 S40 Z3) was able to enhance ECC durability in a sulfate environment as a result of enhancements of 15.4% in compressive strength.

3.2. Flexural Strength

The flexural strengths of each mix design at concrete ages of 28, 150, 180, 210 days were measured using 350 x 100 x 30 mm prism specimens. Both PVA-ECC and PP-ECC showed multiple cracking patterns and strain hardening behaviors during the bending test. Fig.5 and Fig.6 illustrate the fiber bridging action and the bending test setup, respectively.

Fig. 5 Fiber bridging in the 28-day L30 S40 Z3-PP specimen at rupture

Fig. 6 Bending test of the 28-day L30 S40 Z3-PP specimen

The ECC specimens exhibited a far more complicated behavior under the bending test, especially with regard to deflection, than they did under the compressive test. This is because the compressive strength of cement composites such as ECC containing polymeric fibers is mainly influenced by the characteristics of the mortar used. In fact, neither the distribution of fibers nor the fiber-matrix bonding has any significant effect on the compressive strength of ECCs. These parameters, however, have great impacts on ECC's flexural behavior so that the study of fiber reinforced concrete behavior under bending or tension requires the impact of a combination of factors to be considered simultaneously. Put simply, any material added to the ECC mixture might lead to changes in the characteristics of the matrix, fiber-matrix interface, and fiber distribution.

Fig. 7 shows the flexural strengths of the specimens treated under lab conditions. Clearly, the mixtures reinforced with PVA fivers exhibited higher flexural strengths at all concrete ages than did the corresponding ones reinforced with PP fibers. This is due to the higher mechanical properties, particularly the higher tensile strength of PVA fibers than that of PP ones, and the higher PVA-matrix bond strength compared to that of the PP-matrix interface. The lower bond strength of the PP-matrix is due to the frictional bonding, rather than a chemical one, at this interface [40] . This is while both chemical and frictional bonds are at work at the interface of the PVA fibers with the matrix.
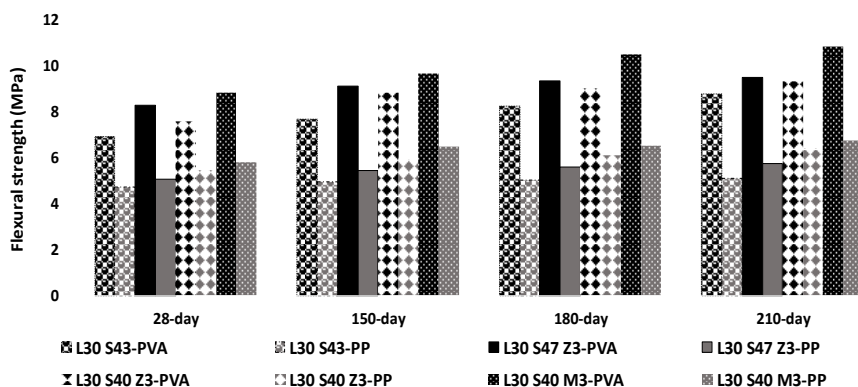
Fig. 7 Flexural strengths at different ages of specimens treated under lab conditions

The specimens with mix designs containing silica fume recorded the highest flexural strengths regardless of their fiber type or concrete age; this was attributed to the higher pozzolanic activity of silica fume compared to those of zeolite and BFS. Moreover, specimens containing silica fume and either type of fiber exhibited flexural strengths higher than did those made of other mixtures (Fig.7); this was also ascribed to the higher pozzolanic activity of silica fume that gave rise to stronger bonds at the fiber-matrix interface. In addition to its higher pozzolanic activity, silica fume leads to a more uniform distribution and, thereby, a more efficient use of fibers. The high flexural strength of mixtures containing silica fume is more pronounced when they are reinforced with PVA fibers because silica fume enhances only the frictional bonds at the PP-matrix interface but it increases both the chemical and frictional bonds at the PVA-matrix one.

An 18% increment in the BFS content of L30 S47 Z3 relative to that of L30 S40 Z3 led to an enhancement in the flexural strength of the specimens with PVA fibers but a slight decrease in that of specimens with PP fibers (Fig.7). This might be related to the effects of increased BFS content on the fiber-matrix interface that vary with the type of fibers used. More specifically, BFS increases in the studied range were observed to reduce the chemical bond strength at the PVA-matrix interface but they improved fiber distribution, the overall result of which was an increment in the specimen's flexural strength. In the case of PP fibers, however, increased BFS content, in contrast to zeolite or cement, reduced the frictional bond strength at the fiber-matrix interface although it improved fiber distribution. As a result, PP fiber slippage was observed to happen because of the poor chemical bond and the reduced frictional bond at their interface with the matrix.

Comparison of L30 S43 and L30 S40 Z3 differing only in their zeolite contents reveals that zeolite increases in the studied range enhanced flexural strength in specimens containing either fiber type and at all concrete ages (Fig.7), indicating that zeolite not only improved fiber distribution but enhanced the chemical bond as well; hence, the observed increase in flexural strength. Moreover, zeolite was observed to have a more pronounced effect on increasing flexural strength in specimens reinforced with PVA fibers while it had almost no such effect on the chemical bonds of PP fibers.

Fig.8 compares the variations in flexural strength in the specimens exposed to the sulfate medium with those of the control mixes. Clearly, the specimens reinforced with PP fibers, regardless of the mix design used or the concrete age, exhibited less reductions in their flexural strengths than did the corresponding ones reinforced with PVA fibers. For

instance, a reduction of 30% was observed in the flexural strength measurements, of the L30 S40 Z3-PVA specimens at the age of 210 days while the same parameters showed reductions of 25.4%, in L30 S40 Z3-PP which indicate flexural strength values by 15.3% higher in the PP-ECC specimens subjected to a sulfate attack relative to those recorded for the PVA-ECC ones. This is probably due to the higher quality and homogeneity of the PP-ECC specimens, due to their denser materials induced by lack of interfacial chemical bonds, than the PVA-ECC ones. A reduction of 26.1% flexural strength was recorded for the 210-day L30 S47 Z3-PVA specimen subjected to the sulfate attack while the same measurement for L30 S40 Z3-PVA showed 22.7% reduction. These values indicate that an 18% increment in BFS (L30 S47 Z3 vs L30 S40 Z3) was able to enhance ECC durability in a sulfate environment as a result of enhancements of 13% flexural strength.

Similar to the changes observed in compressive strength, higher reductions were observed in the flexural strength of the specimens containing silica fume (Fig.8), probably because of the deterioration of the cement paste by C-S-H conversion into magnesium silicate hydrate (M-S-H). These observations bear witness to the superior performance of zeolite with respect to concrete strength over silica when the specimen is under a sulfate attack.
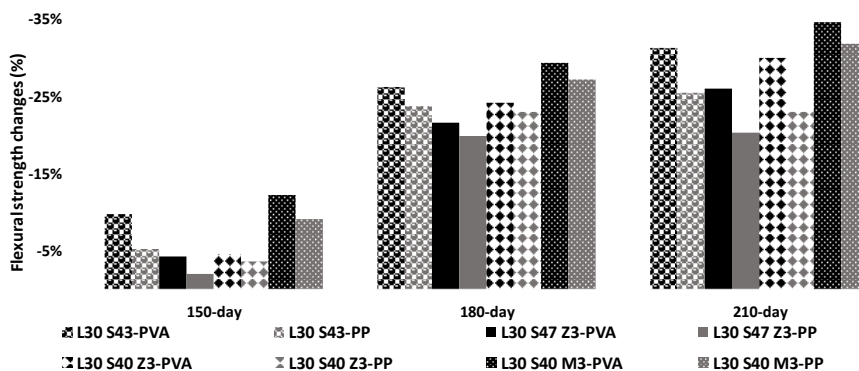
Fig. 8 Variations in flexural strength in specimens cured in the 5% magnesium sulfate solution compared with the control ones

Fig.8 also indicates that, compared to mixtures containing zeolite (namely, L30 S43 and L30 S40 Z3), those lacking in zeolite exhibited a lower resistance against the sulfate environment in terms of flexural strength. this may be explained by the pozzolanic activity of zeolite that consumes it to make a denser matrix, thereby limiting the formation of ettringite.

3.3. Midspan Deflection

Fig.9 shows the MSD values obtained for the specimens treated under lab conditions at different concrete ages. A glance at Fig.9 reveals the significantly higher MSD values of the PP-ECC specimens at all concrete ages than those of the PVA-ECC ones. This is because the lack of chemical bonds at the PP-matrix interface causes the fibers bridging across crack edges to slip due to their insufficient elongation. In contrast, the slippage distance of the PVA fibers is limited because of the presence of both the chemical and frictional bonds at the fiber-matrix interface; this might have been the main reason underlying the higher MSD values of the PP-ECC specimens. It must be reminded that the slippage of PP fibers was clearly observed during the bending test as shown in Fig.5.
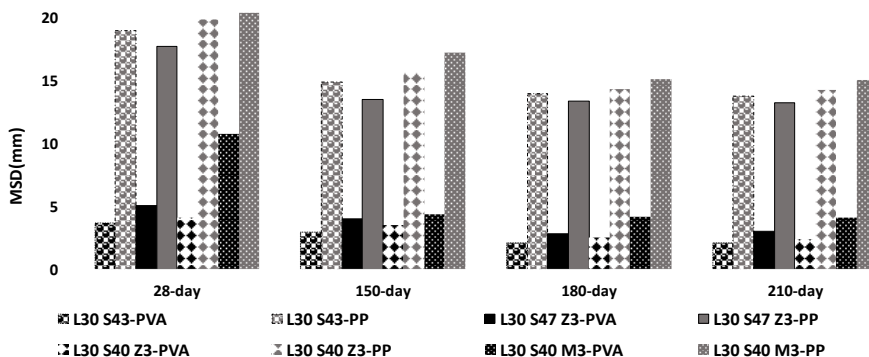
Fig. 9 MSD values at different concrete ages measured in specimens treated under lab conditions

Another interesting point observed during the bending test was the differences in crack formation on the tension side between PP-ECC and PVA-ECC specimens (Fig.10). The crack widths in the PVA-ECC specimens are clearly too small to be seen in the absence of sufficient light or with the naked eye. In contrast, crack widths in the PP-ECC specimens are larger and can be easily seen. This could be due to the higher slippage distance of the PP fibers.
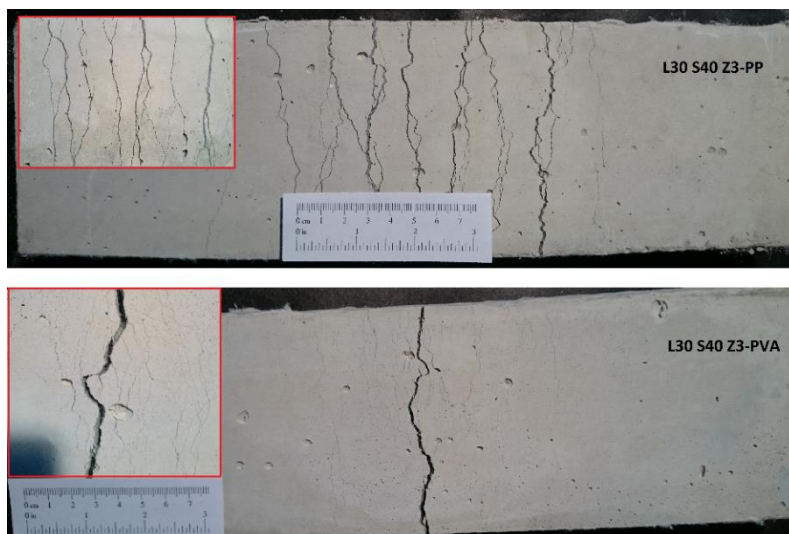
Fig. 10 Crack formation in PP-ECC *vs.* PVA-ECC specimens

The highest MSDs at all concrete ages in both PP-ECC and PVA-ECC specimens were observed in specimens with mixtures containing silica fume, which is probably because of the optimized distribution of fibers and the bond strength at the fiber-matrix interface modified due to the presence of 3% silica fume (Fig.9). Moreover, the increased BFS content gave rise to a 20.4% increment in MSD in PVA-ECC but to a 7.5% decrease in PP-ECC (L30 S47 Z3 vs. L30 S40 Z3), this could be related to the different effects of BFS content on fiber-matrix interfacial bond of PVA-ECC and PP-ECC.
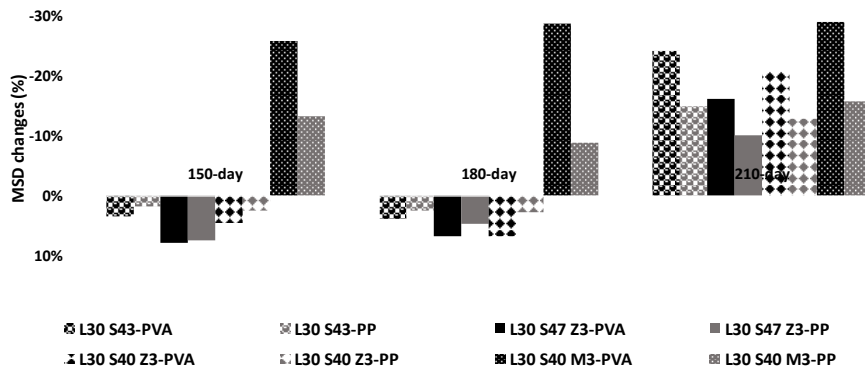
Fig. 11 Variations in MSD values recorded for specimens exposed to the 5%
magnesium sulfate solution compared to those of the control ones

According to Fig. 11, MSD values increased in certain specimens while they decreased in others after treatment in the magnesium sulfate solution. This difference might have arisen from the different effects of magnesium sulfate on matrix toughness and interface bond strength in the different mixtures. One reason that can be claimed for the reduced MSD values in some mixtures is the excessive reduction in their frictional bond strength at the fiber-matrix interface below the permissible range that would allow strain-hardening to occur. On the other hand, the increased MSD values after treatment in the magnesium sulfate solution suggests that both the matrix fracture toughness and the fiber-matrix interface were modified in accordance with the strain-hardening criteria within the micromechanics theory (i.e., due to excessively reduced frictional and chemical bond strengths).

According to Fig. 11, the highest reduction in MSD values both groups of PP-ECC and PVA-ECC specimens were recorded for mixtures containing silica fume, indicating once again that silica fume is not a suitable pozzolan to fight against the adverse effects of the magnesium sulfate solution that is probably due to the conversion of C-S-H to magnesium silicate hydrate (M-S-H) that destroys cement paste, and consequently, causes higher degradation and reduces compressive strength (36). A reduction of 20.8% was observed in the MSD measurements of the L30 S40 Z3-PVA specimens at the age of 210 days while the same parameters showed reduction of 10.8% in L30 S40 Z3-PP which indicate MSD values by 48% higher in the PP-ECC specimens subjected to a sulfate attack relative to those recorded for the PVA-ECC ones.

3.4. Stress-Midspan Deflection Curve

Fig. 12 presents the stress-MSD diagrams for the 28-day PVA-ECC and PP-ECC specimens. Clearly, they all indicate an almost linear pre-cracking behavior for all the mixtures tested in addition to a strain-hardening behavior exhibited by both PVA-ECC and PP-ECC specimens. It is also seen that although the PVA-ECC mixtures obviously exhibit higher flexural strengths, their MSD values are correspondingly lower. It is also interesting to note that, compared to the PP-ECC specimens, the PVA-ECC ones exhibit steeper post-cracking slopes. The difference might be attributed to the high abrasion during the pullout stage resulting from the greater increase in the frictional bond strength at the interface in the PVA-ECC specimens than that in the PP-ECC ones.
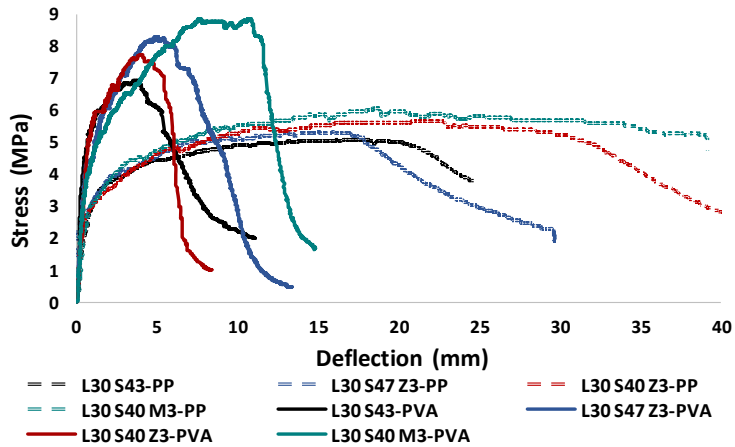
Fig. 12 PVA-ECC stress-MSD diagram

Finally, the PP-ECC specimens do not abruptly rupture after reaching their peak flexural capacity; they, rather, sustain their load-carrying capacity in a milder fashion (i.e., the negative slope in the diagram). This might be explained with recourse to the lower damage incurred by abrasion on the surface of PP fibers than on that of PVA ones.

3.5. Analysis of SEM Images

Based on Fig. 13, the SEM images of a unique mixture (L30 S43) reinforced with different fibers indicate more material bonded to PVA fibers than to PP ones. In addition, the PVA fibers endure severe damages seen as a deep longitudinal crack along the fiber. This could be due to the existence of the high chemical bonds at the PVA-matrix interface, which causes severe damages during the pullout stage. This is while the PP fibers only exhibit a slight abrasion on the surface.
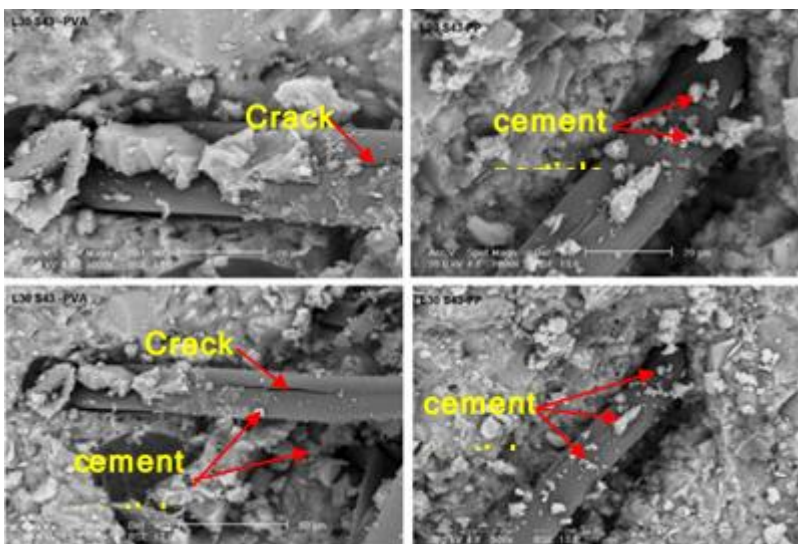
Fig. 13 Post-bending SEM images of 28-day PP-ECC and PVA-ECC specimens
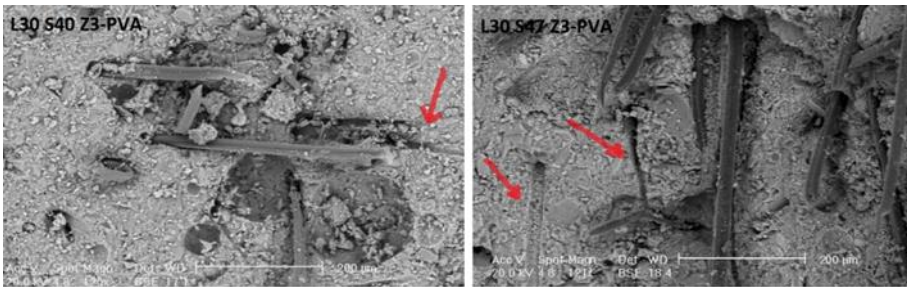
Fig. 14 PVA-ECC fiber pullout path after the bending test

Fig. 14 illustrates the fiber pullout path in L30 S40 Z3-PVA. In fact, after bridging across crack edges, the fibers transfer forces through their development length from one crack edge to the other. The amount of force transferred is a function of both the development length of the fibers and the bond strength at the fiber-matrix interface. The fibers inside the matrix slip if the force applied exceeds fiber capacity. Exploiting this capacity is precisely one of the goals of manufacturing ECCs in this study. Theoretically, on each plane of cracks, the load tolerated by the matrix is taken over by the bridging fibers. The load carried by the bridging fiber is a function of the width opening of the crack and crack opening is a function of fiber bridging characteristics (fiber rupture or fiber slippage). Different combination of fiber-matrix interfacial bond and fiber tensile strength lead to different fiber bridging characteristics, fiber rupture or fiber slippage, and cause differences in the failure mechanism of the ECC [41] . Contrary to intuition, high chemical bond which limits debonding of fiber from matrix is not preferred as it suppresses the fiber slippage as well as multiple cracking creation. Instead, a high frictional bond during fiber slippage is advantageous to maintaining adequate load carrying capacity across the multiple cracks while allowing crack opening to occur in a controlled manner [27] .

4. Conclusion

The mechanical properties and durability of ECC specimens treated in a sulfate medium were experimentally investigated and the effects of silica fume, zeolite, BFS, and fiber type over time were studied on variations in compressive strength, flexural strength, and MSD. Moreover, SEM images were prepared to verify test results. Based on the results obtained, the following conclusions may be drawn:

- Although both PP-ECC and PVA-ECC specimens exhibited multiple cracking patterns and a strain-hardening behavior, the PP-ECC ones showed predominantly higher MSD values and lower compressive and flexural strengths, resulting in their outperformance in a sulfate environment.
- Multiple cracking patterns and crack widths in the PP-ECC specimens were clearly different from those in PVA-ECC ones. The crack width and crack intervals were higher in PP-ECC specimens than those in PVA-ECC ones (PP-ECC crack width was by more than 10 times higher than that of PVA-ECC).
- Compressive and flexural strengths as well as MSD at all concrete ages recorded their highest values in PP-ECC and PVA-ECC specimens containing silica fume and treated under lab conditions. In contrast, the specimens containing silica fume and treated in the sulfate medium were the weakest (i.e., those with the highest reductions in compressive strength, flexural strength, and MSD). This is evidenced by reductions of 37.5%, 34.7%, and 29% in compressive strength, flexural strength, and MSD, respectively, recorded for the 210-day L30 S40 M3-PVA treated in the sulfate medium.

- From among all the mixtures used in both PP-ECC and PVA-ECC specimens, the L30 S47 Z3 one containing the highest BFS content showed the best performance in a sulfate environment at all concrete ages.
- Although an increment of 18% in BFS reduced compression strength in both PP-ECC and PVA-ECC specimens treated under lab conditions, it had different effects on the flexural strength and MSD values of PP-ECC and PVA-ECC specimens under a sulfate medium at all ECC ages such that it led to higher flexural strength and MSD values in the PVA-ECC specimens but to reduced values of the same parameters in the PP-ECC ones.
- Addition of 3% zeolite was observed to enhance the changes in compressive strength, flexural strength, and MSD in both PP-ECC and PVA-ECC specimens treated in a sulfate medium. Moreover, the increased zeolite addition led to the better performance of the ECC in a sulfate environment as evidenced by the average increases of 5.3%, 9.2%, and 14% in the 210-day compressive strength, flexural strength, and MSD, respectively (L30 S40 Z3-PP vs L30 S43-PP).
- SEM imaging showed that the fibers in the PVA-ECC specimens had experienced severe damages while those in the PP-ECC ones experienced only slight scratches; this was attributed to differences in the fiber-matrix bond strengths of PVA-ECC and PP-ECC which led to early and abrupt rupture of PVA fibers and the resulting lower ductility of the PVA-ECC specimens compared to that of PP-ECC ones.

Declaration of Conflicting Interests

The author(s) declared no potential conflicts of interest with respect to the research, authorship, and/or publication of this article.

References

[1] Almohammad-albakkar M, Behfarnia K. Effects of the combined usage of micro and nano-silica on the drying shrinkage and compressive strength of the self-compacting concrete. Journal of Sustainable Cement-Based Materials. 2020:1-19. https://doi.org/10.1080/21650373.2020.1755382
[2] Xing L, Nie G. Analysis on durability of concrete structure of hydropower stations in China. J Hydroelectric Eng. 2003;29(2):27-31.
[3] Charlwood R. Predicting the long term behaviour and service life of concrete dams: na; 2009.
[4] Almohammad-albakkar M, Behfarnia K. Effects of micro and nano-silica on the fresh and hardened properties of self-consolidating concrete.
[5] Nawy E. Control of cracking in concrete structures. Am Concrete Inst Journal & Proceedings. 1972;69(12). https://doi.org/10.14359/11280
[6] Li K, Ma M, Wang X. Experimental study of water flow behaviour in narrow fractures of cementitious materials. Cement and Concrete Composites. 2011;33(10):1009-13. https://doi.org/10.1016/j.cemconcomp.2011.08.005
[7] Han T-S, Feenstra PH, Billington SL. Simulation of highly ductile fiber-reinforced cement-based composite components under cyclic loading. Structural Journal. 2003;100(6):749-57. https://doi.org/10.14359/12841
[8] Tsukamoto M. Tightness of fiber concrete, Darmstadt concrete. Annual Journal on Concrete and Concrete Structures. 1990;5:215-25.
[9] Li VC, Stang H. Elevating FRC material ductility to infrastructure durability. 2004.
[10] Almohammad-albakkar M, Behfarnia K, Mousavi H. Estimation of drying shrinkage in self-compacting concrete containing micro- and nano-silica using appropriate models. Innovative Infrastructure Solutions. 2022;7(5):324. https://doi.org/10.1007/s41062-022-00914-9

[11] Almohammad-albakkar M, Behfarnia K. Water penetration resistance of the self-compacting concrete by the combined addition of micro and nano-silica. Asian Journal of Civil Engineering. 2021;22(1):1-12. https://doi.org/10.1007/s42107-020-00293-5

[12] Li VC. On engineered cementitious composites (ECC). Journal of advanced concrete technology. 2003;1(3):215-30. https://doi.org/10.3151/jact.1.215

[13] Şahmaran M, Li VC. Durability properties of micro-cracked ECC containing high volumes fly ash. Cement and Concrete Research. 2009;39(11):1033-43. https://doi.org/10.1016/j.cemconres.2009.07.009

[14] Wang K, Jansen DC, Shah SP, Karr AF. Permeability study of cracked concrete. Cement and concrete research. 1997;27(3):381-93. https://doi.org/10.1016/S0008-8846(97)00031-8

[15] Aldea CM, Ghandehari M, Shah SP, Karr A. Estimation of water flow through cracked concrete under load. ACI Structural Journal. 2000;97(5):567-75. https://doi.org/10.14359/9289

[16] Aldea C-M, Shah SP, Karr A. Effect of cracking on water and chloride permeability of concrete. Journal of materials in civil engineering. 1999;11(3):181-7. https://doi.org/10.1061/(ASCE)0899-1561(1999)11:3(181)

[17] Aldea C-M, Shah SP, Karr A. Permeability of cracked concrete. Materials and structures. 1999;32(5):370-6. https://doi.org/10.1007/BF02479629

[18] Zhu Y, Zhang H, Zhang Z, Dong B, Liao J. Monitoring the cracking behavior of engineered cementitious composites (ECC) and plain mortar by electrochemical impedance measurement. Construction and Building Materials. 2019;209:195-201. https://doi.org/10.1016/j.conbuildmat.2019.03.132

[19] Banthia N, Sheng J. Fracture toughness of micro-fiber reinforced cement composites. Cement and Concrete Composites. 1996;18(4):251-69. https://doi.org/10.1016/0958-9465(95)00030-5

[20] Lim YM, Li VC. Durable repair of aged infrastructures using trapping mechanism of engineered cementitious composites. Cement and Concrete Composites. 1997;19(4):373-85. https://doi.org/10.1016/S0958-9465(97)00026-7

[21] Maalej M, Quek S, Ahmed S, Zhang J, Lin V, Leong K. Review of potential structural applications of hybrid fiber Engineered Cementitious Composites. Construction and Building Materials. 2012;36:216-27. https://doi.org/10.1016/j.conbuildmat.2012.04.010

[22] Qudah S, Maalej M. Application of Engineered Cementitious Composites (ECC) in interior beam-column connections for enhanced seismic resistance. Engineering Structures. 2014;69:235-45. https://doi.org/10.1016/j.engstruct.2014.03.026

[23] Pan Z, Wu C, Liu J, Wang W, Liu J. Study on mechanical properties of cost-effective polyvinyl alcohol engineered cementitious composites (PVA-ECC). Construction and Building Materials. 2015;78:397-404. https://doi.org/10.1016/j.conbuildmat.2014.12.071

[24] Şahmaran M, Al-Emam M, Yıldırım G, Şimşek YE, Erdem TK, Lachemi M. High-early-strength ductile cementitious composites with characteristics of low early-age shrinkage for repair of infrastructures. Materials and Structures. 2015;48(5):1389-403. https://doi.org/10.1617/s11527-013-0241-z

[25] Meng D, Lee C, Zhang Y. Flexural and shear behaviours of plain and reinforced polyvinyl alcohol-engineered cementitious composite beams. Engineering Structures. 2017;151:261-72. https://doi.org/10.1016/j.engstruct.2017.08.036

[26] Wu C, Li VC. CFRP-ECC hybrid for strengthening of the concrete structures. Composite Structures. 2017;178:372-82. https://doi.org/10.1016/j.compstruct.2017.07.034

[27] Zhang Z, Zhang Q. Matrix tailoring of engineered cementitious composites (ECC) with non-oil-coated, low tensile strength PVA fiber. Construction and Building Materials. 2018;161:420-31. https://doi.org/10.1016/j.conbuildmat.2017.11.072

[28] Arulanandam PM, Sivasubramnaian MV, Chellapandian M, Murali G, Vatin NI. Analytical and Numerical Investigation of the Behavior of Engineered Cementitious Composite Members under Shear Loads. Materials. 2022;15(13):4640. https://doi.org/10.3390/ma15134640

[29] Maheswaran J, Chellapandian M, Sivasubramanian MV, Murali G, Vatin NI. Experimental and Numerical Investigation on the Shear Behavior of Engineered Cementitious Composite Beams with Hybrid Fibers. Materials. 2022;15(14):5059. https://doi.org/10.3390/ma15145059

[30] Lepech M, Li VC, editors. Durability and long term performance of engineered cementitious composites. Proceedings of the International Workshop on HPFRCC in Structural Applications; 2005.

[31] Gao S, Zhao X, Qiao J, Guo Y, Hu G. Study on the bonding properties of Engineered Cementitious Composites (ECC) and existing concrete exposed to high temperature. Construction and Building Materials. 2019;196:330-44. https://doi.org/10.1016/j.conbuildmat.2018.11.136

[32] Kan L-l, Shi R-x, Zhu J. Effect of fineness and calcium content of fly ash on the mechanical properties of Engineered Cementitious Composites (ECC). Construction and Building Materials. 2019;209:476-84. https://doi.org/10.1016/j.conbuildmat.2019.03.129

[33] Wu H-L, Yu J, Zhang D, Zheng J-X, Li VC. Effect of morphological parameters of natural sand on mechanical properties of engineered cementitious composites. Cement and Concrete Composites. 2019;100:108-19. https://doi.org/10.1016/j.cemconcomp.2019.04.007

[34] Jiang L, Niu D. Study of deterioration of concrete exposed to different types of sulfate solutions under drying-wetting cycles. Construction and Building Materials. 2016;117:88-98. https://doi.org/10.1016/j.conbuildmat.2016.04.094

[35] Hashemi S. Experimental study on mechanical properties of different lightweight aggregate concretes. Engineering Solid Mechanics. 2014;2(3):201-8. https://doi.org/10.5267/j.esm.2014.4.003

[36] Behfarnia K, Farshadfar O. The effects of pozzolanic binders and polypropylene fibers on durability of SCC to magnesium sulfate attack. Construction and Building Materials. 2013;38:64-71. https://doi.org/10.1016/j.conbuildmat.2012.08.035

[37] Hekal EE, Kishar E, Mostafa H. Magnesium sulfate attack on hardened blended cement pastes under different circumstances. Cement and Concrete Research. 2002;32(9):1421-7. https://doi.org/10.1016/S0008-8846(02)00801-3

[38] Al-Amoudi OSB. Attack on plain and blended cements exposed to aggressive sulfate environments. Cement and Concrete Composites. 2002;24(3-4):305-16. https://doi.org/10.1016/S0958-9465(01)00082-8

[39] Park Y-S, Suh J-K, Lee J-H, Shin Y-S. Strength deterioration of high strength concrete in sulfate environment. Cement and concrete research. 1999;29(9):1397-402. https://doi.org/10.1016/S0008-8846(99)00106-4

[40] Ananthi A, Karthikeyan J. Combined Performance of Polypropylene Fibre and Weld Slag in High Performance Concrete. Journal of The Institution of Engineers (India): Series A. 2017;98(4):405-12. https://doi.org/10.1007/s40030-017-0248-5

[41] Suthiwarapirak P, Matsumoto T, Kanda T. Multiple cracking and fiber bridging characteristics of engineered cementitious composites under fatigue flexure. Journal of materials in civil engineering. 2004;16(5):433-43. https://doi.org/10.1061/(ASCE)0899-1561(2004)16:5(433)

Research Article

Physico-durability aspects of partial substitution via pelletized fly ash lightweight nano-silica concrete

Waleed A. Abbas[*a], Mohammed L. Abbas[b]

Civil Engineering Dept., University of Technology- Iraq, Al-Sinaa Street, 10066 Baghdad, Iraq

Article Info	Abstract
	This study's main goal is to examine the durability and shrinkage properties of high-performance lightweight concrete (HPLC) which uses lightweight synthetic fly ash instead of some natural coarse aggregate. By combining 90% fly ash and 10% Portland cement by weight in a tilted rotating pan at room temperature and curing the aggregate for 28 days, the synthetic aggregate was created using the cold bonded pelletization procedure. Then, ten combination samples were made using HPLCs by substituting natural coarse aggregate for fly ash aggregate at percentages of 0, 10, 20, 30, and 40% of the aggregate's total volume with a water binder (w/b) ratio of 0.35 both with and without the addition of nano-SiO₂ (nS). Durability characteristics, rapid chloride penetration and water permeability, were tested for 28 and 90 days, while drying shrinkage and weight loss were examined for 61 days. Results demonstrated a lower performance with control mix in terms of durability and shrinkage characteristics with increasing the coarse aggregate replacement (%) of lightweight aggregate (LWA). Additionally, nS improved the transport qualities by reducing the porosity traits and detrimental effects of synthetic LWAs. On the other hand, nS particle-related permeability decreases up to 23.34% due to a larger surface area and smaller particle size that made a permeability channel more meandering or partially closed. HPLCs mixes greatly reduce the overall shrinkage strain when adding 3% nS to HPLC specimens by 11.73% over 61 days. The statistical models that were derived indicated that the independent variables have a statistically significant impact.

1. Introduction

Due to the lack of landfills and the vast amounts of solid waste materials, controlling solid waste management is one of the most difficult problems in our nation and around the world. Reusing and recycling demolition waste is crucial as a result of lessening this issue and looking for an environmentally friendly answer. For instance, enormous amounts of pulverized fly ash are produced by coal-fired thermal plants, yet lesser amounts can be used in the building sector. Due to the severe lack of natural aggregates, synthetic aggregate utilization in the building industry has received significant attention. Thus, the manufacturing of synthetic aggregates addresses two issues: decreasing environmental harm and averting the loss of natural resources, paving the way for sustainable growth. Cold bonding and sintering are efficient ways to manufacture lightweight aggregates. Low strength synthetic aggregates are produced via cold bonding, which requires little energy and relies on the pozzolanic reaction of fly ash to assemble tiny particles into pellet. Pelletization, a procedure that involves mixing fly ash with the right quantity of water and a binder like cement in a pelletizer, can be used to create artificial lightweight fly ash aggregates that are then further hardened using the cold bonding technique [1 – 6]. Thomas, J. and Harilal, B. [7] provide a framework for assessing the sustainability of cold-

bonded aggregates. Social, environmental, and economic aspects served as the primary evaluation criterion. These three sustainability pillars. Utilized were cold-bonded aggregates made from waste products like fly ash and quarry dust. According to this finding, cold-bonded aggregates are viable and should be taken into account when producing used concrete. The volume of binder and the distance to the raw material source were both mentioned as important considerations.

Civil infrastructures are commonly vulnerable to severe loading conditions and harsh environments, especially for structures in aggressive environments. Therefore, durability is an important feature of concrete since it strongly affects structures' maintenance costs and service life. Concrete service life is mainly influenced by permeability associated with harmful agents like chloride, water permeability, carbon dioxide (CO_2), etc. Permeability is one of the fundamental characteristics of concrete structures, as it is closely associated with durability. Concrete durability depends strongly on the ability of concrete to prevent the entry of aggressive chemical species. For this reason, the permeability of concrete is a key indicator and major index for this ability [8 - 9].

The interfacial transition zone (ITZ) between coarse aggregate and cement paste is well established to have an effect on the durability of concrete. In general, when light weight aggregate (LWA) is used, the ITZ is better than when normal weight aggregate (NWA) used [10]. In general, LWAs have more porosity than NWAs. The permeability of LWC might not always be greater than that of NWC. Increasing porosity, enhancing the transition zone between the surface, enhancing cement hydration owing to internal curing, and limiting micro cracking that may affect chloride ions and water transport in the concrete are just a few of the ways that LWCs differ from NWCs. Since linking the pore system has been crucial, the transport properties of LWC in comparison to NWC rely on which of these variables is prominent. The quality of the LWC matrix is typically more significant in regulating the concrete's transport properties [11-12].

The growth of high strength-performance concrete for specific applications results from the retro-gradation of concrete structures in aggressive environments due to its better engineering and performance properties, mainly common characteristics of good workability, high strength, low porosity, and fine pore structure. These, in turn, enhance the concrete resistance to the penetration of harmful substances like chloride ions, carbon dioxide (CO_2), oxygen, and water permeability [13].

In recent years, the incorporation of cementitious materials such as fly ash, silica fume, and ground granulated blast furnace slag (GGBFS) into concrete has been shown to increase the resistance to the deterioration of aggressive media and permeations while lowering the cost of concrete production, preserving resources and energy, and reducing the impact of environmental pollution [14]. The addition of nano-silica has generally improved the concrete performance due to experimental results [15-16] according to its pozzolanic reaction and filler effect. [17] Reported the pozzolanic reaction and the rate of cement hydration increased when the addition of nS because of the nS small particle size, which provides a larger surface area. In their discussion of the impact of 3.8% colloidal nS on the durability characteristics of self-compacting concrete (SCC), Quercia et al. [18] discovered that the pore was less linked and finer. Mohseni E. and Ranjbar M. [13] presented the durability properties of high-performance concrete incorporation nano TiO_2 and fly ash. They concluded the concrete containing nano-TiO_2 significantly improved durability performance in capillary water absorption and chloride diffusion and resistance to sulphuric acid attack by including the replacement of cement of 1% nanoparticles and 30% FA combination. [19] has been claimed that the inclusion of nano-SiO_2 and TiO_2 can refine pore strctures, reducing the permeability of concrete to chloride. For up to 56 days, Kayyali O. and Haque M. [20] looked at the drying shrinkage of LWC with coarse and fine sintered

fly ash aggregate. In terms of dry density and compressive strength, the concrete had values of 1900 kg/m³ and 70 MPa, respectively. They came to the conclusion that LWC shrank less while drying than NWC. In a 57-day study, Gesoğlu et al. [21] investigated the drying, restricted, and autogenous shrinkage of high strength concrete containing synthetic fly ash and blast furnace slag aggregates. Cold bonding was used to create the substitute aggregates. The test findings showed that high-strength concrete with 20% synthetic slag aggregate had better mechanical properties. Additionally, slag aggregate added to high strength concrete prolonged the cracking period and resulted in a finer crack with decreased free shrinkage. All high strength concretes, including those with synthetic aggregates, also showed a discernible decline. Atmaca et al. [22] looked into how 3% nS particles affected HSLWCs' compressive strength, sorptivity, splitting tensile strength, and gas permeability. They came to the conclusion that, in 28 and 90 days, nS particles in HSLWCs provide better compressive strength and splitting tensile strength. The included nS samples showed a decrease in gas permeability and water sorptivity.

The results of an investigation by Kasm M. et al. [23] studied the effect of the micro-steel fiber, pelletized fly ash lightweight aggregate, and microsilica content on the mechanical properties of high-performance cementitious composite (HPCC) and shrinkage behavior showed that the steel fiber volume fraction had a positive effect. Microsilica also has the ability to neutralize the drawbacks of synthetic lightweight aggregate. Kseniia U. [24] demonstrated in his research for a C25/30 concrete with cold-bonded fly ash aggregate, that the linear expansion coefficient is 14.8×10^{-6} K^{-1}, the modulus of elasticity is 18×10^{9} Pa, the compressive strength after 28 days is 37.8 MPa, and the flexural strength is 4.9 MPa. The kinetics of heat emission and cement hydration were unaffected by water presoaking lightweight aggregates, while air shrinkage deformation was positively affected.

By using the cold-bonded approach, Jiayi L. et al. [25] created a novel type of artificial lightweight aggregates from a type of municipal woody biomass waste ash (MWBA). Municipal woody biomass waste ash aggregate (MWBAA) performance was examined in relation to the effects of varying cement content 5, 10, 15, and 20%, curing time 3, 7, 14, and 28 days, and rotation speed 30, 40, 50, and 60 rpm on particle size fractions of fraction 4 mm–10 mm, 10 mm–16 mm, 16 mm–20 mm. The water content 20-33%, rotation speed 30, 40, 50, and 60 rpm, and rotation angle 30–60°. The bulk density of the MWBAA ranges from 841 to 1058 kg/m³. Additionally, it was shown that 27–29% water concentration is ideal for MWBAA manufacture. The rotation speed and angle that produced the maximum granulation efficiency were 55° and 60 rpm. The MWBAA with 20% cement content had the maximum compressive strength after 28 days of curing was 2.6 MPa. In order to successfully recycle MWBA and maybe granulate MWBA into lightweight aggregate that can be used in concrete, the study offers an alternate option. The work suggests a different way to efficiently recycle MWBA and perhaps even granulate it into lightweight material that can be used in concrete.

Therefore, the primary objective of this work is to investigate the shrinkage and durability properties of nano high performance lightweight concrete. In order to create HPLCs, fly ash was cold-bonded pelletized to create the alternative LWA. LWAs from 0 to 40% by 10% increments were used to partially replace the typical coarse aggregate. Thus, ten distinct HPLC mixes with and without nS were created, each with a 420 kg/m³ binder content and a 0.35 w/b ratio. The water permeability, capillary water absorption, chloride ion permeability, drying shrinkage, and weight loss of the created concrete mixtures were all examined to determine their durability.

2. Experimental Study

2.1. Materials

This experiment made use of Portland cement (PC) type I complies with [BS. EN197-1], fly ash (FA) meets the requirements of ASTM C618 [26], nano-SiO₂ (nS), and high range water reducing admixture (HRWRA) had a specific gravity of 1.07 and was used as a superplasticizer (SP). The physical characteristics and chemical compositions of the materials used are stipulated in Table 1.

Table 1. Chemical compositions and physical characteristics of materials used

	PC	FA	nS
Physical Characteristics			
Fineness (Blain) (cm^2/g)	3950	3800	-
Specific Gravity (s.g.)	3.16	2.06	2.3
Specific surface area (BET) (m^2/g)	-	-	150 ± 15
Average primary particle size (nm)	-	-	14
Chemical composition (%)			
Silicon Dioxide, SiO_2	19.7	57.2	99.8
Calcium Oxide, CaO	62.13	2.24	-
Ferric Oxide, Fe_2O_3	2.9	7.1	-
Aluminum Oxide, Al_2O_3	5.15	24.4	-
Sulfur Trioxide, SO_3	2.65	0.29	-
Magnesium Oxide, MgO	1.2	2.4	-
Sodium Oxide, Na_2O	0.17	0.38	-
Potassium Oxide, K_2O	0.89	3.37	-
Loss on Ignition	2.99	1.52	≤ 1.0

2.2. Synthetic Aggregates

The fabrication of the synthetic LWAs in the pelletized machine at room temperature began the experimental program with the cold bonding of FA and PC. As shown in (Fig. 1), a pelletizer machine for this has an 80 cm diameter and a 35 cm depth. The horizontal angle of the pelletizer disc was 45 degrees, and its rotational speed was 42 rpm. The dry powder, which was poured out into the pelletizing pan and allowed to mix until a well-blended-mixture was reached to create the synthetic LWA, was composed of 90% FA class (F) and 10% PC by weight. The pressurized water injection mechanism controlled the amount of water sprayed to be about 20% by weight of the dry mixed mixture. In this procedure, the coagulant was water. After 10 minutes of the first stage's length, the spheroidal fly ash pellets were obtained. A further 10 minutes of agglomeration time is required for appropriate stiffness and compressed fresh pellets. After the pelletization process is complete, the fresh pellets must be saved in sealed plastic bags for a 28-day self-curing period in the curing room to harden at a temperature and relative humidity of 22°C and 70%, respectively. Ultimately, the solidified LWAs were sieved as lightweight coarse aggregate (4-16 mm) to replace the coarse natural utilized to create HPLCs. According to ASTM C 127[27], specific gravity and 24-hour water absorption for LWAs were approximately 1.64g/cm³ and 21.12%, respectively. The fine and coarse materials used

were sand and gravel, which naturally have specific gravities of 2.7 and 2.67, respectively. Table 2 displays the sieve analysis grade for natural and LWA.
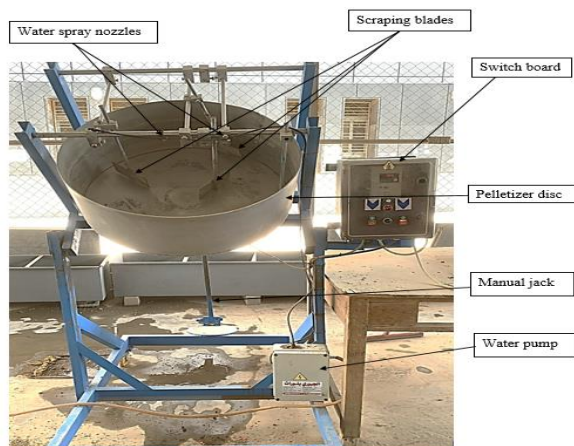
Fig. 1 Pelletizer machine

Table 2. Physical characteristics and sieve analysis of aggregates

Sieve size	Natural Aggregate		Lightweight Aggregate (%)
	Sand	Gravel	
(mm)			4-16 mm
16	100	100	100
8	100	31	81
4	95	0.3	0
2	59	0	0
1	37.8	0	0
0.5	24	0	0
0.25	6	0	0
Fineness modulus (%)	2.79	5.68	5.15
Specific gravity	2.70	2.67	1.64

2.3. Mixes Proportion Details

The second part of the investigation program, which involved the creation of ten HPLC mixes total and showed how LWAs can partially replace natural coarse aggregate at different volume fractions ranging from 0% to 40% in increments of 10%, revealed the durability and shrinkage properties of concrete mixes. The next step was to plan two series: the first involved replacing synthetic coarse lightweight aggregate with coarse natural aggregate free of nanoparticles, and the second involved replacing LWAs with natural coarse aggregate that had nanoparticles. To provide the necessary workability, various concentrations of HRWRA were utilized. To create HPLC mixtures, a 30 L capacity power-driven rotating pan apparatus was employed. The control mix contained only natural aggregate. The goal of all the mixes was to get a $150\ mm \pm 20\ mm$ slump. To achieve consistent workability, different concentrations of HRWRA (SP) have been utilized in each mixture.

Table 3. Mix proportions details for HPLCs

Mix series	Mix designation	w/b	binder	PC	FA	nS	water	SP	sand	Gravel	LWA
Series I	nS0%, LWA0%	0.35	420	336.0	84	0.0	147.0	6.3	942.5	932.0	0.0
	nS0%, LWA10%	0.35	420	336.0	84	0.0	147.0	6.3	942.5	838.8	57.2
	nS0%, LWA20%	0.35	420	336.0	84	0.0	147.0	6.3	942.5	745.6	114.5
	nS0%, LWA30%	0.35	420	336.0	84	0.0	147.0	6.3	942.5	652.4	171.7
	nS0%, LWA40%	0.35	420	336.0	84	0.0	147.0	6.3	942.5	559.2	229.0
Series II	nS3%, LWA0%	0.35	420	323.4	84	12.6	147.0	9.2	936.4	926.0	0.0
	nS3%, LWA10%	0.35	420	323.4	84	12.6	147.0	9.2	936.4	833.4	56.9
	nS3%, LWA20%	0.35	420	323.4	84	12.6	147.0	9.2	936.4	740.8	113.8
	nS3%, LWA30%	0.35	420	323.4	84	12.6	147.0	9.2	936.4	648.2	170.6
	nS3%, LWA40%	0.35	420	323.4	84	12.6	147.0	9.2	936.4	555.6	227.5

* All weights are in **kg/m³** units.

2.4. Test Methods

Regarding BS EN (12390-8)[28], the water penetration depth of HPC containing LWA for 28 and 90 days was adapted. For this, 150 mm cube specimens were pressurized with water at a pressure of $500 \mp 50 \ kPa$ for 72 hours. The middle section of the specimens was divided, and the greatest pressurized water penetration was gauged in millimeters. The average outcomes of three samples of the mix were considered for each testing interval. If the water penetration does not rise by 30 mm after concrete comes into contact with aggressive media, chemical attacks might be regarded to be resistant. ASTM C1202[29] was used to analyze the rapid chloride permeability test (RCPT) for HPLC. As stated in[29], the middle portion of each cylinder specimen measuring approximately $100 \times 200 \ mm$ was cut into three-disc samples measuring 50 mm in height and 100 mm in diameter. At 28 and 90 days, the test was conducted. The disk samples were then placed on a test cell with one side of the specimens in contact with 0.3M sodium hydroxide and the other in contact with a 3% solution of sodium chloride. A direct voltage of $60 \mp 01V$ was applied between the faces. Every 30 minutes, data on the concrete's resistance to chloride ion permeability were archived in order to track the charge that moved through

the samples over the course of six hours. The total charge in $A.s$ ($amperes \times seconds = coulombs$) that passed through the specimens was determined using Simpson's integration and present and time historical knowledge[28]. The drying shrinkage of HPLCs was calculated through three $70 \times 70 \times 280\ mm$ prisms due to ASTM C157[30]. The gage length was settled on the top surface of each specimen by the mean of the glued pin as soon as demolding the prisms. An electronic dial gauge extensometer was used to measure the change length over 200 mm, accurate to 0.002 strains. For the first 21 days, measurements were taken every day; thereafter, they were taken three times per week. Investigations into weight loss were conducted using the same prism. Weight loss and strain variations due to drying shrinkage were recorded over a 61-day period at a drying temperature of 23.2 °C and a relative humidity of 50.5%.

3. Results and Discussions

3.1. Water Permeability

The test uses a range of pressures to calculate the depth of water penetration into the concrete. (Fig. 2) displays the variation in the water penetration depth of HPLCs at 28 and 90 days. As anticipated, the HPC incorporating LWA had water penetration rates at 90 days that are less than 28 days. Additionally, adding LWA to HPC resulted in the construction of more water-absorbent concretes, and the effect grew stronger when LWA content was increased. It is obvious from (Fig. 2) that the water penetration depth goes an upward trend with partial replacement of natural aggregate by LWA. When adding 3% nS with the same replacement amount of LWA, there is a tendency for decline. The lowest value of water penetration depth was measured for nS3%, LWA 0% as 11.5 and 7.5mm, in contrast to the largest penetration depth, which was recorded for nS0 %, LWA40% as 27mm and 21mm at 28 and 90 days, respectively. The porous nature of LWAs accounts for the high penetration depth. Under pressure, water can easily pass-through aggregates, resulting in deeper water penetration in the HPC than that of the mix nS0%, LWA0%, which contains LWAs.
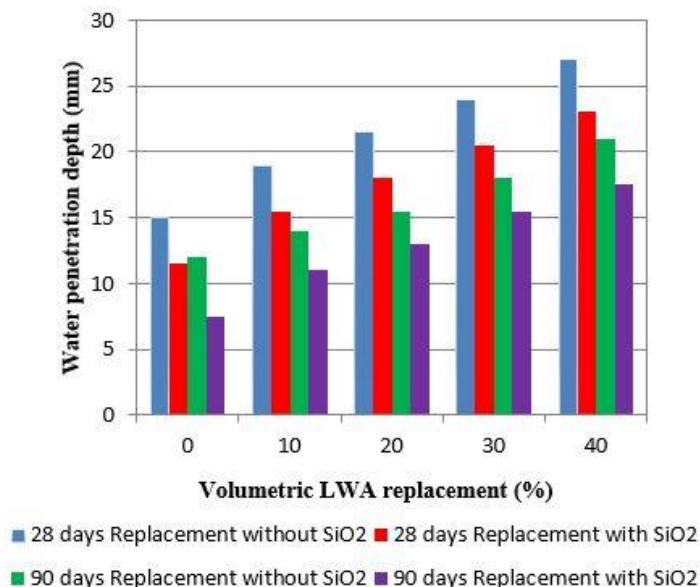
Fig. 2 The 28- and 90-days water penetration values of HPLCs.

This reply supports the findings of some researchers who claimed that numerous synthesized LWAs in concrete increased water penetration [31]. However, when 3%nS particles are added with the same level of LWA substitution, there is a noticeable drop of roughly 14.5-23.3 %. Since the pore structure of HPC substantially affects its endurance, it can be said that adding nS as a mineral admixture has a good impact on the mechanism. However, by filling the voids during the development of the cement paste using aggregate, the ITZ might be impacted [32]. HPLC notices a systematic reduction in water permeability after the addition of concrete with 3%nS particles. The water permeability reached 37.5% when 3%nS was added. The findings of several investigations [33-34] are supported by these findings. In general, high depth water permeability is a sign of low concrete material durability [35]. It is clear that using nS particles as cementitious material significantly lowers the water permeability of HPLC while maintaining the same level of LWA replacement.

3.2. Rapid Chloride Penetration

The infiltration of water containing chloride and other hostile ions into the concrete is the main factor influencing the physical and chemical deterioration process. This procedure, which primarily regulates the microstructure of concrete is connected to water infiltration and ion transport [36]. The total charged A.s (coulombs) passed through concrete disc specimens during 6 hours as a function of electro-migration, which was determined by ASTM C 1202[29] which confirmed concrete's resistance to chloride ion penetration.

(Fig. 3) displays graphically the total charge that was passed through HPLCs throughout the course of 28 and 90 days.
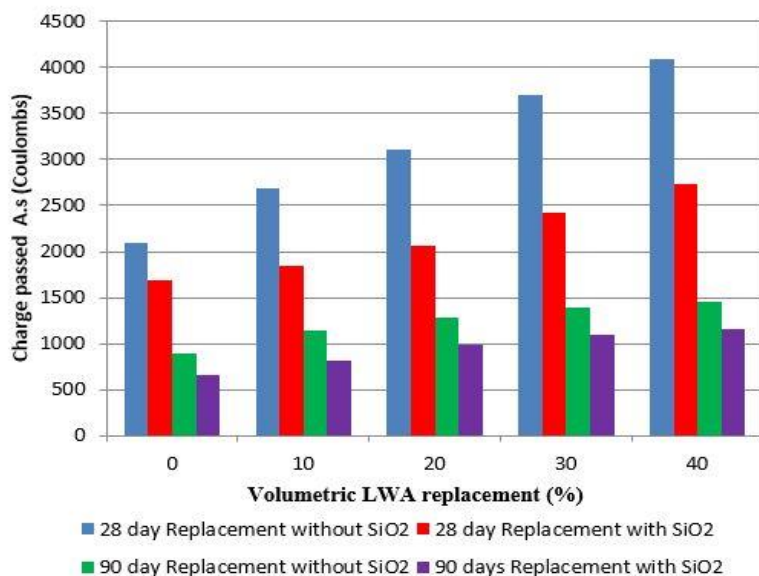
Fig. 3 The 28 and 90-day RCPT values of HPLCs

As the LWAs were replaced with natural aggregate, the results demonstrate a steady rise in chloride-ion permeability. With an increase in the replacement amount, this effect becomes much more noticeable. High chloride permeability refers to the maximum charge that has been observed passing through HPCs, including LWAs, at a coarse aggregate replacement of 40% of 4089 A.s (coulombs) at 28 days without nS. According to ASTM

C1202[29], the total charge transmitted through HPLCs in contrast to LWAs without nS particles in the range between 2000-4000A.s resulted in a moderate categorization of chloride penetration. The pozzolanic reaction and effects of the filler nS particles, which make the ion pathway more difficult or partially blocked are evident from (Fig. 3) that the HPLCs showed a notable diminish to the second series after the addition of 3% nS particles, with the same replacement of LWAs[37]. For 28 days, the 2nd series charges passed were measured as 1690.6A.s, 1847.3A.s, 2067.8 A.s, 2429.1A.s, and 2740A.s for replacements 0-40% of LWAs with nS particles, and the decrease percentages were 19.52%, 31.32%, 33.30%, 34.34%, and 32.99% respectively. Moreover, zero and ten replacement percentages were classified as low chloride permeability, while 20%, 30%, and 40% were classified as moderate chloride permeability concerning ASTM C 1202[29]. These classes were shown to have low chloride permeability with 30 and 40% at 90 days, despite having been seen as very low in terms of 0%, 10%, and 20% coarse aggregate replacement with nS particles. The chloride permeability values are also significantly impacted by the extended testing period of 28 to 90 days.

3.3. Drying Shrinkage and Weight Loss

Long-term drying shrinkage depends on curing temperature, degree of hydration, w/c, relative humidity, aggregate type and characteristics, drying period, admixtures, and cement composition. (Fig. 4) and (Fig. 5) show the changes in total shrinkage for HPC with LWA at a 61-day drying time.

Overall, it is evident that as drying progresses for all mixes gradually reduces the total shrinkage rate of HPC including LWA. On the other hand, (Fig. 4) demonstrates how the drying shrinkage rate rose as LWA largely replaced the natural aggregate. The majority of the entire shrinkage's growth nearly occurred in the first three weeks. The lowest shrinkage strain of 448 $\mu\varepsilon$ for series I in (Fig. 4) was recorded at 61 days for nS% and LWA0%, while HPC contained 40% LWA was recorded the largest shrinkage value 597$\mu\varepsilon$. The total shrinkage strain of HPCs was reduced by 6.47, 16.07, 24.77, and 33.26 %, respectively, for mixtures of nS0% and LWA10%, nS0% and LWA20%, nS0% and LWA30%, nS0% and LWA40%, when compared to the control mix of nS0% and LWA0%. The usage of LWA in the mixtures may be referred to as the cause of the increase in the overall shrinkage strain of HPCs in this study. Additionally, the high porosity of LWA and its reduced stiffness as a result of its rapid absorption rate contribute to concrete's increased drying shrinkage. These results were reported by other previous researchers [21, 38-39].

From (Fig. 5) for series Ⅱ, its evident the influence of replacing cement with nS was to fade the strain development of the drying shrinkage. The addition of 3%nS to the HPLC mixes resulted in a notable improvement in the drying shrinkage by 9.37%, 9.01%, 11.73%, 10.37%, and 9.88% after 61 days, respectively. This improvement was seen in comparison to the two series, as shown in (Fig. 5) the results were confirmed the findings in the study conducted by [40-41]. An extreme fall development at an early age test in the values of drying shrinkage of HPLCs according to (Fig. 5) although the strain development of HPLCs was affected by nS incorporation, LWA coarse aggregate replacement and aggregate type have the main role especially at the initial reading. Moreover, nS efficiency displayed a positive effect and seemed to be more pronounced on the higher coarse aggregate replacement of LWA than at the lowest replacement in strain development. For instance, the drying shrinkage for series Ⅰ, $448, 477, 520, 559, and 597\mu\varepsilon$. In comparison, it is found for series Ⅱ, $406, 434, 459, 502, and 538\ \mu\varepsilon$. (Figs. 6 & 7) depicts series I and II, respectively, the changes in weight loss over time as a result of the drying period. Similar tendencies to the drying shrinkage were revealed by HPC combined with LWA. However,

adding LWA to HPC showed a greater weight reduction, although 3% nS containing HPLWCs showed a smaller weight loss than the series I.
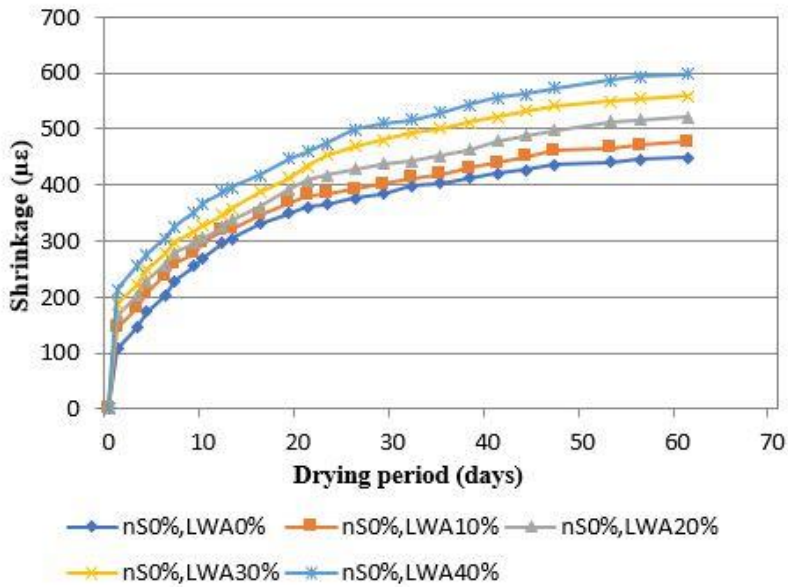
Fig. 4 Drying shrinkage for HPLCs without nS
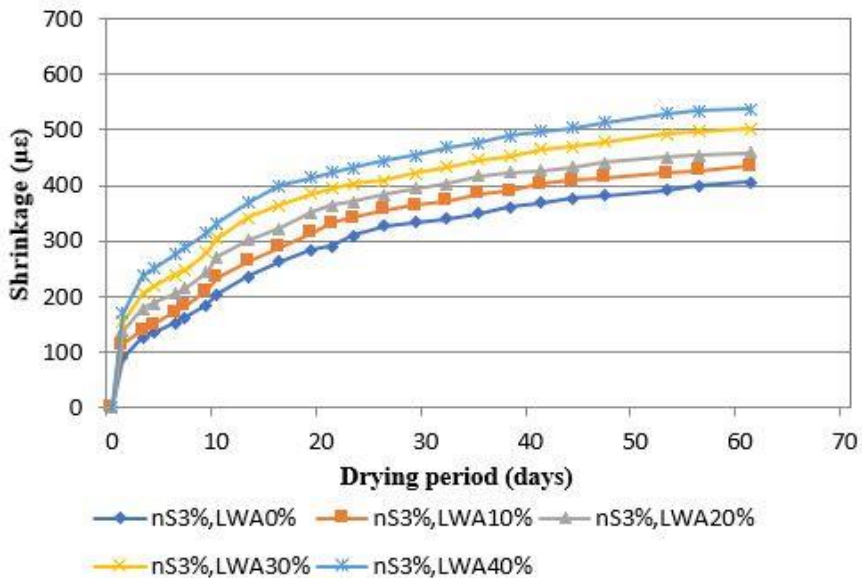
Fig. 5. Drying shrinkage for HPLCs with nS.
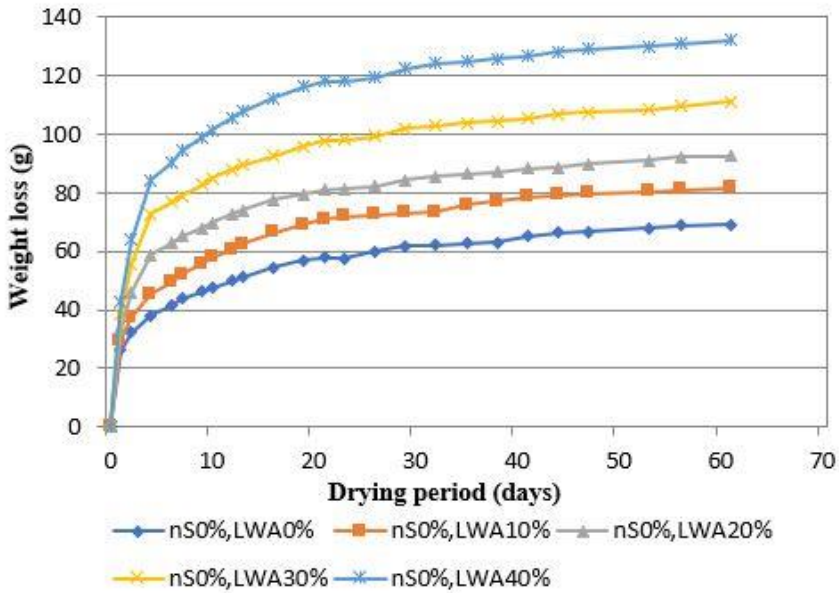
Fig. 6 Weight loss for HPLCs without nS.

After a week of drying, the difference in weight loss between the HPLC series I and II was easier to identify. It was subsequently discovered that the disparities tend to get bigger as the drying time gets longer. The percentage of weight loss increased when NWAs were switched out for LWAs, but this rise in percentage was more obvious as the coarse aggregate replacement rose.
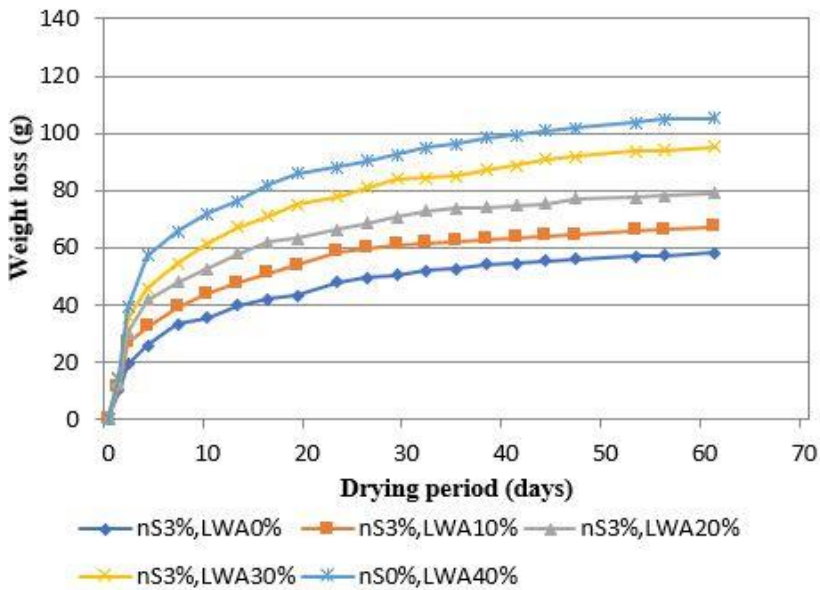
Fig. 7 Weight loss for HPLCs with nS.

For instance, the maximum weight loss for nS0% and LWA 0% in series I was 69.22 gr as opposed to 81.60, 91.57, 111.02, and 132.18 gr for nS0% and LWA 10%, nS0%, and LWA 20%, nS0%, and LWA 30%, and nS0% and LWA 40%, respectively. The incorporation of nS into HPLC combination inhibits weight loss. For instance, a maximum weight loss of series II of nS3% and LWA0%, nS3% and LWA10%, nS3% and LWA20%, nS3% and LWA30%, nS3% and LWA40% was 58.24, 67.31, 78.99, 95.18 and 105.12 gr, respectively, compared with series I with the same coarse aggregate replacement without nS. The results of weight loss measurements using HPLCs suggested that there is no direct correlation between weight loss and drying shrinkage readings. The single weight loss parameter cannot adequately explain the variations in the drying shrinkage of concrete since the shrinkage of concrete is coupled to other parameters and weight loss [42-43].

4. Statistical Analysis

The results of the analysis of variance (ANOVA) are shown in Table 4 to show whether the status of an independent variable has any impact on the dependent variables or not. The statistical evaluation of GLM-ANOVA method was performed with Minitab 17 software and a multiple linear regression method was performed with SPSS 26 software. Durability characteristics, such as water permeability and chloride penetration, were assigned as dependent variables and studied. Calculation of the experimental parameter validation was done using the general linear model analysis of variance (GLM-ANOVA), as indicated in the equations below; Eq(1) for water permeability and Eq(2) for chloride penetration. Figs. 8 & 9 show the normal P-P plot standardized residual for water permeability and rapid chloride penetration models, respectively. The independent criteria, however, were coarse aggregate replacement, Ns(%), and testing age on the 28 and 90 days.

When used in a statistical study with a 0.05 significant level, the parameter is acceptable as a significant factor smaller than that. Additionally, the percent contribution was determined to provide a general understanding of the strength of each independent parameter's influence on the dependent component. By dividing the sequential sum of squares value of an independent factor by the sum of squares of each dependent factor, the percent contributions shown in the eighth column were determined. The effectiveness of the independent component is shown by a larger percent contribution value. All independent variables have a statistically significant impact on the water permeability and chloride penetration; it may be inferred from the statistical analysis in Table 4. However, for the chloride penetration of concrete mixtures, the coarse aggregate replacement is not a statically important quantity. The most efficient independent component for the water permeability is the coarse aggregate replacement, which has a contribution value of 58.89%. The nS parameter, with values of 12.65 and 11.10%, respectively, has the least impact on the water permeability and chloride penetration. According to a statistical analysis of the RCPT results, the most important variable affecting the combinations is testing age, which has a contribution value of 66.04%. The coarse aggregate replacement has also had an impact on the RCPT model, though not to the same extent as water permeability.

$$W.P. = 18.283 - 1.133 \times Ns + 0259 \times C.A.R. -0.081 \times T.A. \qquad (1)$$

$$R.C.P. = 3151.975 - 212.607 \times Ns + 25.753 \times C.A.R. -25.095 \times T.A. \qquad (2)$$

Where, W.P.: Water Permeability (mm.), Ns: Nano silica (%), C.A.R.: Coarse Aggregate Replacement (%), T.A.: Testing Age (days), R.C.P.: Rapid Chloride Penetration [A.s (coulombs)].
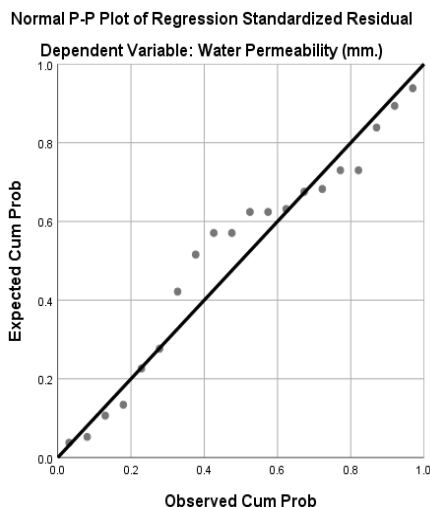
Fig. 8 Normal P-P plot standardized residual for water permeability model
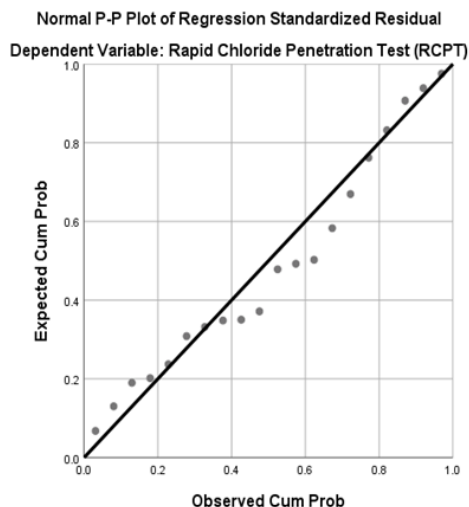
Fig. 9 Normal P-P plot standardized residual for rapid chloride penetration model

Table 4. A statistical analysis of concrete's durability characteristics.

Dependent Element	Unbiased Variable	Squares Added Sequentially	Computed F	R-Square %	P Value	Significance	Contribution %
Water Permeability	The coarse aggregate replacement (%)	269.125	172.350		0.000	Yes	58.89
	nS (%)	57.800	148.060	98.3	0.000	Yes	12.65
	Testing age (days)	125.000	320.200		0.000	Yes	27.35
	Error	5.075	-		-	-	1.11
	Total	457.000	**375.872**		0.000	-	-
Rapid Chloride Penetration	The coarse aggregate replacement (%)	2659772	5.66		0.000	Yes	14.50
	nS (%)	2034072	17.31	90.1	0.000	Yes	11.10
	Testing age (days)	12104124	102.98		0.000	Yes	66.04
	Error	1527957	-		-	-	8.33
	Total	18325925	58.341		0.000	-	-

5. Conclusions

The following conclusions can be reached in light of the research's findings and the materials used:

- Each HPLC combination was made to produce a slump of 150±20 mm. Because nS have a tiny particle size and large surface area, the amount of HRWRA was increased from 6.3 - 9.2 % with the introduction of 3% nS to keep within the range of the required slump.

- When compared to the reference mix, a systematic rise in chloride penetration was seen as the LWAs increased due to the porous structure and high level of permeability. The pozzolanic reaction and filler effect of the nS particles, which make the ion pathway more difficult or partially blocked, caused the HPLCs with nS particles to exhibit a striking decrease in chloride permeability with the same coarse aggregate replacement of LWAs.

- As was predicted, the coarse aggregate replacement of LWAs in the mixtures led to an increase in the water penetration rates. It has been shown that the permeability decreases by up to 23.34% when nS particles are used.

- Regardless of the LWA coarse aggregate replacement, it was found that the total shrinkage strains at 61 days were higher for lightweight concrete than for normal weight concrete. This was attributed to LWA's reduced stiffness from high absorption and high porosity, which also contributed to an increase in concrete's drying shrinkage.

- The presence of 3% nS in HPLC specimens reduces drying shrinkage of 61 days by 9.37%, 9.01%, 11.73%, 10.37%, and 9.88%, respectively, while maintaining the same coarse aggregate replacement of LWA. Additionally, nS efficiency demonstrated a favorable impact on LWA coarse aggregate replacement at higher levels than at the lowest levels during strain development. Summarizing the findings, it can be said that nS can be added to LWAs to counteract their negative effects.

- The addition of nS reduced the rate of weight loss due to the drying of the concrete. Especially for mixtures having a higher rate of coarse aggregate replacement of LWA. The research showed that nS incorporation, LWA coarse aggregate replacement, aggregate type and porosity have the main role in affecting the weight loss of concrete especially at the initial readings.

- The statistical analysis of the experimental test results indicated that the most important factor influencing chloride penetration was testing age, whereas it was a coarse aggregate replacement for water permeability. Moreover, the statistical evaluation exhibited that coarse aggregate replacement had no effect on chloride penetration. But it could be realized from the statistical evaluation that the least influential parameter on water permeability and RCPT was nS particles .

References

[1] Kayali O. Fly ash lightweight aggregates in high performance concrete. Construction and Building Materials. 2008;22(12):2393-9. https://doi.org/10.1016/j.conbuildmat.2007.09.001
[2] Joseph G, Ramamurthy K. Influence of fly ash on strength and sorption characteristics of cold-bonded fly ash aggregate concrete. Construction and Building Materials [Internet]. 2009;23(5):1862-70. https://doi.org/10.1016/j.conbuildmat.2008.09.018
[3] Baykal G, Döven AG. Utilization of fly ash by pelletization process; theory, application areas and research results. Resources, Conservation and Recycling. 2000;30(1):59-77. https://doi.org/10.1016/S0921-3449(00)00042-2

[4] Zakaria M, Cabrera JG. Performance and durability of concrete made with demolition waste and artificial fly ash-clay aggregates. Waste Management. 1996;16(1-3):151-8. https://doi.org/10.1016/S0956-053X(96)00038-4

[5] Tajra F, Elrahman MA, Stephan D. The production and properties of cold-bonded aggregate and its applications in concrete: A review. Construction and Building Materials. 2019;225:29-43. https://doi.org/10.1016/j.conbuildmat.2019.07.219

[6] Raj KR, Vasudev R. Experimental Investigation on Artificial Light Weight Fly Ash Aggregates in Concrete. Lecture Notes in Civil Engineering. 2022;171:73-84. https://doi.org/10.1007/978-3-030-80312-4_7

[7] Thomas J, Harilal B. Sustainability evaluation of cold-bonded aggregates made from waste materials. Journal of Cleaner Production. 2019;237. https://doi.org/10.1016/j.jclepro.2019.117788

[8] Du H, Gao HJ, Pang SD. Improvement in concrete resistance against water and chloride ingress by adding graphene nanoplatelet. Cement and Concrete Research [Internet]. 2016;83:114-23. https://doi.org/10.1016/j.cemconres.2016.02.005

[9] Valentini L, Ferrari G, Russo V, Štefančič M, Zalar Serjun V, Artioli G. Use of nanocomposites as permeability reducing admixtures. Journal of the American Ceramic Society. 2018;101(9):4275-84. https://doi.org/10.1111/jace.15548

[10] Zhang MH, Gjørv OE. Microstructure of the interfacial zone between lightweight aggregate and cement paste. Cement and Concrete Research. 1990;20(4):610-8. https://doi.org/10.1016/0008-8846(90)90103-5

[11] Liu X, Chia KS, Zhang MH. Development of lightweight concrete with high resistance to water and chloride-ion penetration. Cement and Concrete Composites [Internet]. 2010;32(10):757-66. https://doi.org/10.1016/j.cemconcomp.2010.08.005

[12] Chia KS, Zhang MH. Water permeability and chloride penetrability of high-strength lightweight aggregate concrete. Cement and Concrete Research. 2002;32(4):639-45. https://doi.org/10.1016/S0008-8846(01)00738-4

[13] Mohseni E, Ranjbar MM, Tsavdaridis KD. RETRACTED:Durability properties of high-performance concrete incorporating nano-TiO2and fly ash. American Journal of Engineering and Applied Sciences. 2015;8(4):519-26. https://doi.org/10.3844/ajeassp.2015.519.526

[14] Shi H sheng, Xu B wan, Zhou X chen. Influence of mineral admixtures on compressive strength, gas permeability and carbonation of high performance concrete. Construction and Building Materials [Internet]. 2009;23(5):1980-5. https://doi.org/10.1016/j.conbuildmat.2008.08.021

[15] Raiess Ghasemi AM, Parhizkar T, Ramezanianpour AA. Influence of colloidal nano-SiO2 addition as silica fume replacement material in properties of concrete. 2nd. International Conference on Sustainable Construction Materials and Technologies. 2010;23-30. Universita Politecnica delle Marche, Ancona, Italy. ISBN 978-1-4507-1488-4. www.claisse.info/Proceedings.htm, 2010.

[16] Li H, Xiao HG, Yuan J, Ou J. Microstructure of cement mortar with nano-particles. Composites Part B: Engineering. 2004;35(2):185-9. https://doi.org/10.1016/S1359-8368(03)00052-0

[17] Belkowitz JS. AN INVESTIGATION OF NANO SILICA IN THE CEMENT HYDRATION PROCESS [Internet]. ProQuest LLC. 2009.

[18] Quercia G, Spiesz P, Hüsken G, Brouwers HJH. SCC modification by use of amorphous nano-silica. Cement and Concrete Composites [Internet]. 2014;45:69-81. https://doi.org/10.1016/j.cemconcomp.2013.09.001

[19] Zhang MH, Li H. Pore structure and chloride permeability of concrete containing nano-particles for pavement. Construction and Building Materials [Internet]. 2011;25(2):608-16. https://doi.org/10.1016/j.conbuildmat.2010.07.032

[20] Kayyali OA, Haque MN. A new generation of structural lightweight concrete. American Concrete Institute, ACI Special Publication. 1997;SP-171:569-88.

[21] Gesoglu M, Güneyisi E, Ismael ANI, Öz HÖ. Internal curing of high-strength concretes using artificial aggregates as water reservoirs. ACI Materials Journal. 2015;112(6):809-19. https://doi.org/10.14359/51687904

[22] Atmaca N, Abbas ML, Atmaca A. Effects of nano-silica on the gas permeability, durability and mechanical properties of high-strength lightweight concrete. Construction and Building Materials [Internet]. 2017;147:17-26. https://doi.org/10.1016/j.conbuildmat.2017.04.156

[23] Mermerdaş K, İpek S, Algın Z, Ekmen Ş, Güneş İ. Combined effects of microsilica, steel fibre and artificial lightweight aggregate on the shrinkage and mechanical performance of high strength cementitious composite. Construction and Building Materials. 2020;262. https://doi.org/10.1016/j.conbuildmat.2020.120048

[24] Usanova K. Properties of Cold-Bonded Fly Ash Lightweight Aggregate Concretes. Lecture Notes in Civil Engineering. 2020;70:507-16.

[25] Lin J, Mo KH, Goh Y, Onn CC. Potential of municipal woody biomass waste ash in the production of cold-bonded lightweight aggregates. Journal of Building Engineering. 2023;63(January):1-27. https://doi.org/10.1016/j.jobe.2022.105392

[26] ASTM C618. Coal Fly Ash and Raw or Calcined Natural Pozzolan for Use. Annual Book of ASTM Standards. 2019;04.02:1-5. https://doi.org/10.1520/C0618-19

[27] ASTM C127. Relative Density (Specific Gravity) and Absorption of Coarse Aggregate. Annual Book of ASTM Standards. 2015;04.02:1-5. https://doi.org/10.1520/C0127-15

[28] British Standards Institution BSI. Depth of penetration of water under pressure. BS EN 12390-8:2000. 2003;(August):420-57. ICS 91.100.30 , Feb., 2009 .

[29] ASTM C1202. Electrical Indication of Concrete's Ability to Resist Chloride Ion Penetration. Annual Book of ASTM Standards [Internet]. 2013;04.02:1-8. https://doi.org/10.1520/C1202-19

[30] ASTM C157. Length Change of Hardened Hydraulic-Cement Mortar and Concrete. Annual Book of ASTM Standards. 2014;04.02:1-7. https://doi.org/10.1520/C0157_C0157M-08

[31] Liu X, Chia KS, Zhang MH. Water absorption, permeability, and resistance to chloride-ion penetration of lightweight aggregate concrete. Construction and Building Materials [Internet]. 2011;25(1):335-43.. https://doi.org/10.1016/j.conbuildmat.2010.06.020

[32] Güneyisi E, Gesoʇlu M, Booya E, Mermerdaş K. Strength and permeability properties of self-compacting concrete with cold bonded fly ash lightweight aggregate. Construction and Building Materials. 2015;74:17-24. https://doi.org/10.1016/j.conbuildmat.2014.10.032

[33] Du H. Properties of ultra-lightweight cement composites with nano-silica. Construction and Building Materials [Internet]. 2019;199:696-704. https://doi.org/10.1016/j.conbuildmat.2018.11.225

[34] Güneyisi E, Gesoglu M, Azez OA, Öz HÖ. Physico-mechanical properties of self-compacting concrete containing treated cold-bonded fly ash lightweight aggregates and SiO2 nano-particles. Construction and Building Materials. 2015;101:1142-53. https://doi.org/10.1016/j.conbuildmat.2015.10.117

[35] Ahmad S, Adekunle SK, Maslehuddin M, Azad AK. Properties of Self-Consolidating Concrete Made Utilizing Alternative Mineral Fillers. Construction and Building Materials. 2014;68:268-76. https://doi.org/10.1016/j.conbuildmat.2014.06.096

[36] Oh BH, Cha SW, Jang BS, Jang SY. Development of high-performance concrete having high resistance to chloride penetration. Nuclear Engineering and Design. 2002;212(1-3):221-31. https://doi.org/10.1016/S0029-5493(01)00484-8

[37] Du H, Du S, Liu X. Effect of nano-silica on the mechanical and transport properties of lightweight concrete. Construction and Building Materials [Internet]. 2015;82:114-22. https://doi.org/10.1016/j.conbuildmat.2015.02.026

[38] Zhang MH, Li L, Paramasivam P. Shrinkage of high-strength lightweight aggregate concrete exposed to dry environment. ACI Materials Journal. 2005;102(2):86-92. https://doi.org/10.14359/14301

[39] Zhuang YZ, Zheng DD, Ng Z, Ji T, Chen XF. Effect of lightweight aggregate type on early-age autogenous shrinkage of concrete. Construction and Building Materials [Internet]. 2016;120:373-81. https://doi.org/10.1016/j.conbuildmat.2016.05.105

[40] Sadrmomtazi A, Barzegar A. Assessment of the effect of nano-SiO 2 on physical and mechanical properties of self-compacting concrete containing rice husk ash. 2nd International Conference on Sustainable Construction Materials and Technologies. 2010; Universita Politecnica delle Marche, Ancona, Italy. ISBN 978-1-4507-1488-4. www.claisse.info/Proceedings.htm, 2010.

[41] Wang, X. F., Huang, Y. J., Wu, G. Y., Fang, C., Li, D. W., Han, N. X., and Xing F. Effect of nano-SiO2 on strength, shrinkage and cracking sensitivity of lightweight aggregate concrete. Construction and Building Materials. 2018;175:115-25. https://doi.org/10.1016/j.conbuildmat.2018.04.113

[42] Gesoglu M, Özturan T, Güneyisi E. Shrinkage cracking of lightweight concrete made with cold-bonded fly ash aggregates. Cement and Concrete Research. 2004;34(7):1121-30. https://doi.org/10.1016/j.cemconres.2003.11.024

[43] Wiegrink K, Marikunte S, Shah SP. Shrinkage cracking of high-strength concrete. ACI Materials Journal. 1996;93(5):409-15. https://doi.org/10.14359/9844

Technical Note

Experimental investigation of behaviour of concrete mixed and cured with Nembe seawater

Uchechi G. Eziefula*1,a, Uchenna C. Egbufor2,b, Chioma L. Udoha2,c

¹Department of Civil Engineering, Faculty of Engineering, University of Agriculture and Environmental Sciences, Umuagwo, Nigeria
²Department of Agricultural and Bio-Environmental Engineering Technology, School of Engineering Technology, Imo State Polytechnic, Omuma, Nigeria

Article Info	Abstract
	Freshwater is conventionally used to produce concrete, but freshwater scarcity has become a significant challenge worldwide. The aim of this study is to experimentally investigate the workability and strength of Portland cement concrete mixed and cured with Nembe seawater. The initial and final setting times and slump of fresh concrete mixed with freshwater and seawater were determined. Four sets of concrete specimens were produced for the compressive strength tests: concrete cast and cured with freshwater, cast with freshwater and cured with seawater, cast with seawater and cured with freshwater, and cast and cured with seawater. The use of seawater for mixing concrete decreased the initial setting time of the cement paste and the slump of concrete by approximately 36% and 54%, respectively. Concrete specimens mixed with seawater and cured with freshwater exhibited the highest compressive strengths at the 60th and 90th days of curing. Although the concrete mixed with seawater yielded slightly higher compressive strengths than concrete mixed with freshwater, the difference between using freshwater and seawater as mixing and curing water in terms of compressive strength was minimal.

1. Introduction

Concrete is a widely used construction material composed of cement, fine aggregate, coarse aggregate, and water. The demand for concrete structures has increased in recent decades because of their advantages, such as local availability of constituent materials, cost-effectiveness, and good durability. Urbanisation and globalisation have contributed to the rising demand for concrete structures. The increased use of concrete for constructing buildings and civil engineering structures indicates that more constituent materials are required to meet the current demand for concrete. Because of the enormous material and energy resources consumed during concrete production, there is a need to improve the sustainability of concrete. Sustainable construction aims at utilising recyclable materials in building new structures, minimising waste generation, and reducing energy and material consumption. Previous studies on the environmental impacts of concrete mainly focused on energy and material consumption and carbon dioxide emissions; however, little is known about its water consumption and the practical measures required to minimise such consumption [1].

Water is used for mixing concrete components and curing concrete, and it plays a significant role in determining the strength and durability of concrete. When water is mixed with cement, a paste that binds the aggregate particles together produces a stiff mass in a hardened state. Water is also used for curing, a critical process that enhances the

493

strength development and durability of concrete. Conventionally, freshwater has been used to produce concrete, but freshwater scarcity is a significant challenge facing the world in the 21st century. Although water covers approximately 70% of the earth's surface, water scarcity affects every continent [2]. Water stress affects over two billion people globally, and sub-Saharan Africa has more water-stressed countries than any region [2]. The concrete industry competes for freshwater with many essential sectors, such as agriculture and food processing. With the current water scarcity in Nigeria and many other countries, there is an urgent need to seek alternative water sources for concrete production. The use of seawater instead of freshwater is justified because the construction industry annually utilises 16.6×10^9 m³ (16.6 km³) of water globally for concrete production (based on 2012 concrete consumption values) [1]. In some countries (for example, the United Arab Emirates), most of the water used for concrete production is obtained through seawater desalination [3], which increases production costs. The use of seawater in concrete is expected to increase globally as the freshwater supply decreases. Approximately 97% of the earth's water is found in the oceans, 2% is frozen freshwater trapped in glaciers and ice caps, and less than 1% is accessible freshwater [4]. Seawater refers to water in the seas and oceans, and it is salty. Seawater contains small amounts of salts and smaller amounts of other substances, including dissolved organic and inorganic materials. The principal ions in seawater are chloride, sodium, sulphate, calcium, magnesium, and potassium. The specific amounts of these salts in seawater vary but generally comprise approximately 99% of all sea salts. Sodium chloride is the most abundant salt in seawater, constituting over 90% of the total salt weight [5]. Freshwater includes water from ponds, lakes, streams, rivers, ice caps, glaciers, icebergs, and below the soil surface (groundwater). Freshwater generally contains lower concentrations of dissolved salts and other total dissolved solids than seawater.

Previous studies have suggested the possibility of using seawater in mixing and curing cement-based materials. Despite the wide acceptance that seawater is unsuitable for structural concrete, some structures have been successfully built using seawater concrete [6]. Recent research indicates no significant adverse effects of seawater on the mechanical properties of seawater concrete [7], and long-term exposure tests suggest high prospects of using seawater as a material in reinforced concrete [8]. Mbadike and Elinwa [9] analysed the effect of saltwater on the compressive and flexural strengths of concrete for different target strengths. They used freshwater specimens as the control and found that saltwater reduced the concrete strength by approximately 8%. Osuji and Nwankwo [10] evaluated the effect of seawater collected from the Escravos area of the Niger Delta on the compressive strength of concrete. They observed that concrete cast and cured with seawater exhibited approximately 15% higher 28-day strength than concrete cast with freshwater. Lim et al. [11] investigated the strength and corrosion behaviours of seawater-mixed and seawater-cured mortar containing fly ash in various replacement percentages. They reported that utilising seawater as the mixing water can yield comparable compressive strength as freshwater, particularly when cured for extended periods. Younis et al. [6] found that using seawater in concrete initially increased concrete strength up to the seventh day, and a decrease of approximately 7%–10% was observed for Mix B compared to those for Mix A after 28 days. Liu et al. [12] found that seawater and sea sand increased the compressive strength of concrete but decreased the compressive elastic modulus. Teng et al. [13] reported that the use of seawater and sea-sand slightly increases the early-age strength of ultra-high performance concrete but slightly decreases the strength at seven days and above. Vafaei et al. [14] investigated the mechanical properties of fibre-reinforced seawater sea-sand concrete subjected to elevated temperatures. Choi et al. [15] assessed the early-age mechanical properties and microstructures of Portland cement mortars produced with various supplementary cementitious materials exposed to seawater and found that the effect of seawater exposure was more significant on flexural

strength than compressive strength. Sun et al. [16] investigated the physical degradation behaviour of cement mortars at three different relative humidity levels based on variations in the physical appearance, dynamic elastic modulus, and microstructure. Lin et al. [17] examined the combined effects of expansive agents and glass fibres on the fracture performance of seawater and sea-sand concrete and found that the optimal expansive agent content was 3%–6%, which increased with increasing glass fibre content. Bachtiar et al. [18] studied the effect of seawater as a curing/mixing constituent on high-performance concrete and observed that seawater-treated concrete contained increased hydration components (tobermorite and ettringite).

Concrete is reinforced with steel bars to improve its tensile resistance to applied loads. A significant concern in using seawater for mixing and curing concrete is the corrosion of steel reinforcement bars in structural concrete. The significant chloride ion concentration of seawater, which can range from 14,000 to 34,000 ppm [19], accelerates the corrosion process in concrete. Hence, preparing structural concrete with seawater is typically discouraged if conventional steel reinforcement is applied. Nonetheless, unreinforced concrete or concrete reinforced with non-corrosive reinforcement, such as fibre-reinforced polymers, can be mixed with seawater if potable water is scarce [20]. This is because not all types of concrete require reinforcement, depending on the intended application. The application of seawater for mixing concrete constituents might affect the durability of plain and reinforced concrete; however, understanding the durability of seawater-mixed concrete is a critical factor limiting its widespread adoption, and further research is required for clarification [21].

The justification for research on seawater in concrete stems from the fact that large volumes of freshwater are used for cement-based construction each year, and freshwater is becoming a relatively scarce resource. Some coastal areas with limited freshwater supply are abundantly surrounded by seawater. With the current water supply shortage in Nigeria and other parts of the world, there is a need to further explore seawater as an alternative water source for concrete production. The aim of this study is to experimentally investigate the workability and strength of Portland cement concrete mixed and cured with Nembe seawater. Nembe seawater was used for mixing and curing concrete, with the concrete specimens mixed with and cured in freshwater adopted as the control.

2. Materials and Methods

2.1. Materials

Cement: Grade 42.5 Portland–limestone cement manufactured according to NIS 444-1:2003 [22] specifications was purchased from a cement depot in Owerri, Imo State, Nigeria. The properties of the cement provided by the manufacturer are listed in Table 1.

Aggregates: Clean river sand dredged from Otammiri River in Ihiagwa, Owerri West Local Government Area, Imo State, was used as the fine aggregate. Crushed granite of 20 mm nominal size processed at a quarry plant in Ishiagu, Ebonyi State, Nigeria, was used as the coarse aggregate.

Water: Two sets of water were used for mixing the concrete ingredients and curing the hardened concrete samples. Freshwater was obtained from a borehole tap at the Structural Engineering Laboratory of the Department of Civil Engineering, Federal University of Technology, Owerri. The seawater was obtained from Nembe waterside, a water transportation route between Port Harcourt in Rivers State and the Nembe Kingdom in Bayelsa State. The seawater was temporarily stored in air-tight plastic containers and transported to the laboratory.

Table 1. Properties of Portland–limestone cement

Property	Value
Fineness	2%
Specific gravity	3.1
Density	1,440 kg/m^3
Initial setting time	120 min
Final setting time	300 min

2.2 Methods

2.2.1 Materials

Before the constituent materials were utilised, they were subjected to preliminary characterisation tests. The cement was in a dry state and free from lumps. The fine aggregate was free from deleterious substances and had a specific gravity of 2.63, fineness modulus of 2.92, water absorption of 1.6%, and bulk density of 1570 kg/m^3. The coarse aggregate had the following physical and mechanical properties: fineness modulus = 4.15, specific gravity = 2.73, water absorption = 1.3%, bulk density = 1520 kg/m^3, aggregate impact value = 25%, and Los Angeles abrasion value = 12%. The particle size distribution curves of the fine and coarse aggregates are shown in Figure 1. The freshwater and seawater were subjected to physiochemical tests to determine their physical and chemical compositions. Table 2 lists the physiochemical properties of the freshwater and seawater samples.
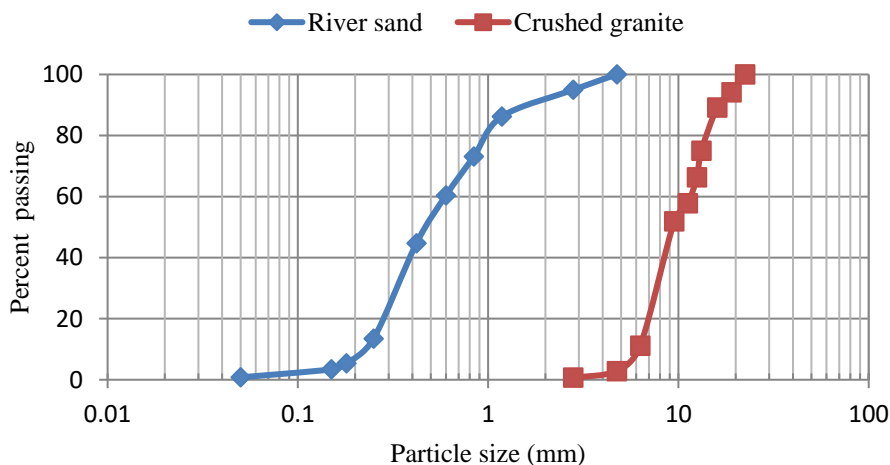
Fig. 1 Particle size distribution curves of river sand and crushed granite

The hardened concrete specimens were denoted by two letters, 'F' and 'S', representing freshwater and seawater, respectively. Each specimen was identified with two letters, such that the first letter indicated the mixing water, whereas the second letter indicated the curing water. For example, 'FS' represented a concrete specimen cast with freshwater and cured with seawater. Four sets of hardened concrete were produced, as listed in Table 3.

Table 2. Physiochemical properties of freshwater and seawater samples

Test	Freshwater	Seawater
pH	7.2	7.9
Electrical conductivity	1,053 micro s/cm	57.9 micro s/cm
Chloride	230 mg/L	19,352 mg/L
Sulphate	110 mg/L	2,649 mg/L
Nitrate	-	-
Calcium	63 mg/L	412 mg/L
Magnesium	28 mg/L	1,272 mg/L
Sodium	-	10,556 mg/L
Potassium	-	880 mg/L
Iron	-	0.14 mg/L
Chromium	-	0.03 mg/L
Phosphate	-	1.10 mg/L
Acidity	-	-
Alkalinity	-	0.8 mg/L
Salinity	-	35.7 mg/L
Total dissolved solids	1,500 mg/L	34,482 mg/L
Total suspended solids	-	-
Odour	Unobjectionable	Unobjectionable
Hardness	-	20.90 mg/L

Table 3. Details of concrete specimens

Notation	Meaning
FF	Concrete mixed and cured with freshwater
FS	Concrete mixed with freshwater and cured with seawater
SF	Concrete mixed with seawater and cured with freshwater
SS	Concrete mixed and cured with seawater

2.2.3 Tests

The setting times and slump of the fresh concrete and the compressive strength of the hardened concrete were determined. The slump of the fresh concrete was evaluated according to BS EN 12350-2:2009 [27], and the compressive strengths of the hardened concrete cubes were measured according to BS EN 12350-3:2009 [28]. The values reported in this paper were obtained as the mean of three measured values. Compressive strength is typically investigated in experimental studies because its test is relatively easy to perform, and the obtained results fairly represent an estimated measure of other mechanical properties, such as flexural strength and splitting tensile strength.

3. Results and Discussion

3.1 Properties of Constituent Materials

The specific gravity of the river sand was within the range used for normal fine aggregate. The fineness modulus of the river sand confirms that the sizes of the fine aggregate particles lie between medium and coarse sands; thus, the river sand is suitable for

manufacturing normal-strength concrete. The aggregate impact and Los Angeles abrasion values of the coarse aggregate satisfied the requirements for manufacturing normal-strength concrete. According to Shetty [29], the aggregate impact value and Los Angeles abrasion value should not exceed 30% for wearing-surface concrete and 45% and 50%, respectively, for non-wearing-surface concrete.

The seawater contained significantly high amounts of chloride and sulphate ions, and sodium, magnesium, potassium, and calcium are the main constituent elements detected in the seawater. The amounts of these ions and elements in the seawater were significantly higher than those in the freshwater. Moreover, the seawater contained significantly higher amounts of total dissolved solids than the freshwater (Table 2). The chloride content of the seawater used in this study is within the typical range for seawater reported in the literature [19]. High contents of chloride and sulphate ions affect the pH of water, which significantly impacts the strength development of concrete [30]. Water with a pH ranging between 6.0 and 8.0 has no significant effect on the compressive strength of concrete [31,32]. The pH values of both water types are somewhat comparable, and the pH of Nembe seawater (7.9) is within the range obtained for different seawaters (7.4–8.4) [33].

Chemical reactions between seawater and cement occur during the diffusion of sulphate and chloride ions in the seawater in concrete. Generally, the chemical reactions of seawater on concrete are generated by sulphate attacks, and crystallisation is the primary attacking mode [34]. Sodium, potassium, and magnesium sulphates (Na_2SO_4, K_2SO_4, and $MgSO_4$) present in seawater may induce sulphate attacks in concrete because they can initially react with calcium hydroxide [$Ca(OH)_2$] present in the set cement formed via hydration of dicalcium silicate (C_2S) and tricalcium silicate (C_3S). The sulphate attacks eventually lead to the formation of gypsum. The chemical reaction of the cement paste with the high-chloride content of seawater is generally slight [34]. A possible chemical reaction between seawater and cement is as follows [35].

$$3Ca(OH)_2 + 3Na_2SO_4 \rightarrow 3CaSO_4 + 6NaOH \quad\quad\quad\quad\quad\quad\quad (1)$$

$$CaCl_2 + 2NaOH \rightarrow Ca(OH)_2 + 2NaCl \quad\quad\quad\quad\quad\quad\quad\quad\quad (2)$$

3.2 Setting Time and Slump

The setting time and slump values of the concrete samples mixed with freshwater and seawater are listed in Table 4. The initial setting time of the concrete specimen mixed with freshwater was significantly longer than that mixed with seawater. Compared with freshwater, the use of seawater in Portland-cement concrete decreased the initial setting time of cement by approximately 36% (Table 4). The behaviour is attributed to the high concentration of chloride ions in seawater. The sodium hydroxide produced during the formation of gypsum reacts with salts in the seawater (for example, calcium chloride), leading to the formation of sodium chloride and additional calcium hydroxide (Eq. (2)). These chlorides and chloride ions accelerate the hydration of C_3S pastes, shortening the initial setting time of the seawater-mixed concrete (Table 4). The reduced initial setting time may necessitate applying appropriate retarding admixtures when the rapid setting is undesirable. However, the final setting times of the specimens mixed with freshwater and seawater were approximately equal.

The slump of fresh concrete mixed with freshwater was higher than that of seawater; seawater decreased the slump by approximately 54%. Thus, the concrete produced with seawater was less workable and more viscous than that with freshwater. The total dissolved solids and possible suspended particles in the seawater might have likely increased the seawater viscosity (compared to the freshwater viscosity) and contributed

to the decreased slump. Another probable reason for the reduced slump of the seawater concrete sample is the accelerated cement hydration owing to the presence of chloride and sulphate ions in the seawater.

Table 4. Setting times and slump values of fresh concrete

Test	CFW	CSW
Initial setting time (min)	88	56
Final setting time (min)	296	299
Slump (mm)	79	36
CFW = Concrete mixed with freshwater; CSW = Concrete mixed with seawater		

Chloride ions react with sodium hydroxide to produce additional calcium hydroxide, inducing a faster setting and quicker fluidity loss. For the adopted water–cement ratio, the fresh concrete samples containing freshwater and seawater exhibited medium workability, as their slump values ranged between 25 and 100 mm [36]. Superplasticisers may be added to concrete mixed with seawater to maintain an appreciable consistency level and, thus, improve the workability of the concrete mixture.

3.3 Compressive Strength

The compressive strengths of the test specimens cured in freshwater and seawater up to the 90th day were obtained (Figure 2). The different casting and curing conditions were analysed by comparing the parameters with the control condition, that is, the FF specimens. The rates of increase in the compressive strength of concrete specimens mixed and cured with freshwater and seawater were similar; that is, the compressive strength increased with curing age, irrespective of mixing and curing (Figure 2). The strength development rates were high within the first few days and decreased at later curing ages.
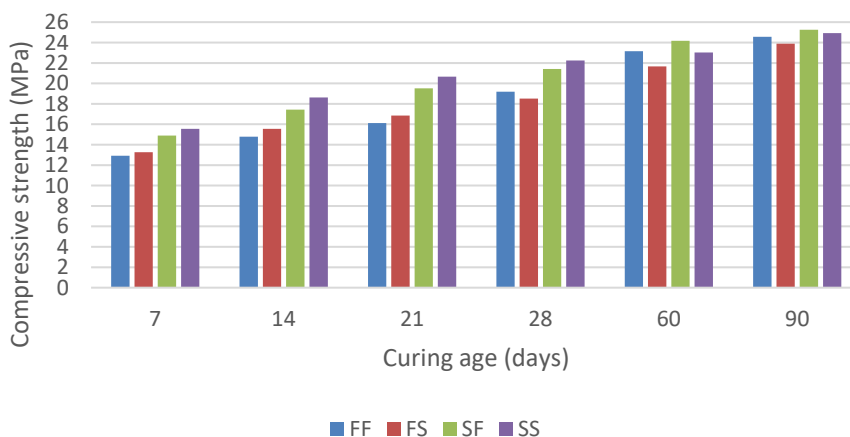
Fig. 2 Compressive strength values for FF, FS, SF, and SS specimens

On the 7th day, the FS specimens had the highest compressive strength than those of the SF, FS, and FF specimens; this trend was also observed on the 14th day. The seawater-mixed concrete underwent an earlier gain in compressive strength before 28 days than the freshwater-mixed concrete. This strength increment might be caused by the improved, densified microstructure of concrete owing to accelerated hydration in the presence of

chloride ions. The FF specimens had lower compressive strength values than the FS specimens up to the 21st day, but from the 28th day, they exhibited higher strengths than the FS specimens. In addition, the SF specimens had higher compressive strength values than the FS specimens. Moreover, the FS specimens had the lowest compressive strength comparatively at the later stages. The low strength of the FS specimens could be caused by a lack of adequate hydration, which may be attributed to the thin layer of minerals covering the cement paste [11]. These minerals might have limited moisture penetration in the specimen essential for continuous hydration. By the 90th day, no significant differences between the compressive strength values for specimens subjected to different mixing and curing conditions were observed. Hence, the hydration rates of the FF and SS specimens decreased by then. The relative decrease in the rate of compressive strength gain of the SF and SS specimens after the 28th day may be attributed to the crystallisation of salt in the seawater [34].

4. Conclusions

In this study, the behaviour of concrete mixed and cured with Nembe seawater was investigated. The behaviour of concrete mixed and/or cured with seawater is somewhat linked to the chemical reactions between seawater and cement in concrete. Seawater induces the formation of gypsum and the accelerated hydration of C_3S pastes, leading to the formation of chloride and sulphate salts. The use of seawater for mixing concrete shortened the initial setting time of the cement paste and reduced the slump of the concrete. Generally, the concrete specimens mixed and cured in fresh water at the earlier curing ages (7, 14, and 21 days) had lower compressive strengths than specimens mixed and cured in seawater. Among the four groups of concrete experimentally analysed in this study, concrete specimens mixed and cured with seawater exhibited the highest compressive strengths up to the 28th day. However, concrete specimens mixed with seawater and cured with freshwater exhibited the highest compressive strengths at the 60th and 90th days of curing. From approximately the 60th day of curing, seawater curing negatively influenced the compressive strength of the concrete. Although the concrete specimens mixed with seawater yielded slightly higher compressive strength values than concrete specimens mixed with freshwater, the difference between using freshwater and seawater as mixing and curing water in terms of compressive strength is minimal.

The use of seawater for casting and curing concrete may be necessitated at construction sites close to the sea where portable freshwater is unavailable or inaccessible. Plain concrete may be mixed with seawater in locations where potable water is scarce. Such concrete may be applied to construction cases where unreinforced concrete is acceptable, such as concrete pavements and footpaths. However, adequate measures must be adopted when using seawater in producing reinforced concrete to prevent or minimize corrosion, such as painting or coating the reinforcement bars or using corrosion-resistant reinforcements (for example, fibre-reinforced polymers). Further studies should be conducted to clarify the influence of seawater on concrete properties, such as the long-term strength properties of concrete mixed or cured with seawater. In addition, the durability and microstructural characteristics of seawater concrete should be investigated in detail.

References

[1] Miller SA, Horvath A, Monteiro PJM. Impacts of booming concrete production on water resources worldwide. Nature Sustainability. 2018;1:69-76. https://doi.org/10.1038/s41893-017-0009-5
[2] United Nations Educational, Scientific and Cultural Organization [Internet]. The United Nations world water development report 2021: valuing water - facts and figures. 2021

[cited   2022   Dec   03].   Available   from: https://unesdoc.unesco.org/ark:/48223/pf0000375751

[3] Fattah KP, Al-Tamimi AK, Hamweyah W, Iqbal F. Evaluation of sustainable concrete produced with desalinated reject brine. International Journal of Sustainable Built Environment. 2017;6:183-190. https://doi.org/10.1016/j.ijsbe.2017.02.004

[4] National Oceanic and Atmospheric Administration [Internet]. How much water is in the ocean?   2021   Feb   26   [cited   2022   Dec   03].   Available   from: https://oceanservice.noaa.gov/facts/oceanwater.html

[5] The United States Geological Survey [Internet]. Why is the ocean salty? [cited 2022 Dec 03]. Available from: https://www.usgs.gov/faqs/why-ocean-salty

[6] Younis A, Ebead U, Suraneni P, Nanni A. Fresh and hardened properties of seawater-mixed   concrete.   Construction   and   Building   Materials.   2018;190:276-286. https://doi.org/10.1016/j.conbuildmat.2018.09.126

[7] Xiao J, Qiang C, Nanni A, Zhang K. Use of sea-sand and seawater in concrete construction: current status and future opportunities. Construction and Building Materials. 2017;155:1101-1111. https://doi.org/10.1016/j.conbuildmat.2017.08.130

[8] Nishida T, Otsuki N, Ohara H, Garba-Say ZM, Nagata T. Some considerations for applicability of seawater as mixing water in concrete. Journal of Materials in Civil Engineering.   2015;27(7):B4014004.   https://doi.org/10.1061/(ASCE)MT.1943-5533.0001006

[9] Mbadike EM, Elinwa AU. Effect of salt water in the production of concrete. Nigerian Journal of Technology. 2011;30(2):105-110.

[10] Osuji SO, Nwankwo E. Marine water effect on compressive strength of concrete: a case study of Escravos area of Nigerian Delta. Nigerian Journal of Technology. 2015;34(2):240-244. https://doi.org/10.4314/njt.v34i2.4

[11] Lim ED, Roxas CL, Gallardo R, Nishida T, Otsuki N. Strength and corrosion behavior of mortar mixed and/or cured with seawater with various fly ash replacement ratios. Asian Journal of Civil Engineering (BHRC). 2015;16(6):835-849 .

[12] Liu J, Fan X, Liu J, Jin H, Zhu J, Liu W. Investigation on mechanical and micro properties of concrete incorporating seawater and sea sand in carbonized environment. Construction   and   Building   Materials.   2021;307:124986. https://doi.org/10.1016/j.conbuildmat.2021.124986

[13] Teng J-G, Xiang Y, Yu T, Fang Z. Development and mechanical behaviour of ultra-high-performance seawater sea-sand concrete. Advances in Structural Engineering. 2019;22(14):3100-3120. https://doi.org/10.1177/1369433219858291

[14] Vafaei D, Ma X, Hassanli R, Duan J, Zhuge Y. Microstructural and mechanical properties of fiber-reinforced seawater sea-sand concrete under elevated temperatures. Journal of   Building   Engineering.   2022;50:104140. https://doi.org/10.1016/j.jobe.2022.104140

[15] Choi SI, Park JK, Han TH, Pae J, Moon J, Kim MO. Early-age mechanical properties and microstructures of Portland cement mortars containing different admixtures exposed to   seawater.   Case   Studies   in   Construction   Materials.   2022;16:e01041. https://doi.org/10.1016/j.cscm.2022.e01041

[16] Sun H, Liu S, Yu F, Zhang X, Wu C, Xing F, et al. Behaviour of cement binder exposed to semi-immersion in chloride-rich salt solutions and seawater with different RH levels. Cement   and   Concrete   Composites.   2022;131:104606. https://doi.org/10.1016/j.cemconcomp.2022.104606

[17] Lin M, He S, Qiao S, Xiong Z, Qiu Y, Zhang J, et al. Combined effects of expansive agents and glass fibres on the fracture performance of seawater and sea-sand concrete. Journal   of   Materials   Research   and   Technology.   2022;20:1839-1859. https://doi.org/10.1016/j.jmrt.2022.08.019

[18] Bachtiar E, Rachim F, Makbul R, Tata A, Irfan-Ul-Hassan M, Kırgız MS, et al. Monitoring of chloride and Friedel's salt, hydration components, and porosity in high-performance

concrete. Case Studies in Construction Materials. 2022;17:e01208. https://doi.org/10.1016/j.cscm.2022.e01208

[19] Li P, Li W, Sun Z, Shen L, Sheng D. Development of sustainable concrete incorporating seawater: a critical review on cement hydration, microstructure and mechanical strength. Cement and Concrete Composites. 2021;121:104100. https://doi.org/10.1016/j.cemconcomp.2021.104100

[20] Montanari L, Suraneni P, Tsui-Chang M, Khatibmasjedi M, Ebead U, Weiss J, et al. Hydration, pore solution, and porosity of cementitious pastes made with seawater. Journal of Materials in Civil Engineering. 2019;31(8):04019154. https://doi.org/10.1061/(ASCE)MT.1943-5533.0002818

[21] Ebead U, Lau D, Lollini F, Nanni A, Suraneni P, Yu T. A review of recent advances in the science and technology of seawater-mixed concrete. Cement and Concrete Research. 2022;152:106666. https://doi.org/10.1016/j.cemconres.2021.106666

[22] NIS 444-1:2003. Quality standard for ordinary Portland cement - part 1: composition, specification and conformity criteria for common cements. Standards Organisation of Nigeria, Lagos, 2003.

[23] Asiedu RO. Using lateritic gravel as all-in aggregate for concrete production. Journal of Engineering, Design and Technology. 2016;15(3):305-316. https://doi.org/10.1108/JEDT-01-2016-0001

[24] Food and Agriculture Organization of the United Nations [Internet]. Concrete. 2018 [cited 2022 Dec 03]. Available from: www.fao.org/docrep/s1250e/S1250E08.htm

[25] Ettu LO, Ibearugbulem OM, Ezeh JC, Anya UC. The suitability of using laterite as sole fine aggregate in structural concrete. International Journal of Scientific and Engineering Research. 2013;4(5):502-507.

[26] BS 8110-1:1997. Structural use of concrete - part 1: code of practice for design and construction, British Standards Institution, London, 1997.

[27] BS EN 12350-2:2009. Testing fresh concrete - slump test. British Standards Institution, London, 2009.

[28] BS EN 12390-3:2009. Testing hardened concrete - compressive strength of test specimens. British Standards Institution, London, 2009.

[29] Shetty MS. Concrete technology: theory and practice. 6th revised ed. New Delhi: S. Chand; 2012.

[30] Kucche KJ, Jamkar SS, Sadgir PA. Quality of water for making concrete: a review of literature. International Journal of Scientific and Research Publications. 2015;5(1): 1-10.

[31] Neville AM, Brooks II. Concrete technology. 2nd ed. Essex: Pearson Education Limited; 2010.

[32] Lasker AI. Concrete technology practices. New Delhi: Narosa Publishing House; 2015.

[33] Venkatesana G, Kumara A, Perumal P. Fresh and hardened properties of five non-potable water mixed and cured concrete: a comprehensive review. Construction and Building Materials. 2021;309:125089. https://doi.org/10.1016/j.conbuildmat.2021.125089

[34] Weigan FM. Effect of seawater for mixing and curing on structural concrete. The IES Journal Part A: Civil & Structural Engineering. 2010;3(4):235-243. https://doi.org/10.1080/19373260.2010.521048

[35] Yaseen SA, Yiseen GA, Poon CS, Li Z. Influence of seawater on the morphological evolution and the microchemistry of hydration products of tricalcium silicates (C3S). ACS Sustainable Chemistry and Engineering. 2020;8(42):15875-15887. https://doi.org/10.1021/acssuschemeng.0c04440

[36] Dhir RK, Jackson N. Concrete. In: Jackson N, Dhir RK, editors. Civil engineering materials. 5th ed. Basingstoke (GB): Palgrave; 1996. p. 161-298. https://doi.org/10.1007/978-1-349-13729-9

Research Article

Experimental study on stress-strain characteristics of ultra high strength concrete and its effect on stress block parameters for flexural design of building

Brijesh Singh[a*], Pranay Singh[b], Parmanand Ojha[c], Abhishek Singh[d]

Centre for Construction Development and Research, National Council for Cement and Building Materials, India

Article Info	Abstract
	Flexural design of reinforced concrete members in structures such as buildings, bridges, etc. presented in various standards are based on the equivalent rectangular stress block and stress-block parameters for high strength concrete. However, with design of high strength concrete mixes these existing stress block parameters for normal and high strength concrete have become redundant and does not give a true representation of the obtained stress-strain curves for ultra-high strength concrete. The primary stress-strain characteristics affecting the stress block parameters are strain at peak stress, the ultimate strain and the shape of the rising limb of the curves. Past studies have confirmed a varying behaviour of all these characteristics in the stress strain curves at higher strength. The present study first evaluated the stress strain curves for high strength concrete from 90 to 140 MPa. The characteristics of the curves were coMPared with those of normal and high strength concrete. Based on the observed stress strain characteristics, the modified stress block parameters for the ultra-high strength concrete are presented. The proposed stress block was coMPared with the Indian standard IS456 and European design standard EC: 02-2004. The proposed stress block will be useful for the required modification and updating of various standards pertaining to the flexural design of ultra-high strength concrete with cylindrical compressive strength in from 90 to 140MPa.

1. Introduction

Various standards propose a stress block based flexural design methodology for concrete structures. This rectangular stress block is modified using the stress block parameters to give an accurate representation of the observed stress-strain behaviour of concrete. The actual stress strain curves for the concrete have a rising limb at peak and a falling limb. With appropriate choice of the stress block parameters these characteristics can be incorporated in the rectangular stress blocks. The use of the equivalent rectangular stress distribution was initially suggested by Emperger [1], which was refined by Whitney [2] for use in ultimate strength design, and then empirically confirmed by Hognestad et al, [3] and Mattock et al, [4]. Hognestad et al, [3] first introduced the rectangular stress block model based on experimental investigation on normal strength concrete. The rectangular stress block dimensions utilized in regular concrete members cannot be used for high and ultra-high strength concrete members safely, [5]. The applicability of ACI 318-95 rectangular stress block parameters to higher strength concretes was investigated by Attard and Stewart (1998) [6]. They demonstrated that the ultimate moment capacity for a rectangular section made of ductile single reinforcement is largely unaffected by the stress block model. Bernardo & Lopes [7] conducted an experimental investigation on the

evolution of depth of neutral axis at failure with the ductility at bending on High Strength Concrete (HSC) beams. Different current RC design codes [8,9] have used equivalent rectangular concrete stress blocks that depend simply on the strength of concrete. It was discovered that, in coMParison to the experimental values, the theoretical formulations based on the usage of the concrete's rectangular block diagram to compute the depth of neutral axis at failure produced significantly smaller values. As a result, it was determined that the ACI 318-1989 rectangular stress block diagram was insufficient for HSC beams. According to Cetin and Carrasquillo [10], no one equation of different codes and previous research appears to accurately describe the flexural strength of HSC, and as a result, measured values should be used rather than hypothesized ones. Another crucial factor in the ultimate strength design is the ultimate concrete compressive strength. Although it is not necessary for the ultimate flexural strength of reinforced concrete cross sections, this variable has a noticeable iMPact on the final curvature. According to Mattock et al. [4], 0.003 is a fairly conservative estimate of the ultimate strain of concrete. Many design codes have also approved this value (NZS 3101 2006; ACI 318-08 2008; AS 3600 2009). According to Kahn et al. [11], the ultimate value of 0.003 is accurate up to 102 MPa for concrete and offered the best forecast of the ultimate moment. The limit of 0.003 for concrete under compression may be increased for higher strength concrete, according to Mansur et al ,[12] The final concrete strain results from Ibrahim and MacGregor (1996) were significantly higher than the limitation value of 0.003. However, they came to the conclusion that the value of 0.003 adopted by the ACI code seems suitable as a cautious lower bound of experimental results based on the reported values in prior testing of C-shaped specimens. The assumed stress strain behaviour and stress block parameters for the evaluation of flexural capacity of the beams as given in IS 456 [13] is presented in Figure 1. The strain at the peak stress is assumed to be 2500 microstrains and the peak strain as 3500 microstrains. Based on the assumed stress block the flexural capacity of the members are established. The stress block assumed in Eurocode EC 02: 2004 [14] is shown in Figure 2. The assumed stress-strain behaviour in Eurocode varies with the variation on the compressive strength of the concrete and therefore gives a more accurate representation of the actual stress-strain behaviour at different strength of concrete. These stress-strain characteristics and the resulting stress block parameters have underlying effect on the mechanical [15,16], fracture [17] and durability [18] properties of the concrete.
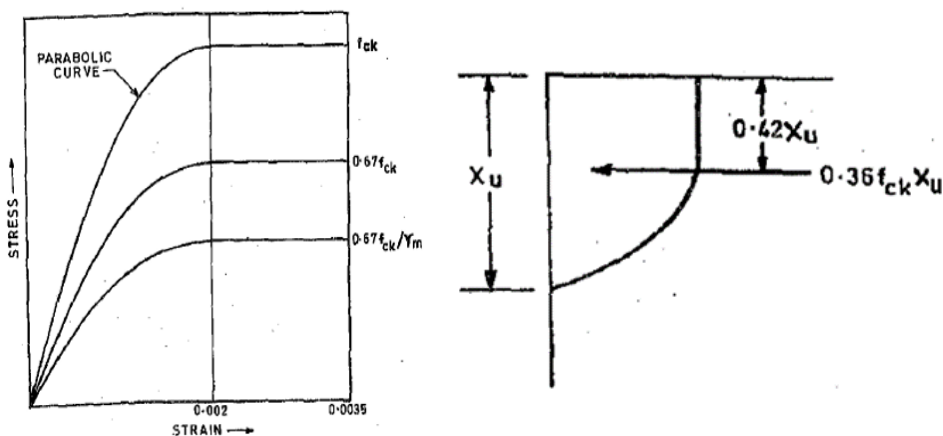
Fig. 1 Stress-Strain behaviour & Stress block parameters adopted in IS 456:2000 [13]

fck(Mpa)	Upto 50	55	60	70	80	90
εc2(%)	2	2.2	2.3	2.4	2.5	2.6
εcu2(%)	3.5	3.1	2.9	2.7	2.6	2.6
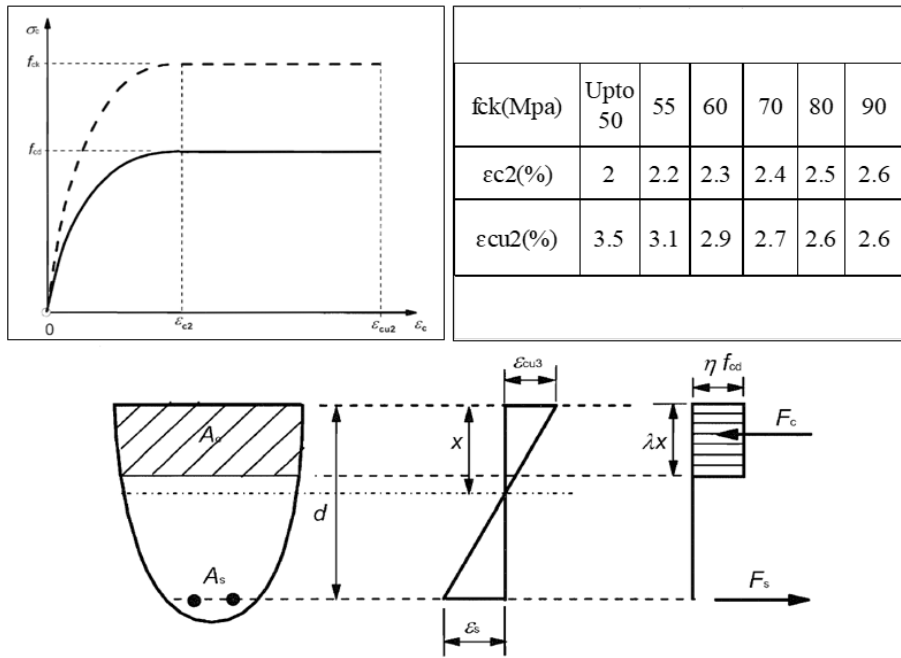
Fig. 2 Stress strain behaviour and stress block in Eurocode EC 02-2004 [14]

The primary aim of the present study is to calculate the stress block parameters "K' (strength reduction factor) and k_2 (factor for depth of resultant compressive force) using experimental strain measurements. The model proposed in European Design Standard EC: 02-2004 was examined in this study, and stress block parameters was converted into those utilised in the IS code design technique. The outcomes of the experiments were then coMPared to the design parameters.

2. Concrete Ingredients

In this study cementitious material with a broad range of particle size distribution were selected which leads to a higher packing density of concrete. The physical and chemical properties of cementitious material are given in Tables 1 & 2 respectively. Cementitious Materials used in the study are OPC53, GGBS, Flyash, ultrafine GGBS, and Silica fume conforming to IS 269[19], IS 16714[20], IS 3812[21], IS 16715[22], IS 15388[23] respectively. Nano-silica was also used to fill the pores of Nano-size. Similarly, to increase the packing density of solid materials, three different types of aggregates were used namely Quartz sand, Ground Quartz, and River sand. The properties of the materials are given in Table 1 and 2.

Table 1. Physical properties of materials

S. No.	Properties	Cement	G.G.B.S	Flyash	UFGGBS	Silica Fume	Nano Silica
1.	Fineness(m^2/kg)	323	400	310	2026	16701	24000
2.	Specific Gravity	3.15	2.93	2.28	2.88	2.28	2.21

Table 2. Chemical properties of materials

S. No.	Properties	Cement	G.G.B.S	Flyash	UFGGBS	Silica Fume
1	Loss of Ignition (LOI)	2.3	0.33	0.4	0.17	2.73
2	Silica (SiO_2)	20.71	34.41	60.95	33.05	85.03
3	Iron oxide (Fe_2O_3)	4.08	1.18	5.7	0.58	-
4	Aluminum oxide (Al_2O_3)	5.15	18.45	26.67	20.40	-
5	Calcium oxide (CaO)	59.96	36.46	2.08	33.14	-
6	Magnesium oxide (MgO)	4.57	7.00	0.69	7.62	-
7	Sulphate (SO_3)	1.84	0.097	0.29	0.19	-
8	Na_2O	0.42	0.30	0.06	0.19	0.73
9	K_2O	0.56	0.37	1.46	0.58	2.96
10	Chlorides	0.012	0.022	0.009	0.016	-

3. Mix Design Details

In the present study, the proportion of individual cementitious material was decided using the Modified Andreasen and Andersen equation [24,25,26]. From mixes that were mathematically optimized based on their Residual Sum of Squares (RSS) value using an excel solver, three final mixes were cast in the laboratory for a study on their Stress-strain behavior. The details of the mix composition of these optimized mixes are given in Table 3. The total cementitious content used is between 950 to 1000 kg/m³. To attain better particle packing density, a combination of fine aggregates was used i.e., Ground quartz, Fine quartz sand, and coarse quartz sand. The nano-silica was used as 3% replacement for OPC content.

Table 3. Mix Proportion for the experimental study

Mix ID	Mix 1	Mix 2	Mix 3
w/binder	0.17	0.17	0.17
Cement	597	707	636
Flyash	85	42	95
GGBS	165	0	110
Silica fume	135	180	139
Nano Silica	18	21	20
Admixture (%)	1	1	1
FQS	922	734	922
GQ	256	0	256
CQS	0	534	0
Total binder content (kg/m³)	1000	950	1000

4. Stress-strain Study on Ultra-High Strength Concrete

Concrete samples were tested in a strain-controlled, closed-loop servo hydraulic compression testing system with 3000kN capacity in order to determine the stress strain properties of the high strength concrete. In order to measure strain, a compress meter and a Linear Variable Displacement Transducers (LVDT) were placed at the halfway point of the height (Figure-3). CoMPared with normal strength and high strength Concrete, the effect of specimen geometry on the compressive strength is very small for ultra-high strength concrete. For recording the strain, LVDT and compress meter were utilized based on the recording channels available in the strain-controlled machine. The LVDT and

compress meter readings are reported in the study. Generally, the LVDT is suitable for capturing complete stress strain response but accuracy is not at par with compress meter due to error coming from platen-to-platen measurement and larger gauge length. For the compression test, a slow rate of loading in the range of 0.4 μm/sec was used in order to get a complete stress-strain curve. Normal strength concrete fails gradually after attaining its peak load, but high strength and ultra-high strength concrete bursts upon reaching their peak loads [27, 28, 29, 30,34,35]. The recorded stress strain curves are shown in Figure-4 to Figure-6. In the Figures for each specimen the peak stress and the strain at peak stress are given in the legend for each sample.

Fig. 3 Testing setup for Stress Strain Curve determination

The strain at peak stress and the ultimate strain at failure for the specimen are recorded and are shown in the Figure 3 to Figure 5. As depicted in the stress strain plots for ultra-high strength concrete the strain at peak stress and the ultimate strain at failure coincides. The stress strain curves for the concrete above 90MPa compressive strength depicts a straight-line path for the rising limb. Also, the post peak behaviour is negligible leading to equal values for the strain at peak stress and the ultimate strain at failure. Also, the stress-strain curves for the LVDT shows a higher strain value as coMPared to the compress meter values. The reason can be attributed to the difference in gauge length ratios adopted for the compress meter and Linear Variable Displacement Transducer (LVDT). From the curve, one can conclude that specimen with smaller gage length ratio show more ductility than that of larger ratio. This was because the measurement using larger gage ratio can detect more cracks processed within the gage length region during loading stage. The platen-to-platen axial measurements were widely used, especially in ultra-high strength concrete because the test technique was able to capture all cracks within the specimen tested. In ultra-high strength concrete, sudden spalling of concrete cylinder surface makes it difficult to get a post peak behavior [31,32,33]. Thus, the platen-to-platen measurements include extra deformation from the weak contact between loading plate and specimen, consequently the stress-strain curves become more brittle. It was concluded that strain values measured in the stress-strain curve are strongly dependent on the gage length ratio used in compression test. Deformations measured from specimen surface give strain values of stress-strain curve. After peak load, concrete begins to spall and disturb strain measurement in specimen. However, deformations from platen to platen give stable behavior. This makes platen to platen strain measurements popular. Based on the observed stress strain behaviour stress block parameters were derived and discussed in section-5.
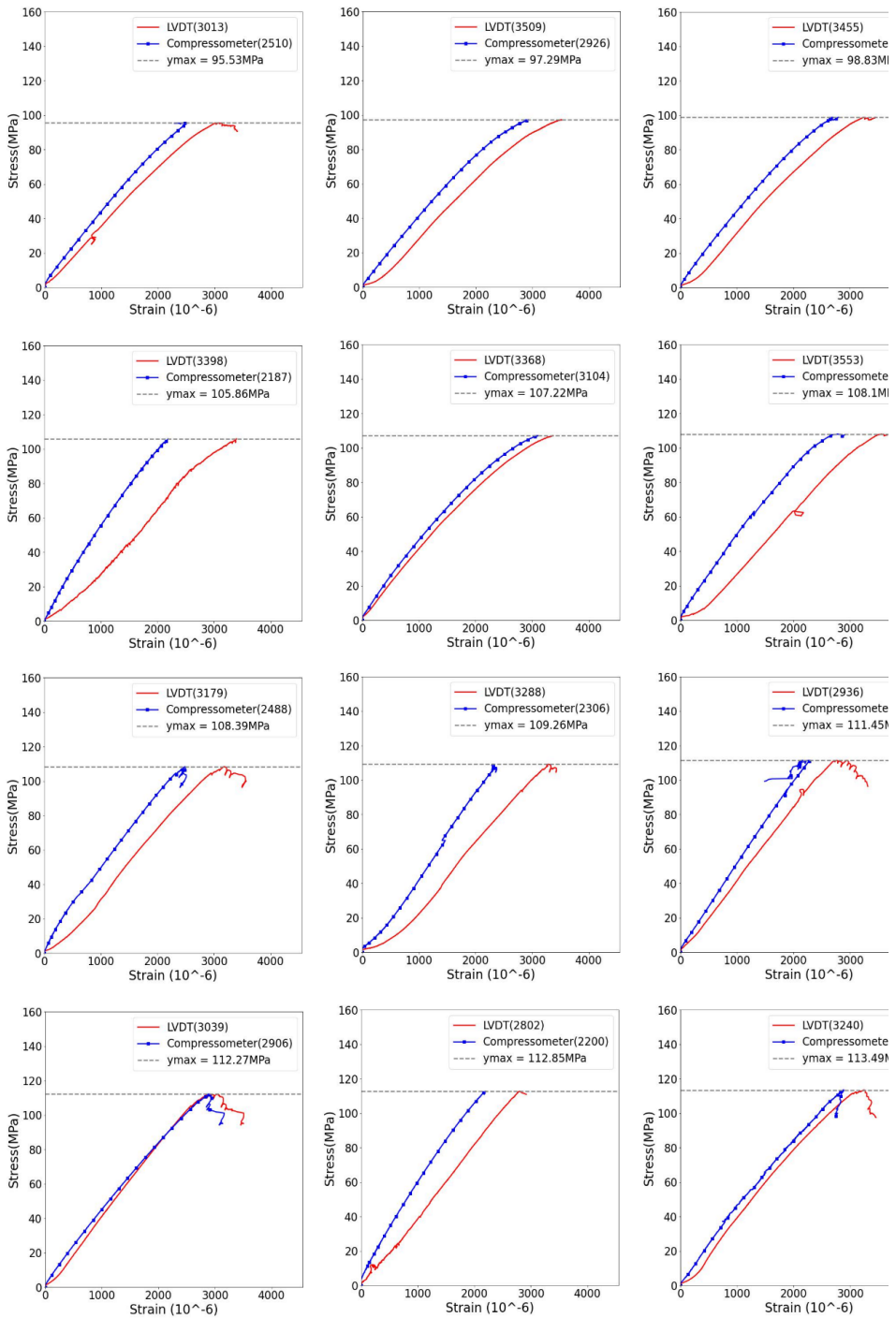
Fig. 4 Stress strain characteristics of Concrete (Compressive strength between 95 MPa to 113 MPa)
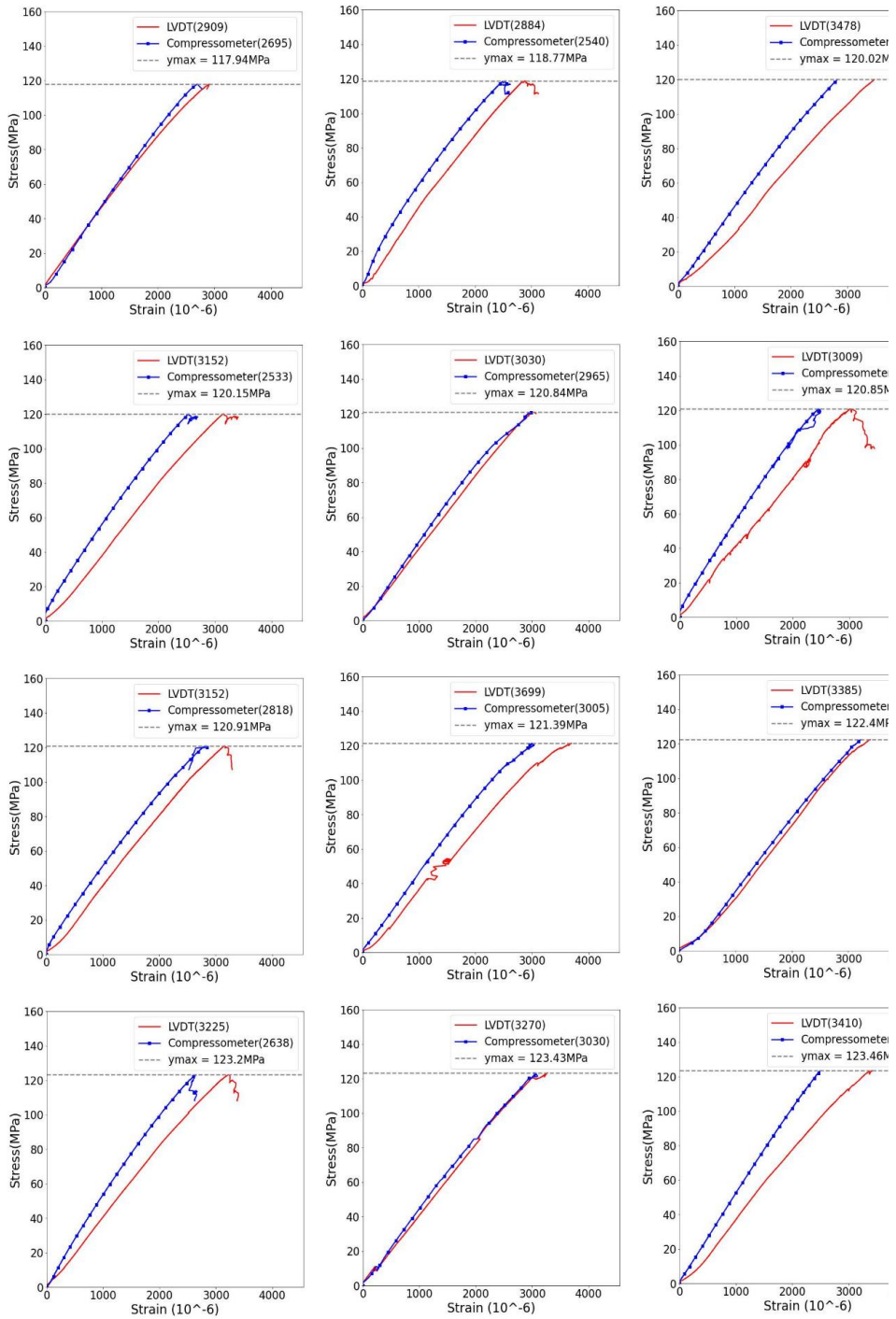
Fig. 5 Stress strain characteristics of Concrete (Compressive strength between 113 MPa to 123 MPa)
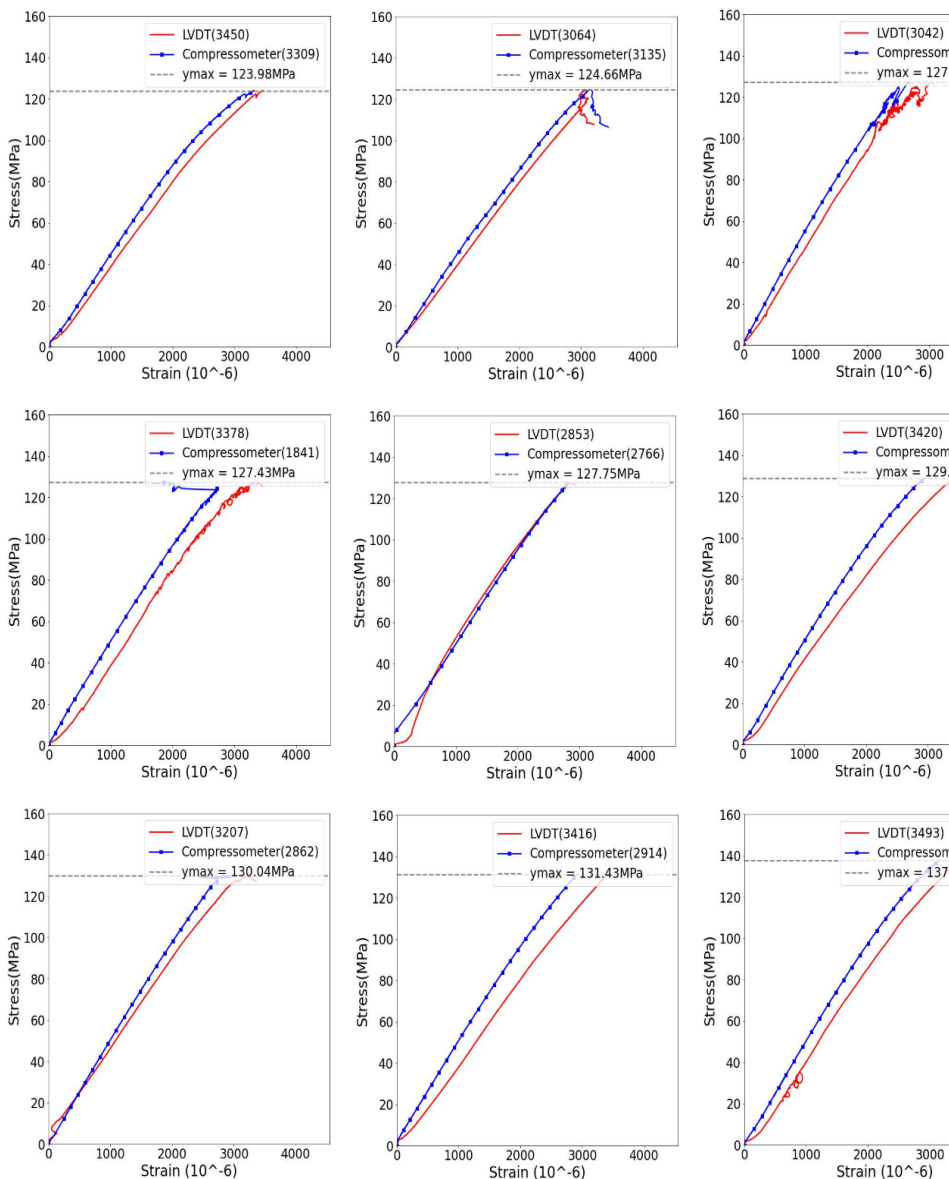
Fig. 6 Stress strain characteristics of Concrete (Compressive strength between 123 MPa to 138 MPa)

5. Determination of Stress-block Parameters and Moment Capacity from Experimentally Obtained Strain Values Using IS: 456 and Eurocode

As presented in past studies the total compressive force and its line of action from the extreme compression fiber can be expressed in terms of three stress block parameters k_1, k_2, and k_3. k_1 is known as shape factor and is defined as the factor for converting the area of rectangular stress into the assumed shape stress block based on stress strain behaviour. Mathematically it can be evaluated using Equation (1).

$$k1 = \frac{Area\ of\ actual\ stress\ block}{Area\ of\ rectangular\ stress\ block\ envalope} \tag{1}$$

The second stress block parameter k2 is related to the evaluation of location of the resultant compressive force of the stress block. Mathematically it is the ratio of the depth of resultant compressive force to depth of neutral axis. Equation (2) gives the mathematical formulation for stress block parameter k2.

$$k2 = \frac{\begin{array}{c}Depth\ of\ Centroid\ of\ Assumed\ stress\ block\\ from\ extreme\ compression\ fiber\end{array}}{Depth\ of\ Neutral\ Axis} \tag{2}$$

The third stress block parameter k3 is a factor for consideration of stress reduction and reduces the maximum ordinate of stress block. Parameter k3 is evaluated as product of two factors – (i) factor of consideration of long-term effect including the way load is applied (αcc), and (ii) factor for conversion of conversion of cube to cylinder strength. Equation (3) and (4) presents the mathematical formulation and implication of the stress block parameter k3.

$$k3 = \alpha_{cc} \text{ x S1} \tag{3}$$

$$ordinate\ of\ stress\ block = \frac{k3 * f_{ck}}{\Upsilon_{mc}} \tag{4}$$

Based on literature, the value for αcc in Equation (2) was taken as 0.85. In Equation (4) fck is the characteristic compressive strength of concrete and Ymc is the partial factor of safety of concrete. According to Indian standard code of concrete IS 456:2000, Ymc was taken as 1.5 in the present study.

For simplification, the two stress block parameters k1 and k3 can be combined to single stress block parameters as stated in equation (5):

$$K = \frac{k1 * k3}{\Upsilon_{mc}} \tag{5}$$

Also, the stress block parameters can be presented in terms of two factors r1 and r2 which represents the strain at peak stress (εc) and ultimate strain at failure (εcu). These two factors are mathematically presented in Equations (6) and (7):

$$r1 = \frac{\varepsilon_c}{\varepsilon_{cu}} \tag{6}$$

$$r2 = \frac{\varepsilon_{cu} - \varepsilon_c}{\varepsilon_{cu}} \tag{7}$$

These stress block parameters and the factors are primarily depended on the following stress strain characteristics of a particular concrete type:

Shape of the rising limb of the stress-strain curve: The stress strain behaviour of normal strength concrete (upto 50 MPa) shows a parabolic rising limb (Figure-4). This has been widely adopted by standard codal provisions around the world. But with increase in strength of the concrete the behaviour of the rising limb changes significantly. As presented by Singh et al. [20] the rising limb of the stress-strain curve for high strength

concrete assumes a straight-line path. In the present study for the concrete strength above 90 MPa the rising limb depicts a nearly perfect straight line with only a little deviation.

Strain at peak stress, Ultimate Strain at failure and their difference: For normal strength concrete, up to 55 MPa, Indian standard code assumes a constant value of 2000 micro strains and 3500 micro strains as the strain at peak stress and ultimate strain respectively. With increase in strength concrete, these values also vary significantly leading to variation in the stress block and stress block parameters. As reported by Singh et al, [20] with increase in the compressive strength of the concrete the difference between these two strain values shrinks and ultimately gets vanished. As observed in the experimental investigation of concrete cylinders above 90MPa strength, there exist no much difference between the strain value at peak stress and the ultimate strain. The change leads to removal of upper rectangular portion of the assumed stress block in IS 456:2000. The variation in the stress block with changes in stress-strain characteristics due to increase in compressive strength is shown in Figure 7. The Figure 7A shows a rectangular stress block which will be modified using the stress block parameters based on the stress strain characteristics. Figure 7B is a typical stress block parameter with parabolic and rectangular portion. The parabolic stress block seems to be a good representation of actual stress-strain curve up to 55 MPa compressive strength. With increase in the compressive strength the parabolic portion becomes linear as show in Figure 7C. This gives a triangular stress block with rectangular upper part. This stress block gives satisfactorily representation of stress-strain behaviour up to 90 MPa. Above 90 MPa the upper rectangular portion shrinks and ultimately dies out giving a stress block as presented in Figure 7D. Based on these shapes of stress blocks the parameters and factors can be evaluated for the flexural design of concrete structures with different concrete compressive strength.

Table 4 shows the calculated stress block parameters for different strength range of concrete. The equations for calculating these parameters are given above as Equation (1) to (7). The stress block parameters k_1 and k_2 can be represented in terms of factor r_1 and r_2. The calculation of the stress block parameter for concrete above 90 MPa strength can also be done by adopting $r_1=1$, and $r_2=0$ in the stress block parameters for the 55 MPa to 90MPa concrete.

Table 4. Stress-block parameters for different strength of concrete

Upto 55 MPa (Fig 7B)	55 MPa to 90 MPa (Fig 7C)	Above 90 MPa (Fig 7D)
$k1 = \frac{2}{3}r1 + r2$	$k1 = \frac{1}{2}r1 + r2$	$k1 = \frac{1}{2}$
$k2 = [\frac{2}{3}r1\left(r2 + \frac{3}{8}r1\right) + r2(\frac{r2}{2})]/k1$	$k2 = [\frac{1}{2}r1\left(r2 + \frac{1}{3}r1\right) + r2(\frac{r2}{2})]/k1$	$k2 = \frac{1}{3}$
$k3 = \alpha_{cc} * S1$	$k3 = \alpha_{cc} * S1$	$k3 = \alpha_{cc} * S1$

Based on the evaluated stress block parameters the total compressive force and its line of action can be calculated for the flexural design of reinforced concrete structures. The total compressive strength in terms of stress block can be evaluated using equation (8) as follows:

$C_u = width\ of\ beam * area\ of\ actual\ stress\ block$

$= b * k1 * area\ of\ rectangular\ stress\ block = b * k1 * k3 * \left(\frac{fck}{Y_{mc}}\right) * x_u$

$$= K * fck * b * x_u \qquad \left\{K = k3 * \frac{fck}{Y_{mc}}\right\} \tag{8}$$

(a)

(b)

(c)

(d)
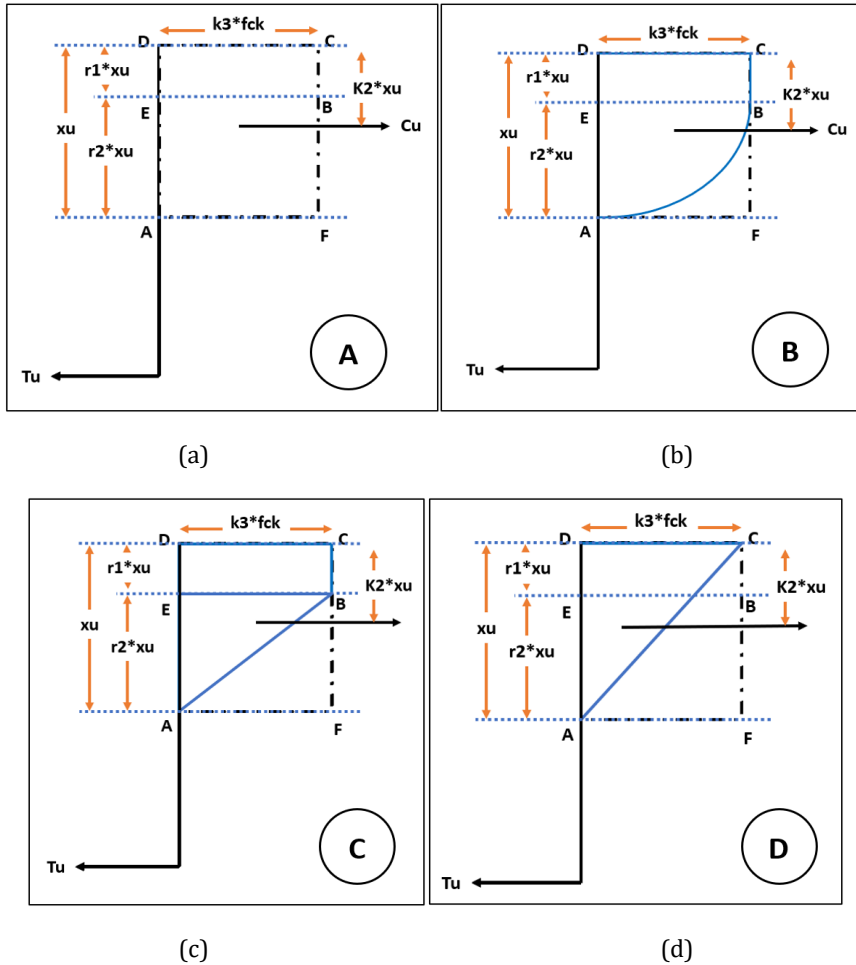
Fig. 7 (a) Rectangular stress-block, (b) Parabolic stress block (55MPa), Triangular stress-block (55MPa to 90 MPa), (d) Triangular stress block (above 90 MPa)

Calculation of neutral axis for balanced section (x_u) can be made using equation (9) as follows:

$$\frac{x_u}{d} = \frac{\frac{fy}{Y_s} * A_{st}}{K * fck * b * d} = \frac{\varepsilon_c}{\varepsilon_c + \varepsilon_{su}} \tag{9}$$

In equation 9, d represents the depth of the centroid of the tension reinforcement from the extreme compression fiber of the concrete (effective depth), fy is the yield strength of the reinforcement, Ast is the area of tension reinforcement, Ys is the partial factor of safety for steel (=1.15 as per IS456-2000), and εsu is the ultimate strain in tension steel (= 0.002+0.87*(fy/Es(modulus of elasticity of steel)).

The lever arm for calculation of moment capacity can be made using equation (10) as follows:

$$l = Lever\ arm\ = d - (k2 * x_u) \tag{10}$$

And the corresponding Moment capacity can be calculated using equation (11) as follows:

$$M_u = C_u * l \tag{11}$$

$$M_u = T_u * l \qquad \{T_u = \frac{fy * Ast}{\Upsilon_s}\} \tag{12}$$

Euro-code give a slightly different approach for evaluation of flexural capacity of reinforced concrete than IS 456:2000. The total compressive force in Eurocode is evaluated using equation (13) as given below:

$$C_u = \lambda * \eta * fcd * b * x_u \tag{13}$$

In equation 13, λ defines the effective height of the compression zone, η defines the effective strength, and fcd represents design compressive strength of the concrete. f_{cd} is given as follow in equation (14).

$$fcd = \alpha_{cc} * \frac{S1}{\Upsilon_{CC}} \tag{14}$$

The IS code equivalent of 13 has been suggested by Singh et al. [20] and is given in equation (15):

$$C_u = K' * fck * b * x_u \qquad \{K' = \lambda * \eta * \alpha_{cc} * \frac{S1}{\Upsilon_{cc}}\ and\ \lambda = 2 * k2\} \tag{15}$$

The depth of neutral axis can be calculated as per euro-code using equation (16) as given below:

$$\frac{x_u}{d} = \frac{1 - 0.44}{k4}\ , if\ cylinderical\ strength < 50MPa \tag{16}$$

$$\frac{x_u}{d} = \frac{1 - 0.54}{k4}\ , if\ cylinderical\ strength > 50MPa \tag{17}$$

$$k4 = 1.25 * (0.6 + (0.0014 * \frac{1000000}{\varepsilon_{cu}})) \tag{18}$$

Moment capacity for balanced section as per Eurocode is given using equation (19) as given below:

$$Mu = C_u * (d - k2 * x_u) = C_u * (d - \frac{\lambda}{2} * x_u) \tag{19}$$

Using equation 11 and equation 19, moment capacities as per IS code and Euro code respectively for a beam of 200mm wide (b = 200mm), 400 mm deep (D = 400 mm) with clear cover of 25 mm is evaluated. Table 5 presents Moment calculation based on Modified IS code and Modified Eurocode methods.

6. Recommended Modifications in Codal Provisions for Incorporation of Ultra High Strength Concrete

Based on the findings of the present study following changes can be made to incorporate the design of ultra-high strength concrete structures:

- Modifications in the strain at peak stress and ultimate strain:

Eurocode EC02-2004 gives equations for evaluating the strength based strain values for concrete upto with compressive strength above 50MPa. The equations for strain at yield strain and the ultimate strain merges at 2600 microstrains. The equations from the Eurocode are presented as follows:

$$\varepsilon c2(o/oo) = 2.0 + 0.085(fck - 50)^{0.53} \tag{20}$$

$$\varepsilon cu2(o/oo) = 2.6 + 35 * \left[\frac{90 - fck}{100}\right]^4 \tag{21}$$

The strain value calculated from equation (20) can be applied to evaluate the ultimate strain of the concrete with compressive strength above 90MPa. The equation (20) can be used to give both the strain at ultimate strain and the peak strain as given in equation (22):

$$\varepsilon c2(o/oo) = \varepsilon cu2(o/oo) = 2.0 + 0.085(fck - 50)^{0.53} \quad \{for \; fck > 90MPa\} \tag{22}$$

The coMParison of the experimental values with the values calculated using equation (22) are presented in Figure (7). The Figure suggests that the equation presented in equation (22) agrees well with the experimental value. Although a high coefficient of correlation is not observed (r2=0.35), still the Eurocode based equation is suitable for design as it is safer for most of the experimental samples as well as it is neither too conventional to be uneconomical.
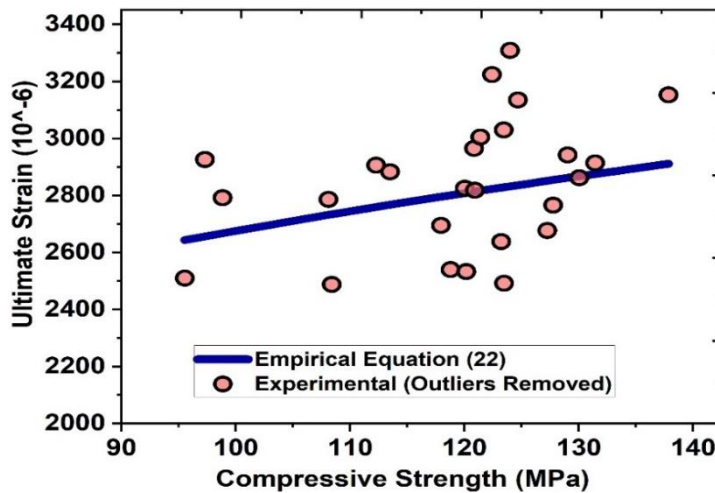
Fig. 7 CoMParison of the strain values obtained from equation (22) with the experimental values (Compressometer)

- Modifications in the equation for calculation of moment of resistance of rectangular section:

Indian standard code IS456 gives the equations for depth of neutral axis and moment of resistance for rectangular section as per equation (23) and (24) as follows:

$$\frac{x_u}{d} = \frac{0.87 * fy * Ast}{0.36 * fck * b * d} \tag{23}$$

$$Mulim = 0.36 * \frac{xu, max}{d} * \left(1 - 0.42 * \frac{xu, max}{d}\right) * bd^2 * fck \tag{24}$$

Table 5. Moment calculation based on Modified IS code and Modified Eurocode methods

Cyd str	Calculations for IS Code based stress block Parameters				Calculations for Euro-Code based stress block Parameters			
	K	k_2	$X_u(max)/d$	Moment	K'(EC)	$\lambda/2$	$X_u(max)/d$	Moment
95.53	0.26	0.33	0.38	236.90	0.29	0.35	0.32	228.18
97.29	0.26	0.33	0.41	261.08	0.29	0.35	0.34	247.17
98.83	0.26	0.33	0.40	259.06	0.29	0.35	0.33	246.55
105.86	0.26	0.33	0.34	243.25	0.29	0.35	0.30	238.02
107.22	0.26	0.33	0.43	296.11	0.29	0.35	0.35	278.52
108.10	0.26	0.33	0.40	283.05	0.29	0.35	0.33	269.44
108.39	0.26	0.33	0.37	267.52	0.29	0.35	0.32	257.94
109.26	0.26	0.33	0.36	258.68	0.29	0.35	0.30	251.59
111.45	0.26	0.33	0.34	254.61	0.29	0.35	0.30	249.43
112.27	0.26	0.33	0.41	300.26	0.29	0.35	0.34	284.48
112.85	0.26	0.33	0.35	260.19	0.29	0.35	0.30	254.42
113.49	0.26	0.33	0.41	302.32	0.29	0.35	0.34	286.69
117.94	0.26	0.33	0.39	303.61	0.29	0.35	0.33	290.10
118.77	0.26	0.33	0.38	296.40	0.29	0.35	0.32	285.11
120.02	0.26	0.33	0.40	316.48	0.29	0.35	0.34	300.80
120.15	0.26	0.33	0.38	299.40	0.29	0.35	0.32	288.09
120.84	0.26	0.33	0.42	326.40	0.29	0.35	0.34	308.56
120.85	0.26	0.33	0.37	296.00	0.29	0.35	0.31	285.86
120.91	0.26	0.33	0.40	318.43	0.29	0.35	0.34	302.73
121.39	0.26	0.33	0.42	330.04	0.29	0.35	0.35	311.54
122.40	0.26	0.33	0.44	344.16	0.29	0.35	0.36	322.39
123.20	0.26	0.33	0.39	313.65	0.29	0.35	0.33	300.41
123.43	0.26	0.33	0.42	336.94	0.29	0.35	0.35	317.77
123.46	0.26	0.33	0.37	304.98	0.29	0.35	0.32	294.00
123.98	0.26	0.33	0.44	352.84	0.29	0.35	0.36	329.60
124.66	0.26	0.33	0.43	345.91	0.29	0.35	0.35	325.01
127.24	0.26	0.33	0.39	326.42	0.29	0.35	0.33	312.12
127.43	0.26	0.33	0.31	264.37	0.29	0.35	0.27	263.86
127.75	0.26	0.33	0.40	333.28	0.29	0.35	0.33	317.51
129.02	0.26	0.33	0.41	347.16	0.29	0.35	0.34	328.47
130.04	0.26	0.33	0.41	345.15	0.29	0.35	0.34	327.57
131.43	0.26	0.33	0.41	351.98	0.29	0.35	0.34	333.38
137.84	0.26	0.33	0.43	383.53	0.29	0.35	0.35	360.13

For concrete with compressive strength of 90 MPa equation (23) and (24) can be modified based on the obtained stress blocks as given in equation (25) and (26):

$$\frac{x_u}{d} = \frac{0.87 * fy * A_{st}}{0.26 * fck * b * d} \tag{25}$$

$$Mulim = 0.26 * \frac{xu, max}{d} * \left(1 - 0.33 * \frac{xu, max}{d}\right) * bd^2 * fck \tag{26}$$

For Eurocode the equation for the moment can be obtained by merging equations 15 and 19 and putting the values of the stress block parameters. The equation is given as follow in equation (27):

$$\begin{aligned} Mu = K' * fck * b * x_u * \left(d - \frac{\lambda}{2} * x_u\right) &= K' * fck * b * \frac{x_u}{d} * \left(1 - \frac{\lambda}{2} * \frac{x_u}{d}\right) * d^2 \\ &= 2.29 * fck * b * \frac{x_u}{d} * \left(1 - 0.35 * \frac{x_u}{d}\right) * d^2 \end{aligned} \tag{27}$$

The coMParison of the moments based on the modified IS code procedure and the Modified Eurocode procedure is shown in Figure 8.

As shown in the Figure 8, with few deviations originating from the experimentally obtained strain values, the moment capacity of the beam increases with the increase in the compressive strength. Also, the moments calculated from both the methods differs marginally. The Indian standard code gives a slightly higher value than the corresponding moment calculated from the Eurocode method. The variation arises because the calculations in Eurocode are based on the cylindrical compressive strength whereas Indian standard code is based on the cubical compressive strength. The adopted cube to cylindrical compressive strength in the present study does not coincides with values proposed by Eurocode. However, the variation is not much significant and lies below 5%.
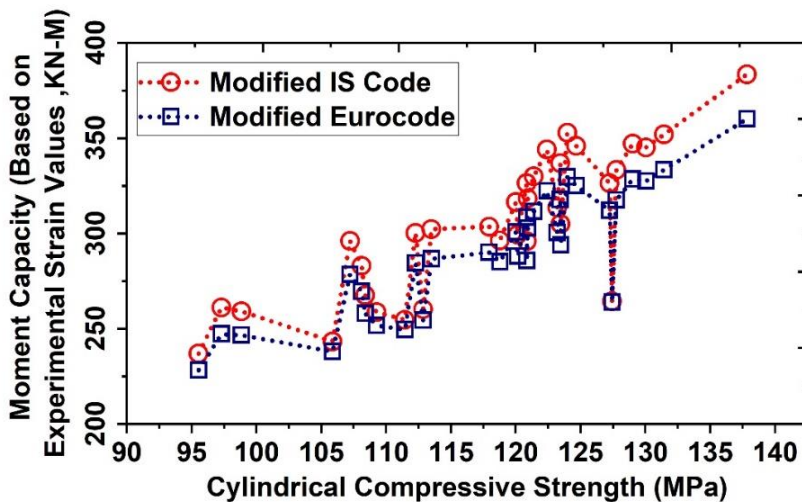

Fig 8. CoMParison of evaluated moments from Modified IS code (equation. 26) and Modified Eurocode (equation 27) methods based on experimental strain values for concrete

7. Conclusions

The stress strain characteristics of concrete changes significantly with increase in concrete compressive strength. Specifically, above 90 MPa the stress strain curves for concrete

becomes ideally straight with negligible post peak behaviour. The change in the stress strain characteristics for higher strength concrete makes the existing stress block parameters unsuitable for design of ultra-high strength concrete. The present study attempted to evaluate the stress block parameters for ultra-high strength concrete based on the experimentally determined stress strain characteristics for ultra-high strength concrete. The findings of the study can be concluded as follows:

- The stress strain curves for the concrete above 90MPa compressive strength depicts a straight-line path for the rising limb. Also, the post peak behaviour is negligible leading to equal values for the strain at peak stress and the ultimate strain at failure.
- The stress-strain curves for the LVDT shows a higher strain value as coMPared to the compress meter values. The reason can be attributed to the difference in gauge length ratios adopted for the compress meter and LVDT. Also, the LVDT was attached between the platen and was affected by the strain in greater length of the specimens therefore it gives a higher strain value than the compress meter for similar stress level.
- Based on the observed stress-strain characteristics, the existing stress block with a parabolic and rectangular parts was modified. The modifications proposed includes adoption of a triangular stress block instead of a parabolic stress block. Also, since the strain at peak stress and the ultimate strain coincides, the proposed stress block doesn't have an idealized rectangular upper part.
- Due to the modifications in the shape of the stress block, the stress block parameters also changed. The shape factor k_1 assumes a value of 0.5. The stress block parameter k_2 which gives the location of resulting compressive strength has a value of 0.33 in the modified stress block for compressive strength above 90MPa to 140MPa
- The study indicates that the stress-block parameters which governs the flexural design of RC members needs modifications in existing standards by appropriately taking care of changes in shape factor and stress reduction factor which is depending upon the stress strain characteristics of ultra-high strength concrete wherein strain at peak stress and ultimate strain coincides.

The proposed stress block gives a better representation of the actual stress strain characteristics for the concrete above compressive strength of 90 MPa. The study is supposed to help in updating the existing standards for incorporating the flexural design of ultra-high strength reinforced concrete structures.

Acknowledgements

References

[1] Emperger F. Ein graphischer Nachweis der Tragfahigkeit und aller in einem Tragwerke aus Eisenbeton auftretenden Spannungen. Beton und Eisen. 1904; 4:5 306-320.
[2] Whitney CS. Design of reinforced concrete members under flexure or combined flexure and direct compression. ACI Journal Proceedings, ACI 1937.
[3] Hognestad E, Hanson NW, et al. Concrete stress distribution in ultimate strength design. ACI Journal Proceedings, ACI 1955.
[4] Mattock AH, Kriz LB, et al. Rectangular concrete stress distribution in ultimate strength design. ACI Journal Proceedings, ACI 1961.

[5] Oztekin E, Pul S, Husem M. Determination of rectangular stress block parameters for High Performance Concrete. Engineering Structures, 2003; 25: 371-376. https://doi.org/10.1016/S0141-0296(02)00172-4

[6] Attard MM, Stewart MG. Two parameter stress block for High-Strength Concrete. ACI Structural Journal, 1998; 95:3 305- 317. https://doi.org/10.14359/548

[7] Bernardo LFA, Lopes SMR. Neutral axis depth versus flexural ductility in High-Strength Concrete Beams. J. Struct. Eng., 2004; 130:3 452-459. https://doi.org/10.1061/(ASCE)0733-9445(2004)130:3(452)

[8] ACI Committee 318 (2008) "Building Code Requirements for Reinforced Concrete and Commentary ACI 318M-08", Manual of Concrete Practice. American Concrete Institute. Michigan. pp 465. USA.

[9] Standards New Zealand, NZS 3101 (2006), "Concrete Structures Standard, Part 1 - The Design of Concrete Structures", Wellington, New Zealand.

[10] Cetin A, Carrasquillo RL. High- Performance Concrete: Influence of Coarse Aggregates on Mechanical Properties. Journal of ACI Materials, 1998; 95: 252-261. https://doi.org/10.14359/369

[11] Kahn LF, Meyer KF. Rectangular stress block for nonrectangular compression zone. ACI Structural Journal, 1995; 92:3. https://doi.org/10.14359/1131

[12] Mansur MA, Chin MS, Wee TH. Flexural behavior of high-strength concrete beams. ACI Structural Journal, 1997; 94:6 663-673. https://doi.org/10.14359/9726

[13] IS: 456-2000, "Code of Practice for Plain and Reinforced Concrete", Bureau of Indian Standards, New Delhi.

[14] Eurocode 2-2004: Design of concrete structures, European Committee for Standardization.

[15] Ojha, PN, Singh B, Singh P, Singh A, Mandre MK. Study on effect of fly ash and limestone powder on compressive strength of roller coMPacted concrete for dam construction. Journal of Asian Concrete Federation, vol. 8, no. 1, pp. 37-51, Jun.

[16] Ojha PN, Singh B, Prakash S, Singh P, Mandre MK, Kumar S. Effect of high ratio fly ash on roller coMPacted concrete for dam construction. Research on Engineering Structures and Materials, 2022. https://doi.org/10.17515/resm2022.374ma1216

[17] Ojha PN, Singh P, Singh B, Singh A, Mittal P. Fracture behavior of plain and fiber-reinforced high strength concrete containing high strength steel fiber. Research on Engineering Structures and Materials, 2022. https://doi.org/10.17515/resm2022.377ma1228

[18] Ojha PN, Kumar S, Kaura P, Singh B, Singh P. Experimental investigation on effect of corrosion on curvature- ductility relationship of RCC member in flexure. vol. 9, pp. 74-86, May 2022.

[19] IS: 269-2015, 2020, "Ordinary Portland Cement - Specification (Sixth Revision)", Bureau of Indian Standards, New Delhi.

[20] IS: 16714-2018, 2018, "Ground Granulated Blast Furnace Slag for Use in Cement, Mortar & Concrete- Specification", Bureau of Indian Standards, New Delhi.

[21] IS 3812 (2013), "Pulverised Fuel Ash - Specification, Part 1: For use in cement, cement mortar and concrete", Bureau of Indian Standards, New Delhi.

[22] IS 16715-2018, "Ultrafine Ground Granulated Blast Furnace Slag - Specification".

[23] IS 15388 (2003), "Silica Fume - Specification", Bureau of Indian Standards, New Delhi

[24] Hüsken G, Brouwers HJH. A new mix design concept for earth-moist concrete: A theoretical and experimental study. Cement and Concrete Research, 2008; p. 1246 – 1259. https://doi.org/10.1016/j.cemconres.2008.04.002

[25] Yu QL, Spiesz P, Brouwers HJH. Development of cement-based lightweight composites - Part 1: Mix design methodology and hardened properties. Cement and Concrete Composites, 2013; p. 17 – 29. https://doi.org/10.1016/j.cemconcomp.2013.03.030

[26] Ojha PN, Mittal P, Singh A, Singh B, Arora VV. Optimization and evaluation of ultra-high-performance concrete. Journal of Asian Concrete Federation, vol. 6, no. 1. Asian

Concrete Federation, pp. 26-36, Jun. 30, 2020. https://doi.org/10.18702/acf.2020.6.6.1.26

[27] Singh B, Patel V, Ojha PN, Arora VV. Analysis of stress block parameters for high strength concrete. Journal of Asian Concrete Federation, vol. 6, no. 1. Asian Concrete Federation, pp. 1-9, Jun. 30, 2020. https://doi.org/10.18702/acf.2020.6.6.1

[28] Singh B, Arora VV, Patel V. Experimental study on stress strain behaviour of normal and high strength unconfined concrete. Indian Concrete Journal, 2020; 94:4 10-19.

[29] Singh B, Arora VV, Patel V. Study on stress strain characteristics of high strength concrete. Indian Concrete Journal 2018; 92:6 37-43.

[30] Arora VV, Singh B, Durability Studies on Prestressed Concrete made with Portland Pozzolana Cement, Indian Concrete Journal, 2016; 90:8, 41-48.

[31] Ojha PN, Trivedi A, Singh B, S AKN, Patel V, Gupta RK. High performance fiber reinforced concrete - for repair in spillways of concrete dams. Research on Engineering Structures and Materials, 2021. https://doi.org/10.17515/resm2021.252ma0128

[32] Singh B, Ojha PN, Trivedi A, Patel V, Arora VV. Development Of Empirical Equations For Prediction Of Flexural And Split Tensile Strength For Normal And High Strength Concrete With Granite And Calc-Granulite Aggregate, Indian Concrete Journal, November 2021; 95:11 36-46.

[33] Ojha PN, Singh B, Singh A, Patel V, Arora VV. Experimental study on creep and shrinkage behaviour of high strength concrete for application in high rise buildings. Indian Concrete Journal, 2021; 95:2 30-42.

[34] Arora VV, Singh B, Patel V, Daniel Y, Mohapatra BN. Stress-Strain Behaviour and Performance Evaluation of High Strength Steel Fibre Reinforced Concrete. Indian Concrete Journal, 2019; 93:12 54-61.

[35] Arora VV, Singh B, Patel V, Trivedi A. Evaluation of modulus of elasticity for normal and high strength concrete with granite and calc-granulite aggregate," Structural Concrete, vol. 22, no. S1, Jan. 2021 https://doi.org/10.1002/suco.202000023

[36] Ojha PN, Singh B, Kaura P, Singh A. Lightweight geopolymer fly ash sand: an alternative to fine aggregate for concrete production. Research on Engineering Structures and Materials, 2021 https://doi.org/10.17515/resm2021.257ma0205

Supplementary Material

Table 1. Strain at peak stress/ultimate strain for the specimens tested

Individual			Average		
Strength	LVDT	compressometer	Strength	LVDT	compressometer
95.53	3013	2510			
97.29	3509	2926			
98.83	3455	2792			
105.86	3398	2187	103.8	3345.4	2637.4
107.22	3368	3104			
108.1	3553	2786			
108.39	3179	2488			
109.26	3288	2306			
111.45	2936	2165			
112.27	3039	2906			
112.85	2802	2200			
113.49	3240	2883			
117.94	2909	2695			
118.77	2884	2540	117.2	3057.4	2634.8
120.02	3478	2825			
120.15	3152	2533			
120.84	3030	2965			
120.85	3009	2453			
120.91	3152	2818			
121.39	3699	3005			
122.4	3385	3224			
123.2	3225	2638			
123.43	3270	3030			
123.46	3410	2492			
123.98	3450	3309	124.9	3290.5	2823.5
124.66	3064	3135			
127.24	3042	2677			
127.43	3378	1841			
127.75	2853	2766			
129.02	3420	2942			
130.04	3207	2862			
131.43	3416	2914	133.1	3372.0	2976.3
137.84	3493	3153			

Table 2. Stress-block Parameters (IS code)

Cyd str	Cube/ Cyd	Cube Str	Ec	Ecu	r_1	r_2	k_1	S_1	k_3	Ymc	K	k_2
95.53	1.10	105.08	2510	2510	1.00	0.00	0.50	0.91	0.77	1.5	0.26	0.33
97.29	1.10	107.02	2926	2926	1.00	0.00	0.50	0.91	0.77	1.5	0.26	0.33
98.83	1.10	108.71	2792	2792	1.00	0.00	0.50	0.91	0.77	1.5	0.26	0.33
105.86	1.10	116.45	2187	2187	1.00	0.00	0.50	0.91	0.77	1.5	0.26	0.33
107.22	1.10	117.94	3104	3104	1.00	0.00	0.50	0.91	0.77	1.5	0.26	0.33
108.1	1.10	118.91	2786	2786	1.00	0.00	0.50	0.91	0.77	1.5	0.26	0.33
108.39	1.10	119.23	2488	2488	1.00	0.00	0.50	0.91	0.77	1.5	0.26	0.33
109.26	1.10	120.19	2306	2306	1.00	0.00	0.50	0.91	0.77	1.5	0.26	0.33
111.45	1.10	122.60	2165	2165	1.00	0.00	0.50	0.91	0.77	1.5	0.26	0.33
112.27	1.10	123.50	2906	2906	1.00	0.00	0.50	0.91	0.77	1.5	0.26	0.33
112.85	1.10	124.14	2200	2200	1.00	0.00	0.50	0.91	0.77	1.5	0.26	0.33
113.49	1.10	124.84	2883	2883	1.00	0.00	0.50	0.91	0.77	1.5	0.26	0.33
117.94	1.10	129.73	2695	2695	1.00	0.00	0.50	0.91	0.77	1.5	0.26	0.33
118.77	1.10	130.65	2540	2540	1.00	0.00	0.50	0.91	0.77	1.5	0.26	0.33
120.02	1.10	132.02	2825	2825	1.00	0.00	0.50	0.91	0.77	1.5	0.26	0.33
120.15	1.10	132.17	2533	2533	1.00	0.00	0.50	0.91	0.77	1.5	0.26	0.33
120.84	1.10	132.92	2965	2965	1.00	0.00	0.50	0.91	0.77	1.5	0.26	0.33
120.85	1.10	132.94	2453	2453	1.00	0.00	0.50	0.91	0.77	1.5	0.26	0.33
120.91	1.10	133.00	2818	2818	1.00	0.00	0.50	0.91	0.77	1.5	0.26	0.33
121.39	1.10	133.53	3005	3005	1.00	0.00	0.50	0.91	0.77	1.5	0.26	0.33
122.4	1.10	134.64	3224	3224	1.00	0.00	0.50	0.91	0.77	1.5	0.26	0.33
123.2	1.10	135.52	2638	2638	1.00	0.00	0.50	0.91	0.77	1.5	0.26	0.33
123.43	1.10	135.77	3030	3030	1.00	0.00	0.50	0.91	0.77	1.5	0.26	0.33
123.46	1.10	135.81	2492	2492	1.00	0.00	0.50	0.91	0.77	1.5	0.26	0.33
123.98	1.10	136.38	3309	3309	1.00	0.00	0.50	0.91	0.77	1.5	0.26	0.33
124.66	1.10	137.13	3135	3135	1.00	0.00	0.50	0.91	0.77	1.5	0.26	0.33
127.24	1.10	139.96	2677	2677	1.00	0.00	0.50	0.91	0.77	1.5	0.26	0.33
127.43	1.10	140.17	1841	1841	1.00	0.00	0.50	0.91	0.77	1.5	0.26	0.33
127.75	1.10	140.53	2766	2766	1.00	0.00	0.50	0.91	0.77	1.5	0.26	0.33
129.02	1.10	141.92	2942	2942	1.00	0.00	0.50	0.91	0.77	1.5	0.26	0.33
130.04	1.10	143.04	2862	2862	1.00	0.00	0.50	0.91	0.77	1.5	0.26	0.33
131.43	1.10	144.57	2914	2914	1.00	0.00	0.50	0.91	0.77	1.5	0.26	0.33
137.84	1.10	151.62	3153	3153	1.00	0.00	0.50	0.91	0.77	1.5	0.26	0.33

Table 3. Stress-block Parameters (Eurocode)

Cyd str	Cube/Cyd	Cube Str	Ec	Ecu	λ	η	αcc	S1	Ycc	K'(EC)	k2
95.53	1.10	105.08	2510	2510	0.70	0.80	0.85	0.91	1.5	0.29	0.35
97.29	1.10	107.02	2926	2926	0.70	0.80	0.85	0.91	1.5	0.29	0.35
98.83	1.10	108.71	2792	2792	0.70	0.80	0.85	0.91	1.5	0.29	0.35
105.86	1.10	116.45	2187	2187	0.70	0.80	0.85	0.91	1.5	0.29	0.35
107.22	1.10	117.94	3104	3104	0.70	0.80	0.85	0.91	1.5	0.29	0.35
108.1	1.10	118.91	2786	2786	0.70	0.80	0.85	0.91	1.5	0.29	0.35
108.39	1.10	119.23	2488	2488	0.70	0.80	0.85	0.91	1.5	0.29	0.35
109.26	1.10	120.19	2306	2306	0.70	0.80	0.85	0.91	1.5	0.29	0.35
111.45	1.10	122.60	2165	2165	0.70	0.80	0.85	0.91	1.5	0.29	0.35
112.27	1.10	123.50	2906	2906	0.70	0.80	0.85	0.91	1.5	0.29	0.35
112.85	1.10	124.14	2200	2200	0.70	0.80	0.85	0.91	1.5	0.29	0.35
113.49	1.10	124.84	2883	2883	0.70	0.80	0.85	0.91	1.5	0.29	0.35
117.94	1.10	129.73	2695	2695	0.70	0.80	0.85	0.91	1.5	0.29	0.35
118.77	1.10	130.65	2540	2540	0.70	0.80	0.85	0.91	1.5	0.29	0.35
120.02	1.10	132.02	2825	2825	0.70	0.80	0.85	0.91	1.5	0.29	0.35
120.15	1.10	132.17	2533	2533	0.70	0.80	0.85	0.91	1.5	0.29	0.35
120.84	1.10	132.92	2965	2965	0.70	0.80	0.85	0.91	1.5	0.29	0.35
120.85	1.10	132.94	2453	2453	0.70	0.80	0.85	0.91	1.5	0.29	0.35
120.91	1.10	133.00	2818	2818	0.70	0.80	0.85	0.91	1.5	0.29	0.35
121.39	1.10	133.53	3005	3005	0.70	0.80	0.85	0.91	1.5	0.29	0.35
122.4	1.10	134.64	3224	3224	0.70	0.80	0.85	0.91	1.5	0.29	0.35
123.2	1.10	135.52	2638	2638	0.70	0.80	0.85	0.91	1.5	0.29	0.35
123.43	1.10	135.77	3030	3030	0.70	0.80	0.85	0.91	1.5	0.29	0.35
123.46	1.10	135.81	2492	2492	0.70	0.80	0.85	0.91	1.5	0.29	0.35
123.98	1.10	136.38	3309	3309	0.70	0.80	0.85	0.91	1.5	0.29	0.35
124.66	1.10	137.13	3135	3135	0.70	0.80	0.85	0.91	1.5	0.29	0.35
127.24	1.10	139.96	2677	2677	0.70	0.80	0.85	0.91	1.5	0.29	0.35
127.43	1.10	140.17	1841	1841	0.70	0.80	0.85	0.91	1.5	0.29	0.35
127.75	1.10	140.53	2766	2766	0.70	0.80	0.85	0.91	1.5	0.29	0.35
129.02	1.10	141.92	2942	2942	0.70	0.80	0.85	0.91	1.5	0.29	0.35
130.04	1.10	143.04	2862	2862	0.70	0.80	0.85	0.91	1.5	0.29	0.35
131.43	1.10	144.57	2914	2914	0.70	0.80	0.85	0.91	1.5	0.29	0.35
137.84	1.10	151.62	3153	3153	0.70	0.80	0.85	0.91	1.5	0.29	0.35

Table 4. Moment Capacity (IS code)

Cyd str	Cube/Cyd	Cube Str	Ec	Ecu	Esu	K	k_2	Xu(max)/d	Moment
95.53	1.10	105.08	2510.00	2510.00	4175.00	0.26	0.33	0.38	236.90
97.29	1.10	107.02	2926.00	2926.00	4175.00	0.26	0.33	0.41	261.08
98.83	1.10	108.71	2792.00	2792.00	4175.00	0.26	0.33	0.40	259.06
105.86	1.10	116.45	2187.00	2187.00	4175.00	0.26	0.33	0.34	243.25
107.22	1.10	117.94	3104.00	3104.00	4175.00	0.26	0.33	0.43	296.11
108.10	1.10	118.91	2786.00	2786.00	4175.00	0.26	0.33	0.40	283.05
108.39	1.10	119.23	2488.00	2488.00	4175.00	0.26	0.33	0.37	267.52
109.26	1.10	120.19	2306.00	2306.00	4175.00	0.26	0.33	0.36	258.68
111.45	1.10	122.60	2165.00	2165.00	4175.00	0.26	0.33	0.34	254.61
112.27	1.10	123.50	2906.00	2906.00	4175.00	0.26	0.33	0.41	300.26
112.85	1.10	124.14	2200.00	2200.00	4175.00	0.26	0.33	0.35	260.19
113.49	1.10	124.84	2883.00	2883.00	4175.00	0.26	0.33	0.41	302.32
117.94	1.10	129.73	2695.00	2695.00	4175.00	0.26	0.33	0.39	303.61
118.77	1.10	130.65	2540.00	2540.00	4175.00	0.26	0.33	0.38	296.40
120.02	1.10	132.02	2825.00	2825.00	4175.00	0.26	0.33	0.40	316.48
120.15	1.10	132.17	2533.00	2533.00	4175.00	0.26	0.33	0.38	299.40
120.84	1.10	132.92	2965.00	2965.00	4175.00	0.26	0.33	0.42	326.40
120.85	1.10	132.94	2453.00	2453.00	4175.00	0.26	0.33	0.37	296.00
120.91	1.10	133.00	2818.00	2818.00	4175.00	0.26	0.33	0.40	318.43
121.39	1.10	133.53	3005.00	3005.00	4175.00	0.26	0.33	0.42	330.04
122.40	1.10	134.64	3224.00	3224.00	4175.00	0.26	0.33	0.44	344.16
123.20	1.10	135.52	2638.00	2638.00	4175.00	0.26	0.33	0.39	313.65
123.43	1.10	135.77	3030.00	3030.00	4175.00	0.26	0.33	0.42	336.94
123.46	1.10	135.81	2492.00	2492.00	4175.00	0.26	0.33	0.37	304.98
123.98	1.10	136.38	3309.00	3309.00	4175.00	0.26	0.33	0.44	352.84
124.66	1.10	137.13	3135.00	3135.00	4175.00	0.26	0.33	0.43	345.91
127.24	1.10	139.96	2677.00	2677.00	4175.00	0.26	0.33	0.39	326.42
127.43	1.10	140.17	1841.00	1841.00	4175.00	0.26	0.33	0.31	264.37
127.75	1.10	140.53	2766.00	2766.00	4175.00	0.26	0.33	0.40	333.28
129.02	1.10	141.92	2942.00	2942.00	4175.00	0.26	0.33	0.41	347.16
130.04	1.10	143.04	2862.00	2862.00	4175.00	0.26	0.33	0.41	345.15
131.43	1.10	144.57	2914.00	2914.00	4175.00	0.26	0.33	0.41	351.98
137.84	1.10	151.62	3153.00	3153.00	4175.00	0.26	0.33	0.43	383.53

Table 5. Moment Capacity (Eurocode)

Cyd str	Cube/Cyd	Cube Str	Ec	Ecu	k_4	K'(EC)	$\lambda/2$	Xu(max)/d	Moment
95.53	1.10	105.08	2510.00	2510.00	1.45	0.29	0.35	0.32	228.18
97.29	1.10	107.02	2926.00	2926.00	1.35	0.29	0.35	0.34	247.17
98.83	1.10	108.71	2792.00	2792.00	1.38	0.29	0.35	0.33	246.55
105.86	1.10	116.45	2187.00	2187.00	1.55	0.29	0.35	0.30	238.02
107.22	1.10	117.94	3104.00	3104.00	1.31	0.29	0.35	0.35	278.52
108.10	1.10	118.91	2786.00	2786.00	1.38	0.29	0.35	0.33	269.44
108.39	1.10	119.23	2488.00	2488.00	1.45	0.29	0.35	0.32	257.94
109.26	1.10	120.19	2306.00	2306.00	1.51	0.29	0.35	0.30	251.59
111.45	1.10	122.60	2165.00	2165.00	1.56	0.29	0.35	0.30	249.43
112.27	1.10	123.50	2906.00	2906.00	1.35	0.29	0.35	0.34	284.48
112.85	1.10	124.14	2200.00	2200.00	1.55	0.29	0.35	0.30	254.42
113.49	1.10	124.84	2883.00	2883.00	1.36	0.29	0.35	0.34	286.69
117.94	1.10	129.73	2695.00	2695.00	1.40	0.29	0.35	0.33	290.10
118.77	1.10	130.65	2540.00	2540.00	1.44	0.29	0.35	0.32	285.11
120.02	1.10	132.02	2825.00	2825.00	1.37	0.29	0.35	0.34	300.80
120.15	1.10	132.17	2533.00	2533.00	1.44	0.29	0.35	0.32	288.09
120.84	1.10	132.92	2965.00	2965.00	1.34	0.29	0.35	0.34	308.56
120.85	1.10	132.94	2453.00	2453.00	1.46	0.29	0.35	0.31	285.86
120.91	1.10	133.00	2818.00	2818.00	1.37	0.29	0.35	0.34	302.73
121.39	1.10	133.53	3005.00	3005.00	1.33	0.29	0.35	0.35	311.54
122.40	1.10	134.64	3224.00	3224.00	1.29	0.29	0.35	0.36	322.39
123.20	1.10	135.52	2638.00	2638.00	1.41	0.29	0.35	0.33	300.41
123.43	1.10	135.77	3030.00	3030.00	1.33	0.29	0.35	0.35	317.77
123.46	1.10	135.81	2492.00	2492.00	1.45	0.29	0.35	0.32	294.00
123.98	1.10	136.38	3309.00	3309.00	1.28	0.29	0.35	0.36	329.60
124.66	1.10	137.13	3135.00	3135.00	1.31	0.29	0.35	0.35	325.01
127.24	1.10	139.96	2677.00	2677.00	1.40	0.29	0.35	0.33	312.12
127.43	1.10	140.17	1841.00	1841.00	1.70	0.29	0.35	0.27	263.86
127.75	1.10	140.53	2766.00	2766.00	1.38	0.29	0.35	0.33	317.51
129.02	1.10	141.92	2942.00	2942.00	1.34	0.29	0.35	0.34	328.47
130.04	1.10	143.04	2862.00	2862.00	1.36	0.29	0.35	0.34	327.57
131.43	1.10	144.57	2914.00	2914.00	1.35	0.29	0.35	0.34	333.38
137.84	1.10	151.62	3153.00	3153.00	1.31	0.29	0.35	0.35	360.13

Technical Note

Influence of B₄C particle size on the mechanical behavior of A356 aluminium composites

Zeeshan Ali[1,a], V Muthuraman[2,b], P Rathnakumar[1,c], P Gurusamy[3,d], Madeva Nagaral[4,e]

[1]*Department of Mechanical Engineering, Navodaya Institute of Technology, Raichur, Karnataka, India*
[2]*Vels Institute of Science, Technology and Advanced Studies, Chennai, India*
[3]*Department of Mechanical Engineering, Chennai Institute of Technology, Chennai, India*
[4]*Aircraft Research and Design Centre, HAL, Bengaluru, Karnataka, India*

Article Info	Abstract
	The influence of adding B₄C particulates with a 40 and 90 μm sizes on the compressive strength, tensile strength and impact toughness of the A356 alloy is being studied. In the Al alloy matrix, 40 and 90 μm -sized micro B₄C particulates are employed as reinforcements. In the A356 alloy, composites are created utilizing the liquid melt process in increments of 3 and 6 weight percent. Using an energy dispersive spectroscope (EDS) and a scanning electron microscope (SEM), samples are examined for microstructural characterization. According to ASTM standards, mechanical characteristics including tensile, hardness, compression, and toughness are assessed. The consistent distribution of B4C particles in the A356 alloy is seen in SEM micrographs, and this is supported by EDS analysis. Additionally, the inclusion of B₄C reinforcement improves the compression and impact strength of the base matrix A356 alloy, which is especially noticeable in the case of reinforced composites that are 6 wt. % of 40 μm B₄C in size.

1. Introduction

Due to its beneficial qualities, such as light weight, corrosion resistance, high stiffness, and cost efficiency when compared to currently utilized metals, aluminum is extensively employed in aerospace, automotive, and structural applications. Aluminum has a density that is around one-third that of iron and copper, and its corrosion resistance negates the need for protective coatings. Recent growth in research suggests that there is still more room for advancement in the use of aluminum. Utilizing aluminum with increased characteristics will satisfy both economic and environmental needs [1].

Aluminum metal matrix composites (AMMC) may be treated in a number of ways, including liquid metallurgy, solid metallurgy, in situ procedures, etc. However, liquid metallurgy is preferred owing to its cheap cost, ease of processing, and superior characteristics. The primary issue with processing AMMC is the wettability of the ceramic particles, which may be solved by coating the reinforcement, which is one of the methods to improve wettability [2]. Ti coating has shown superior results for improving the wettability of B₄C. By creating a thin coating of Ti around the B₄C particles, the K₂TiF₆ halide salt, which is evenly mixed with B₄C during casting, has improved the bonding between Al and B₄C and the mechanical characteristics of the material. Aluminum is combined with B₄C and graphite using a mechanical stirrer. The homogenous dispersion of particles in the metal matrix is facilitated by the use of a mechanical stirrer and

*Corresponding author: madev.nagaral@gmail.com
[a] orcid.org/0000-0002-7439-6656; [b] orcid.org/0000-0001-9891-0165; [c] orcid.org/0000-0003-2768-4601;
[d] orcid.org/0000-0003-1641-9415; [e] orcid.org/0000-0002-8248-7603

vigorous stirring. In liquid metallurgy, reinforcing particles are added in two steps, assisting with homogenous distribution and preventing particulate aggregation [3].

In general, aluminum-based MMCs provide a significant improvement in elasticity modulus, strength, and wear resistance compared to unreinforced alloys. The reinforcing particle size, shape, and volume fraction, the matrix material, and the response at the interface all have an impact on the properties of composites. Hard ceramic particles such as SiO_2, SiC, Al_2O_3, TiB_2, B_4C, etc. may be added to the Al matrix to reinforce it and increase its characteristics [4]. Al_2O_3 and SiC ceramic particles are the most often utilized materials for aluminum reinforcement. Due to its great hardness it is the third hardest substance after diamond and boron nitride boron carbide (B_4C) might be used as a replacement to silica and aluminum oxide [5]. High strength, low density, exceptionally high hardness, strong wear resistance, and good chemical stability are some of B_4C's appealing qualities. As a result, B_4C particle reinforcement of aluminum results in increased specific strength, elastic modulus, wear resistance, and thermal stability [6].

According to the literature review, SiC and Al_2O_3 particle reinforcements are the focus of the majority of investigations on aluminum-based MMCs. TiC particulate reinforcement of aluminum matrix is, however, comparatively underutilized. Despite the fact that powder metallurgy gives MMCs higher mechanical characteristics, liquid state processing offers certain significant benefits. Better matrix-particle bonding, simpler matrix structure management, cheap processing costs, closer net form, and a broad range of material options are a few of them. There are two techniques for manufacturing MMCs in a liquid state, and they are both dependent on the temperature at which the particles are added to the melt. The vortex is utilized to introduce reinforcement particles in both processes. Micro-particles are particularly cost-effective due to their cheap cost and simplicity of dispersion during manufacturing.

Stir casting is considered as the most effective and cost-effective technique out of all of them. However, this technique has always resulted in a large number of structural flaws in composite materials. Some significant structural flaws of stir cast composites include poor wettability, uneven distribution of reinforcement particles, segregation and agglomeration of reinforcement [7]. The compressive and impact characteristics of the A356 reinforced with micron B_4C particles MMC's manufactured by stir casting technique, however, are little understood. Aluminum-boron carbide composites are crucial, particularly in the aerospace industry, where there is a growing need for lightweight materials. The development of A356 micron B_4C composites with different particle sizes and weight percentages of B_4C particulates is suggested in light of the aforementioned findings.

In this work, the mechanical characteristics of A356 alloy-based composites containing 40 and 90 μm sized B_4C particles were examined utilizing the liquid metallurgical process at different weight percentages (3 and 6 wt. % B_4C). Based on the literature, smaller particles create agglomeration in the prepared composites, whereas larger particle addition creates de-bonding particles from the matrix. Hence, an attempt was made to develop an A356 alloy with varying boron carbide particle-reinforced composites and investigate the effect of the optimum reinforcing particle size on the mechanical properties of the composites.

2. Experimental Details

By using liquid metallurgy, metal matrix composites with 3 and 6 wt. % of B_4C particles and size of 40 and 90 μm are created. A356 alloy is employed as the matrix material and B_4C particles with an average size of 40 μm are used as reinforcements in the fabrication

of MMCs. Table 1 is showing chemical composition of A356 alloy and Table 2 is representing chemistry of B_4C particles.
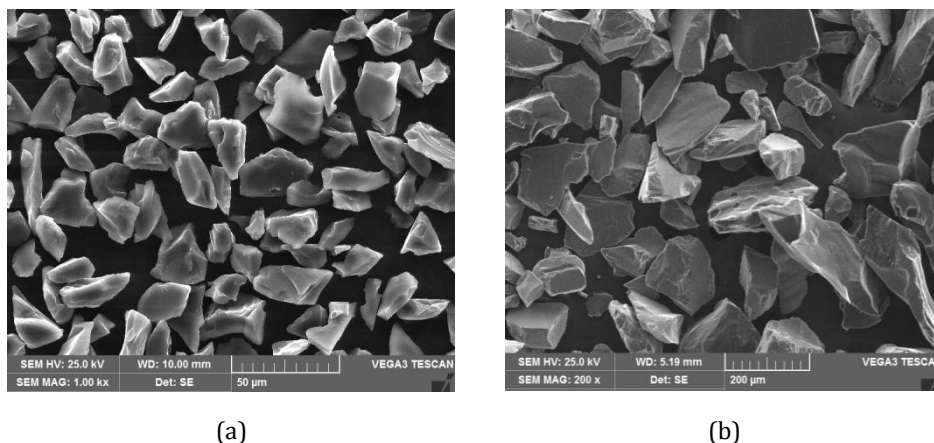

(a)   (b)

Fig.1 SEM images of (a) 40 µm B_4C (b) 90 µm B_4C particles

Table 1. Chemical Composition of A356 Alloy

Element	Symbol	Wt %
Silicon	Si	6.98
Magnesium	Mg	0.35
Iron	Fe	0.10
Titanium	Ti	0.15
Copper	Cu	0.01
Nickel	Ni	0.013
Zinc	Zn	<0.015
Tin	Sn	<0.005
Manganese	Mn	<0.005
Aluminum	Al	Balance

Table 2. Chemical composition of B_4C

Total Boron	Total Carbon	Total Iron	Total Boron + Carbon
77.5%	21.5%	0.2%	99.8%

2.1. Preparation of Composites

A356 alloy with 40 and 90 micron sized B_4C particles reinforced composites were created using the liquid metallurgical approach. An A356 alloy ingots were charged into the furnace by taking calculated quantity to melt. A356 alloy has a 660°C melting temperature. The maximum melting temperature of 750°C was used to melt the A356 alloy. A chromel-alumel thermocouple was used to measure the temperature. Hexachloroethane (C_2Cl_6) in solid form was then used to degas the liquid metal o remove the unwanted gases from the molten metal. The molten metal was stirred to form a vortex using a zirconium-coated stainless-steel impeller. The impeller was immersed 60 % below the height of the molten metal from the melt's surface and the stirrer rotates at a speed of 300 rpm. The pre-heated B_4C particles were added to the vortex. The A356 alloy with 3 weight percentage of B_4C composites were then placed into a permanent cast

iron mould with dimensions of 120 mm in length and 15 mm in diameter [8]. Similarly, A356 alloy with 6 wt. % of boron carbide particles reinforced composites were synthesized in the similar way. Further, based on the microstructural analysis, the tensile strength, hardness, compressive strength and impact toughness of the A356 alloy of 40 and 90 μm sized B_4C reinforced composites were evaluated and compared with the as-cast A356 alloy. Figure 2 shows cast aluminum specimen.

Fig. 2 Cast aluminum specimen

2.2. Testing of Composites

The microstructural specimens were polished using 220 to 1000 grit emery sheets before being subjected to diamond paste polishing and microstructural examination by SEM and EDS [9]. The specimens were etched with Keller's reagent. According to ASTM E10 standard, the hardness test was performed using Brinell hardness testing equipment. ASTM E8 and E9 standards were used to conduct the tensile and compression tests. According to ASTM E23 standard, the Charpy impact test was performed using an impact test machine.

3. Results and Discussion

3.1. Microstructural Study

The microstructure of the cast A356 aluminum alloy is seen in Fig. 3(a). A356 composites with 40 and 90 μm sized particles of 3% and 6% wt.% B_4C content are shown in Fig. 3(b-e). As shown in figures, the SEM micrographs show a very equal distribution of B_4C particles throughout the matrices (Fig. 3b-e). The porosity of the MMC is decreased by uniformly dispersed particles, which also improve overall strength and other qualities. From the micrographs it is revealed that the boron carbide particles distributed uniformly in the matrix material. The bonding between the A356 alloy and boron carbide particles is strong and helps in enhancing the properties.

Energy dispersive spectrographs (EDS) of the cast A356 aluminum alloy is seen in Fig. 4 (a) A356-3 wt.% of 40 and 90 μm sized B_4C particulates reinforced composites, and A356-6 wt. % of 40 and 90 μm sized B_4C particulates reinforced composites are shown in Fig. 4 (b-e). The B (Boron) and C (Carbon) components in the composites help to identify the presence of B_4C particles.

(a)

(b)

(c)

(d)

(e)
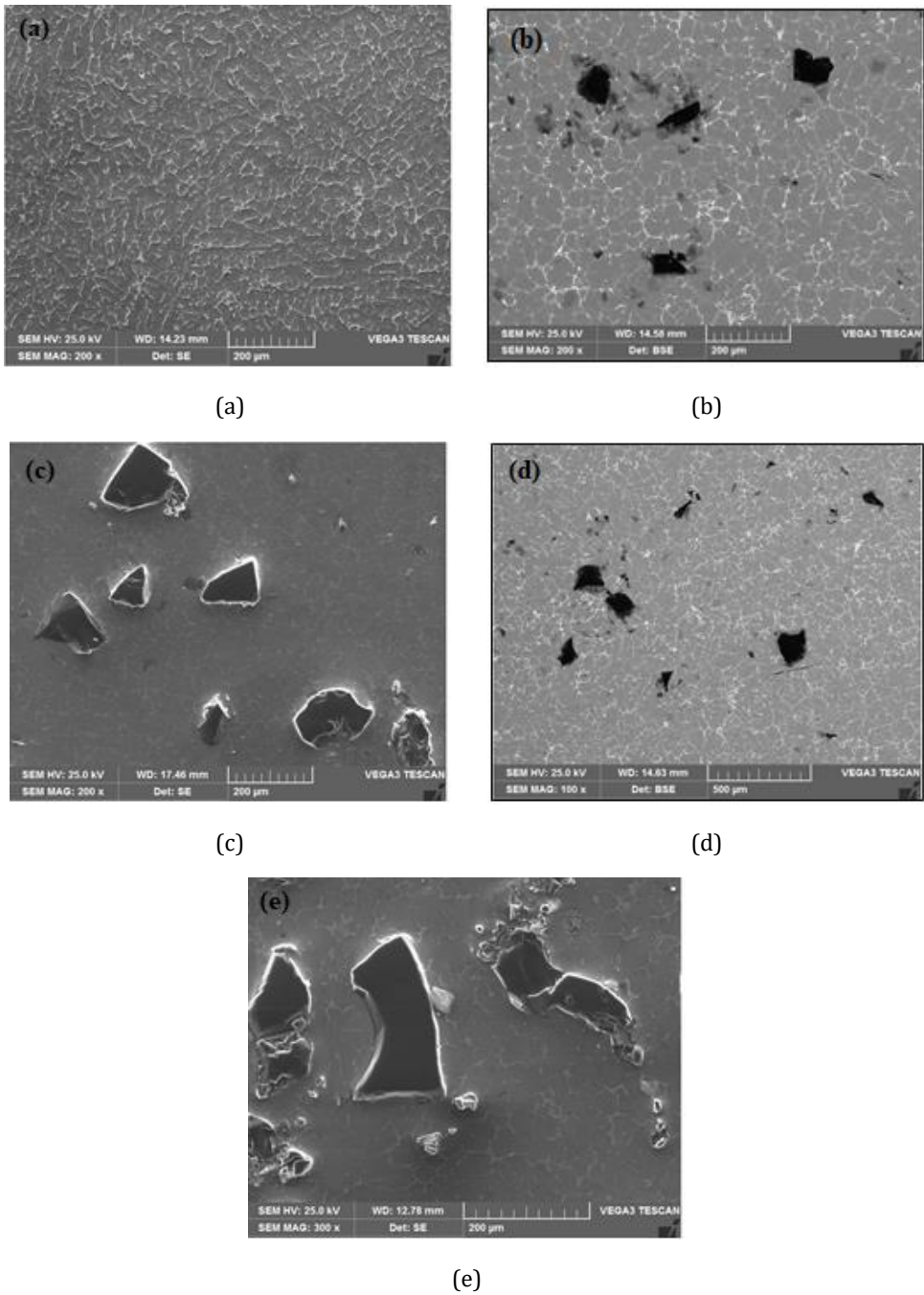
Fig. 3 SEM image of a) A356 alloy b) 3 wt.% 40μm B$_4$C c) 3 wt.% 90μm B$_4$C d) 6 wt.% 40μm B$_4$C e) 6 wt.% 90μm B$_4$C
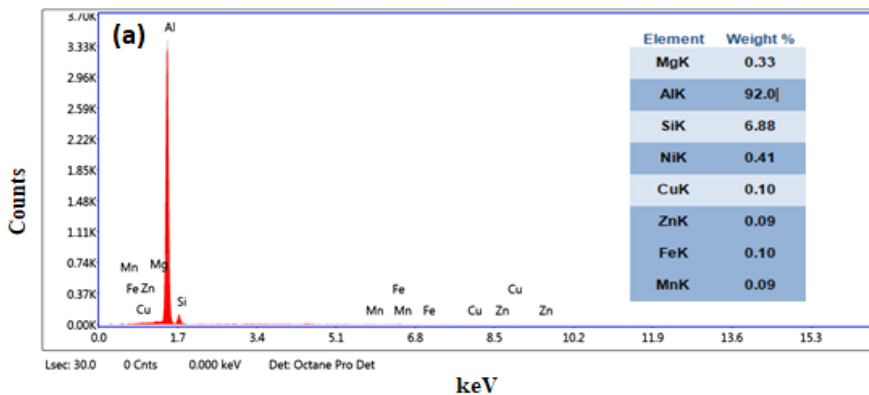
(a)
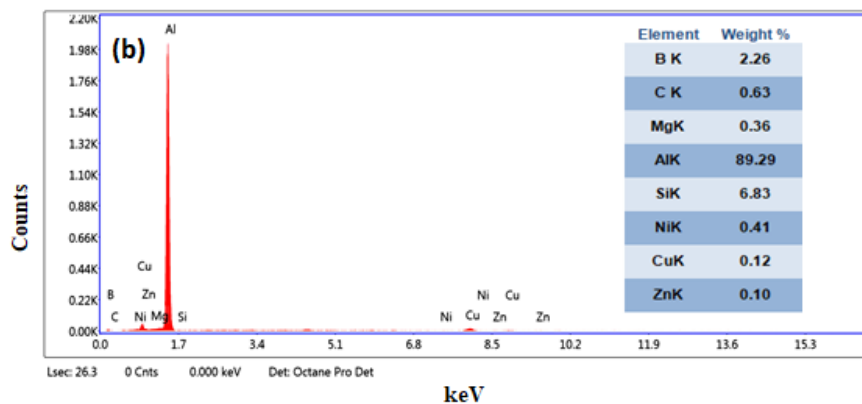
(b)
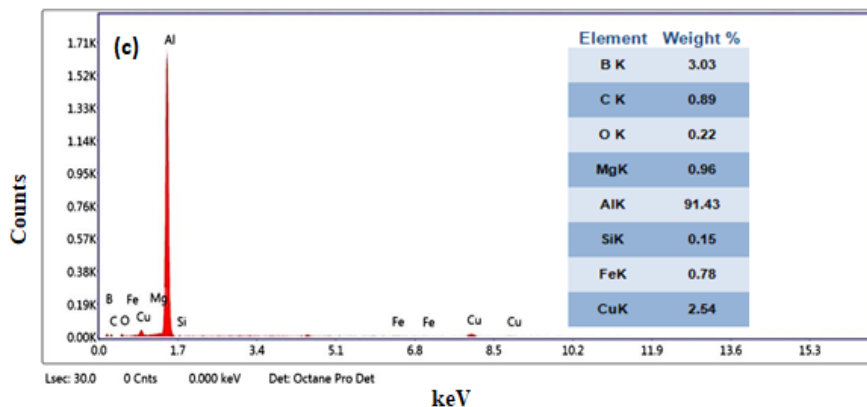
(c)
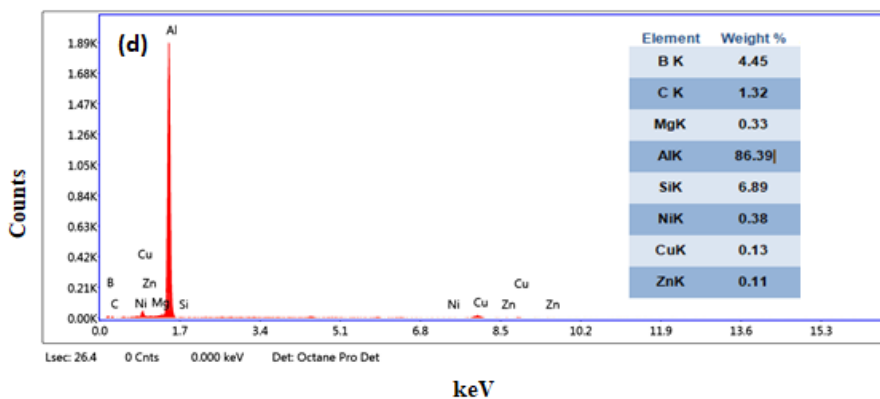
(d)
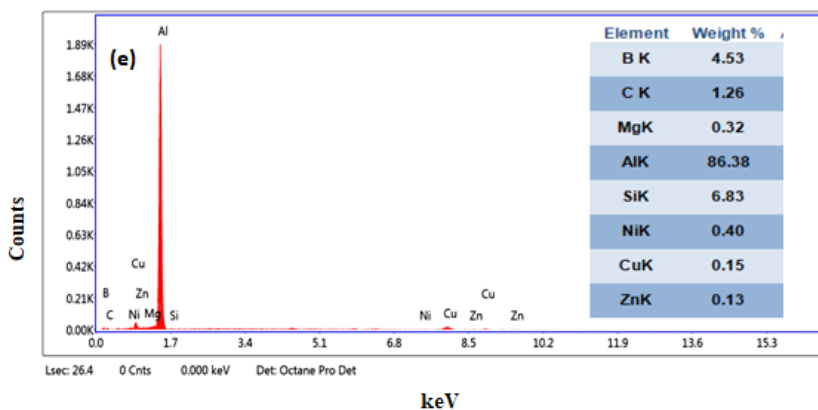
(e)

Fig. 4 SEM image of a) A356 alloy b) 3 wt.% 40µm B_4C c) 3 wt.% 90µm B_4C d) 6 wt.% 40µm B_4C e) 6 wt.% 90µm B_4C

3.2. Tensile Properties

To analyze tensile parameters such as ultimate tensile strength and yield strength, the tensile behavior of all the composite sample preparations is determined. The computerized universal testing apparatus received the specimens by hydraulic loading. The weights that caused the specimen to break and reach the yield point were noted. Fig. 5, 6 and Table 3 depicts how adding B_4C particles of 40 and 90 µm in size affected the samples' ultimate tensile strength and yield strength. In a nutshell, both direct and indirect strengthening plays a significant role in the strengthening [10]. With the addition of 6 wt. % 40 and 90 µm size B_4C, the ultimate tensile strength and yield strength both exhibit an improvement. This improvement is mostly attributable to an increase in dislocation density and their accumulation behind the uniformly dispersed B_4C. The changes in the matrix microstructure brought on by the presence of reinforcement particles lead to indirect strengthening. The mismatch in the coefficient of thermal expansion between B_4C and A356 alloy causes an increase in dislocation density in the A356- B_4C composites, which leads to indirect strengthening [11]. As the weight

percentage of B₄C rises, so does the density of these thermally generated dislocations, increasing the indirect strengthening contribution as well. On the other hand, work hardening behavior seems to be the cause of this progressive improvement.

Table 3. Tensile properties of A356 alloy and its B₄C composites with standard deviation

Material Composition	B₄C Particle Size (micron)	Ultimate Tensile Strength (MPa)	Yield Strength (MPa)
A356 Alloy	--	162.5 ± 0.95	126.4 ± 1.11
A356 – 3 wt. % B₄C	40	183.2 ± 0.75	151.4 ± 1.02
A356 – 6 wt. % B₄C		206.4 ± 1.10	182.0 ± 0.72
A356 – 3 wt. % B₄C	90	179.2 ± 1.01	148.2 ± 1.15
A356 – 6 wt. % B₄C		198.4 ± 1.07	168.7 ± 0.76

± - SD (Standard Deviation)
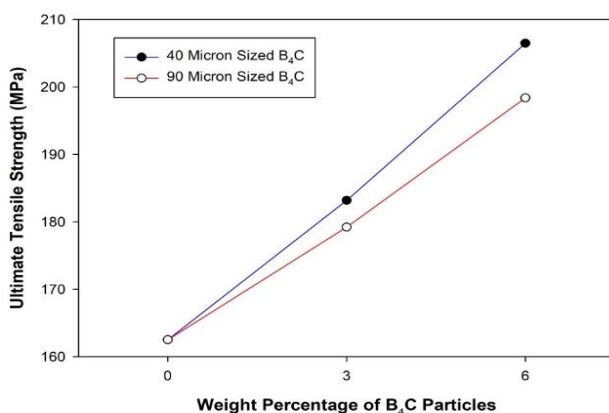
Fig. 5 Ultimate tensile strength of A356 with B₄C composites

In composite materials, the presence of a larger weight percentage of B₄C boosted the strengthening effect and load absorption. When compared to the unreinforced A356 alloy, the aluminum alloy containing reinforcement particles such boron carbide reinforcement supplied the highest tensile strength, according to earlier study findings [12]. Particle reinforcement increased strength and provided greater resilience to tensile stresses. The highest tensile strength of composites is provided through load transmission from the matrix to the reinforcing particles.

If an applied stress at which considerable internal damage (particle fracture and/or interfacial failure) occurs is taken into account, the impact of reinforcement as a function of matrix yield stress and tensile strength may be somewhat rationalized. The distribution of residual tension and the size of the particles are two important variables that will affect this stress. The impact of particle size is significant since the average fracture stress of the B₄C particles decreases as particle size rises. Therefore, in composites reinforced with big particles, particle breakage will occur at lower applied stress levels and therefore, will be reduced. Additionally, the overall interfacial area will shrink as particle size rises. Particle size is unlikely to have a significant impact on the interfacial strength. Therefore, when the particle size rises, the percentage of particle damage caused by particle breakage is anticipated to rise.

The uniformity of the particle dispersion may have an impact on the tensile characteristics of these materials. These have been shown to be quite homogenous in the current situation (Fig. 3b-e), and it is thought that they will not significantly affect the trends of the current work. The presence of any clusters, however, may impair strength and ductility by causing localized damage. Such clusters might be seen in this context as areas of potential harm that exist before loading. It should be emphasized that composites reinforced with small particulates, which seem to have more strength and ductility than materials containing coarse particles, are often more prone to have any such clustering. It is obvious that any such zones of clustering must be minimized if optimal performance is sought, particularly for the tiny particle reinforced composites.
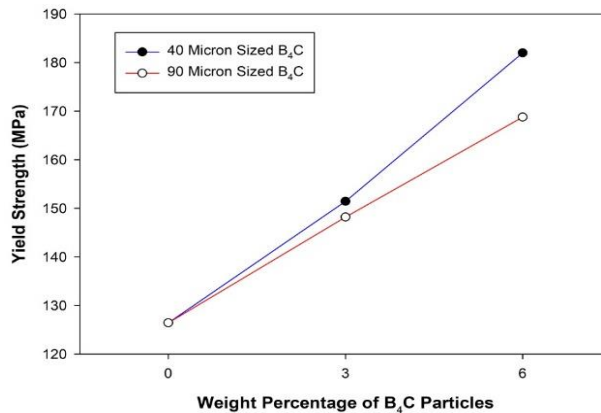
Fig. 6 Yield strength of A356 with B_4C composites

3.3. Hardness Measurements

Brinell hardness tester was used to measure the composites' hardness. Test specimens were carved out of each composite composition and polished before testing in order to achieve a flat and smooth surface finish. Brinell hardness is assessed by pressing a hard steel or carbide sphere with a certain diameter into a material's surface under a predetermined force for a predetermined amount of time, then measuring the diameter of the indentation that remains after the test. By dividing the applied force, in kilograms, by the actual surface area of the indentation, in square millimeters, one may get the Brinell hardness number. For aluminum castings, a 500 kilograms load is applied for 30 seconds. Each sample underwent several hardness tests, with the average result used to calculate the specimen's hardness.

Fig. 7 and Table 4 compares the hardness of A356 alloy with composites supplemented with 40 and 90 μm sized B_4C particulates at 3 and 6 weight percentages. The graph clearly shows that the hardness of the A356 alloy in both 40 and 90 μm of 3 and 6 wt. percent sized composites rises as the weight percentage of reinforcing particles increases [13, 14]. The basic matrix A356 alloy has a hardness of 60.3 BHN. The hardness of A356 alloy is 65.4 BHN with 3 wt. percent of 40 μm B4C particle reinforced composites, and it is 76.3 BHN with 6 wt. percent of 40 μm B4C particle reinforced composites. Similarly, in the case of 3 and 6 weight percentages of 90 mμ sized B_4C particulates reinforced A356 alloy composites it is 64.1 and 73 BHN respectively.

Table 4. Hardness of A356 alloy and its B_4C composites with standard deviation

Material Composition	B_4C Particle Size (micron)	Hardness (BHN)
A356 Alloy	--	60.33 ± 1.22
A356 – 3 wt. % B_4C	40	65.43 ± 0.80
A356 – 6 wt. % B_4C		76.30 ± 1.05
A356 – 3 wt. % B_4C	90	64.13 ± 1.00
A356 – 6 wt. % B_4C		73.03 ± 0.77

± - SD (Standard Deviation)

The data show that the hardness of B_4C composites with a 40 μm size 6 wt. % is greater than that of B_4C composites with 3 wt. %. The improvement in hardness is more pronounced in composites supplemented with smaller particle and larger in quantity. This enhancement is caused by the particles' excellent wetability in the matrix of the A356 alloy and is also evident from microstructural tests. The bonding between the reinforcement and the matrix alloy increases as particle size decreases [15, 16].
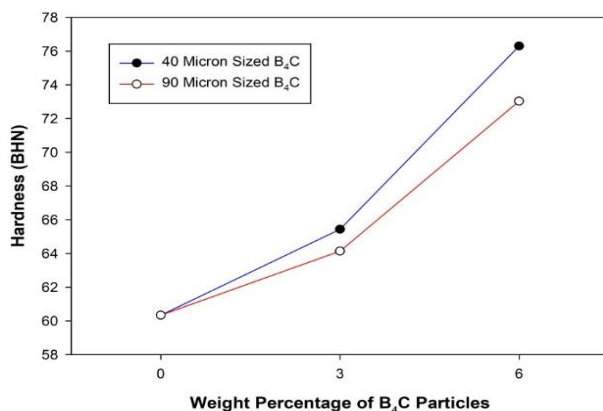
Fig. 7 Hardness of A356 with B_4C composites

3.4. Compression Strength

The Universal Testing Machine does compression testing (UTM). On the UTM's base plate is affixed the cylindrical test specimen. The specimen being utilized has a diameter that is equal to its height. The specimen is progressively loaded until it has been crushed by 50% (height). When applying higher weights, displacement also rises up to a certain point before abruptly falling till it reaches a height beyond which it can no longer be squeezed.

Fig. 8 and Table 5 compares the compressive strength of composites reinforced with 3 and 6 weight percent of 40 and 90 μm B_4C particles with that of A356 alloy. When B_4C particles with sizes of 40 and 90 μm are added, the compressive strength of the A356 alloy rises. Furthermore, as compared to composites reinforced with 40 μm sized B_4C particulates exhibit better compressive strength. The basic matrix of the A356 alloy has a compressive strength of 548.6 MPa.

Table 5. Compression strength of A356 alloy and its B_4C composites with standard deviation

Material Composition	B_4C Particle Size (micron)	Compression Strength (MPa)
A356 Alloy	--	548.60 ± 2.36
A356 – 3 wt. % B_4C	40	602.33 ± 3.51
A356 – 6 wt. % B_4C		675.87 ± 3.25
A356 – 3 wt. % B_4C	90	589.57 ± 3.10
A356 – 6 wt. % B_4C		657.13 ± 4.17

± - SD (Standard Deviation)

The compressive strength of A356 alloy is 602.3 MPa with 3 wt. percent of 40 μm B_4C particle reinforced composites, and it is 675.9 MPa with 6 wt. percent of 40 μm B_4C particle reinforced composites. Similarly, in the case of 3 and 6 weight percentages of 90 mμ sized B_4C particulates reinforced A356 alloy composites it is 589.6 and 657.1 respectively. This improvement is the result of the matrix's hard B_4C particles, which have a higher compressive strength [17, 18]. Additionally, the higher resistance of crushing 40 μm 6 wt. % B_4C particles is the reason for the increased strength in 40 μm sized particle reinforced composites as compared to 3 wt. % reinforced composites.
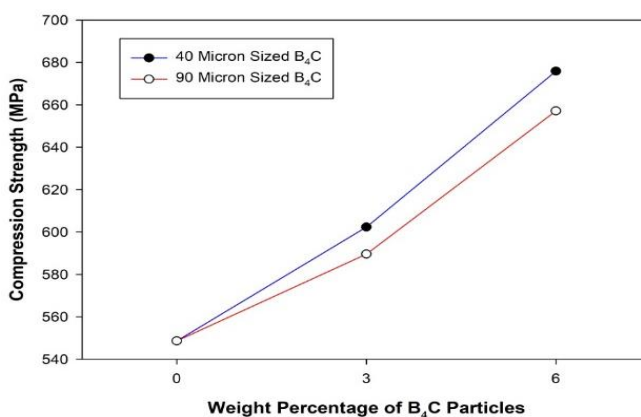
Fig. 8 Compression strength of A356 with B_4C composites

3.5. Impact Strength

Fig. 9 and Table 6 compares the impact toughness of A356 alloy with 40 and 90 μm sized B_4C reinforced composites. In reinforced composites with 40 and 90 μm sized particle sizes, the impact toughness of the A356 alloy is enhanced by 3 and 6 weight percent. A356 alloy with 6 weight percent Boron carbide in 40 μm composites demonstrate greater impact toughness than composites with 3 weight percent B_4C particles. The greater resistance of smaller particles to debonding during impact loading accounts for the majority of the improvement in impact toughness in 40 μm B_4C composites.

There is no void formation or debonding at the interface of the matrix and the particle reinforcements, indicating improved interfacial bonding between the matrix and the reinforcements [19, 20]. The uniformity produced by the homogeneous dispersion of B_4C particles in the matrix improves the matrix-reinforcement bonding as well as the impact

strength of composites. Under the impact loading, the homogeneous particles could clearly be distinguished. The SEM analyses in figure 3 lend credence to this hypothesis.

As a result, particle cracking dominates the failure mechanism. This outcome is consistent with the literature, which states that particle breakage occurs when the contact is stronger than the individual particles. Therefore, it seems that the failure results from an accumulation of internal damage brought on by particle breakage and matrix material deformation [21, 22].

Table 6. Impact strength of A356 alloy and its B_4C composites with standard deviation

Material Composition	B_4C Particle Size (micron)	Impact Strength (J)
A356 Alloy	--	1.10 ± 0.1
A356 – 3 wt. % B_4C	40	1.45 ± 0.05
A356 – 6 wt. % B_4C		1.90 ± 0.03
A356 – 3 wt. % B_4C	90	1.35 ± 0.04
A356 – 6 wt. % B_4C		1.88 ± 0.02

± - SD (Standard Deviation)
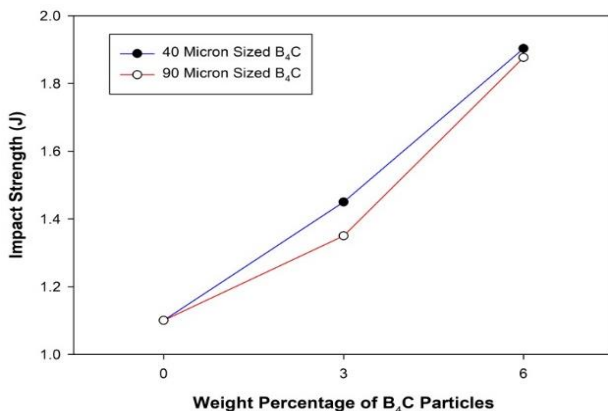
Fig. 9 Impact strength of A356 with B_4C composites

4. Conclusions

The following general findings are drawn from this study on the synthesis and characterization of composites reinforced with B_4C particles of various sizes made of the A356 alloy:

- Stir casting is an effective method for producing reinforced composites made of A356 alloy that include 3 and 6 weight percent of B_4C particulates that are 40 and 90 μm in size.
- Energy dispersive analysis (EDS) confirms the existence of B_4C particles in the form of C elements in composites made of A356 and B_4C that are 40 and 90 μm in size.
- SEM micrographs show a very equal distribution of B_4C particles throughout the matrix.
- The inclusion of 40 and 90 μm sized B_4C particles enhances the tensile properties of A356 composites with 3 and 6 wt.%B_4C. Additionally, as cast A356

alloy and composites reinforced with 6 wt.% percent 40 μm sized B_4C particles exhibit better tensile properties than composites reinforced with 3 wt.% B_4C. The inclusion of 40 and 90 μm sized B_4C particles enhances the hardness of A356 composites with 3 and 6 wt.% B_4C. Additionally, as cast A356 alloy and composites reinforced with 6 wt.% percent 40 μm sized B_4C particles exhibit better hardness than composites reinforced with 3 wt.% B_4C. The addition of B_4C particles results in an increase in the compressive strength of the A356 matrix. Furthermore, compared to 3 wt. % B_4C composites, the A356 alloy with 6 wt. % 40 μm sized B_4C particle reinforced composites show greater compressive strength.

- The inclusion of B_4C particles increases the impact toughness of the A356 matrix. Furthermore, compared to 3 wt. % 40 μm sized B_4C composites, the A356 alloy supplemented with 6 wt.% percent 40 μm sized B_4C particle demonstrates greater impact toughness.

References

[1] Bharath V, Auradi V, Nagaral M. Fractographic characterization of Al2O3p particulates reinforced Al2014 alloy composites subjected to tensile loading. Frattura ed Integrità Strutturale, 2021; 15(57): 14-23. https://doi.org/10.3221/IGF-ESIS.57.02

[2] Harti J, Prasad TB, Nagaral M, Rao KN. Hardness and tensile behavior of Al2219-TiC metal matrix composites. Journal of Mechanical Engineering and Automation, 2016; 6(5A): 8-12.

[3] Ali Z, Muthuraman V, Rathnakumar P, Gurusamy P, Nagaral M. Investigation on the tribological properties of copper alloy reinforced with Gr/ZrO2 particulates by stir casting route. Materials Today: Proceedings, 2020; 33: 3449-3453. https://doi.org/10.1016/j.matpr.2020.05.351

[4] Balaraj V, Nagaraj K, Nagaral M, Auradi V. Microstructural evolution and mechanical characterization of micro Al2O3 particles reinforced Al6061 alloy metal composites. Materials Today: Proceedings, 2021; 47: 5959-5965. https://doi.org/10.1016/j.matpr.2021.04.500

[5] Ali Z, Muthuraman V, Rathnakumar P, Gurusamy P, Nagaral M. Studies on mechanical properties of 3 wt.% of 40 and 90 μm size B4C particulates reinforced A356 alloy composites. Materials Today: Proceedings, 2022; 52: 494-499. https://doi.org/10.1016/j.matpr.2021.09.260

[6] Gurusamy P, Muthuraman V, Raj SHK, Kumar JL. Performance and experimental analysis of Al-Al2O3 metal matrix composites. International Journal of Vehicle Structures & Systems, 2022; 14(2): 257-259. https://doi.org/10.4273/ijvss.14.2.20

[7] Shetty RP, Mahesh TS, Ali Z, Veeresha G, Nagaral M. Studies on mechanical behavior and tensile fractography of boron carbide particles reinforced Al8081 alloy advanced metal composites. Materials Today: Proceedings, 2022; 52: 2115-2120. https://doi.org/10.1016/j.matpr.2021.12.397

[8] Nagaral M, Auradi V, Kori SA, Reddappa HN, Jayachandran, Shivaprasad V. Studies on 3 and 9 wt. % of B4C particulates reinforced Al7025 alloy composites. In AIP Conference Proceedings, 2017; 1859, 1: 020019. https://doi.org/10.1063/1.4990172

[9] Prasad GP, Chittappa HC, Nagaral M, Auradi V. Influence of B4C reinforcement particles with varying sizes on the tensile failure and fractography of LM29 alloy composites. Journal of Failure Analysis and Prevention, 2020; 20(6): 2078-2088. https://doi.org/10.1007/s11668-020-01021-6

[10] Nithin K, Kumar HS, Hemanth RT, Nagaral M, Auradi V, Veeresha RK. Microstructural characterization, mechanical and taguchi wear behavior of micro-titanium carbide particle-reinforced Al2014 alloy composites synthesized by advanced two-stage

casting method. Journal of Bio and Tribo-Corrosion, 2022;8(109):1-16. https://doi.org/10.1007/s40735-022-00709-6

[11] Krishna Prasad S, Samuel Dayanand, Rajesh , Madeva Nagaral, Auradi V, Rabin Selvaraj. Preparation and Mechanical Characterization of TiC Particles Reinforced Al7075 Alloy Composites, Advances in Materials Science and Engineering, 2022, Article ID 7105189, https://doi.org/10.1155/2022/7105189. https://doi.org/10.1155/2022/7105189

[12] Kumar HSV, Kempaiah UN, Nagaral M. Impact, tensile and fatigue failure analysis of boron carbide particles reinforced Al-Mg-Si (Al6061) alloy composites. Journal of Failure Analysis and Prevention, 2021; 21: 2177-2189. https://doi.org/10.1007/s11668-021-01265-w

[13] Nagaral M, Deshapande RG, Auradi V, Satish BP, Samuel D, Anilkumar MR. Mechanical and wear characterization of ceramic boron carbide-reinforced Al2024 alloy metal composites. Journal of Bio-and Tribo-Corrosion, 2021; 7(1):1-12. https://doi.org/10.1007/s40735-020-00454-8

[14] Nagaral M, Auradi V, Kori SA, Vijaykumar H. Investigations on mechanical and wear behavior of nano Al2O3 particulates reinforced AA7475 alloy composites. Journal of Mechanical Engineering and Sciences, 2019; 13(1):4623-4635. https://doi.org/10.15282/jmes.13.1.2019.19.0389

[15] Pankaj RJ, Nagaral M, Shivakumar R, Jayasheel IH. Impact of boron carbide and graphite dual particulates addition on wear behaviour of A356 alloy metal matrix composites. Journal of Metals, Materials and Minerals, 2020; 30(4):106-112. https://doi.org/10.55713/jmmm.v30i4.642

[16] Pathalinga PG, Chittappa HC, Nagaral M, Auradi V. Effect of the reinforcement particle size on the compressive strength and impact toughness of LM29 alloy B4C composites. Structural Integrity and Life, 2019;5 (7):231-236.

[17] Sallahauddin Attar, Madeva Nagaral, Reddappa HN, V Auradi V. Effect of B4C particles addition on wear properties of Al7075 alloy composites. American Journal of Materials Science, 2015; 5(3C): 53-57.

[18] Nagaral M, Shivananda BK, Auradi V, Kori SA. Development and mechanical wear Al2024 nano B4C composites for aerospace applications. Strength, Fracture and Complexity, 2020; 13 (1): 1-13. https://doi.org/10.3233/SFC-190248

[19]Nagara M, Auradi V, Bharath V. Mechanical characterization and fractography of 100 micron sized silicon carbide particles reinforced Al6061 alloy composites. Metallurgical and Materials Engineering, 2022; 28 (1): 17-32. https://doi.org/10.30544/639

[20] Chandrasekhar GL, Y Vijayakumar Y, Nagaral M, Anilkumar C. Microstructural evaluation and mechanical behavior of nano B4C reinforced Al7475 alloy metal composites. International Journal of Vehicle Structures & Systems, 2021; 13(5). https://doi.org/10.4273/ijvss.13.5.24

[21] Fazil N, Venkataramana V, Nagaral M, Auradi V. Synthesis and mechanical characterization of micro B4C particulates reinforced AA2124 alloy composites. International Journal of Engineering and Technology UAE, 2018; 7 (2.23): 225-229. https://doi.org/10.14419/ijet.v7i2.23.11954

[22] Nagaral M, Attar S, Reddappa HN, Auradi V, Kumar S, Raghu S. Mechanical behavior of Al7075-B4C particulate reinforced composites. Journal of Applied Mechanical Engineering, 2015; 4(6): 1000186.

Review Article

Effect of various interface bond tests and their failure behavior on substrate and overlay concrete -A Review

Kavendra Pulkit[*a], Babita Saini[b], HD Chalak[c]

Department of Civil Engineering, National Institute of Technology, (Civil engineering department), Kurukshetra, (Haryana) India

Article Info	Abstract
	Concrete is a widely used building material in the construction sector. Still, the lifespan of concrete is limited because many factors can influence the performance of concrete structures, which can be classified based on physical, chemical, and mechanical changes that occur during their service life. In addition, the structure's lifespan is being reduced due to adverse environmental conditions and loads. These require maintenance, restoration, or reconstruction. Therefore, considerable concrete remediation is necessary, and the best option is to repair it. However, the cost associated with restoring the deteriorating concrete structures is higher. The repaired concrete strength mainly depends on the interface layer, situated between the substrate (old) and overlay (new) concrete. The interface layer strength primarily depends on interface adhesion, friction, aggregate interlock, bonding agent, compaction, cleanliness, moisture content, concrete age, roughness, and time-dependent variables. Multiple tests are available to analyse the bonding behavior between substrate-overlay concrete. However, no particular method is available to access the bond strength. This paper describes various methods and techniques used by researchers to evaluate bond strength. The reviewed summary has shown that concrete repair is the best solution, and higher-strength concrete uses show better shear results; also, conventional concrete is more economical than higher-strength concrete. Among all the available tests the bi-surface shear test and slant shear test are the more suitable method to determine the bond strength.

1. Introduction

The interfacial bonding between damaged concrete structures and newly applied repair materials is one of the significant issues for the structure functionality, safety, and durability. At the interfaces of the concrete, a strong bond is required to make it stronger and prevent failure. There are millions of old buildings in Indian cities in degrading condition. These structures create a problem for individuals and their properties (1). For example, 14,375 and 10,500 old structures in Mumbai main city and suburban, respectively, require restoration, but, the reconstruction cost is higher. However, it can be overcome by repairing the existing structure. The repairing cost mainly depends on the old concrete properties, like the type of concrete, compressive strength, age of concrete, or other environmental conditions such as freeze-thaw weathering (2), temperature change, creep, shrinkage, fatigue, etc. Rehabilitation and repair enhance the life of degraded concrete structures by using new concrete because the old concrete cannot regain strength near the fresh concrete. The major factors involved in the bond strength are Van Der Waals (VDW) force and mechanical interlocking, which are mainly influenced by the bonding, the shrinkage difference, and interface roughness of substrate-overlay concrete(3–6). The

541

interface layer is the main area of concern because it is a very weak part of the bonding [7]–[11], and the bonding mechanism diagram has been shown in Fig. 1.
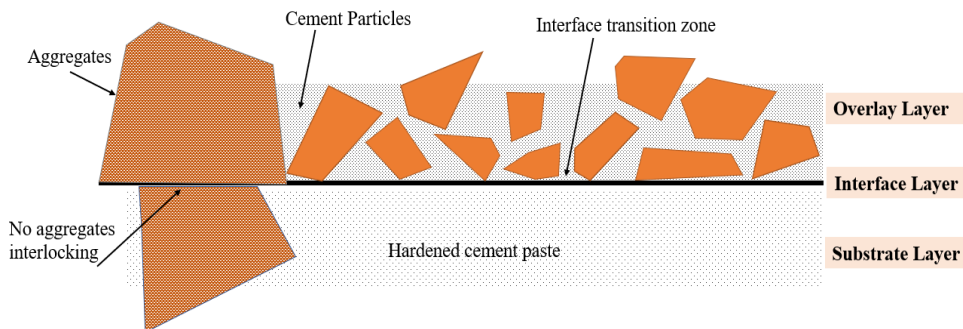

Fig. 1 Substrate-overlay concrete mechanical interlocking (7)

The bond between the substrate and overlay depends on the interface layer. In the bond mechanism, VDW forces, surface profile-related frictional interlock and exposed aggregate-induced mechanical interlock play an important role(8).The interface bond always depends on the chemical, mechanical or physical relation by the formation of the new layer as the interface. Based on the existence of the layer location the substrate–overlay composite is divided into three layers. Based on the scale these are termed macro-scale, mesoscopic and microscopic and the bond mechanics has been shown in Fig. 2. The newly formed gel is present in form of three layers.
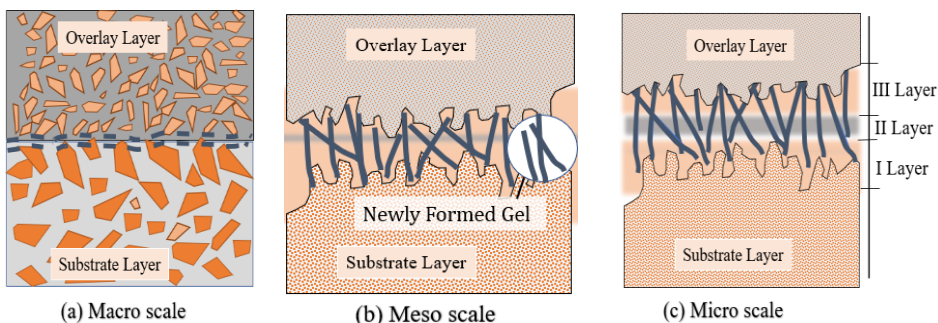
Fig. 2 Scale representation of the interface between substrate-overlay concrete (7)

- I layer–is also known as the penetration layer and it consists of mainly spike types calcium silicate hydrate (C–S–H) with smaller amounts of $Ca(OH)_2$, which is generated within the concrete substrate and contains young ingredients that react with active chemical components in the substrate concrete.
- II layer - it is also known as the highly affected layer or weakest layer; this layer is characterized by high porosity and highly oriented crystal constituents.
- III layer - it is also known as lower impacted layer or lower affected layer, which has almost the same micro-structure as overlay concrete.

From Fig. 2, it is clear that the surface roughness and presence of microcracks also affect the hydration product chain. Wang et al. (9) defined the chemical behavior of the OPC-based repair materials through the C-S-H gels process and stated that the chemical creates adhesion to the concrete substrate. Other than this various factors are involved in standardizing the bonding test procedure, such as the loading condition, interface layer

behavior, and geometry (10). Unfortunately, there is no suitable method to evaluate the accurate bond strength of the interface (11). However, some studies have recommended the tests mentioned below to estimate the bond strength between substrate and overlay concrete (11–13).

2. Objective of the Study

The primary objective of this research was to find out the suitable bond strength test of substrate and overlay concrete. Also, an effort has made to find the relation among the studied tests, different geometry and material properties. The failure patterns based on stress condition is also expected.

3. Literature Study

In this section, the test procedures and methods for evaluating interface bonding have been discussed. In real life, the interfaces between concrete layers are usually loaded in pure shear mode, pure tension mode, shear-compression mode, and shear-tension mode. The related geometry used in various tests and their shape have been shown in Table 1 and Fig. 3 respectively.

3.1 Direct and Indirect Tension Tests (Pure Tension)

These tests are useful for carrying out the bonding behavior between the substrate and the overlay concrete. In these tests, stress is determined by the effect of pure shear (14)(15). Various tests and their loading conditions have been described below.

3.1.1 Pull Off Test (POT)

It is suitable for assessing bond strength in the field and the laboratory. Because of its simplicity, many codes of practice recommended this test for quality assessment. This test applies a direct tensile force on an interface layer; but, this test method is complex due to several factors, such as damage by drilling, inappropriate gluing of the loading disc, system misalignment, interface geometry, and related stress disturbance. These types of complexity cause substrate failure. The testing guidelines are given in the ICRI code (16), and the test setup has been shown in Fig. 3(p). The minimum requirement for pull-off strength according to ACI 546-06 is 1.7-2.1 MPa at 28 d. Julio et al. (17) showed a strong relationship between the SST and POT; however, Yildirim et al. (18)stated no correlation between these two methods. Fig. 4 shows the relationships discovered by Julio et al. (17) and Yildirim et al. (18) with slant shear strength and pull-off strength. The difference between the SST and POT bond strength can be seen directly in Fig. 4 due to the various parameters, such as loading rate, differential shrinkage magnitude, specimen size, testing apparatus, etc. Some researchers used various types of materials to analyze the pull-off strength.

Thongchom et al. (19) investigated the effect of higher temperature on POT bonding and found that the bond strength and fracture energy reduced due to high temperature. The main disadvantage of this test is that the specimen gest partly destroyed during testing and the complexity of bonding. Further research is needed to resolve this issue. POT bond strength can be seen directly in Fig. 4 due to the various parameters, such as loading rate, differential shrinkage magnitude, specimen size, testing apparatus, etc. The expected failure mode have been shown in Fig 7(a) with loading diagram for POT.
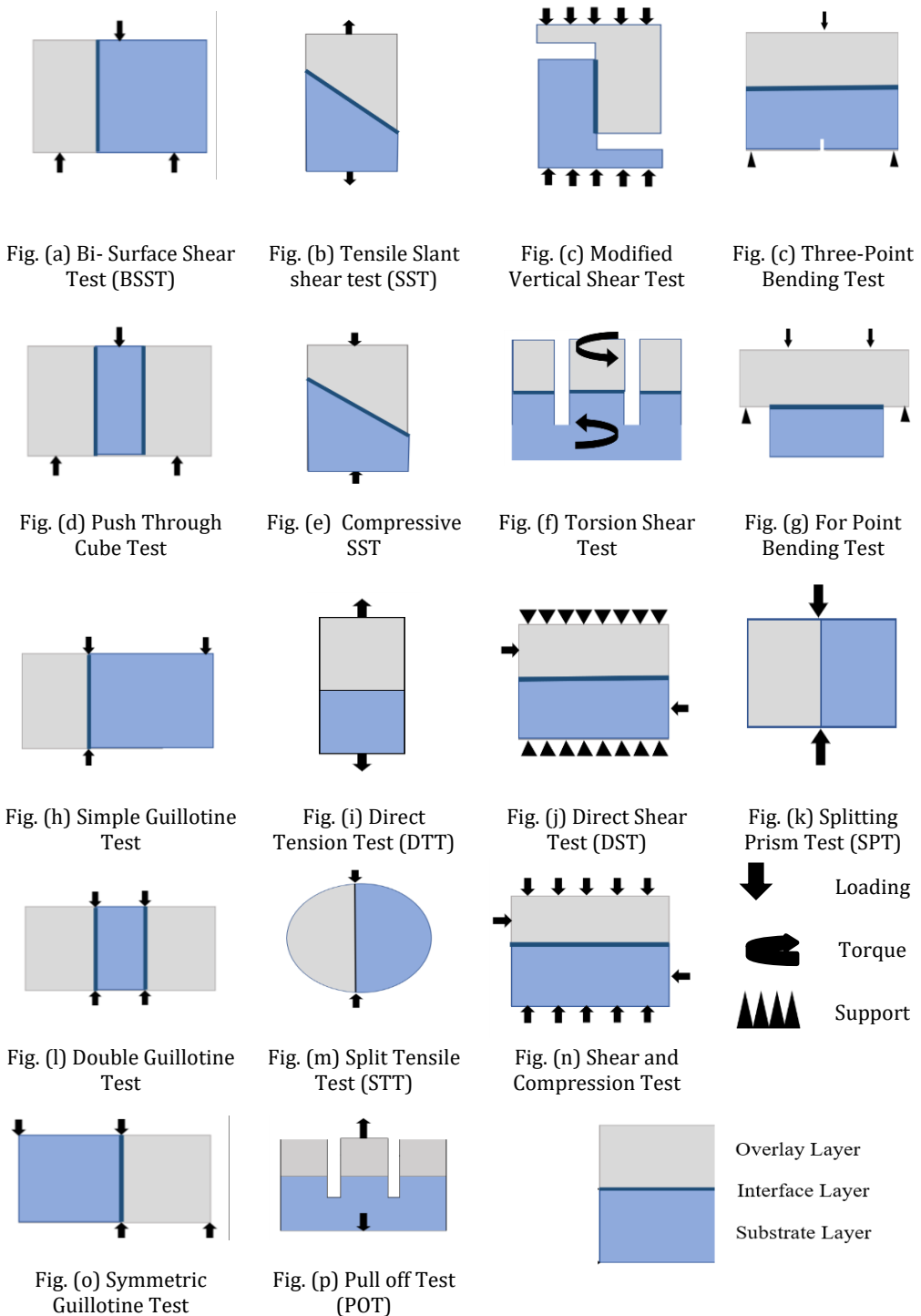
Fig. 3 Specimen shapes of various tests with loading conditions (15)
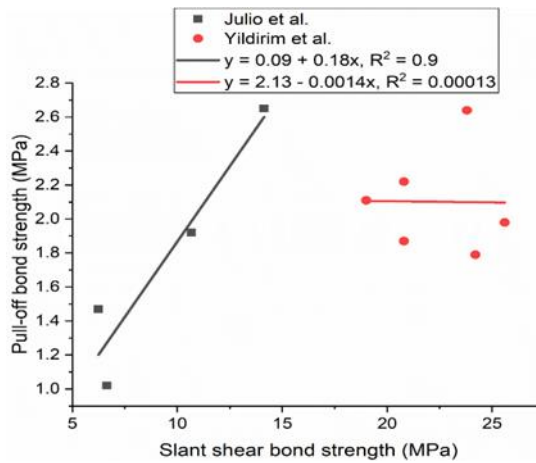
Fig. 4 Relationship between SST and POT (17)(18)

3.1.2 Direct Tension Test

This test examines the tensile bond strength between substrate and overlay material. In this test, two opposite tensile stresses are applied using two steel plates to a composite specimen. The test setup has been shown in Fig. 3(i). The expected failure mode have been shown in Fig 7(b) with loading diagram for DTT. There is no specific provision in American Society for Testing and Materials (ASTM)78 (20) to determine direct tensile strength. However, ASTM C 496 shows the procedure of splitting tensile strength measurement (21). Kim et al. (22) stated that comparing tensile and shear bond strength is challenging but usually related.

3.1.3 Splitting Prism Test

To determine the tensile strength of prismatic specimen STT is used, and the test setup has been shown in Fig. 3(k). According to ASTM C 496 (21), this test is good to determine the interface bond strength; but, some factors can influence the test technique, such as the freezing and thawing of specimens (23).

Table 1. Various interface bond tests and their geometry

Test Name	Size of tests
POT	40×40×160 (Cohesive and mixed failure)(32)
	150×150×150 φ (14)
	300×300×70 (Substrate failure) (10)
	35×50 and 110×50 with α= 180° (33)
	300×650×80 (Overlay failure) (34)
	600×800×100 and 500×500×70 (35)
DTT	100×100×300 (Partial interface failure) (13)
	Φ=100,h=200 (Cohesive and mixed mode) (36)
Splitting prism/ Cylinder test	150×50with α= 180° and 200×100 with α= 0° (33)
	Φ = 100, h=200and 40×40×160 (37)
Splitting cylinder test	Φ = 100 h= 200 (Substrate failure) (10)
	100×100×100 and 100×100×400and φ = 160, h= 320 (Interface failure and Mixed failure) (38)
BSST	150×50, h= 150 (Substrate Failure) (14)
	40 ×40 ×160 (39)

	50×150×150 and 100×150×150 (Adhesive, Cohesive and Mixed failure) (40) 38 ×51 × 153 (Mixed failure) (41) 50×150×150 (Shear failure) (24)
Modified vertical shear test	150×150×600 with α= 30° (12) 300×150×300 (33) 100x100x300 (Cohesive failure) (36) 150×150×150 (Close to interface) (42) 254×546×127 (At connectors failure) (43)
SST	102×76×394 with α=60° and 70° (Cohesive and mixed failure) (32) 100×100×300 (Substrate Failure)(10) 75×150 α= 42° (Within the substrate) (11) 75x150 α= 30° (37) Φ= 150 α= 30° h= 300, φ = 75 30° h= 150 , 100x100×400, 200x200×100 (With Epoxy no interface failure) (44) 75 ×150, α = 30° (45)
Flexural Bond test	150×150×500 (Mixed failure) (11) 100×100×400 (Shearing failure) (39) 100×100×500, 100×100×250 (Interface failure)(46)

Where, φ – Diameter of specimen, h- Slant height and α is slant angle. All dimension are in mm.

The expected failure mode has been shown in Fig 7(d) with loading diagram for SPT. According to Momayez (14) and Ju et al. (24), this test is more suitable to find bond strength; The test procedure is simple and utilizes the same specimen for the BSST and the loading procedure is simple for   the split cylinder test. Zhang et al (25) recommended this test for actual engineering application with the use of 5 to 20 mm size gravel, which improve the bond strength by nearly 24%; but, Pedro Miguel Duarte Santos (26) stated that the SPT is inappropriate to determine the bond strength and further recommended investigation at later age.

Some authors (25,27–29)found the split bond strength with different sizes of gravel, surface patterns and different overlay materials. With the use of the gravel patterns, the bond strength was increased by 60.3% as compared to the chipped surface (30). Bond strength testing of split prism specimens was performed using a modified version of ASTM C496, with results of 1.5 MPa for the 0.05 mm texture and the bond strength was nearly 3.7 MPa for the rough texture (31).

3.1.4 Splitting Cylinder Test

A simple cylindrical specimen is used to determine the tensile bond strength. This test is easy to perform on composite material, and the test setup has been shown in Fig. 3(m). The procedure for the above test is as per ASTM C1404 (47) and ASTM C1583 (48). In this test, the interface layer is more critical. It is affected by impact loading that causes various types of failure due to damage at the interface (49); but, is unaffected by the surface preparation as per International Concrete Repair Institute (ICRI) 210.3 (50) classification. The expected failure mode have been shown in Fig 7(c) with loading diagram for pure tensile bond test.

According to Hu et al. (49), the Split tensile bond strength of the composite section is related to the compressive strength and split tensile strength of old and new concrete. Zhu et al. (51) recommended a factor of 0.738 for compressive strength and 0.96 for splitting tensile strength to convert cubic strength to cylindrical strength for steel fibre reinforced concrete. The STT (Brazilian test) can be used to estimate a repair cementitious failure envelope more efficiently (52).

Qian et al. (53) found that the splitting tensile strength did not change significantly after 150 d freeze-thaw cycles for substrate concrete. According to Tayeh et al. (54), the bond strength was unusually high in this case. Due to the simplicity of this test, some researchers performed the STT on composite cubes (55), prisms (51), or cylinders (56) to evaluate the correlation between various tests. Michael and M. Sprinkel (57) described the tensile bond strength into five groups, shown in Table 2.

Table 2. Split tensile bond strength classification based on bond strength (57)

Strength (MPa)	≥ 2.1	1.7-2.1	1.4-1.7	0.7-1.4	0-0.7
Category	Excellent	Very good	Good	Fair	Poor

Tayeh et al. (58) described a correlation between splitting tensile and slant shear strength, given in Fig. 5. Graybeal et al. (59) stated that the flexure strength test and the splitting cylinder test are related and showed higher bond strengths than the pull-off strength. The splitting tensile strength increased more for composite specimens with both limestone sand and glass powder applied to high-roughness surfaces than applied to drilled holes surfaces (38).
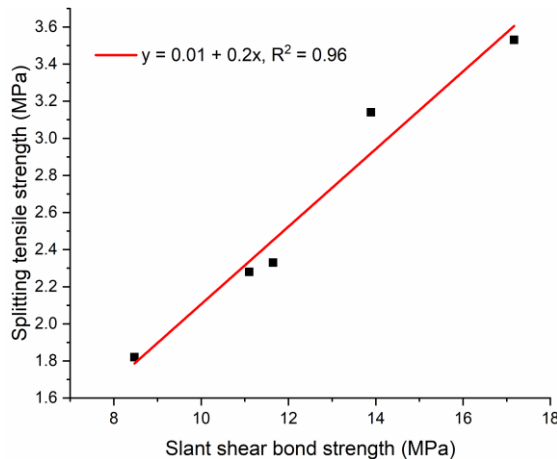
Fig. 5 Correlation of SST and STT (55)

3.2 Pure Shear Tests

Pure shear stress is assumed to act between the substrate and repair layers in the pure shear test. Various tests are available to determine interface shear strength, like torsion shear test (2), push through cube test (7), BSST (60–62), modified vertical shear test (57) (61), DST (63), and a mixed-mode of them.

3.2.1 Bi-Surface Shear Test

Momayez et al. developed BSST to determine substrate and overlay concrete bond strength (64). The test process is like the direct shear test (DST), but has a single shear plane and a single load arrangement. The primary advantage of this is that the loads applied uniformly to the composite concrete specimen through the steel plates. The test setup of the BSST has been shown in Fig. 3(a); however, this test method highly depends on the bonding agent, moisture content of the substrate surface, and the surface preparation method (42).

In this test, the specimen is prepared by filling two-third of the mould with existing concrete and the remaining one-third with new concrete. This test procedure is complicated due to the bonding material, substrate wetness, and surface preparation. The expected failure mode has been shown in Fig 8(a) with loading diagram for BSST. Kabay et al. (62) studied the effect of surface preparation on bond behaviour of composite with BSST and evaluated that smooth surfaces showed bond strength of nearly 2.9 MPa; whereas, the bond strength increased up to 134% for the rough surface. The use of a bond agent enhances the BSST bond strength but as compared to the shot blast treatment it is lower for the bond agent (40).

On the other hand, Lee et al. (65) used Ultra High Performance Concrete (UHPC) to overlay with Normal Strength Concrete (NSC) substrate and found that UHPC performed better in bonding due to high strength. This test also offers better results using mortar instead of concrete; but, there is a lack of correlations between the bond strength obtained by SST and other tests(66). Only Al-Rubaye et al. (60) found the relationship between bond strength, and it was reported that, by using SST and BSST, the Slant Shear Bond Strength (SSBS) was two to three times higher than the BSST strength. This is because the high compressive stresses that take place in a SST cause more friction and locking, which increases the shear failure load (14). To solve the problems of poor durability and low bearing capacity of existing concrete reinforcement, a BSST between reactive powder concrete (RPC) and ordinary concrete (OC) was conducted and it was found that RPC has better bonding performance with ordinary concrete. The bonding strength of the RPC and steel mesh-reinforced OC structure can be increased by 1.37–3.11 times compared with the OC-OC interface (67).

Hak-Chul et al.(68) investigated a relationship between BSST strength and Ca/Si ratio. The shear bond strength increases as the Ca/Si ratio at the interface increases. Because the Ca/Si ratio is an indirect measure of C-S-H and Calcium Hydroxide (CH), therefore an interface with high C-S-H contents is strong.

3.2.2 Modified Vertical Shear Test

The modified vertical shear test is helpful to determine the bond strength when reinforcement crosses the interface layer. It is also known as the L-shaped test or push-off test, and the test setup has been shown in Fig. 3(c). In this test, two L shape sections are used, and their inner interface is joined together by cross reinforcement, having a gap at both ends. The loading acting at the outer part is to be continued in the testing procedure until the interface fails in shear. The expected failures mode have been shown in Fig 8(c) with loading diagram for Modified vertical shear test. The push-off shear mainly depends on specimen size, bonding preparation, thickness, and shear reinforcement (29)(69). The use of shear reinforcement has a greater impact on the bond strength. It has been discovered that the interfacial bond strength decreases in geosynthetic fibre (70). A geosynthetic interlayer creates shear plane which allows the layers to debond more easily. However, by the use of fibers and grid reinforcement, shear and tensile bond strengths increased 331% and 456% respectively as compared to un-strengthened specimen (71). This higher bond strength was due to the conversion of interface shear failure into compressive failure due to, the fiber addition. Javidmehr et al. (72) used a grooving pattern at the interface to reduce shear reinforcement; due to the ultimate load increases as the roughness of the interface increases. The bond strength in this test is influenced by Compressive Strength (CS) rather than shear reinforcement. CS increases ultimate shear strength while decreasing cracks and residual strength (57). When the CS of the concrete was increased, the ultimate shear strength of the push-off specimens increased (61). Other than this, increasing adhesive thickness reduces maximum loads at the overlap side (73). Cattaneo et al. (72) discovered an analytical study of concrete bonding. The push-off test does not allow for the application of reversal cyclic loads.

3.2.3 Torsion Shear Test

It is like the POT; the only difference between this test and the POT is the torque application. The test setup has been shown in Fig. 3(f). A torsional moment (T) is applied at the top to determine bond strength, and T is increased until failure. Equation (1) shows the relationship between shear stress and the torsional moment (2). Dowan Kim and Sungho Mun (74) developed a torsion test for repairing of tack coat to understand its performance and define application standards.

$$Shear\ stress = \frac{16}{\pi}.\frac{T}{\emptyset^3} \tag{1}$$

Where ϕ is the core diameter.

3.2.3 Direct Shear Test

The DST is the most used test for determining bond shear strength. This test can be conducted using a single (75) or double shear plane (76). The specimen for this test is cast in a cube with half substrate concrete or half repair concrete, and the test setup has been shown in Fig. 3(j). This test applies opposite compressive forces to the composite specimen, each acting on a separate specimen region. Nowadays, the cube specimen is modified into a "butterfly" double wedge specimen with slits around the interface edge (63).

3.2.4 Guillotine Test

The guillotine test is a standard bond test that measures the substrate - overlay concrete bond strength. A compressive load is applied on the shear box, producing shear stress at the composite specimen's bond interface. This test is divided into three categories: the simple guillotine test, the double guillotine test, and the symmetric guillotine test, based on the loading or overlay material position and the systematic test setup have been shown in Fig. 3(h), Fig. 3(l), and Fig. 3(0) respectively. The expected failure mode have been shown in Fig 8(d) with loading diagram for Guillotine test.

Delatte et al. (77) suggested that the guillotine test is a laboratory test with limited use in situ due to the difficulty of loading conditions. In this test, bond strength is directly influenced by the overlay's mechanical and physical qualities (7).

3.2.5 Slant Shear Test

The SST is a standard bond test that was developed in 1976. Several standards, including BS EN12615 (78), ASTM C1042 (79), ASTM C881 (80), and ASTM C882 (81), are available to describe this test; various measures for the SST have been shown in Table 3 (44). In this test, cylinders or prismatic moulds are used to determine the bond strength by dividing the substrate-overlay concrete at various angles. The bond interface surface is prepared after casting the substrate concrete. Then, repair concrete over the substrate is cast after a specified time interval. In SST, the specimen is subjected to compressive, and shear stresses simultaneously. The expected failure mode has been shown in Fig 9(a) and Fig.9(b) with loading diagram for SST (compression) and SST (tensile), respectively. The bond strength is depending on various parameters like surface preparation, bonding agent, angle, and specimen size.

Table 3. Standards for SST(44)

Standard	Cross-section (mm)	Height (mm)	Angle with the vertical
ASTM C881	150 φ	300	30°
ASTM C882	75 φ	150	30°
NEP18-872	100×100	300	30°
BS EN12615	40×40	160	30°
BS EN12615	100×100	400	30°

Pedro Miguel Duarte Santos (82) and Harris et al. (83) found that bond strength mainly depends on surface preparation. According to Salim et al. (84), the bond strength of interface is affected by the substrate concrete's compressive and flexural strength, rather than the surface preparation. The minimum requirement of SSBS according to ACI 546-06, is 14-21 MPa at 28 d. Different specimens have been used to conduct SST based on different standards. The test setup has been shown in Fig.3(b) and Fig.3(e). The difference in SSBS by using different standards was observed by Diab et al.(44).
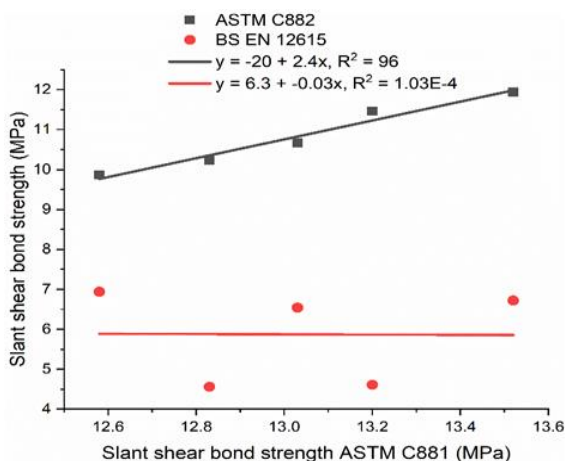
Fig. 6 Correlation of different standards for SST (44)

It has been noted that the coefficient of variation in results conducted by ASTM C881 was less than ASTM C882 and BS EN 12615. A higher value of SSBS was obtained when the test was conducted on cylindrical specimens than prism specimens. Fig. 6 compares different standards of SST and shows a strong correlation between both cylindrical specimens by ASTM C881 and ASTM C882. There was no correlation between prisms specimen of BS EN12615 and ASTM C881. Similarly, the SSBS and CS are related linearly; due to the use of PVA content compressive strength and SSBS increase in the same manner (85).

In addition to specimen size, angle with the vertical also influences the SSBS. For example, Harris et al. (83) showed substrate failure at 60° angle. However, adhesive failure was observed at 70° angle for the brushed interface between NSC and UHPC. In addition to repair and concrete strength, SST performance is dependent on bond and contact area. Increasing interface bond angle increases mixed failure risk. Zhang et al. (86) studied the different types of surface preparation on the substrate layer and found that the bond

strength of the surface-milled and grooved composite increases with the curing; because, milling surface preparation removes laitance, pores, and other defects from the old concrete surface; that leads to better bond with overlay concrete. Similarly, the water jetting surface treatment increases bond strength up to 56% (87).

The surface angle orientation impacts the concrete mixture's bond strength (88). Wood (89) investigated how the slant angle of the interface layer influences the bond behaviour. The interface surface was inclined to vertical and varied from 10° to 50°. A slant angle of 40° or fewer causes adhesive failure, while a slant angle of more than 40° causes cohesive failure. According to Sun et al. (90), specimens with 45° inclination were unsuitable for SST due to greater compressive stress. Cohesive failure reduces interfacial bond strength. Numerous researchers (14)(40)(44)(45)(17)(82)(88,91–95), and ASTM C881 and ASTM C882 recommend 30° slant angle is best to determine the bond strength of substrate - overlay concrete. However, the widespread use of a single 30° slant angle is insufficient. A variety of slant angles should be studied to complete the interfacial behaviour gap (91)-(92). Gomaa et al. (96) used three slant angles, 20°, 25°, and 30°, to analyse the failure envelope of the specimen surfaces with the Mohr-Coulomb criterion. The failure occurred at a smaller angle because the interface joint was sliding along the interface layer.

3.2.6 Flexural Bond Test

Bending tests are used to determine the flexural strength of concrete. Based on the available literature, this test method is simple for evaluating the interface bonding [101]. In this test, a simple prismatic section is used, and the test setup has been shown in Fig. 3(c). Half of the prism is cast initially. Then, the overlay material is used in the remaining part. The stress distribution of this test is complex and depends on the contact plane's location and direction. In pure bending, only compressive and tensile stresses are important. However, in shear bending, both compressive and tensile stresses are important, along with shear stress. The expected failure mode have been shown in Fig 9(c) with loading diagram for flexural bond test. The bond strength determined by this test depends on the substrate concrete's strength, the surface preparation, and materials type. Aaleti et al. (97) describe the durability of tests with UHPC in bridge decks to enhance the service life of the decks. Numerous novel studies are conducted to verify the interface bonding behaviour. Some authors used a new frustum, split Hopkinson pressure bar (98), Double Sleeve Test (11) (99) to estimate the actual bond strength.

4. Failure Study

From the previous studies it can be stated that the bond between the substrate layer or overlay layer is a very crucial parameter that cannot be defined clearly; because, it depends on various factors like, subterete and overlay layer properties, selection of materials for both layer and other environmental factors. To determine the failure criteria of the composite section it is necessary to predict the numerous tests with the interface layer. Many types of tests available to determine the bonding behaviour based on the stress criteria has been shown in Fig. 7, Fig. 8 and Fig. 9 respectively. Three types of common failures that can occur based on material failure with stress are substrate failure, overlay failure and interface failure or mixed mode failure. The bond strength is directly influenced by the interface layer failure; but the substrate failure did not fulfil the demand of the direct measurement of bond strength. Similarly, the overlay failure shows that the overlay materials are not sufficient.
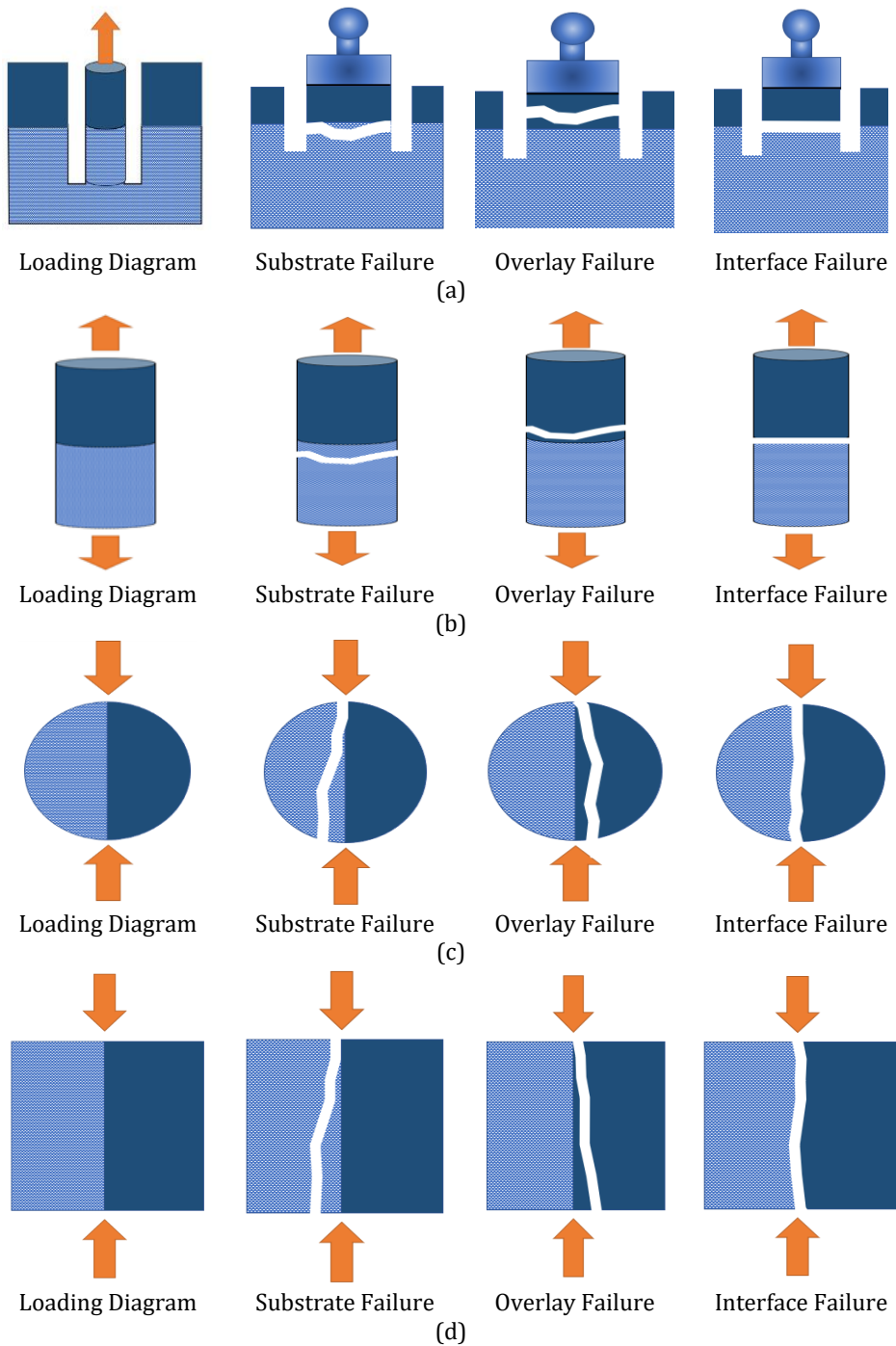
Fig 7. Loading diagram of pure tensile bond test with expected failure mode (a) Pull off test, (b) Direct tension test, (c) Splitting cylinder test and (d) Splitting prism test
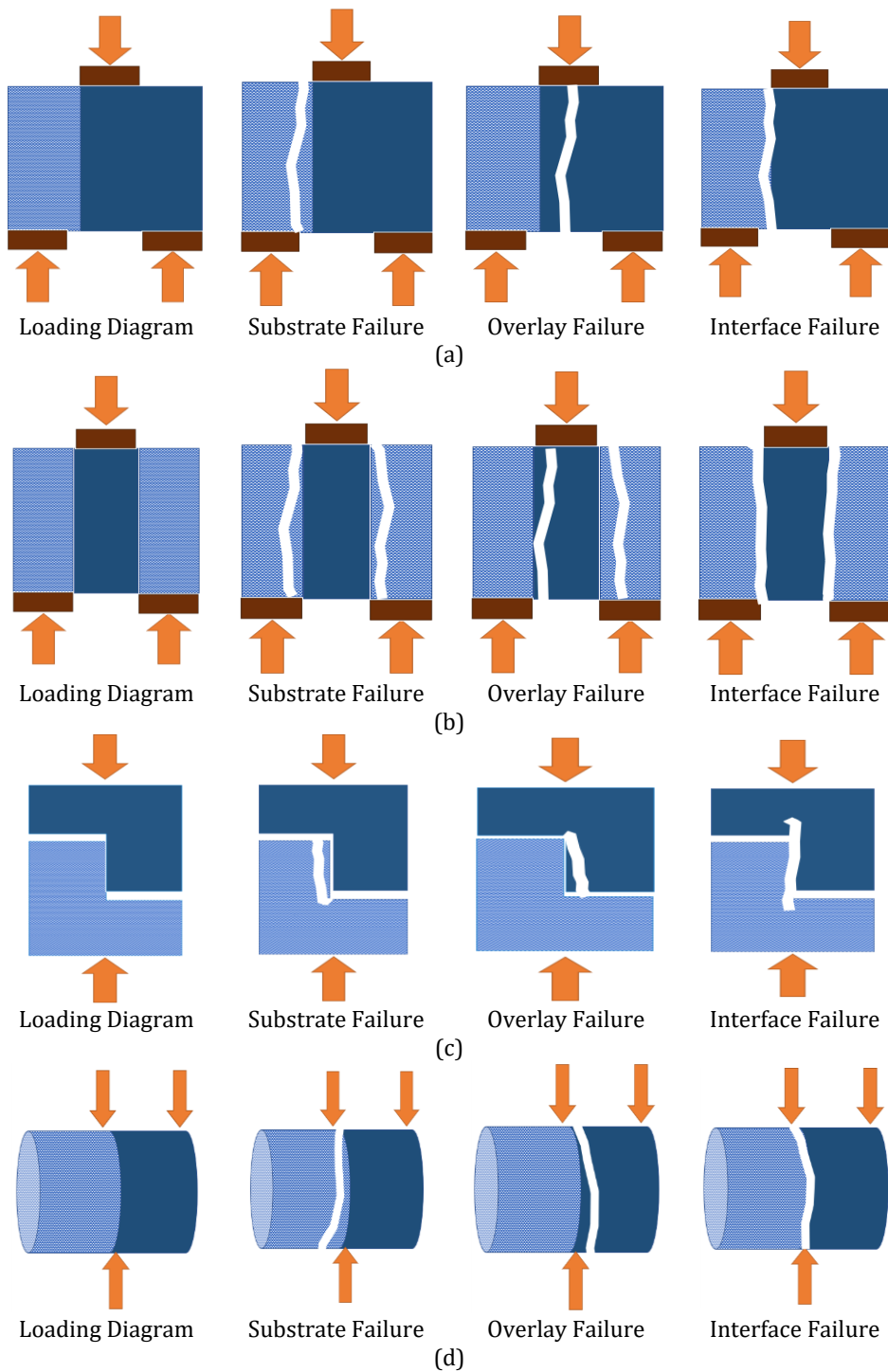
Fig 8. Loading diagram of pure compression bond test with expected failure mode (a) Bi surface shear test, (b) Push through cube test, (c) Modified vertical shear test and (d) Guillotine test
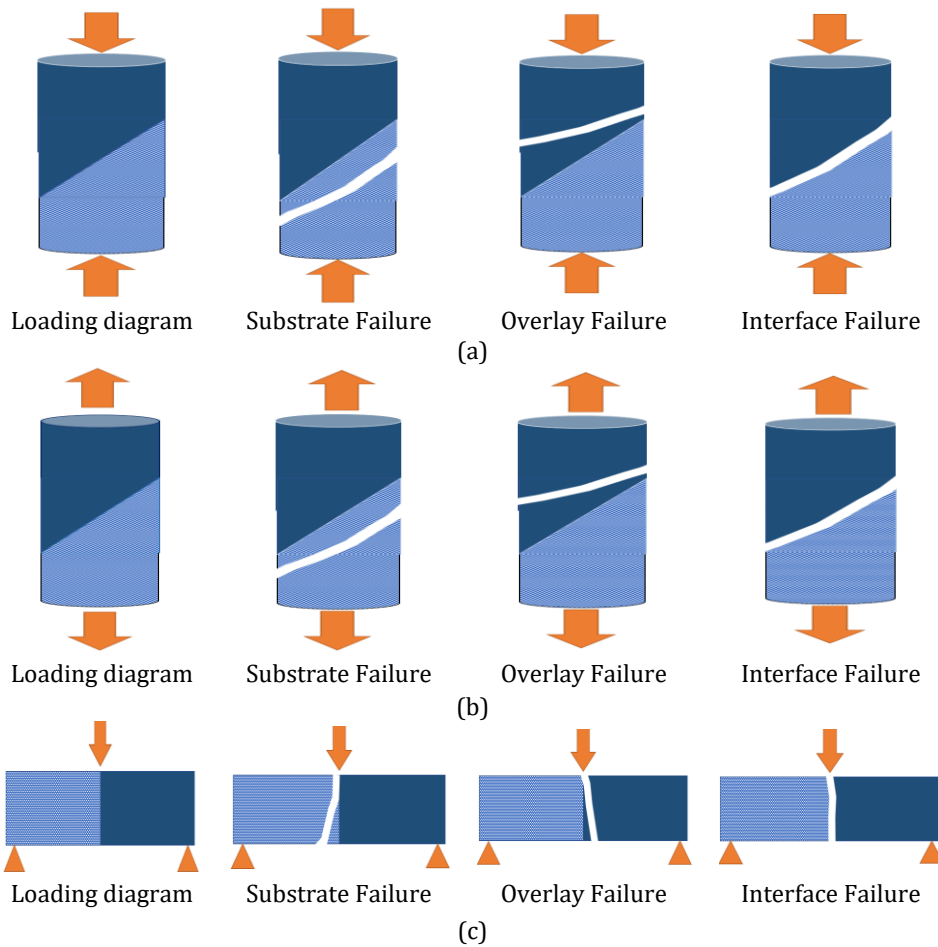
Fig 9. Loading diagram of mixed mode of stress bond test with expected failure mode
(a) SST (compression), (b) SST (Tensile) and (c) Three- point bending test

Other than this, partial failure or mixed mode failure can occur due to the stress applied to it (83). Although each of these failure types give useful information regarding the performance of the system, only the interface failure mode accurately defines the bond. When Epoxy is used at the interface layer, a thin layer was formed over the substrate which leads to substrate failure (30).

Sun et al. (90) determined the failure pattern with the use of UHPC as an overlay on NSC by SST and STT, it was observed that most of the specimens failed in the substrate or partial interface failure. Similarly, Based on the test specimen and failure characteristics under various experimental conditions, six types of interfacial shear failure were recorded and most of the failures occurred partial failure; due to the UHPC surface attached to the partial thin layer of NSC (100). The interfacial failure modes were determined with double-sided DST and most specimens failed partially interface with NSC or completely NSC, and a few failed within the interface (49). Liao et al. (101) found the bond behavior with mortar and the failure was characterized into two patterns, uncracked or cracked failure. From the failure mode, it is clear that mortar thickness influenced the failure behavior. Ganesh et al. (30) expected the bond behavior with model analysis and found that the maximum difference in the experimental bond strength and model bond strength was nearly 12%. It

is critical to understand that the result of a specimen that did not fail at the bonding interface (for example, a pull-off test that failed in the substrate concrete) will show interface bond stress at specimen failure, not interface bond strength (59).

Rather than the layer failure the full failure is subdivided into adhesive failure and cohesive failure based on the loading process. Numerous authors (14)(12)(17)(28)(102)(103) have researched both adhesive and cohesive parameters to avoid failure. Failure of an adhesive occurs when the plane of failure is parallel to the contact surface. When the material compressive strength exceeded, cohesion failure occurred (92). the basic parameter defined by Naderi et al. (104) that affects the bond strength and mode of failure are described as:

- Substrate soundness- Many authors (77)(105)(106) focused on how this parameter affects the strength and mode of failure, and it is noticed that increasing roughness can also lead to a change in failure mode, from the adhesive mode to the cohesive mode.
- Shrinkage of the new layer- According to (82) the slant-shear strength increases as the difference in age between the two different concretes increases (107).
- Interface angle- it also influences the failure mode. It can be stated that adhesive failure cannot be prevented only by adequately defining the interface angle.
- According to Austin et al. (108), who investigated the SST failure modes, the normal/shear stress ratio is controlled by the interface angle. It is suggested to test different interface angles, for each surface treatment, to obtain a bond failure envelope. Zambas (109) examined the effects of the slant angle on the bond behavior of new-to-old concrete interfaces. The inclination angle of the interface from vertical was in the range of 10° to 50°. Test results showed that when the slant angle is not greater than 40°, failure occurs along the interface, which is referred to as an adhesive failure, and that when the slant angle exceeds 40°, the weakest concrete is crushed, which is regarded as a cohesive failure.

5. Conclusion

- Past studies have covered the effect of various factors on interface layer bonding, workability, surface roughness, bonding agent, surface moisture condition, overlay materials strength, age of concrete, specimen size, micro-cracking, shrinkage of concrete, cohesion in the substrate concrete, aggregate interlock, and other time-dependent factors. Most past studies have focused on testing the efficiency of different test setups to determine a perfect bond. The roughness substrate surface improves binding strength over a smooth surface.
- Due to the simplicity most of the researcher used SST, STT followed by POT and avoided the mixed mode of test due to complexity.
- POT test showed better results for bond strength but its complexity restricts its use. The main disadvantage of this test is that the specimen partly destroyed during testing and the complexity of bonding.
- Bond strength by the SST shows higher bond strength than BSST and SST is chiefly used to test the bond strength of substrate-overlay concrete because of the simplicity of the test.
- The interference failure is observed in most of the cases due to, the lack of EBA.
- The above results are based on the various research observations; further research is required to explore suitable methods, materials and surface techniques.
- The BSST is more suitable to find bond strength; The test procedure is simple and utilizes the same specimen as the BSST and the loading procedure is simple like the split cylinder test.

- By using SST and BSST, the SSBS was two to three times higher than the BSST strength. This is because the high compressive stresses that take place in a SST cause more friction and locking, which increases the shear failure load.
- The guillotine test is a laboratory test with limited use due to the difficulty of loading conditions. In this test, bond strength is directly influenced by the overlay's mechanical and physical properties.
- When Epoxy is used at the interface layer, a thin layer was formed over the substrate which leads to substrate failure in most cases.

Conflicts of Interest

"The authors declare no conflict of interest."

References

[1] Naresh Kamath. Mumbai building collapse: 25,000 old buildings are dilapidated, so why do lakhs refuse to move? Hindustan Times. 2017 Sep 1.
[2] Silfwerbrand J. Shear bond strength in repaired concrete structures. Mater Struct. 2003;36(6):419-24. https://doi.org/10.1007/BF02481068
[3] Wang X, Dong S, Ashour A, Han B. Bond of nanoinclusions reinforced concrete with old concrete: Strength, reinforcing mechanisms and prediction model. Constr Build Mater [Internet]. 2021;283:122741. https://doi.org/10.1016/j.conbuildmat.2021.122741
[4] Semendary AA, Svecova D. Factors affecting bond between precast concrete and cast in place ultra high performance concrete (UHPC). Eng Struct [Internet]. 2020;216(May):110746. https://doi.org/10.1016/j.engstruct.2020.110746
[5] Carbonell MA, Mumuñoz M, Harris DK, AM, Ahlborn TM. Bond Performance between Ultrahigh-Performance Concrete and Normal-Strength Concrete. 2014, 26(8): 04014031. https://doi.org/10.1061/(ASCE)MT.1943-5533.0000890
[6] Hassan Fardoun, David Begg. Shear strength between ultra-high-performance concrete and old concrete. In: 6th International Conference on Civil, Architecture and Transport Engineering (ICCATE-2017) London (UK) Dec 4-6, 2017 Shear. International Institute of Engineers; 2017.
[7] Beushausen H, Alexander MG. Bond strength development between concretes of different ages. Mag Concr Res. 2008;60(1):65-74. https://doi.org/10.1680/macr.2007.00108
[8] Yazdi MA, Dejager E, Debraekeleer M, Gruyaert E, Van Tittelboom K, De Belie N. Bond strength between concrete and repair mortar and its relation with concrete removal techniques and substrate composition. Constr Build Mater [Internet]. 2020;230:116900. https://doi.org/10.1016/j.conbuildmat.2019.116900
[9] Wang YS, Peng K Di, Alrefaei Y, Dai JG. The bond between geopolymer repair mortars and OPC concrete substrate: Strength and microscopic interactions. Cem Concr Compos [Internet]. 2021;119(February):103991. https://doi.org/10.1016/j.cemconcomp.2021.103991
[10] Abo Sabah SH, Hassan MH, Muhamad Bunnori N, Megat Johari MA. Bond strength of the interface between normal concrete substrate and GUSMRC repair material overlay. Constr Build Mater. 2019 Aug 20;216:261-71. https://doi.org/10.1016/j.conbuildmat.2019.04.270
[11] Farzad M, Shafieifar M, Azizinamini A. Experimental and numerical study on bond strength between conventional concrete and Ultra High-Performance Concrete (UHPC). Eng Struct. 2019 May 1;186:297-305. https://doi.org/10.1016/j.engstruct.2019.02.030
[12] Saldanha R, Júlio E, Dias-Da-Costa D, Santos P. A modified slant shear test designed to enforce adhesive failure. Constr Build Mater. 2013;41:673-80. https://doi.org/10.1016/j.conbuildmat.2012.12.053

[13.] Zhang Y, Zhu P, Liao Z, Wang L. Interfacial bond properties between normal strength concrete substrate and ultra-high performance concrete as a repair material. Constr Build Mater. 2020 Feb 28;235. https://doi.org/10.1016/j.conbuildmat.2019.117431

[14] Momayez A, Ehsani MR, Ramezanianpour AA, Rajaie H. Comparison of methods for evaluating bond strength between concrete substrate and repair materials. Cem Concr Res. 2005 Apr;35(4):748-57. https://doi.org/10.1016/j.cemconres.2004.05.027

[15] Espeche AD, León J. Estimation of bond strength envelopes for old-to-new concrete interfaces based on a cylinder splitting test. Constr Build Mater. 2011 Mar;25(3):1222-35. https://doi.org/10.1016/j.conbuildmat.2010.09.032

[16] ICRI. Guide to using in-situ tensile pull-off tests to evaluate bond of concrete surface materials. Concr Repair Man. 2004;(March).

[17] Júlio ENBS, Branco FAB, Silva VD. Concrete-to-concrete bond strength: Influence of an epoxy-based bonding agent on a roughened substrate surface. Mag Concr Res. 2005 Oct;57(8):463-8. https://doi.org/10.1680/macr.2005.57.8.463

[18] Yildirim G, Şahmaran M, Al-Emam MKM, Hameed RKH, Al-Najjar Y, Lachemi M. Effects of compressive strength, autogenous shrinkage, and testing methods on bond behavior of high-early- strength engineered cementitious composites. ACI Mater J. 2015;112(3):409-18. https://doi.org/10.14359/51687188

[19] Thongchom C, Lenwari A, Aboutaha RS. Bond properties between carbon fibre-reinforced polymer plate and fire-damaged concrete. Int J Adhes Adhes. 2020 Mar 1;97. https://doi.org/10.1016/j.ijadhadh.2019.102485

[20] ASTM-C78. Standard test method for flexural strength of concrete (using simple beam with third-point loading) [Internet]. 2002. Available from: www.astm.org

[21] ASTM C496. Standard test method for splitting tensile strength of cylindrical concrete specimens. 1996.

[22] Kim JJ, Reda Taha M. Experimental and numerical evaluation of direct tension test for cylindrical concrete specimens. Adv Civ Eng. 2014 ; 1-8 156926. https://doi.org/10.1155/2014/156926

[23] ASTM-C/496. Splitting tensile strength of cylindrical concrete specimens [Internet]. 2004. Available from: www.astm.org,

[24] Ju Y, Shen T, Wang D. Bonding behavior between reactive powder concrete and normal strength concrete. Constr Build Mater [Internet]. 2020;242:118024. https://doi.org/10.1016/j.conbuildmat.2020.118024

[25] Zhang J, Ding X, Zhao Q. Experimental and numerical investigation of scattering gravels on the surface bond strength of self-compacting concrete. Constr Build Mater. 2017 Aug 1;145:11-9. https://doi.org/10.1016/j.conbuildmat.2017.03.219

[26] Pedro Miguel Duarte Santos, and Eduardo Nuno Brito Santos Júlio. Factors affecting bond between new and old concrete. ACI Mater J. 2011; 108(4): 449-456.

[27] Harris DK, Carbonell Muñoz MA, Gheitasi A, Ahlborn TM, Rush S V. The challenges related to interface bond characterization of ultra-high-performance concrete with implications for bridge rehabilitation practices. Adv Civ Eng Mater. 2015;4(2):75-101. https://doi.org/10.1520/ACEM20140034

[28] Santos PMD, Julio ENBS. Factors affecting bond between new and old concrete. Vol. 108, ACI Materials Journal. 2011. 108(4): 449-56. https://doi.org/10.14359/51683118

[29] Ganeshan M, Venkataraman S. Interface shear strength evaluation of self compacting geopolymer concrete using push-off test. J King Saud Univ - Eng Sci [Internet]. 2020; 34(2) : 98-107

[30] Ganesh P, Ramachandra Murthy A. Simulation of surface preparations to predict the bond behaviour between normal strength concrete and ultra-high performance concrete. Constr Build Mater. 2020 Jul 30;250. https://doi.org/10.1016/j.conbuildmat.2020.11887 1

[31] Al-Basha AJ, Toledo WK, Newtson CM, Weldon BD. Ultra-High Performance Concrete Overlays for Concrete Bridge Decks. In: IOP Conference Series: Materials Science and Engineering. Institute of Physics Publishing; 2019. https://doi.org/10.1088/1757-899X/471/3/032007

[32] Carbonell MA, Mu˜muñoz M, Harris DK, Asce AM, Ahlborn TM, Asce M, et al. Bond performance between ultrahigh-performance concrete and normal-strength concrete. J Mater Civ Eng. 2014;26(8). https://doi.org/10.1061/(ASCE)MT.1943-5533.0000890

[33] Zanotti C, Randl N. Are concrete-concrete bond tests comparable? Cem Concr Compos. 2019 May 1;99:80-8. https://doi.org/10.1016/j.cemconcomp.2019.02.012

[34] Bonaldo E, Barros JAO, Lourenço PB. Bond characterization between concrete substrate and repairing SFRC using pull-off testing. Int J Adhes Adhes. 2005 Dec;25(6):463-74. https://doi.org/10.1016/j.ijadhadh.2005.01.002

[35] Courard L, Piotrowski T, Garbacz A. Near-to-surface properties affecting bond strength in concrete repair. Cem Concr Compos. 2014 Feb;46:73-80. https://doi.org/10.1016/j.cemconcomp.2013.11.005

[36] López-Carreño RD, Pujadas P, Cavalaro SHP, Aguado A. Bond strength of whitetoppings and bonded overlays constructed with self-compacting high-performance concrete. Constr Build Mater. 2017 Oct 30;153:835-45. https://doi.org/10.1016/j.conbuildmat.2017.07.136

[37] Benyahia A, Ghrici M, Choucha S, Omran A. Characterization of fiber reinforced self-consolidating mortars for use in patching damaged concrete. Lat Am J Solids Struct. 2017;14(6):1124-42. https://doi.org/10.1590/1679-78253718

[38] Gadri K, Guettala A. Evaluation of bond strength between sand concrete as new repair material and ordinary concrete substrate (The surface roughness effect). Constr Build Mater [Internet]. 2017;157:1133-44. https://doi.org/10.1016/j.conbuildmat.2017.09.183

[39] Yue Li, Weiliang Bai, Tongfei Shi. A study of the bonding performance of magnesium phosphate cement on mortar and concrete. Constr Build Mater. 2017 Jul 1;142:459-68. https://doi.org/10.1016/j.conbuildmat.2017.03.090

[40] Santos DS, Santos PMD, Dias-Da-Costa D. Effect of surface preparation and bonding agent on the concrete-to-concrete interface strength. Constr Build Mater. 2012 Dec;37:102-10. https://doi.org/10.1016/j.conbuildmat.2012.07.028

[41] Valikhani A, Jahromi AJ, Mantawy IM, Azizinamini A. Experimental evaluation of concrete-to-UHPC bond strength with correlation to surface roughness for repair application. Constr Build Mater. 2020 Mar 30;238. https://doi.org/10.1016/j.conbuildmat.2019.117753

[42] Beushausen H, Höhlig B, Talotti M. The influence of substrate moisture preparation on bond strength of concrete overlays and the microstructure of the OTZ. Cem Concr Res. 2017 Feb 1;92:84-91. https://doi.org/10.1016/j.cemconres.2016.11.017

[43] Júlio ENBS, Dias-da-Costa D, Branco FAB, Alfaiate JMV. Accuracy of design code expressions for estimating longitudinal shear strength of strengthening concrete overlays. Eng Struct. 2010;32(8):2387-93. https://doi.org/10.1016/j.engstruct.2010.04.013

[44] Diab AM, Abd Elmoaty AEM, Tag Eldin MR. Slant shear bond strength between self compacting concrete and old concrete. Constr Build Mater. 2017 Jan 15;130:73-82. https://doi.org/10.1016/j.conbuildmat.2016.11.02

[45] Mirmoghtadaei R, Mohammadi M, Ashraf Samani N, Mousavi S. The impact of surface preparation on the bond strength of repaired concrete by metakaolin containing concrete. Constr Build Mater. 2015 Apr 1;80:76-83. https://doi.org/10.1016/j.conbuildmat.2015.01.018

[46] Qin R, Hao H, Rousakis T, Lau D. Effect of shrinkage reducing admixture on new-to-old concrete interface. Compos Part B Eng. 2019 Jun 15;167:346-55. https://doi.org/10.1016/j.compositesb.2018.11.087

[47] ASTM 1404. Standard test method for bond strength of adhesive systems used with concrete as measured by direct tension [Internet]. 2010. Available from: ASTM International, West Conshohocken, PA, 2020.

[48] ASTM-C1583. Standard test method for tensile strength of concrete surfaces and the bond strength or tensile strength of concrete repair and overlay materials by direct tension [Internet]. 2013. p. 1-4. Available from: ASTM International, West Conshohocken, PA, 2020

[49] Hu B, Meng TF, Li Y, Li DZ, Chen L. Dynamic splitting tensile bond behavior of new-to-old concrete interfaces. Constr Build Mater. 2021 Apr 26;281. https://doi.org/10.1016/j.conbuildmat.2021.122570

[50] ICRI. Guide for Selecting and Specifying Materials for Repair of Concrete Surfaces [Internet]. 2015. Available from: info@icri.org

[51] Zhu H, Li C, Gao D, Yang L, Cheng S. Study on mechanical properties and strength relation between cube and cylinder specimens of steel fiber reinforced concrete. Adv Mech Eng. 2019;11(4):1-12. https://doi.org/10.1177/1687814019842423

[52] Espeche AD, León J. Estimation of bond strength envelopes for old-to-new concrete interfaces based on a cylinder splitting test. Constr Build Mater [Internet]. 2011;25(3):1222-35. https://doi.org/10.1016/j.conbuildmat.2010.09.032

[53] Qian Y, Zhang D, Ueda T. Tensile bond between substrate concrete and normal repairing mortar under freeze-thaw cycles. Proc 4th Int Conf Durab Concr Struct ICDCS 2014. 2014;(July):385-92. https://doi.org/10.5703/1288284315427

[54] Tayeh BA, Abu Bakar BH, Megat Johari MA, Voo YL. Mechanical and permeability properties of the interface between normal concrete substrate and ultra high performance fiber concrete overlay. Constr Build Mater. 2012 Nov;36:538-48. https://doi.org/10.1016/j.conbuildmat.2012.06.013

[55] Ahmed SI, Shaikh FA, Jakhrani SH, Mushtaq MY, Sidiqy JA. Mechanical behavior of normal concrete reinforced with kantharo suter fiber. Civ Eng J. 2017;3(7):487-95. https://doi.org/10.28991/cej-2017-00000107

[56] Słowik M, Akram A. Length effect at testing splitting tensile strength of concrete. Materials (Basel). 2022;15(1). https://doi.org/10.3390/ma15010250

[57] Michael M. Sprinkel PE, Celik Ozyildirim. Evaluation of high performance concrete overlays placed on route 60 over LYNNHAVEN inlet in VIRGINIA. Qual Life Res [Internet]. 2000;3(2):1689-99.

[58] Tayeh BA, Abu Bakar BH, Megat Johari MA. Characterization of the interfacial bond between old concrete substrate and ultra high performance fiber concrete repair composite. Mater Struct Constr. 2013 May;46(5):743-53. https://doi.org/10.1617/s11527-012-9931-1

[59] Graybeal B. Bond of Field-Cast Grouts to Precast Concrete Elements FHWA [Internet]. 2017. Available from: www.fhwa.dot.gov/research

[60] Al-Rubaye M, Muteb H, Al-Rubaye MM, Yousef RF, Muteb HH. Experimental evaluation of bond strength performance between normal concrete substrate and different overlay materials. Journal of Engineering Science and Technology. 2020; 15(6) : 4367 – 4382

[61] Rahal KN, Khaleefi AL, Al-Sanee A. An experimental investigation of shear-transfer strength of normal and high strength self compacting concrete. Eng Struct [Internet]. 2016;109:16-25. https://doi.org/10.1016/j.engstruct.2015.11.015

[62] Kabay N, Kızılkanat AB. Mechanical properties of concrete to concrete interfaces under uniaxial and shear forces. Pamukkale Univ J Eng Sci. 2018;24(6):1037-42. https://doi.org/10.5505/pajes.2018.72246

[63] Ray I, Davalos JF, Luo S. Interface evaluations of overlay-concrete bi-layer composites by a direct shear test method. Cem Concr Compos. 2005;27:339-47. https://doi.org/10.1016/j.cemconcomp.2004.02.048

[64] A. Momayez H. Rajaie, and M. R. Ehsani AAR. Bi-surface shear test for evaluating bond between existing and new concrete. ACI Mater J. 2005;35 (4): 748-757.

[65] Lee HS, Jang HO, Cho KH. Evaluation of bonding shear performance of ultra-high-performance concrete with increase in delay in formation of cold joints. Materials (Basel). 2016;9(5): 362. https://doi.org/10.3390/ma9050362

[66] Santos PD. Assessment of the shear Strength between concrete layers. Departemento De Engenharia Civil Faculdade De Ciencias E Tecnologia Unversidade De Coimbra. 2009; November.

[67] Du G, Xu B, Bu L. Experimental study and numerical simulation of the interfacial bonding performance of ordinary concrete reinforced with reactive powder concrete. J Build Eng [Internet]. 2022;62(September):105352. https://doi.org/10.1016/j.jobe.2022.105352

[68] Hak-Chul S, Zhifu W. Interfacial Properties between New and Old Concretes [Internet]. 2010. Available from: http://www.claisse.info/Proceedings.htm

[69] Ahmad Waseem S, Singh B. Shear strength of interfaces in natural and in recycled aggregate concrete [Internet]. 2017; 44(3):1-36. https://doi.org/10.1139/cjce-2016-0317

[70] Sudarsanan N, Karpurapu R, Amrithalingam V. An investigation on the interface bond strength of geosynthetic- reinforced asphalt concrete using Leutner shear test. Constr Build Mater [Internet]. 2018;186:423-37. https://doi.org/10.1016/j.conbuildmat.2018.07.010

[71] Liu Y, Tafsirojjaman T, Dogar AUR, Hückler A. Bond behaviour improvement between infra-lightweight and high strength concretes using FRP grid reinforcements and development of bond strength prediction models. Constr Build Mater [Internet]. 2021;270:121426. https://doi.org/10.1016/j.conbuildmat.2020.121426

[72] Javidmehr S, Empelmann M. Shear bond between ultra-high performance fibre reinforced concrete overlays and normal strength concrete substrates. Sustainability. 2021;13(15). https://doi.org/10.3390/su13158229

[73] Alachek I, Reboul N, Jurkiewiez B. Bond behaviour improvement between infra-lightweight and high strength concretes using FRP grid reinforcements and development of bond strength prediction models. Int J Adhes Adhes. 2020;98(December 2019):1-13.

[74] Kim D, Mun S. Development of an interface shear strength tester and a model predicting the optimal application rate of tack coat. Constr Mater. 2021;1(1):22-38. https://doi.org/10.3390/constrmater1010002

[75] Li S. Durability and bond of high-performance concrete and repaired Portland cement concrete. Australian Science Teachers' Journal. 1997 48; 30-35.

[76] Chen Pu-woie, Fu Xuli, Chung D D L. Improving the bonding between old and new concrete. Cem Concr Res. 1995;25(3):491-6. https://doi.org/10.1016/0008-8846(95)00037-D

[77] Norbert J. Delatte Dawn Marie Wade, and David W. Fowler J. Laboratory and field testing of concrete bond development for expedited bonded concrete overlays. ACI Mater J. 2000;97(3). https://doi.org/10.14359/4622

[78] BS-12615. Products and systems for the protection and repair of concrete structures. Test methods. Determination of slant shear strength. 1999:1-8.

[79] ASTM C1042. Standard test method for bond strength of epoxy-resin systems used with concrete by slant shear. ASTM Int. 2005;i:1-3.

[80] ASTM-C881/C881M. Standard specification for epoxy-resin-base bonding systems for concrete. Current [Internet]. 2002;06:4-9. Available from: ASTM International, West Conshohocken, PA, 2020

[81] American Society for Testing and Materials. ASTM. Standard test methods for tensile properties of thin plastic sheeting, method C882. Annu B ASTM Stand [Internet]. 2010;87(Reapproved):3-5. Available from: www.astm.org

[82] Pedro Miguel Duarte Santos, Eduardo Nuno Brito Santos Júlio. Factors affecting bond between new and old concrete. ACI Mater J. 2014; 108: 449-456

[83] Harris DK, Carbonell Muñoz MA, Gheitasi A, Ahlborn TM, Rush S V. The challenges related to interface bond characterization of ultra-high-performance concrete with implications for bridge rehabilitation practices. Adv Civ Eng Mater. 2015;4(2):75-101. https://doi.org/10.1520/ACEM20140034

[84] Salim LG, Al-Baghdadi HM, Muteb HH. Reactive Powder Concrete with Steel, Glass and Polypropylene Fibers as a Repair Material. Civ Eng J. 2019 Nov 1;5(11):2441-9. https://doi.org/10.28991/cej-2019-03091422

[85] Kristiawan S, Santosa B, Purwanto E, Caesar RA. Slant shear strength of fibre reinforced polyvinyl acetate (PVA) modified mortar. In: MATEC Web of Conferences. EDP Sciences; 2018; 195. https://doi.org/10.1051/matecconf/201819501016

[86] Zhang B, Kang J, Li J, Liang J, Wang J. Evaluation of interface rapid bond strength between normal concrete and ternary system fast setting and rapid hardening self-compacting concrete. Constr Build Mater [Internet]. 2022;347(May):128515. https://doi.org/10.1016/j.conbuildmat.2022.128515

[87] Zhang S, Li Q, Yuan Q, Yang S, Dai X. Effect of roughness on bonding performance between Portland cement concrete and magnesium phosphate cement concrete. Constr Build Mater [Internet]. 2022;323(January):126585. https://doi.org/10.1016/j.conbuildmat.2022.126585

[88] Mohammadi M, Mir Moghtadaei R, Ashraf Samani N. Influence of silica fume and metakaolin with two different types of interfacial adhesives on the bond strength of repaired concrete. Constr Build Mater [Internet]. 2014;51:141-50. https://doi.org/10.1016/j.conbuildmat.2013.10.048

[89] Wood AM. Structural repairs to the monuments of the Acropolis-the Parthenon. Proc Inst Civ Eng Civ Eng. 1993;97(4):155. https://doi.org/10.1680/icien.1993.25302

[90] Sun N, Song Y, Hou W, Zhang H, Wu D, Li Y, et al. Interfacial Bond Properties between Normal Strength Concrete and Epoxy Resin Concrete. 2021;1-14, 556109. https://doi.org/10.1155/2021/5561097

[91] Zanotti C, Banthia N, Plizzari G. A study of some factors affecting bond in cementitious fiber reinforced repairs. Cem Concr Res. 2014;63:117-26. https://doi.org/10.1016/j.cemconres.2014.05.008

[92] Eymard M, Plassiard JP, Perrotin P, Le Fay S. Interfacial strength study between a concrete substrate and an innovative sprayed coating. Constr Build Mater [Internet]. 2015;79:345-56. https://doi.org/10.1016/j.conbuildmat.2014.12.031

[93] He Y, Zhang X, Hooton RD, Zhang X. Effects of interface roughness and interface adhesion on new-to-old concrete bonding. Constr Build Mater. 2017;151:582-90. https://doi.org/10.1016/j.conbuildmat.2017.05.049

[94] Abu-Tair AI, Rigden SR, Burley E. Testing the bond between repair materials and concrete substrate. ACI Mater J. 1996;93(6):553-8. https://doi.org/10.14359/9861

[95] Knab LI, Spring CB. Evaluation of test methods for measuring the bond strength of portland cement based repair materials to concrete. Cem Concr Aggregates. 1989;11(1):3-14. https://doi.org/10.1520/CCA10096J

[96] Gomaa E, Gheni AA, Kashosi C, ElGawady MA. Bond strength of eco-friendly class C fly ash-based thermally cured alkali-activated concrete to portland cement concrete. J Clean Prod. 2019 Oct 20;235:404-16. https://doi.org/10.1016/j.jclepro.2019.06.268

[97] Aaleti S, Sritharan S. Quantifying bonding characteristics between UHPC and normal-strength concrete for bridge deck application. J Bridg Eng. 2019 Jun;24(6):04019041. https://doi.org/10.1061/(ASCE)BE.1943-5592.0001404

[98] Hu B, Li Y, Liu Y. Dynamic slant shear bond behavior between new and old concrete. Constr Build Mater. 2020 Mar 30;238. https://doi.org/10.1016/j.conbuildmat.2019.117779

[99] Piancastelli EM, Magalhães AG, Silva FJ, Rezende MAP, Santos WJ, Carrasco EVM, et al. Bond strength between old and new concretes with focus on the strengthening of reinforced concrete columns - slant shear test versus double sleeve test. Appl Mech Mater. 2017 Apr;864:324-9. https://doi.org/10.4028/www.scientific.net/AMM.864.324

[100] Zhang Y, Zhang C, Zhu Y, Cao J, Shao X. An experimental study: various influence factors affecting interfacial shear performance of UHPC-NSC. Constr Build Mater [Internet]. 2020;236:117480.

[101] Liao W, Wang H, Li M, Ma C, Wang B. Large scale experimental study on bond behavior between polymer modified cement mortar layer and concrete. Constr Build Mater. 2019 Dec 20;228; 16751.https://doi.org/10.1016/j.conbuildmat.2019.116751

[102] Júlio ENBS, Branco FAB, Silva VD, Lourenço JF. Influence of added concrete compressive strength on adhesion to an existing concrete substrate. Build Environ. 2006 Dec;41(12):1934-9. https://doi.org/10.1016/j.buildenv.2005.06.023

[103] Santos PMD, Júlio ENBS, Silva VD. Correlation between concrete-to-concrete bond strength and the roughness of the substrate surface. Constr Build Mater. 2007 Aug;21(8):1688-95. https://doi.org/10.1016/j.conbuildmat.2006.05.044

[104] Naderi M. Analysis of the slant shear test. J Adhes Sci Technol. 2009 Jan 1;23(2):229-45. https://doi.org/10.1163/156856108X369589

[105] Austin S, Robins P, Pan Y. Tensile bond testing of concrete repairs. Mater Struct [Internet]. 1995;28(5):249. https://doi.org/10.1007/BF02473259

[106] Garbacz A, Górka M, Courard L. Effect of concrete surface treatment on adhesion in repair systems. Mag Concr Res [Internet]. 2005 Feb 1;57(1):49-60. https://doi.org/10.1680/macr.2005.57.1.49

[107] Haach VG, Vasconcelos G, Lourenço ;, Auxiliar P, Catedrático P. Characterization of the tensile and shear bond strength of concrete block masonry. In: 8o Congresso Nacional de Mecânica Experimental. 2010;

[108] Austin S, Robins P, Pan Y. Shear bond testing of concrete repairs. Vol. 29, Cement and Concrete Research. 1999; https://doi.org/10.1016/S0008-8846(99)00088-5

[109] Zambas C. Structural repairs to the monuments of the acropolis - the parthenon. Proc Inst Civ Eng - Civ Eng [Internet]. 1992 Nov 1;92(4):166-76. https://doi.org/10.1680/icien.1992.21497

Research Article

Comprehensive analysis of specimen's properties and fiber type on the performance of Indian origin fine aggregates-based composite

Muppalla Venkata Sai Surya Pratap Chowdary[*,1,a], SS. Asadi[1,b], C. Raveendra Reddy[2,c]

[1]Department of Civil Engineering, Vignan's Foundation for Science, Technology and Research (Deemed to be University), Vadlamudi-522213, India
[2]Department of S&H, NBKR Institute of Science and Technology (Autonomous), Gudali-524413, India

Article Info	Abstract
	A versatile concept in the field of Engineered Cementitious Composite (ECC) is Eco-friendly ECC. The materials and properties of specimens will influence the characteristics. In this present study, locally available fine aggregates (50% River sand + 50% M-Sand (16.3316^0 N, 80.3514^0 E)) and 2% PVA fibers-based Mix-1, local sand and sisal fibers based Mix-2 (1% sisal fibers + 1% PVA fibers) are considered. The flowability is slightly reduced from Mix-1 to Mix-2. All considered mixes showed good self-consolidation properties (Deformability factor (D.F.) <2.75 based on Li, 2008). For analysis of the mechanical characteristics, different specimens are considered. The compressive and flexural properties negligibly reduced by the size of specimens. But compressive strength moderately reduced by shape (cube to cylindrical specimens). The compressive ratio is between 1.45 to 1.6. The split tensile properties are moderately reduced with the size specimens. All these mechanical characteristics are slightly reduced by the usage of sisal fibres. To determine the durability properties, Rapid chloride penetration (RCPT) test conducted. However, these properties also negligibly influenced by the sisal fibres. It indicates that the sisal fibres can be used for the partial replacement of PVA fibres in the local sand-based mixes. To analyse this, SEM and XRD analysis conducted. Their performance also validated based on Roychand et al, 2016. The hydration of particles and arrangement of fibres are responsible for the significant performance of this Eco-friendly ECC.

1. Introduction

Engineered Cementitious Composite (ECC) is one of the enormous building composites. This is utilizing worldwide as an alternative to conventional concrete due to its tremendous performance [1, 2]. The characteristics of the composites, such as high strength, self-consolidation, crack resistance, etc., are mainly dependent on the properties of the materials [3, 4]. A high dosage of cement in the preparation increases the strength. But it may cause early-age cracks. So a suitable combination of cement with pozzolanic materials is required in the preparation of ECC [5, 6].

Past researchers have studied fly ash's influence on the cement dosage (F/C) and fine aggregates on the composite's performance. Li, 2008. [7] analyzed the influence of silica sand with an F/C ratio on the composite characteristics. The silica sand of 200μm grain size and F/C of 1.2 improved the self-consolidation, mechanical, and durability characteristics. But the economic conditions of silica sand are necessitating alternatives.

Sherir et al., 2018. [8] analysed the impact of mortar sand on the properties. The composite' flowability and durability were reduced with the usage of mortar sand, but it showed a negligible impact on the mechanical characteristics. The increased content of fly ash has negatively impacted the properties of the composite. It indicates that the properties of fine aggregates and F/C are considerable in the preparation. Apart from this, other materials also will influence the characteristics of the composite.

The crack propagation in this composite can arrest by using fibers, especially Polyvinyl alcohol (PVA) fibers. These bridge the cracks under heavy loads or seismic forces, but fibers' performance depends on the chemical ingredients and oiling agents. Li et al, 2002. [9] studied the impact of the proprietary oiling agents at different concentrations on the PVA fibers' performance. ECC's mechanical characteristics were optimized at 1.2% (weight ratio of oil to fiber) of oiling agents. At this, the debonding energy was also reduced. Fahad et al., 2019. [10] studied the influence of chemical ingredients such as alkyl ketone dimer (AKD), the copolymer of polyurethane, and acrylic epoxy-modified polysiloxane, etc. with oiling agents on the performance of fibers. The flexural characteristics were improved and the composite' debonding energy was reduced with these chemical ingredients with the oiling agents. Pakravan et al, 2015. [11] studied the influence of fibers' properties. For this, PVA fibers and Polypropylene (PE) fibers were considered. The Kidney shaped PVA fibers improved ductility with the combination of polypropylene fibers. Choi et al, 2012. [12] studied the influence of hybridization on performance. The PVA fibers were replaced with Polyethylene terephthalate (P.E.) at different proportions. This combination of fibres has improved performance and reduced construction costs. The usage of PVA fibres are responsible for the environmental problems. To reduce these problems, the usage of natural fibres is necessary. While analysing the test results, the properties of specimens also need to consider due to it may influence the properties. It is helpful to choose the type (shape and size) of elements (The strength may vary by properties) for construction purpose.

In this research work, the impact of specimens' properties and fibres such as sisal fibres and PVA fibres on the Manufactured sand-based mixes have been analysed. The experiments are planned based on future studies on structural components like Paver blocks, bricks, and slabs, etc. Specimens' properties and fibre types are essential factors in these elements. Very limited research done on natural fibres usage in this composite. To analyse its impact, especially sisal fibres at different properties of specimens is necessary for the comprehensive development of elements. It is responsible for the sustainable growth of developing countries like India, Bangladesh, Srilanka, Nepal, etc. In future, these elements can be supplied from Andhra Pradesh (16.3316^0 N, 80.3514^0 E) with affordable prices to different parts of India and other adjacent countries.

2. Experimental Program

In this present study, Fig. 1 (methodology) is considered to analyse the impact of the various factors (influence materials and properties of specimens) on the characteristics. The standard and supplementary materials were considered based on environmental and performance factors. For this, PVA fibres were replaced partially with Sisal fibres and locally available fine aggregates were used in place of Silica sand. The different size and shapes of specimens were considered to analyse the mechanical characteristics. Flowability and durability properties of the composite also determined. The microstructural analysis was conducted to analyse the influence of materials on these properties. Keeping all these into consideration, this research work was planned and executed to obtain Eco-friendly ECC. This methodology was step by step given below.

2.1. Materials

In this study, OPC-53 grade cement is used as per IS 12269-1987 [13]. Class-F fly ash was used to eliminate early-age cracks, according to ASTM 2012a [14]. Locally available River sand (RS) and M-Sand (MS) are used as an alternative to silica sand, as mentioned in Table 2 as per IS 383-2016 [15]. The chemical composition of materials in preparation was mentioned in the Table 1. PVA fibres of 12mm in length and 39μm were used with 0.2% oiling agents to reduce debonding energy. Sisal fibres are used as supplementary material for PVA fibres. These fibres are compatible with the length of PVA fibres. Turbopol CEA50 superplasticizer was used according to ASTM C494 [16]. Taping water in laboratory used. The fibers such as PVA and sisal fibers used in this investigation was shown in the following Fig.4. and Fig.5.

Table 1. Chemical composition

Chemical composition (%)	Cement	Fly ash	RS	MS
Cao	64.35	2.78	0.61	3.45
Sio_2	20.23	59.07	88.75	70.13
Al_2o_3	4.67	25.63	2.92	15.75
Fe_2o_3	3.98	4.57	3.27	2.63
Tio_2	2.56	0.83	0.46	0.25
Mgo	0.45	1.22	0.21	3.67
others	3.76	5.9	4.51	4.15

Table 2. Sieve analysis of local materials

IS sieve size (mm)	Weight retained		Remarks
	RS	MS	
10	0	0	
4.75	17	16	
2.36	176	203	
1.18	181	175	Indian Zone-II category
0.6	256	253	
0.3	189	176	
0.15	152	147	

Fig. 2, and Fig. 4 illustrate the unoiled PVA fibers and Oiled fibers, respectively. The oiling agents applied about 0.2% on the surface of PVA fibers to reduce debonding energy. Initially, these fibers are taken from the local supplied company with a length of 12mm. These fibers are responsible for environmental problems such as toxicity, and disposal problems. To avoid this, sisal fibers are considered in this study. As mentioned in Fig.5, Sisal fibers can collect from the sisal plant (Fig. 3). These are natural fibers that consist of cellulose and moisture. So, need to treat before mixing with other materials in ECC [18,19]. Alkaline treatment is one of the acceptable techniques for treating natural fibers. In this method, fibers are cleaned and dipped in a 6% concentration of NaOH solution for 30min. These are neutralized with 2% of HCL before being dried for 3h at 80°C in the oven based on past researchers [19]. After that, fibers are cut in 12mm lengths for suitability with PVA fibers that do not affect the composite's mixing process.
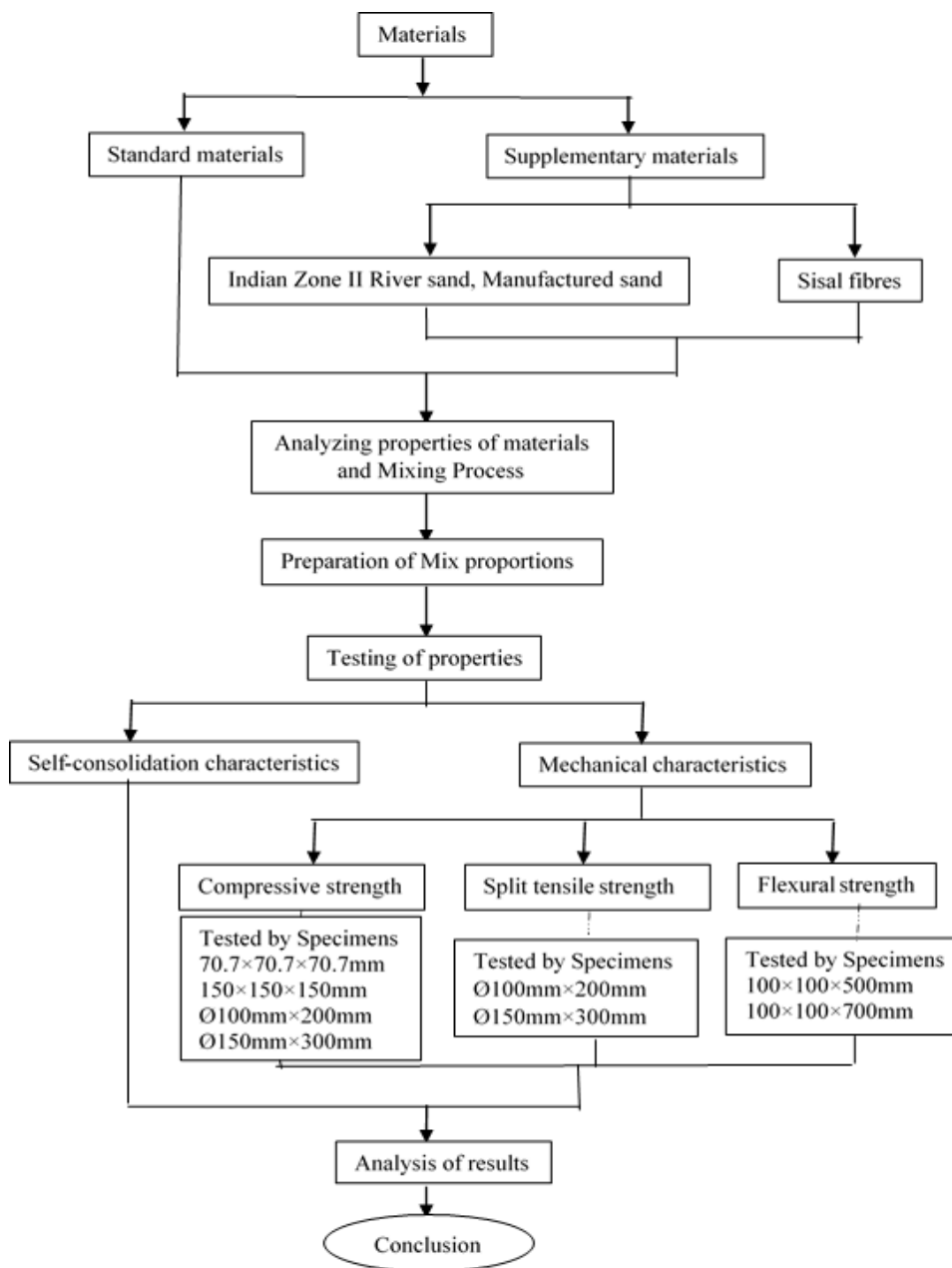
Fig. 1 Methodology with various factors

Fig. 2 Untreated PVA fibres

Fig. 3 Sisal Plant [17]

Fig. 4 Treated (or) Oiled PVA fibres

Fig. 5 Treated Sisal fibers

2.2. Mixing Process

This is one of the critical factors that will decide the performance. In this study, the mixing process was considered based on past researchers [20,21] and our experimental studies. A pan mixer with 120L capacity and 1440rpm was used to mix the materials at a constant speed. Initially, cement, fly ash, and fine aggregates are mixed for 3min. For this mix, PVA fibers are added and mixed for 2min. Later, the Turbopol CEA50 and water are added and blended for 3min. This mixing process was used for the preparation of samples to analyze the characteristics of ECC.

2.3. Mix proportions

The mixing proportions mentioned in the Table 3 were considered in this study to determine the impact of the specimen's properties, hybridization of fibers, and locally available fine aggregates. These mixtures are the local sand based (50% of River sand + 50% of M-sand) and sisal fiber (1% PVA+1% Sisal fibers) based mixes. The specimens of cube (70.7×70.7×70.7mm, 150×150×150mm), cylindrical (Ø150mm×300mm, Ø100mm×200mm), and prism specimens of 100mm×100mm×500mm, 100mm×100mm×700mm were prepared with that mix proportions. The PVA fibres replaced by Sisal fibers based on volume.

Table 3. Mix proportions

Mix	Ingredients (kg/m³)									
	CE	F	water	River sand	M-sand	PVA	SS	PCE	F/C	w/b
1	483	676	320	213	214	26	-	4.55	1.4	0.27
2	483	676	320	213	214	13	13	4.55	1.4	0.27

PVA: Polyvinyl alcohol, SS: Sisal fibres, CE: Cement, F: fly ash, w/b: water/ binder, PCE: Polycarboxylate ether

2.4. Curing of Specimens

Water curing under air submersion was preferred in this study based on past research investigations. Zhu et al. [22] analyzed the impact of different curing conditions such as water curing under air submersion and room-air storage on the hardening characteristics of ECC. These characteristics were improved with the water curing under air submersion compared to the room-air storage. This indicates that the appropriate curing conditions are water curing under air submersion. After 28 days of curing, all the specimens are placed in a room for 1 to 2 days before testing to analyze the characteristics of ECC.

3. Experimental Tests:

3.1. Flowability and Self-consolidation Test

The fresh properties were determined by the T_{50} slump cone test, as per ASTM 1611 [23]. For this, a slump cone was placed on the steel plate of 900mm×900mm. After pouring of composite into a slump cone, allowed to spread on the steel plate. The deformability factor (DF) for all these mixtures was measured based on the following formulae mentioned in Eq (1), and that should be less than 2.75

$$DF = \frac{(D1 - D0)}{D0} \tag{1}$$

where D_1=Average diameter of the two orthogonal, D_0= slump cone's bottom diameter

3.2. Hardening Properties

3.2.1. Compressive Test

The compressive characteristics were determined under a compression testing machine with a 140kg/cm²/min rate of loading as per IS 516-2013 [24]. For this, cubes 70.7mm×70.7mm×70.7mm, and 150mm×150mm×150mm and cylindrical specimens of Ø100mm×200mm, Ø150mm×300mm were used. These two cube specimens are considered to determine the impact of the cube's size on the compressive characteristics of the composite. The two sizes of cylindrical specimens were used to assess the impact of the cylinder's size on the composite. From this, the compressive ratio (compressive strength of cube to cylinder) was also determined. The compressive setup for this study was shown in Fig. 6(a), Fig. 6(b).

3.2.2. Split Tensile Test

The split tensile properties of the composite mixes were determined under the split tensile testing machine with the 1.2N/mm²/min as per IS 5816-1999 [25]. For this, cylindrical specimens of Ø100mm×200mm, and Ø150mm×300mm were used. These two cylindrical specimens are considered to determine the impact of the specimen's size on the split tensile properties. The split tensile test setup for this analysis was shown in Fig. 6(C).

3.2.3. Flexural Test

The flexural properties were determined under the flexural testing machine as per IS 516-1959 [26]. For this, prism specimens of 70.7mm×70.7mm×70.7mm 150mm× 150mm×150mm were used. These two prism specimens are considered to determine the impact of the specimen's size on the flexural properties of the ECC. The flexural test setup for this analysis was shown in Fig. 7.

Cube specimen
70.7×70.7×70.7mm
150×150×150mm

(a) Schematic Compressive test setup-cubes

Cylindrical specimen
Ø100mm×200mm
Ø150mm×300mm

Cylindrical specimen
Ø100mm×200mm
Ø150mm×300mm

(b) Schematic Compressive test   (c) Schematic Split tensile test setup-cylinders
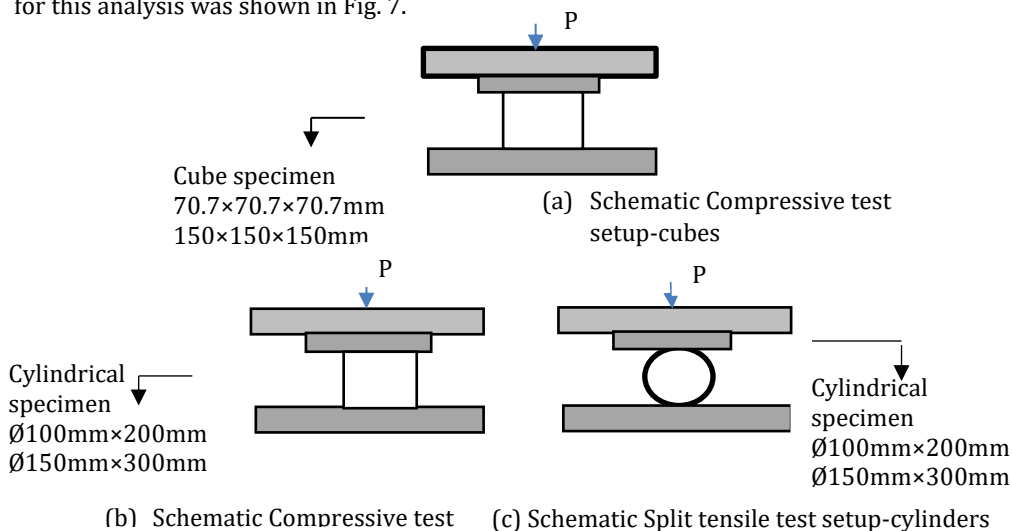
Fig. 6 Specimens under compression and split-tensile test

Four-point loading

Prism specimen
100×100×500mm
100×100×700mm
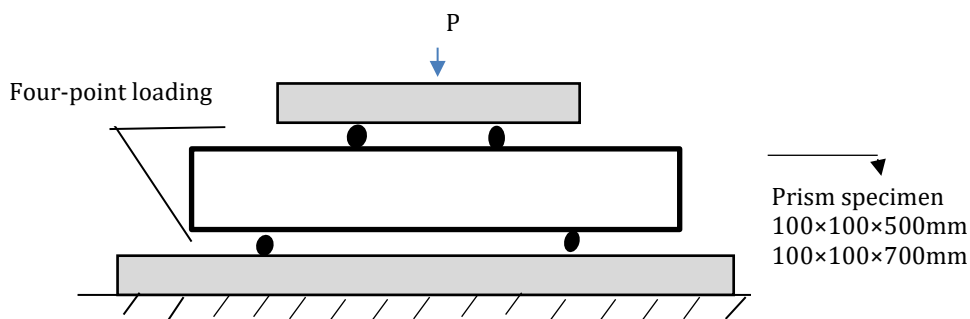
Fig. 7 Schematic representation of specimens under Flexural test

Where, P=Specimens (cubes, cylinder, prisms) under loading

Fig. 6 represents the schematic setup of compression and split tensile test. The cube specimens of 70.7mm×70.7mm×70.7mm and 150mm×150mm×150mm and cylindrical specimens of Ø100mm×200mm and Ø150mm×300mm were considered for compression test. These cylindrical specimens were also used for analyzing split tensile characteristics. Fig. 7 represents the schematic setup of the flexural test. For this, prism specimens of 100mm×100mm×500mm and 100mm×100mm×700mm were considered. The four-point loading was applied to these specimens to study the characteristics of ECC. All these test setups were followed and applied loading conditions were based on Indian standards.

3.3. Durability Test

RCPT test was conducted in this study to determine the durability of ECC. For this, Ø100mm×50mm size disc specimens were used to determine these characteristics in terms of chloride ion penetration as per ASTMC1202 [27]. The NaOH and NaCl solutions are poured into the RCPT reservoirs to measure the intensity of chloride ions. The schematic RCPT test setup is mentioned in Fig. 8.
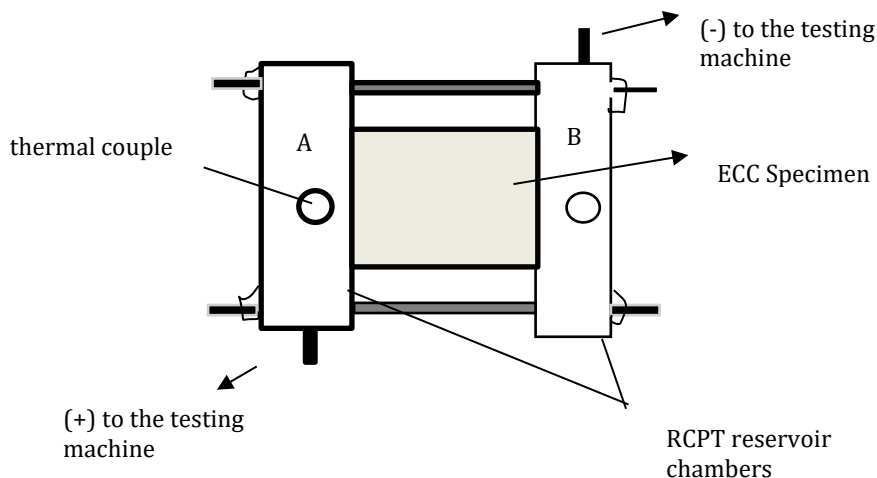
Fig. 8 RCPT schematic test setup

Fig. 8 illustrates the schematic test setup of the RCPT. It has an ECC specimen between the two chambers, and silica sealant was used to avoid any gaps between them. Chambers A and B are the reservoirs that contain 3% NaOH solution and 3%NaCl solutions, respectively. These solutions are poured into the chambers to measure the intensity of chloride ion penetration. This indicates the durability of the composite mixtures.

4. Test Results and Discussions

4.1. Flowability and Self-Consolidation Characteristics

The fresh properties of the composite were measured with the T_{50} slump cone test. These results for the local sand (50% of River sand+50% of M-Sand) based mixes and sisal fibre-based (1% of PVA fibres+1% of sisal fibres) are mentioned in the Table 4. The sisal fiber based mixes also showed good self-consolidation (S.C.) characteristics. The D.F. <2.75 indicates good S.C. (based on the Li, 2008).

Table 4. Fresh properties of ECC mixtures

Mix id	Mix-1	Mix-2
Slump flow	510	505
T_{50} (sec)	2.52	2.55
D.F.	1.55	1.525
S.C.	Good	Good

Where T50(sec) indicates flow time, D.F. indicates Deformability factor, S.C. indicates self-consolidation. For good self-consolidation characteristics, the deformability factor <2.75

The composite's flowability was slightly reduced due to the addition of sisal fibres, which were treated by alkaline treatment. The flow time of the composite is increased with the replacement of sisal fibres from mix-1 to mix-2. But all the mixtures showed good-self consolidation properties.

4.2. Mechanical Characteristics

4.2.1. Compressive Characteristics

The compressive properties were determined by cube specimens of 70.7mm×70.7mm×70.7mm and 150mm×150mm×150mm, cylindrical specimens of Ø100mm×200mm and Ø150mm×300mm. These test results were shown in Fig.9 to Fig.13. These compressive characteristics were reduced with the size of specimens. The compressive strength of the Mix-1 local sand based mixes is reduced by 0.478% from the 70.7mm×70.7mm×70.7mm specimen to 150mm×150mm×150mm specimens. This is a very marginal decrease in the strength. Mix-1's compressive characteristics were also marginally reduced from cylindrical specimens Ø100mm×200mm to Ø150mm×300mm. The compressive strength for the Mix-2 (1% PVA fibres + 1% Sisal fibres) mixes is reduced marginally from 70.7mm×70.7mm×70.7mm specimen to 150mm×150mm×150mm specimens. Mix-1's compressive characteristics were also reduced marginally from cylindrical specimens Ø100mm×200mm to Ø150mm×300mm. It indicates that the impact of size of the specimens on the characteristics is negligible. So small-size specimens such as the cube, and cylindrical specimens can be used to analyse the compressive characteristics of ECC. But the shape of specimens is needed to consider for the study of composite' compressive strength. These characteristics are reduced by 30-35% from the cube specimens (70.7mm×70.7mm×70.7mm, 150mm× 150mm×150mm) to cylindrical specimens (Ø100mm×200mm, Ø150mm×300mm). The compressive ratio (compressive strength of cube to compressive strength of cylinder) based on these specimens for these ECC mixtures is between 1.45 to 1.6. These cube specimens are considerable in the design of beams and cylindrical specimens are significant for columns.
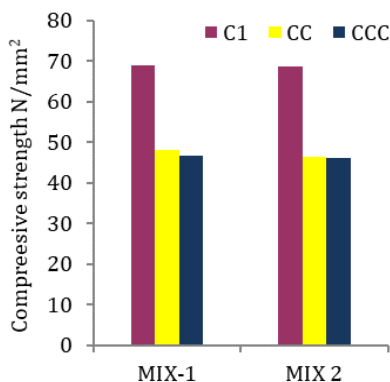
Fig. 9 Compressive strength of (C1 with CC, CCC)
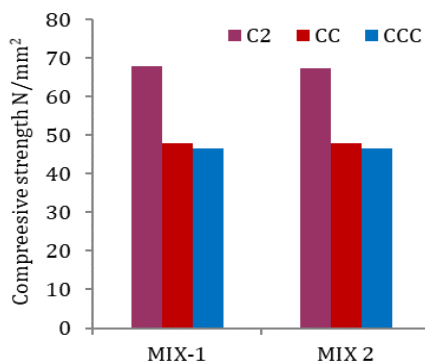
Fig. 10 Compressive strength of (C2 with CC, CCC)

Where C1 denotes 70.7×70.7×70.7mm, C2 denotes150×150×150mm, CC denotes Ø100mm×200mm, CCC denotes Ø150mm×300mm

Fig.9 represents the impact of cube specimen 70.7mm×70.7mm×70.7mm and cylindrical specimens Ø100mm×200mm, Ø150mm×300mm on the characteristics of Mix-1,2. Fig.10 represents the impact of cube specimens 150mm×150mm×150mm and cylindrical specimens Ø100mm×200mm, Ø150mm×300mm on the characteristics of Mix-1,2. The

compressive characteristics are slightly impacted by the size of specimens. But are highly influenced by the specimens 'shape.
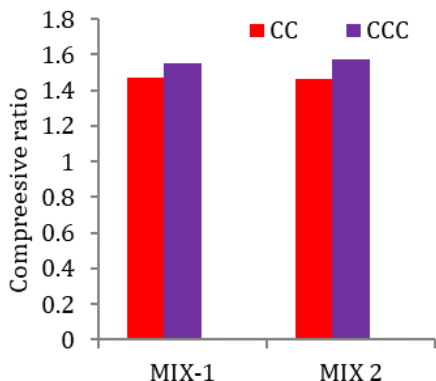
Fig. 11 Compressive ratio (C1 with CC, CCC)
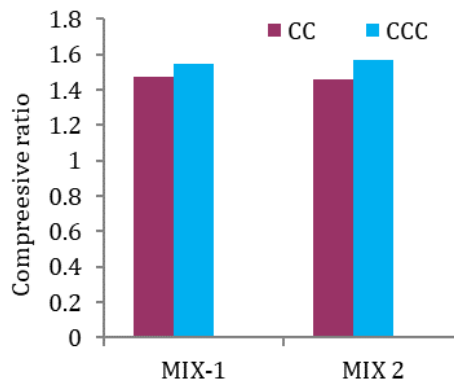
Fig. 12 Compressive ratio (C2 with CC, CCC)

Fig. 11 and Fig. 12 illustrates the compressive ratio of the cube specimens to cylindrical specimens. These compressive ratios of Mix-1 and Mix-2 are lies between 1.45 to 1.6. The compressive ratio equation mentioned below can be implemented to analyse the impact of hybridization of fibres, specimens' properties, and local fine aggregates on the compressive characteristics of ECC.

$$A = B(x) + C \qquad (2)$$

A= Cube's compressive strength, B=cylindrical compressive strength, X=compressive ratio =1.45 to 1.6, C=Compressive strength (1 to 3N/mm^2) due to miscellaneous factors,

For this experimental analysis C=0
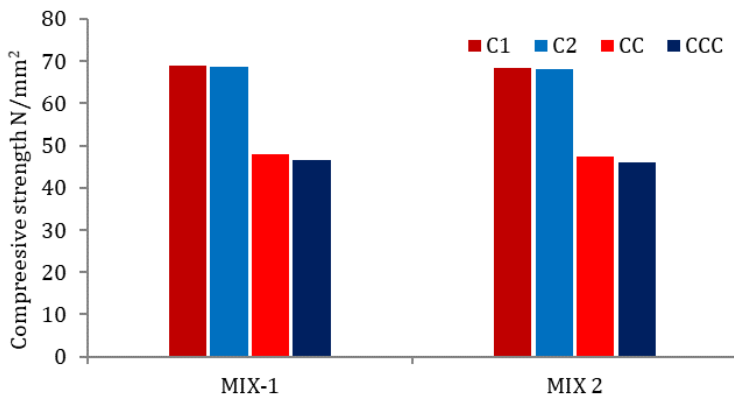
Fig. 13 Compressive characteristics of ECC mixtures

Fig.13 represents the impact of hybridization (sisal fibres and PVA fibres), locally available fine aggregates (river sand, M-sand), and specimens' properties (shape, size) on the compressive characteristics of ECC. In this, the two cube (70.7mm×70.7mm×70.7mm, 150mm×150mm×150mm) and cylindrical Ø100mm×200mm, Ø150mm×300mm)

compressive strengths for mixes were mentioned. It showed that small-sized cubes and cylindrical specimens can be considered for analysing the compressive characteristics but the shape of specimens and compressive ratio needed to be considered.

4.2.2. Split tensile characteristics

The split tensile properties were determined by the cylindrical specimens of Ø100mm×200mm and Ø150mm×300mm. These test results were shown in Fig.14. These split tensile characteristics were reduced by the size. The split tensile characteristics of Mix-1 were reduced by 7.41% from the cylindrical specimens Ø100mm×200mm to Ø150mm×300mm. The split tensile characteristics of Mix-2 were reduced by 7.69 % from the cylindrical specimens of Ø100mm×200mm to Ø150mm×300mm. These characteristics are marginally reduced from Mix-1 to Mix-2. It indicates that the size of cylindrical specimens can highly influence the split tensile characteristics.
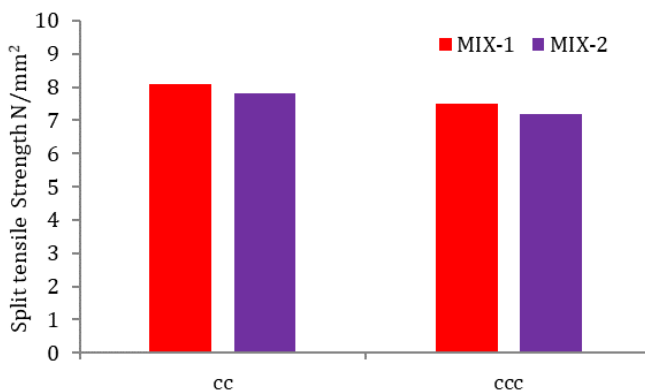
Fig. 14 Split characteristics of ECC mixtures

Fig.14 represents the influence of hybridization (sisal fibres and PVA fibres), locally available fine aggregates (river sand, M-sand), and specimens' properties (shape, size) on the split tensile characteristics of ECC. In this, the cylindrical Ø100mm×200mm Ø150mm×300mm) split tensile strengths for mixes Mix-1 and Mix-2 were mentioned. This showed that appropriate size cylindrical specimens (Ø150mm×300mm) could be considered for analyzing the split tensile properties.

4.2.3. Flexural Characteristics

The flexural properties were determined by the prism specimens of 100mm×100mm×500mm, 100mm×100mm×700mm. These test results were shown in Fig.15. These flexural characteristics were reduced by the size. The flexural properties of Mix-1 were reduced by 5.21% from the prism specimens 100mm×100mm×500mm, to 100mm×100mm×700mm. The flexural characteristics of Mix-2 were reduced by 5.09% from the prism specimens 100mm×100mm×500mm to 100mm×100mm×700mm. It indicates that the size of prismatic specimens negligibly impacted the flexural characteristics.

Based on this, the relation between the split tensile and flexural characteristics of ECC mixtures was mentioned in Eq (3).

$$Ff = Fs(y) + L \tag{3}$$

Where F_f=Flexural characteristics of ECC, F_s= Split tensile characteristics of ECC, Y= Factor of split tensile characteristics to flexural characteristics=1.5 to 1.7, L= Flexural strength (0.1to 0.4N/mm^2) due to miscellaneous factors, for this study L=0
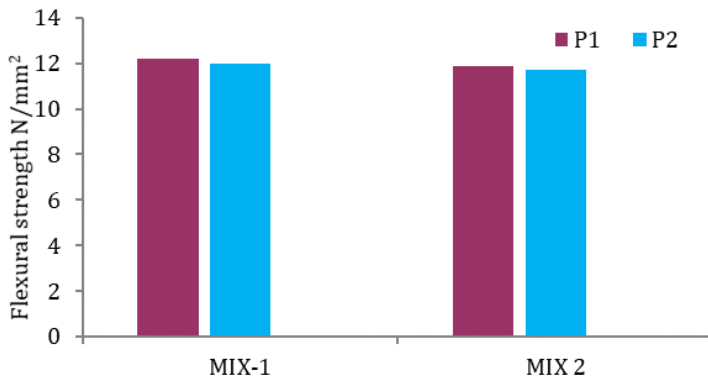
Fig. 15 Flexural characteristics of ECC mixtures

Where P1 denotes prismatic specimen-100mm×100mm×500mm, P2 denotes prismatic specimen-100mm×100mm×700mm

4.3. Durability Characteristics

To analyze the durability characteristics of ECC mixtures, the RCPT test was conducted. These characteristics are measured as the intensity of chloride ion penetration. For this, Ø100×50mm size specimens were cast and placed in the RCPT apparatus to analyze the impact of sisal fibres on the local sand (50% of river sand + 50% of M-sand) based mixes. These mixtures showed that negligible increase in chloride ion penetration, the microstructure (SEM and XRD) of these mixtures was shown in Fig.16 to Fig.18. The microstructure of these mixes is almost similar and densified. So, sisal fibres can be used with partial replacement of PVA fibres in the local sand (river sand + M-sand) based composite mixes.
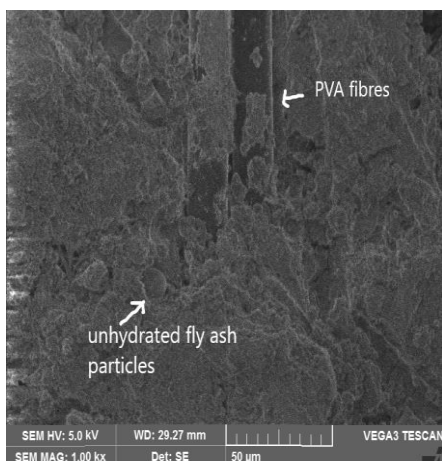
Fig. 16 SEM image of Mix-1
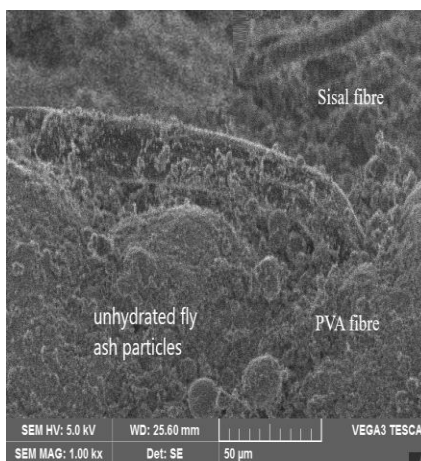
Fig.17 SEM image of Mix-2

The hydration of materials and arrangement of fibres and its properties are responsible for slight difference in the portlandite (P), quartz (Q) content (unhydrated particles) in the matrix of composite. It is responsible for the slight difference in durability. This kind of

phenomenon and XRD pattern is validated with the (Roychand et al., 2016) past researcher study [28]. The arrangement of fibres and hydration of particles (formation of C-S-H and CH gels) responsible for performance. Based on these results, sisal fibres can use an alternative to PVA fibres for prepare Eco-friendly ECC.
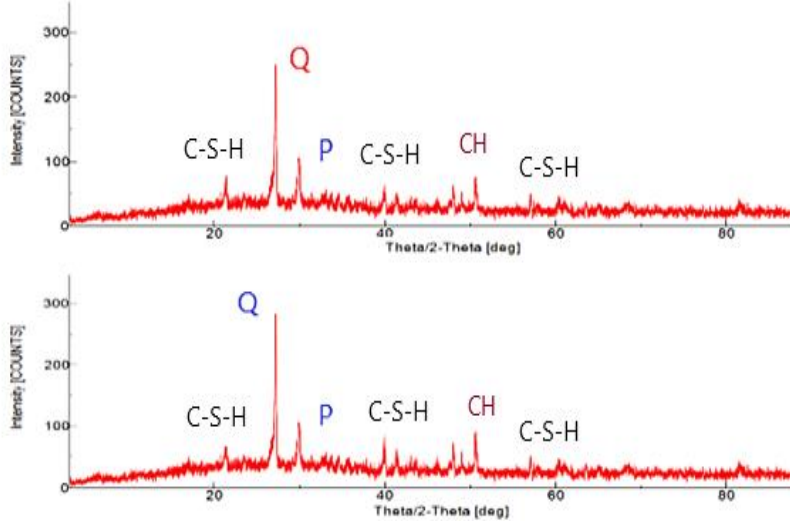
Fig.18 XRD of ECC-Mixes (Top Mix-1, Bottom Mix-2)

5. Conclusions

Based on the experimental analysis on the performance of Synthetic fibres (PVA) and natural (Sisal) fibres-based composites, the following conclusions are given.

- The characteristics of ECC-Mixes mainly depends on the properties of specimens and materials. To analyse the impact of sisal fibres on the characteristics, different specimens are considered. The cube specimens of (150mm×150mm×150mm and 70.7mm×70.7mm×70.7mm), cylindrical specimens (Ø100×200mm and Ø150×300mm), prism specimens (100mm×100mm×500mm and 100mm×100mm×700mm) considered.
- The compressive characteristics were slightly decreased by the increased size of specimens. But highly influenced by the shape of specimens. These characteristics were decreased by 30-35% from cube specimens to cylindrical specimens. The compressive ratio (compressive strength of cube specimens to cylindrical specimens) of these mixes is between 1.45 to 1.6.
- Specimens' size moderately influenced the split tensile properties. These characteristics were reduced by 7-10% from the cylindrical specimens of Ø100×200mm to Ø150×300mm. So appropriate size of cylindrical specimen is Ø150×300mm for analysing the split tensile characteristics. At this, the minimum required strength is determined. The flexural characteristics were slightly influenced by the size of the specimens.
- But these mechanical characteristics were slightly reduced with sisal content (or) dosage of sisal fibres. Shape of specimens highly influenced the compressive characteristics compared to their size. The flowability slightly reduced by usage of sisal fibres compared to PVA fibres based mixes. All these considered mixes showed good self-consolidation characteristics (Deformability factor (D.F.) <2.75 based Li, 2008).

- However, durability characteristics are also slightly reduced from Mix-1 to Mix-2. These test results indicate that the sisal fibres can use an alternative to traditional PVA fibres. The performance of these mixes is validated with the past researcher (Roychand et al, 2016) study. By observing Scanning Electron Microscopy (SEM) and X-ray diffraction analysis (XRD) results, the arrangement of fibres and Hydration of particles are responsible for these characteristics.

Acknowledgement

Abbreviations:

ECC	Engineered Cementitious Composite
M-Sand	Manufactured sand
PVA	Poly Vinyl alcohol
D.F.	Deformability factor
RCPT	Rapid chloride penetration test
SEM	Scanning Electron Microscopy
XRD	X-ray diffraction Analysis

References

[1] Elmoaty AEMA, Morsy AM, Harraz AB. Effect of Fiber Type and Volume Fraction on Fiber Reinforced Concrete and Engineered Cementitious Composite Mechanical Properties. Buildings. 2022;12(12); 2108. https://doi.org/10.3390/buildings12122108

[2] Zhang P, Hu J, Yu J, Weng Y, Zhang D. Enhancing mechanical properties of engineering cementitious composite by defoamer. Construction and Building Materials. 2022; 339; 127670. https://doi.org/10.1016/j.conbuildmat.2022.127670

[3] Baviskar S, Dwivedi A, Patil H. Analysis and development of the Composite Sustainable Condition Index for elevated service reservoir (ESR) by DER method. Journal of Building Pathology and Rehabilitation. 2002; 7(1). https://doi.org/10.1007/s41024-022-00177-y

[4] Patil H, Dwivedi A. Impact of Nano ZnO particles on the characteristics of the cement mortar. Innovative. Infrastructure. Solutions. 2021; 6; 222. https://doi.org/10.1007/s41062-021-00588-9

[5] Ali M, Soliman A, Nehdi M. Hybrid-fiber reinforced engineered cementitious composite under tensile and impact loading. Materials & Design. 2017; 117; 139–149. https://doi.org/10.1016/j.matdes.2016.12.047

[6] Wu HL, Yu J, Zhang D, Zheng JX, Li VC. Effect of morphological parameters of natural sand on mechanical properties of engineered cementitious composites. Cement and Concrete Composites. 2019;100;108–119. https://doi.org/10.1016/j.cemconcomp.2019.04.007

[7] Li VC. Engineered Cementitious Composites (ECC) - Material, Structural, and Durability Performance. Concrete Construction Engineering Handbook. CRC Press. 2008.

[8] Sherir MA, Hossain KM, Lachemi M. Fresh state, mechanical & durability properties of strain hardening cementitious composite produced with locally available aggregates and high volume of fly ash. Construction and Building Materials. 2018; 189;253–264. https://doi.org/10.1016/j.conbuildmat.2018.08.204

[9] Li VC, Wu C, Wang S, Ogawa A, Saito T. Interface Tailoring for Strain-Hardening Polyvinyl Alcohol-Engineered Cementitious Composite (PVA-ECC). ACI Materials Journal, 2002;99(5). https://doi.org/10.14359/12325

[10] Fahad AM, Mingxue W, Jiayong C, Huapeng Z. Study on PVA fibre Surface modification for strain-hardening cementitious composites (PVA-SHCC). Construction and Building materials.2019;197;107-116. https://doi.org/10.1016/j.conbuildmat.2018.11.072

[11] Pakravan H, Jamshidi M, Latifi M. The effect of hybridization and geometry of polypropylene fibres on engineered cementitious composites reinforced by polyvinyl alcohol fibres. Journal of Composite Materials. 2015; 50(8); 1007–1020. https://doi.org/10.1177/0021998315586078

[12] Choi WC, Yun HD, Kang JW, Kim SW. Development of recycled strain-hardening cement-based composite (SHCC) for sustainable infrastructures. Composites Part B: Engineering.2012;43(2);627–635. https://doi.org/10.1016/j.compositesb.2011.11.060

[13] IS: 12269: 1987 ''Specifications for 53 grade Ordinary Portland Cement'', Bureau of Indian Standards, New Delhi.

[14] ASTM: 2012a. "Standard specifications for coal fly ash and raw or calcinated natural puzzolan for use in concrete'', ASTMC618, West Conshohocken.

[15] IS: 383 :2016 ''Specifications for Coarse and Fine aggregates from Natural sources for Concrete'', Bureau of Indian Standards, New Delhi.

[16] ASTM: 2013 ''Standard specifications for chemical admixtures for concrete'', ASTM C494/C494M, West Conshohocken.

[17] Y Li, Shen YO. The use of sisal and henequen fibres as reinforcements in composites. Biofibre Reinforcements in Composite Materials 2015;6;165-210.

[18] Kumre A, Rana RS, Purohit R. A Review on mechanical property of sisal glass fibre reinforced polymer composites. Materials Today: proceedings. 2017;4;3466–3476.

[19] Yusof FM, Wahab NA, Rahman NLA, Kalam A, Jumahat A, Taib CFM. Properties of treated bamboo fiber reinforced tapioca starch biodegradable composite. Materials Today: Proceedings. 2019; 16; 2367–2373. https://doi.org/10.1016/j.matpr.2019.06.140

[20] Zhou J, Qian S, Sierra Beltran M G, Ye G, Breugel K, Li VC. Development of engineered cementitious composites with limestone powder and blast furnace slag. Materials and Structures. 2009;43(6);803–814. https://doi.org/10.1617/s11527-009-9549-0

[21] Ismail MK, Hassan AAA, Lachemi M. Performance of Self-Consolidating Engineered Cementitious Composite under Drop-Weight Impact Loading. Journal of Materials in Civil Engineering. 2019;31(3). https://doi.org/10.1061/(asce)mt.1943-5533.0002619

[22] Zhu Y, Zhang Z, Yao Y, Guan X. Effect of Water-Curing Time on the Mechanical Properties of Engineered Cementitious Composites. Journal of materials in civil engineering, 2016;28(11);1-6.

[23] ASTM C :1611 "Standard test Method for Slump Flow of Self-Consolidating Concrete'', Am Soc Test Mater, West Conshohocken, PA, USA, 2014;1-15.

[24] IS :516 :2013 ''Method of tests for strength of concrete'', Bureau of Indian Standards, New Delhi.

[25] IS: 5816: 1999 ''Specifications for splitting tensile strength of concrete-method of the test'', Bureau of Indian Standards, New Delhi.

[26] IS: 516: 1959 ''Method of tests for strength of concrete'', Bureau of Indian Standards, New Delhi.

[27] ASTM C1202: 2010 ''Standard specification for rapid chloride penetrable test ASTM'', West Conshohocken.

[28] Roychand R, Silva SD, Law D, Setunge S. Micro and Nano Engineered High Volume Ultrafine Fly Ash Cement Composite with and without Additives. International Journal of Concrete Structures and Materials. 2016; 10(1); 113–124. https://doi.org/10.1007/s40069-015-0122-7

Research Article

Optimized properties of concrete at various exposure conditions

Mahesh Patil[*1,a], Shailendrakumar Dubey[2,b], Hiteshkumar Patil[3,c]

[1]Kavayitri Bahinabai Chaudhari North Maharashtra University, Jalgaon-425001 (MS), India
[2]Civil Engineering Department at SSVPS BSD COE, Dhule (MS)-424005, India
[3]The Shirpur Education Society's, Shirpur R. C. Patel Institute of Technology, India, district Dhule- 425405 (MS) India

Article Info	Abstract
	This research explores the testing of M40 grade concrete results under various exposure scenarios. The characteristics of concrete are investigated at the plastic and hardening stages. The characteristics of concrete at both stages vary depending on the exposure circumstances. The rheological qualities of the concrete as well as its strength characteristics under various exposure situations are investigated. It has been noted that as exposure conditions deteriorate, cement content gradually rises while W/C and water content decrease. This research is more beneficial for predicting the diverse properties of concrete under various exposure conditions. This will also aid in reducing losses incurred during construction and structural decay. During the investigation, the correlation matrix and Principal Component Analysis (PCA) are used to evaluate the interrelationship of the experimental variables, which yields more accurate results and predictions of the various characteristics of concrete. A Multivariate Linear Regression (MLR) model developed for the prediction of concrete qualities in the plastic and hardens stages. The MLR model found to be best matched to experimental data, and its forecast is correct. The Response Surface Method (RSM) used to find the optimal properties of the concrete in all types of exposure scenarios.

Nomenclature

Cement	C	Compressive Strength (MPa)	CS
Sand	S	Split Tensile Strength	SPT
Water	W	Flexural Strength	FS
Water Cement Ratio	W/C	Compaction Factor	CF
Principle Component Analysis	PCA	Setting time test	ST
Multiple Linear Regression	MLR	Fine Aggregate	FA
Response Surface Regression Method	RSR	Coarse Aggregate	CA
Water Cement Ratio	W/C	Admixture	ADM

1. Introduction

Concrete serves as the most adaptable building material on the planet. It has the title of "biggest man-made substance" with an average per capita usage exceeding 2 kg[1,2]. Concrete is the preferred material for a wide range of uses including buildings, bridge, roadway pavement, industrial structures, liquid storage structures, retaining structures and so on. Concrete's well-known characteristics such as availability of ingredients, acceptable technical qualities for a wide range of structural applications, flexibility,

diversity, relative low cost and so on are credited with this feat. Furthermore, when compared to other building materials, concrete has an outstanding ecological characteristic. With the on-going increase in infrastructure and residential building, particularly in emerging Asia, Africa, and South America, the demand of cement and concrete is increasing and it is expected to rise further [3,4]. In recent times, the concrete building industry in India has grown significantly. Cement output in the country has more than doubled in the last 12 years, rising from 45.25 million tonnes in 1989-90 (the start of the decontrol era) to 215 million tonnes produced in 2019-20. India is now the second-biggest cement manufacturer behind China, which is a commendable feat [5, 6].

The exposed circumstances [7–10] determines the structure's durability requirements, choice of materials, proportion, design and construction. As a result, if the exposure class is chosen correctly, it will provide great durability of concrete buildings, reducing routine maintenance and costs. The durability of concrete is affected by factors such as relative humidity, quality of raw material, water to cement ratio, aggregate to cement ratio, coarse aggregate to fine aggregate ratio, concrete age, concrete compaction and temperature. As per IS 456:2000[11], various exposure circumstances are classified according to their impact as follows.

a) Mild exposure: Concrete surfaces protected from the elements or extreme conditions, with the exception of coastal areas.

b) Moderate exposure: Concrete exposed to condensation and rain, concrete submerged in water continually, concrete in contact with or buried beneath non-aggressive soil/ground water, and concrete surfaces shielded from saturated salt air in coastal locations.

c) Severe exposure: Concrete exposed to coastal region, concrete immersed completely in saltwater, concrete surfaces subjected to severe rain, alternating absorbing and drying or frequent freezing while wet.

d) Very Severe exposure: Concrete in touch with or buried in aggressive subsoil/ground water; wet concrete surfaces exposed to saltwater spray, toxic gasses, or high freezing weather.

e) Extreme exposure: Tidal zone surfaces; members in direct touch with liquid/solid hostile substances.

The testing of M40 grade concrete under various exposure situations is explored in this study. Investigations on the properties of concrete at the plastic and hardening stages are conducted. Based on the exposure conditions, concrete's properties change at both stages. It is researched how the concrete behaves rheologically and how strong it is in different exposure scenarios. It has been observed that cement content steadily increases while W/C and water content decrease when exposure circumstances intensify. This study is more useful for forecasting concrete's varied properties under various exposure scenarios. This will help to minimize damages from construction and structural deterioration. The research uses the correlation matrix and Principal Component Analysis (PCA) to assess how the experimental variables interact, producing more precise results and predictions of the different properties of concrete. For the purpose of predicting concrete properties during the plastic and hardening phases, a Multivariate Linear Regression (MLR) model is also being developed. The MLR model's prediction is accurate and it best matches the experimental data. In all kinds of exposure circumstances, the Response Surface Method (RSM) is also utilized to identify the concrete's ideal property because of its high coefficient of determination. The RSM provides the best match to experimental data and makes reliable predictions (R^2).

Main objectives of this research to scrutinize behaviour, rheological properties and strength characteristics of concrete under diverse environmental exposure conditions. Novelty of this experimental work is introduction of statistical tools Correlation Matrix, PCA, MLR and RSR for optimization purpose in construction industry.

2. Methodology

This research investigates the testing of M40 grade concrete under various exposure scenarios. It provides a good understanding on the influence of environmental exposure circumstances on concrete strength. Environmental exposure circumstances are unavoidable but its bad impact can be reduced. Research is done on the characteristics of concrete during its plastic and hardening stages. The characteristics of concrete alter at both stages depending on the exposure circumstances. This research may be helpful for the construction industry in future for optimization purpose. Research has been done on the rheological behaviour of concrete and its strength characteristics under various exposure conditions. When exposure conditions get worse, it has been observed that cement content progressively rises while W/C and water content fall. This study is more helpful for predicting the various properties of concrete under different exposure scenarios. It can be helpful in reduction of construction-related losses and structural deterioration damages. Figure 1 shows the research outline of the work carried out during the work. During the current experimental study, mathematical models like correlation, PCA, MLR and RSM established. These provide the most accurate predictions, best matched to the experimental data. The RSM models optimized the concrete properties in plastic and harden stage and also predict the accurate results.
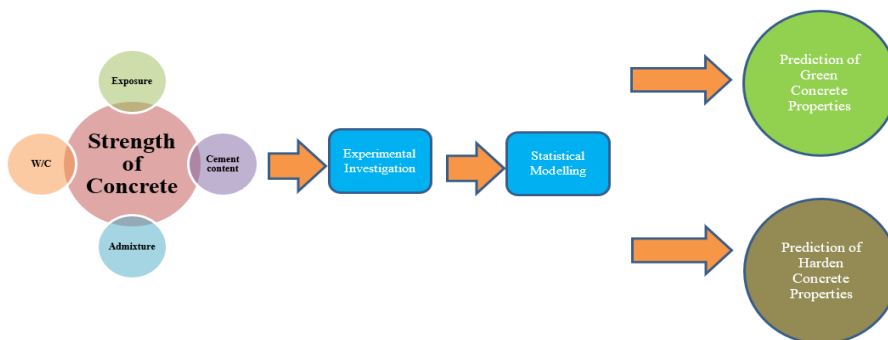
Fig. 1 Research Outline

3. Materials and Proportions

PPC cement manufactured by Ambuja Company in accordance with IS 1489-part 1:1991 [12] was used for the experiment. The detailed physical characteristics of the cement are shown in Table 1 (A). Table 1 (B) displays the characteristics of fine and coarse aggregates, which are in accordance with IS 383:2016[13]. Super plasticizer utilized to make the concrete more workable without compromising its strength or addition of excess water. The super plasticizers used was a high range water reducing Admixture sold by Fosroc under the trade name Auramix 200. Table 1 (C) displays characteristics of chemical Admixture (Superplasticizer) Auramix 200. Vibrating table utilized to compress freshly mixed concrete for one minute time period. 56 mix proportions by weight are taken into consideration for the investigation of various sorts of exposure conditions, proportions are listed in Table 1 (D).

Table 1. Materials Properties

Cement IS 1489 (Part1):1991		
Property	Results	IS code Specification
Fineness	6.5 %	< 10%
Setting Time (Initial)	36 min	> 30 min
Setting Time (Final)	290 min	< 600 min
Soundness	6.5mm	< 10mm
3 days compressive Strength	19.26 MPa	> 16 MPa
7 days compressive Strength	39.35 MPa	> 22 MPa
28 days compressive Strength	60.63 MPa	> 33 MPa
Aggregates, IS 383:2016		
Property	Fine Aggregate	Coarse Aggregate
Fineness Modulus	2.6	6.2
Specific Gravity	2.65	2.8
Water Absorption	0.5%	0.55%
Density	1440 kg/m³	1910 kg/m³

Properties of chemical Admixture (Superplasticizer) Auramix 200 by Fosroc

Specific Gravity: 1.05
pH = 6
Chloride Content: Nil
Alkali Content < 1g
Appearance: Yellowish to brownish Liquid

Mix Proportions designed as per IS 10262:2019 (5)

Sr. No	C	FA	CA	W/C	Sr. No	C	FA	CA	W/C	Sr. No	C	FA	CA	W/C
1	1	1.21	2.46	0.3	21	1	2.46	4.22	0.5	41	1	1.48	2.65	0.45
2	1	1.57	3.03	0.36	22	1	0.8	1.62	0.3	42	1	1.48	2.65	0.45
3	1	1.83	3.41	0.4	23	1	1.06	2.04	0.36	43	1	1.21	2.46	0.3
4	1	2.16	3.85	0.45	24	1	1.25	2.32	0.4	44	1	1.57	3.03	0.36
5	1	2.46	4.22	0.5	25	1	1.48	2.65	0.45	45	1	1.83	3.41	0.4
6	1	2.52	4.15	0.5	26	1	1.73	2.96	0.5	46	1	1.83	3.41	0.4
7	1	2.52	4.15	0.5	27	1	1.73	2.96	0.5	47	1	1.83	3.41	0.4
8	1	0.8	1.62	0.3	28	1	1.73	2.96	0.5	48	1	1.83	3.41	0.4
9	1	1.06	2.04	0.36	29	1	1.21	2.46	0.3	49	1	1.83	3.41	0.4
10	1	1.25	2.32	0.4	30	1	1.57	3.03	0.36	50	1	0.8	1.62	0.3
11	1	1.48	2.65	0.45	31	1	1.83	3.41	0.4	51	1	1.06	2.04	0.36
12	1	1.73	2.96	0.5	32	1	2.16	3.85	0.45	52	1	1.25	2.32	0.4
13	1	1.99	3.27	0.55	33	1	2.16	3.85	0.45	53	1	1.25	2.32	0.4
14	1	1.99	3.27	0.55	34	1	2.16	3.85	0.45	54	1	1.25	2.32	0.4
15	1	1.21	2.46	0.3	35	1	2.16	3.85	0.45	55	1	1.25	2.32	0.4
16	1	1.57	3.03	0.36	36	1	0.8	1.62	0.3	56	1	1.25	2.32	0.4
17	1	1.83	3.41	0.4	37	1	1.06	2.04	0.36					
18	1	2.16	3.85	0.45	38	1	1.25	2.32	0.4					
19	1	2.46	4.22	0.5	39	1	1.48	2.65	0.45					

4. Result and Discussion

The rheological qualities of the M40 concrete as well as its strength characteristics under various exposure situations are examined during the investigation of the research. It has been noted that as exposure conditions deteriorate, cement content gradually rises while WC ratio and water content decrease. The graphical comparisons of the experimental results are shown in Figure 2. It has been found that the rheological and strength

characteristics considerably affected as the exposure condition becomes critical. Table 2 demonstrates comparison of concrete's characteristics exposed to different environmental exposure conditions. For extreme environmental exposure condition, the maximum enhancements in slump, CF, CS, SPT, and FS are 10%, 0.99%, 1.89%, 4.3%, and 6.08%, respectively.
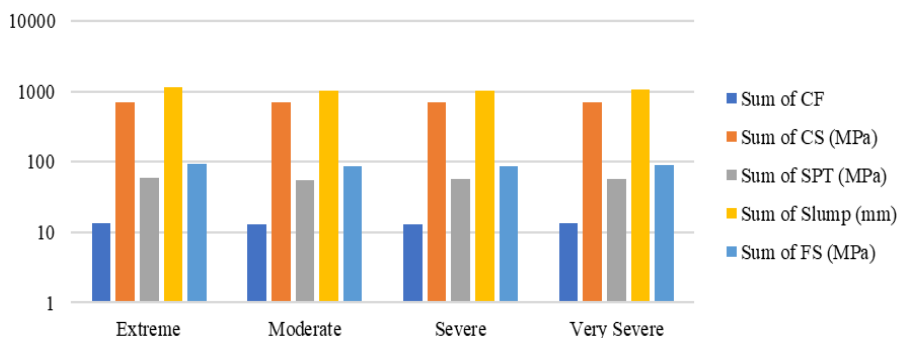
Fig. 2 Test Comparison (Compaction Factor (CF), Compressive strength (CS), Split Tensile Strength (SPT), Slump and Flexural Strength (FS)

Table 2. Percentage Increase for various exposures

Sr. No	Exposure Conditions	% Decrease in Slump	% Increase in CF	% Increase in CS	% Increase in SPT	% Increase in FS
1	Moderate	0	0	0	0	0
2	Sever	1.27	0.23	0.44	0.42	0.13
3	Very Sever	3.03	0.69	0.88	2.46	2.77
4	Extreme	10.05	0.99	1.89	4.3	6.08

In order to meet the requirements for the exposure condition, the strength and rheological qualities must rise as the harshness of the exposure condition increases [13]. Wons et.al [8], Mishra et.al [15] and Park et.al [9] noted same outcomes in their investigation. The experimental data thoroughly examined and evaluated in this part using statistical approaches such as correlation matrix, PCA, MLR, and RSM.

4.1 Correlation Matrix

The correlation study's input is shown in Figure 3. (A) displays the correlation matrix, which reveals interrelationship between experiments' variable. The correlation fluctuates between 1 and -1. Values close to 1 exhibit positive correlation, whereas values close to -1 exhibit negative correlation. Figure 3 illustrates how the relationship between concrete's characteristics and various exposures ranges from 0 to 0.1, additionally; it shows how different exposure conditions have a favorable effect on concrete's properties throughout both the plastic and hardening periods. Both Patil et al. [16], Endait et.al [17] and Baviskar et al. [18] reported the same kind of model results in their research.

4.2 Principal Component Analysis

A Scree plot of PCA's first three components reveals that this model has a variability close to 85.6%for dependent variables. This volatility is beneficial for prediction; shown in Figure 3 (B) (i). Similar to a Scree plot, the component plot of the PCA in Figure 3 (B) (ii) reveals that all of the study's variables are connected to one another. Concrete's compressive, flexural, and split tensile strengths are directly related to the cement content,

CA, FA, and exposure circumstances. Unlike slump, this is directly correlated with Admixture quantity, exposure circumstances, cement content, CA and FA. However, the relationship between these characteristics and the water cement ratio and water content is inverse.

The loading plot in Figure 3 (B) (ii) illustrates the significance of the components for the study's variables. In order to predict the various properties of concrete, Patil et al. [19] and Lu et al. [20] employ correlation matrices; this plot also helps to condense a large number of unimportant variables.

4.3 Multiple Linear Regression (MLR)

A statistical method called multiple regression can be used to look at the relationship between a number of independent factors and one single dependent variable. Using available independent variables, multiple regression analysis seeks to estimate the value of a single dependent variable. Table 3 displays the MLR model's input parameters. Determining the connection between two or more variables is a common task in engineering. One statistical tool that has long captured the curiosity of researchers in this field is regression analysis. Regression modelling is widely believed of as the process of fitting models to data.

A special type of regression model called a linear regression model uses linear predictor functions to describe the data and estimates output parameters from the data. It is important to note that numerous input variables are often used in regression analysis applications, which results in the "multiple linear regression" function. In this instance, MLR analyses observed data and fits a linear equation to determine the correlation between two or more input variables. In multiple linear regression, data are summarized and the relationship between variables is examined. For prediction of concrete properties like slump, CF, CS, SPT and FS, MLR model gives the Equation 1, 2, 3, 4, and 5 respectively. The Charhate et al. [21] and Patil et al. [22] published results from a similar kind of model in their work.

$$\text{Loss in slump (mm)} = -480.93 + 0.63 \cdot W/C + 0.63 \cdot C + 0.35 \cdot FA + 5.7E\text{-}02 \cdot CA - 0.83 \cdot Admx - 4.59 \cdot Exposure\text{-}Extreme + 3.65 \cdot Exposure\text{-}Modrate + 3.55 \cdot Exposure\text{-}Sever \tag{1}$$

$$CF = 2.31 - 1.69E\text{-}02 \cdot W/C - 5.39E\text{-}04 \cdot C - 1.0E\text{-}03 \cdot FA - 4.2E\text{-}04 \cdot CA + 1.24E\text{-}2 \cdot Admx - 6.6E\text{-}03 \cdot Exposure\text{-}Extreme + 4.89E\text{-}03 \cdot Exposure\text{-}Modrate + 1.14E\text{-}3 \cdot Exposure\text{-}Sever \tag{2}$$

$$CS\ (MPa) = 159.0 - 2.38 \cdot W/C - 4.85E\text{-}02 \cdot C - 8.5E\text{-}02 \cdot FA - 2.9E\text{-}2 \cdot CA + 0.86 \cdot Admx - 0.145 \cdot Exposure\text{-}Extreme + 0.43 \cdot Exposure\text{-}Modrate + 0.18 \cdot Exposure\text{-}Sever \tag{3}$$

$$SPT\ (MPa) = 30.87 - 0.7 \cdot W/C - 1.15E\text{-}2 \cdot C - 1.8E\text{-}02 \cdot FA - 8.86E\text{-}3 \cdot CA + 0.24 \cdot Admx - 5.15E\text{-}02 \cdot Exposure\text{-}Extreme + 5.94E\text{-}02 \cdot Exposure\text{-}Modrate - 0.010 \cdot Exposure\text{-}Sever \tag{4}$$

$$FS\ (MPa) = 53.78 - 0.80 \cdot W/C - 2E\text{-}2 \cdot C - 3.61E\text{-}02 \cdot FA - 1.3E\text{-}02 \cdot CA + 0.40 \cdot Admx - 9.26E\text{-}02 \cdot Exposure\text{-}Extreme + 0.18 \cdot Exposure\text{-}Modrate - 1.2E\text{-}2 \cdot Exposure\text{-}Sever \tag{5}$$

Figure 4 (a) displays the prediction for slump loss and its corresponding means, Figure 4 (b) displays the prediction for CF and its corresponding means, Figure 4 (c) displays the prediction for CS and its corresponding means, Figure 4 (d) displays the prediction for SPT and its corresponding means, Figure 4 (e) displays the prediction for FS and its corresponding means, and Figure 4 (f) displays the performance of the MLR model. Since the values of R2 for slump loss, CF, CS, SPT, and FS are sequentially 0.903, 0.903, 0.952,

0.954, and 0.988, it can be concluded that the MLR model provides the best match to the empirical data and makes accurate predictions. A strong model is indicated by a reasonably high F-value. The MLR model predicts the flexural strength of concrete more precisely than it does the other parameters because the MLR model for FS has higher values for R2 and F. The changes in properties of the concrete is mainly due to meet the requirements for the exposure condition, the strength and rheological qualities must rise as the severity of the exposure condition increases. Several studies have confirmed such parallel sorts of outcomes [10,21,23–25].
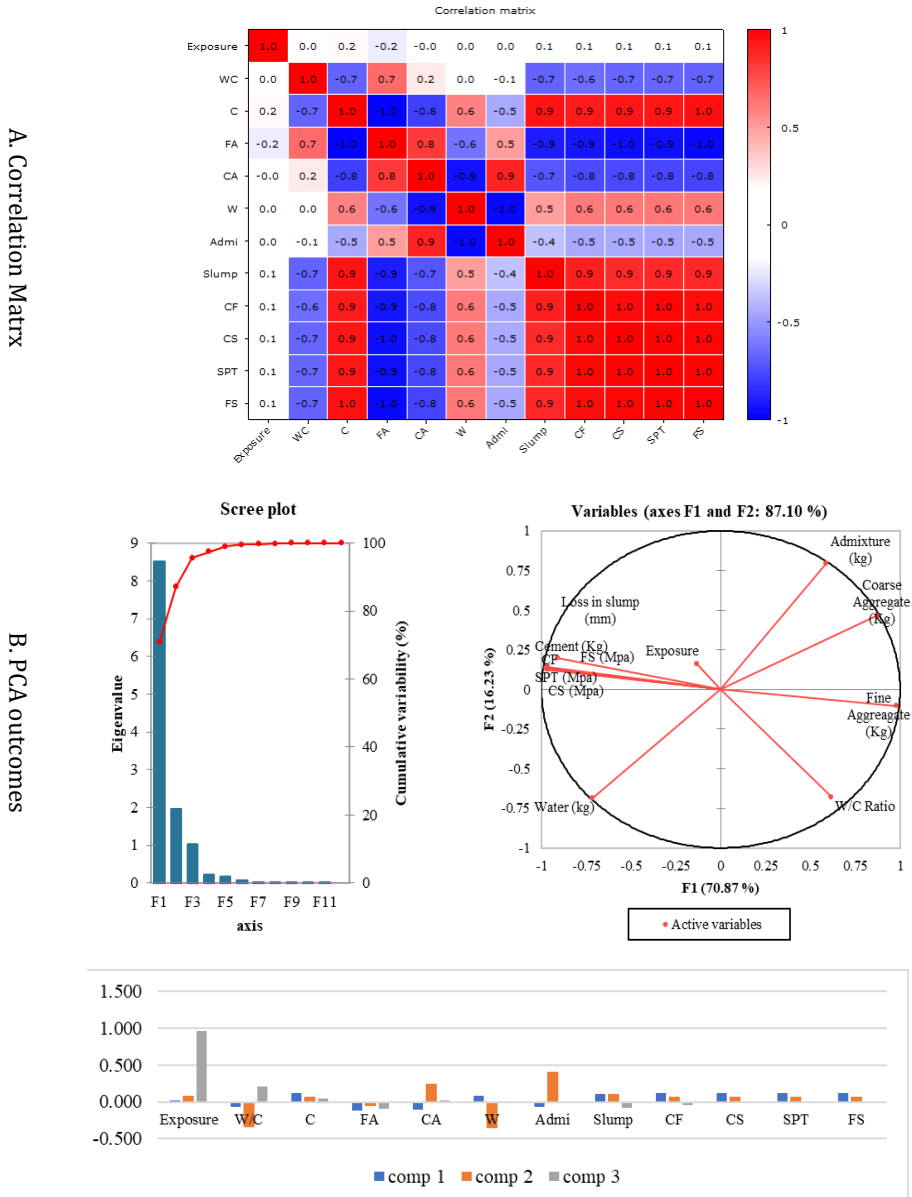
Fig. 3 (A) Correlation Matrix (B) PCA outcomes (i) Scree Plot (ii) Component Plot (iv) Loading Plot

Table 3. Experimental results

Sr No	Expo sure	W/C Ratio	Cement (Kg)	FA (Kg)	CA (Kg)	Water (kg)	Adm (kg)	Slump (mm)	CF	CS (MPa)	SPT (MPa)	FS (MPa)
1	1	0.3	494	597.45	1215	148	4.94	122	0.99	52	4.65	7.56
2	1	0.36	412	645.95	1248	148	4.12	68	0.96	50	4.18	6.71
3	1	0.4	370	674.8	1260	148	3.7	47	0.92	49	3.83	6.12
4	1	0.45	329	707.54	1266	148	3.29	45	0.91	47	3.51	5.3
5	1	0.5	300	736.56	1264	148	3	43	0.9	46	3.37	4.82
6	1	0.55	300	754.97	1243	148	3	41	0.9	46	3.37	4.71
7	1	0.6	300	754.97	1243	148	3	44	0.9	46	3.31	4.7
8	1	0.3	639	508.98	1035	191.58	0	149	0.99	53	4.78	8.27
9	1	0.36	533	562.9	1087	191.58	0	141	0.99	53	4.69	7.85
10	1	0.4	479	594.24	1110	191.58	0	99	0.98	52	4.58	7.3
11	1	0.45	426	629.25	1126	191.58	0	83	0.97	51	4.39	6.96
12	1	0.5	384	661.12	1135	191.58	0	46	0.93	50	4.09	6.33
13	1	0.55	349	691.1	1138	191.58	0	49	0.91	47	3.55	5.6
14	1	0.6	349	691.1	1138	191.58	0	48	0.91	47	3.55	5.56
15	2	0.3	494	597.45	1215	148	4.94	119	0.99	52	4.65	7.44
16	2	0.36	412	645.95	1248	148	4.12	62	0.96	50	4.17	6.49
17	2	0.4	370	674.8	1260	148	3.7	52	0.92	49	3.82	6.08
18	2	0.45	329	707.54	1266	148	3.29	51	0.91	47	3.5	5.3
19	2	0.5	300	736.56	1264	148	3	51	0.9	46	3.29	4.52
20	2	0.55	300	736.56	1264	148	3	54	0.9	46	3.22	4.41
21	2	0.6	300	736.56	1264	148	3	45	0.9	46	3.22	4.33
22	2	0.3	639	508.98	1035	191.58	0	146	0.99	53	4.77	8.14
23	2	0.36	533	562.9	1087	191.58	0	136	0.99	53	4.69	7.78
24	2	0.4	479	594.24	1110	191.58	0	94	0.98	52	4.56	7.24
25	2	0.45	426	629.25	1126	191.58	0	82	0.97	51	4.34	6.8
26	2	0.5	384	661.12	1135	191.58	0	55	0.93	49	4.08	6.32
27	2	0.55	384	661.12	1135	191.58	0	43	0.93	49	3.94	6.2
28	2	0.6	384	661.12	1135	191.58	0	48	0.92	49	3.83	6.13
29	3	0.3	494	597.45	1215	148	4.94	118	0.98	52	4.62	7.38
30	3	0.36	412	645.95	1248	148	4.12	47	0.93	50	4.12	6.48
31	3	0.4	370	674.8	1260	148	3.7	42	0.92	48	3.77	5.87
32	3	0.45	329	707.54	1266	148	3.29	50	0.91	47	3.45	5.18
33	3	0.5	329	707.54	1266	148	3.29	44	0.91	46	3.44	5.16
34	3	0.55	329	707.54	1266	148	3.29	47	0.9	46	3.39	5.15
35	3	0.6	329	707.54	1266	148	3.29	51	0.9	46	3.38	4.99
36	3	0.3	639	508.98	1035	191.58	0	146	0.99	53	4.77	8.1
37	3	0.36	533	562.9	1087	191.58	0	133	0.99	52	4.66	7.63
38	3	0.4	479	594.24	1110	191.58	0	93	0.98	52	4.53	7.22
39	3	0.45	426	629.25	1126	191.58	0	72	0.96	51	4.31	6.79
40	3	0.5	426	629.25	1126	191.58	0	72	0.96	51	4.28	6.78
41	3	0.55	426	629.25	1126	191.58	0	72	0.96	51	4.26	6.76
42	3	0.6	426	629.25	1126	191.58	0	69	0.96	50	4.24	6.73
43	4	0.3	494	597.45	1215	148	4.94	108	0.98	52	4.6	7.35
44	4	0.36	412	645.95	1248	148	4.12	51	0.93	50	4.12	6.43
45	4	0.4	370	674.8	1260	148	3.7	41	0.91	48	3.64	5.77
46	4	0.45	370	674.8	1260	148	3.7	55	0.91	48	3.63	5.73
47	4	0.5	370	674.8	1260	148	3.7	54	0.91	48	3.58	5.7
48	4	0.55	370	674.8	1260	148	3.7	50	0.91	48	3.58	5.69
49	4	0.6	370	674.8	1260	148	3.7	55	0.91	48	3.56	5.67
50	4	0.3	639	508.98	1035	191.58	0	144	0.99	53	4.7	7.97
51	4	0.36	533	562.9	1087	191.58	0	131	0.99	52	4.66	7.6
52	4	0.4	479	594.24	1110	191.58	0	92	0.97	51	4.51	7.13
53	4	0.45	479	594.24	1110	191.58	0	90	0.97	51	4.44	7.06
54	4	0.5	479	594.24	1110	191.58	0	88	0.97	51	4.42	7.03
55	4	0.55	479	594.24	1110	191.58	0	86	0.97	51	4.41	7
56	4	0.6	479	594.24	1110	191.58	0	83	0.97	51	4.4	6.99

Where   1= Moderate exposure, 2= Severe Exposure, 3= Very Severe, 4= Extreme Exposure

4.4 Response Surface Method

The relationship between a response variable and a group of experimental variables or factors is studied using RSM techniques. These procedures are often applied after selecting a few key controllable factors and identifying the factor settings that maximise the response. The RSM Model's input parameters are listed in Table 3. The variables are exposure, W/C, cement, FA, CA, water, and admixture. RSM chooses the variable combination that produces the best response for the dependent variables Slump, CF, CS, SPT, and FS. RSM approaches are used to investigate the association between a response variable and a collection of experimental variables or factors. Figure 5 displays the RSM model's output, which consists of two plots: a Pareto chart and a normal probability chart. Normal probability graphs display the effects of the factors or their interactions and can be employed to identify significant effects. Equations 6, 7, 8and 9 provide RSM predictions for slump at extreme, moderate, severeand very severe environmental exposure conditionsrespectively. These predictions provide the ideal slump value for each exposure. Equations 10, 11, 12, and 13 provide the optimal CF value for each exposure by providing RSM predictions for CF at extreme, moderate, severe, and very severe exposure conditions respectively.

Equations 14, 15, 16, and 17 provide RSM predictions for CS at extreme moderate, severe, and very severe levels, respectively, providing the ideal CS value for each exposure. Equations 18, 19, 20, and 21 provide RSM predictions for SPT at extreme, moderate, severe, and very severe levels, respectively, providing the ideal SPT value for each exposure. Equations 22, 23, 24, and 25 provide the optimal FS value for each exposure by providing RSM predictions for FS at extreme, moderate, severe, and very severe levels, respectively. The RSM model's pareto chart displays the independent variables in the experiment in descending order of importance. RSM calculates S (error estimate); the lower the value of S, the better the fit of the model to the data. Figure 5 (2) illustrates that the RSM model performs better for CF prediction than the Slump, CS, SPT, and FS models because the S value for the CF is lower than the S values for the Slump, CS, SPT, and FS models. The R^2 value, which represents how well the model matches the data, is used to assess the RSM model's performance. Figure 5 illustrates how well the RSM model fits Slump, CF, CS, SPT, and FS, with R^2 values of 0.986, 0.985, 0.987, 0.999, and 0.997, respectively. Similar results have been confirmed by numerous investigations[26-31].
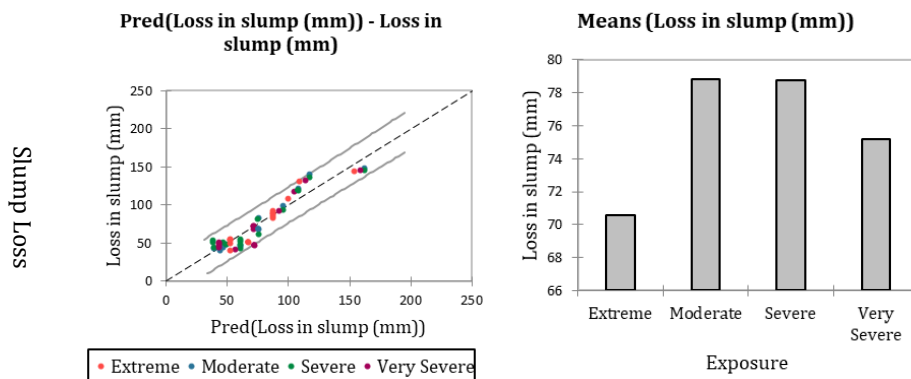
Compaction Factor
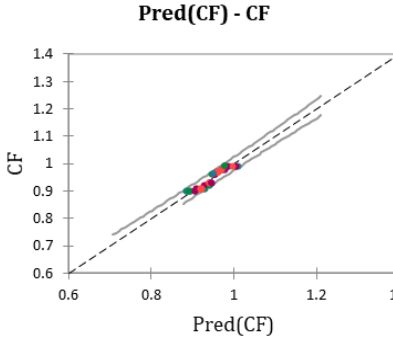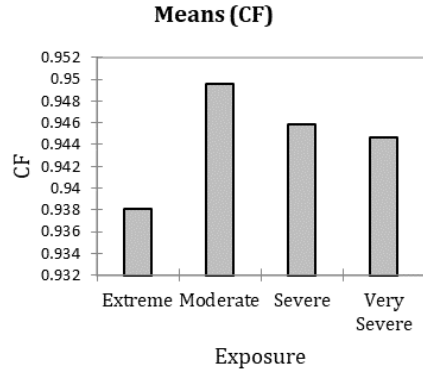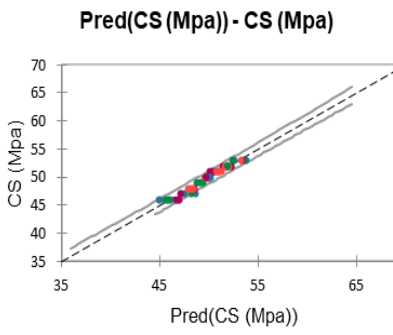
Compressive Strength

Split Tensile Strength

Pred(FS (Mpa)) - FS (Mpa)

Means (FS (Mpa))

Flexural Strength
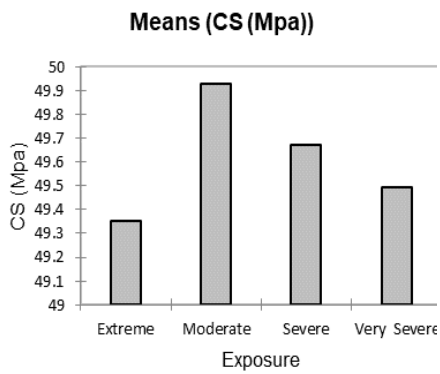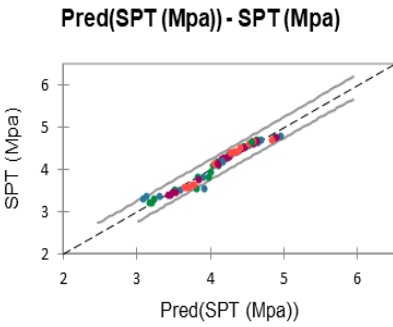
Performance of the MLR Model
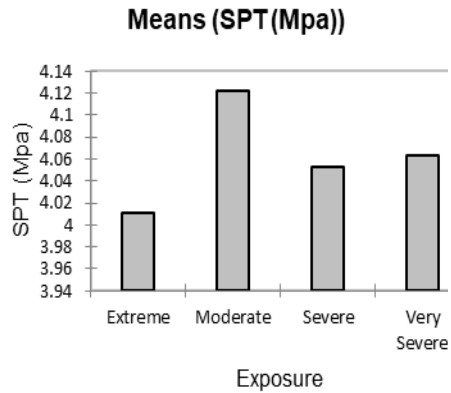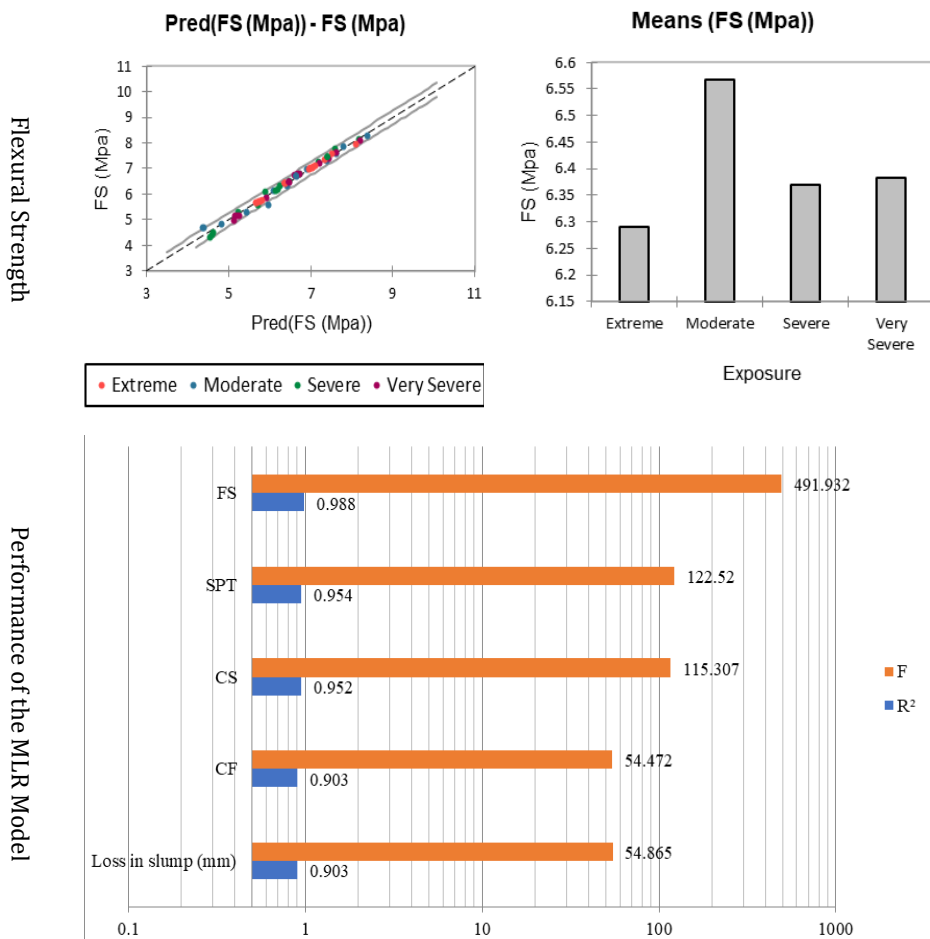
Fig. 4 Outcomes of the MLR Model for a) Slump Loss 2) CF 3) CS 4) SPT 5) FS 6) Performance of the Model

Test	Exposure	Test	
Slump	Extreme	Slump = 1377103 + 738422 W/C - 1909 C - 353 FA - 1639 CA - 297 W - 8837 Adm - 145 W/C*W/C + 0.599 C*C + 0.310 FA*FA + 0.538 CA*CA + 440 Adm*Adm- 253 W/C*C - 547 W/C*FA - 109 W/C*CA - 892 W/C*W - 1579 W/C*Adm + 0.595 C*FA + 1.022 C*CA	(6)
	Moderate	Slump =1441317 + 761663 W/C - 1931 C - 417 FA - 1645 CA - 388 W - 8923 Adm- 145 W/C*W/C + 0.599 C*C + 0.310 FA*FA + 0.538 CA*CA + 440 Adm*Adm- 253 W/C*C - 547 W/C*FA - 109 W/C*CA - 892 W/C*W - 1579 W/C*Adm + 0.595 C*FA + 1.022 C*CA	(7)
	Severe	Slump = 1419836 + 753743 W/C - 1924 C - 395 FA - 1644 CA - 357 W - 8884 Adm - 145 W/C*W/C + 0.599 C*C + 0.310 FA*FA	(8)

		+ 0.538 CA*CA + 440 Adm*Adm- 253 W/C*C - 547 W/C*FA - 109 W/C*CA - 892 W/C*W- 1579 W/C*Adm+ 0.595 C*FA + 1.022 C*CA	
CF	Very Severe	Slump = 1400693 + 745956 W/C - 1917 C - 374 FA - 1642 CA - 328 W - 8849 Adm - 145 W/C*W/C + 0.599 C*C + 0.310 FA*FA + 0.538 CA*CA + 440 Adm*Adm- 253 W/C*C - 547 W/C*FA - 109 W/C*CA - 892 W/C*W- 1579 W/C*Adm+ 0.595 C*FA + 1.022 C*CA	(9)
	Extreme	CF=1213 + 2670 W/C - 2.39 C - 0.065 FA - 2.125 CA + 0.361 W - 10.64 Adm- 0.011 W/C*W/C + 0.000825 C*C + 0.000377 FA*FA + 0.000766 CA*CA+ 0.437 Adm*Adm - 0.963 W/C*C - 1.474 W/C*FA - 0.691 W/C*CA - 2.948 W/C*W- 2.97 W/C*Adm + 0.000714 C*FA + 0.001491 C*CA	(10)
	Moderate	CF=1260 + 2706 W/C - 2.41 C - 0.145 FA - 2.115 CA + 0.270 W - 10.79 Adm- 0.011 W/C*W/C + 0.000825 C*C + 0.000377 FA*FA + 0.000766 CA*CA+ 0.437 Adm*Adm - 0.963 W/C*C - 1.474 W/C*FA - 0.691 W/C*CA - 2.948 W/C*W- 2.97 W/C*Adm + 0.000714 C*FA + 0.001491 C*CA	(11)
	Severe	CF=1222 + 2694 W/C - 2.40 C - 0.109 FA - 2.111 CA + 0.324 W - 10.73 Adm- 0.011 W/C*W/C + 0.000825 C*C + 0.000377 FA*FA + 0.000766 CA*CA+ 0.437 Adm*Adm - 0.963 W/C*C - 1.474 W/C*FA - 0.691 W/C*CA - 2.948 W/C*W- 2.97 W/C*Adm + 0.000714 C*FA + 0.001491 C*CA	(12)
	Very Severe	CF=1202 + 2681 W/C - 2.39 C - 0.080 FA - 2.113 CA + 0.359 W - 10.69 Adm- 0.011 W/C*W/C + 0.000825 C*C + 0.000377 FA*FA + 0.000766 CA*CA+ 0.437 Adm*Adm - 0.963 W/C*C - 1.474 W/C*FA - 0.691 W/C*CA - 2.948 W/C*W- 2.97 W/C*Adm + 0.000714 C*FA + 0.001491 C*CA	(13)
CS	Extreme	CS =-40337 + 11151 W/C + 59.0 C + 16.7 FA + 24.3 CA + 30.7 W + 276 Adm- 1.0 W/C*W/C - 0.0202 C*C - 0.0039 FA*FA - 0.0052 CA*CA - 7.2 Adm*Adm- 4.3 W/C*C - 3.2 W/C*FA - 4.6 W/C*CA - 10.7 W/C*W + 4.3 W/C*Adm- 0.0233 C*FA - 0.0217 C*CA	(14)
	Moderate	CS=-38792 + 11031 W/C + 58.4 C + 16.4 FA + 23.6 CA + 29.3 W + 278 Adm- 1.0 W/C*W/C - 0.0202 C*C - 0.0039 FA*FA - 0.0052 CA*CA - 7.2 Adm*Adm- 4.3 W/C*C - 3.2 W/C*FA - 4.6 W/C*CA - 10.7 W/C*W + 4.3 W/C*Adm- 0.0233 C*FA - 0.0217 C*CA	(15)
	Severe	CS=-37881 + 11070 W/C + 58.1 C + 15.9 FA + 23.3 CA + 28.3 W + 277 Adm- 1.0 W/C*W/C - 0.0202 C*C - 0.0039 FA*FA	(16)

SPT		- 0.0052 CA*CA - 7.2 Adm*Adm- 4.3 W/C*C - 3.2 W/C*FA - 4.6 W/C*CA - 10.7 W/C*W + 4.3 W/C*Adm- 0.0233 C*FA - 0.0217 C*CA	
	Very Severe	CS=-41033 + 11103 W/C + 59.3 C + 17.2 FA + 24.4 CA + 31.5 W + 279 Adm- 1.0 W/C*W/C - 0.0202 C*C - 0.0039 FA*FA - 0.0052 CA*CA - 7.2 Adm*Adm- 4.3 W/C*C - 3.2 W/C*FA - 4.6 W/C*CA - 10.7 W/C*W + 4.3 W/C*Adm- 0.0233 C*FA - 0.0217 C*CA	(17)
	Extreme	SPT=-9990 + 10062 W/C + 10.67 C + 5.41 FA + 4.68 CA + 7.97 W + 42.6 Adm+ 2.18 W/C*W/C - 0.00322 C*C - 0.001415 FA*FA - 0.00077 CA*CA- 1.331 Adm*Adm - 3.81 W/C*C - 3.96 W/C*FA - 3.54 W/C*CA- 10.23 W/C*W- 3.17 W/C*Adm - 0.00435 C*FA - 0.00307 C*CA	(18)
	Moderate	SPT=-9944 + 10049 W/C + 10.66 C + 5.43 FA + 4.64 CA + 7.94 W + 42.8 Adm+ 2.18 W/C*W/C - 0.00322 C*C - 0.001415 FA*FA - 0.00077 CA*CA- 1.331 Adm*Adm - 3.81 W/C*C - 3.96 W/C*FA - 3.54 W/C*CA- 10.23 W/C*W- 3.17 W/C*Adm - 0.00435 C*FA - 0.00307 C*CA	(19)
	Severe	SPT=-9933 + 10051 W/C + 10.65 C + 5.42 FA + 4.64 CA + 7.93 W + 42.8 Adm+ 2.18 W/C*W/C - 0.00322 C*C - 0.001415 FA*FA - 0.00077 CA*CA- 1.331 Adm*Adm - 3.81 W/C*C - 3.96 W/C*FA - 3.54 W/C*CA- 10.23 W/C*W- 3.17 W/C*Adm - 0.00435 C*FA - 0.00307 C*CA	(20)
	Very Severe	SPT=-9925 + 10055 W/C + 10.65 C + 5.42 FA + 4.64 CA + 7.91 W + 42.8 Adm+ 2.18 W/C*W/C - 0.00322 C*C - 0.001415 FA*FA - 0.00077 CA*CA- 1.331 Adm*Adm - 3.81 W/C*C - 3.96 W/C*FA - 3.54 W/C*CA- 10.23 W/C*W- 3.17 W/C*Adm - 0.00435 C*FA - 0.00307 C*CA	(21)
	Extreme	FS=-2867 + 876 W/C + 6.1 C + 2.14 FA - 0.2 CA + 3.67 W + 28.1 Admi + 0.40 W/C*W/C - 0.00244 C*C - 0.00016 FA*FA + 0.00046 CA*CA + 0.03 Admi*Admi - 0.27 W/C*C - 0.77 W/C*FA - 0.09 W/C*CA - 1.0 W/C*W+ 0.5 W/C*Admi - 0.00321 C*FA - 0.00155 C*CA	(22)
	Moderate	FS =-2449 + 918 W/C + 6.0 C + 1.92 FA - 0.4 CA + 3.19 W + 28.0 Adm + 0.40 W/C*W/C - 0.00244 C*C - 0.00016 FA*FA + 0.00046 CA*CA + 0.03 Adm*Adm - 0.27 W/C*C - 0.77 W/C*FA - 0.09 W/C*CA - 1.0 W/C*W+ 0.5 W/C*Adm - 0.00321 C*FA - 0.00155 C*CA	(23)
	Severe	FS=-2425 + 903 W/C + 6.0 C + 1.93 FA - 0.4 CA + 3.18 W + 28.0 Adm + 0.40 W/C*W/C - 0.00244 C*C - 0.00016 FA*FA + 0.00046 CA*CA	(24)

+ 0.03 Adm*Adm - 0.27 W/C*C - 0.77 W/C*FA - 0.09 W/C*CA
- 1.0 W/C*W+ 0.5 W/C*Adm - 0.00321 C*FA - 0.00155 C*CA

Very Severe	FS=-2822 + 890 W/C + 6.1 C + 2.12 FA - 0.2 CA + 3.60 W + 28.3 Adm + 0.40 W/C*W/C - 0.00244 C*C - 0.00016 FA*FA + 0.00046 CA*CA + 0.03 Adm*Adm - 0.27 W/C*C - 0.77 W/C*FA - 0.09 W/C*CA - 1.0 W/C*W+ 0.5 W/C*Adm - 0.00321 C*FA - 0.00155 C*CA	(25)

Test	Pareto Chart	Normal Probability Plot	R²	S
Slump			0.986	4.028
CF			0.985	0.0041
CS			0.987	0.26
SPT			0.999	0.016
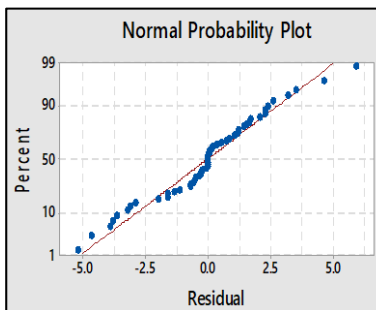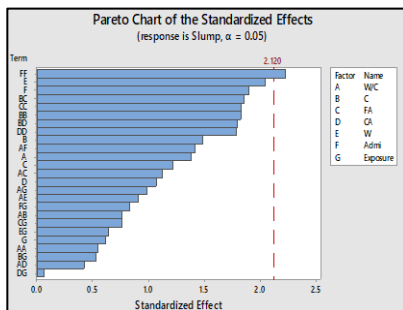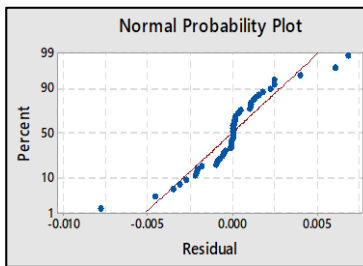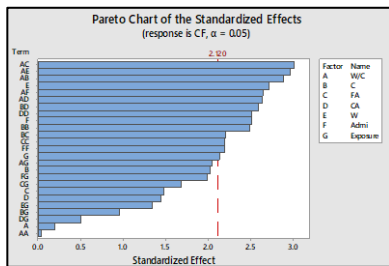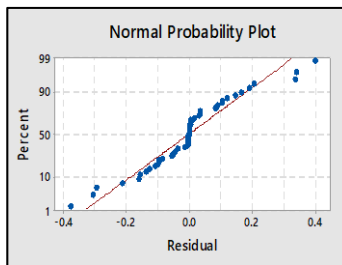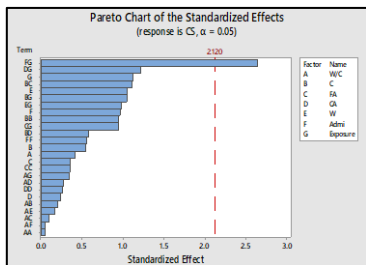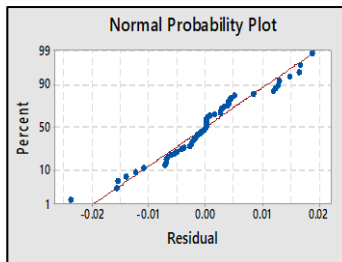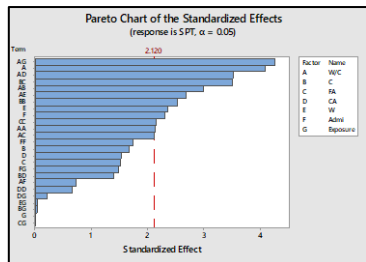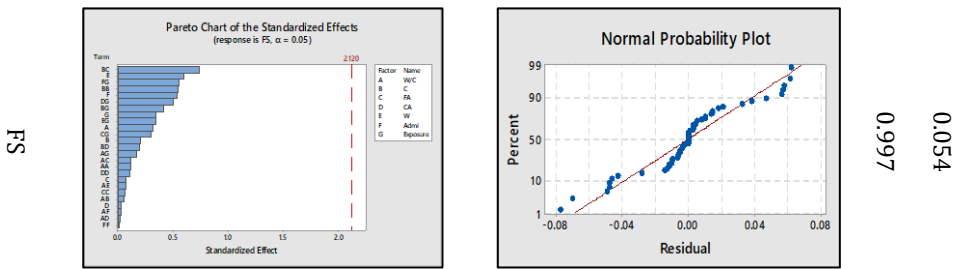
Fig. 5 RSM Model outcomes for (1) Slump (2) CF (3) CS (4) SPT (5) FS

5. Summary and Conclusion

A series of experiments have been conducted in this study to examine behaviour, rheological properties and strength characteristics of concrete under diverse environmental exposure conditions. IS 456:2000 [11] recommends, M40 be the minimum grade of concrete for extreme environmental exposure condition explored in this experimental work at both plastic and hardening stage.

Statistical tools such correlation matrices, PCA, MLR, and RSM were used to extensively analyze and assess the experimental data. The research uses correlation matrix and Principal Component Analysis (PCA) to produce precise results in order to assess interaction of experimental variables. Multivariate Linear Regression (MLR) model was developed to predict concrete properties during the plastic and hardening process. RSM techniques used to establish relationship between a response variable and a group of experimental variables.

The following inferences could be made in light of the experimental findings

- It had been observed that cement content steadily increases while W/C and water content decrease when exposure circumstances intensify.
- As the exposure condition worsens, rheological and strength parameters are significantly altered.
- Maximum enhancements in slump, CF, CS, SPT and FS for extreme environmental exposure conditions seem to be 10%, 0.99%, 1.89%, 4.3%, and 6.08%, respectively.
- Strength and rheological properties must improve as the exposure condition's abrasiveness rises in order to satisfy the exposure condition's demands.
- Correlations shows positive impact of various exposure conditions on properties of concrete throughout both the plastic and hardening periods as the relationship between concrete's features and different exposures varies from 0 to 0.1.
- According to a Scree plot of PCA's first three components, model has a variability of 85.6% for dependent variables. Compressive strength, flexural strength and split tensile strength are directly related to cement content, CA, FA and exposure circumstances. However, there is an inverse correlation between these traits and the water cement ratio.
- RSM model performs better for CF prediction than the Slump, CS, SPT, and FS models as "S" value for the CF is lower than the S values for the Slump, CS, SPT, and FS models. RSM model fits Slump, CF, CS, SPT, and FS, with R^2 values of 0.986, 0.985, 0.987, 0.999, and 0.997, respectively.
- It can be concluded that the MLR model provides the best match to the actual data and produces reliable prediction.

- In all kinds of exposure circumstances, the Response Surface Method (RSM) is also utilized to identify the concrete's ideal property. The RSM also matches experimental data the best because of its high coefficient of determination and its forecast is precise (R^2).

Declarations

- Conflict of Interest

The corresponding author confirms on behalf of all authors that no one's financial or personal interest conflict with the research described in this publication.

- **Author Contributions Statement**
  1) Experimental work was done by the first author.
  2) The manuscript's second and third authors each offer ideas, reviews, and additional effort.
  3) All authors reviewed the manuscript.

References

[1] Darban S, Tehrani HG, Karballaeezadeh N. Presentation a new method for determining of bridge condition index by using analytical hierarchy process. 2020 ;(March). https://doi.org/10.20944/preprints202003.0420.v1

[2] Pacheco-Torgal F, Miraldo S, Ding Y, Labrincha JA. Targeting HPC with the help of nanoparticles: An overview. Vol. 38, Construction and Building Materials. 2013. p. 365-70. https://doi.org/10.1016/j.conbuildmat.2012.08.013

[3] Tang F. Brief analysis on sampling and testing method of concrete specimen of building materials. MATEC Web Conf. 2018; 175. https://doi.org/10.1051/matecconf/201817501015

[4] Narmatha M, Felixkala DT. Meta kaolin -The Best Material for Replacement of Cement in Concrete. IOSR J Mech Civ Eng. 2016; 13(04):66-71. https://doi.org/10.9790/1684-1304016671

[5] Cavazos JS, González G, Kharissova O V, Ortega B, Peña L, Osorio M, et al. Effect of Nanoparticles on Mechanical Properties of Cement-Sand Mortar Applications. Adv Chem Eng Sci. 2017; 7:270-6. https://doi.org/10.4236/aces.2017.73020

[6] Jyothi Nikhila C, Chaitanya Kumar JD. Partial Replacement of Cement with Metakaolin in High Strength Concrete. Int J Engg Res Sci Tech [Internet]. 2015;4(4). Available from: http://www.ijerst.com/currentissue.php

[7] Ghadzali NS, Ibrahim MHW, Mohd Sani MSH, Jamaludin N, Desa MSM, Misri Z. Properties of concrete containing different type of waste materials as aggregate replacement exposed to elevated temperature - A review. IOP Conf Ser Earth Environ Sci. 2018; 140(1). https://doi.org/10.1088/1755-1315/140/1/012139

[8] Wons M, Camara L, Esteves I, Trentin PO, Medeiros-Junior RA. Evaluation of concrete self-healing with different fly ash contents and cracking ages by means of ultrasonic pulse velocity and compressive strength tests. J Build Pathol Rehabil [Internet]. 2021; 6(1):10. https://doi.org/10.1007/s41024-021-00104-7

[9] Park JK, Kim MO. The effect of different exposure conditions on the pull-off strength of various epoxy resins. J Build Eng [Internet]. 2021; 38:102223. https://doi.org/10.1016/j.jobe.2021.102223

[10] Eneowaji DO, Ucheowaji O. Effect of Exposure of Cement on the Compressive Strength of Concrete. J Eng Res Reports. 2021;20(6):24-32. https://doi.org/10.9734/jerr/2021/v20i617324

[11] Indian Code. IS:456 (2000) Plain and Reinforced Concrete Code of Practice. In: Bureau of Indian Standards, New Delhi. 2000.

[12] Indian Standard. IS: 1489 (Part 1):1991 Portland Pozzolona Cement Specification. In: Bureau of Indian Standards, New Delhi. THIRD. INDIA: Bureau of Indian Standards; 1991. p. 57.

[13] Indian Standard. IS 383 : 2016 Coarse and Fine Aggregate for Concrete - Specification. In: Bureau of Indian Standards, New Delhi. 2016.

[14] Indian Standard. IS 10262: 2019 Concrete Mix Proportioning- Guidelines. In: Bureau of Indian Standards (BIS). 2019. p. 1-40.

[15] Mishra RK, Ghosh P, Kulshreshtha M. Evaluation of strength of concrete on different initial exposure condition. Curr Mater Sci. 2020; 13.

[16] Patil HS, Dwivedi AK. Rheology of self-compacting concrete nanocomposites. Int J Recent Technol Eng. 2019; 8(2):554-7. https://doi.org/10.35940/ijrte.B1603.078219

[17] Endait M, Juneja A. New correlations between uniaxial compressive strength and point load strength of basalt. Int J Geotech Eng [Internet]. 2015; 9(4):348-53. https://doi.org/10.1179/1939787914Y.0000000073

[18] Baviskar S, Dwivedi A, Patil H. Analysis and development of the Composite Sustainable Condition Index for elevated service reservoir (ESR) by DER method. J Build Pathol Rehabil. 2022 Dec 16; 7(1):34. https://doi.org/10.1007/s41024-022-00177-y

[19] Patil H, Dwivedi A. Impact of nano ZnO particles on the characteristics of the cement mortar. Innov Infrastruct Solut [Internet]. 2021; 6(4). https://doi.org/10.1007/s41062-021-00588-9

[20] Lu K, Jin Y, Chen Y, Yang Y, Hou L, Zhang Z, et al. Review for order reduction based on proper orthogonal decomposition and outlooks of applications in mechanical systems. Mechanical Systems and Signal Processing. 2019. https://doi.org/10.1016/j.ymssp.2019.01.018

[21] Charhate S, Subhedar M, Adsul N. Prediction of Concrete Properties Using Multiple Linear Regression and Artificial Neural Network. J Soft Comput Civ Eng. 2018; 2(3):27-38.

[22] Patil H, Dwivedi A, Bidkar K. Prediction of upgraded properties of the concrete with the wash sand waste. J Build Pathol Rehabil [Internet]. 2022; 7(1):33. https://doi.org/10.1007/s41024-022-00171-4

[23] Alaneme George U, Mbadike Elvis M. Modelling of the mechanical properties of concrete with cement ratio partially replaced by aluminium waste and sawdust ash using artificial neural network. SN Appl Sci [Internet]. 2019; 1(11):1-18. https://doi.org/10.1007/s42452-019-1504-2

[24] Bidkar KL, Jadhao PD. Prediction of strength of remixed concrete by application of orthogonal decomposition, neural analysis and regression analysis. Open Eng. 2019; 9(1):434-43. https://doi.org/10.1515/eng-2019-0053

[25] Khademi F, Akbari M, Mohammadmehdi S, Nikoo M. Multiple linear regression, artificial neural network, and fuzzy logic prediction of 28 days compressive strength of concrete. Front Struct Civ Eng. 2017; 11(1):90-9. https://doi.org/10.1007/s11709-016-0363-9

[26] Patil H, Dwivedi A. Prediction of properties of the cement incorporated with nanoparticles by principal component analysis (PCA) and response surface regression (RSR). Mater Today Proc. 2021; 43:1358-67. https://doi.org/10.1016/j.matpr.2020.09.170

[27] Selvaraj S, Sivaraman S. Prediction model for optimized self-compacting concrete with fly ash using response surface method based on fuzzy classification. Neural Comput Appl [Internet]. 2019; 31(5):1365-73. https://doi.org/10.1007/s00521-018-3575-1

[28] Salem Alsanusi, Loubna Bentaher. Prediction of Compressive Strength of Concrete from Early Age Test Result Using Design of Experiments (RSM). Int J Civil, Environ Struct Constr Archit Eng. 2015;

[29] Gopalakrishnan R, Nithiyanantham S. Effect of ZnO Nanoparticles on Cement Mortar for Enhancing the Physico-Chemical, Mechanical and Related Properties. Adv Sci Eng Med. 2020; 12(3):348-55. https://doi.org/10.1166/asem.2020.2505

[30] Alyamac KE, Ghafari E, Ince R. Development of eco-efficient self-compacting concrete with waste marble powder using the response surface method. J Clean Prod. 2016; https://doi.org/10.1016/j.jclepro.2016.12.156

[31] Borucka-Lipska J. Acid Resistance, Water Permeability and Chloride Penetrability of Concrete Containing Crushed Basalt as Aggregates. Neural Comput Appl [Internet]. 2016 Apr; 31(2):137-50.

Research Article

Deformation and stress analysis of rotating functionally graded hollow cylindrical body for variable heat generation

Rakesh Kumar Sahu[1,a], Lakshman Sondhi[1,b], Shubhankar Bhowmick[2,c], Royal Madan*[3,d]

[1]Department of Mechanical Engineering, Shri Shankaracharya Group of Institute, Bhilai, India
[2]Department of Mechanical Engineering, National Institute of Technology Raipur, Raipur, India
[3]Department of Mechanical Engineering, G H Raisoni Institute of Engineering & Technology, Nagpur, India

Article Info	Abstract
	In the present study, one-dimensional steady-state temperature variation with variable heat generation was considered and thermo-mechanical stress and deformation analysis on a hollow functionally graded cylinder were then performed. A governing differential equation with a variable coefficient is solved using Navier's equation by applying thermal and mechanical boundary conditions. The effect of internal pressure and temperature, rotation, gravity, and heat generation, and their combined effect such as rotation and heat generation, gravity and heat generation, rotation, gravity, and heat generation were studied in a cylindrical body. The gradation properties varied radially as per power-law variation. The grading parameter ranging between -2 to 3, changes the material properties in the radial direction. A critical grading index was identified that lowers the induced stresses and hence an improvement in the performance of functionally graded cylinders can be obtained under the influence of a combination of loads. The validation of the results was carried out with published literature.

1. Introduction

In functionally graded materials (FGM) the properties change with distance because of changes in composition, microstructure, or porosity gradient [1]. The change in composition can be stepped-wise or continuously varying depending on the fabrication route selected, for ex., a layer-wise FGM is obtained in the case of powder metallurgy and continuously varying type in centrifugal casting [2]. Mainly the choice of functionally graded material selected is a combination of a metal-ceramic type wherein the metal provides the toughness and ceramic the wear resistance, therefore, the structure then obtained has potential applications in areas like nuclear energy, defense, biomedical, aerospace, energy-based, semiconductor, and cutting tools to name a few [3]. Various methods are available for the fabrication of FGMs such as solid-based, liquid-based, and gas-based, but for the fabrication of axisymmetric structures, a centrifugal casting method was found to be an effective fabrication technique [4–6]. To ascertain the performance of such structures, a prior analysis would be advantageous, as it saves costs, time, and other resources. Hence, modeling and analysis of structures (Plate, shell, disk, and cylinder) are of interest to researchers [7–9]. There are two approaches to model the properties of functionally graded materials; in the first approach, the material properties are varied based on the volume fraction variation of metal and ceramic. The variation of

volume fraction variation can be as per laws like power-law, exponential law, and sigmoid law [10] or by assuming a variation of properties like exponentially, power-law, and others. The effective estimation of the mechanical property of the material in which the volume fraction changes can be carried out using methods such as rule of mixture, modified rule of mixture, Mori-Tanaka, and others [11].

Cylindrical structures are employed in a wide range of engineering applications, including marine, reactor, rocket components, and automotive, to name a few [12]. When compared to isotropic material, a functionally graded cylinder has a larger energy absorption capacity [13, 14]. A nonlinear finite element approach was employed to study buckling in a cylindrical panel for several lamination arrangements and boundary conditions [15]. The pressure-bearing capability of shells under blast loading was solved using Lame's approach [16]. Elastic-plastic stress analysis of an FG solid cylinder subjected to homogenous heat generation was performed based on Tresca's yield criteria [17]. Under uniform internal pressure, the complementary functions approach was used to investigate stress distribution in hollow cylinders, disks, and spheres [18]. Finite element analysis has been employed to investigate the temperature distribution in a wet cylinder liner and bonded T-joints [19, 20]. Free vibration and buckling analysis of functionally graded beams were performed using the finite element approach [21]. Analytical and experimental analysis of an isotropic material was carried out to investigate the yield criteria of plasticity models [22].

The power series method was used to calculate displacements and stresses in an exponentially graded thick cylinder under internal pressure [23]. For variable thickness, a cylindrical shell under internal pressure was considered to perform stress analysis using first-order shear deformation theory (FSDT) [24]. The Bessel function was used to develop a closed-form solution of an FG hollow cylinder exposed to thermo-mechanical loading assuming steady-state temperature distribution along the radial and longitudinal directions [25]. The energy method was used in an FG piezoelectric rotating cylinder under the influence of electrical, thermal, and mechanical loads [26]. For the FG pressure vessel, an analytical solution for non-uniform pressure loading was solved using FSDT [27]. The FG rotating thick cylinder shell problem was addressed using a multi-layered approach under arbitrary non-uniform internal pressure [28]. In [29], investigated the hollow cylinder problem in two different ways: Firstly, the hollow cylinder is made of a multi-layered material with variable material properties on each layer; the material properties in the second case were continually changing. A closed-form solution to the exponentially graded hollow cylinder problem was used to investigate stress distribution under thermo-mechanical loads [30]. By employing Fredholm's integral equation thermal stresses and displacement of a functionally graded cylindrical vessel were studied [31]. An elasto-plastic thermo-mechanical analysis of a thick-walled cylinder when subjected to internal pressure and the temperature has been performed using the Successive Approximation Method, and they found that the effect of boundary temperature on radial and tangential stress is insignificant [32]. Thermo-mechanical fatigue analysis and failure location in the cylinder head were investigated [33]. A fast Fourier transform and finite element method were combinely employed in the thermo-mechanical analysis of a thick cylinder [34]. Elastic analysis of a thick cylinder and spherical pressure vessel made up of functionally graded material (FGM) was studied and found a significant reduction in stresses when compared with homogeneous material [35]. Finite element analysis has been employed to analyze the thermo-elastic analysis of a rotating FGM circular disk [36]. A lot of research in the fabrication and analysis of functionally graded structures is going on. Studies on static and dynamic analysis on FGM plates have been performed by authors using methods such as higher-order shear deformation theory [37–39], and sinusoidal shear deformation [40] to name a few.

In this paper, using Navier's equation a thermal and mechanical analysis of a rotating FG hollow cylinder was performed. Considering one-dimensional steady-state thermal heat conduction, stress and deformation analysis were performed when a cylinder is subjected to combined thermal and rotational effects. For property variation in a radial direction, the individual and combined effects of rotation, gravity, and heat generation on stresses: radial, tangential, and von Mises were investigated. To the best of the author's knowledge, there is no study in which the effect of variable heat generation on stresses is considered, such situations are practical in the case of functionally graded materials. The material properties of FGMs such as Young's modulus, density, coefficient of thermal expansion, conductivity, and heat generation was considered as per power law variation. The proposed method is simple and validated with benchmark solutions. The study will benefit researchers and industries in understanding the effects of individual loadings and the combination of them such as gravity, rotation, and variable heat generation. Thus, the research will help industry personnel in selecting suitable grading parameters for different cases before the fabrication of such structures.
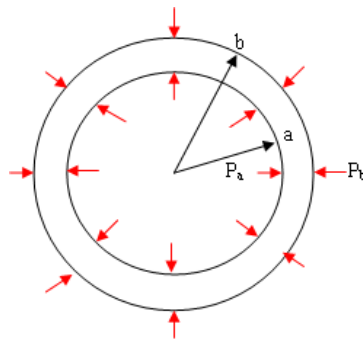
Fig. 1 Hollow cylinder

2. Mathematical Formulation

A rotating hollow cylinder is considered whose inner and outer radius are '*a*' and '*b*'. Variation of material properties of rotating hollow cylinder is a function of radial direction '*r*'. Let displacement component '*u*' is the function of radial direction. The displacement relation for combined thermal and mechanical strain is given by;

$$\varepsilon_r = \frac{du}{dr} = \frac{1}{E_r}\left[\sigma_r - \vartheta\sigma_\theta\right] + \alpha_r T_r \text{ and } \varepsilon_\theta = \frac{u}{r} = \frac{1}{E_r}\left[\sigma_\theta - \vartheta\sigma_r\right] + \alpha_r T_r \tag{1}$$

The stress-strain relations are given by,

$$\sigma_r = \frac{E_r}{(1+\vartheta)(1-2\vartheta)}\left[\varepsilon_r(1-\vartheta) + \vartheta\varepsilon_\theta - (1+\vartheta)\alpha_r T_r\right]$$

$$\sigma_\theta = \frac{E_r}{(1+\vartheta)(1-2\vartheta)}\left[\vartheta\varepsilon_r + (1-\vartheta)\varepsilon_\theta - (1+\vartheta)\alpha_r T_r\right] \tag{2}$$

Concerning the body force and inertia term the equation thus becomes,

$$r\frac{d}{dr}\sigma_r + (\sigma_r - \sigma_\theta) + \rho_r\left(\omega^2 - \frac{g}{a}\right)r^2 = 0 \tag{3}$$

By employing the power law in the material properties, we get;

$$E_r = E_a(r)^{n_1}, \quad \alpha_r = \alpha_a(r)^{n_2}, \quad k_r = k_a(r)^{n_3}, \quad \rho_r = \rho_a(r)^{n_4}, \quad q_r = q_a(r)^{n_5} \tag{4}$$

Solving Eq. (1-4), the displacement formulation thus becomes

$$r\frac{d}{dr}\left[E_r\lambda\left\{(1-\vartheta)\frac{du}{dr}+\vartheta\frac{u}{r}-(1+\vartheta)\alpha_r T_r\right\}\right]+E_r\lambda\left[(1-\vartheta)\frac{du}{dr}+\vartheta\frac{u}{r}-(1+\vartheta)\alpha_r T_r\right]$$
$$-E_r\lambda\left[\vartheta\frac{du}{dr}+(1-\vartheta)\frac{u}{r}-(1+\vartheta)\alpha_r T_r\right]+\rho_r(\omega^2-\frac{g}{a})r^2=0 \tag{5}$$

where,

$$\lambda = \frac{1}{(1+\vartheta)(1-2\vartheta)} \tag{6}$$

Above eq. (5) can also be written as here we required the values for temperature and its derivative. The formulation for the temperature profile is separately calculated in section 2.1

$$Ar^2u'' + Bru' + Cu = Ur^{n_2+P_4+1} + Vr^{n_2-n_3+n_5+3} + Wr^{n_2+1} + Sr^{n_4-n_1+3} \tag{7}$$

where,

$$A = E_a\lambda(1-\vartheta), \quad B = n_1 E_a\lambda(1-\vartheta) + E_a\lambda(1-\vartheta), \quad C = E_a\lambda\vartheta n_1 + E_a\lambda\vartheta - E_a\lambda$$
$$U = \frac{1}{(1-2\vartheta)}\left[E_a\alpha_a Q_4 P_4 + E_a\alpha_a Q_4 n_1 + E_a\alpha_a Q_4 n_2\right], \quad V = \frac{\beta_1 E_a\alpha_a}{(1-2\vartheta)}\left[n_5 - n_3 + n_1 + n_2 + 2\right]$$
$$W = \frac{Q_3 E_a\alpha_a}{(1-2\vartheta)}\left[n_1 + n_2\right], \quad S = -\rho_a\left[\omega^2 - \left(\frac{g}{a}\right)\right] \tag{8}$$

2.1 Temperature Formulation

A one-dimensional steady-state heat conduction equation includes variable conductivity and temperature variation.

$$\frac{1}{r}\frac{d}{dr}\left[rk_r\frac{d}{dr}(T_r)\right]+q_r=0 \tag{9}$$

And boundary conditions for thermal are given by,

$$T_r = T_a \text{ at } r = a \text{ and } T_r = T_b \text{ at } r = b \tag{10}$$

Differentiating the above eq.(9) of the heat conduction equation to obtain the Navier equation for temperature,

$$A_1 r^2 T_r'' + B_1 r T_r' + C_1 T_r = \gamma_1 r^{n_5-n_3+2} \tag{11}$$

where

$$A_1 = k_a, \quad B_1 = k_a(n_3+1), \quad C_1 = 0, \quad \gamma_1 = -q_a$$

After solving eq.(11),

$$T_r = Q_3 + Q_4 r^{P_4} + \beta_1 r^{n_5 - n_3 + 2} \quad , \quad \frac{dT}{dr} = Q_4 P_4 r^{P_4 - 1} + \beta_1 (n_5 - n_3 + 2) r^{n_5 - n_3 + 1} \tag{12}$$

$$P_3 = 0 \, , \quad P_4 = \frac{A_1 - B_1}{A_1} = -n_3$$

Using the boundary condition find-out the value of Q_3 and Q_4 yields,

$$Q_4 = \frac{T_a - T_b}{a^{P_4} - b^{P_4}} - \frac{\beta_1 \left(a^{n_5 - n_3 + 2} - b^{n_5 - n_3 + 2} \right)}{a^{P_4} - b^{P_4}} \quad \text{and} \quad Q_3 = T_a - \beta_1 a^{n_5 - n_3 + 2} - Q_4 a^{P_4} \tag{13}$$

2.2 Solution of Displacement Equation

The displacement formulation has a general solution and a particular solution. Now general part of the solution, u_g is obtained by assuming,

$$u_g = Q r^P \tag{14}$$

Substitute the above eq.(14) in the homogeneous form of eq.(7) to get,

$$A P^2 + (B - A) P + C = 0 \tag{15}$$

The above eq. (15) has 2 real roots P_1 and P_2 as,

$$P_{1,2} = \frac{(A - B) \pm \sqrt{(B - A)^2 - 4AC}}{2A} \tag{16}$$

Thus, the general solution is,

$$u_g = Q_1 r^{P_1} + Q_2 r^{P_2} \tag{17}$$

Now particular part of the solution u_p is assumed to have the form

$$u_p = I r^{n_2 + P_4 + 1} + J r^{n_2 - n_3 + n_5 + 3} + L r^{n_2 + 1} + M r^{n_4 - n_1 + 3} \tag{18}$$

Solving, we get,

$$\begin{aligned}
&\left[A(n_2 + P_4 + 1)(n_2 + P_4) + B(n_2 + P_4 + 1) + C \right] I r^{n_2 + P_4 + 1} + \\
&\left[A(n_2 + n_5 - n_3 + 3)(n_2 + n_5 - n_3 + 2) + B(n_2 + n_5 - n_3 + 3) + C \right] J r^{n_2 - n_3 + n_5 + 3} \\
&+ \left[A(n_2 + 1)n_2 + B(n_2 + 1) + C \right] L r^{n_2 + 1} + \left[A(n_4 - n_1 + 3)(n_4 - n_1 + 2) + B(n_4 - n_1 + 3) + C \right] M r^{n_4 - n_1 + 3} \\
&= U r^{n_2 + P_4 + 1} + V r^{n_2 - n_3 + n_5 + 3} + W r^{n_2 + 1} + S r^{n_4 - n_1 + 3}
\end{aligned} \tag{19}$$

On solving the above equation, the following form is obtained.

$$\mathbf{I} = \frac{\mathbf{U}}{\mathbf{A}\left[(n_2 + P_4 + 1)(n_2 + P_4)\right] + \mathbf{B}\left[n_2 + P_4 + 1\right] + \mathbf{C}}$$

$$\mathbf{J} = \frac{\mathbf{V}}{\mathbf{A}\left[(n_2 + n_5 - n_3 + 3)(n_2 + n_5 - n_3 + 2)\right] + \mathbf{B}\left[(n_2 - n_3 + n_5 + 3)\right] + \mathbf{C}}$$

$$\mathbf{L} = \frac{\mathbf{W}}{\mathbf{A}\left[(n_2 + 1)(n_2)\right] + \mathbf{B}\left[(n_2 + 1)\right] + \mathbf{C}}$$
(20)

$$\mathbf{M} = \frac{\mathbf{S}}{\mathbf{A}\left[(n_4 - n_1 + 3)(n_4 - n_1 + 2)\right] + \mathbf{B}\left[(n_4 - n_1 + 3)\right] + \mathbf{C}}$$

Now the complete solution 'u' is the sum of the general part of the solution and the particular part of the solution as,

$$u = u_g + u_p$$
(21)

Thus,

$$u = Q_1 r^{P_1} + Q_2 r^{P_2} + I r^{n_2 + P_4 + 1} + J r^{n_2 - n_3 + n_5 + 3} + L r^{n_2 + 1} + M r^{n_4 - n_1 + 3}$$
(22)

Substituting eq.(22) in eq.(1) and (2), the stress and strain distributions can be written as,

$$\varepsilon_r = Q_1 p_1 r^{P_1 - 1} + Q_2 p_2 r^{P_2 - 1} + I\left(n_2 + P_4 + 1\right)r^{n_2 + P_4} + J\left(n_2 - n_3 + n_5 + 3\right)r^{n_2 - n_3 + n_5 + 2}$$
$$+ L\left(n_2 + 1\right)r^{n_2} + M\left(n_4 - n_1 + 3\right)r^{n_4 - n_1 + 2}$$
(23)

$$\varepsilon_\theta = Q_1 r^{P_1 - 1} + Q_2 r^{P_2 - 1} + I r^{n_2 + P_4} + J r^{n_2 - n_3 + n_5 + 2} + L r^{n_2} + M r^{n_4 - n_1 + 2}$$
(24)

$$\sigma_r = E_a \lambda \begin{bmatrix} Q_1\left\{(1-\vartheta)P_1 + \vartheta\right\}r^{n_1 + P_1 - 1} + Q_2\left\{(1-\vartheta)P_2 + \vartheta\right\}r^{n_1 + P_2 - 1} + I r^{n_1 + n_2 + P_4}\left\{(1-\vartheta)(n_2 + P_4 + 1) + \vartheta\right\} + \\ J r^{n_1 + n_2 + n_5 - n_3 + 2}\left\{(1-\vartheta)(n_2 + n_5 - n_3 + 3) + \vartheta\right\} + L r^{n_1 + n_2}\left\{(1-\vartheta)(n_2 + 1) + \vartheta\right\} + \\ M r^{n_4 + 2}\left\{(1-\vartheta)(n_4 - n_1 + 3) + \vartheta\right\} - (1+\vartheta)\alpha_a\left\{Q_3 r^{n_1 + n_2} + Q_4 r^{n_1 + n_2 + P_4} + \beta_1 r^{n_1 + n_2 + n_5 - n_3 + 2}\right\} \end{bmatrix}$$
(25)

The boundary condition of stresses is used to determine the constant Q_1 and Q_2. Considering the mechanical boundary condition on the inner side and outer side surface of the cylinder as

$$\sigma_r = -P_a \text{ at } r = a \text{ and } \sigma_r = -P_b \text{ at } r = b$$
(26)

Substituting the stress boundary condition in eq.(25), the constants become,

$$Q_1 = \frac{\phi_{22}X - \phi_{12}Y}{\phi_{11}\phi_{22} - \phi_{12}\phi_{21}} \text{ and } Q_2 = \frac{\phi_{11}Y - \phi_{21}X}{\phi_{11}\phi_{22} - \phi_{12}\phi_{21}}$$
(27)

$$\phi_{11} = E_a \lambda\left[P_1(1-v) + v\right]a^{n_1 + P_1 - 1} \qquad \phi_{12} = E_a \lambda\left[P_2(1-v) + v\right]a^{n_1 + P_2 - 1}$$
$$\phi_{21} = E_a \lambda\left[P_1(1-v) + v\right]b^{n_1 + P_1 - 1} \qquad \phi_{22} = E_a \lambda\left[P_2(1-v) + v\right]b^{n_1 + P_2 - 1}$$
(28)

$$X = -Z(a) - P_a \qquad Y = -Z(b) - P_b$$
(29)

$$Z(a) = E_a\lambda \begin{bmatrix} Ia^{n_1+n_2+P_4}\{(1-\vartheta)(n_2+P_4+1)+\vartheta\} + Ja^{n_1+n_2+n_5-n_3+2}\{(1-\vartheta)(n_2+n_5-n_3+3)+\vartheta\} \\ +La^{n_1+n_2}\{(1-\vartheta)(n_2+1)+\vartheta\} + Ma^{n_4+2}\{(1-\vartheta)(n_4-n_1+3)+\vartheta\} \\ -(1+\vartheta)\alpha_a\{Q_3a^{n_1+n_2} + Q_4a^{n_1+n_2+P_4} + \beta_1a^{n_1+n_2+n_5-n_3+2}\} \end{bmatrix} \quad (30)$$

$$Z(b) = E_a\lambda \begin{bmatrix} Ib^{n_1+n_2+P_4}\{(1-\vartheta)(n_2+P_4+1)+\vartheta\} + Jb^{n_1+n_2+n_5-n_3+2}\{(1-\vartheta)(n_2+n_5-n_3+3)+\vartheta\} + \\ Lb^{n_1+n_2}\{(1-\vartheta)(n_2+1)+\vartheta\} + Mb^{n_4+2}\{(1-\vartheta)(n_4-n_1+3)+\vartheta\} \\ -(1+\vartheta)\alpha_a\{Q_3b^{n_1+n_2} + Q_4b^{n_1+n_2+P_4} + \beta_1b^{n_1+n_2+n_5-n_3+2}\} \end{bmatrix} \quad (31)$$

3. Result and Discussion

3.1 Functionally Graded Properties

The variation in material parameters such as Young's modulus of elasticity, thermal expansion coefficient, density, and thermal conductivity along the cylinder radius is shown in Fig. 2 to Fig. 5. When the grading parameter (**n**) is zero it represents isotropic material behaviour. When the grading parameter (**n**) is positive the material properties increase as the radius increases, whereas when the parameter (**n**) is negative the material properties decrease as the radius increases.
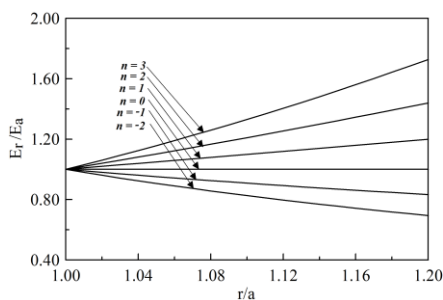
Fig. 2 Young's modulus variation
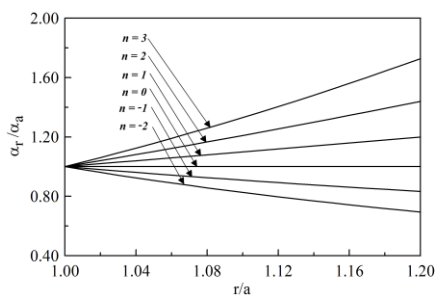
Fig. 3 Thermal expansion coefficient
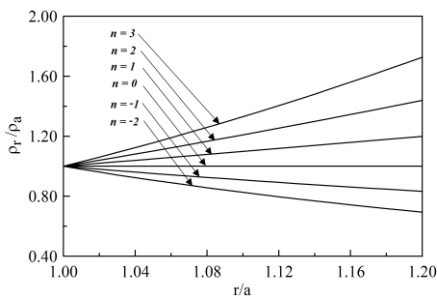
Fig. 4 Density variation
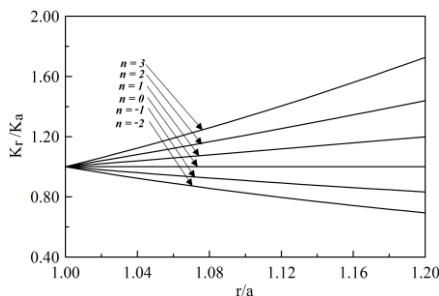
Fig. 5 Thermal conduction coefficient

3.2 Validation

Table 1. Geometrical and mechanical properties

Physical properties		Material properties						Boundary condition			
a m	b m	E_a GPa	α_a per ^0C	k_a W/mk	ρ_a kg/m^3	q_a kj/m^3	ϑ	P_a MPa	P_b MPa	T_a ^0C	T_b ^0C
1	1.2	200	1.2*10^{-6}	15	7800	50*10^3	0.3	50	0	10	0

The grading index $n_1 = n_2 = n_3 = n_4 = n_5 = n$ is selected as -2 to 3 and the results of the present method are compared with the literature [41]. Because for this particular range of **n,** the composition of metal and ceramic in a functionally graded material is a desired one. Beyond this range of **n**, an FGM would have an excessive amount of one phase, which would be inappropriate for real-world applications. Stress and displacement of FG hollow cylinder are reported at an angular velocity (ω) = 50 rps. Furthermore, the analysis was extended for FG hollow cylinder under the influence of rotation, gravitational force, and varying internal heat generation.

Stress distribution along the radial direction of the cylinder is investigated by the von Mises stress $\sigma^* = \sqrt{2}|\sigma_r - \sigma_\theta|$ for different values of the power law material index [42].
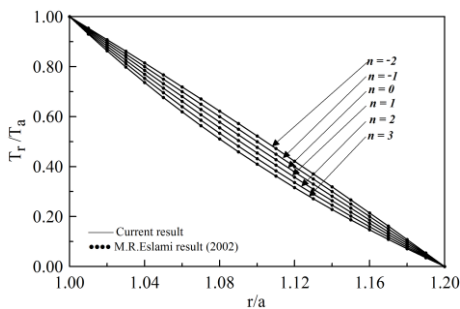
Fig. 6 Radially distributed temperature
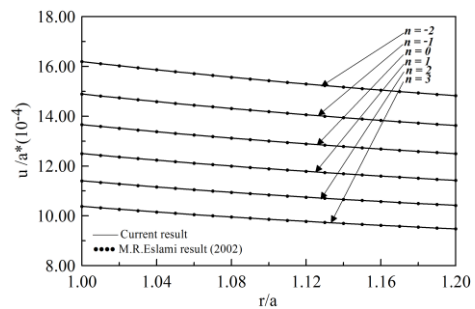
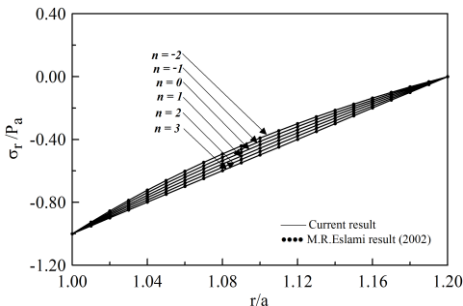Fig. 7 Radially distributed displacement
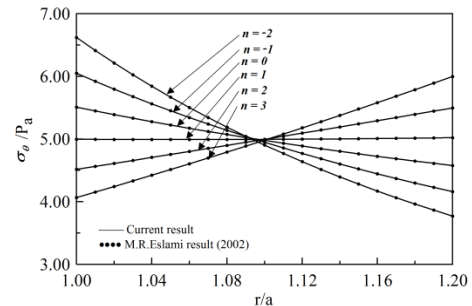

Fig. 8 Radially distributed radial stress

Fig. 9 Radially distributed tangential stress

Fig. 6 shows a decrease in T_r/T_a ratio from the inner to the outer radius of the cylinder. Temperature distribution and displacement are plotted for an index value of -2 to 3 as shown, whereas the negative value of the index shows a higher value of temperature & displacement as compared to the positive value of the index value.

For the negative value of the grading parameter, the magnitude of temperature is higher compared to the positive value of grading parameters. Fig. 7 to Fig. 9 show the radial displacement, radial stress, and tangential stress for aspect ratio **b/a** = 1.2. It is clear that the displacement decreases from the inner to outer radius, the magnitude is maximum for the negative grading parameter and minimum for the positive grading parameter, and least for indices, **n** = 3. The radial stress is maximum for the negative grading index and minimum for the positive grading index. Similarly, the tangential stress is maximum at the inner radius and for a negative grading index i.e., **n**<1, a reverse trend is seen beyond, (**r/a**) =1.10 and so the tangential stress reaches a maximum value at **r/a**=1.20 for positive grading index i.e., **n**>1.

3.3 Effect of Rotation in a Hollow Cylindrical Body

Fig. 10-14 shows the distribution of temperature, displacement, radial stress, tangential, and von Mises stress due to rotation effect only. Because of the rotational effect on the cylindrical body, the displacement and stresses induced are higher compared to the non-rotating case. Displacement is higher for a negative value of **n** as compared to a positive value of **n**. Radial stress is also higher for the negative value of **n** as compared to the positive value of **n** and compressive throughout the radial direction. For a negative value of **n**, the tangential and von Mises stresses are higher at the inner radius and then start converging up to **r/a** = 1.08 (approximately), after that tangential and von Mises stresses are diverging in nature. Stresses and displacement are higher due to the influence of rotation which can be seen when comparing the respective figures of section 3.2 with section 3.3. This analysis proposed an idea for a rotating hollow cylindrical body.

3.4 Effect of Gravity in Hollow Cylindrical Body

Fig. 15-19 shows the distribution of temperature, displacement, radial stress, tangential, and von Mises stress due to the gravity effect only. The maximum displacement attained is lesser than rotation. The nature of the variation of displacement and stresses is similar to that obtained in the previous case (section 3.3). Due to the effect of gravity, the results of displacement and stresses are lesser.

3.5 Effect of Variable Heat Generation in a Cylindrical Body

Fig. 20-24 shows the distribution of temperature, displacement, radial stress, tangential, and von Mises stress due to the variable heat generation effect. Fig. 20 shows the temperature distribution along the radial direction with variable heat generation. Here, the relationship between displacement and material grading index is inversely proportional i.e. for a negative value of **n**, the displacement is higher as compared to the positive value of **n**. The relation between displacement and radius of a hollow cylindrical body is inverse i.e. displacement is higher at **r**=0 and decreases as **r** increases.

The relation between radial stress and grading index is inversely proportional i.e. for a negative value of **n** radial stress is higher as compared to the positive value of **n**, the nature of tangential stress and von Mises stress is similar to the previous cases (section 3.3) but the magnitude is lesser. The results obtained in this case are higher as compared to the reference due to the influence of variable heat generation which is visible when comparing the figure of section 3.2 with section 3.5. This analysis proposed an idea for a hollow cylindrical body with variable heat generation.

3.6 Effect of rotation and gravity in cylindrical body

Fig. 25-29 shows the distribution of temperature, displacement, radial stress, tangential, and von Mises stress due to the influence of rotation and gravity together. The result obtained for displacement and stresses are similar to the result obtained in section 3.3 but the magnitude obtained is less as compared to section 3.3 (only rotation) because of

the combined influence of rotation & gravity. Magnitude is higher because of the influence of rotation & gravity. This analysis proposed an idea for hollow cylindrical body under the influence of rotation and gravity.
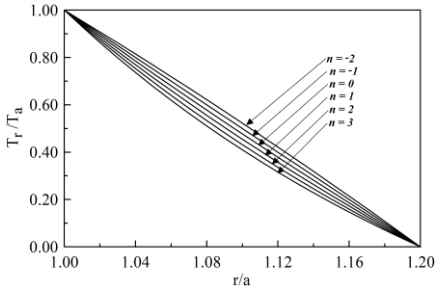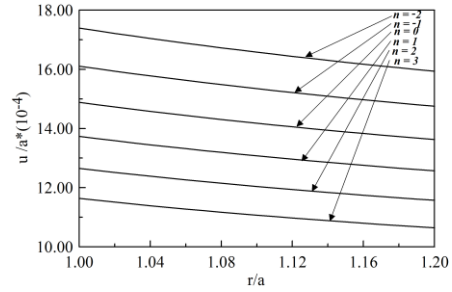

Fig. 10 Temperature distribution
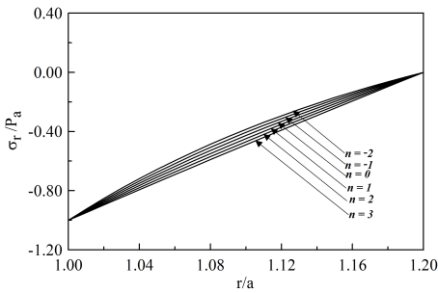

Fig. 11 Displacement results
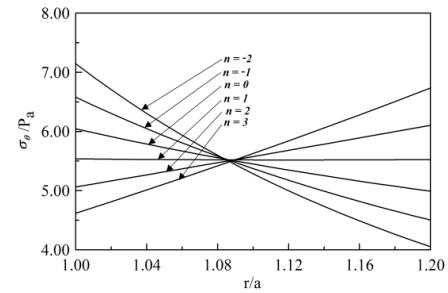

Fig. 12 Radial stress distribution

Fig. 13 Tangential stress distribution
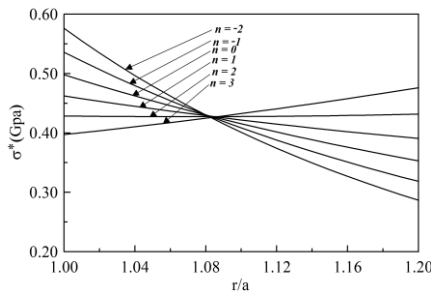
Fig. 14 von Mises stress along radial direction
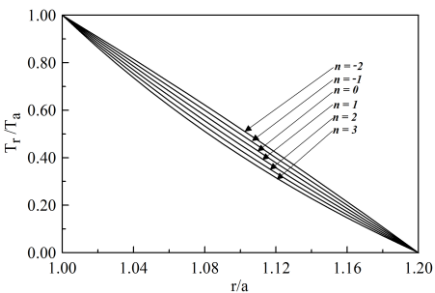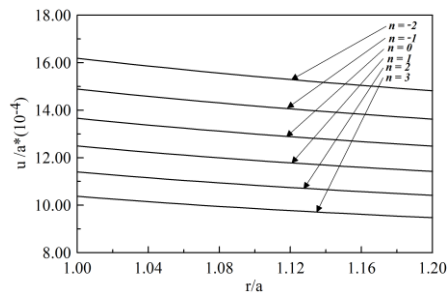

Fig. 15 Temperature distribution
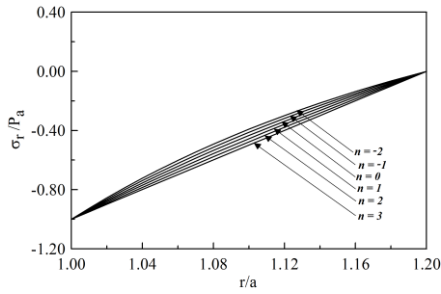

Fig. 16 Displacement results
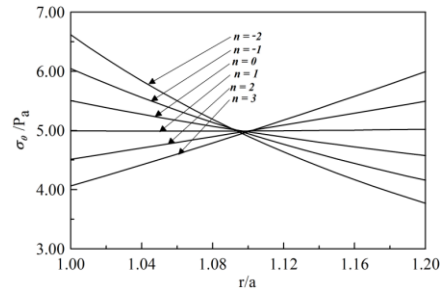
Fig. 17 Radial stress distribution

Fig. 18 Tangential stress distribution

Fig. 19 von Mises results along radial direction

Fig. 20 Temperature distribution

Fig. 21 Displacement results

Fig. 22 Radial stress distribution

Fig. 23 Tangential stress distribution
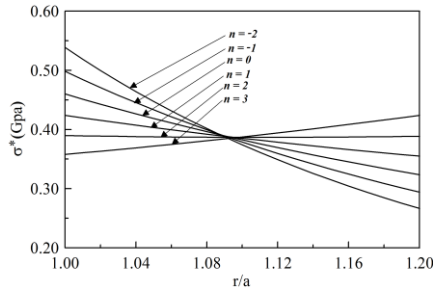
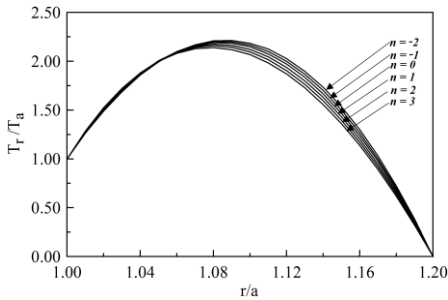Fig. 24 von Mises results along radial direction

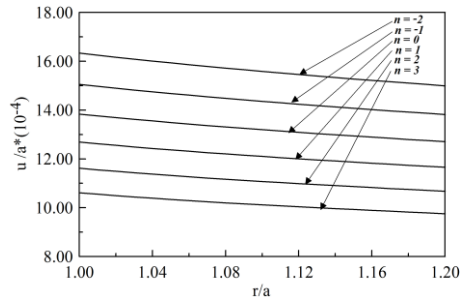Fig. 25 Temperature distribution
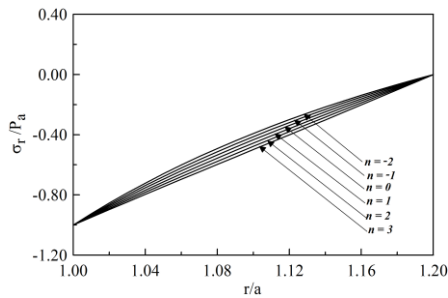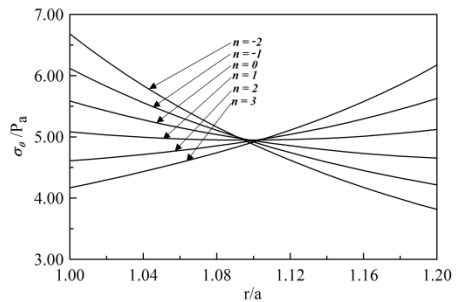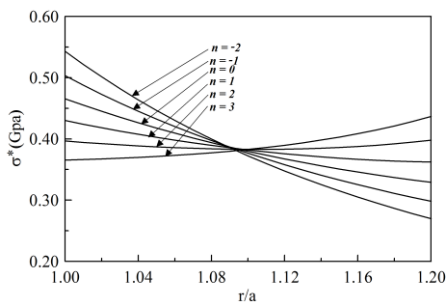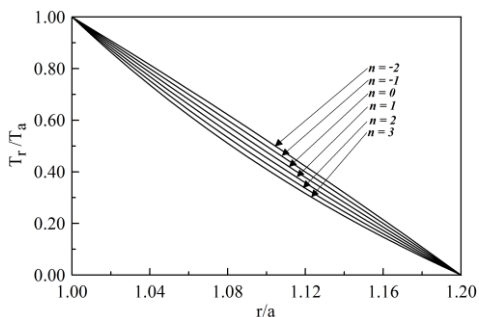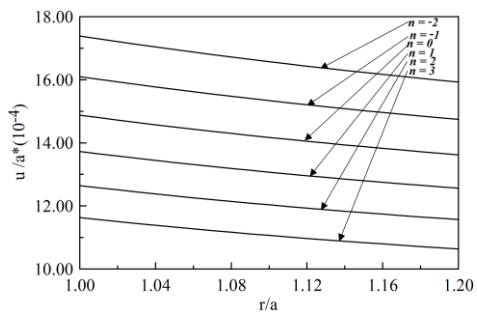
Fig. 26 Displacement results

Fig. 27 Radial stress distribution

Fig. 28 Tangential stress distribution

Fig. 29 von Mises results along radial direction

3.7 Effect of Rotation and Variable Heat Generation in a Cylindrical Body

Fig. 30-34 shows the distribution of temperature, displacement, radial stress, tangential, and von Mises stress due to rotation and variable heat generation. The nature of variation of displacement and stresses along the radius is similar to the previous cases and the relation of grading index with displacement and stresses is also similar to that discussed in previous cases. Due to the combined influence of rotation and variable heat generation, the result of displacement and stresses are higher compared to the previous cases. The combined effect of rotation and variable heat generation is visible when comparing the figures of sections 3.2, 3.3, 3.4, 3.5, and 3.6 with this present section. The variation of temperature is abrupt along the radius. This analysis proposed the idea of a hollow cylindrical body with the influence of rotation and heat generation.

Fig. 30 Temperature distribution

Fig. 31 Displacement results

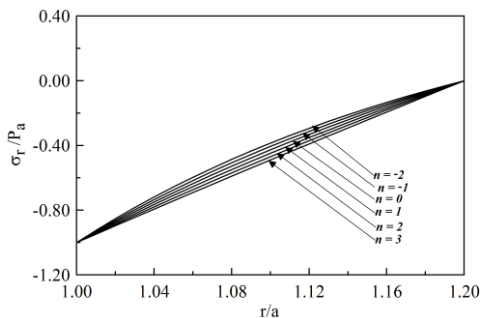Fig. 32 Radial stress distribution

Fig. 33 Tangential stress distribution

Fig. 34 von Mises results along radial direction

3.8 Effect of Gravity and Variable Heat Generation in Hollow Cylindrical Body

Fig. 35-39 shows the distribution of temperature, displacement, radial stress, tangential, and von Mises stress due to gravity and variable heat generation. Due to the combined loading of gravity and heat generation the results are less as compared to sections 3.3, 3.5, 3.6, and 3.7 but higher as compared to the reference & section 3.4 while comparing the figures. So this analysis proposed an idea of hollow cylindrical body influenced by gravity and variable heat generation.

Fig. 35 Temperature distribution
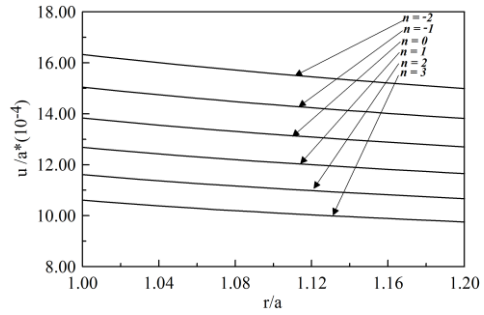
Fig. 36 Displacement results
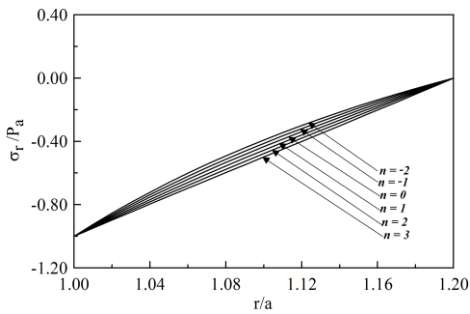
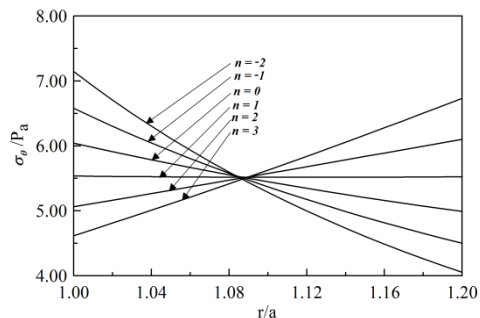Fig. 37 Radial stress distribution

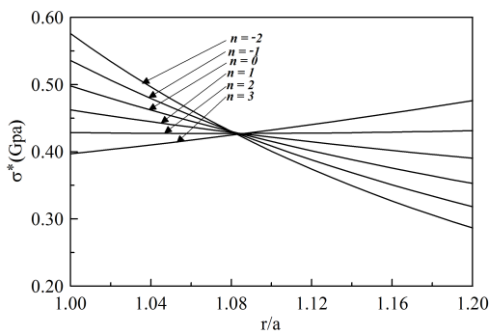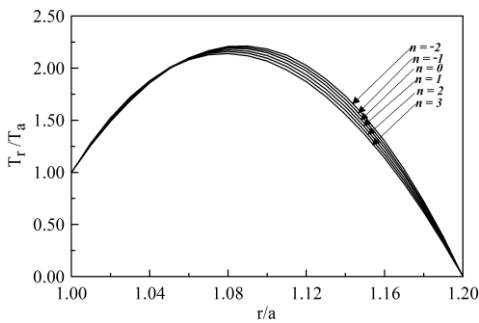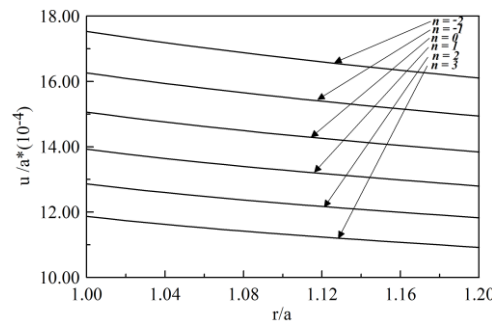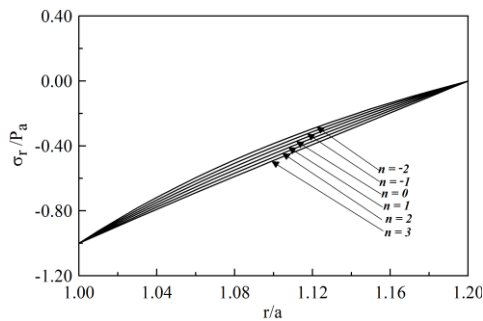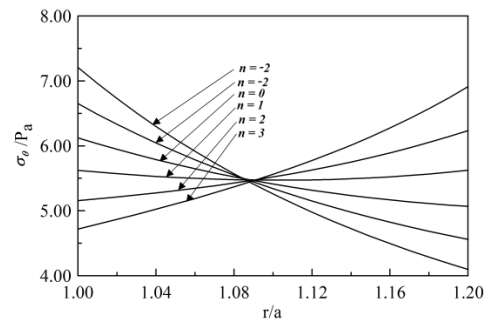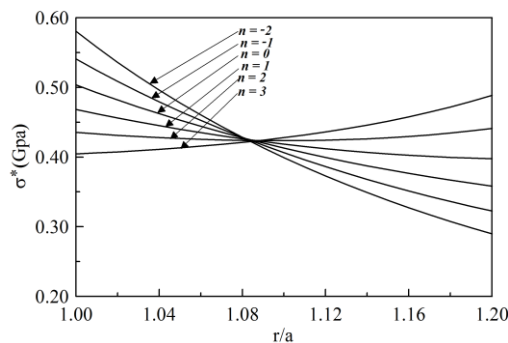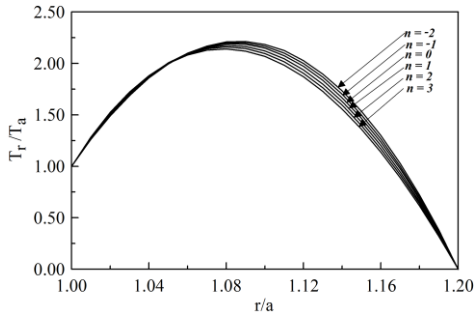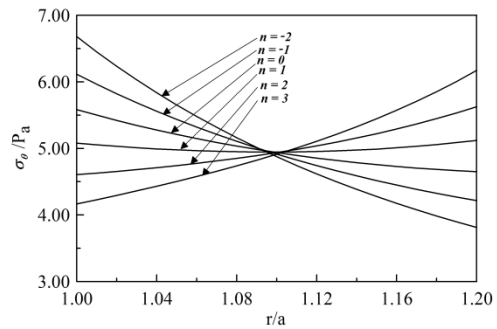Fig. 38 Tangential stress distribution
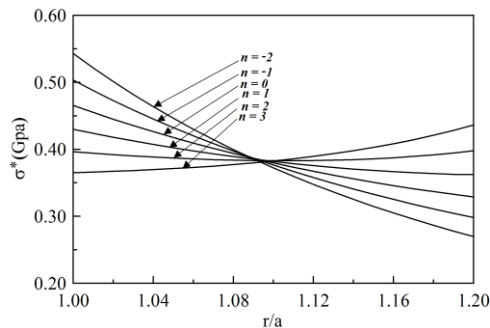
Fig. 39 von Mises results along radial direction

3.9 Effect of Rotation, Gravity and Variable Heat Generation in Hollow Cylindrical Body

Fig. 40-44 shows the distribution of temperature, displacement, radial stress, tangential, and von Mises stress due to rotation, gravity, and variable heat generation. In all the cases, the negative value of the grading index shows a higher value of radial stress as compared to the positive grading index. A reverse trend is seen in the variation of tangential stress along the radius, i.e., the tangential stress is converging type at the beginning and becomes equal at the center (*r/a*=1.09 approx.) irrespective of the grading parameter. Beyond this, the tangential stress shows a diverging behavior. In the converging part, the negative index yields a higher value of tangential stress as compared to the positive value of the index. The von Mises stress distribution is plotted in the radial direction from the inner side to the outer surface of the cylinder. The von Mises stresses are convergent up to the mid-surface after reaching a critical point and then the trend reverses. The nature of the convergent and divergent von Mises stress is similar to that of tangential stress distribution. The result obtained is higher as compared to the reference and all above sections except section 3.7 which is observed when comparing the results of all sections discussed in this paper. So, this analysis proposed the idea of a hollow cylindrical body combined with rotation, gravity, and variable heat generation.

A power-law variation of material property is considered in the present study. The power law is applied directly to the material properties and not to the volume fraction variation of functionally graded materials. The other aspect of analyzing these structures is layer-wise or continuously graded. The difference between these two methods is that in a layer-wise structure the stress distribution obtained is discontinuous and stress jumps can be seen at the interface. On the other hand, when the change in material composition is smoother there will be no jump at the interface. It is always preferred to vary the composition in a smoother fashion such that the causes of delamination can be prohibited which may arise due to the difference in thermo-mechanical properties of a material selected for the fabrication of functionally graded structures. The distribution of stresses varies smoothly along the radial direction. And so, the selection of grading parameters plays a crucial role in improving the performance of functionally graded materials.
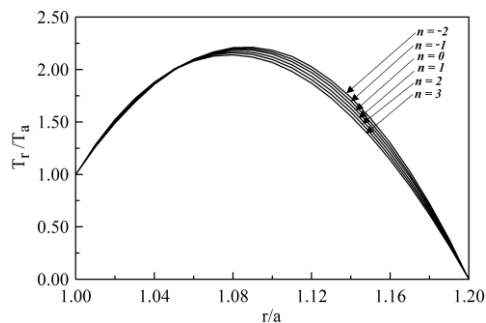
Fig. 40 Temperature distribution
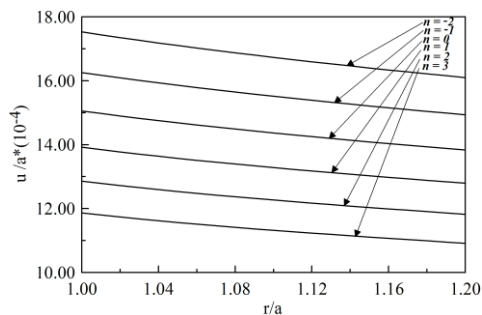
Fig. 41 Displacement results
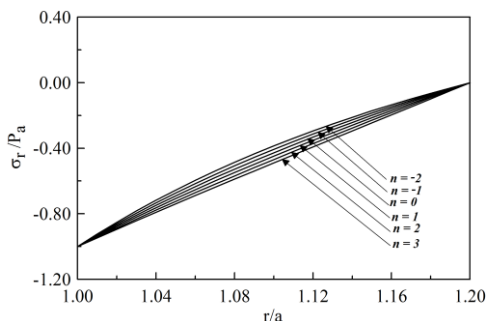
Fig. 42 Radially Distributed Radial Stress
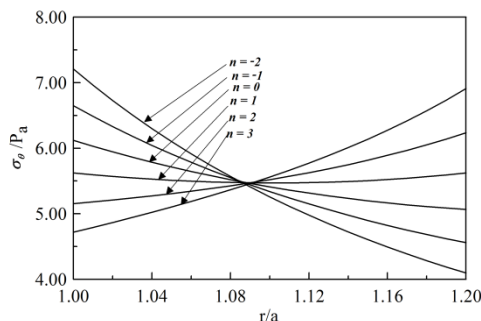
Fig. 43 Tangential stress distribution
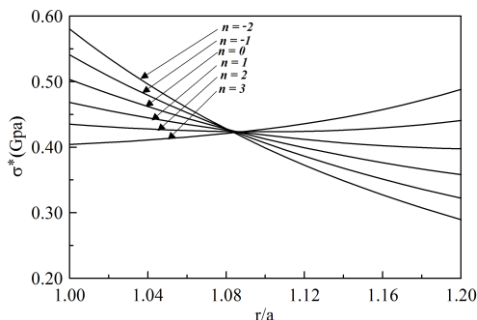
Fig. 44 von Mises results along radial direction

4. Conclusion

Thermo-mechanical stress analysis of the FG hollow cylinder has been performed for varying grading indices under the effect of grading parameters, rotational speed, gravitational force, and heat generation. By employing Navier's method, the problem was solved considering variable heat generation in a cylinder.

- The fabrication of such structures is possible using centrifugal casting and additive manufacturing techniques; the centrifugal casting technique is very well suited for fabricating axisymmetric structures whereas there are no such limitations in additive manufacturing. In centrifugal casting, the gradation variation will be continuous whereas in additive manufacturing because of layer-wise deposition a layer-wise graduation is expected.
- Due to the increments in grading parameters, the strength of the hollow cylindrical body is improving resulting in lowering the displacement and radial stresses. The von Mises stresses decrease till a certain value of **b/a** is reached beyond this von Mises stresses of FG hollow cylindrical body increase. The magnitude of von-Mises stress is higher at the inner radius of FG hollow cylindrical body and lesser at the outer radius, but for **n** = 3 the variation in von Mises stress is almost uniform.
- For **n**>1, the tangential stresses of FG hollow cylindrical body increase radially but for **n**<1, it decreases; and for **n**=1, the variation in tangential stress is almost uniform along the radial direction.
- From the analysis of the hollow cylindrical body, it was found that the radial displacement varies inversely with the grading index whereas the tangential stress increases with **n** when **n** is greater than unity. Similarly, von Mises stress

is directly proportional to a grading index greater than 2 and inversely to a grading index less than 2.

Nomenclature

a	Inner radius (m)	ρ_r	Density function (kg/m^3)
b	Outer radius (m)	q_r	Heat generation function (kJ/m^3)
r	Radial direction (m)	E_a	Young's modulus at 'a' (MPa)
u	Displacement component (m)	α_a	CTE at 'a' ($per\ ^0C$)
ε_r	Radial strain	k_a	TCC at 'a' (W/mk)
ε_θ	Tangential strain	$\rho_{a,}$	Density at 'a' (kg/m^3)
σ_r	Radial stress (MPa)	q_a	Heat generation at 'a' (kJ/m^3)
σ_θ	Tangential stress (MPa)	n_1, n_2, n_3, n	Material index
u', T'	1st order differential	T_r	Temperature function (^0C)
u'', T''	2nd order differential	T_a	Temperature at 'a' (^0C)
ω	Rotation (rad/s)	T_b	Temperature at 'b' (^0C)
g	Gravity (m/s^2)	$Q_3, Q_4,$ P_3, P_4	Thermal constants
E_r	Young's modulus function (MPa)	$Q_1, Q_2,$ P_1, P_2	Displacement constants
α_r	CTE function ($per\ ^0C$)	P_a	Pressure at inside (MPa)
k_r	Thermal conduction coefficient (TCC) function (W/mk)	P_b	Pressure at outside (MPa)

References

[1] Saleh B, Jiang J, Ma A, et al. Review on the Influence of Different Reinforcements on the Microstructure and Wear Behavior of Functionally Graded Aluminum Matrix Composites by Centrifugal Casting. Met Mater Int 2020; 26: 933-960. https://doi.org/10.1007/s12540-019-00491-0

[2] Mortensen A, Suresh S. Functionally graded metals and metal-ceramic composites: Part 1 Processing. null 1995; 40: 239-265. https://doi.org/10.1179/imr.1995.40.6.239

[3] Madan R, Bhowmick S. A review on application of FGM fabricated using solid-state processes. Advances in Materials and Processing Technologies 2020; 6: 608-619. https://doi.org/10.1080/2374068X.2020.1731153

[4] Parihar RS, Setti SG, Sahu RK. Recent advances in the manufacturing processes of functionally graded materials: a review. Science and Engineering of Composite Materials 2018; 25: 309-336. https://doi.org/10.1515/secm-2015-0395

[5] Saleh B, Jiang J, Fathi R, et al. 30 Years of functionally graded materials: An overview of manufacturing methods, Applications and Future Challenges. Composites Part B: Engineering 2020; 201: 108376. https://doi.org/10.1016/j.compositesb.2020.108376

[6] Verma RK, Parganiha D, Chopkar M. A review on fabrication and characteristics of functionally graded aluminum matrix composites fabricated by centrifugal casting method. SN Appl Sci 2021; 3: 227. https://doi.org/10.1007/s42452-021-04200-8

[7] Abdalla HMA, Casagrande D, De Bona F, et al. An optimized pressure vessel obtained by metal additive manufacturing: Preliminary results. International Journal of Pressure Vessels and Piping 2021; 192: 104434. https://doi.org/10.1016/j.ijpvp.2021.104434

[8] Arefi M, Firouzeh S, Mohammad-Rezaei Bidgoli E, et al. Analysis of porous micro-plates reinforced with FG-GNPs based on Reddy plate theory. Composite Structures 2020; 247: 112391. https://doi.org/10.1016/j.compstruct.2020.112391

[9] Lakshman S, Subhashis S, Kashinath S, et al. Limit elastic speeds of functionally graded annular disks. FME Transactions 2018; 46: 603-611. https://doi.org/10.5937/fmet1804603S

[10] Madan R, Bhowmick S. A numerical solution to thermo-mechanical behavior of temperature dependent rotating functionally graded annulus disks. AEAT; ahead-of-print. Epub ahead of print 7 June 2021. https://doi.org/10.1108/AEAT-01-2021-0012

[11] Madan R, Bhowmick S. Modeling of functionally graded materials to estimate effective thermo-mechanical properties. WJE; ahead-of-print. Epub ahead of print 26 January 2021. DOI: 10.1108/WJE-09-2020-0445. https://doi.org/10.1108/WJE-09-2020-0445

[12] Sharma D, Kaur R. Thermoelastic analysis of FGM hollow cylinder for variable parameters and temperature distributions using FEM. Nonlinear Engineering 2020; 9: 256-264. https://doi.org/10.1515/nleng-2020-0013

[13] Bacciocchi M, Luciano R, Majorana C, et al. Free Vibrations of Sandwich Plates with Damaged Soft-Core and Non-Uniform Mechanical Properties: Modeling and Finite Element Analysis. Materials 2019; 12: 2444. https://doi.org/10.3390/ma12152444

[14] Menasria A, Kaci A, Bousahla AA, et al. A four-unknown refined plate theory for dynamic analysis of FG-sandwich plates under various boundary conditions. Steel and Composite Structures 2020; 36: 355-367.

[15] Liang K, Li Z. A novel nonlinear FE perturbation method and its application to stacking sequence optimization for snap-through response of cylindrical shell panel. Computers & Mathematics with Applications 2022; 112: 154-166. https://doi.org/10.1016/j.camwa.2022.03.002

[16] Chen Z-F, Wang H-J, Sang Z, et al. Theoretical and Numerical Analysis of Blasting Pressure of Cylindrical Shells under Internal Explosive Loading. JMSE 2021; 9: 1297. https://doi.org/10.3390/jmse9111297

[17] Ozturk A, Gulgec M. Elastic-plastic stress analysis in a long functionally graded solid cylinder with fixed ends subjected to uniform heat generation. International Journal of Engineering Science 2011; 49: 1047-1061. https://doi.org/10.1016/j.ijengsci.2011.06.001

[18] Tutuncu N, Temel B. A novel approach to stress analysis of pressurized FGM cylinders, disks and spheres. Composite Structures 2009; 91: 385-390. https://doi.org/10.1016/j.compstruct.2009.06.009

[19] Çelebi Kavdir E, Aydin MD. The stress analysis on two different adhesively bonded t-joints via 3d nonlinear finite element method. Journal of Thermal Engineering 2020; 170-179. https://doi.org/10.18186/thermal.729864

[20] Trung KN. The temperature distribution of the wet cylinder liner of v-12 engine according to calculation and experiment. Journal of Thermal Engineering 2021; 7: 1872-1884. https://doi.org/10.18186/thermal.1051265

[21] Falsonea G, La Valle G. Dynamic and buckling of functionally graded beams based on a homogenization theory. Res. Eng. Struct. Mater., 2021; 7(4): 523-538. https://doi.org/10.17515/resm2021.259st0216

[22] Esener E, Unlu A. Analytical evaluation of plasticity models for anisotropic materials with experimental validation. Res. Eng. Struct. Mater., 2022; 8(1): 75-89.

[23] Tutuncu N. Stresses in thick-walled FGM cylinders with exponentially-varying properties. Engineering Structures 2007; 29: 2032-2035. https://doi.org/10.1016/j.engstruct.2006.12.003

[24] Ghannad M, Rahimi GH, Nejad MZ. Elastic analysis of pressurized thick cylindrical shells with variable thickness made of functionally graded materials. Composites Part B: Engineering 2013; 45: 388-396. https://doi.org/10.1016/j.compositesb.2012.09.043

[25] Jabbari M, Bahtui A, Eslami MR. Axisymmetric mechanical and thermal stresses in thick short length FGM cylinders. International Journal of Pressure Vessels and Piping 2009; 86: 296-306. https://doi.org/10.1016/j.ijpvp.2008.12.002

[26] Rahimi GH, Arefi M, Khoshgoftar MJ. Application and analysis of functionally graded piezoelectrical rotating cylinder as mechanical sensor subjected to pressure and thermal loads. Appl Math Mech-Engl Ed 2011; 32: 997-1008. https://doi.org/10.1007/s10483-011-1475-6

[27] Khoshgoftar MJ, Rahimi GH, Arefi M. Exact solution of functionally graded thick cylinder with finite length under longitudinally non-uniform pressure. Mechanics Research Communications 2013; 51: 61-66. https://doi.org/10.1016/j.mechrescom.2013.05.001

[28] Nejad MZ, Jabbari M, Ghannad M. Elastic analysis of axially functionally graded rotating thick cylinder with variable thickness under non-uniform arbitrarily pressure loading. International Journal of Engineering Science 2015; 89: 86-99. https://doi.org/10.1016/j.ijengsci.2014.12.004

[29] Shi Z, Zhang T, Xiang H. Exact solutions of heterogeneous elastic hollow cylinders. Composite Structures 2007; 79: 140-147. https://doi.org/10.1016/j.compstruct.2005.11.058

[30] Habib E-S, El-Hadek MA, El-Megharbel A. Stress Analysis for Cylinder Made of FGM and Subjected to Thermo-Mechanical Loadings. Metals 2018; 9: 4. https://doi.org/10.3390/met9010004

[31] Peng XL, Li XF. Thermoelastic analysis of a cylindrical vessel of functionally graded materials. International Journal of Pressure Vessels and Piping 2010; 87: 203-210. https://doi.org/10.1016/j.ijpvp.2010.03.024

[32] Saeedi S, Kholdi M, Loghman A, et al. Thermo-elasto-plastic analysis of thick-walled cylinder made of functionally graded materials using successive approximation method. International Journal of Pressure Vessels and Piping 2021; 194: 104481. https://doi.org/10.1016/j.ijpvp.2021.104481

[33] Yang W, Pang J, Wang L, et al. Thermo-mechanical fatigue life prediction based on the simulated component of cylinder head. Engineering Failure Analysis 2022; 135: 106105. https://doi.org/10.1016/j.engfailanal.2022.106105

[34] M. Dehghan. An Approximate Thermo-Mechanical Solution of a Functionally Graded Cylinder Using Hybrid Integral Transform and Finite Element Method. Journal of Solid Mechanics 2022; 14: 17-36.

[35] Chen YZ, Lin XY. Elastic analysis for thick cylinders and spherical pressure vessels made of functionally graded materials. Computational Materials Science 2008; 44: 581-587. https://doi.org/10.1016/j.commatsci.2008.04.018

[36] Go J, Afsar AM, Song JI. Analysis of Thermoelastic Characteristics of a Rotating FGM Circular Disk by Finite Element Method. Advanced Composite Materials 2010; 19: 197-213. https://doi.org/10.1163/092430410X490473

[37] Frahlia H, Bennai R, Nebab M, et al. Assessing effects of parameters of viscoelastic foundation on the dynamic response of functionally graded plates using a novel HSDT theory. Mechanics of Advanced Materials and Structures 2022; 1-15. https://doi.org/10.1080/15376494.2022.2062632

[38] Bennai Riadh, Mellal Fatma, Nebab Mokhtar, et al. On wave dispersion properties of functionally graded plates resting on elastic foundations using quasi-3D and 2D HSDT. Earthquakes and Structures 2022; 22: 447-460.

[39] Mellal F, Bennai R, Nebab M, et al. Investigation on the effect of porosity on wave propagation in FGM plates resting on elastic foundations via a quasi-3D HSDT. null 2021; 1-27. https://doi.org/10.1080/17455030.2021.1983235

[40] Nebab M, Ait Atmane H, Bennai R, et al. Effect of variable elastic foundations on static behavior of functionally graded plates using sinusoidal shear deformation. Arab J Geosci 2019; 12: 809. https://doi.org/10.1007/s12517-019-4871-5

[41] Jabbari M, Sohrabpour S, Eslami MR. Mechanical and thermal stresses in a functionally graded hollow cylinder due to radially symmetric loads. International Journal of Pressure Vessels and Piping 2002; 5. https://doi.org/10.1016/S0308-0161(02)00043-1

[42] Eslami MR, Babaei MH, Poultangari R. Thermal and mechanical stresses in a functionally graded thick sphere. International Journal of Pressure Vessels and Piping 2005; 82: 522-527. https://doi.org/10.1016/j.ijpvp.2005.01.002

Research Article

Air blast response of sandwich structures with auxetic cores under in-plane and axial loadings

Kadir Günaydın[a], Orhan Gülcan[b]

General Electric Aerospace, Gebze, Kocaeli, Turkey

Article Info	Abstract
	Blast loading due to an explosion nearby may generate severe damages on the target. Therefore, engineering structures need to be designed by considering blast loads due to terrorist attacks, accidental explosions or natural disasters. Sandwich structures are good candidates for blast loading applications and core section of these panels are very important to absorb blast loads. This study focused on blast resistance of sandwich structures with lattice core designs. Sandwich panels with honeycomb cores and re-entrant and double arrowhead auxetic cores, which are common and easy to produce in comparison to other type of lattice structures, were used to investigate the impact of core design on front and back face sheet thicknesses, total absorbed energy and maximum stress under in-plane and axial loading due to an explosion. Results revealed that sandwich structures absorb more energy when loaded along axial direction than in-plane direction. According to the simulation results, double arrowhead core outperformed by showing the lowest stress, front and back face displacement and the highest total energy absorption.

1. Introduction

Military vehicles, marine structures and buildings undergo very high loads with very high strain rates due to the detonation of an explosive nearby. When an explosive is detonated, a shock wave with a high velocity and pressure is released from the explosive and moves towards the target. This shock wave or blast loading may generate severe damages on the target. Therefore, these structures need to be designed by considering these loads, or specifically blast loads [1].

To increase the blast resistance of engineering applications, different studies have been performed on blast analysis of different types of structures and materials in literature. Sandwich structures with crushable cores (Fig. 1) are good candidates for blast loading applications since cores between front and back face sheets can dissipate a very large amount of energy in a blast scenario and weakens the transmitted shockwave to back face sheets and therefore protects the vital structures from failure [2]. Core design and core type selection is very important for air blast loading applications of sandwich structures. In literature, different types of sandwich structures with different types of cores have been investigated in terms of their blast performance [3-6]. One of the core types used in sandwich structures to increase blast resistance is auxetic core. When a material or structure is subjected to tensile loading, it extends in longitudinal direction and contracts in lateral direction. The negative value of the ratio of contraction strain to extension strain is called Poisson's ratio which is close to 1/3 for most materials but in rubbery materials it approaches to 1/2. Apart from these materials, some materials show negative Poisson's ratio characteristics [7]. Negative Poisson's ratio, or auxetic, materials expand laterally

when stretched and contract laterally when compressed [8]. Auxetic structures have unique mechanical, indentation, deformation and viscoelastic behaviors [9]. As stated by Prawoto, auxetic materials find their usage in different industrial applications where specific applications need negative Poisson's ratio, large shear resistance, higher hardness, lower fatigue crack propagation, large toughness and modulus resilience and / or vibration absorption characteristics [10]. For instance, auxetic structures have been used effectively in crashworthiness tubes in automotive and aerospace applications to increase energy absorption capability and without increasing the total weight considerably. Studies showed that auxetic foam filled tubes had 41.3% and 14.3% higher energy absorption capability than empty tubes and tubes with conventional foam filled, respectively [11]. In another study, it was stated that specific energy absorption of anti-tetrachiral and re-entrant lattices filled tubes were 28.5% and 20.6% higher than empty tube, respectively [12]. It was also stated that tubes with auxetic foam filled had better progressive collapse compared to empty tubes and tubes with conventional foam filled [13].
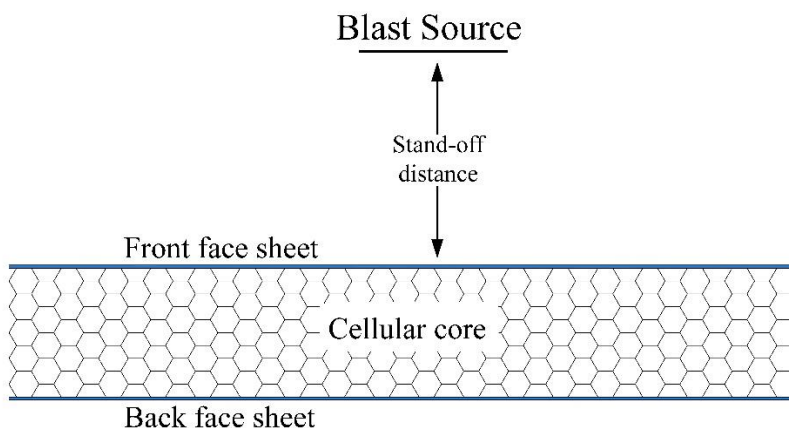
Fig. 1 Blast mitigation concept using a sandwich panel

In a blast loading, auxetic structures move towards impacted area due to their unique negative Poisson's ratio characteristics causing more densification and larger energy absorption at impacted area [14]. Due to these unique characteristics, different types of auxetic structures have been used as core structure in sandwich structures for blast loading applications. For instance, reentrant auxetic structures have been used for blast loading applications in literature [15, 16]. Qi et al. investigated ballistic response of honeycomb sandwich structures with aluminum face sheets and aluminum regular, rectangular-shaped, and re-entrant hexagons cores. They stated that sandwich structures with re-entrant hexagons cores showed the highest blast resistance due to negative Poisson's ratio characteristics [17]. Jin et al. investigated the blast resistance of sandwich structures with graded and cross-arranged auxetic re-entrant cell honeycomb cores. They stated that, compared to ungraded and regular-arranged cores, these structures showed higher resistance against blast loads and the highest blast resistance was observed in structures where cross-arranged graded honeycomb cores with higher density of the upper layer were used [18]. Imbalzano et al. investigated blast performance of sandwich structures with re-entrant auxetic core and stated that re-entrant auxetic core increased the plastic energy dissipation by 50% and decreased back face sheet displacement by 30% when compared with equivalent monolithic steel plates [2]. Qi et al. evaluated blast performance of sandwich panels with honeycomb core and re-entrant hexagonal cells both numerically and experimentally. They stated that these structures showed higher blast resistance than conventional honeycomb structures of the same size, areal density and

material [19]. Wang et al. stated that sandwich structures with three-dimensional double V auxetic core showed higher blast resistance and less back face deflection than solid plate [20]. Yang et al. stated that sandwich structures with auxetic core showed better blast performance than traditional panels and this performance can be increased by increasing the number of layers and Poisson's ratio of core [21]. Imbalzano et al. investigated blast resistance of auxetic composite sandwich structures and equivalent honeycomb structures. They stated that in both structures, core and front face sheets completely absorbed the impact energy, but auxetic composite sandwich structures resulted in less stress on back face sheets. Energy dissipation increased and stress on back face sheet reduced when number of layers increased in auxetic composite sandwich structures [22]. Hajmohammad et al. investigated blast response of sandwich structures with nanocomposite face sheets reinforced by carbon nanotubes and auxetic honeycombs core. Their results revealed that reinforcing face sheets with 0.1% carbon nanotubes decreased the maximum dynamic deflection by 59% [23]. Xiao et al investigated the high velocity impact response of sandwich beams with auxetic re-entrant hexagonal aluminum honeycomb core experimentally and numerically. They stated that during impact, local indentation with negative Poisson's ratio deformation and then global deformation were observed and when re-entrant wall thickness increased, negative Poisson's ratio deformation characteristics decreased [24]. Lan et al. investigated the blast resistance of cylindrical sandwich structures with three different cores: aluminum foam core, hexagonal honeycomb core, and auxetic honeycomb core. They stated that structures with auxetic honeycomb cores showed higher blast resistance than that with aluminum foam cores and hexagonal honeycomb cores. Their numerical results revealed that blast performance of structures with all types of cores increased with an increase in curvature and face sheet thickness. Increasing back face sheet thickness was more effective than increasing front face sheet thickness in panels with auxetic honeycomb cores in terms of blast resistance. This result came out to be opposite for the other two core configuration [25]. Novak et al. investigated blast resistance of sandwich composite structures with 3D chiral auxetic core. Experimental results revealed that sandwich composite structures with chiral auxetic core resulted in higher specific energy absorption than a core with a positive Poisson's ratio materials of the same porosity and mass [14]. Lan et al. investigated the blast response of a curved structure with three-dimensional double arrow auxetic core [26]. Luo et al. investigated blast resistance of sandwich structures with composite face sheets and re-entrant and honeycomb cores. Their results revealed that structures with honeycomb cores showed less stress at back face sheet. On the other hand, panels with re-entrant cores showed the best anti-explosion performance at front face sheet. Panel deformation from blast loading was due to crushable cells with auxetic behavior for panels with re-entrant cores and to whole panel bending for panels with honeycomb cores [27].

The studies in literature cover the mechanical and blast performance of sandwich structures with different cores in single lattice structure orientation. However, to the best of authors' knowledge, no study has so far focused on the blast resistance of sandwich structures with different type of auxetic cores under in-plane and axial loadings. To fill the gap of showing efficiency of lattice structure orientation, in this study, blast resistance of sandwich structures with AISI 4340 steel front and back face sheets and different types of AA5083-H116 aluminum alloy auxetic structures as core geometries were investigated by using CONWEP (conventional weapons effects program) blast loading model. Honeycomb cores and re-entrant and double arrowhead auxetic cores were used as design variables and front and back face sheet thicknesses, total absorbed energy and maximum stress under in-plane and axial loadings were evaluated as design outputs. The contribution focuses only on through numerical investigations since experimental studies are not practical in view of the special loading regime. However, the employed CONWEP framework which is already based on experimental investigation partially fills this gap. A

similar approach was used by Walkowiak et al. [28] where they investigated different core topologies in sandwich panels subjected to air blast loading. However, the distinguishing feature of the present study is the analysis of different loading regimes in terms of in-plane and axial loading directions. The rest of the paper is organized as follows: Section 2 describes the numerical method details used for blast loading analysis, Section 3 reveals the analysis results and relations between core type and design outputs, and finally the paper is concluded with a Conclusion section which lists main findings from the study.

2. Materials and Methods

In the present study, AISI 4340 steel front and back face sheets with 1.25x640x640 mm dimensions and AA5083-H116 aluminum alloy auxetic cores with 50x640x640 mm dimensions were used. The highest dimensions for the sandwich structure were selected in accordance with the computational efficiency and the current study in literature. The material properties of AISI 4340 steel and AA5083-H116 aluminum alloy are shown in Table 1. AISI 4340 steel material is characterized by its high yield stress and low ductility, on the other hand, AA5083-H116 aluminum alloy is characterized by its high specific energy absorption [22].

Table 1. Material properties of AISI 4340 steel and AA5083-H116 aluminum alloy [2]

	AISI 4340	AA5083-H116
Density (kg/m3)	7850	2750
Elastic modulus (GPa)	210	70
Poisson's ratio	0.3	0.3
Melting temperature (K)	1800	893
Yield stress (MPa)	792	215
Stress hardening (MPa)	510	280

Three different core geometries were used: honeycomb core and re-entrant and double arrowhead auxetic cores. The geometries were modelled by using Siemens NX 12 software. The dimensions of each unit cells for each core geometries are shown in Fig. 2.
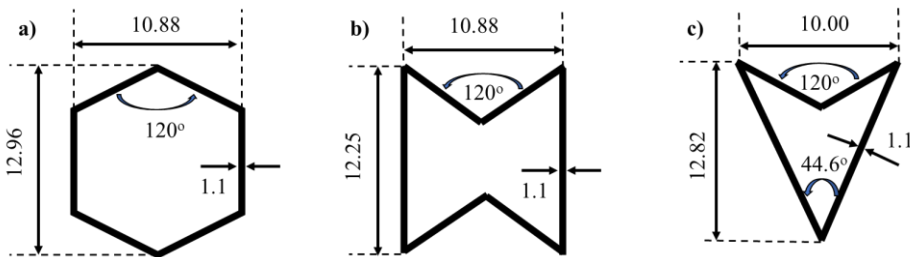
Fig. 2 Dimensions of unit cell geometries: a) honeycomb, b) re-entrant, c) double arrowhead

By using unit cell topologies, sandwich structure core geometries were modelled. The dimension of the unit cell topologies is selected in terms of obtaining the equal core thickness in different designs. These sandwich structures were intended to be loaded in axial and in-plane directions. The in-plane direction is the direction where the orientation of the cell walls is as much parallel as to the bonding axis [29]. The loading directions for

each core geometry and related sandwich structures are shown in Fig. 3 and 4, respectively.
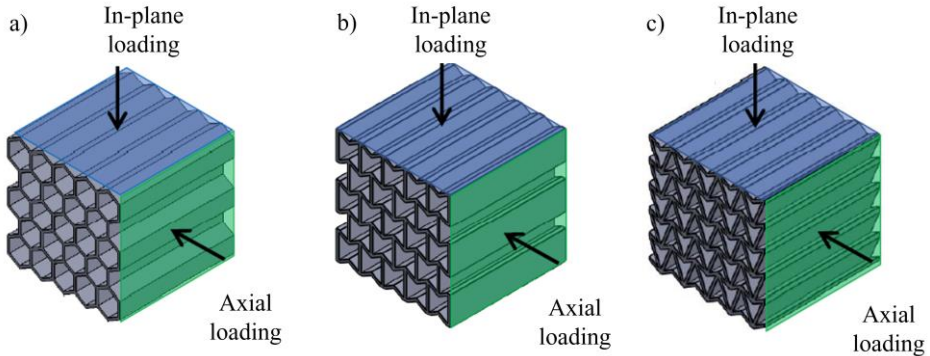
Fig. 3 Loading directions for: a) honeycomb, b) re-entrant, c) double arrowhead lattice structure cores

Blast loading applications were performed by using CONWEP (conventional weapons effects program) blast loading model in Abaqus 6.14. In CONWEP, the blast originated from the source creates pressure and it decays with time, as expressed below:

$$P(\text{t}) = P_{so} \left[1 - \frac{t - T_a}{T_0} \right] \exp \left[\frac{-Ax(t - T_a)}{T_0} \right] \tag{1}$$

in which P(t) – MPa is the pressure at the time t - sec, P_{so} – MPa is the peak incident pressure, T_o – ms is the positive phase duration, A is the decay coefficient, and T_a - ms is the arrival time of the shock wave. The explosive mass (1 kg TNT) was placed at the center of sandwich structure and 100 mm away from the front face. The mass of the explosive is determined as a result of different amount of explosive mass trials in order to define the optimum emerged blast that the sandwich structures are able to mitigate. In order to apply boundary conditions, all the edges of the sandwich structures are clamped, and a quarter model is constituted with symmetric boundary conditions to reduce the computational time as seen in Fig. 5. Johnson Cook material parameters and model are utilized in the simulations to describe the rate-dependent behavior of metallic alloys used in the simulations.
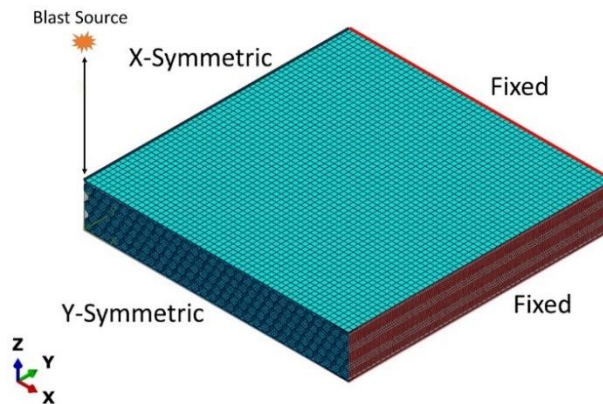
Fig. 5 A quarter sandwich structure model meshed with 5 mm shell elements (S4R) and boundary conditions

The general contact algorithm of shell elements is incorporated using hard contact formulation, while the tangential behavior is described with a penalty friction formulation with a friction coefficient of 0.3. For the discretization, 5 mm thick shell elements (S4R) were used for both core topologies and front and back face sheets (Figure 5) as a result of convergence study with compromising the computational time [22]. Front and back face displacements and total energy absorption values were calculated at 1.5 ms after the blast takes place.
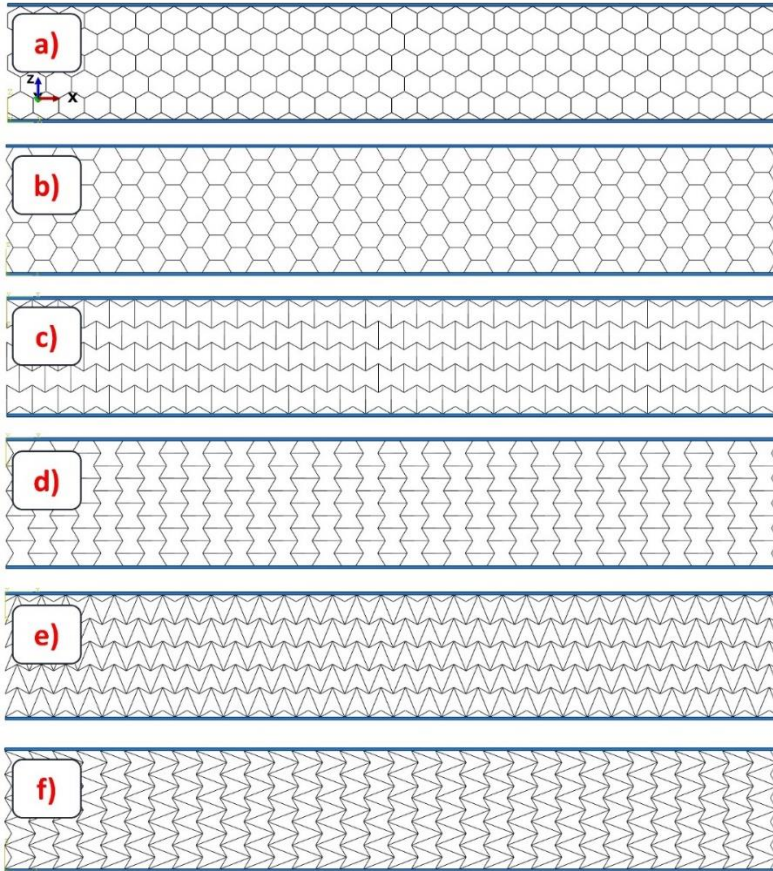
Fig. 4 Sandwich structures with: a) in-plane honeycomb core , b) axial honeycomb core, c) in-plane re-entrant core, d) axial re-entrant core, c) in-plane double arrowhead core, d) axial double arrowhead core

3. Results and Discussions

3.1. Von Misses Stresses

Von Misses stress distribution on the sandwich structures with honeycomb core under in-plane and axial loading conditions are shown in Fig. 6a and 6b, respectively. When explosive mass is detonated, an air blast shock wave propagates towards the sandwich panel. After the first interaction between shock wave and sandwich structure, the front face sheet is deformed elastically and plastically, and the shock wave is redistributed on the core. When the back face sheet deflection is maximized, the sandwich panels rebound, and some amount of both the front and the back face sheet deflections are recovered [25].

As shown in Fig. 6, the honeycomb core shows bending-dominated behavior meaning that expansion and deformation of the core from center of the sandwich structure to the sides are present [22]. It can also be stated that the blast energy is dissipated in the core through three mechanisms: breakage of honeycomb cell walls, honeycomb core compaction and plastic deformation [30]. It was observed that in-plane loading resulted in higher stresses than axial loading (1257 MPa vs 1160 MPa).
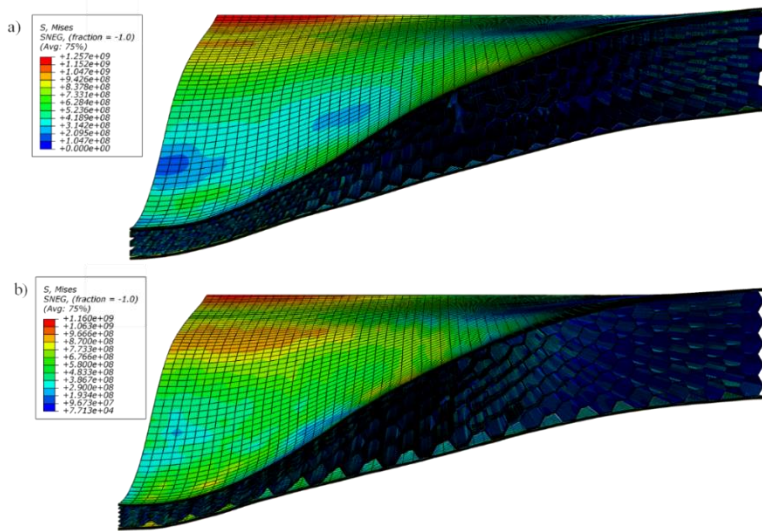
Fig. 6 Stress distribution on quarter sandwich structures with honeycomb core under:
a) in-plane loading, b) axial loading

Von Misses stress distribution on the sandwich structures with re-entrant core under in-plane and axial loading conditions are shown in Fig. 7a and 7b, respectively. Contrary to the sandwich structures with honeycomb core, the maximum stress on the sandwich structure with re-entrant core is higher when loaded in axial direction compared to the in-plane loading (1297 MPa vs 1198 MPa). Similar results (1090 MPa vs 1049 MPa) were also observed in sandwich structures with double arrowhead core as shown in Fig. 8. For the three different core topologies, the maximum and the minimum stress values were observed on sandwich structure with re-entrant core under axial loading and that with double arrowhead core under in-plane loading, respectively.
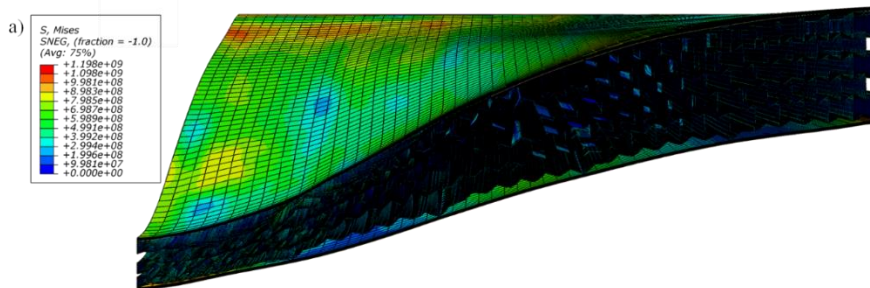
Fig. 7 Stress distribution on quarter sandwich structures with re-entrant core under:
a) in-plane loading
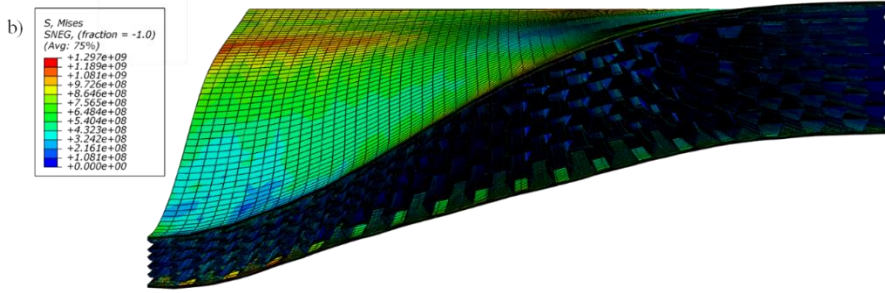
Fig. 7(cont) Stress distribution on quarter sandwich structures with re-entrant core under: b) axial loading
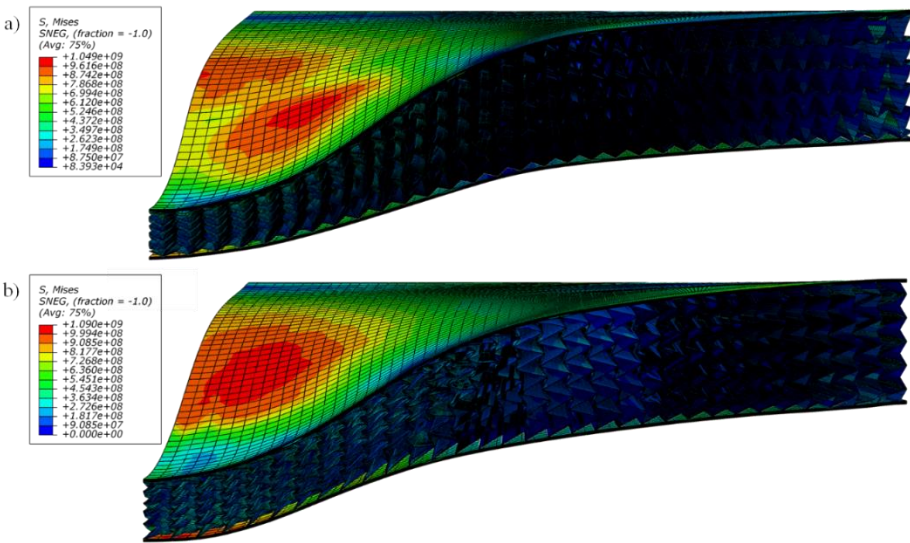
Fig. 8 Stress distribution on quarter sandwich structures with double arrowhead core under: a) in-plane loading, b) axial loading

3.2. Front Face Displacements

Fig. 9 shows the front face displacements for different core topologies under in-plane and axial loading conditions. For all core topologies, it is clear that front face progressively deforms up to its maximum displacement at a certain time, then due to the auxetic effect and redistribution of the load on the entire core, the displacement decreases and the front face tries to get back its original shape [31]. In Table 2, the maximum front face displacement, maximum displacement times and deviations comparing to honeycomb lattice structures response in in-plane direction are displayed. For sandwich structures with honeycomb core, the maximum displacements were observed at 0.80 ms with a value of 117.6 mm and 0.78 ms with a value of 116.4 mm for in-plane and axial loading conditions, respectively. For the in-plane and axial loading of sandwich structures with re-entrant and double arrowhead core topologies, the maximum displacements were observed at 0.88 ms with a value of 107.2 mm, at 0.80 ms with a value of 106.1 mm, at 0.70 ms with a value of 89.0 mm and at 0.74 ms with a value of 90.2 mm, respectively. The highest displacement was observed with honeycomb core topology under in-plane loading

condition. On the other hand, the lowest displacement was observed with double arrowhead core topology under in-plane loading condition. Loading along axial direction resulted in lower maximum front face displacement for sandwich structures with honeycomb and re-entrant cores, but the situation is opposite for sandwich structures with double arrowhead core.
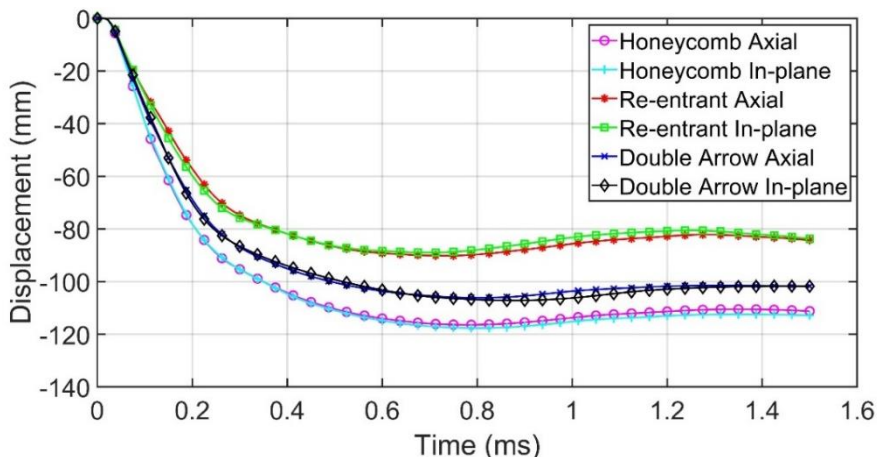
Fig. 9 Front face displacements

Table 2. Maximum front face sheet displacements, maximum displacement times and deviations comparing to honeycomb lattice structures response in in-plane direction

	Orientation	Time (ms)	Maximum Displacement (mm)	Deviation (%)
Honeycomb	Axial	0.780	116.393	-1.04
	In-plane	0.803	117.621	-
Re-entrant	Axial	0.803	106.136	-9.76
	In-plane	0.878	107.156	-8.90
Double Arrowhead	Axial	0.735	90.147	-23.36
	In-plane	0.698	88.983	-24.35

Table 3. Front face displacements at 1.5 ms and deviations comparing to honeycomb lattice structures response in in-plane direction

	Orientation	Displacement (mm)	Deviation (%)
Honeycomb	Axial	111.22	-1.41
	In-plane	112.82	-
Re-entrant	Axial	101.66	-9.89
	In-plane	101.77	-9.79
Double Arrowhead	Axial	84.28	-25.30
	In-plane	83.75	-25.77

The final front face displacements at 1.5 ms for all topologies are shown in Table 3. Axial loading resulted in slightly less final front face displacement than in-plane loading for honeycomb cores. However, the loading direction has insignificant effect on final front face

displacement for re-entrant and double arrowhead cores. Honeycomb cores showed higher final front face displacements than re-entrant and double arrowhead cores. It can be concluded that sandwich structures with double arrowhead core outperformed in terms of front face displacement.

3.3. Back Face Displacements

Fig. 10 shows the back face displacements for different core topologies under in-plane and axial loading conditions. For all core topologies, similar displacement behavior was observed compared to front face displacement. The maximum displacement values, times and deviations in comparison to honeycomb lattice structure's response to the blast load in in-plane direction of back sheets for all lattice structures are shown in Table 4. For sandwich structures with honeycomb core, the maximum displacements were observed at 0.80 ms with a value of 80.7 mm and 0.77 ms with a value of 73.0 mm for in-plane and axial loading conditions, respectively. For the in-plane and axial loading of sandwich structures with re-entrant and double arrowhead core topologies, the maximum displacements were observed at 0.87 ms with a value of 78.8 mm, at 0.80 ms with a value of 70.6 mm, at 0.70 ms with a value of 54.9 mm and at 0.73 ms with a value of 63.8 mm, respectively. Similar to the front face displacement, the highest displacement was observed with honeycomb core topology under in-plane loading condition. On the other hand, the lowest displacement was observed with double arrowhead core topology under in-plane loading condition. Loading along axial direction resulted in lower maximum back face displacement for sandwich structures with honeycomb and re-entrant cores, but the situation is opposite for sandwich structures with double arrowhead core.
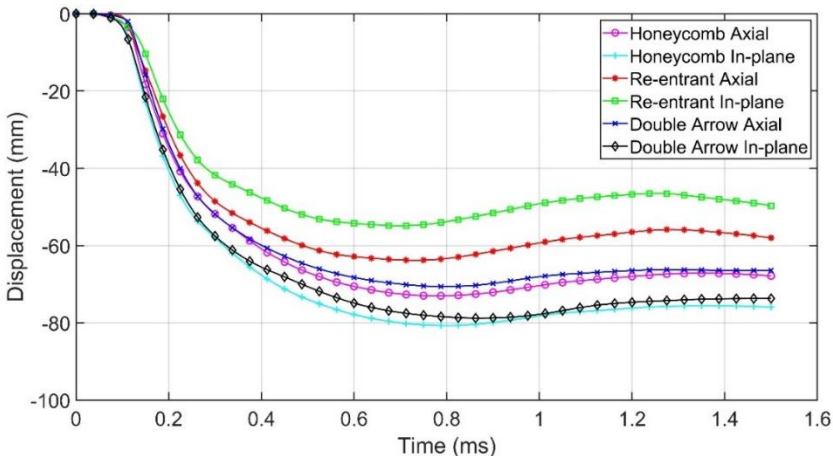
Fig. 10 Back face displacements

The final back face displacements at 1.5 ms for all topologies are shown in Table 5. Axial loading resulted in less final back face displacement than in-plane loading for honeycomb and re-entrant cores. However, the situation is opposite for sandwich structures with double arrowhead core. For both in-plane and axial loading, honeycomb cores showed higher final back face displacements than re-entrant and double arrowhead cores. Similar to the front face displacement, sandwich structures with double arrowhead core outperformed in terms of back face displacement. A comparison between back and front face displacements can reveal that back face displacements are lower than front face displacements indicating that sandwich structure core dissipated some of the energy transmitted from the front face to the back face. This can reduce the structural damages behind the sandwich structure due to air blast loading [20].

Table 4. Maximum back face sheet displacements, maximum displacement times and deviations comparing to honeycomb lattice structures response in in-plane direction

	Orientation	Time (ms)	Maximum Displacement (mm)	Deviation (%)
Honeycomb	Axial	0.77	73.01	-9.50
	In-plane	0.80	80.68	-
Re-entrant	Axial	0.80	70.60	-12.49
	In-plane	0.87	78.79	-2.34
Double	Axial	0.73	63.81	-20.91
Arrowhead	In-plane	0.70	54.89	-31.97

Table 5. Back face displacements at 1.5 ms and deviations comparing to honeycomb lattice structures response in in-plane direction

	Orientation	Displacement (mm)	Deviation (%)
Honeycomb	Axial	67.8	-10.62
	In-plane	75.94	-
Re-entrant	Axial	66.45	-12.50
	In-plane	73.70	-2.95
Double Arrowhead	Axial	58.02	-23.61
	In-plane	49.71	-34.54

3.4. Total Energy Absorption

Total energy absorption of sandwich structures with different core topologies are shown in Table 6. It is clear that sandwich structures absorbed more energy when loaded along axial direction than in-plane direction. The highest and the lowest total energy absorption were observed with double arrowhead core under axial loading and honeycomb core under in-plane loading, respectively.

Table 6. Total energy absorption and deviations comparing to honeycomb lattice structures response in in-plane direction

	Orientation	Absorbed energy (kJ)	Deviation (%)
Honeycomb	Axial	167.67	1.27
	In-plane	165.56	-
Re-entrant	Axial	192.26	16.13
	In-plane	191.24	75.90
Double Arrowhead	Axial	198.24	19.73
	In-plane	181.31	9.51

This can be attributed to the fact that in re-entrant and double arrow core topologies, cells are stretched towards the center of the panel where first interaction between the air blast wave and sandwich structure takes place which increases its energy absorption. On the other hand, in honeycomb core topology, cells at the middle are nearly fully compacted and the other cells are partially compacted [32]. As stated earlier, due to the expansion and

deformation of the honeycomb core from center of the sandwich structure to the sides [22], the center of the sandwich structure weakens and smaller magnitude of blast loading can deform the core when compared to re-entrant and double arrowhead cores where the center of the sandwich structure is densified with the application of blast load due to the auxetic behavior of the cells and higher magnitude of blast loading is necessary to further deform the panel. Therefore, more energy is absorbed by re-entrant and double arrowhead core when compared with honeycomb core.

5. Conclusions

In the present study, the effectiveness of different core topologies in sandwich structures under air blast loading was studied. Different loading conditions (in-plane and axial loadings) were also investigated to understand the core topology behavior. The key findings can be summarized as follows:

- Double arrowhead core showed the lowest stress, front and back face displacement under in-plane loading. It showed the highest total energy absorption under axial loading.
- Honeycomb core showed the highest front and back face displacement and the lowest total energy absorption under in-plane loading condition.
- Re-entrant core showed the highest stress under axial loading.
- Sandwich structures absorbed more energy when loaded along axial direction than in-plane direction.
- In-plane and axial loading have different effects on front and back face displacements, stress and total energy absorption of different core topologies. For instance, axial loading resulted in higher stresses than in-plane loading for re-entrant and double arrowhead core. However, the opposite situation was observed for honeycomb core. Axial loading resulted in lower maximum front and back face displacement and less final back face displacement for sandwich structures with honeycomb and re-entrant cores, but the opposite situation was observed for double arrowhead core. Finally, it was observed that a slight or insignificant effect of loading direction on final front face displacement was revealed for all core topologies.

Reducing the effect of air blast loading due to an explosion nearby on the target (especially military applications) is one of the important design criteria. This study showed that by using sandwich panels with honeycomb cores or auxetic cores, the damage due to an explosion on the application can be significantly mitigated due to the energy absorbed by the core geometry. As a future study, experimental verification of numerical studies will be performed and optimum core and loading conditions will be proposed to prevent the any structural application from damages due to air blast loading.

References

[1] Makwana DR, Thakur DG, Sentilkumar K. Numerical analysis and effects on rigidity of combat vehicle structure due to blast load. Procedia Structural Integrity, 2018, 14: 44-52. https://doi.org/10.1016/j.prostr.2019.05.007

[2] Imbalzano G, Tran P, Ngo, TD, Lee PVS. A numerical study of auxetic composite panels under blast loadings. Composite Structures, 2016, 135: 339-352. https://doi.org/10.1016/j.compstruct.2015.09.038

[3] Xue Z, Hutchinson JW. A comparative study of impulse-resistant metal sandwich plates. International Journal of Impact Engineering, 2004, 30 (10): 1283-1305. https://doi.org/10.1016/j.ijimpeng.2003.08.007

[4] Huang W, Zhang W, Huang X, Jiang X, Li Y, Zhang L. Dynamic response of aluminum corrugated sandwich subjected to underwater impulsive loading: Experiment and numerical modeling. International Journal of Impact Engineering, 2017, 109: 78-91. https://doi.org/10.1016/j.ijimpeng.2017.06.002

[5] Zhang C, Cheng Y, Zhang P, Duan X, Liu J, Li Y. Numerical investigation of the response of I-core sandwich panels subjected to combined blast and fragment loading. Engineering Structures, 2017, 151: 459-471. https://doi.org/10.1016/j.engstruct.2017.08.039

[6] Fahr P, Yazici M, Shukla A. Shock response of filled corrugated sandwich structures under extreme temperatures. Journal of Sandwich Structures & Materials, 2018, 20 (1): 130-149. https://doi.org/10.1177/1099636216650987

[7] Lakes R. Advances in negative Poisson's ratio materials. Advanced Materials, 1993, 5 (4): 293-296. https://doi.org/10.1002/adma.19930050416

[8] Rothenburg L, AI. Berlin A, Bathurst R. Microstructure of isotropic materials with negative Poisson's ratio. Nature, 1991, 354: 470-472. https://doi.org/10.1038/354470a0

[9] Yang W, Li Z-M, Shi M, Xie B-H, Yang M-B. Review on auxetic materials. Journal of Materials Science, 2004, 39: 3269-3279. https://doi.org/10.1023/B:JMSC.0000026928.93231.e0

[10] Prawoto Y. Seeing auxetic materials from the mechanics point of view: A structural review on the negative Poisson's ratio. Computational Materials Science, 2012, 58: 140-153. https://doi.org/10.1016/j.commatsci.2012.02.012

[11] Mohsenizadeh S, Alipour R, Nejad AF, Rad MS, Ahmad Z. Experimental investigation on energy absorption of auxetic foam-filled thin-walled square tubes under quasi-static loading. Procedia Manufacturing, 2015, 2: 331-336. https://doi.org/10.1016/j.promfg.2015.07.058

[12] Günaydın K, Gülcan O, Türkmen HS. Experimental and numerical crushing performance of crash boxes filled with re-entrant and anti-tetrachiral auxetic structures. International Journal of Crashworthiness, 2022, https://doi.org/10.1080/13588265.2022.2115962

[13] Mohsenizadeh S, Alipour R, Rad MS, Nejad AF, Ahmad Z. Crashworthiness assessment of auxetic foam-filled tube under quasi-static axial loading. Materials and Design, 2015, 88: 258-268. https://doi.org/10.1016/j.matdes.2015.08.152

[14] Novak N, Starčevič L, Vesenjak M, Ren Z. Blast response study of the sandwich composite panels with 3D chiral auxetic core. Composite Structures, 2019, 210: 167-178. https://doi.org/10.1016/j.compstruct.2018.11.050

[15] Al-Rifaie H, Sumelka W. The development of a new shock absorbing uniaxial graded auxetic damper (UGAD). Materials, 2019, 12 (16): 2573. https://doi.org/10.3390/ma12162573

[16] Al-Rifaie H, Sumelka W. Improving the blast resistance of large steel gates-numerical study. Materials, 2020, 13 (9): 2121. https://doi.org/10.3390/ma13092121

[17] Qi C, Yang S, Wang D, Yang LJ. Ballistic resistance of honeycomb sandwich panels under in-plane high-velocity impact. Scientific World Journal, 2013, 25: 892781. https://doi.org/10.1155/2013/892781

[18] Jin X, Wang Z, Ning J, Xiao G, Liu E, Shu X. Dynamic response of sandwich structures with graded auxetic honeycomb cores under blast loading. Composites Part B: Engineering, 2016, 106: 206-217. https://doi.org/10.1016/j.compositesb.2016.09.037

[19] Qi C, Remennikov A, Pei L, Yang S, Yu Z, Ngo T. Impact and close-in blast response of auxetic honeycomb-cored sandwich panels: Experimental tests and numerical simulations. Composite Structures, 2017, 180: 161-178. https://doi.org/10.1016/j.compstruct.2017.08.020

[20] Wang Y, Zhao W, Zhou G, Wang C. Analysis and parametric optimization of a novel sandwich panel with double-V auxetic structure core under air blast loading.

International Journal of Mechanical Sciences, 2018, 142-143: 245-254. https://doi.org/10.1016/j.ijmecsci.2018.05.001

[21] Yang D, Zhang X, Wu B. The influence factors of explosion and shock resistance performance of auxetic sandwich defensive structures. Journal of Shanghai Jiaotong University, 2018, 52(4): 379-387.

[22] Imbalzano G, Linforth S, Ngo TD, Lee PVS, Tran P. Blast resistance of auxetic and honeycomb sandwich panels: Comparisons and parametric designs. Composite Structures, 2018, 183: 242-261. https://doi.org/10.1016/j.compstruct.2017.03.018

[23] Hajmohammad MH, Kolahchi R, Zarei MS, Nouri AH. Dynamic response of auxetic honeycomb plates integrated with agglomerated CNT-reinforced face sheets subjected to blast load based on visco-sinusoidal theory. International Journal of Mechanical Sciences, 2019, 153-154: 391-401. https://doi.org/10.1016/j.ijmecsci.2019.02.008

[24] Xiao D, Chen X, Li Y, Wu W, Fang D. The structure response of sandwich beams with metallic auxetic honeycomb cores under localized impulsive loading-experiments and finite element analysis. Materials and Design, 2019, 176: 107840. https://doi.org/10.1016/j.matdes.2019.107840

[25] Lan X, Feng S, Huang Q, Zhou T. A comparative study of blast resistance of cylindrical sandwich panels with aluminum foam and auxetic honeycomb cores. Aerospace Science and Technology, 2019, 87: 37-47. https://doi.org/10.1016/j.ast.2019.01.031

[26] Lan X, Huang Q, Zhou T, Feng S. Optimal design of a novel cylindrical sandwich panel with double arrow auxetic core under air blast loading. Defence Technology, 2020, 16: 617-626. https://doi.org/10.1016/j.dt.2019.09.010

[27] Luo F, Zhang S, Yang D. Anti-explosion performance of composite blast wall with an auxetic re-entrant honeycomb core for offshore platforms. Journal of Marine Science and Engineering, 2020, 8: 182. https://doi.org/10.3390/jmse8030182

[28] Walkowiak M, Reinicke U, Anders D. Numerical investigation of different core topologies in sandwich-structured composites subjected to air-blast impact. Applied Sciences, 2022, 12 (18): 9012. https://doi.org/10.3390/app12189012

[29] Zhou J, Liu H, Dear JP, Falzon BG, Kazancı Z. Comparison of different quasi-static loading conditions of additively manufactured composite hexagonal and auxetic cellular structures. International Journal of Mechanical Sciences, 2023, 244: 108054. https://doi.org/10.1016/j.ijmecsci.2022.108054

[30] Yan Z, Liu Y, Yan J, Wang B, Bai F, Shi Z, Huang F. Anti-blast performance of 3D-printed sandwich panels with auxetic hexagonal and regular hexagonal honeycomb cores. Engineering Structures, 2022, 272: 114996. https://doi.org/10.1016/j.engstruct.2022.114996

[31] Kalubadanage D, Remennikov A, Ngo T, Qi C. Experimental study on damage magnification effect of lightweight auxetic honeycomb protective panels under close-in blast loads. Thin-Walled Structures, 2022, 178: 109509. https://doi.org/10.1016/j.tws.2022.109509

[32] Bohara RP, Linforth S, Ghazlan A, Nguyen T, Remennikov A, Ngo T. Performance of an auxetic honeycomb-core sandwich panel under close-in and far-field detonations of high explosive. Composite Structures, 2022, 280: 114907. https://doi.org/10.1016/j.compstruct.2021.114907

Review Article

A review on optimization of process parameters of fused deposition modeling

Naveen Kumar Suniya*,a, Arvind Kumar Verma,b

Department of Production and Industrial Engineering, MBM University, Jodhpur, India

Article Info	Abstract
	The purpose of this review is to explore various techniques used in the optimization of process parameters of 3D printing machines for different applications. Fused Deposition Modeling (FDM) is an emerging technology that has been widely used in diverse areas including new product development, mould manufacturing, etc. FDM is the process of depositing the material in a layer-by-layer manner to manufacture the part. FDM provides a lot of flexibility in fabricating a part. Many complex parts can be manufactured by FDM easily which are very difficult to manufacture through conventional manufacturing methods. However, build-in time, manufacturing speed, and mechanical strength of FDM fabricated parts are still challenging and critical. The quality of FDM fabricated parts is affected by various machining parameters, such as air gap, build orientation, infill percentage, raster angle, raster width, layer thickness, etc. The selection of significant process parameters needs to be identified and optimized as per the usage of apart. Many researchers have used different techniques, such as the design of experiment (DOE) technique, response surface method(RSM), genetic algorithm(GA), artificial neural network(ANN), and fuzzy, to optimize the FDM process parameters to improve the desired part quality, such as mechanical properties, and dimensional accuracy. This survey paper attempts to critically review various research articles published on the optimization of process parameters to improve the performance parameters of FDM.

1. Introduction

Additive Manufacturing (AM) is a process to fabricate components by incrementally adding materials layer-by-layer using details available in a CAD model. Contrary to the traditional subtractive machining processes to generate a shape by removing materials, additive manufacturing builds a component by adding the material to the desired places. This additive process reduces material wastage and manufacturing time.AM was developed initially as a technique for rapid prototyping to visualize, test, and authenticate a design, before end-user production of the design. However, with recent developments, now AM can rapidly fabricate components with complex shapes without much geometric restriction under more comfortable work conditions. It is currently used in various fields, from industrial products to medical appliances, as a production technology [57]. Over the years, many additive manufacturing processes, such as photo-polymerization, fused deposition modeling, material jetting, and powder bed fusion, have been developed. However, fused deposition modeling (FDM), also called the extrusion method, is one of the most popular additive manufacturing techniques due to its ability to create complex components from a wide range of materials.

FDM utilizes a long thermoplastic fiber that passes through a CNC-controlled and temperature-controlled moving extrusion head to deposit material at the desired locations. FDM

incrementally builds components by laying a thin layer over the top of the previous layer [84]. Fig. 1 shows a block diagram of FDM. Due to its capacity to generate complicated parts in a faster production cycle time than traditional machining procedures, FDM is now regarded as a quick manufacturing approach. Due to its use of the net shape manufacturing principle and lack of additional tooling requirements, FDM also has the advantage of being the least expensive production system. Despite these benefits, creating components for end use with FDM is still a difficult task since FDM has a number of process parameters that affect the quality, mechanical characteristics, manufacturing process, and dimensional accuracy of the part.

Air gap, build orientation, infill proportion, raster angle, layer height, and other characteristics of the FDM process are some of them. These process parameters need to be carefully chosen according to the application for which a part is made using FDM. Some process parameters are more important than others for a given output need.

In order to achieve the best results, it is necessary to identify and optimize these important process characteristics. The various experimental or statistical design of experiment (DOE) methodologies have been studied and used by several researchers over the years to optimize the FDM process parameters for the mechanical characteristics and component quality.The Taguchi approach, genetic algorithms (GA), grey relational, fractional factorial, artificial neural networks (ANN), fuzzy logic, ANOVA, , and other DOE techniques are frequently employed.
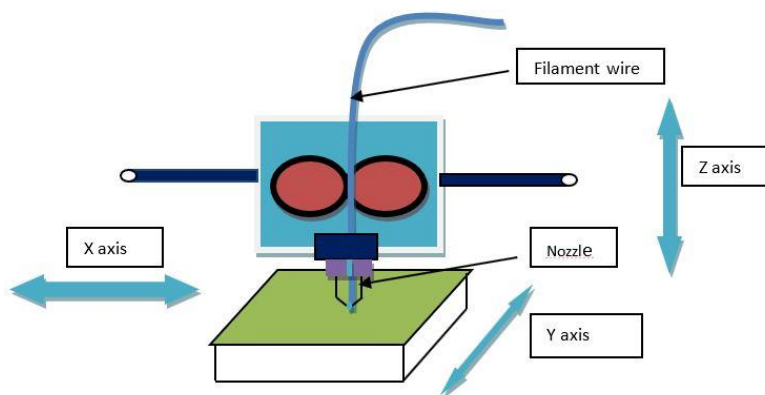
Fig. 1 Block diagram of FDM

This article aims to present a state-of-the-art review of the current research on FDM process parameter optimization focusing on enhancing mechanical properties, reducing build time, and improving part quality. The remaining part of the paper is organized as follows: section 2 briefly explains various FDM process parameters. Section 3 discusses commonly used materials. Section 4 reviews the optimization of various process parameters and section 5 concludes the paper and gives future research directions.

2. Process Parameters of FDM

FDM has many process parameters which affect the quality of fabricated parts. Following are the most widely studied FDM process parameters:

1. Build orientation: FDM 3D printed parts have inherently anisotropic mechanical properties, i.e., the parts are much stronger in the XY direction than in the Z direction. Build orientation is the orientation of the part on the print table. In FDM, a part can be printed at any orientation. However, build orientation affects the strength of the part in different

directions, the requirement of supports during printing, and the surface finish of different surfaces of the part [53]. As shown in fig 2, the same part requires a different amount of support structure during printing based on its build orientation.
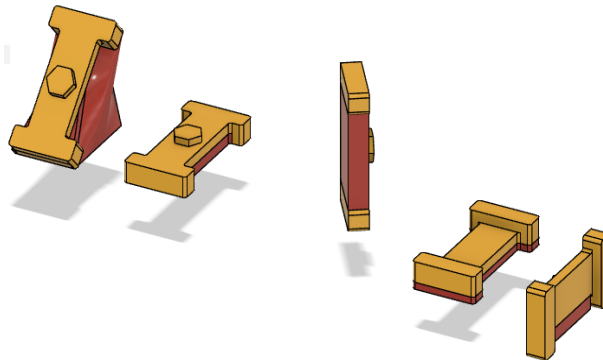
Fig. 2 Various build orientations of a part. The golden shade shows the part and the red shade shows the support structure

2. Layer thickness: Layer thickness, also called layer height, is the thickness of the material of a layer deposited by the FDM process. The layer thickness parameter affects the surface finish and build-time of a part. Layer thickness depends on the tip size, printing speed, and material [42]. Fig 3 shows the effect of different layer thicknesses on the surface finish of an FMD printed part.
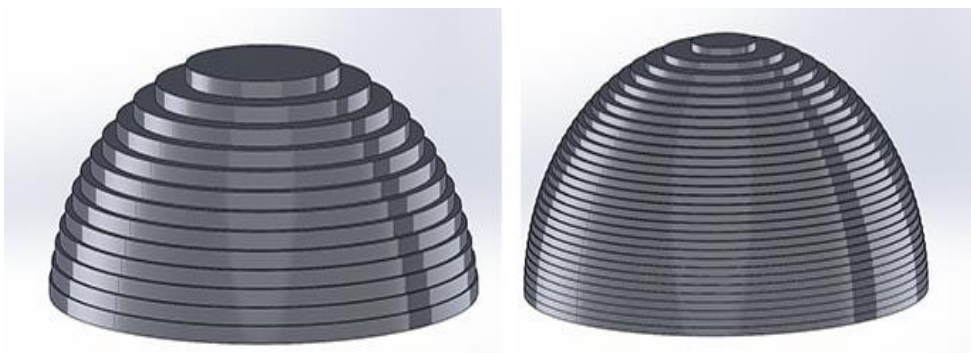
(a) Larger layer thickness   (b) Smaller layer thickness

Fig. 3Effect of the layer thickness of the surface finish of a part

3. Extrusion temperature: Extrusion temperature is the temperature at which the filament material is heated inside the nozzle during the FDM process. It depends on the printing material and printing speed.

4. Print Speed: Print speed is the speed, normally specified in mm/sec, of the printing head in the XY plane of the 3D printer. Print speed affects the build time [13]. After a certain level, it also affects the strength of printed parts [38].

5. Bed temperature: It is the temperature of the top surface of the 3D printer bed. The adhesion between the first printed layer and the printing bed is dependent on the bed temperature. It is reported that a bed temperature slightly above the glass transition

temperature of the printing material provides good adhesive property. Good adhesion is required to avoid the part warping and improve the dimensional accuracy of the part. [41]
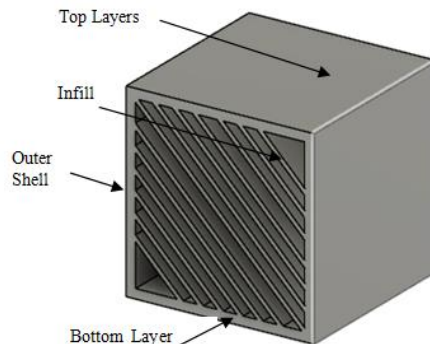
Fig. 4 Structure of a 3D printed part

6. Raster Angle: A layer in a 3D FDM printed part consists of a number of linear segments of the molten metal, called raster, extruded from the nozzle. Raster angle is the angle from the x-axis of the build table at which the printing head deposits a raster of a layer (see fig 5). The typical values of the raster angle are in the range of 0°to 90° in a step of 15° [13, 42]. Typically, raster angles of two adjacent layers differ by 90°. Raster angle affects the directional mechanical property of printed parts.
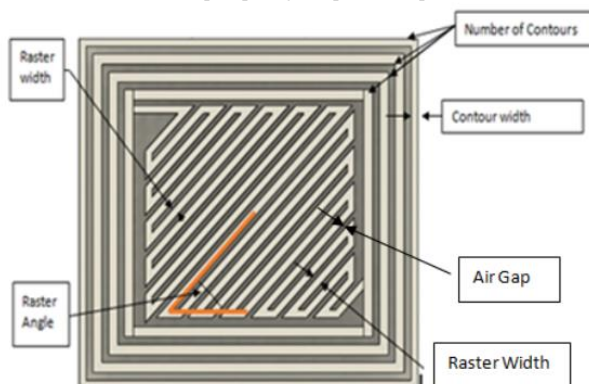
Fig. 5 FDM tool path parameters

7. Raster width: Raster width, also called road width, refers to the width of a raster. The value of raster width varies based on the diameter of the nozzle [13, 42].A larger value will increase the strength of the interior of the part [42].
8. Air gap: Air gap is the distance between two adjacent rasters of a layer (Fig 5). If two adjacent rasters overlap with each other, then Air gap is negative.
9. Infill Density: The outer surface of a 3D printed part is normally solid but the internal structure of the part is filled with various styles of infills. Infill density is the percentage of the volume of infill filament material with the total volume of the part covered with the infills. Typically 20% infill density is used for parts used only for visualization and higher infill density is used for end-use parts to achieve the required mechanical properties

(strength and mass). Infill density plays a major role in the mechanical strength of an FDM printed part [13]

10. Infill pattern: Infill pattern is the structure and shape of the infill to fill the internal space of a part. Commonly used infill patterns are shown in fig 6. Infill patterns influence the mechanical properties and printing time of parts.

11. Contour width: Outer solid shells of an FDM part are printed as a set of contours of molten material. Contour width (fig 5) is the width of a contour [13].

12. Contour air gap: Contour air gap is the distance between two adjacent contours when the part fill style is selected as multiple contours [13].

HoneyComb **Gyroid** **Triangular**

Grid **Hexagonal** **Concentric**
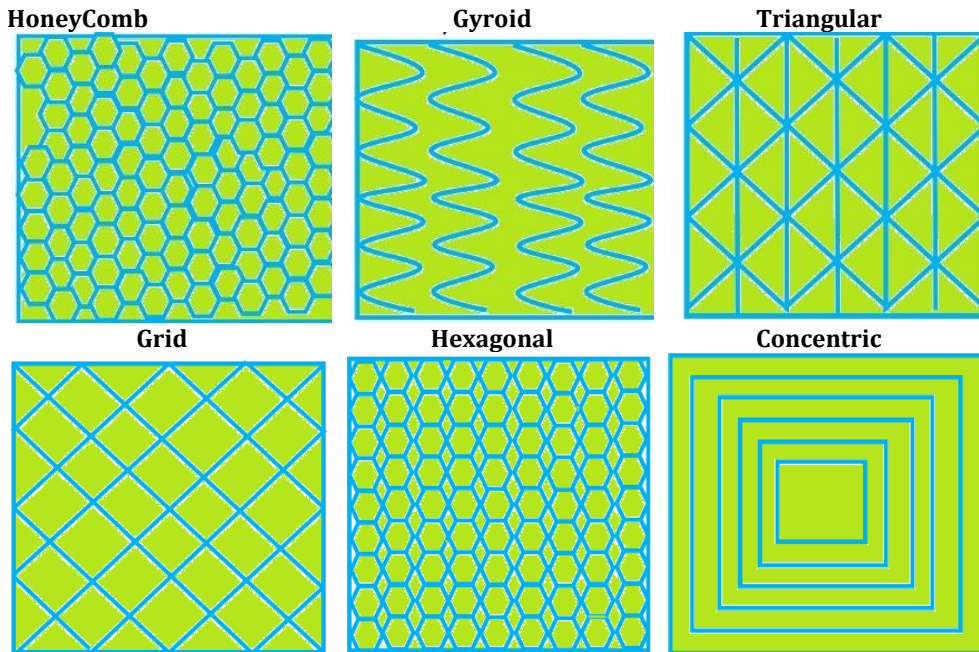
Fig. 6 Commonly used infill patterns

13. Perimeter to raster air gap: It is the distance between the edge of the raster fill and the innermost contour [13].

14. The number of contours: It is the number of contours in the shell of a part [13].

3. FDM 3D printing Materials

With the growing popularity and capability of FDM 3D printing, researchers are experimenting with various thermoplastics and their composites to fabricate parts using FDM. In this section, commonly used thermoplastics in FDM were discussed in brief. Table 1 summarizes the properties useful for 3D printing of these materials. Following are the commonly used materials in FDM:

3.1. Acrylonitrile Butadiene Styrene (ABS)

ABS is a thermoplastic, amorphous polymer that is widely used in FDM. ABS is styrene, butadiene, and acrylonitrile copolymer. ABS has two critical mechanical properties: impact resistance and toughness. The melting point of ABS is 230°C [13].

3.2. Polylactic Acid (PLA)

In FDM, PLA is one of the most commonly utilized thermoplastics. PLA is produced from corn, sugarcane starch roots, and so forth. Since PLA is a biodegradable and renewable thermoplastic, PLA is becoming increasingly more popular. Additionally, it offers manufacturing prototypes and functioning parts with good quality and precision and uses less energy and temperature. Further, it does not require a heated bed. However, it is prone to jamming the printer nozzle during printing. When compared to ABS, PLA has a stronger tensile strength, a lower warp, and a lower ductility [13]. PLA is currently used in various applications, such as packaging of food, and medical implants. The melting point of PLA ranges between 170 and 180 °C depending on the amount of residual monomer.

3.3. Nylon

Nylon is a family of petroleum-based synthetic polymers composed of polyamides. From the FDM point of view, Nylon's characteristics are comparable to those of ABS. If more flexible and durable parts are needed, nylon can be used. It has a high level of toughness and impact resistance, but it is extremely vulnerable to moisture as nylon is hygroscopic. Moisture absorption degrades filament properties leading to poor quality parts. The melting point of nylon ranges between 190 and 350 °C.

3.4. Polyethylene Terephthalate (PET)

PET is a strong, stiff synthetic fiber of the polyester family of polymers and is a popular material for FDM. PET is commercially available in a variety of forms, such as PETP, PETG, GPET, and PETT. It is employed in the production of water bottles and food packaging. The melting point of PET is 260 °C.

3.5. Polyether Ether Ketone (PEEK)

PEEK is an organic thermoplastic polymer of the polyaryletherketone family. It is a heat-resistant material with better mechanical and chemical characteristics than PLA and ABS. PEEK is used in human prostheses due to its potential bone healing property. The melting point of PEEK is 343 °C.

3.6. High Impact Polystyrene (HIPS)

HIPS, also known as PS (Polystyrene), is an amorphous thermoplastic material. HIPS has comparable mechanical properties to ABS but it is cheaper than ABS. However, it has low flexibility but it can be bonded, punched, and sawn successfully. It's widely utilized in the toy industry and on building signage. The melting point of HIPS ranges between 150 to 180°C.

Table 1. Common properties of various thermoplastics

Material/Property	PLA	ABS	HIPS	PET	Nylon	PC
Extrude temp. °C	180-220	210-240	220-230	230-255	235-270	270-315
Bed temp. °C	20-55	80-11-	50-60	55-70	60-80	90-120
T_g (°C)	60-65	105-110	100	70-78	47-60	145-150

4. Modeling and Optimization Techniques Used in The Investigation of The FDM Process

For easy comprehension of this review paper, this section briefly discusses various optimization techniques used to investigate the effect of various process parameters on the quality and desired properties of FDM printed parts.

4.1. Genetic Algorithm

Darvin proposed the genetic algorithm (GA) with the Theory of Evolution and the Survival of the Fittest as its guiding principle. The algorithm generates a set of random initial population, called chromosomes and then optimizes the population using a number of operations. Cromosomes are normally represented as integer strings. In order to generate a new population and to found best optimum solution, several procedures including reproduction, cross-over and mutation are utilized, as well as the solution from the prior population. The best chromosomes (around 20%) are saved during reproduction for the next population on the basis of fitness function. The crossover of two parent strings generates offspring (new solutions) by switching around the genes or portions of the chromosomes. Mutation is a technique to raise in population variety caused by the random modification of parts of one solution. The belief that the incoming population would be better than the outgoing one serves as motivation. Based on the fitness function, solutions are chosen to create new solutions (Off springs). This process is repeated until the end condition is satisfied. For more details, researchers could refer to [89].

4.2. Grey Analysis:

Various researchers implemented Grey relational analysis to determine the best combination of the process parameters to achieve the desired performance parameters on the basis of grey relational grade [32]. In Grey Analysis, firstly experimental data is preprocessed using normalization. Normalized data of each experimental run is used to determine the Grey Relational coefficient for the same. Grey relation grade is calculated by averaging the grey relational coefficient for each sequence. High grey relational grade provides the optimum process parameters setting for the desired performance parameters. Researchers might consult [31] for further information.

4.3. Particle Swarm Optimization (PSO)

In a study published in 1995, Kennedy and Ebehart introduced the PSO global heuristic search method. PSO has seen significant revisions since 1995. Particles in PSO follow the best moving particles at any given time to move through the problem space. Every particle in the problem space keeps track of its coordinate position, which aids in identifying the current optimal solution. Particles are assessed using a fitness function following each repetition. Compared to other optimization techniques, PSO can achieve a point of convergence more quickly. Only a few parameters can be used to calculate the optimal value. Reducing the number of particles can boost the PSOs performance [83].

4.4. Factorial Design Method

Researchers can examine the effects of multiple independent variables and the extent of their interaction simultaneously using the factorial design method. In statistics, a full factorial design is made up of two or more variables in the experiment design, each of which has discrete possible values or levels, and whose experimental units take on any possible combination of these levels across all variables. This method can be used to study the effects of each component on the response variables as well as the effects of the interactions among the factors on the response variable [65].

4.5. Taguchi Methodology

The Taguchi method integrates the statistical and mathematical techniques to optimize performance traits through the selection of design parameters. With fewer experiments, Taguchi technique discovers some effects resulting from statistical fluctuation. Additionally, the Taguchi approach identifies the ideal experimental setting with the least amount of variability. The noise factor which is difficult to regulate, is the primary contributor to unpredictability. In contrast, the signal or control factor is simple to manage. The Taguchi method is a statistical quality control technique where the level of controllable factors, input process parameters, or

independent variables are chosen in a way to minimize the variation in responses caused by uncontrollable or noise factors like humidity, vibration, and environmental temperature [65].

4.6. Response Surface Method (RSM)

RSM combines mathematical and statistical techniques for modelling and optimization. The fundamental goal of this approach is to optimize the responses that are affected by numerous input parameters or factors. RSM uses the design of experiments to gather enough data. The relationship between the controllable input parameters and the results can be established using RSM [65].

4.7. Teaching Learning Based Optimization (TLBO)

The teaching-learning procedure in a classroom is replicated by the TLBO algorithm. The top solution from the most recent iteration is regarded as a teacher, and all other solutions are regarded as students. The majority of students complies with teacher's instructions and benefit from peer teaching. An academic field corresponds to an independent variable or candidate solution feature in the TLBO algorithm. The Teacher Phase and Learners Phase are two crucial phases in the TLBO algorithm [66]. Students interact with one another to enhance their knowledge in the learner phase while teachers refine the knowledge of all students in the teacher phase.

4.8. Artificial Neural Network (ANN)

Artificial neural networks (ANNs) are effective data modelling and analysis tools that can construct the complicated input-output relationship. ANNs are inspired by the human brains learning from experience paradigm. A neural network is made up of numerous simple computing units, known as neuron, that are arranged in the shape of a massively connected network. Each input link has a weight, and each neuron computes a weighted total of all the links it receives. Using a training dataset made up of input and output, a network is trained by methodically altering the weights of the networks. An artificial neural network can successfully depict the nonlinear and interaction effects using experimental data sets [66].

5. Research on FDM Process Parameters Optimization

Many researchers optimized the process parameters of Fused Deposition Modeling. This section provides a comprehensive and critical literature review to analyze the effect of various process parameters of FDM on dimensional accuracy, surface roughness, tensile strength, compressive strength, build cost, etc. This section includes research papers published during the last two decades, i.e., from 2001 to 2022.

Table 2. Research articles related to optimization of process parameters of FDM based on filament materials

Material	Researchers
ABS	Anitha et al.[4] ,Nazan et. al.[52] , Asadollahi-Yazdi et al. [5], Lunetto et al.[39], Dong et al.[15], Vishwas et al. [84], Yadav et al. [88], Raju et al. [63], Gurrala et al. [25], Haque et al. [28], Eswaran et al. [18], Sood et al. [74], Khan et al. [33], Rao et al. [66], Mahmood et al. [43], Sajan et al. [72], Wankhede et al. [87], Chaudhari et al. [9], Dev et al. [12], Srinivasan et al. [76], Fountas et al. [21].
PLA	Sharma et al. [73], Tontowi et al. [80], Pazhamannil et al. [57], Qattawi et al. [60], Rajpurohit et al. [61], Beniak et al. [6], Fountas et al. [21], Deshwal et al. [11], Rao et al. [67], Beniak et al. [7]
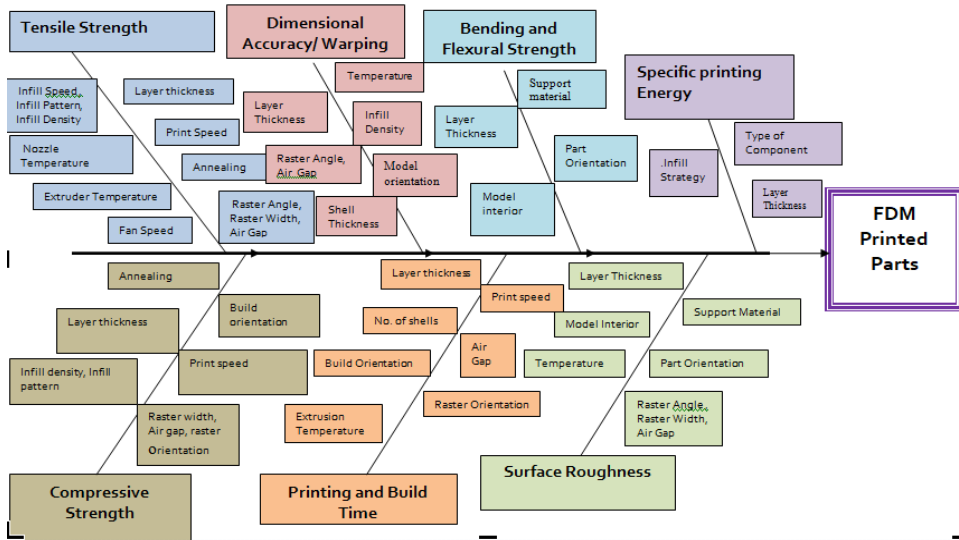
Fig. 7Cause and effect diagram for FDM parts

Various research papers using different keywords in titles, abstracts, and keyword sections of various scientific databases were searched and the relevant published articles (journal and conference papers) were selected from four major science publishers: Taylor and Francis, Springer Link, Science Direct, and Inder science. Around 80 papers were finally selected for this survey. A cause-and-effect diagram (Fig. 7) was developed based on factors identified in these research articles that affect various responses. Process parameters of FDM were optimized based on the response requirement. Table 2 provides the summary of various optimization techniques implemented in the research articles published on the optimization of process parameters of FDM. The following subsections describe the research in this domain. Table 2 shows the classification of research articles related to the optimization of process parameters of FDM based on filament material used to fabricate the parts.

5.2. Surface Roughness

The quality of parts manufactured by FDM depends on several parameters. Surface finish is an important quality parameter useful in many real-life engineering problems. Many attempts have been made in the last few decades to improve the surface finish of FDM printed parts. This literature review attempts to study the effect of various process parameters on the surface roughness of printed parts.

Anitha et al. [4] analyzed the effect of various process parameters, for instance, layer thickness, raster width, and speed of deposition on surface roughness. Optimal settings of these process parameters to minimize surface roughness were found with the help of the Taguchi L18 orthogonal array. It was found that layer thickness is the most significant factor among all the considered parameters that affect the surface roughness [4]. Byun et al. [92] introduced a method to determine optimal part orientation using the genetic algorithm to improve the average weighted surface roughness (AWSR) generated due to the staircase effect [90]. Kumar et al. [68] proposed a robust process optimization to improve the surface roughness from feature and dimensional accuracy. The raster angle and air gap, were reported as significant factors for surface roughness [92]. Nancharaiah et al. [50] investigated the effect of layer thickness, road width, air gap, and raster angle on surface roughness. It was found that road width is another factor other than layer thickness that affects the surface roughness and dimensional accuracy of parts manufactured by FDM [50]. Raju et al. [63] investigated the effect of layer thickness, support material, model interior, and part orientation on surface roughness,

tensile strength, flexural modulus, and hardness. It was reported in the research that surface roughness increases with the value of support structure from high density to low density and decreases with infill style or model interior from low to high density [63]. Taguchi's 'L18' orthogonal array was used as the design of the experiment. In this research, multi-responsive optimization has been implemented by Particle Swarm Optimization (PSO), Bacterial Foraging Optimization (BFO), and hybrid PSO-BFO to improve the surface roughness, hardness, tensile strength, flexural modulus.

Sharma et. al [73] have reported the optimization and process capability analysis for surface properties of 3D printed functional prototypes of polyvinyl chloride (PVC) reinforced with polypropylene (PP) and hydroxyapatite (HAP) for possible bio-sensing applications. Various experiments according to Taguchi's L9 orthogonal array were conducted to investigate the surface properties of FDM filament comprising PVC, PP, and HAP. This research considered infill density, layer thickness, and deposition speed as process parameters to minimize the surface roughness. It was found that infill density is the most influential factor affecting the surface roughness. It has been observed in this research that with the increase in infill density from low level to medium level, the surface finish of the parts has been improved [73].

The surface roughness of parts fabricated by FDM can be improved by treating them chemically. Galantucci et al. [22] have investigated the effect of process parameters and post-processing on the surface roughness of a part. The study was conducted in two phases. In the first phase, the effect of various process parameters on surface roughness was analyzed. It was found that layer thickness and raster angle affect surface roughness of ABS printed part. In the second phase, the prototype was treated with a solution of 90% dimethyl ketone and 10% water for 300 seconds. Significant improvement in surface roughness of part was observed [22]. Tiwary et al. [78] further studied the effect of layer thickness, extrusion width, and emersion time in the solutions having different compositions (1) 100% 1,2- Dichloroetahne, (2) 90% Acetone + 10% distilled water and (3) 50% 1,2-Dichloroetane + 50% Acetone. It was concluded that layer thickness, extrusion width, and immersion time significantly influence the surface roughness of ABS printed parts [78].

Apart from controlling the various machining parameters, Khan et al. [33] analyzed the effect of chemical post-processing on the surface roughness of an ABS specimen containing flat, inclined, and curved surfaces. Specimens were treated with vaporized acetone and significant improvement in surface roughness was observed. It was also observed that surface roughness was largely affected by the air gap [33].

Li et al. [36] investigated the effect of post-processing parameters such as immersion time, temperature, and concentration of chloroform solution on the surface roughness of PLA-printed parts. PLA printed test specimens were exposed to hot vapors of chloroform solution in a special heating thermostatic system. PLA is soluble in chloroform at room temperature. It was observed that surface roughness after treating with chemical first decreases and then increases. It was observed that 5 minutes is the optimal time for optimum surface roughness. It was also reported that temperature affects surface roughness significantly. Table 3 illustrates the major research works that studied the impact of process parameters on surface roughness [36].

Nagendra et al. [48] investigated the effect of infill density, infill style, layer thickness, print temperature, and raster angle on the surface quality of the printed part of nylon and aramid. Taguchi DOE was utilized to determine the optimum values of factors. As a result, the improved surface finish was found at the optimal condition of 0.2 mm layer thickness, tetrahedral infill style, 90 % infill density, 90-degree raster angle, and 280 C print temperatures [48]. Patil et al. [56] developed an optimization model to analyze the effect of various process parameters such as infill style, infill density, printing speed, and layer thickness on surface roughness. It was concluded that layer thickness is the most influencing factor for surface roughness. Infill pattern

also affects the surface roughness. Gyroid infill style provides better results for surface roughness [56].

Table 3. Optimization techniques used to identify the impact of process parameters on surface roughness

Authors	Material	Optimization Technique	Process Parameters	Performance Parameters
Sharma et al. [73]	PLA	Taguchi Philosophy	1.Layer thickness 2. Infill density 3. Deposition speed	1. Surface roughness
Anitha et al. [4]	ABS	Taguchi Philosophy	1. Layer thickness, 2. speed of deposition 3. road width	1. Surface finish
Asadollahi-Yazdi et al. [5]	ABS	NSGA -II	1. Layer thickness 2. Part orientation	1. Build time 2. Tensile Strength 3. Surface Roughness 4. Material
Raju et al. [63]	ABS	Hybrid PSO-BFO	1. Layer thickness, 2. Support material, 3. Model interior 4. Part orientation	1.Surface roughness 2.Hardness 3. Tensile Strength 4. Flexural Modulus
Khan et al. [33]	ABS	Taguchi Philosophy	1. Raster Angle (degree) 2. Raster Width (mm) 3. Air gap (mm) 4. Temperature (C) 5. Time (s)	1. Surface Roughness
Haque et al. [28]	ABS	DOE with face cantered composite design(FCCCD)	1. Layer thickness, 2. Part orientation, 3. Raster width, 4. Overlap distance	Surface Roughness
Sajan et al. [72]	ABS	Taguchi L'27'	1. Bed Temperature 2. Nozzle Temperature 3. Print Speed 4. Infill	1. Circularity error 2. Surface Roughness

			5. Layer thickness	
			6. Number of loops	
Wankhede et al. [87]	ABS	Taguchi 'L8'	1. Layer thickness	1. Surface roughness
			2. Infill density	
			3. Support style	

5.3. Discussion and Future Aspects

From the above research works, it can be concluded that surface finish is affected by layer thickness, road width, raster angle, and air gap, significantly. Low layer thickness reduces the staircase effect and improves the surface finish. Print orientation also affects the surface finish. It was observed that the top surface is better finished than the side surfaces. Therefore, it is recommended to build the shortest side surface in the z-direction. ABS and PLA parts can be further treated with acetone and chloroform to improve surface finish.

5.4. Mechanical Properties

Many researchers studied the effect of various process parameters on the mechanical properties of FDM printed parts. Montero et al. [45] investigated the effect of raster orientation, air gap, bead width, colour, and model temperature on the tensile strength of the parts fabricated by FDM. Raster orientation and air gap were found two significant factors that affect the tensile strength [45]. Ahn et al. [91] observed that the tensile strength and compressive strength of parts fabricated with a negative air gap were observed to be 65-72% and 85-90% as compared to the corresponding injection-molded ABS parts, respectively [91]. Bellini and Güçeri [70] investigated the effect of deposition angle and part orientation on tensile strength and flexural strength using experimental and analytical techniques. Rodriguez et al. (2003) introduced and developed a mathematical model based on an approximate minimization algorithm to find the optimal settings of parameters for better tensile strength and stiffness [70]. Weinmann et al. [93] recommended a small air gap and low layer thickness to achieve better yield strength and ultimate strength [93]. Lee et al. [34] optimized the process parameters values to maximize the elastic performance. It was found that air gap, raster angle and layer thickness was the most influential factors [34].

Lee et al. [35] fabricated a cylindrical specimen to analyse the effect of build orientation on the compressive strength of printed parts. The compressive strength of the axial FDM specimen was 41.26 MPa, which was 11.6% greater than the transverse FDM specimen. It is important to study the influence of various parameters on compressive strength for improving the service life of parts due to the anisotropic and brittle nature of parts fabricated by FDM [35]. Panda et al. [55] examined the influence of layer thickness, orientation, raster angle, raster width, and air gap on the tensile strength of parts fabricated by ABS P400. The Bacterial Foraging technique (BFO) was implemented to determine the theoretical optimal value of process parameters to achieve better strength [55]. Sood et al. [75] developed an equation to determine the optimal setting to achieve desired compressive strength through quantum-behaved particle swarm optimization (QPSO)[75]. Rao et al. [66] formulated the single objective and multi-objective problems based on fused deposition modelling and solved these problems with the help of the Teaching Learning Based Optimization (TLBO) algorithm [66]. This research used two case studies to formulate these problems based on the empirical model developed by Sood et. al (2009). Qattawi et al. [60] used ASTM D638 type IV specimen of PLA to investigate the effect of building direction, infill percent, print speed, extrusion temperature, layer height, and infill pattern on tensile strength, dimensional accuracy, and ductility. In this research, various parameters were considered at 4 levels and optimized the process parameters using the response surface method. It is observed in this research that the dimensional accuracy is affected by building

direction, extrusion temperature, and layer height more than infill percentage, infill pattern, and printing speed [60]. Higher extrusion temperature and larger layer height were suggested to improve the mechanical properties of the printed part. Mishra et al. [44] attempted to identify the effect of layer thickness, raster width, contour chamber part orientation, and air gap on compressive strength. It was concluded that part orientation, contour number, and gaps between raster have a significant effect on compressive strength. An equation was developed to compute compressive strength from process parameters using RSM [44].

Vishwas et al. [84] experimentally identified the impact of the independent variables (layer thickness, shell thickness, and part orientation) on the dependent variable (ultimate tensile strength, dimensional accuracy, and manufacturing time of printed parts). ASTM standard D638-10specimenof ABS and Nylon were printed. Using Taguchi L9 orthogonal array, it was concluded that raster angle and shell thickness are the most significant process parameters for the ultimate tensile strength and dimensional accuracy for ABS and Nylon printed parts [84]. Dong et al. [15] studied the effect of the extruder temperature, print speed, fan speed, and layer height on the tensile strength. Lattice structure was used as a specimen to identify the effect of all independent variables mentioned above on the dependent variable. The lattice structure was deconstructed into horizontal and inclined struts. Taguchi's 'L16' orthogonal array was implemented to investigate which factor is most influential. In this research, it was found that fan speed is the most significant factor for inclined strut but for horizontal strut it is layer thickness [15]. Rajpurohit et al. [61] concluded that the highest tensile strength was obtained at the 0° raster angle and a lower value of layer height. The tensile strength of the parts fabricated using PLA improves as raster width increases but after a certain value of raster width, the tensile strength decreases [61].

Nagaraj et al. [47] found the optimal values of infill density, print speed, and layer thickness to achieve desired tensile strength for FDM printed ABS parts. The maximum tensile strength, 24.66 N/mm^2, was achieved with 80% infill density, 100 mm/min speed, and 0.2 mm layer thickness [47]. Luo et al. [40] developed and proposed dual nozzle FDM technology for continuous carbon fiber composite 3D printing. Various volume fractions of carbon fiber composite materials were achieved by inserting layers of carbon fiber into the model fabricated using PLA. The tensile strength of the fabricated part with a volume fraction of 40% Carbon fiber and 60 % of PLA was 287.9% better than parts fabricated with pure PLA [40]. Gebisa et al. [24] developed a regression model to predict the tensile strength of ULTEM 9085 thermoplastic material based on an experimental study to identify the effect of the air gap, raster angle, raster width, contour width, and contour number. It was concluded that the raster angle was the most influential factor among all considered factors [24]. Rao et al. [67] implemented a full factorial ANOVA analysis to study the effect of layer thickness, print temperature, and infill style on the tensile strength of parts fabricated by carbon fiber PLA. The maximum tensile strength (26.59 MPa) was obtained for a 0.1 mm layer thickness, cubic infill style, and 220 ^{0}C extrusion temperature [67].

Beniak et al. [6] fabricated a cylindrical specimen to investigate the effect of annealing on tensile strength and compressive strength of FDM printed volcano PLA parts. Tensile strength and compressive strength were found to be maximum when parts were heated after fabrication for 20 minutes in a heating chamber [6]. Deshwal et al. [7] fabricated the ASTM D 638 V standard specimen using PLA by varying process parameters of FDM. The RSM-based center composite design was developed to determine parameter combinations. A hybrid technique like GA-ANN, GA-RSM, and GA-ANFIS was deployed to determine the optimized value of process parameters to achieve maximum tensile strength. The maximum tensile strength, 47.0212 MPa, was achieved with infill density of 100%, temperature of 210 ^{0}C, and speed of 124.778 mm/s by GA-ANN, with an accuracy of 99.89% [7]. Kumar et al. [92] obtained desired tensile strength of carbon-reinforced PLA thermoplastic by optimizing process parameters according to Taguchi L9 experimental design. The optimum tensile strength, 21.961 MPa, of the fabricated part,was

achieved at 80 % infill density, 80mm/sec print speed, and 100 microns layer thickness [92]. Kain et al. [30] identified the effect of infill orientation on the mechanical performance of parts fabricated by FDM. Parts were fabricated using wood filament of PLA. In the wood filament of PLA, wood dust, cork, and other powdered wood derivatives are mixed with PLA. It was reported that parts fabricated with 25% wood fiber achieved better tensile strength [30]. Pazhamannil et al. [57] investigated the influences of nozzle temperature, layer thickness, and infill density on the tensile strength of the ASTM D638 specimen of PLA. It was found that the tensile strength of the specimen decreased with higher layer thickness. The main cause behind the above observation is the poor inter-layer bonding with large micro-voids at higher layer thickness and hence lower tensile strength. As the nozzle temperature increases, the tensile strength increases significantly. At high nozzle temperature, the intermolecular diffusion occurs across the interface for a longer period which increases the rate of neck growth gradually. The interface disappears which causes a decrease in the void density of the specimen [57]. Yadav et al. [88] discussed the effects of infill density, material density, and extrusion temperature on the tensile strength of ABS, PETG, and multi-material test pieces. Multi-material by merging ABS and PETG was fabricated in a ratio of 50:50 and 30 test pieces of ASTM D638 type-IV specimen with different inputs were printed to optimize the process parameters for multi-material using GA-ANN. It was found that extrusion temperature was the most influential factor that affects tensile strength. Higher extrusion temperature favors the high tensile strength of the test pieces up to a certain limit. The tensile strength of PETG is 44 N/mm^{2}at the extrusion temperature of 225 ^{0}C at 40% infill density was reported. The hybrid GA-ANN tool maximized the tensile strength of PETG to 46 N/mm^2 [88]. Fountas et al. [20] optimized the compressive strength using various evolutionary algorithms such as dragonfly (DA), ant lion algorithm (ALO), grey wolf algorithm (GWO), and wale optimization algorithm (WOA) by considering the equation developed by Sood et al. [75] and found better result in less number of iteration as compared to QPSO [20].

Dev et al. [12] have conducted a multi-objective optimization study to investigate the effect of layer thickness, build orientation, and infill patterns on material consumption and compressive strength. The Taguchi L9 orthogonal array was used for experimental design. Non- sorting genetic algorithm (NSGA-II) was used to optimize the objective function. It was concluded that the sample fabricated with 80% infill with gyroid pattern, 0.2 mm layer thickness, and 90^0 build orientations provide almost equal compressive strength with a lesser amount of material as compared to solid ABS part [12].

Srinivasan et al. [76] conducted an RSM-CCD-based experimental study to investigate the factors affecting the hardness and tensile strength of parts fabricated using ABS. Infill density and layer thickness were the two most significant factors that affect both responses. Maximum tensile strength was obtained when the infill style was triangular and trailed by grid and cubic [76]. Ramesh et al. [64] found that infill density has a higher contribution to improve tensile strength, to be maximum at 100% infill density and 0.1 mm layer thickness. Table 4 shows the summary of research works conducted to optimize the process parameters of FDM to achieve desired mechanical strength [64].

Dev et al. [12] combined Response Surface Methodology (RSM) and Genetic Algorithm to determine the optimal values of layer thickness, nozzle temperature, and print head speed to achieve desired flexural strength of the ABS printed part. As a result, the Flexural strength (58.3862 MPa) was predicted at a layer thickness of 0.120 mm, 224.958^0 C nozzle temperature, and 30.356 mm/s using the above-developed GA- RSM model is validated through experiments and only 0.69% deviation from predicted flexural strength was found [12]. Kam et al. [29] investigated the effect of infill style and infill density on the printed parts' tensile strength and Izod impact values. It was concluded that the tensile strength and Izod impact values improve with infill density [29]. Feng et al. [19] developed a machine-learning model to reduce the residual stress and warpage effect based on FEM simulation [19].

 Mubeen et al. [46] identified the influence of layer thickness, print temperature, infill density, and infill pattern on the impact strength of PLA. It is observed that layer thickness is the most significant factor for impact strength compared to other factors. Lower the layer thickness, the higher the impact strength [46]. Tosto et al. [82] improved the mechanical properties and the density of the sintered part manufactured by metal polymer filament by optimization of various process parameters of FDM. Flow rate is the most significant factor in enhancing mechanical properties and sample density. As a result, better mechanical properties were observed with layer thickness from 90 to 140 micrometres [82]. Lim et al. [37] investigated the effect of nozzle diameter, layer thickness, and infill percentage on the strength of prosthetic socket, Fabrication time, and weight of the prosthetic socket. It was observed that the optimum performance parameters could be achieved at the combination of 1.0 mm nozzle diameter, 0.48 mm layer thickness, and 30% infill density. PCR-TOPSIS was used to find the optimal process parameters condition [37]. Muhamedagic et al. [95] investigated the effect of layer height, print speed, raster angle, and wall thickness on the tensile strength of the specimen built using short carbon fiber reinforced polymide composite. The reduced cubic model was established using RSM and the correlation between selected process parameters and performance parameter was anlyzed by ANOVA. The layer thickness and raster angle were found most influential factors for tensile strength [95]. Ahmed et al. [2] identified the influence of layer thickness, build orientation, infill density, and print speed on tensile strength, Young's modulus, and flexural strength. Build orientation was the most significant factor which affects tensile strength, Young's modulus, and flexural strength. The optimal setting of various process parameters for FDM using oil palm fiber composite was flat (0 degree) build orientation, 10 mm/s printing speed, 0,4 mm layer thickness, and 50% infill density [2].

Table 4. Summary of major research in optimization of process parameters optimization of fused deposition modeling for mechanical properties

Authors	Material	Optimization Technique	Process Parameters	Performance Parameters
Tontowi et al. [80]	PLA	RSM, Taguchi	1. layer thickness	1. Tensile strength
			2. Temperature	2. Dimensional accuracy.
			3. Raster angle	
Asadollahi-Yazdi et al. [5]	ABS	NSGA-II	1. layer thickness	1.Build time
			2.Part orientation	2. Tensile strength
				3. Surface Roughness
				4.Material
Pazhamannil et al. [57]	PLA	ANN	1. Nozzle temperature(C)	1.Tensile strength
			2. Layer thickness	
			3. Infill speed	
			4. Tensile strength	
Beniak et al. [6]	Volcano PLA thermoplastic	NSGA-II	Annealing time	1. Tensile strength
				2. Compressive Strength
Dong et al. [15]	ABS	Taguchi Philosophy	1. Extruder Temperature	1. Tensile Strength
			2. Print Speed	
			3. Fan Speed	
			4. Layer Height	
Vishwas et al. [84]	ABS, Nylon	Taguchi Philosophy	1. Shell thickness	1. ultimate tensile Strength

			2. Model Orientation	2. Dimensional accuracy.
			3. Layer Thickness	
Yadav et al. [88]	ABS	GA-ANN	1. Infill density	1. Tensile strength
			2. Material Density	
			3. Extrusion temperature	
Qattawi et al. [60]	PLA	Taguchi Philosophy	1. Building Direction	1. Young's Modulus
			2. Infill Percent	2. Tensile Strength
			3. Print Speed	3. Ductility
			4. Extrusion Temperature	
			5. Layer height	
			6. Infill pattern	
Rajpurohit et al. [62]	PLA	Taguchi Philosophy	1. Raster Angle	1. Tensile strength
			2. Raster Width	
			3. Layer Height	
Raju et al. [63]	ABS	Hybrid PSO-BFO	1. Layer thickness	1. Surface Roughness
			2. Support Material	2. Hardness
			3. Model Interior	3. Tensile Strength
			4. Part Orientation	4. Flexural Modulus
Garg et al. [23]	ABS	Factorial Design	1. layer thickness	1. Compressive Strength
			2. Raster angle	
			3. Orientation	
			4. Raster width	
			5. Air gap	
Rao et al. [66]	ABS P400	TLBO	1. layer thickness	1. Compressive Strength
			2. Orientation	
			3. Raster angle	
			4. Raster Width	
			5. Air Gap	
Mishra et al. [44]	Rigid Plastic	RSM-FCCD	1. Cotour Number	1. Compressive Strength
			2. Layer thickness (mm)	
			3. Raster width	
			4. Part Orientation	
			5. Raster Angle	
			6. Air Gap	
Fountas et al. [21]	PLA	RSM	1. layer thickness	1. Tensile strength
			2. Shell thickness	
			3. Infill density	
			4. Part Orientation	
			5. Printing Speed	
Dev et al. [12]	ABS	Taguchi Philosophy, NSGA-II	1. layer thickness	1. Compressive Strength
			2. orientation angle	2. Material usage
			3. Infill density with pattern	
Deshwal et al. [11]	PLA	GA-ANN GA-ANFIS	1. Infill density	1. Tensile strength
			2. Temperature	

		GA-RSM	3. Speed	
Srinivasan et al. [77]	ABS	RSM-CCD	1. Infill density	1. Tensile strength
			2. Infill pattern	
			3. Layer thickness	
Ramesh et al. [65]	Nylon	Taguchi Philosophy, NSGA-II	1. Print speed	1. Tensile strength
			2. Layer Height	2. Impact Strength
			3. Infill density	3. Shore D-hardness
				4. Flexural Strength
Gebisa et al. [25]	ULTEM 9085 thermoplastic	Full Factorial Design	1. Air gap	1. Tensile strength
			2. Raster Angle	
			3. Raste width	
			4. Contour Number	
			5. Contour width	
Fountas et al. [20]	ABS	DA	1. Layer thickness	1. Compressive strength
		ALO	2. Orientation	2. Sliding wear
		GWO	3. Raster angle	
		MFO	4. Raster width	
		WOA	5. Air gap	
Rao et al. [68]	PLA	Full Factorial design	1. layer thickness	1. Tensile strength
			2. Infill pattern	
			3. Temperature	

5.5. Effect of Post-Processing on Mechanical Properties of Parts Printed Using FDM Technology

Torres et al. [82] investigated the effect of process parameters including the layer thickness, infill density, and post-processing heat-treatment time at 100^0C on the shear properties of FDM printed PLA parts. Infill density and layer thickness were the most influential factors for the strength, whereas infill density, and post-processing for ductility. Wach et al. [86] fabricated PLA specimen parts at different temperatures and processed them at 215^0C to increase the degree of crystallinity. The flexural strength of the samples improved with the increase in the degree of crystallinity of FDM-PLA by 11–17%. Pagano et al. [55] investigated the effect of annealing on the mechanical properties of PLA parts. It was concluded that annealing has no effect on tensile strength but significantly affected the Young modulus (stiffness).

5.6. Discussion and Future Aspects

Tensile strength is one of the most analyzed mechanical properties of FDM printed parts. It can be concluded from existing research works that layer thickness and build orientation are the most significant factors that affect the tensile strength of parts. Tensile strength was found to be maximum at 0^0-part orientation. The smaller layer thickness leads to better tensile strength. Apart from these two factors, infill density and number of shells, air gap, and raster angle also play an important role in tensile strength. Many researchers studied the effect of various process parameters on the compressive strength of FDM printed parts and concluded that infill density, infill shape, and the number of shells are the most significant factors impacting compressive strength. Very few works are reported that studied the flexural strength of FDM printed parts. Flexural strength was found to be maximum at 100% infill density and low layer thickness. Based on reviewed articles, the impact of process parameters including extrusion temperature, infill pattern, raster width, infill pattern, and their combinations can be analyzed in the future to build a part with good flexural strength. Annealing of the FDM parts improves the stiffness but does not affect tensile strength, significantly. Only a few articles have been

published on multi-objective optimization of process parameters of FDM to improve the mechanical properties of parts. Hence, there is a scope for further research in this direction.

5.7. Dimensional Accuracy

The dimensional accuracy of an FDM printed part is influenced by many factors including material characteristics, part geometry, and FDM process parameters. Wang et al. [86] observed that thermoplastic fiber shrinks when it cools down from melting temperature to glass transition temperature, which causes dimensional inaccuracy in parts [86]. Nazan et al. [52] investigated the effect of layer temperature, infill density, first layer thickness, and other layer thickness on the dimensional accuracy of parts. Cuboids of size 30mm x 100mm x 5mm were printed and RSM-central composite design was implemented to optimize different process parameters to reduce the warping of the parts [52]. Sood et. al [74] presented an experimental investigation on the effect of various process parameters, such as part orientation, layer thickness, raster angle, raster width, and air gap along with their combinations on the dimensional accuracy of FDM printed ABSP400 parts. Shrinkage was observed along the x and y-axis of the build platform and the thickness of the printed part along the z-axis was always found to be more than the design value. Taguchi's 'L27' orthogonal array was used to determine the significance of parameters and their interactions before recommending the optimum level of parameters. Grey Taguchi methodology has been adopted to minimize the combination of all objectives, i.e., minimizing the percentage change in the dimension along all the axes [74]. Dani et al. [10] implemented multi-objective optimization of process parameters, including build material, the number of layers, support structure, build time, and part orientation to reduce dimensional inaccuracy [10]. Sahu et al. [71] conducted an experimental study and integrated fuzzy logic with the Taguchi method for decision-making in selecting the optimal set of parameters to improve dimensional accuracy. The results of the multi-response predicted model was validated by conducting a confirmation test [71]. Peng et al. [59] implemented a fuzzy interface system to convert three outputs including build time, dimensional accuracy, and warp deformation into one comprehensive response. A model was developed relating the comprehensive response and the four input variables namely, line width compensation, extrusion velocity, filling velocity, and layer thickness using second-order response surface methodology and further validated by the artificial neural network [59]. Gurrala et al. [25] developed a functional relationship between the independent variable and response variable. In this study, the model interior, the horizontal direction along the xy plane, and the vertical direction along the xz plane were considered the independent variable. This paper concluded that the effect of the depositing direction along the horizontal direction was found predominant through ANOVA. The width and shrinkage were varying as the length of the part increased [25]. Dimensional accuracy is an important factor for the fit and finish requirement of assembly. The dimensional accuracy of the printed part deviates from the CAD model due to the heating and cooling cycle of the FDM process. Equbal et al. [16] incorporated the parametric optimization of FDM to enhance the dimension accuracy of parts fabricated by ABS and concluded that raster angle and raster width affect the dimensional accuracy significantly [16]. Narang et al. [51] recommended lower layer thickness to achieve better dimensional accuracy and surface roughness [51]. Tontowi et al. [80] optimized the process parameter of the 3D printer to improve the quality of poly-lactic acid printed parts. Layer thickness, temperature, and raster angle were selected as process parameters. This study investigated the effect of process parameters on tensile strength and dimensional accuracy.RSM and Taguchi methods were used to develop equations between dependent variables, i.e. tensile strength and dimensional accuracy, and independent variables, i.e., layer thickness, temperature, and raster angle. It was found that tensile strength was prominently affected by layer thickness rather than raster angle or temperature. This study also compared two different methodologies of design of experiments: RSM Taguchi methods and concluded that RSM could significantly reduce the dimensional error and improve the tensile strength as compared to the Taguchi method [80].

Cekic et al. [8] compared the dimensional accuracy of parts fabricated using PLA and PLA-wood composite and concluded that PLA wood composite parts' dimensional accuracy was found better than PLA parts [8]. Sajan et al. [72] conducted an experimental investigation to identify the effect of six parameters including bed temperature, nozzle temperature, print speed, infill percentage, layer thickness, and the number of loops on circularity and surface finish. Bed temperature, number of loops, nozzle temperature, print speed, layer thickness, and infill affect the circularity and surface roughness in descending order [72]. Mahmood et al. [43] investigated the effect of 13 parameters on dimensional accuracy and geometric characteristics of benchmarked components fabricated using ABS material. It was found that deviation increased with more features. The number of shells was found to be the most significant factor affecting dimensional accuracy. Layer thickness, infill speed, infill shell spacing multiplier, number of shells, and extruder temperature were the most influencing factors for geometric characteristics [43]. Eswaran et. al [18] used Taguchi's 'L9' orthogonal array to optimize the process parameter such as infill density, horizontal orientation, and vertical orientation to minimize the circularity error of the printed part. In this study, It was observed that 50% infill density, 0 degrees horizontal, and vertical orientation minimizes the circularity error of the considered printed part [18]. Beniak et al. [7] investigated the effect of layer thickness and extrusion temperature on dimensional accuracy through ANOVA. This research concluded that printing temperature has a significant effect on the shape and dimensional tolerance. Agarwal et al. [1] analyzed the impact of wall thickness, infill density, print bed temperature, print speed, layer thickness, and extrusion temperature on dimensional accuracy. This research concluded that layer thickness and print speed significantly impact the dimensional accuracy of the printed parts. Therefore, low layer thickness and high print speed were suggested to achieve better dimensional accuracy [1].

Table 5. presents the summary of research articles published to investigate the effect of various process parameters on dimensional accuracy.

Authors	Material	Optimization Technique	Process Parameters	Performance Parameters
Tontowi et al. [81]	PLA	RSM, Taguchi	1. Layer thickness	1. Tensile strength
			2. Temperature	2. Dimensional accuracy.
			3. Raster angle	
Nazan et al. [53]	ABS	Response Surface Method	1. layer temperature	1. Warping
			2. infill density	
			3. first layer thickness	
			4. other layer thickness	
Beniak et al. [6]	Volcano PLA thermoplastic	NSGA-II	1. Annealing time	1. Tensile strength
				2. Compressive Strength
Sood et al. [75]	ABS	Taguchi 'L27' and Grey Rational Method	1. Layer thickness,	Dimensional Accuracy
			2. Raster angle,	
			3. Raster width,	
			4. Air gap,	
			5. Build Orientation	

Eswaran et al. [18]	ABS	Taguchi 'L9'	1. Infill density,	1.Circularity Error Internal
			2. Horizontal orientation,	2.Circularity error External
			3. vertical orientation	
Mahmood et al. [44]	ABS	Taguchi L'27'	1. Chamber Temp.	Dimensional Accuracy
			2. Layer Thickness	
			3. Extruder Temp.	
			4. Platform Temp.	
			5. No. of shells	
			6. Infill shell spacing multiplier	
			7. Inset distance multiplier	
			8. Floor/roof thickness	
			9. Infill density	
			10. Infill speed	
			11. Outline speed(mm/s)	
			12. Inset speed(mm/s)	
Sajan et al. [73]	ABS	Taguchi L'27'	1. Bed Temperature	1. Circularity error
			2. Nozzle Temperature	2. Surface Roughness
			3. Print Speed	
			4. Infill	
			5. Layer thickness	
			6. Number of loops	

5.8. A short discussion and future aspects:

The critical literature review concludes that dimensional accuracy is significantly affected by layer thickness, extrusion temperature, and the number of shells. The low layer thickness was recommended to improve dimensional accuracy. Shrinkage and expansion were observed along the X and Y directions and the Z direction, respectively. Thus, orientation is also an important factor that affects dimensional accuracy. It is required to further investigate the effect of other factors, such as the number of contours, contour width, raster angle, and raster width on dimensional accuracy. Many researchers have considered the two-level or three-level factors to reduce the deviation in dimension. Taguchi method and response surface methodology were used for experimental modeling and optimization. In the future, optimization of process parameters considering more than three-level using modern optimization techniques, such as GA, TLBO, QPSO, can be investigated.

5.9. Build Time

The adoption of additive manufacturing for mass production in industries is still challenging due to the large build time of parts. Fused deposition modeling fabricates the parts in the layer-by-layer manner. It consumes a lot of time to fabricate even a small part. Failure of part printing due to blocked nozzle also increased the build time of parts. Similarly, other part characteristics and machining parameters also affect the build time. Build time can be optimized by selecting the optimum setting of various process parameters. Thrimurthulu et al. [79] presented a multi-criteria genetic algorithm to determine optimal settings of part orientation to enhance surface finish and reduce printing time [79]. Nancharaiah [50] observed that raster angle and air gap influence the build time greatly. Build time can be reduced by selecting a higher layer thickness and positive air gap [50]. Gurrala et al. [25] developed a model to investigate the effect of layer thickness, raster angle, part orientation, contour width, and part raster width on build time and support structure volume using a full factorial design of experiments. It was concluded that layer thickness, part orientation, contour width, and raster width affect the build time significantly [25]. Ali et al. [3] reduced the build time by selecting high layer thickness, positive air gap, and larger raster width. High layer thickness, positive air gap, and larger raster width fulfill the aggregate model in less number of slices. This results in reduced build time [3]. Espalin et al. [17] explored build process deviation to improve surface roughness and build time by integrating two legacy FDM machines. Build time was reduced by 53% more than the standard FDM process [17]. Rathee et al. [69] conducted an experimental case study using a cylindrical specimen to investigate the effect of layer thickness, shell width, air gap, raster width, raster orientation, and build orientation to reduce the build time. Quadratic response surface equations relating build time and the considered factors for each spatial orientation (rotation around different axes) were developed using a central composite design (CCD) approach.

Table 6. Summary of major research in optimization of process parameters optimization of fused deposition modeling for build time

Authors	Material	Optimization Technique	Process Parameters	Performance Parameters
Hallmann et al. [28]	Water Soluble filament	Simulation in MATLAB	The angle of the 3RRR mechanism	1. Build Time
				2. Support Structure
Asadollahi-Yazdi et al. [5]	ABS	NSGA-II	1.Layer thickness	1.Build time
				2. Tensile strength
			2.Part orientation	3. Surface Roughness
				4.Material
Chaudhari et al. [9]	ABS	Taguchi 'L9'	1. layer thickness,	1. Production Time
			2. infill,	
			3. orientation	2. Production cost
			4. post-processing	

The outcome of the study showed that layer thickness and air gap were the most significant parameters for all the spatial orientations [69]. Srivastava et al. [77] implemented multi-

objective optimization using RSM embedded fuzzy logic to determine the optimal setting of process parameters to improve build time and reduce support structure volume simultaneously. The intermediate value of layer height and air gap were found optimal for a multi-objective function [77]. Patil et al. [58] conducted multi-objective optimization using the grey rational method to find out the optimal settings of FDM parameters to enhance surface finish, reduce build time, and consumption of filament. This study concluded that a triangular infill pattern, 70% infill density, 100 mm/h printing speed, and 0.2 mm layer thickness are the optimum value of the considered parameters to improve the objective. Table 6 illustrates a brief description of research articles that investigated the impact of process parameters on build time [58].

5.10. A Short Discussion and Future Aspects

It was found from the critical literature review that the build time was reduced by selecting high layer thickness, larger raster width, and positive air gap. Some of the researchers also investigated the effect of part orientation on build time. Various orientations to print a part required different volumes of the support structure. Thus, the time to print support structure and part vary with part orientation. The effect of some process parameters, such as extrusion temperature, raster angle, and shell thickness, is still unexplored. Layer thickness also affects surface roughness and dimensional accuracy adversely. One further research direction could be multi-objective optimization to study the effect of various process parameters on surface roughness, dimensional accuracy, and build time.

5.11. Other Responses

The effect of various process parameters of FDM on support structure minimization, energy consumption, build cost, etc. are still least explored. Few experimental investigations to identify the effect of various process parameters on these responses have been conducted. Lunetto et al. [39] investigated the effect of types of components, material, infill styles, and layer thickness on specific printing energy, specific energy consumption, and process time using the regression method. The results of the study reported that the contribution due to the non-printing phases, i.e., switch-on, idling, heating, and calibration, on the total process time and energy consumption can be modeled as a constant. A linear correlation was highlighted between build time and energy demand for printing during the printing phase [39]. Dani et al. [10] recommended 0°build orientation to reduce support structure, build time, and build cost [10]. Raut et al. [94] fabricated the ABS parts in various orientations and identified the effect of build orientation on the required number of layers, time to fabricate the part, support structure volume, and total cost. Build orientation 0°about the y-axis was found optimal for tensile strength and build cost [94].

Table 7. optimization techniques used to identify the impact of process parameters on other performance parameters such as specific printing energy, specific energy consumption, production cost, etc.

Authors	Material	Optimization Technique	Process Parameters	Performance Parameters
Lunetto et al. [40]	ABS PC ABS	Linear Correlation method	1. Type of Component	1.Specific Printing Energy (SPE)
			2. Infill Strategy	2.The Specific Energy Consumption (SEC)
			3. layer thickness	

Fountas et al. [21]	PLA	RSM	1. layer thickness	1. Tensile strength
			2. Shell thickness	
			3. Infill density	
			4. Part Orientation	
			5. Printing Speed	
Chaudhari et al. [9]	ABS	Taguchi 'L9'	1. layer thickness,	1. Production Time
			2. infill,	
			3. orientation	2. Production cost
			4. post-processing	

6. Conclusion

This literature review attempted to critically analyze and discuss FDM process parameters and their impact on various properties of FDM printed parts. Various optimization tools such as GA, RSM, Taguchi etc., are also summarized which are commonly used in this research. This work explored the existing research that has been carried out on the optimization of process parameters of FDM using various tools such as genetic algorithm, grey analysis, factorial design method, Taguchi methodology, response surface method, teaching learning-based optimization, artificial neural network. In these optimization methods, attempts are made to identify the significant parameters responsible for a desired property. Many works have been reviewed that focuses on the mechanical properties, quality of parts, and efficiency of the FDM process but very few research were conducted to improve the 3D printer design, identification of newer printing material and preventive maintenance of 3D printer. The following could be the potential future research directions:

- ABS and PLA are the two most commonly used materials to print the parts. Other materials such as Nylon, PETG, and HIPS, can be used as thermoplastic filament for future research.
- Some process parameters, such as infill pattern, shell width, air gap, annealing, contour width, number of contours are less analyzed compared to layer thickness, build orientation, raster width, etc. The least known parameter such as annealing, support structures may be considered as a variable for future research direction.
- There is limited research on multi-objective optimization of process parameters of fused deposition modeling, which can be another direction for future work.
- 3D printing in different planes to reduce or eliminate the support structure can also be a research direction for future work, which is very challenging.
- Future research may be possible on "3D printing on the uneven surface" and "3d printing for repairing the broken parts".

References

[1] Agarwal KM, Shubham P, Bhatia D, Sharma P, Vaid H, Vajpeyi R. Analyzing the impact of print parameters on dimensional variation of ABS specimens printed using fused deposition modelling (FDM). Sensors International. 2022 Jan 1;3:100149. https://doi.org/10.1016/j.sintl.2021.100149

[2] Ahmad MN, Ishak MR, Mohammad Taha M, Mustapha F, Leman Z, Anak Lukista DD, Ghazali I. Application of Taguchi method to optimize the parameter of fused deposition modeling (FDM) using oil palm fiber reinforced thermoplastic composites. Polymers. 2022 May 24;14(11):2140. https://doi.org/10.3390/polym14112140

[3] Ali F, Chowdary BV, Maharaj J. Influence of some process parameters on build time, material consumption, and surface roughness of FDM processed parts: inferences based on the Taguchi design of experiments. InProceedings of The 2014 IACJ/ISAM Joint International Conference 2014 Sep.

[4] Anitha R, Arunachalam S, Radhakrishnan P. Critical parameters influencing the quality of prototypes in fused deposition modelling. Journal of Materials Processing Technology. 2001 Dec 3;118(1-3):385-8. https://doi.org/10.1016/S0924-0136(01)00980-3

[5] Asadollahi-Yazdi E, Gardan J, Lafon P. Multi-objective optimization of additive manufacturing process. IFAC-PapersOnLine. 2018 Jan 1;51(11):152-7. https://doi.org/10.1016/j.ifacol.2018.08.250

[6] Beniak J, Holdy M, Križan P, Matúš M. Research on parameters optimization for the Additive Manufacturing process. Transportation Research Procedia. 2019 Jan 1;40:144-9. https://doi.org/10.1016/j.trpro.2019.07.024

[7] Beniak J, Križan P, Šooš Ľ, Matúš M. Research on shape and dimensional accuracy of FDM produced parts. InIOP conference series: materials science and engineering 2019 Mar 1 (Vol. 501, No. 1, p. 012030). IOP Publishing. https://doi.org/10.1088/1757-899X/501/1/012030

[8] Cekic A, Begic-Hajdarevic D, Muhamedagic K, Guzanovic N. Experimental investigations of process parameters influence on dimensional accuracy and mechanical properties of FDM manufactured parts. InProceedings of 29th DAAAM International Symposium on Intelligent Manufacturing and Automation, Zadar, ISSN 2018 Jan 1 (pp. 1726-9679).

[9] Chaudhari M, Jogi BF, Pawade RS. Comparative study of part characteristics built using additive manufacturing (FDM). Procedia Manufacturing. 2018 Jan 1;20:73-8. https://doi.org/10.1016/j.promfg.2018.02.010

[10] Dani T, Kamdi P, Nalamwar G, Borse V. Multi objective optimization of built orientation for rapid prototyping of connecting rod. International Journal of scientific research and management. 2013;1(1):13-8.

[11] Deshwal S, Kumar A, Chhabra D. Exercising hybrid statistical tools GA-RSM, GA-ANN and GA-ANFIS to optimize FDM process parameters for tensile strength improvement. CIRP Journal of Manufacturing Science and Technology. 2020 Nov 1;31:189-99. https://doi.org/10.1016/j.cirpj.2020.05.009

[12] Dev S, Srivastava R. Experimental investigation and optimization of FDM process parameters for material and mechanical strength. Materials Today: Proceedings. 2020 Jan 1;26:1995-9. https://doi.org/10.1016/j.matpr.2020.02.435

[13] Dey A, Yodo N. A systematic survey of FDM process parameter optimization and their influence on part characteristics. Journal of Manufacturing and Materials Processing. 2019 Jul 29;3(3):64. https://doi.org/10.3390/jmmp3030064

[14] Dev S, Srivastava R. Optimization of fused deposition modeling (FDM) process parameters for flexural strength. Materials Today: Proceedings. 2021 Jan 1;44:3012-6. https://doi.org/10.1016/j.matpr.2021.02.436

[15] Dong G, Wijaya G, Tang Y, Zhao YF. Optimizing process parameters of fused deposition modeling by Taguchi method for the fabrication of lattice structures. Additive Manufacturing. 2018 Jan 1;19:62-72. https://doi.org/10.1016/j.addma.2017.11.004

[16] Equbal A, Sood AK, Ansari AR, Equbal A. Optimization of process parameters of FDM part for minimiizing its dimensional inaccuracy. International Journal of Mechanical and Production Engineering Research and Development. 2017;7(2):57-65.

[17] Espalin D, Ramirez JA, Medina F, Wicker R. Multi-material, multi-technology FDM: exploring build process variations. Rapid Prototyping Journal. 2014 Apr 14. https://doi.org/10.1108/RPJ-12-2012-0112

[18] Eswaran P, Sivakumar K, Subramaniyan M. Minimizing error on circularity of FDM manufactured part. Materials Today: Proceedings. 2018 Jan 1;5(2):6675-83. https://doi.org/10.1016/j.matpr.2017.11.324

[19] Feng Q, Maier W, Möhring HC. Application of machine learning to optimize process parameters in fused deposition modeling of PEEK material. Procedia CIRP. 2022 Jan 1;107:1-8. https://doi.org/10.1016/j.procir.2022.04.001

[20] Fountas NA, Kechagias JD, Manolakos DE, Vaxevanidis NM. Single and multi-objective optimization of FDM-based additive manufacturing using metaheuristic algorithms. Procedia Manufacturing. 2020 Jan 1;51:740-7. https://doi.org/10.1016/j.promfg.2020.10.104

[21] Fountas NA, Kostazos P, Pavlidis H, Antoniou V, Manolakos DE, Vaxevanidis NM. Experimental investigation and statistical modelling for assessing the tensile properties of FDM fabricated parts. Procedia Structural Integrity. 2020 Jan 1;26:139-46. https://doi.org/10.1016/j.prostr.2020.06.017

[22] Galantucci LM, Lavecchia F, Percoco G. Experimental study aiming to enhance the surface finish of fused deposition modeled parts. CIRP annals. 2009 Jan 1;58(1):189-92. https://doi.org/10.1016/j.cirp.2009.03.071

[23] Garg A, Tai K, Lee CH, Savalani MM. A hybrid $$\text {M} 5^\prime $$-genetic programming approach for ensuring greater trustworthiness of prediction ability in modelling of FDM process. Journal of Intelligent Manufacturing. 2014 Dec;25(6):1349-65.. https://doi.org/10.1007/s10845-013-0734-1

[24] Gebisa AW, Lemu HG. Influence of 3D printing FDM process parameters on tensile property of ULTEM 9085. Procedia Manufacturing. 2019 Jan 1;30:331-8. https://doi.org/10.1016/j.promfg.2019.02.047

[25] Gurrala PK, Regalla SP. Optimization of support material and build time in fused deposition modeling (FDM). InApplied Mechanics and Materials 2012 (Vol. 110, pp. 2245-2251). Trans Tech Publications Ltd. https://doi.org/10.4028/www.scientific.net/AMM.110-116.2245

[26] Gurrala PK, Regalla SP. DOE based parametric study of volumetric change of FDM parts. Procedia materials science. 2014 Jan 1;6:354-60. https://doi.org/10.1016/j.mspro.2014.07.045

[27] Hallmann M, Goetz S, Schleich B, Wartzack S. Optimization of build time and support material quantity for the additive manufacturing of non-assembly mechanisms. Procedia CIRP. 2019 Jan 1;84:271-6.https://doi.org/10.1016/j.procir.2019.03.197

[28] Haque ME, Banerjee D, Mishra SB, Nanda BK. A numerical approach to measure the surface roughness of FDM build part. Materials Today: Proceedings. 2019 Jan 1;18:5523-9.https://doi.org/10.1016/j.matpr.2019.07.659

[29] Kam M, Ipekci A, Sengul O. Taguchi optimization of fused deposition modeling process parameters on mechanical characteristics of PLA+ filament material. Scientia Iranica. 2022 Feb 1;29(1):79-89.

[30] Kain S, Ecker JV, Haider A, Musso M, Petutschnigg A. Effects of the infill pattern on mechanical properties of fused layer modeling (FLM) 3D printed wood/polylactic acid (PLA) composites. European journal of wood and wood products. 2020 Jan;78(1):65-74.https://doi.org/10.1007/s00107-019-01473-0

[31] Kalsi NS, Sehgal R, Sharma VS. Grey-based Taguchi analysis for optimization of multi-objective machining process in turning. International Journal of Strategic Decision Sciences (IJSDS). 2013 Apr 1;4(2):79-95.

[32] Kanchana J, Prasath V, Krishnaraj V. Multi response optimization of process parameters using grey relational analysis for milling of hardened Custom 465 steel. Procedia Manufacturing. 2019 Jan 1;30:451-8. https://doi.org/10.1016/j.promfg.2019.02.064

[33] Khan MS, Mishra SB. Minimizing surface roughness of ABS-FDM build parts: An experimental approach. Materials Today: Proceedings. 2020 Jan 1;26:1557-66. https://doi.org/10.1016/j.matpr.2020.02.320

[34] Lee BH, Abdullah J, Khan ZA. Optimization of rapid prototyping parameters for production of flexible ABS object. Journal of materials processing technology. 2005 Oct 30;169(1):54-61.https://doi.org/10.1016/j.jmatprotec.2005.02.259

[35] Lee CS, Kim SG, Kim HJ, Ahn SH. Measurement of anisotropic compressive strength of rapid prototyping parts. Journal of materials processing technology. 2007 Jun 12;187: 627-30. https://doi.org/10.1016/j.jmatprotec.2006.11.095

[36] Li B, Yang J, Gu H, Jiang J, Zhang J, Sun J. Surface roughness of PLA parts by FDM with chemical treatment. InJournal of Physics: Conference Series 2021 Jun 1 (Vol. 1948, No. 1, p. 012199). IOP Publishing. https://doi.org/10.1088/1742-6596/1948/1/012199

[37] Lim GD, Abd Latif MJ, Alkahari MR, Yob MS, Musa M, Rahman MN, Rajaandra P, Nguyen HQ. Parameter Optimization of Fused Deposition Modeling Process for 3D Printed Prosthetic Socket using PCR-TOPSIS Method. International Journal of Nanoelectronics & Materials. 2022 Mar 2;15.

[38] Miazio Ł. Impact of print speed on strength of samples printed in FDM technology. Agricultural Engineering. 2019;23. DOI 10.1515/agriceng-2019-0014

[39] Lunetto V, Priarone PC, Galati M, Minetola P. On the correlation between process parameters and specific energy consumption in fused deposition modelling. Journal of Manufacturing Processes. 2020 Aug 1;56:1039-49. https://doi.org/10.1016/j.jmapro.2020.06.002

[40] Luo H, Tan Y, Zhang F, Zhang J, Tu Y, Cui K. Selectively enhanced 3D printing process and performance analysis of continuous carbon fiber composite material. Materials. 2019 Oct 28;12(21):3529. https://doi.org/10.3390/ma12213529

[41] Spoerk M, Gonzalez-Gutierrez J, Sapkota J, Schuschnigg S, Holzer C. Effect of the printing bed temperature on the adhesion of parts produced by fused filament fabrication. Plastics, Rubber and Composites. 2018 Jan 2;47(1):17-24. https://doi.org/10.1080/14658011.2017.1399531

[42] Mohamed OA, Masood SH, Bhowmik JL. Optimization of fused deposition modeling process parameters: a review of current research and future prospects. Advances in manufacturing. 2015 Mar;3(1):42-53. https://doi.org/10.1007/s40436-014-0097-7

[43] Mahmood S, Qureshi AJ, Talamona D. Taguchi based process optimization for dimension and tolerance control for fused deposition modelling. Additive Manufacturing. 2018 May 1;21:183-90. https://doi.org/10.1016/j.addma.2018.03.009

[44] Mishra SB, Abhishek K, Satapathy MP, Mahapatra SS. Parametric appraisal of compressive strength of FDM build parts. Materials Today: Proceedings. 2017 Jan 1;4(9):9456-60. https://doi.org/10.1016/j.matpr.2017.06.203

[45] Montero M, Roundy S, Odell D, Ahn SH, Wright PK. Material characterization of fused deposition modeling (FDM) ABS by designed experiments. Society of Manufacturing Engineers. 2001 May;10(13552540210441166):1-21.

[46] Mubeen MA, Rani PS, Optimization of Fused deposition modeling process parameters for impact strength carbon fiber (PLA). Journal of Engineering Sciences. 2022; 13(5):323-332.

[47] Nagaraj C, Mishra D, Tirupati T. Optimization of the FDM Process parameters to attain the desired strength of ABS specimens. Int J Recent Technol Eng (IJRTE). 2019;8(4).

[48] Nagendra J, Srinath MK, Sujeeth S, Naresh KS, Prasad MG. Optimization of process parameters and evaluation of surface roughness for 3D printed nylon-aramid composite. Materials Today: Proceedings. 2021 Jan 1;44:674-82. https://doi.org/10.1016/j.matpr.2020.10.609

[49] Nancharaiah TR, Raju DR, Raju VR. An experimental investigation on surface quality and dimensional accuracy of FDM components. International Journal on Emerging Technologies. 2010 Jan;1(2):106-11.

[50] Nancharaiah T. Optimization of process parameters in FDM process using design of experiments. Int J Emerg Technol. 2011;2(1):100-2.

[51] Narang R, Chhabra D. Analysis of process parameters of fused deposition modeling (FDM) technique. International Journal on Future Revolution in Computer Science & Communication Engineering. 2017 Oct;3(10):41-8.

[52] Nazan MA, Ramli FR, Alkahari MR, Sudin MN, Abdullah MA. Process parameter optimization of 3D printer using Response Surface Method. Methodology. 2006;15:17.

[53] Ngo TD, Kashani A, Imbalzano G, Nguyen KT, Hui D. Additive manufacturing (3D printing): A review of materials, methods, applications and challenges. Composites Part B: Engineering. 2018 Jun 15;143:172-96. https://doi.org/10.1016/j.compositesb.2018.02.012

[54] Pagano C, Basile V, Modica F, Fassi I. Micro-FDM process capability and post-processing effects on mechanical properties. InAIP Conference Proceedings 2019 Aug 26 (Vol. 2139, No. 1, p. 190002). AIP Publishing LLC. https://doi.org/10.1063/1.5121694

[55] Panda SK, Padhee S, Anoop Kumar SO, Mahapatra SS. Optimization of fused deposition modelling (FDM) process parameters using bacterial foraging technique. Intelligent information management. 2009 Nov 30;1(02):89. https://10.4236/iim.2009.12014

[56] Patil P, Raykar SJ, Bhamu J, Singh D. Modelling and Analysis of Surface Roughness in Fused Deposition Modeling Based on Infill Patterns. Indian Journal of Engineering and Materials Sciences (IJEMS). 2022 Nov 5;29(1):92-9. https://10.56042/ijems.v29i1.45585

[57] Pazhamannil RV, Govindan P, Sooraj P. Prediction of the tensile strength of polylactic acid fused deposition models using artificial neural network technique. Materials Today: Proceedings. 2021 Jan 1;46:9187-93.
https://10.56042/ijems.v29i1.45585

[58] Patil P, Singh D, Raykar SJ, Bhamu J. Multi-objective optimization of process parameters of Fused Deposition Modeling (FDM) for printing Polylactic Acid (PLA) polymer components. Materials Today: Proceedings. 2021 Jan 1;45:4880-5.
https://doi.org/10.1016/j.matpr.2021.01.353

[59] Peng A, Xiao X, Yue R. Process parameter optimization for fused deposition modeling using response surface methodology combined with fuzzy inference system. The International Journal of Advanced Manufacturing Technology. 2014 Jul;73(1):87-100.
https://doi.org/10.1007/s00170-014-5796-5

[60] Qattawi A, Alrawi B, Guzman A. Experimental optimization of fused deposition modelling processing parameters: a design-for-manufacturing approach. Procedia Manufacturing. 2017 Jan 1;10:791-803. https://doi.org/10.1016/j.promfg.2017.07.079

[61] Rajpurohit SR, Dave HK. Effect of process parameters on tensile strength of FDM printed PLA part. Rapid Prototyping Journal. 2018 Oct 25. https://doi.org/10.1108/RPJ-06-2017-0134

[62] Rajpurohit SR, Dave HK. Analysis of tensile strength of a fused filament fabricated PLA part using an open-source 3D printer. The International Journal of Advanced Manufacturing Technology. 2019 Apr;101(5):1525-36. https://doi.org/10.1007/s00170-018-3047-x

[63] Raju M, Gupta MK, Bhanot N, Sharma VS. A hybrid PSO–BFO evolutionary algorithm for optimization of fused deposition modelling process parameters. Journal of Intelligent Manufacturing. 2019 Oct;30(7):2743-58. https://doi.org/10.1007/s10845-018-1420-0

[64] Ramesh M, Panneerselvam K. Mechanical investigation and optimization of parameter selection for Nylon material processed by FDM. Materials Today: Proceedings. 2021 Jan 1;46:9303-7. https://doi.org/10.1016/j.matpr.2020.02.697

[65] Rao RV. Advanced modeling and optimization of manufacturing processes: international research and development. London: Springer; 2011.

[66] Rao RV, Rai DP. Optimization of fused deposition modeling process using teaching-learning-based optimization algorithm. Engineering Science and Technology, an International Journal. 2016 Mar 1;19(1):587-603. https://doi.org/10.1016/j.jestch.2015.09.008

[67] Rao VD, Rajiv P, Geethika VN. Effect of fused deposition modelling (FDM) process parameters on tensile strength of carbon fibre PLA. Materials Today: Proceedings. 2019 Jan 1;18:2012-8. https://doi.org/10.1016/j.matpr.2019.06.009

[68] Ravi Kumar Y, Rao CS, Janardhan Reddy TA. A robust process optimisation for fused deposition modelling. International journal of manufacturing technology and management. 2008 Jan 1;14(1-2):228-45. https://doi.org/10.1504/IJMTM.2008.017497

[69] Rathee S, Srivastava M, Maheshwari S, Siddiquee AN. Effect of varying spatial orientations on build time requirements for FDM process: A case study. Defence technology. 2017 Apr 1;13(2):92-100. https://doi.org/10.1016/j.dt.2016.11.006

[70] Rodrı´ guez JF, Thomas JP, Renaud JE. Design of fused-deposition ABS components for stiffness and strength. J. Mech. Des.. 2003 Sep 1;125(3):545-51. https://doi.org/10.1115/1.1582499

[71] Sahu RK, Mahapatra SS, Sood AK. A study on dimensional accuracy of fused deposition modeling (FDM) processed parts using fuzzy logic. Journal for Manufacturing Science & Production. 2013 Oct 25;13(3):183-97. https://doi.org/10.1515/jmsp-2013-0010

[72] Sajan N, John TD, Sivadasan M, Singh NK. An investigation on circularity error of components processed on Fused Deposition Modeling (FDM). Materials Today: Proceedings. 2018 Jan 1;5(1):1327-34. https://doi.org/10.1016/j.matpr.2017.11.218

[73] Sharma R, Singh R, Batish A. On multi response optimization and process capability analysis for surface properties of 3D printed functional prototypes of PVC reinforced with PP and HAp.

Materials Today: Proceedings. 2020 Jan 1;28:1115-22. https://doi.org/10.1016/j.matpr.2020.01.092

[74] Sood AK, Ohdar RK, Mahapatra SS. Improving dimensional accuracy of fused deposition modelling processed part using grey Taguchi method. Materials & design. 2009 Dec 1;30(10):4243-52. https://doi.org/10.1016/j.matdes.2009.04.030

[75] Sood AK, Ohdar RK, Mahapatra SS. Experimental investigation and empirical modelling of FDM process for compressive strength improvement. Journal of Advanced Research. 2012 Jan 1;3(1):81-90.https://doi.org/10.1016/j.jare.2011.05.001

[76] Srinivasan R, Pridhar T, Ramprasath LS, Charan NS, Ruban W. Prediction of tensile strength in FDM printed ABS parts using response surface methodology (RSM). Materials today: proceedings. 2020 Jan 1;27:1827-32. https://doi.org/10.1016/j.matpr.2020.03.788

[77] Srivastava M, Rathee S, Maheshwari S, Kundra TK. Multi-objective optimisation of fused deposition modelling process parameters using RSM and fuzzy logic for build time and support material. International Journal of Rapid Manufacturing. 2018;7(1):25-42.

[78] Tiwary V, Arunkumar P, Deshpande AS, Khorate V. Studying the effect of chemical treatment and fused deposition modelling process parameters on surface roughness to make acrylonitrile butadiene styrene patterns for investment casting process. International Journal of Rapid Manufacturing. 2015;5(3-4):276-88. https://doi.org/10.1504/IJRAPIDM.2015.074807

[79] Thrimurthulu KP, Pandey PM, Reddy NV. Optimum part deposition orientation in fused deposition modeling. International Journal of Machine Tools and Manufacture. 2004 May 1;44(6):585-94. https://doi.org/10.1016/j.ijmachtools.2003.12.004

[80] Tontowi AE, Ramdani L, Erdizon RV, Baroroh DK. Optimization of 3D-printer process parameters for improving quality of polylactic acid printed part. International Journal of Engineering and Technology. 2017 Apr;9(2):589-600. DOI: 10.21817/ijet/2017/v9i2/170902044

[81] Torres J, Cotelo J, Karl J, Gordon AP. Mechanical property optimization of FDM PLA in shear with multiple objectives. Jom. 2015 May;67(5):1183-93. https://doi.org/10.1007/s11837-015-1367-y

[82] Tosto C, Tirillò J, Sarasini F, Sergi C, Cicala G. Fused deposition modeling parameter optimization for cost-effective metal part printing. Polymers. 2022 Aug 10;14(16):3264. https://doi.org/10.3390/polym14163264

[83] Tyagi K, Tyagi K. A comparative analysis of optimization techniques. Int. J. Comput. Appl. 2015 Dec;131(10):6-12.

[84] Vishwas M, Basavaraj CK, Vinyas M. Experimental investigation using taguchi method to optimize process parameters of fused deposition Modeling for ABS and nylon materials. Materials Today: Proceedings. 2018 Jan 1;5(2):7106-14. https://doi.org/10.1016/j.matpr.2017.11.375.

[85] Wach RA, Wolszczak P, Adamus-Wlodarczyk A. Enhancement of mechanical properties of FDM-PLA parts via thermal annealing. Macromolecular Materials and Engineering. 2018 Sep;303(9):1800169. https://doi.org/10.1002/mame.201800169

[86] Wang TM, Xi JT, Jin Y. A model research for prototype warp deformation in the FDM process. The International Journal of Advanced Manufacturing Technology. 2007 Aug;33(11):1087-96.https://doi.org/10.1007/s00170-006-0556-9

[87] Wankhede V, Jagetiya D, Joshi A, Chaudhari R. Experimental investigation of FDM process parameters using Taguchi analysis. Materials Today: Proceedings. 2020 Jan 1;27:2117-20. https://doi.org/10.1016/j.matpr.2019.09.078

[88] Yadav D, Chhabra D, Garg RK, Ahlawat A, Phogat A. Optimization of FDM 3D printing process parameters for multi-material using artificial neural network. Materials Today: Proceedings. 2020 Jan 1;21:1583-91. https://doi.org/10.1016/j.matpr.2019.11.225

[89] Zeng Z, Sammut K, Lian L, He F, Lammas A, Tang Y. A comparison of optimization techniques for AUV path planning in environments with ocean currents. Robotics and Autonomous Systems. 2016 Aug 1;82:61-72. https://doi.org/10.1016/j.robot.2016.03.011

[90] Byun HS, Lee* KH. Determination of the optimal part orientation in layered manufacturing using a genetic algorithm. International journal of production research. 2005 Jul 1;43(13):2709-24. https://doi.org/10.1080/00207540500031857

[91] Ahn SH, Montero M, Odell D, Roundy S, Wright PK. Anisotropic material properties of fused deposition modeling ABS. Rapid prototyping journal. 2002 Oct 1. https://doi.org/10.1108/13552540210441166

[92] Kumar MA, Khan MS, Mishra SB. Effect of fused deposition machine parameters on tensile strength of printed carbon fiber reinforced PLA thermoplastics. Materials Today: Proceedings. 2020 Jan 1;27:1505-10. https://doi.org/10.1016/j.matpr.2020.03.033

[93] Weinmann J, Ip H, Prigozhin D, Escobar E, Mendelson M, Noorani R. Application of design of experiments (DOE) on the processing of rapid prototyped samples. In2003 International Solid Freeform Fabrication Symposium 2003.http://dx.doi.org/10.26153/tsw/5569

[94] Raut S, Jatti VS, Khedkar NK, Singh TP. Investigation of the effect of built orientation on mechanical properties and total cost of FDM parts. Procedia materials science. 2014 Jan 1;6:1625-30. https://doi.org/10.1016/j.mspro.2014.07.146

[95] Muhamedagic K, Berus L, Potočnik D, Cekic A, Begic-Hajdarevic D, Cohodar Husic M, Ficko M. Effect of Process Parameters on Tensile Strength of FDM Printed Carbon Fiber Reinforced Polyamide Parts. Applied Sciences. 2022 Jun 14;12(12):6028. https://doi.org/10.3390/app12126028

Research Article

Energy and exergy analysis of a solar energy-based power generation system

Ali Koç[1,a], Ayşenur Özdemir[1,b], Özkan Köse[1,c], Yıldız Koç[1,d,*] Hüseyin Yağli[2,e]

[1] Department of Mechanical Engineering, Iskenderun Technical University, Hatay, Turkey
[2] Department of Mechanical Engineering, Gaziantep University, Gaziantep, Turkey

Article Info	Abstract
	Nowadays, energy is obtained from both fossil fuels and renewable energy sources. The use of fossil fuels causes climate change and global warming. The use of renewable energy systems ensures the reduction of greenhouse gas emissions and, as a result, the reduction of global warming. In this study, a solar-based electricity generation facility, which is one of the renewable energy sources, is discussed. The power generation potential of the solar system with integrated Rankine cycle under the changing climatic conditions of Iskenderun, which is a region with high solar energy potential, is investigated by thermodynamic analysis. A solar power tower was selected as the solar energy system in the facility. In the facility, electrical energy is obtained by sending the heat energy obtained from the solar power tower to the steam Rankine cycle. Energy and exergy analysis were performed to find the performance of the facility and the main sources of exergy destruction. As a result of the thermodynamic analysis, the net power obtained from the system increased with the increase of the input heat. During the day, 495.3 MWh/day of heat entered the system and 202.3 MWh/day of net power was obtained from this heat. The highest exergy destruction in the system occurred at 12:00. The highest exergy destruction occurred in the receiver at this hour and was calculated as 13.83 MW. The daily average energy and exergy efficiencies of the system were found to be 40.8% and 66.08%, respectively.

1. Introduction

The energy and environmental overlook of the world have become much worse day by day. Besides, the increase in technological developments along with the population significantly is increased the energy demand. To meet this demand, it is clearly seen in global data that coal, natural gas and oil are the most used fuels [1]. However, in addition to the limited use of fossil fuels, the negative effects of the pandemic period and political conflicts between countries as well as the limited fossil fuels is obstructed access to fossil fuels. This situation has revealed the necessity of using renewable energy sources more [2]. At the same time, fossil fuel usage has caused global climate change and increased health risks. Using renewable energy sources instead of fossil fuels is making it a necessity [3]. Solar energy has a huge energy source [4]. Solar energy is one of the most important renewable energy sources, an alternative to fossil fuels. Solar energy is an environmentally friendly, safe, practical, renewable energy source [5-6]. The use of renewable energy concerns sectors of activity such as industry, buildings, transportation and agriculture [7]. Recently, the efficiency of solar energy technologies has increased significantly and is more easily accessible. Despite the high installation costs of solar energy technologies, low operating cost makes them attractive. In addition, while fluctuations in the prices of fossil

fuels are observed, solar energy is relatively stable for long periods [8]. For this reason, today, solar energy-based technologies are developed to meet the increasing energy demand [9]. Exergy analysis is an important method in the thermodynamic analysis of power systems. Exergy analysis is widely used, especially in revealing the quality of a system design and examining the improvement potential of the equipment used. When compared with the first law analysis, losses in the system could be determined both quantitatively and qualitatively with the exergy analysis [5].

Ahmadi and Toghraie[10] studied the steam cycle of a power plant in Iran. The system performance was examined by carrying out energy and exergy analysis of the cycle and its equipment. As a result of the analysis, it was found that the highest exergy destruction is performed in Boiler. Altarawneh et al. [11] performed the energy and exergy analysis of the hybrid fuel thermal power plant in Jordan. As a result of the analysis, it was found that the boiler caused the highest exergy destruction in the plant. In order to improve the performance of the plant, it has been suggested to increase the performance of the boiler. Although solar energy systems are used in many areas, the remarkable results obtained from solar tower power plants bring this field into the forefront. The steam Rankine cycle is the most widely used in concentrated solar energy from solar-based technologies. In low and medium-temperature applications, the organic Rankine cycle (ORC) is a promising alternative to the steam Rankine cycle. While water is used in the Steam Rankine cycle, organic fluid is used in the ORC. The choice of working fluid for ORC depends on the temperature of the heat source, ranging from 70°C to 400°C [12]. However, since turbine inlet temperature is high in the present study, the steam Rankine cycle is preferred. Some studies are focusing on solar tower power plants. Xu et al. [5] evaluated the performance of the solar tower power plant by performing energy and exergy analysis. They found that the central receiver and power cycle have the highest energy and exergy efficiency, respectively. Yagli et al. [13] performed parametric optimization of a solar power tower plant for the Iskenderun region. They found that the highest net power generation was at 1000°C at tower outlet temperatures varying between 500°C and 1000°C. The energy and exergy efficiencies of the plant were calculated as 45.81% and 47.19%, respectively. Zolfagharnasab et al. [14] investigated a solar tower with the Rankine cycle from a thermodynamic point of view. It was determined that the exergy efficiency of the receiver decreased from 57% to 52% with the increase in ambient temperature. It has been found that the increase in wind speed decreases energy and exergy efficiency. In addition, they found the optimum values of molten salt outlet temperature and velocity as 650 K and 2 m/s, respectively. Salilih et al. [15] analyzed a small-scale industrial waste heat-assisted solar tower power plant in their study. They claimed that using nanofluids instead of water as the cooling fluid in the condenser increases the solar system's efficiency. Different power cycles utilizing solar energy have also been used. Siddiqui and Almitani [16] performed the energy and exergy analysis of a solar tower system using the supercritical carbon dioxide cycle as the power cycle. The system was operated between 8 am and 4 pm. For a turbine inlet temperature of 600°C, a net power of 80 MW was obtained. It was also found that the highest exergy destruction was in the heliostat. Atif and Al-Sulaiman [17] performed the energy and exergy analysis of the solar tower-based supercritical carbon dioxide cycle. In the constant turbine inlet temperature, they obtained net power of 40 MW. In the plant, it was observed that the heliostat caused the highest exergy destruction. Moreover, today, Hybrid systems are being developed to meet energy demand via solar energy. Nafchi et al. [18] discussed a system including a solar tower and a hydrogen-fueled gas turbine. In the proposed system, the solar tower is caused the highest exergy destruction and cost. Boukelia et al. [19] proposed a new combined solar-assisted geothermal power plant and examined its thermodynamic performance. This power plant was compared with the conventional solar power plant and it was concluded that the proposed plant increased the thermodynamic performance by more than 30%. The solar

tower was not only used for power generation. Li et al. [20] proposed a new combined heat and power system integrating a solar tower system with thermal energy storage and an absorption heat pump. With this system, 6214 kWh electrical energy and 14502 MJ thermal energy were produced. In the proposed system, the utilization efficiency of solar energy was obtained as 15.96%. In a study performed by Acar and Dincer [21], they examined the multiple production systems that could produce electricity, heat, air-conditioning, cooling and hot water. While the highest exergy efficiency of the system was found as 28%, the maximum electricity production was calculated as 550 kW. Colakoglu and Durmayaz [22] evaluated the energy and exergy analysis of a triple combined cycle including the solar tower. The energy and exergy efficiency of the proposed system were found to be 51.99% and 37.99%, respectively.

As seen above, although there are many studies on the solar tower, there are very few studies performed by depending on the thermodynamic analysis of the solar tower considering hourly wind speed, ambient temperature and solar energy per unit area. In addition, a few studies on solar tower design using the EBSILON®Professional simulation program in system design is executed.

This study is aimed to generate power by using the useful heat obtained from the solar tower, where the renewable energy source is used along with the steam Rankine cycle in the environmental conditions of the Iskenderun region of Hatay province. Firstly the wind speed, ambient temperature and DNI values that change throughout a day in June in Iskenderun for the installation of a solar power tower are determinated. Secondly the heat amount obtained from solar tower and efficiency of receiver is evaluated. Then According to the first and second laws of thermodynamics, the energy and exergy analysis of the proposed system is performed and the hourly thermodynamic performance of the system is performed for a day.

2. Material and Method

Today, the decrease in fossil-based resources and the deterioration in supply chains show how necessary the use of renewable energy is. These environmentally friendly sustainable systems are very important to choose the most suitable system according to the meteorological indicators of the area used. The fact that Iskenderun is one of the places with the highest solar radiation values brings the use of solar energy systems to the fore. In this study, a system that is powered by solar energy has been designed for the Iskenderun region, which is a region rich in terms of solar energy. The system consists of a solar power tower and a steam Rankine cycle. The schematic representation of the power system is given in Figure 1.

The radiation coming from the solar by means of the mirrors called heliostat is reflected to the receiver located on the top of the solar tower and then energy absorbed by the receiver is transferred to the working fluid in steam Rankine cycle. The working fluid, water, exits from the tower as superheated steam at 80 bar pressure and 950 °C, and the superheated steam is transmitted to the turbine. Here, the steam expands, and then mechanical power is generated. Meanwhile, the temperature of the fluid drops, and its pressure drops to 0.10 bar. The fluid pressure is increased to 80 bar again by using the pump and the working fluid is transferred to the tower. So the cycle is completed. (1→4).

The wind speed, ambient temperature and DNI values that change throughout a day in June in Iskenderun, which was chosen for the installation of a solar power tower, are given in Table 1. Wind speed varies between 2.14-5.39 m/s during the day. The ambient temperature increases towards noon and decreases towards evening. It reaches the highest ambient temperature of 30.79°C 12 pm. The DNI value shows a similar change to

the ambient temperature. The DNI value, which is low in the morning hours, rises to 815.71 W/m2 at noon. Then, the DNI value decreases to 33.37 W/m2 until 18 pm.
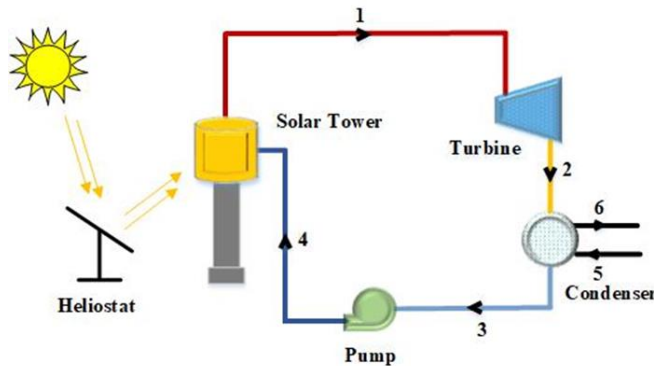

Fig. 1 Schematic representation of solar tower-assisted power generation system

Table 1. Changing wind speed, ambient temperature and DNI values of the Iskenderun region throughout the day [23]

Hours	Wind speed (m/s)	Ambient temperature (°C)	DNI (W/m^2)
06:00	2.14	23.02	14.93
07:00	2.35	25.27	105.88
08:00	2.65	27.22	281.59
09:00	3.11	28.75	468.72
10:00	3.60	29.89	646.86
11:00	4.12	30.56	747.28
12:00	4.61	30.79	815.71
13:00	5.00	30.66	801.62
14:00	5.27	30.18	709.79
15:00	5.39	29.32	548.23
16:00	5.29	28.07	361.73
17:00	4.82	26.49	171.29
18:00	3.53	24.28	33.37

Thermodynamic analysis of the proposed solar energy-assisted power generation system is made. As a result of the analysis, the energy and exergy efficiencies of the system and the irreversibilities in the system are determined. The design parameters of the proposed system are given in Table 1.

While performing the thermodynamic analysis of the system, it is assumed that the system operates in a steady state, its kinetic and potential energies are neglected, and the turbines and pumps are adiabatic. In line with these assumptions, the mass, energy and exergy balances of the proposed system are respectively written as in Eq. (1), Eq. (2) and Eq. (3) [24,25].

Table 1. The design parameters of the proposed system

Parameter	Value
Ambient pressure, P_0	101.325 kPa
Working fluid	Water
Heliostat field, A_h	150000 m²
Turbine inlet temperature	950 °C
Turbine inlet pressure	80 bar
Condenser pressure	0.10 bar
Coolant inlet temperature	10 °C
Coolant outlet temperature	31.81 °C

$$\sum \dot{m}_i = \sum \dot{m}_e \tag{1}$$

$$\sum \dot{Q}_i + \sum \dot{W}_i + \sum \dot{m}_i h_i = \sum \dot{Q}_e + \sum \dot{W}_e + \sum \dot{m}_e h_e \tag{2}$$

$$\sum \dot{Ex}_i^Q + \sum \dot{Ex}_i^W + \sum \dot{m}_i \psi_i = \sum \dot{Ex}_e^Q + \sum \dot{Ex}_e^W + \sum \dot{m}_e \psi_e + \dot{Ex}_{dest} \tag{3}$$

ψ, $\dot{Ex}^Q$ and $\dot{Ex}^W$ denote specific exergy, the exergy of heat, and work, respectively. The specific exergy, the exergy of heat and work are calculated with the formulas given in Eq. (4), Eq (5) and Eq. (6) [24]. The energy and exergy balance relations of each component of the system given in Figure 1 are given in Table 2.

$$\psi = (h - h_0) - T_0(s - s_0) \tag{4}$$

$$\dot{Ex}^Q = \left(1 - \frac{T_0}{T}\right)\dot{Q} \tag{5}$$

$$\dot{Ex}^W = W \tag{6}$$

Table 2. Energy and exergy balance relationships of each component in the proposed system [24-26]

Component	Energy and Exergy Balance Relationship
Solar tower	$\dot{m}_1 h_1 = \dot{Q}_{tower} + \dot{m}_4 h_4$ $\dot{m}_4 \psi_4 + \dot{Ex}_{tower}^Q = \dot{m}_1 \psi_1 + \dot{Ex}_{dest}$
Turbine	$\dot{m}_1 h_1 = \dot{m}_2 h_2 + \dot{W}_t$ $\dot{m}_1 \psi_1 = \dot{m}_2 \psi_2 + \dot{W}_t + \dot{Ex}_{dest}$
Condenser	$\dot{m}_2 h_2 + \dot{m}_5 h_5 = \dot{m}_3 h_3 + \dot{m}_6 h_6$ $\dot{m}_2 \psi_2 + \dot{m}_5 \psi_5 = \dot{m}_3 \psi_3 + \dot{m}_6 \psi_6 + \dot{Ex}_{dest}$
Pump	$\dot{m}_3 h_3 + \dot{W}_p = \dot{m}_4 h_4$ $\dot{m}_3 \psi_3 + \dot{W}_p = \dot{m}_4 \psi_4 + \dot{Ex}_{dest}$

The energy efficiency of the solar receiver and the exergy efficiency of the solar tower are given in Eq. (7) and Eq. (8), respectively.

$$\eta_{I,rec} = \frac{\dot{Q}_{rec,i} - \dot{Q}_{rec,loss}}{\dot{Q}_{rec,i}} \tag{7}$$

$$\eta_{II,rec} = \frac{\dot{m}_1 \psi_1 - \dot{m}_4 \psi_4}{\dot{Ex}_{tower}^Q} \tag{8}$$

$\dot{Ex}_{tower}^Q$ is found by Eq. (9).

$$\dot{E}x_{tower}^{Q} = \left(1 - \frac{T_0}{T_{surface}}\right) \dot{Q}_{rec,i} \tag{9}$$

Here, $T_{surface}$ is the average temperature of the fluid entering and leaving the receiver. $\dot{W}_{net}$ refers to the net power produced by the solar power tower and it is calculated with the formula given in Eq. (10). The energy and exergy efficiencies of the proposed solar power tower are obtained using Eq. (11) and Eq. (12).

$$\dot{W}_{net} = \dot{W}_t - \dot{W}_p \tag{10}$$

$$\eta_I = \frac{\dot{W}_{net}}{\dot{m}_1 h_1 - \dot{m}_4 h_4} \tag{11}$$

$$\eta_{II} = \frac{\dot{W}_{net}}{\dot{m}_1 \psi_1 - \dot{m}_4 \psi_4} \tag{12}$$

3. Results and Discussions

When the climatic conditions of Iskenderun are examined, it is seen that Iskenderun is a suitable region for solar energy and electricity generation systems. In the study, a solar power tower system is proposed for the Iskenderun region and a thermodynamic analysis is made. The power plant works with solar energy during daylight hours. By entering parameters of the wind, DNI and the ambient temperature into the EBSILON®Professional simulation program, the heat entering the receiver, the heat output and the receiver losses are calculated. Also, the flow rate of the working fluid was changed throughout the day and thus the outlet temperature of the receiver was kept constant at 950 °C. In this way, the heat obtained from the system was also increased. Firstly, the analysis of the solar tower is carried out. The heat coming to the receiver from the solar and receiver losses, which change throughout the day, have been determined and their changes are shown in Figure 2.
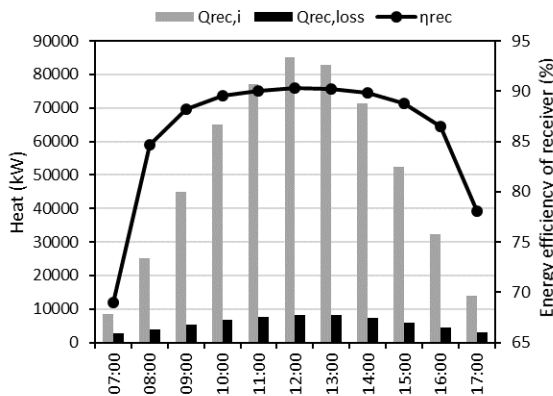
Fig. 2 The change of heat entering the receiver, receiver loss and efficiency during the day

The lowest heat coming to the receiver and minimum heat loss resulting from receiver is performed at 07:00 in the morning. The highest heat from the solar reaches the receiver at 12 pm as 85.04 MW. The heat loss in the receiver is 8.26 MW. The energy efficiency of the tower is found from the values of heat entering the receiver and receiver losses. The highest and lowest energy efficiency of the receiver is found as 90.29% and 69.02%,

respectively. It is observed that the energy efficiency of the receiver increased when the DNI is high. The change in exergy efficiency of the tower during the day is shown Figure 3.
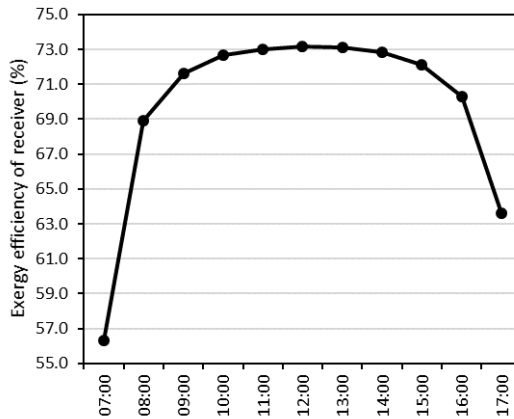

Fig. 3 The change in exergy efficiency of the receiver during the day

As seen in Figure 3, it is observed that the exergy efficiency of the receiver decreases during the low hours of the DNI value and increases during the high hours. When the DNI is 105.88 W/m², the exergy efficiency is 55.60% at 07:00. The DNI value increases to 815.71 W/m² at 12 pm. The exergy efficiency of the tower increases to 72.13% with this increase. Exergy efficiency decreases towards evening hours again. It is found that the exergy efficiency of the receiver varies inversely with the energy efficiency. The variation of the mass flow rate of the working fluid in the solar power tower system between 06:00 and 18:00 is given in Figure 4.
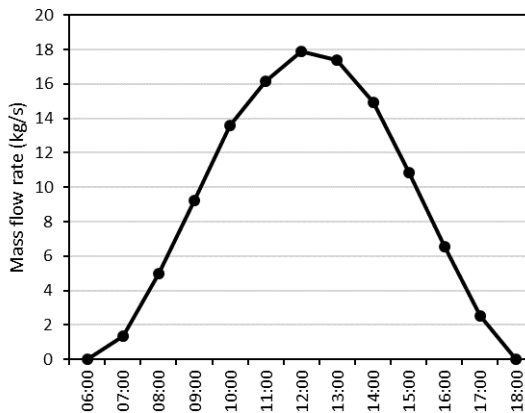
Fig. 4 The change of the mass flow rate of the working fluid during the day

While the mass flow rate of the water increases towards the noon hours, it decreases towards the evening hours. The mass flow rate is highest at 12 pm and is founded as 17.89 kg/s. The variation of the heat value entering the steam Rankine cycle from the tower during the day and the DNI are given in Figure 5.

667
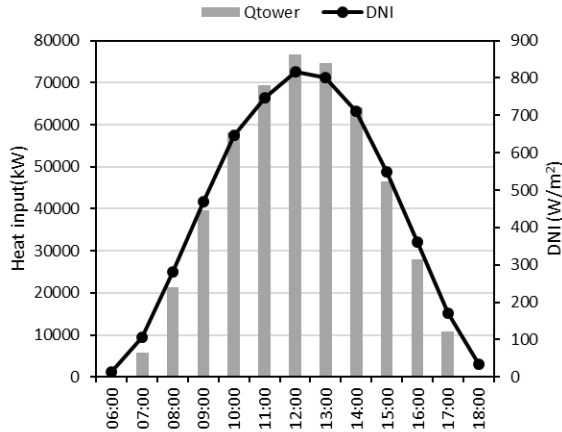
Fig. 5 The changing in the values of heat entering the solar power tower and DNI during the day

While the DNI values are 105.88 W/m^2 and 171.29 W/m^2, the heat inputs are found to be 5893 kW and 10778 kW, respectively. It is calculated as 76778 kW for the highest DNI value. While the DNI value is 801.62 W/m^2 at 13:00, 74636 kW of heat entered the tower. The heat input increases proportionally with the DNI value. The power generated from the turbine with the heat entering during the day and the net power are given in Figure 6.
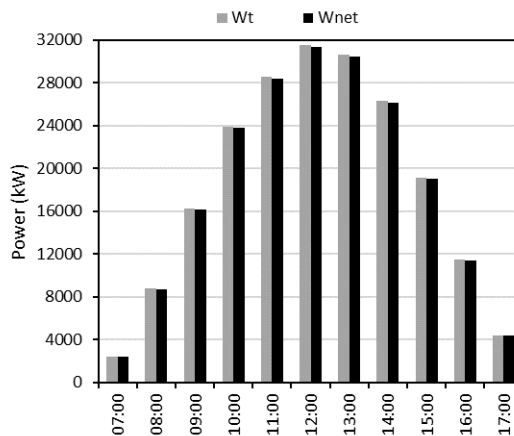
Fig. 6 The change of the power generated in the turbine and the net power in the solar power tower system during the day

Power production of 28539.8 kW, 31552.5 kW and 30672.3 kW were obtained from the turbine at 11:00, 12:00 and 13:00, respectively. The net power produced is 28366.2 kW, 31360.6 kW and 30485.8 kW, respectively. The lowest net power in the system is calculated as 2406.3 kW in the DNI value of 105.88 W/m^2. Total heat of 495.3 MWh/day enters the tower throughout the day. A power of 202.3 MWh/day was produced with this heat input. The change of exergy destruction occurring in the system and the component of the system during the day is given in Figure 7.
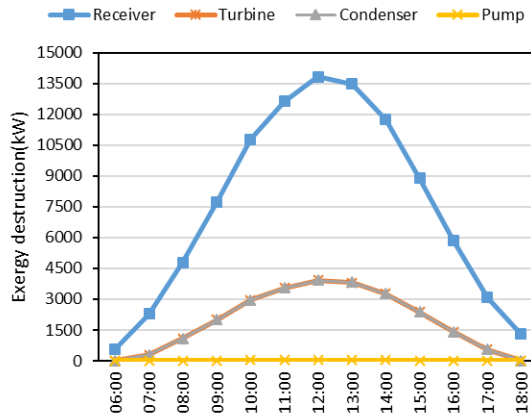
Fig. 7 The variation of exergy destruction in the overall system and its components during the day

The exergy destruction of all components increases during the hours when the value of DNI and ambient temperature are high. The exergy destruction of the tower, turbine, condenser and pump at 12 pm is calculated as 13.83 MW, 3.93 MW, 3.93 MW and 36.81 kW, respectively. The highest exergy destruction occurred in the tower. The values of exergy destruction occurring in the turbine and condenser during the day are close. The lowest exergy destruction occurred in the pump. A similar change to the ambient temperature occurred in the component. The changing in the energy and exergy efficiency of the solar power tower system throughout the day is given in Figure 8.
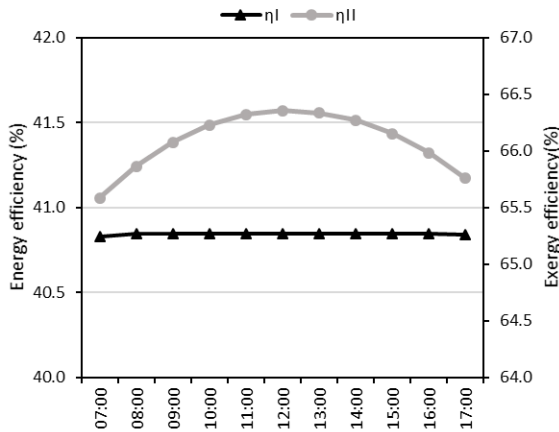
Fig. 8 The changing in the energy and exergy efficiency of the solar power tower system throughout the day

As can be seen in Figure 8, the average daily energy efficiency of the solar power tower system is around 40.8%. There is no significant change in the energy efficiency of the system during the day. The exergy efficiency varies between 65.6% and 66.35%. The ambient temperature changing during the day causes a change in the exergy efficiency. The high ambient temperature increases the exergy efficiency. Therefore, the highest exergy efficiency is reached at 12 pm. The average exergy efficiency of the system is obtained as 66.08%. Dunham et al. analyzed steam Rankine cycle that operates at the 20 MPa and 1100

ºC. Correspondingly, they appeared that efficiency of system is about 45% [27]. Besides, Zhang et al evaluated the steam Rankine cycle that has 38 MPa and 700 ºC. They asserted that efficiency of the proposed system is calculated as about 51% [28]. Xu et al. [5] investigated the effect of DNI on energy efficiency. They stated that if the DNI value increases from 100 W/m² to 1000 W/m², the efficiency of the solar receiver also increases from about 45% to 90%. They found that the solar system has the highest exergy destruction. 550 °C of turbine inlet temperature, the efficiency of the power cycle was calculated as 37.5%. Similar results with the literature were obtained. In the studies in the literature, solar power tower systems were made for a certain DNI value. There are not many studies examining the effect of climatic conditions on the performance of that region for a particular region. The proposed system does not harm the environment and it has been found to be good in terms of performance when installed in a region rich in solar energy such as İskenderun. The thermodynamic properties of the fluid at each state in the system are given in Table 3.

Table 3. The state points of the solar power tower system

State	Pressure (bar)	Temperature (°C)	Enthalpy (kJ/kg)	Density (kg/m³)	Volume flow rate (m³/s)	Entropy (kJ/kgK)	Exergy (kJ/kg)
1	80.00	950.00	4,493.77	14.27	1.25	7.8410	2,117.53
2	0.10	120.56	2,726.65	0.06	324.74	8.5511	134.58
3	0.10	45.81	191.81	989.84	0.02	0.6492	1.41
4	85.00	46.60	202.51	993.17	0.02	0.6559	10.08
5	2.00	10.00	42.21	999.75	0.50	0.1511	3.22
6	1.95	31.81	133.47	995.13	0.50	0.4616	0.10

4. Conclusions

The use of solar energy, one of the renewable energy sources, is increasing day by day to meet the energy demand increases. In the study, it is integrated with the current steam Rankine cycle and the maximum potential energy production of the proposed system for the region where the solar energy potential is high was evaluated. Iskenderun of Turkey, which has a high solar energy potential is selected as region and the solar power tower system was investigated by performing energy and exergy analysis. Values such as wind speed, ambient temperature and DNI change during the day. In the case of the installation of this Integrated system in the Iskenderun region, the losses occurring in the receiver, the effect of these changing values on the receiver efficiency and system performance have been examined. As a result of the analysis, the following findings are obtained:

- The heat entering the receiver and the receiver losses are shown similar changes with the DNI value. High heat input and receiver efficiency are obtained during the hours when the DNI value was high. The highest receiver efficiency is found to be 90.29%.
- The exergy efficiency of the receiver in the system increases with the increase of the value of DNI. The heat entering the steam Rankine cycle from the solar tower increases with the increase of this value. The heat input is found to be 76,778 kW for the highest DNI value of 815.71 W/m². The high heat input increased the net power produced in the steam Rankine cycle. The solar tower received 495.3 MW of heat throughout the day and generated 202.3 MW of net power.
- The highest exergy destruction in the system was caused by the solar tower. The highest exergy destruction of the solar tower, turbine, condenser and pump

occurred at 12 pm and it is calculated that it was 13.83 MW, 3.93 MW, 3.93 MW and 36.81 kW, respectively.

- The average daily energy and exergy efficiencies of the solar power tower system are around 40.8% and 66.08%, respectively. It is concluded that the exergy efficiency varies similarly with the ambient temperature during the day.

In addition, the installation of a renewable energy integrated power system in the current study will reduce both greenhouse gas emissions and external dependence on energy. In addition to these, the economic dimension of the implementation of the system should also be investigated.

Symbols

h	Specific enthalpy [kJ/kg]
s	Entropy [kJ/kgK]
P	Pressure [kPa]
T	Temperature [K]
$\dot{m}$	Mass flow rate [kg/s]
$\dot{Q}$	Heat flow rate [kW]
$\dot{W}$	Power [kW]
η	Efficiency [%]
ψ	Specific exergy [kJ/kg]
DNI	Direct normal irradiance [W/m^2]

Subscripts

I	energy
II	exergy
e	exit
i	inlet
$dest$	destruction
p	pump
rec	receiver
t	turbine
0	ambient temperature

Acknowledgment

References

[1] Ibrahim TK, Mohammed MK, Awad OI, Abdalla AN, Basrawi F, Mohammed MN, A comprehensive review on the exergy analysis of combined cycle power plants. Renew Sustain Energy Rev. 2018;90(April):835-50. https://doi.org/10.1016/j.rser.2018.03.072

[2] Okoroigwe E, Madhlopa A. An integrated combined cycle system driven by a solar tower: A review. Renew Sustain Energy Rev [Internet]. 2016;57:337-50. https://doi.org/10.1016/j.rser.2015.12.092

[3] Panwar NL, Kaushik SC, Kothari S. Role of renewable energy sources in environmental protection: A review. Renew Sustain Energy Rev [Internet]. 2011;15(3):1513-24. https://doi.org/10.1016/j.rser.2010.11.037

[4] Harsito C, Triyono T, Rovianto E. Analysis of Heat Potential in Solar Panels for Thermoelectric Generators using ANSYS Software. Civ Eng J. 2022;8(7):1328-38. https://doi.org/10.28991/CEJ-2022-08-07-02

[5] Xu C, Wang Z, Li X, Sun F. Energy and exergy analysis of solar power tower plants. Appl Therm Eng [Internet]. 2011;31(17-18):3904-13. https://doi.org/10.1016/j.applthermaleng.2011.07.038

[6] Kannan N, Vakeesan D. Solar energy for future world: - A review. Renew Sustain Energy Rev. 2016;62:1092-105. https://doi.org/10.1016/j.rser.2016.05.022

[7] Laabid A, Saad A, Mazouz M. Integration of Renewable Energies in Mobile Employment Promotion Units for Rural Populations. Civ Eng J. 2022;8(7):1406-34. https://doi.org/10.28991/CEJ-2022-08-07-07

[8] Kabir E, Kumar P, Kumar S, Adelodun AA, Kim KH. Solar energy: Potential and future prospects. Renew Sustain Energy Rev. 2018;82(September 2016):894-900. https://doi.org/10.1016/j.rser.2017.09.094

[9] Modi A, Bühler F, Andreasen JG, Haglind F. A review of solar energy based heat and power generation systems. Renew Sustain Energy Rev [Internet]. 2017;67:1047-64. https://doi.org/10.1016/j.rser.2016.09.075

[10] Ahmadi GR, Toghraie D. Energy and exergy analysis of Montazeri Steam Power Plant in Iran. Renew Sustain Energy Rev. 2016;56:454-63. https://doi.org/10.1016/j.rser.2015.11.074

[11] Altarawneh OR, Alsarayreh AA, Al-Falahat AM, Al-Kheetan MJ, Alrwashdeh SS. Energy and exergy analyses for a combined cycle power plant in Jordan. Case Stud Therm Eng [Internet]. 2022;31:101852. https://doi.org/10.1016/j.csite.2022.101852

[12] Desai NB, Bandyopadhyay S. Thermo-economic comparisons between solar steam Rankine and organic Rankine cycles. Appl Therm Eng [Internet]. 2016;105:862-75. https://doi.org/10.1016/j.applthermaleng.2016.04.055

[13] Yağlı H, Karakuş C, Koç Y, Çevik M, Uğurlu İ, Koç A. Designing and exergetic analysis of a solar power tower system for Iskenderun region. Int J Exergy. 2019;28(1):96-112. https://doi.org/10.1504/IJEX.2019.097273

[14] Zolfagharnasab MH, Aghanajafi C, Kavian S, Heydarian N, Ahmadi MH. Novel analysis of second law and irreversibility for a solar power plant using heliostat field and molten salt. Energy Sci Eng. 2020;8(11):4136-53. https://doi.org/10.1002/ese3.802

[15] Salilih EM, Abu-Hamdeh NH, Alsulami RA, Rawa MJH, Aljinaidi AA, Alazwari MA, et al. Annual performance analysis of small scale industrial waste heat assisted solar tower power plant and application of nanofluid. J Taiwan Inst Chem Eng [Internet]. 2021;124:216-27. https://doi.org/10.1016/j.jtice.2021.04.019

[16] Siddiqui ME, Almitani KH. Energy and exergy assessment of S-CO2 Brayton cycle coupled with a solar tower system. Processes. 2020;8(10). https://doi.org/10.3390/pr8101264

[17] Atif M, Al-Sulaiman FA. Energy and exergy analyses of solar tower power plant driven supercritical carbon dioxide recompression cycles for six different locations. Renew Sustain Energy Rev [Internet]. 2017;68:153-67. https://doi.org/10.1016/j.rser.2016.09.122

[18] Nafchi FM, Baniasadi E, Afshari E, Javani N. Performance assessment of a direct steam solar power plant with hydrogen energy storage: An exergoeconomic study. Int J Hydrogen Energy [Internet]. 2022;47(62):26023-37. https://doi.org/10.1016/j.ijhydene.2022.01.250

[19] Boukelia TE, Arslan O, Bouraoui A. Thermodynamic performance assessment of a new solar tower-geothermal combined power plant compared to the conventional solar tower power plant. Energy [Internet]. 2021;232:121109. https://doi.org/10.1016/j.energy.2021.121109

[20] Li X, Wang Z, Yang M, Yuan G. Modeling and simulation of a novel combined heat and power system with absorption heat pump based on solar thermal power tower plant. Energy [Internet]. 2019;186:115842. https://doi.org/10.1016/j.energy.2019.07.172

[21] Acar C, Dincer I. Exergetic performance assessment of an integrated solar energy system. Int J Exergy. 2016;19(2):161-72. https://doi.org/10.1504/IJEX.2016.075603

[22] Colakoglu M, Durmayaz A. Energy, exergy, economic and emission saving analysis and multiobjective optimization of a new multi-generation system based on a solar tower with triple combined power cycle. Sustain Energy Technol Assessments [Internet]. 2022;52:102289. https://doi.org/10.1016/j.seta.2022.10228 9

[23] TSMS. Turkish State Meteorological Service. 2016.

[24] Çengel YA, Boles. MA. Termodinamik Mühendisik Yaklaşımıyla. 2008.

[25] Köse Ö, Koç Y, Yağlı H. Energy, exergy, economy and environmental (4E) analysis and optimization of single, dual and triple configurations of the power systems: Rankine Cycle/Kalina Cycle, driven by a gas turbine. Energy Convers Manag. 2021;227:113604. https://doi.org/10.1016/j.enconman.2020.113604

[26] Yağli H. Examining the receiver heat loss, parametric optimization and exergy analysis of a solar power tower (SPT) system. Energy Sources, Part A Recover Util Environ Eff. 2020;42(17):2155-80. https://doi.org/10.1080/15567036.2020.1748765

[27] Dunham, MT, Iverson BD. High-efficiency thermodynamic power cycles for concentrated solar power systems. Renewable and Sustainable Energy Reviews. 2014:30, 758-770. https://doi.org/10.1016/j.rser.2013.11.010

[28] Zhang,Z, Zhou R., Ge ., Zhang J, & Wu, X. Perspectives for 700° C ultra-supercritical power generation: Thermal safety of high-temperature heating surfaces. Energy.2020:190, 116411. https://doi.org/10.1016/j.energy.2019.116411

Research on

Engineering

Structures

Materials

Content

Research Group